

AD-A277 517



INTERNATIONAL
REVIEW OF
RARE EARTH
SCIENCE
AND TECHNOLOGY
VOLUME 301

Rare Earth Doped Semiconductors

EDITORS

Gernot S. Pomrenke

Paul B. Klein

Dietrich W. Langer

DTIC
ELECTE
MAR 28 1994
S E D

Approved for public release
Distribution unlimited

94 3 25 026

Approved for public release;
distribution unlimited.

94-09375



94 3 22 048

Rare Earth Doped Semiconductors

Rare Earth Doped Semiconductors

Symposium held April 13-15, 1993, San Francisco, California, U.S.A.

EDITORS:

Gernot S. Pomrenke

Air Force Office of Scientific Research
Bolling AFB, Washington, DC, U.S.A.

Paul B. Klein

Naval Research Laboratory
Washington, DC, U.S.A.

Dietrich W. Langer

University of Pittsburgh
Pittsburgh, Pennsylvania, U.S.A.

Accession For	
NTIS CRA&I	<input checked="" type="checkbox"/>
DTIC TAB	<input checked="" type="checkbox"/>
Unannounced	<input type="checkbox"/>
Justification	
By	
Distribution /	
Availability Codes	
Dist	Avail and/or Special
A-1	

MRS

MATERIALS RESEARCH SOCIETY
Pittsburgh, Pennsylvania

This work was supported largely by the Air Force Office of Scientific Research under Grant Number AFOSR-F49620-9310156DEF.

Single article reprints from this publication are available through University Microfilms Inc., 300 North Zeeb Road, Ann Arbor, Michigan 48106

CODEN: MRSPDH

Copyright 1993 by Materials Research Society.
All rights reserved.

This book has been registered with Copyright Clearance Center, Inc. For further information, please contact the Copyright Clearance Center, Salem, Massachusetts.

Published by:

Materials Research Society
9800 McKnight Road
Pittsburgh, Pennsylvania 15237
Telephone (412) 367-3003
Fax (412) 367-4373

Library of Congress Cataloging in Publication Data

Rare earth doped semiconductors: symposium held April 13-15, 1993, San Francisco, California, U.S.A. / editors Gernot S. Pomrenke, Paul B. Klein, Dietrich W. Langer.

p. cm. -- (Materials Research Society symposium proceedings; v. 301)

Includes bibliographical references and index.

ISBN 1-55899-197-2

I. Semiconductors--Congresses. 2. Rare earth metals--Surfaces--Congresses. I. Pomrenke, Gernot S. II. Klein, Paul B. III. Langer, Dietrich W. IV. Series: Materials Research Society symposium proceedings; v. 301.

QC611.8.R37R37 1993
621.3815'2--dc20

93-28259
CIP

Manufactured in the United States of America

Contents

PREFACE	xi
ACKNOWLEDGMENTS	xv
MATERIALS RESEARCH SOCIETY SYMPOSIUM PROCEEDINGS	xvi
PART I: RARE EARTH INCORPORATION	
*MOVPE OF RARE EARTH DOPED III-V SEMICONDUCTORS F. Scholz, J. Weber, K. Pressel, and A. Dörnen	3
MOCVD GROWTH AND PROPERTIES OF ERBIUM-DOPED GaAs Dietrich W. Langer, Yabo Li, Xiao M. Fang, and Victoria Coon	15
MOCVD ERBIUM SOURCES Anton C. Greenwald, William S. Rees, Jr., and Uwe W. Lay	21
PRASEODYMIUM DIOXIDE DOPING OF $\text{In}_{1-x}\text{Ga}_x\text{As}_y\text{P}_{1-y}$ EPILAYER GROWN WITH LIQUID PHASE EPITAXY Kari T. Hjelt, Markku A. Sopanen, Harri K. Lipsanen, Turkka O. Tuomi, and Stanislav Hansenöhr	27
RARE-EARTHS APPLICATIONS IN III-V CRYSTAL GROWTH TECHNOLOGY Leo Zakharenkov	33
*RARE-EARTH DOPING BY ION IMPLANTATION AND RELATED TECHNIQUES Ian G. Brown	39
GROWTH OF Er DOPED Si FILMS BY ELECTRON CYCLOTRON RESONANCE PLASMA ENHANCED CHEMICAL VAPOR DEPOSITION Jim L. Rogers, Walter J. Varhue, and Edward Adams	49
ERBIUM-DOPED SEMICONDUCTOR THIN FILMS PREPARED BY RF MAGNETRON SPUTTERING Hong Koo Kim, Cheng Chung Li, Xiao Ming Fang, James Solomon, Gerald Nykolak, and Philippe C. Becker	55
Er-DOPING IN SILICON BY PULSED LASER IRRADIATION Kenshiro Nakashima	61
Er^{3+} -DOPED SILICON PREPARED BY LASER DOPING T. Asatsuma, P. Dodd, J.F. Donegan, J.G. Lunney, and J. Hegarty	67
MONOCRYSTAL DISLOCATIONLESS Si:Ge, GROWN FROM THE MELT WITH Gd IMPURITY V.V. Borschensky, D.I. Brinkevich, V.V. Petrov, and V.S. Prosolovch	73
EPITAXIAL LAYERS Si:(Sn,Yb) PRODUCED BY THE CRYSTALLIZATION FROM THE MELT-SOLUTION ON THE BASIS OF Sn D.I. Brinkevich, N.M. Kazuchits, and V.V. Petrov	79

*Invited Paper

PART II: RARE EARTH DOPED SILICON

*IC COMPATIBLE PROCESSING OF Si:Er FOR OPTOELECTRONICS F.Y.G. Ren, J. Michel, Q. Sun-Paduan, B. Zheng, H. Kitagawa, D.C. Jacobson, J.M. Poate, and L.C. Kimerling	87
OXYGEN-ENHANCED 1.54 μ m PHOTOLUMINESCENCE OF Er ³⁺ IN SILICON F. Arnaud d'Avitaya, Y. Campidelli, J.A. Chroboczek, P.N. Favennec, H. L'Haridon, D. Moutonnet, and A. Wasieleski	97
HIGH CONCENTRATIONS OF ERBIUM IN CRYSTAL SILICON BY THERMAL OR ION-BEAM-INDUCED EPITAXY OF ERBIUM-IMPLANTED AMORPHOUS SILICON J.S. Custer, A. Polman, E. Snoeks, and G.N. van den Hoven	101
OPTICAL DIRECT AND INDIRECT EXCITATION OF Er ³⁺ IONS IN SILICON A. Majima, S. Uekusa, K. Ootake, K. Abe, and M. Kumagai	107
EFFECT OF THE Er ³⁺ CONCENTRATION ON THE LUMINESCENCE OF Ca _{1-x} Er _x F _{2+x} THIN FILMS EPITAXIALLY GROWN ON Si(100) A.S. Barriere, S. Raoux, P.N. Favennec, H. L'Haridon, and D. Moutonnet	113
CORRELATION OF ELECTRICAL, STRUCTURAL, AND OPTICAL PROPERTIES OF ERBIUM IN SILICON J.L. Benton, D.J. Eaglesham, M. Almonte, P.H. Citrin, M.A. Marcus, D.L. Adler, D.C. Jacobson, and J.M. Poate	119
Er LUMINESCENCE IN Si: A CRITICAL BALANCE BETWEEN OPTICAL ACTIVITY AND PUMPING EFFICIENCY S. Coffa, F. Priolo, G. Franzó, V. Bellani, A. Carnera, and C. Spinella	125
1.54 μ m PHOTOLUMINESCENCE OF ERBIUM IMPLANTED HYDROGENATED AMORPHOUS SILICON M. Kechouane, N. Beldi, T. Mohammed-Brahim, H. L'Haridon, M. Salvi, M. Gauneau, and P.N. Favennec	133

PART III: OPTICAL, ELECTRICAL AND STRUCTURAL PROPERTIES

*ELECTRONIC PROPERTIES AND THEIR RELATIONS TO OPTICAL PROPERTIES IN RARE EARTH DOPED III-V SEMICONDUCTORS Akihito Taguchi, Kenichiro Takahei, and Jyoji Nakata	139
*EFFECTS OF YTTERBIUM ADDITION ON LIQUID PHASE EPITAXIAL GROWTH OF InGaAs/InP HETEROSTRUCTURES A. Davis, H.M. Dauplaise, J.P. Lorenzo, G.O. Ramseyer, and J.A. Horrigan	151
ELECTRICAL AND OPTICAL PROPERTIES OF Yb, Er DOPED GaAs T. Benyattou, D. Seghier, G. Brémond, S. Moneger, A. Kalboussi, G. Marrakchi, G. Guillot, C. Lhomer, B. Lambert, Y. Toudic, and A. Le Corre	163
LUMINESCENCE STUDY OF THE INTRA-4f EMISSIONS FROM GaAs:(Er+O) and Al _{1-x} Ga _x As:(Er+O) Jose E. Colon, David W. Elsaesser, Yung Kee Yeo, Robert L. Hengehold, and Gernot S. Pomrenke	169

*Invited Paper

LATTICE LOCATION AND PHOTOLUMINESCENCE OF Er IN GaAs AND $\text{Al}_{0.5}\text{Ga}_{0.5}\text{As}$	175
E. Alves, M.F. da Silva, A.A. Melo, J.C. Soares, G.N. van den Hoven, A. Polman, K.R. Evans, and C.R. Jones	
*OPTICAL ACTIVATION OF ION IMPLANTED RARE-EARTHS	181
P.N. Favenne, H. L'Haridon, D. Moutonnet, M. Salvi, and M. Gauneau	
LUMINESCENCE OF Tm^{3+} IN GALLIUM ARSENIDE GROWN BY METAL-ORGANIC VAPOR PHASE EPITAXY	195
Achim Dörnen, Klaus Pressel, Christoph Hiller, Dieter Haase, Jürgen Weber, and Ferdinand Scholz	
OPTICAL ACTIVITY OF Yb^{3+} IN MeV ION-IMPLANTED InP	201
S. Uekusa, A. Majima, H. Katsumata, Y. Noyori, and M. Kumagai	
PREPARATION AND PROPERTIES OF GALLIUM PHOSPHIDE DOPED BY RARE-EARTH ELEMENTS	207
Sergei L. Pyshkin and Alberto Anedda	
ESR OF RARE EARTH IMPURITIES (Dy^{3+} , Er^{3+} , Yb^{3+}) IN THE NARROW GAP SEMICONDUCTOR PbTe	213
A.M. Gennaro, G.B. Martins, C. Rettori, G.E. Barberis, and C.Y. An	
CORRELATION OF THE LOCATION IN CRYSTAL LATTICE AND OPTICAL ACTIVITY OF Yb IMPURITY IN III-V COMPOUNDS	219
Adrian Kozanecki	
Tm DOPING OF LEAD TELLURIDE	225
Ludmila I. Ryabova and Marina E. Tamm	
THE EFFECT OF RARE-EARTH ELEMENTS ON THE ENTROPY OF RADIATION DEFECTS IONIZATION IN n-TYPE Ge	229
V.V. Petrov, T.D. Kharchenko, and V.Yu. Yavid	

PART IV: EXCITATION MECHANISMS

*EXCITATION AND DE-EXCITATION MECHANISMS OF RARE-EARTH IONS IN III-V COMPOUNDS: OPTICALLY DETECTED MICROWAVE-INDUCED IMPACT IONIZATION OF Yb DOPANT IN InP	239
T. Gregorkiewicz, B.J. Heijmink Liesert, I. Tsimperidis, I. de Maat-Gersdorf, C.A.J. Ammerlaan, M. Godlewski, and F. Scholz	
ANNEALING STUDIES OF Er-IMPLANTED GaAs AND THE EXCITATION MECHANISM OF Er IN GaAs	251
D.W. Elsaesser, J.E. Colon, Y.K. Yeo, R.L. Hengehold, and G.S. Pomrenke	
PHOTOLUMINESCENCE STUDY OF ENERGY TRANSFER PROCESSES IN ERBIUM DOPED $\text{Al}_x\text{Ga}_{1-x}\text{As}$ GROWN BY MBE	257
Tong Zhang, J. Sun, N.V. Edwards, D.E. Moxey, R.M. Kolbas, and P.J. Caldwell	
LUMINESCENCE PROPERTIES OF Yb-DOPED InP	263
H.J. Lozykowski, A.K. Alshawa, G. Pomrenke, and I. Brown	
EXCITATION OF THE 4f-4f EMISSION OF DONOR-TYPE RARE-EARTH CENTERS THROUGH DONOR-ACCEPTOR PAIR STATES (ZnS:Tm)	269
K. Löbe, R. Boyn, and H. Zimmermann	
Eu AND Yb EXCITATION MECHANISMS IN ZnS, CaS, SrS AND InP	275
M. Godlewski, K. Świątek, and B. Monemar	

*Invited Paper

LUMINESCENCE PROPERTIES OF Yb- AND Nd- IMPLANTED CdS A.K. Alshawa, H.J. Lozykowski, T. Li, and I. Brown	281
*ELECTRICALLY PUMPED RARE EARTH DOPED SEMICONDUCTOR LASERS Jacques I. Pankove and Robert Feuerstein	287
EXCITATION AND RELAXATION PROCESSES OF IMPACT EXCITATION EMISSION OF Er^{3+} IONS IN InP T. Kimura, H. Ishida, S. Yugo, R. Saito, H. Isshiki, and T. Ikoma	293
IMPACT EXCITATION OF Er-DOPED GaAs AND THE RARE-EARTH SITES IN III-V COMPOUND SEMICONDUCTORS S.J. Chang, K. Takahei, J. Nakata, and Y.K. Su	299

PART V: NOVEL STRUCTURES AND DEVICES

*NOVEL ELECTRONICS ENABLED BY RARE EARTH ARSENIDES BURIED IN III-V SEMICONDUCTORS S. James Allen, Dan Brehmer, and C.J. Palmström	307
STUDY OF $\text{Sr}_{1-x}\text{Er}_x\text{F}_{2-x}$ LUMINESCENT THIN FILMS EPITAXIALLY GROWN ON InP (100) A.S. Barriere, B. Mombelli, B.Y. Kim, S. Raoux, and A. Garcia	319
OPTICAL AND STRUCTURAL PROPERTIES OF $\text{CaF}_2\text{:Nd}$ FILMS ON Si-BASED SUBSTRATES C.-C. Cho, W.M. Duncan, and H.-Y. Liu	325
MBE GROWTH OF RARE-EARTH DOPED FLUORIDE INSULATORS ON SEMICONDUCTORS FOR LASER APPLICATIONS M. Lui, R.A. McFarlane, and D. Yap	331
*ERBIUM DOPED GALLIUM ARSENIDE—A SELF-ORGANISING LOW DIMENSIONAL SYSTEM A.R. Peaker, H. Efeoglu, J.M. Langer, A.C. Wright, I. Poole, and K.E. Singer	337
Er-DOPED GaAs FOR HIGH SPEED PHOTOCONDUCTOR APPLICATIONS S. Gupta, S. Sethi, P.K. Bhattacharya, and S. Williamson	347
EuTe/PbTe SUPERLATTICES: MBE GROWTH AND OPTICAL CHARACTERIZATION G. Springholz, Shu Yuan, G. Bauer, M. Kriechbaum, and H. Krenn	353
EFFECTS OF MICROSTRUCTURE ON PHOTOLUMINESCENCE OF $\text{SrS:Eu}^{2+}, \text{Sm}^{3+}$ THIN FILMS Susan Z. Hua, L. Salamanca-Riba, M. Wuttig, and P.K. Soltani	359
MICROELECTRONIC DEVICES: PROSPECTS FOR RARE-EARTHS Leo Zakharenkov, Valeri Golubev, and Vitali Kozlovskii	365

PART VI: THEORY AND MODELS

*ELECTRON STRUCTURE AND MECHANISM OF EXCITATION OF THE RARE-EARTH IONS IN THE III-V COMPOUNDS Vadim F. Masterov	373
---	-----

*Invited Paper

*THE THEORY OF RARE-EARTH IMPURITIES IN SEMICONDUCTORS Michel Lannoo and C. Delerue	385
KINETICS OF THE LUMINESCENCE OF ISOELECTRONIC RARE-EARTH IONS IN III-V SEMICONDUCTORS H.J. Lozykowski	397
ELECTRONIC STRUCTURE OF Si DOPED BY RARE EARTH Yb^{3+} Shang Yuan Ren and John D. Dow	403
SIMPLE MODEL FOR RARE-EARTH IMPURITIES IN THE COMPOUND SEMICONDUCTORS Nicolas P. Ilyin and Vadim F. Masterov	409
AUTHOR INDEX	415
SUBJECT INDEX	417

*Invited Paper

Preface

Symposium E on Rare Earth Doped Semiconductors at the 1993 MRS Spring Meeting was considered by many participants as extremely useful with respect to collating information in this field, highlighting new developments, bringing the international research efforts together, and making new contacts. Of course, the outstanding success of the symposium was due in no small part to the efforts of the speakers and authors who presented their work and composed the papers for the proceedings. A joint session on "Rare Earth Doped Silicon," held together with Symposium B, Silicon-Based Optoelectronic Materials, was beneficial to both symposia, highlighting especially erbium doped silicon for optoelectronic applications. The proceedings from this symposium represent one of the first attempts to compile selected research pertaining to rare earths incorporated into technologically important semiconductors.

The properties of rare earth ions in solids have been studied in detail for decades, but until recently this work was restricted to dominantly ionic hosts such as fluorides and oxides, and to a lesser extent to more covalently bonded hosts, such as tetrahedral II-VI semiconductors. The idea of rare earth elements incorporated into covalent semiconductors such as GaAs and Si may be traced to a short communication in 1963 by R.L. Bell [J. Appl. Phys. **34**, 1563 (1963)] proposing a dc-pumped rare earth laser. At about the same time, three unpublished technical reports appeared as a result of U.S. Department of Defense sponsored research in rare earth doped Si, GaAs, and InP to fabricate LEDs. Attempts by Lasher et al., Betz et al., and Richman et al. to identify sharp 4f specific emissions in these hosts essentially failed. Perhaps due to competing research efforts in glasses and II-VI semiconductors, or to the recognition of the difficulty in appreciably doping the materials with rare earths, no substantial efforts [aside from Pyshkin, Sov. Phys. Semicond. **8**, 912 (1975)] were reported for rare earth doped semiconductors until 1979-1981, a period which witnessed increased activity in the Soviet Union (Kasatkin, Masterov, Zakharenkov, and collaborators). These investigations were quickly followed by various definitive investigations at the Fraunhofer IAF in Germany by Ennen, Schneider, Kaufmann, Pomrenke, and collaborators. Closely related research by Klein, Furneaux, and Henry which impacted this area showed that host-impurity energy transfer could produce lasing from a closed shell impurity (Fe) in a semiconductor (InP) [Appl. Phys. Lett. **42**, 638 (1983)]. Research over the last decade has taken a more international flavor, with the interest in large part driven by the possibility of producing efficient, room temperature, electrically excited intracenter emissions for optoelectronic applications. A particularly newsworthy article hinted at lasing in InGaAsP:Er [Appl. Phys. Lett. **49**, 1686 (1986)]. More recently the research interest has focused around erbium doped silicon, due to its optoelectronic possibilities in a developed silicon electronic technology. Internationally, the research efforts have shifted primarily to Japan, U.S.A., France, Italy, the Netherlands, and Great Britain.

The need for this symposium was dictated by the significant recent national and international activities in investigating rare earth doped semiconductors, and by the common themes in issues related to defects, doping, growth, theory, and optoelectronics. The groundwork for the symposium was laid in the fall of 1991, while unsuccessfully attempting to organize a NATO workshop in this area with H. Gislason and B. Wessels. The current forum through the MRS allowed for the cross fertilization among fields in the material sciences, solid state physics, laser physics, spectroscopy, chemistry, and device physics. The objective of the symposium was to bring together the community of investigators, addressing in depth the unique properties of rare earth doped Group III-V, Group IV, and II-VI semiconductors, addressing current trends in research, and identifying the potential for current and future electronic and optoelectronic applications. The symposium aimed to address a broad range of topics from the very fundamental to the more applied. Emphasis was on the III-V and Group

IV material systems, although issues associated with the growth and doping of epitaxial II-VI systems and particular insulators were also desired. Topics which were considered included defect theory, growth and implantation, microstructure, optical and electrical characterization, radiation damage, and specific device applications. These topics are reflected in the subject breakdown for the proceedings.

The symposium was highlighted by advances in doping techniques, developments in models and theory, and the growth and fabrication of novel structures. Special interest focused on erbium doped silicon, microprecipitates of erbium arsenide in the gallium arsenide matrix, and the potential of GaAs:Er in high speed photoconductive applications. Attention was also on Group II-VI semiconductors due to demands on electroluminescent devices for flat panel displays and rare earth doped fluoride insulators for optical waveguide applications.

The incorporation of rare earths into semiconductors was highlighted with three new approaches, including electron cyclotron resonance plasma enhanced chemical vapor deposition, magnetron sputtering, and laser doping. An excellent overview was given by I. Brown on metal plasma techniques for ion implantation with diverse commercial applications through up-scaling. Significant developments were reported for metal-organic epitaxy which proved the technique's capability in producing high quality III-V compounds with large rare earth doping concentrations. F. Scholz reported desirable vapor pressure and melting point precursor parameters for methyl-cyclopentadienyl and isopropyl-cyclopentadienyl compounds. Others reported data on successful erbium doping and deposition using tris(n-butyl cyclopentadienyl)erbium and an erbium amide source.

Significant events in Group IV optoelectronics were reported by L. Kimerling. The first sharp-line, room temperature light emission from a silicon(erbium) LED was demonstrated. The light emission and possible amplification using erbium in a silicon host provides a potential breakthrough technology platform for optoelectronic integration and interconnection. The lead government agencies supporting this work have included AFOSR, the Air Force Rome Lab, and ARPA. Important material problems were addressed, including the diffusivity and solubility of erbium in silicon, which appears to be low relative to common dopants. Other significant developments included the incorporation of high concentrations ($> 10^{20} \text{ cm}^{-3}$) of erbium in silicon, identification of optically and electrically active sites, and the importance of adding oxygen to enhance the erbium 1.54 μm emission.

Several papers focused on understanding the excitation and deexcitation mechanism of GaAs:Er and InP:Yb. T. Gregorkiewicz elaborated on this latter system and the role of bound excitons, non-radiative Auger processes, and electron and hole traps. DLTS measurements are aiding in giving a more complete picture of GaAs:Er. Co-doping with oxygen also appears to enhance the erbium signal in different III-V systems. Work continues in impact excitation and novel device approaches having high speed photoconductive applications. J. Allen and C. Palmstrom addressed a new rare earth based material system which is emerging and which combines semi-metallic rare earth mono-arsenides with compound semiconductors like GaAs and AlAs. These rare earth mono-pnictides will enable buried structures for resonant tunneling and hot electron transistors for quantum multifunctional high speed electron devices.

Timeliness, exceptional speakers, large attendance, and lively discussion contributed to the success of the meeting. Attendees, which numbered over 90 in the regular sessions and over 200 in the joint session, were primarily from universities and selected government labs. The meeting was also visited by some of the original investigators in the area of rare earth doped III-V semiconductors, including Masterov, Pyshkin, and Ennen. Out of the 69 accepted abstracts, 61 were presented in addition to four late news papers. Out of these, 57 papers are published in these proceedings. Especially unique for a symposium of this size was the representation of contributors from 20

different countries. Due to past achievements in this research area by investigators from the former Soviet Union (FSU), special attempts were made to accommodate papers from these new countries. This was shown in the original Spring Meeting Program in which a special poster session was dedicated toward contributions from Russia, Moldova, Belarus, Ukraine, and Uzbekistan. Several of these papers are presented in these proceedings.

It is hoped that these proceedings further the interest of many investigators and aid in stimulating new insights and ideas. Future meetings are already being considered by A. Peaker and separately by V. Masterov. This area of research has the opportunity of expanding into several related research areas. Future potential for lanthanides and even actinides in electronics and optoelectronics include not only rare earth doped semiconductors but also rare earth mono-pnictides and rare earth silicides.

Gernot S. Pomrenke
Paul B. Klein
Dietrich W. Langer

June 1993

Acknowledgments

The editors wish to express their appreciation to the Air Force Office of Scientific Research (AFOSR) which provided the financial support for this symposium. Their interest and generosity have enhanced the exchange of ideas in this area of research.

Many thanks go to the speakers of the contributed papers and reviewers of the papers. Thanks to the following individuals for their part as session chairs in processing the papers and running the sessions: B. Wessels, R. Soref, R. Feuerstein, P.N. Favennec, Y.K. Yeo, J. Pankove, H. Ennen, L. Kimerling, J. Lam, and T. Gregorkiewicz. Appreciation also to the invited speakers for adding immensely to the technical program: S.J. Allen, I. Brown, P.N. Favennec, T. Gregorkiewicz, L. Kimerling, M. Lannoo, A. Davis, V. Masterov, J. Pankove, A. Peaker, F. Scholz, and A. Taguchi. Further thanks go to L. Kimerling, A. Peaker, C. Palmstrom, and H. Ennen for their stimulating remarks during the rump session on the second evening of the program. Special thanks also to J. Langer and K. Takahai for their helpful program inputs and to all other individuals who contributed to the success of the symposium.

Finally, we acknowledge the invaluable assistance of the MRS Headquarters staff in organizing the meeting and processing the proceedings.

MATERIALS RESEARCH SOCIETY SYMPOSIUM PROCEEDINGS

- Volume 279—Beam-Solid Interactions—Fundamentals and Applications, M.A. Nastasi, N. Herbots, L.R. Harriott, R.S. Averbach, 1993, ISBN: 1-55899-174-3
- Volume 280—Evolution of Surface and Thin Film Microstructure, H.A. Atwater, E. Chason, M. Grabow, M. Lagally, 1993, ISBN: 1-55899-175-1
- Volume 281—Semiconductor Heterostructures for Photonic and Electronic Applications, D.C. Houghton, C.W. Tu, R.T. Tung, 1993, ISBN: 1-55899-176-X
- Volume 282—Chemical Perspectives of Microelectronic Materials III, C.R. Abernathy, C.W. Bates, D.A. Bohling, W.S. Hobson, 1993, ISBN: 1-55899-177-8
- Volume 283—Microcrystalline Semiconductors—Materials Science & Devices, Y. Aoyagi, L.T. Canham, P.M. Fauchet, I. Shimizu, C.C. Tsai, 1993, ISBN: 1-55899-178-6
- Volume 284—Amorphous Insulating Thin Films, J. Kanicki, R.A.B. Devine, W.L. Warren, M. Matsumura, 1993, ISBN: 1-55899-179-4
- Volume 285—Laser Ablation in Materials Processing—Fundamentals and Applications, B. Braren, J. Dubowski, D. Norton, 1993, ISBN: 1-55899-180-8
- Volume 286—Nanophase and Nanocomposite Materials, S. Komarneni, J.C. Parker, G.J. Thomas, 1993, ISBN: 1-55899-181-6
- Volume 287—Silicon Nitride Ceramics—Scientific and Technological Advances, I-W. Chen, P.F. Becher, M. Mitomo, G. Petzow, T-S. Yen, 1993, ISBN: 1-55899-182-4
- Volume 288—High-Temperature Ordered Intermetallic Alloys V, I. Baker, J.D. Whittenberger, R. Darolia, M.H. Yoo, 1993, ISBN: 1-55899-183-2
- Volume 289—Flow and Microstructure of Dense Suspensions, L.J. Struble, C.F. Zukoski, G. Maitland, 1993, ISBN: 1-55899-184-0
- Volume 290—Dynamics in Small Confining Systems, J.M. Drake, D.D. Awschalom, J. Klafter, R. Kopelman, 1993, ISBN: 1-55899-185-9
- Volume 291—Materials Theory and Modelling, P.D. Bristowe, J. Broughton, J.M. Newsam, 1993, ISBN: 1-55899-186-7
- Volume 292—Biomolecular Materials, S.T. Case, J.H. Waite, C. Viney, 1993, ISBN: 1-55899-187-5
- Volume 293—Solid State Ionics III, G-A. Nazri, J-M. Tarascon, M. Armand, 1993, ISBN: 1-55899-188-3
- Volume 294—Scientific Basis for Nuclear Waste Management XVI, C.G. Interrante, R.T. Pabalan, 1993, ISBN: 1-55899-189-1
- Volume 295—Atomic-Scale Imaging of Surfaces and Interfaces, D.K. Biegelson, D.S.Y. Tong, D.J. Smith, 1993, ISBN: 1-55899-190-5
- Volume 296—Structure and Properties of Energetic Materials, R.W. Armstrong, J.J. Gilman, 1993, ISBN: 1-55899-191-3

MATERIALS RESEARCH SOCIETY SYMPOSIUM PROCEEDINGS

- Volume 297—Amorphous Silicon Technology—1993, E.A. Schiff, M.J. Thompson, P.G. LeComber, A. Madan, K. Tanaka, 1993, ISBN: 1-55899-193-X
- Volume 298—Silicon-Based Optoelectronic Materials, R.T. Collins, M.A. Tischler, G. Abstreiter, M.L. Thewalt, 1993, ISBN: 1-55899-194-8
- Volume 299—Infrared Detectors—Materials, Processing, and Devices, A. Appelbaum, L.R. Dawson, 1993, ISBN: 1-55899-195-6
- Volume 300—III-V Electronic and Photonic Device Fabrication and Performance, K.S. Jones, S.J. Pearton, H. Kanber, 1993, ISBN: 1-55899-196-4
- Volume 301—Rare-Earth Doped Semiconductors, G.S. Pomrenke, P.B. Klein, D.W. Langer, 1993, ISBN: 1-55899-197-2
- Volume 302—Semiconductors for Room-Temperature Radiation Detector Applications, R.B. James, P. Siffert, T.E. Schlesinger, L. Franks, 1993, ISBN: 1-55899-198-0
- Volume 303—Rapid Thermal and Integrated Processing II, J.C. Gelpey, J.K. Elliott, J.J. Wortman, A. Ajmera, 1993, ISBN: 1-55899-199-9
- Volume 304—Polymer/Inorganic Interfaces, R.L. Opila, A.W. Czanderna, F.J. Boerio, 1993, ISBN: 1-55899-200-6
- Volume 305—High-Performance Polymers and Polymer Matrix Composites, R.K. Eby, R.C. Evers, D. Wilson, M.A. Meador, 1993, ISBN: 1-55899-201-4
- Volume 306—Materials Aspects of X-Ray Lithography, G.K. Celler, J.R. Maldonado, 1993, ISBN: 1-55899-202-2
- Volume 307—Applications of Synchrotron Radiation Techniques to Materials Science, D.L. Perry, R. Stockbauer, N. Shinn, K. D'Amico, L. Terminello, 1993, ISBN: 1-55899-203-0
- Volume 308—Thin Films—Stresses and Mechanical Properties IV, P.H. Townsend, J. Sanchez, C-Y. Li, T.P. Weihs, 1993, ISBN: 1-55899-204-9
- Volume 309—Materials Reliability in Microelectronics III, K. Rodbell, B. Filter, P. Ho, H. Frost, 1993, ISBN: 1-55899-205-7
- Volume 310—Ferroelectric Thin Films III, E.R. Myers, B.A. Tuttle, S.B. Desu, P.K. Larsen, 1993, ISBN: 1-55899-206-5
- Volume 311—Phase Transformations in Thin Films—Thermodynamics and Kinetics, M. Atzmon, J.M.E. Harper, A.L. Greer, M.R. Libera, 1993, ISBN: 1-55899-207-3
- Volume 312—Common Themes and Mechanisms of Epitaxial Growth, P. Fuoss, J. Tsao, D.W. Kisker, A. Zangwill, T.F. Kuech, 1993, ISBN: 1-55899-208-1
- Volume 313—Magnetic Ultrathin Films, Multilayers and Surfaces/Magnetic Interfaces—Physics and Characterization (2 Volume Set), C. Chappert, R.F.C. Farrow, B.T. Jonker, R. Clarke, P. Grünberg, K.M. Krishnan, S. Tsunashima/E.E. Marinero, T. Egami, C. Rau, S.A. Chambers, 1993, ISBN: 1-55899-211-1
- Volume 314—Joining and Adhesion of Advanced Inorganic Materials, A.H. Carim, D.S. Schwartz, R.S. Silbergliitt, R.E. Loehman, 1993, ISBN: 1-55899-212-X
- Volume 315—Surface Chemical Cleaning and Passivation for Semiconductor Processing, G.S. Higashi, E.A. Irene, T. Ohmi, 1993, ISBN: 1-55899-213-8

PART I

Rare Earth Incorporation

MOVPE OF RARE EARTH DOPED III-V SEMICONDUCTORS

F. SCHOLZ, J. WEBER¹, K. PRESSEL², A. DÖRNEN

4. Physikalisches Institut, Universität Stuttgart, Pfaffenwaldring 57,
D-W-7000 Stuttgart 80, Germany

ABSTRACT

Different III-V compound semiconductors have been doped with the rare earth (RE) elements Yb, Er, and Tm using atmospheric pressure metalorganic vapor phase epitaxy. Best results have been obtained using the novel metalorganic compounds tris-isopropyl-cyclopentadienyl-RE as precursors which have an acceptable vapor pressure and can be used as liquids at bubbler temperatures of 60°-90°C. Only Yb has been found to occupy a regular lattice site in InP, whereas the other RE show complex optical spectra because of their incorporation in form of different centers and clusters.

Introduction

In the recent years, Rare Earth elements (RE) incorporated into semiconductor host material have attracted high interest because of their inneratomic optical transitions whose spectral positions are well defined and insensitive to temperature and influences of the host material, because they are screened by outer electronic shells. Nevertheless they can be excited via the semiconductor host material, and therefore, simple spectrally well defined light emitting devices should be feasible. Besides, the study of the excitation and decay processes is an interesting research topic for the interaction of the solid state band structure and single atomic states.

In first attempts, doping by liquid phase epitaxy has been studied [1,2], but the success of these experiments was limited due to the high reactivity of the RE which had to be used in elemental form, and only rather low doping concentrations could be realized. With ion implantation techniques [3-6], high concentrations have been attained, but only in locally well defined small regions. Only the today well developed modern methods like Molecular Beam Epitaxy (MBE) and Metalorganic Vapor Phase Epitaxy (MOVPE) allowed the incorporation of high RE concentrations in a wide range of semiconductor host materials and specially designed epitaxial structures. MBE is mainly limited to phosphorus free material, and so the incorporation of Yb and Er into GaAs and AlGaAs by the latter method has been reported [7-9].

In this contribution, we like to focus on the RE doping of III-V semiconductors by MOVPE. In contrast to MBE, most III-V materials can be grown by this method, and therefore, the doping of various III-Vs with many RE by MOVPE has been published [10-17]. The main aspect will be drawn on the MOVPE technique itself. We will describe the studies about suitable RE precursors as a stringent prerequisite and their application in conventional atmospheric pressure MOVPE. Furthermore, characteristic results will be

¹Now with: Alcatel-SEL Research Center, D-W-7000 Stuttgart, Germany

²Now with: Institut für Halbleiterphysik, D-O-1200 Frankfurt (Oder), Germany

given, mainly for the elements ytterbium (Yb) and erbium (Er) incorporated into InP, and thulium (Tm) in GaAs and GaInP.

METALORGANIC RARE EARTH PRECURSORS

The striking advantage of (metalorganic) vapor phase epitaxy over many other epitaxial methods is the simple control of most properties of the growing structure via the independent control of the gas flows of the different precursors. But this implies that suitable precursors for each element needed are available. This requirement can easily be fulfilled for the elements of the Vth and VIth group of the periodic system with hydrides like PH_3 , AsH_3 , or H_2S (with S as n-type dopant for III-Vs). For the metals, no gaseous precursors do exist, but metalorganic liquid (sometimes solid) compounds have been developed whose rather high vapor pressure enables their transport in gas lines by a carrier gas (commonly high purity H_2). Best known examples are TMGa and TMIIn as Ga and In precursors, respectively.

Therefore, a main problem is the development of suitable precursors, when further elements, e.g. RE, are to be used as dopants. Such compounds should fulfil many requirements as, e.g., acceptable vapor pressure, chemical stability, high purity, and release of the desired element (and only it) at normal MOVPE growth conditions. Liquids can be handled much easier in MOVPE bubblers than solids, therefore rather low melting points are needed. Only very few classes of metalorganic RE compounds are known which might fulfil at least some of these demands.

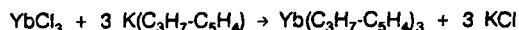
As already known from other doping elements like Mg and Fe, cyclopentadienyl (Cp) compounds could be suitable, and in fact, first RE doping experiments in MOVPE have been done using $(\text{Cp})_3\text{Yb}$ and $(\text{Cp})_3\text{Er}$ as precursors [10,18]. But due to their low vapor pressure, they require extremely high bubbler temperatures of about 200°C [10], and even then, they are still solid ($(\text{Cp})_3\text{Yb}$ has a melting point of 273°C , [19]). Thus, the MOVPE system has to be specially designed with heated gas lines and valves up to $T > 200^\circ\text{C}$ [10], and the doping reproducibility is limited.

Williams, Neuhaufen and Wessels used commercially available precursors like tris-heptafluoro-dimethyloctane-dionate-Yb $[(\text{fod})_3\text{Yb}]$ [14], tris-tetramethylheptanedionate-Er $[(\text{thd})_3\text{Er}]$ [16] and the respective Tm-compound $[(\text{thd})_3\text{Tm}]$ [17]. But even then, still high source temperatures of 120 - 160°C have been found necessary, and due to the solid state nature of these compounds, special source arrangements have been used.

Therefore, we have investigated novel precursors with higher vapor pressure and lower melting point. By replacing one hydrogen atom of the Cp ring by a methyl group, the intermolecular attractive forces can be reduced, and thus the vapor pressure increased and the melting point lowered, as already known from respective Mg compounds. In fact, we found a melting point of 117°C and a vapor pressure of 0.15 Pa at 80°C for the $(\text{MeCp})_3\text{Yb}$ compound synthesized by us [20,21], much better values than those known for $(\text{Cp})_3\text{Yb}$. So we could reduce our bubbler temperature to about 80°C , although we still had to handle a solid compound.

By further increasing the size of the ligand by replacing it by an isopropyl group (iPr), the melting point could be further reduced to 46 - 48°C . The vapor pressure of the resulting compound, $(\text{iPrCp})_3\text{Yb}$ (fig. 1), although not directly measured, seems to be similar to that of $(\text{MeCp})_3\text{Yb}$, as estimated from our growth experiments [22]. It has been synthesized in a

similar way as the respective MeCp-compound via the reaction of dry YbCl_3 and $(\text{iPrCp})\text{K}$ according to



using di-methoxy-ethane as solvent [20]. It is a dark-green solid compound (at room temperature). It can be easily purified by further distillation, therefore the final metalorganic product can be much purer than the RE material in elemental form as used in LPE. Moreover, having stabilized the RE elements inside the Cp molecules, their high reactivity is no longer a problem which otherwise could result in contaminations during storage.

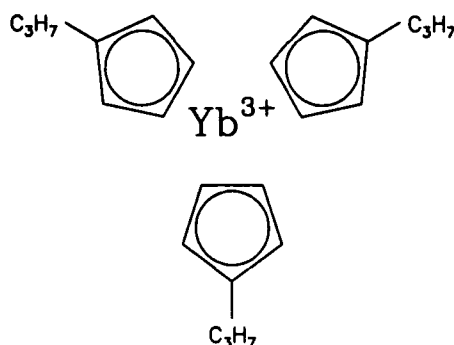


Fig. 1: Chemical structure of the $(\text{iPrCp})_3\text{Yb}$ -precursor

For doping experiments with Er and Tm, the compounds $(\text{MeCp})_3\text{Er}$, $(\text{iPrCp})_3\text{Er}$, and $(\text{iPrCp})_3\text{Tm}$ have been synthesized following the same paths. All iPrCp compounds have similar physical properties with melting points of 46-50°C and thus could be used as liquids at conventional bubbler temperatures (60-90°C) with still high incorporation rates. They have been filled into glass bubblers by distillation and then fitted to our MOVPE system.

MOVPE EXPERIMENTS

For the RE doping, we used a small scale MOVPE kit with conventional gas delivery system including vent-run manifold and a horizontal reaction chamber with rectangular cross-section operated at atmospheric pressure. Growth temperatures between 580°C and 750°C could be established by lamp heating. Adducts as TmIn-TEP [23], DADI [24], TMGa-TEP [23], TMGa-NHiPr_2 [24] have been used as In and Ga precursors, respectively. Although these adducts are chemically more stable than the conventional alkyls thus preventing possible side reactions with the RE precursors, we did not observe a specific (positive or negative) influence of these compounds on our doping results. PH_3 and AsH_3 have been used as P and As precursors, respectively. The bubblers of the above described (MeCp) (for Yb and Er) and (iPrCp) compounds (for Yb, Er and Tm) have been heated to 80°-90°C for obtaining RE doping levels in the range 10^{18} - 10^{19}cm^{-3} . Co-doping experiments with shallow n- and p-type dopants have been carried out using H_2S and DEZn , respectively.

In most experiments, growth rates of 1-2 $\mu\text{m/h}$ have been established in the growth of binary and ternary materials (see below).

DOPING RESULTS

a) Ytterbium

Most of our experiments focused on the system InP:Yb, because it was thought to play the role of a characteristic model of RE in III-Vs. It was already known that Yb occupies an In lattice site [25-29] because of its similar ionic radius. But now, a much wider range of Yb concentrations could be studied as compared to our previous LPE experiments. We found that the Yb incorporation from $(\text{MeCp})_3\text{Yb}$ could be stimulated by raising the growth temperature from 580°C to 670°C reaching concentrations of about $2 \times 10^{19} \text{ cm}^{-3}$ as evaluated by secondary mass spectrometry (SIMS). But then, the surface morphology got worse. Much better surface quality could be obtained with the liquid Yb precursor $(\text{iPrCp})_3\text{Yb}$. Moreover, we found higher Yb photoluminescence (PL) intensities even at low growth temperatures (580°C) although the incorporated Yb concentration was lower. Obviously, the liquid precursor disturbs the InP crystal growth much less than $(\text{MeCp})_3\text{Yb}$, and thus, a higher fraction of Yb can contribute radiatively to the PL signal. This could be due to the lower chemical bonding strength of Yb within the Cp-rings with the large iPr-ligands. Although these findings show, that not all Yb atoms incorporated into the InP host contribute to the optical spectra, we have not found any indication for a saturation limit of this optically active fraction.

In parallel, we observed a drastic difference in the Yb memory effect: We found rather high Yb concentrations in nominally undoped InP layers grown after experiments with $(\text{MeCp})_3\text{Yb}$, whereas no such memory effect was detectable after $(\text{iPrCp})_3\text{Yb}$ grown layers. So in summary, the latter precursor is much better suited for RE doping in terms of reproducibility, crystal quality, and reduced memory effect.

In accordance with results from other authors [30], all our MOVPE grown InP:Yb layers showed n-type conduction without a significant correlation between carrier concentration and Yb concentration. Therefore we conclude, that Yb does not directly influence the electrical conductivity of InP. Former LPE experiments, where p-type conduction has been found [1,2,31], probably have to be explained by extrinsic impurities coming into the LPE melt together with the elemental Yb.

These MOVPE grown layers have been intensively studied by optical spectroscopy. Low temperature ($T=2\text{K}$) photoluminescence (PL) revealed the typical Yb related spectra around $1 \mu\text{m}$ caused by transitions within the 4f-shell of the Yb^{3+} -ion (fig. 2). One missing electron in the 4f-shell can be described by the electronic state ^2F , which splits into $^2\text{F}_{5/2}$ (upper) and $^2\text{F}_{7/2}$ (lower) due to spin-orbit coupling. Further crystal field splitting (due to the T_d symmetry of Yb on an In lattice site) causes the further lines observed in PL (see inset fig. 2). In many layers, one or more phonon replica at lower energies have been observed demonstrating the good quality of the samples. This typical spectrum has been found in our InP:Yb samples regardless of specific growth conditions, Yb precursor, co-doping (if not very high), and epitaxial method (i.e. LPE layers show up the same). They only differ in absolute intensity, mainly caused by differences in Yb concentration.

The same correspondence has been found in time resolved PL measurements: The Yb lines have a constant decay time of $13 \mu\text{sec}$ (at 2K) irrespective of growth method, growth conditions, background carrier type etc.. This has also been found by many other authors in ion implanted samples [32], and LPE [33]

or MOVPE [30,34] grown layers. Therefore, we ascribe it to being an intrinsic property of Yb in InP, i.e. a radiative decay time determined by the influence of the InP crystal field on the Yb atom. It is about 100 times shorter than the decay time of the Yb signal in ionic crystals [35,36].

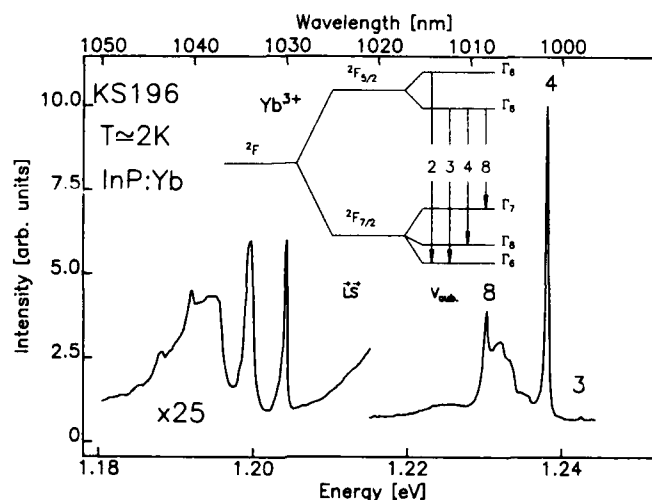


Fig. 2: Low temperature photoluminescence spectrum of an MOVPE grown InP:Yb layer (at about 1.2 eV: Phonon replica). Inset: Term scheme of Yb³⁺ in a cubic crystal field.

Taking into account further spectroscopic data, a model has been proposed where Yb³⁺ in InP is treated as a pseudo acceptor with an energy level 30 meV below the conduction band or a pseudo donor with a level 30 meV above the valence band [37]. The former is in good agreement with DLTS results (DLTS = deep level transient spectroscopy), where a level within the forbidden gap 30 meV below the conduction band has been identified [30], although it is questionable whether the Yb-related defect species giving rise to the electron trap observed in DLTS is identical to the luminescent species [37]. A detailed description would break up this paper, so we refer to the original papers and to further contributions within these proceedings.

When InP was doped simultaneously with Yb and S (n-type) or Zn (p-type), the incorporation rate of these dopants was not influenced by each other (as checked by SIMS) demonstrating again the chemical stability of the Yb precursors against parasitic side reactions. Nevertheless, we found a continuous decrease of the Yb PL intensity for increasing S (above $5 \times 10^{16} \text{ cm}^{-3}$) [22] and Zn concentrations (above $5 \times 10^{17} \text{ cm}^{-3}$). This could be explained (for the n-type co-doping) by a shift of the Fermi level above the pseudo acceptor level. But we cannot exclude some direct interaction of the Yb and S or Zn atom, respectively, leading to a hindered incorporation of Yb on an In lattice site.

b) Erbium

This element is of particular interest for applications in optoelectronic communications due to its inneratomic transition ($^4I_{13/2} \rightarrow ^4I_{15/2}$) at $1.54 \mu\text{m}$ (0.805 eV) which is close to an optical window of the glass fibers. So we studied Er doping of InP as a possible candidate of a light emitting device at this wavelength. As mentioned above, the same types of precursors have been used [38]. We found the same general behaviour: $(\text{iPrCp})_3\text{Er}$ could be used with higher reproducibility and resulted in InP:Er layers with higher crystal quality and PL intensity as compared to the $(\text{MeCp})_3\text{Er}$ precursor. Er concentrations up to $5 \times 10^{18} \text{ cm}^{-3}$ could be obtained. A typical spectrum is depicted in fig.3. In contrast to InP:Yb, its shape remains unchanged even in highly codoped InP:Er:S and InP:Er:Zn samples, and it is very similar to that detected in GaAs:Er [39], which could be resolved to a high number of very sharp lines by high resolution PL [40,41]. Moreover, it resembles to the spectrum of Er in ionic crystals. It cannot be explained by a simple incorporation of Er on a substitutional lattice site, but an incorporation in form of clusters and different interstitial sites has to be taken into account. This is in good agreement with life time experiments: We found decay times of the Er signal of 1-1.5 msec in all kinds of samples (only Er doped and co-doped with S and Zn) and in a wide temperature range from 2 to 150 K, similar to values found in ionic and insulating crystals and glasses [42-44] and other III-Vs [45]. Obviously, the atomic transitions of Er are much less influenced by the semiconductor host than those of Yb in InP.

Although the incorporation of a small fraction of Er on a regular lattice site cannot be excluded, we did not find any indication for that. Insofar, Yb and Er show a very different incorporation behaviour in InP.

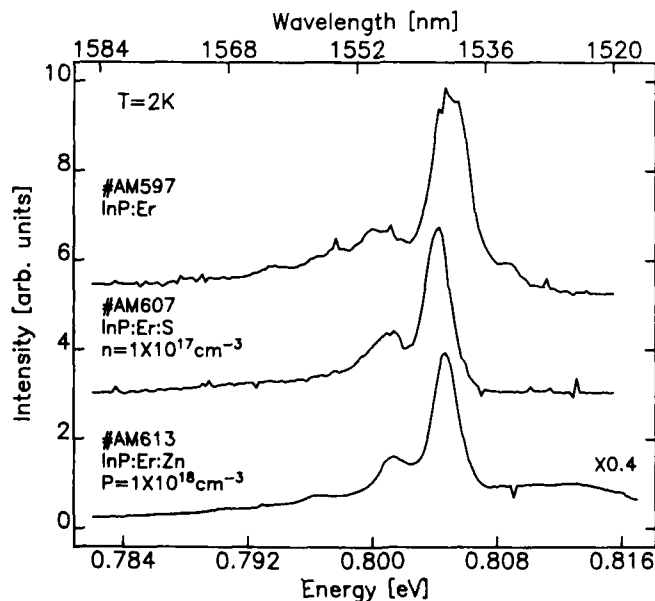


Fig. 3: Low temperature photoluminescence spectra of InP:Er, InP:Er:S, and InP:Er:Zn layers grown by MOVPE

c) Thulium

Thulium was chosen as a further doping candidate, because optical transitions in the accessible range between 1 and 2 μm for two charge states, Tm^{3+} and Tm^{2+} , have been reported [46,47]. This should facilitate the spectroscopic investigations of the excitation and decay processes of the RE, if these transitions occur as well in III-V host material. Using the experience with Yb and Er, $(\text{iPrCp})_3\text{Tm}$ has been chosen as the dopant precursor. Although InP, GaInAs, GaAs, GaInP, and GaP layers doped with Tm have been grown, the typical Tm^{3+} PL spectrum has been observed only in GaAs, GaInP, and very weakly in InP [48].

According to the term scheme of Tm^{3+} , two optical transitions ($^3\text{H}_5 \rightarrow ^3\text{H}_6$ and $^3\text{H}_4 \rightarrow ^3\text{H}_6$) have been expected at wavelengths $\lambda \sim 1.2 \mu\text{m}$ ($\sim 1\text{eV}$) and $\lambda \sim 1.9 \mu\text{m}$ ($\sim 0.65\text{eV}$), respectively. Both transitions could well be resolved in our GaAs:Tm samples for rather high concentrations of $[\text{Tm}] > 10^{18} \text{cm}^{-3}$ (figs. 4 and 5). But as in the case of Er, the number of detected lines was much higher than expected if Tm was incorporated on a substitutional lattice site, and therefore again, we suppose an incorporation in form of different centers [48]. Ion implanted samples showed similar spectra at least for the 1.2 μm transition (fig. 4) [49] demonstrating, that at least a large fraction of Tm forms a specific defect irrespective of the doping method. Zeemann experiments carried out on the most intensive line 1 (at 1.005 eV, see fig. 4) revealed, that this line is caused by a defect with [001] axis, i.e. with D_{2d} symmetry [49], and not with T_d symmetry as for Yb on a regular lattice site.

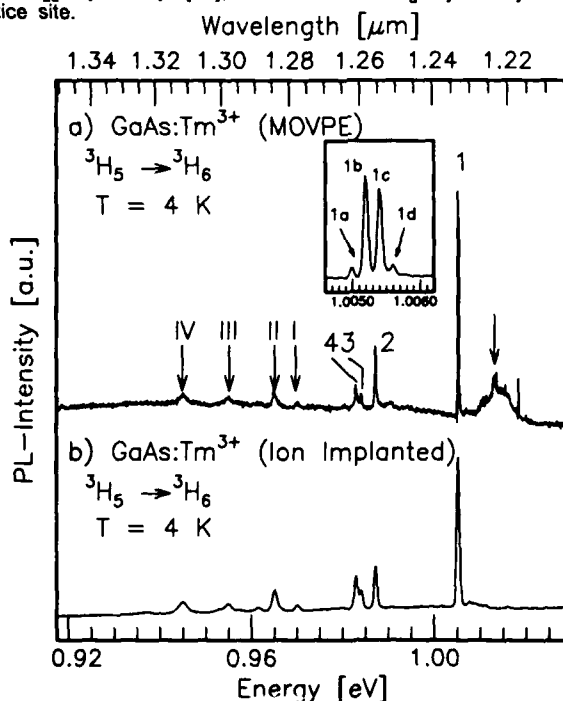


Fig. 4: Low temperature photoluminescence spectra of GaAs:Tm grown by MOVPE (a) and ion implanted (b), transition at 1 eV.

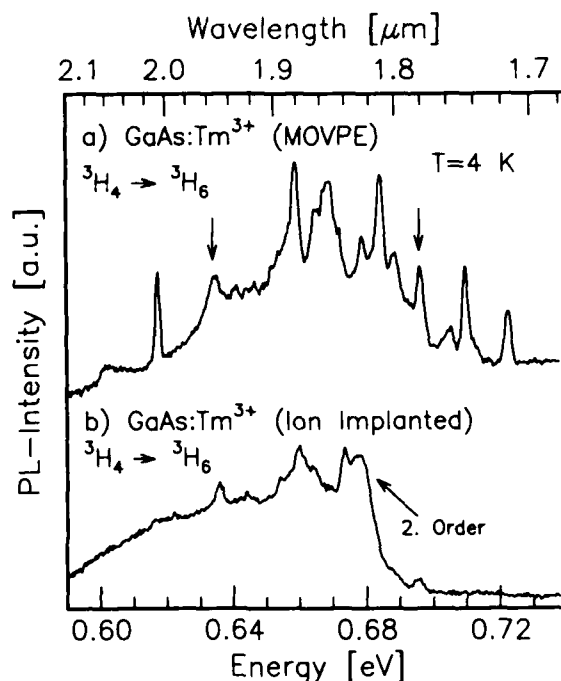


Fig. 5: Low temperature photoluminescence spectra of GaAs:Tm grown by MOVPE (a) and ion implanted (b), transition at 0.65 eV.

A larger difference has been found for the lines at 1.9 μm (fig.5). Therefore, it cannot be excluded that Tm forms different centers in GaAs depending to some extent on the doping process.

Surprisingly, a very strong signal of the $^3\text{H}_5 \rightarrow ^3\text{H}_6$ transition has been detected in GaInP:Tm layers lattice matched to GaAs (fig.6), although the morphology of this material was clearly deteriorated by the Tm doping in contrast to our GaAs samples which remained mirror-like. The intensity is about 3 orders of magnitude stronger than that of GaAs:Tm and reaches about 1/20 of that of the excitonic line of a high quality GaInAsP layer emitting at the same wavelength, although the intensity of the $^3\text{H}_4 \rightarrow ^3\text{H}_6$ transition at 1.9 μm and the Tm concentration, as estimated from SIMS results, are in the same range for both, GaInP and GaAs. This strong Tm signal could easily be detected even at room temperature (fig.6) due to the reduced quenching process of this higher band gap material [17], probably enabling the fabrication of a GaInP:Tm LED.

Unfortunately, we have not been able to find any spectroscopic indication for the $^2\text{F}_{5/2} \rightarrow ^2\text{F}_{7/2}$ transition of Tm^{2+} at about 1.12 μm , even in highly n-type co-doped samples of different materials. We suppose that this transition is not visible in III-V host material.

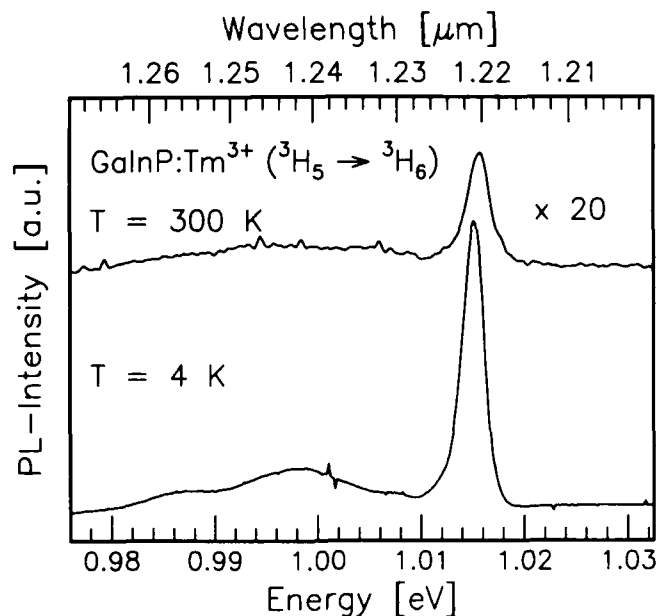


Fig. 6: Low temperature photoluminescence spectra of GaInP at $T=4\text{K}$ (lower) and $T=300\text{K}$ (upper).

CONCLUSIONS

These investigations have shown that MOVPE is well suited to grow RE doped III-V-compound semiconductor layers. The main requirement is the existence of a suitable metalorganic precursor, which could be fulfilled by the synthesis of $(\text{iPrCp})_3\text{RE}$ compounds. These precursors could be used as liquids in an acceptable bubbler temperature range of $60^\circ\text{--}90^\circ\text{C}$ due to their rather high vapor pressure and their stable physico-chemical properties. Good reproducibility has been obtained in the growth of several III-V compounds with Yb, Er and Tm, and no memory effect has been observed in contrast to results obtained with $(\text{MeCp})_3\text{RE}$ compounds.

Although comparably high RE concentrations up to 10^{19}cm^{-3} could be realized for all materials, the detailed optical spectra and thus microscopic incorporation mechanisms obviously depend strongly on III-V compound and RE element. Only Yb is found on a substitutional lattice site in InP, whereas Er is incorporated via different defects and clusters which give rise for complex optical spectra. This has been also reported for Yb in GaAs and GaP [50] and Neodymium (Nd) in GaP [51]. Tm doped into GaAs forms one specific defect with [001] axis (D_{2d} -symmetry) in MOVPE grown and ion implanted samples. Thus, it seems to be different to both, Er and Yb, and therefore, no simple model describing RE in III-V semiconductors can be deduced.

ACKNOWLEDGEMENT

The work described here has been done during the last 5 years, and many people have contributed significant effort. The chemical studies on the precursors have been done by F. Cordeddu, G. Laube, K. Locke, A. Hammel, J. Weidlein and D. Wiedmann. Growth and characterization experiments have been carried out by G. Bohnert, A. Hangleiter, C. Hiller, G. Hörcher, M. Kessler, E. Landsbeck, A. Molassioti, M. Moser, B. Notheisen, D. Ottenwälder, A. Stapor, and K. Thonke. Ion implanted samples for SIMS calibration and further experiments have been provided by H. Ennen (formerly IAF Freiburg) and G.S. Pomrenke (AFSC Bolling). Some SIMS evaluations have been done by M. Gericke and M. Trapp (RTG Mikroanalyse, Berlin). All these contributions are gratefully acknowledged along with fruitful discussions with M. Pilkuhn. This work has been financially supported by the Deutsche Forschungsgemeinschaft under contract no. Pi 71/23.

REFERENCES

- [1] W. Körber, J. Weber, A. Hangleiter, K.W. Benz, H. Ennen, H.D. Müller; *J. Crystal Growth* **79** (1986), 741
- [2] H. Nakagome, K. Takahei, Y. Homma; *J. Crystal Growth* **85**, 345 (1987)
- [3] C. Rochaix, A. Rolland, P. N. Favennec, B. Lambert, A. Le Corre, H. L'Haridon, M. Salvi; *J. Electron. Mat.* **17**, 351 (1988)
- [4] C. Rochaix, A. Rolland, P. N. Favennec, B. Lambert, A. Le Corre, H. L'Haridon, M. Salvi; *Jap. J. Appl. Phys.* **27**, L2348 (1988)
- [5] H. Isshiki, H. Kobayashi, S. Yugo, T. Kimura, T. Ikoma; *Appl. Phys. Lett.* **58**, 484 (1991)
- [6] P.B. Klein, F.G. Moore, H.B. Dietrich; *Appl. Phys. Lett.* **58**, 502 (1991)
- [7] H. Ennen, J. Wagner, H.D. Müller, R.S. Smith; *J. Appl. Phys.* **61**, 4877 (1987)
- [8] A. Rolland, A. Le Corre, P. N. Favennec, M. Gauneau, B. Lambert, D. Lecrosnier, H. L'Haridon, D. Moutonnet, C. Rochaix; *Electron. Lett.* **24**, 956 (1988)
- [9] M. N. Charasse, P. Galtier, A.M. Huber, C. Grattepain, J. Chazelas, J.P. Hirtz; *Electron. Lett.* **24**, 1458 (1988)
- [10] K. Uwai, H. Nakagome, K. Takahei; *J. Crystal Growth* **93**, 583 (1988)
- [11] K. Uwai, H. Nakagome, K. Takahei; *Appl. Phys. Lett.* **50**, 977 (1987)
- [12] K. Takahei, H. Nakagome; *Inst. Phys. Conf. Ser.* **106**, 913 (1990)
- [13] H. Nakagome, K. Takahei; *Jap. J. Appl. Phys.* **28**, L2098 (1989)
- [14] D.M. Williams, B.W. Wessels; *Appl. Phys. Lett.* **56**, 566 (1990)
- [15] A. Taguchi, H. Nakagome, K. Takahei; *J. Appl. Phys.* **68**, 3390 (1990)
- [16] A.J. Neuhalfen, B.W. Wessels; *Appl. Phys. Lett.* **59**, 2317 (1991)
- [17] A.J. Neuhalfen, B.W. Wessels; *Mat. Res. Soc. Symp. Proc. Vol. 240*, p. 195 (1992)
- [18] K. Uwai, H. Nakagome, K. Takahei; *Appl. Phys. Lett.* **51**, 1010 (1987)
- [19] J.M. Birmingham, G. Wilkinson; *J. Am. Chem. Soc.* **78**, 42 (1956)
- [20] A. Hammel, Ph.D. Thesis, University Stuttgart, 1989
- [21] J. Weber, A. Molassioti, M. Moser, A. Stapor, F. Scholz, G. Hörcher, A. Forchel, A. Hammel, G. Laube, J. Weidlein; *Appl. Phys. Lett.* **53**, 2525 (1988)
- [22] J. Weber, M. Moser, A. Stapor, F. Scholz, G. Hörcher, A. Forchel, G. Bohnert, A. Hangleiter, A. Hammel, J. Weidlein; *J. Crystal Growth* **100**, 467 (1990)
- [23] G. Laube, U. Kohler, J. Weidlein, F. Scholz, K. Streubel, R.J. Dieter, N. Karl, M. Gerdon; *J. Crystal Growth*, **45** 93 (1988)
- [24] F. Scholz, A. Molassioti, M. Moser, B. Notheisen, K. Streubel, M. Hostalek, L. Pohl; *J. Crystal Growth* **107**, 365 (1991)

- [25] V.F. Masterov, V.P. Savel'ev, K.F. Shtel'makh, L.F. Zakharenkov; Sov. Phys. Sem. **23**, 1381 (1989)
- [26] V.A. Kasatkin, V.F. Masterov, V.V. Romanov, B.E. Samorukov, K.F. Shtel'makh; Sov. Phys. Sem. **16**, 106 (1982)
- [27] G. Aszodi, J. Weber, Ch. Uihlein, L. Pu-lin, H. Ennen, U. Kaufmann, J. Schneider, J. Windscheif; Phys. Rev. **B31**, 7767 (1985)
- [28] A. Kozanecki, R. Grötschel; J. Appl. Phys. **68**, 517 (1990)
- [29] A. Kozanecki, Phys. Stat. Solidi **A 112**, 777 (1989)
- [30] P.S. Whitney, K. Uwai, H. Nakagome, K. Takahei; Appl. Phys. Lett. **53**, 2074 (1988)
- [31] L.F. Zakharenkov, V.A. Kasatkin, F.P. Kesamanly, B.E. Samorukov, M.A. Sokolova; Sov. Phys. Semicond. **15**, 946 (1981)
- [32] P.B. Klein, Solid State Comm. **65**, 1097 (1988)
- [33] W. Körber, A. Hangleiter; Appl. Phys. Lett. **52**, 114 (1988)
- [34] K. Takahei, A. Taguchi, H. Nakagome, P.S. Whitney; J. Appl. Phys. **66**, 4941 (1989)
- [35] J.A. DeLuca, F.S. Ham; J. Electrochem. Soc. **124**, 1592 (1977)
- [36] G.A. Bogomolova, D.N. Vylegzhanin, A.A. Kaminskii; Sov. Phys. JETP **42**, 440 (1976)
- [37] K. Thonke, K. Pressel, G. Bohnert, A. Stapor, J. Weber, M. Moser, A. Molassioti, A. Hangleiter, F. Scholz; Semicond. Sci. Technol. **5**, 1124 (1990)
- [38] J. Weber, M. Moser, A. Stapor, F. Scholz, G. Bohnert, A. Hangleiter, A. Hammel, D. Wiedmann, J. Weidlein; J. Crystal Growth **104**, 815 (1990)
- [39] P. Galtier, T. Benyattou, J.P. Pocholle, M.N. Charasse, G. Guillot, J.P. Hirtz; Inst. Phys. Conf. Ser. **106**, 327 (1990)
- [40] K. Thonke, H.U. Hermann, J. Schneider; J. Phys. C: Solid State Phys. **21**, 5881 (1988)
- [41] H.U. Hermann, Diploma Thesis, University Stuttgart, 1986 (unpublished)
- [42] S.V.J. Lakshman, Y.C. Ratnakaram; J. Non-cryst. Solids **94**, 222 (1987)
- [43] T.M. Kozhan, V.V. Kuznetzova, I.I. Sergeev, V.S. Khomenko; Zh. Prikl. Spektrosk. **41**, 929 (1984) [Trans. J. Appl. Spectrosc. **41**, 1341 (1984)]
- [44] W.W. Anderson, J. Chem. Phys. **44**, 3283 (1966)
- [45] P.B. Klein, G.S. Pomrenke; Electron. Lett. **24**, 1502 (1988) and references given therein
- [46] S. Hüfner; Optical Spectra of Transparent Rare Earth Compounds; Academic Press, New York, 1978
- [47] Z.K. Kiss, P.N. Yocom; J. Chem. Phys. **41**, 1511 (1964)
- [48] F. Scholz, J. Weber, D. Ottenwälder, K. Pressel, C. Hiller, A. Dörnen, F. Cordeddu, K. Locke, D. Wiedmann; J. Crystal Growth **124**, 470 (1992)
- [49] A. Dörnen, K. Pressel, C. Hiller, D. Haase, J. Weber, F. Scholz; Presentation at MRS Spring Meeting 1993 (San Francisco)
- [50] A. Kozanecki, R. Grötschel; J. Appl. Phys. **64**, 3315 (1988)
- [51] K. Takahei, H. Nakagome; J. Appl. Phys. **72**, 3674 (1992)

MOCVD GROWTH AND PROPERTIES OF ERBIUM DOPED GaAs

DIETRICH W. LANGER*, YABO LI*, XIAO M. FANG** AND VICTORIA COON**

*Electrical Engineering Department, University of Pittsburgh, Pittsburgh, PA 15261

**Microtronics Associates, Inc., 3337 Forbes Ave., Pittsburgh, PA 15213

ABSTRACT

Erbium doped GaAs was grown by metalorganic chemical vapor deposition using a novel liquid precursor: Tris(n-butylcyclopentadienyl)erbium, $\text{Er}(\text{C}_4\text{H}_9\text{C}_5\text{H}_4)_3$. Growth parameters, i.e. temperature, V/III ratio, Er-vapor flow, were investigated. The maximum erbium incorporation in layers with excellent morphology was $1.2 \times 10^{19} \text{ cm}^{-3}$. The erbium-related photoluminescence intensity and the incorporated concentrations, as measured by secondary ion mass spectrometry, were correlated. Based on a simple model for the excitation dependence of the emission, the non-radiative Auger-type process was estimated to be nearly five times that of the energy transfer process from bound excitons to the Er^{3+} ions, which subsequently resulted in the Er-related light emission. Temperature induced quenching of the emission was found to be dominated by transitions with an activation energy of 74 meV.

INTRODUCTION

Erbium-doped GaAs is one of the materials which has been studied intensively because its sharp and temperature-independent $4f$ -intrashell emissions around $1.54 \mu\text{m}$ matches the wavelength of lowest attenuation of silica-based optical fibers.¹⁻⁵ It has been reported that the erbium-related emission lines around $1.54 \mu\text{m}$ are contributed by erbium complexes incorporated into several different sites in GaAs crystal structures.^{1,3} Unlike its ytterbium counterpart, Er^{3+} ion in GaAs has been found to reside either at a cation site or an interstitial site depending on growth procedures.^{2,5} Attention has been paid to the selective formation of specific RE centers in semiconductor hosts to fully utilize all the optically active RE trivalent ions available.

Metalorganic chemical vapor deposition (MOCVD) has been used in the growth of erbium-doped GaAs crystals with simple and reproducible spectra.³ In the past, several erbium source materials have been utilized.^{3,6} As demonstrated in previous studies, liquid precursors of erbium metalorganic compounds are preferable to solid ones because of their high vapor pressures and doping controllability. In this paper we present the results on the growth of erbium-doped GaAs by MOCVD using a new liquid source which contains besides erbium only carbon and hydrogen, elements which are anyway abundant in the growth process. We used Tris(n-butylcyclopentadienyl)erbium [$\text{Er}(\text{C}_4\text{H}_9\text{C}_5\text{H}_4)_3$], commercially available from Strem Chemicals, Inc.. The dependence of erbium concentration in GaAs epilayers on the growth temperature, V/III ratio and the hydrogen (H_2) flow rate through the erbium bubbler has been investigated. The grown samples have been characterized by secondary ion mass spectrometry (SIMS) and photoluminescence (PL).

DESCRIPTION OF EXPERIMENTAL SETUP

The MOCVD growth of GaAs epilayers has been described in detail elsewhere.⁷ Erbium-doped GaAs was grown at atmospheric pressure in a horizontal quartz reactor using Trimethylgallium (TMG) and Tertiarybutylarsine (TBA). Erbium was incorporated into GaAs using the commercial $\text{Er}(\text{C}_4\text{H}_9\text{C}_5\text{H}_4)_3$ with the metal purity of 99.9%. According to the data provided by the manufacturer, the measured boiling point of the synthesized $\text{Er}(\text{C}_4\text{H}_9\text{C}_5\text{H}_4)_3$ is in the range of 230-240°C at 0.1mmHg and the vapor pressure is around 1.0 torr at 200°C.⁸ The epilayers were grown on (100)-oriented Si-doped or undoped GaAs substrates. The growth temperature was varied from 620°C to 680°C. The erbium concentration in the layers was controlled by the erbium source temperature and the H_2 flow through the erbium bubbler which were changed in the range from 175°C to 225°C and from 50SCCM to 210SCCM, respectively. The growth rate was 1-2 $\mu\text{m}/\text{h}$.

Photoluminescence measurements were performed using 488.5nm or 514.5nm lines of an argon-ion laser, a 0.275m Jarrel-Ash monochromator with a 600 grating blazed at 1.0 μm . Operating with relatively wide slits, our spectral resolution was usually limited to about 5nm. A room-temperature InGaAs photodetector and an ORTEC Brookdeal 9503 lock-in amplifier were used. The excitation power density was controlled in the range of 11-19mW/mm². Samples were mounted on the cold finger of a liquid-helium cryostat with temperatures ranging from 4.2K to 300K.

RESULTS AND DISCUSSION

Variation of Growth Parameter

Fig.1 shows the SIMS profile of erbium concentration in a GaAs epilayer grown at 620°C with the H_2 flow rate through the erbium bubbler of 210SCCM and the V/III ratio of 13.5:1. The maximum erbium concentration at the depth of 0.55 μm is around $1.2 \times 10^{19} \text{cm}^{-3}$. The comparison with the real thickness of the epilayer, about 0.75 μm in this case, showed the

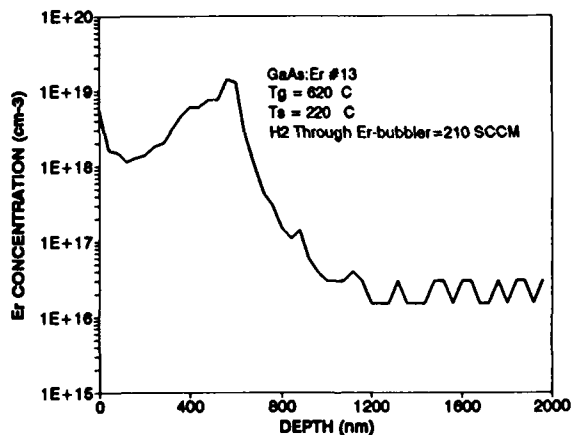


Fig. 1

SIMS profile of an erbium-doped GaAs epilayer.

diffusion of erbium toward the substrate during the growth procedure. The erbium distribution is not uniform, especially near the front surface, which may be related to the segregation of erbium atoms toward the front surface as discussed later. SIMS profiles were obtained with 12 keV oxygen at normal incidence. The SIMS instrument is described

elsewhere.⁹ The dependence of erbium concentration on the $\text{Er}(\text{C}_4\text{H}_9\text{C}_3\text{H}_4)_3$ source temperature was obtained at constant growth temperature and constant H_2 flow rate through the erbium bubbler (620°C and 210SCCM respectively). Source temperatures of 200°C and 220°C resulted in concentrations of $5.5 \times 10^{18} \text{ cm}^{-3}$ and $1.2 \times 10^{19} \text{ cm}^{-3}$ respectively. These erbium doping levels are comparable to those results achieved by MOCVD using $\text{Er}(\text{C}_5\text{H}_5)_3$, $\text{Er}(\text{CH}_3\text{C}_3\text{H}_4)_3$ and $\text{Er}(\text{C}_3\text{H}_7\text{C}_3\text{H}_4)_3$ metalorganic compounds.^{3,6}

The surface morphology of the grown erbium-doped GaAs epilayers was found to depend on the growth temperature, the erbium source temperature and the H_2 flow through the erbium bubbler. Keeping the erbium source temperature at 225°C and a hydrogen flow rate through the bubbler of 210 SCCM, the surface turned out to be cloudy. Whereas grown at the identical temperature (680°C), the sample had a mirror like surface when the gaseous erbium supply was reduced (Erbium source temperature 190°C and 110SCCM flowrate). The observed degradation of morphology is clearly related to the incorporation of erbium into GaAs. The PL measurements indicated that all these samples with cloudy surface exhibited nearly the same PL intensities around $1.54 \mu\text{m}$ despite the differences of erbium source temperatures and H_2 flow rates. One of the cloudy samples - grown with the erbium source at 200°C with 210SCCM of H_2 flow and a V/III ratio of 13.5:1 - exhibited an erbium concentration of $8.0 \times 10^{18} \text{ cm}^{-3}$ according to SIMS measurements. Reducing the growth temperature generally improved the morphology. Optimum morphology with highest Er incorporation was obtained at a growth temperature of 620°C. At this growth temperature, Erbium concentrations as high as $1.2 \times 10^{19} \text{ cm}^{-3}$ have been realized while mirror-like surface morphologies were still maintained. The degradation of the surface morphology induced by the incorporation of rare earths into III-V semiconductor epilayers has been reported previously and attributed to the formation of precipitates with high doping.¹⁰

The erbium concentration in GaAs was found to depend slightly on the temperature at which the epilayer is grown. Keeping constant the erbium source temperature (200°C), the H_2 flow rate through the erbium bubbler (210SCCM) and the V/III ratio (13.5:1), varying the growth temperature from 620°C to 680°C, we measure maximal erbium concentrations of 5.5×10^{18} and $8 \times 10^{18} \text{ cm}^{-3}$ respectively.

Photoluminescence Results

Shown in Fig.2 is the dependence of the erbium-related PL intensity on the erbium concentration as determined by SIMS. At relatively low concentrations, the erbium-related PL intensity was increased with increasing erbium doping. When the erbium concentration exceeded $1.2 \times 10^{19} \text{ cm}^{-3}$, the noticeable decline in PL intensity was observed. This kind of degradation in photoluminescence seems to be characteristic of rare earth doped III-V semiconductor epilayers which has been attributed to a nonuniform distribution of rare earths during the homogenization process as in the case of liquid phase epitaxy growth.¹⁰ Precipitates larger than $1 \mu\text{m}$ were not detected using Normaski microscopy. Therefore a large amount of erbium in complexes with non-(3+)-valence or in the form of smaller precipitates should be responsible for the decrease of PL intensity as the erbium concentration exceeds $1.2 \times 10^{19} \text{ cm}^{-3}$.

Fig.3 shows typical PL spectra of erbium-doped GaAs epilayers obtained at 5.5K, 77K and 300K. Samples used for these PL measurements were all grown at 620°C with a V/III ratio of 13.5:1. At the temperature of 5.5K, the PL spectrum exhibits two distinct peaks, labeled as A at $1.54 \mu\text{m}$ and B at $1.55 \mu\text{m}$. Another relatively weak structure C is also denoted.

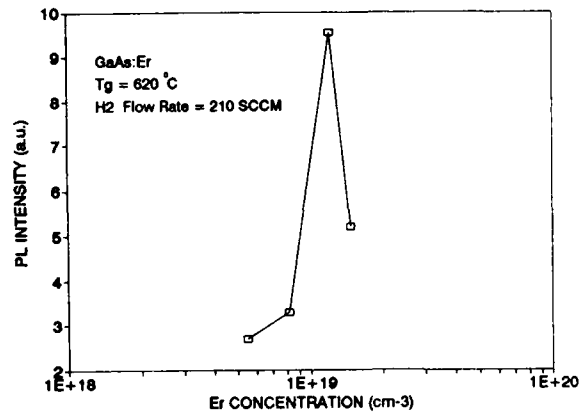


Fig. 2

Dependence of erbium-related PL intensity on the maximal erbium concentration as determined by SIMS measurements.

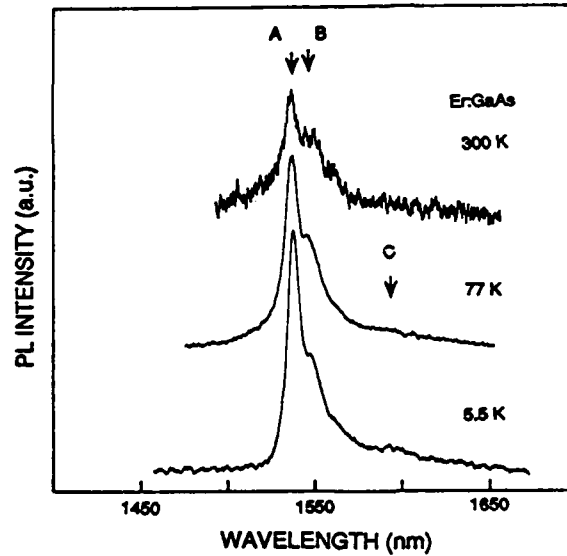


Fig. 3

Photoluminescence spectra of GaAs:Er at 5.5K, 77K and 300K. Baselines are arbitrarily offset.

These emission lines are related to the internal $4f-4f$ transition $^4I_{13/2} \rightarrow ^4I_{15/2}$ of Er^{3+} ($4f^1$) as discussed in Ref. 2. The two main peaks, A and B, shifted to shorter wavelengths by $\sim 2\text{nm}$ with widened line widths as the temperature was increased from 5.5K to 77K. At room temperature, the main peak A was found to locate at $1538 \pm 1\text{nm}$, shifting by less than 1nm from that at 77K. The nonlinear dependence of erbium-related PL intensity on the excitation power has been observed and explained by the non-radiative Auger-type losses during the excitation process.¹¹

The fact that the erbium-related PL spectra were found to be independent of the growth conditions suggests that the observed emission lines are due to the crystal-field induced splitting of Er^{3+} ground state rather than several different erbium sites. The erbium-related emissions were found to depend on the V/III ratio. As the V/III ratio was increased to 27.0, we observed that the main peak A, with the reduced PL intensity, was superimposed on a broad emission band. This might be attributed to the incorporation of some kinds of deep level defects such as EL2 associated with an inappropriately chosen V/III ratio.¹²

The temperature dependence of the PL intensity corresponding to the main peak A is shown in Fig.4. It has been fitted (solid line) to the relationship¹³

$$I(T) = I(0) / [1 + A_1 \exp(-E_1/kT) + A_2 \exp(-E_2/kT)] \quad (1)$$

with the fitting parameters $E_1 = 74 \text{ meV}$, $E_2 = 11 \text{ meV}$, $A_1 = 69$ and $A_2 = 1$. The dominant thermal quenching mechanism is associated with the non-radiative process with an activation energy of E_1 . Takahei et al.¹⁴ proposed that such process may occur through the capture of electrons by excited RE ions from the conduction band at elevated temperatures. The activation energy of 11 meV related to another weak non-radiative process is comparable to the binding energy of excitons in GaAs. This may suggest a likely mechanism in which the bound excitons at Er^{3+} centers are thermally ionized with increasing temperatures.

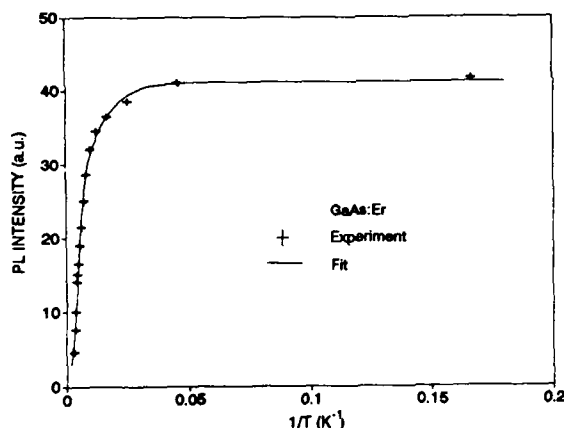


Fig. 4

Temperature dependence of PL intensity related to the main peak A. The solid line is a fit to the data using the analytical expression of eqn.(1).

CONCLUSION

Erbium-doped GaAs has been grown at atmospheric pressure by MOCVD, using a novel metal-organic source, $\text{Er}(\text{C}_4\text{H}_9\text{C}_5\text{H}_4)_3$. Erbium doping as high as $1.2 \times 10^{19} \text{ cm}^{-3}$ was obtained as determined by SIMS measurements. The surface morphology was improved dramatically as the growth temperature was decreased to about 620°C . The incorporated erbium concentration was found to depend on the growth temperature. The erbium-related PL intensity decreased when the doping level exceeded $1.2 \times 10^{19} \text{ cm}^{-3}$ due to the low solubility of erbium atoms in GaAs which may limit the performance of erbium-doped GaAs as to be fabricated in current-injection light emitting devices. The temperature dependence of the photoluminescence showed that thermal quenching is associated with a non-radiative process with an activation energy of 74 meV.

ACKNOWLEDGEMENT

We are grateful to Dr. James Solomon of the University of Dayton Research Institute for carrying out the SIMS measurements. This work was partially supported by the University of Pittsburgh's Materials Research Center operating under AFOSR grant # 91-0441 and by an AFOSR SBIR contract # F49620-92-C-0038.

REFERENCES

1. G. S. Pomrenke, H. Ennen and W. Haydl, J. Appl. Phys. **59**, 601 (1986).
2. H. Ennen, J. Wagner, H. D. Müller and R. S. Smith, J. Appl. Phys. **61**, 4877 (1987).
3. K. Uwai, H. Nakagome and K. Takahei, J. Crystal Growth **93**, 583 (1988).
4. P. Galtier, J. P. Pocholle, M. N. Charasse, B. de Cremoux, J. P. Hirtz, B. Groussin, T. Benyattou and G. Guillot, Appl. Phys. Lett. **55**, 2105 (1989).
5. J. Nakata, M. Taniguchi and K. Takahei, Appl. Phys. Lett. **61**, 2666 (1992).
6. J. Weber, M. Moser, A. Stapor, F. Scholz, G. Bohnert, A. Hangleiter, A. Hammel, D. Wiedmann and J. Weidlein, J. Crystal Growth **104**, 815 (1990).
7. H. G. Lee, H. K. Kim, S. H. Park and D. W. Langer, Proc. of SPIE - Physical Concepts of Materials for Novel Optoelectronic Device Applications I, **1361**, 893 (1990).
8. Ed Meloni, STREM CHEMICALS, INC., private communication.
9. J. S. Solomon, Surf. and Interface Analysis, **10**, 77 (1987).
10. H. Nakagome, K. Takahei and Y. Homma, J. Cryst. Growth, **85**, 345 (1987).
11. X. M. Fang, Y. Li and D. W. Langer, to be published.
12. G. B. Stringfellow, *Organometallic Vapor-Phase Epitaxy: Theory and Practice* (Academic Press, San Diego, 1989), p.289.
13. P. B. Klein, Solid State Commun. **65**, 1097 (1988).
14. K. Takahei, A. Taguchi, H. Nakagome, K. Uwai and P. S. Whitney, J. Appl. Phys. **66**, 4941 (1989).

MOCVD ERBIUM SOURCES*

ANTON C. GREENWALD*, WILLIAM S. REES, Jr.** AND UWE W. LAY**

* Spire Corporation, One Patriots Park, Bedford, MA 01730-2396

** Florida State University, Dittmer Laboratory of Chemistry, Tallahassee, FL 32306

ABSTRACT

The overall objective of this research is to develop source materials for doping AlGaAs. We compared $\text{Er}(\text{C}_5\text{H}_5)_3$ to $\text{Er}\{\text{N}[\text{Si}(\text{CH}_3)_2]_2\}_3$ for purity, decomposition kinetics and doping of germanium films deposited from $\text{Ge}(\text{CH}_3)_4$ in a hydrogen atmosphere. Cyclopentadienyl erbium left large amounts of carbon both in pure metal films, and in the germanium film, at low pressure and temperatures to 850°C. Bis-(tri-methylsilyl) erbium amide decomposed cleanly without carbon, nitrogen or silicon in the deposited film.

INTRODUCTION

The ability to dope III-V compound semiconductors with rare-earth elements could make it possible to produce ionic luminescence whose wavelength is temperature independent. Stable erbium-doped GaAs and AlGaAs diode lasers offer particularly great promise because their 1538 nm wavelength matches that needed for efficient pumping of the Er-doped fibers used in optical amplifiers.¹

Rare earth doping of III-V semiconductors by melt growth processes has generally led to broad photoluminescence (PL) spectra.^{2,3} Ion implantation doping has produced narrow PL spectra, but results were sensitive to annealing parameters.⁴ Because light emitting diodes and lasers are now typically fabricated by metalorganic chemical vapor deposition (MOCVD), and because recent successful results have been reported with rare earth doping of III-V semiconductors by MOCVD,⁵⁻⁸ this approach to achieving narrow-line, temperature-independent, solid-state light sources has reduced risk.

MOCVD is possible if and only if a volatile erbium source compatible with MOCVD of III-V compounds exists. Finding an improved erbium source that contained no oxygen was the objective of this research program. Possible structures for volatile erbium compounds are shown in Figure 1. The betadiketonates (Figure 1a) contain oxygen and were not considered. $\text{Er}(\text{C}_5\text{H}_5)_3$ and $\text{Er}\{\text{N}[\text{Si}(\text{CH}_3)_2]_2\}_3$ (Figures 1b and 1c) were tested.

SYNTHESIS

The cyclopentadienyl erbium material was purchased from a commercial vendor and had tested impurity levels below 1 ppma. The amide was investigated after good results were reported for MOCVD of ZnSe using similar precursors.⁹ $\text{Er}\{\text{N}[\text{Si}(\text{CH}_3)_2]_2\}_3$ was synthesized from $\text{LiN}[\text{Si}(\text{CH}_3)_2]_2$ and ErCl_3 , forming lithium chloride and the erbium-amide.¹⁰ The principal impurity in the resulting product is $\text{LiN}[\text{Si}(\text{CH}_3)_2]_2$, which was separated out by successive sublimations at 5×10^{-2} torr and 80°C. The final residue was sublimed at 140°C, giving a pink powder. The purity of this product is indicated by the NMR data shown in Figure 2. The single very sharp peak implies a total contaminant concentration less than 0.1 ppma.

Decomposition kinetics of $\text{Er}\{\text{N}[\text{Si}(\text{CH}_3)_2]_2\}_3$ are shown in the thermal gravimetric analysis (TGA) in Figure 3. The decomposition point of this material is 257°C. It sublimes rapidly at 175°C. The melting point is 162°C, and the vapor pressure at 120°C is 0.1 torr. For comparison, the published vapor pressure of $\text{Er}(\text{Cp})_3$ is 0.01 torr at 200°C, and the melting point is 285°C.

a) This work was supported by Strategic Defense Initiative Organization and monitored by Air Force Office of Scientific Research, Contract No. F49620-92-C-0060

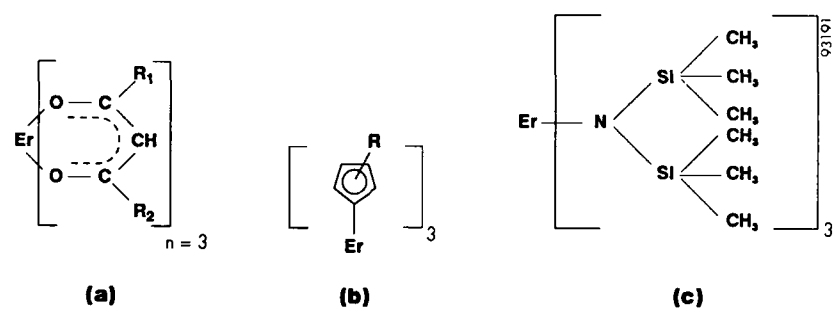


Figure 1 Structure of metalorganic erbium source chemicals, a) β -diketonates, b) cyclopentadienyls, and c) amino-silyls.

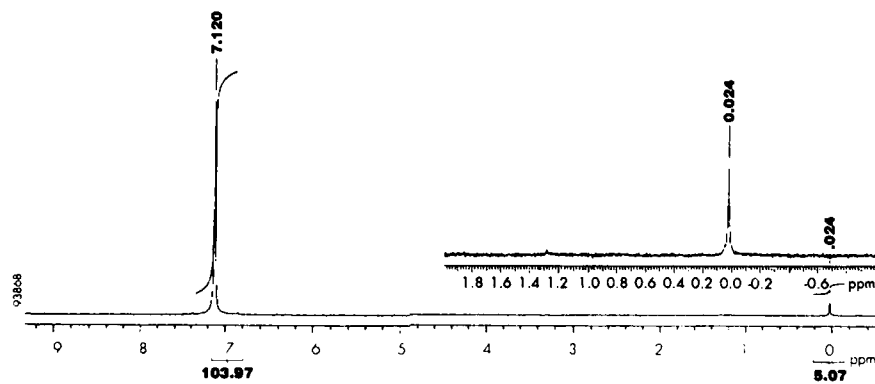


Figure 2 NMR analysis of $\text{Er}[\text{N}(\text{Si}(\text{CH}_3)_3)_2]_3$, showing material purity.

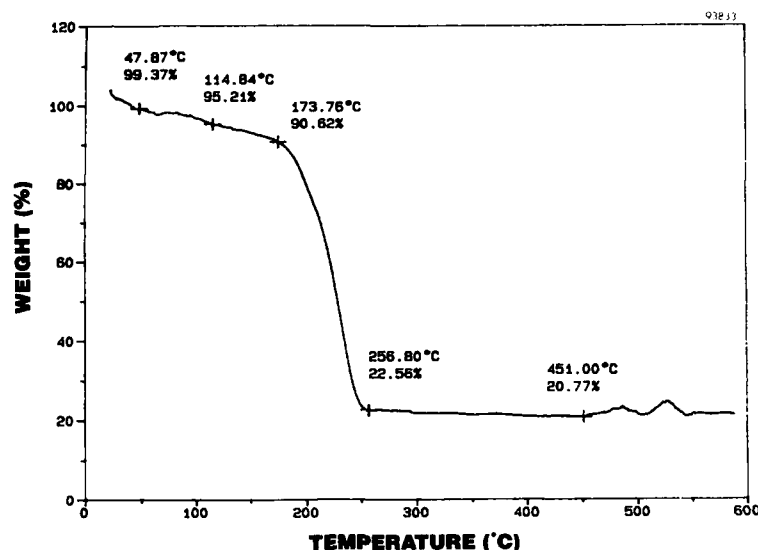


Figure 3 TGA analysis of $\text{Er}\{\text{N}[\text{Si}(\text{CH}_3)_3]_2\}_3$.

CHEMICAL VAPOR DEPOSITION

As the objective of this work is to dope AlGaAs compounds with erbium, the sources were tested at parameters appropriate for epitaxial growth of these III-V compounds. All CVD tests were performed in a hydrogen atmosphere using argon as the carrier gas. The reactor pressure was maintained at either 10 or 75 torr with induction heating of the susceptor to temperatures between 650 and 850°C.

The erbium sources were stored in a stainless steel bubbler. The bubbler was fitted with high temperature valves as were all valves used downstream from these erbium sources. The manifold carrying the erbium vapor was heated in an oven typically 10°C above the temperature of the source to prevent condensation in the lines. The oven assured more uniform temperatures for the valves than the use of heating tape. The gas line from the manifold to the reactor, which contained no valves, was heated by resistance tape to the same temperature as the manifold. There were no deposits in any of the valves or lines except right at the exit slit to the reactor, which could not be directly heated.

Two experiments were performed with each erbium source, deposition of erbium metal alone, and doping a germanium film deposited from $\text{Ge}(\text{CH}_3)_4$. The liquid germanium source had a very high vapor pressure and the pressure of the bubbler holding this compound was independently controlled.

CVD results for the $(\text{Cp})_3\text{Er}$ compound are shown in Figures 4 and 5. The erbium source was maintained at a temperature of 200°C. With a carrier flow of 200 sccm diluted by 4.8 slpm of hydrogen, a metal film 400 nm thick was deposited in two hours at 600°C. The film composition was measured by Rutherford Backscattering Spectroscopy (RBS). Dots in Figure 4 are measured data points while the line is fit using a multilayered model. Carbon content of this film exceeded 90% by atomic ratio.

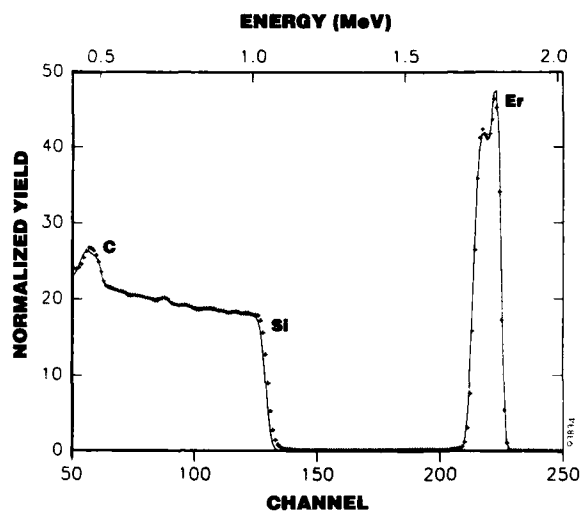


Figure 4 RBS analysis of carbon contaminated erbium film deposited at 600°C from $\text{Er}(\text{Cp})_3$ onto a silicon wafer.

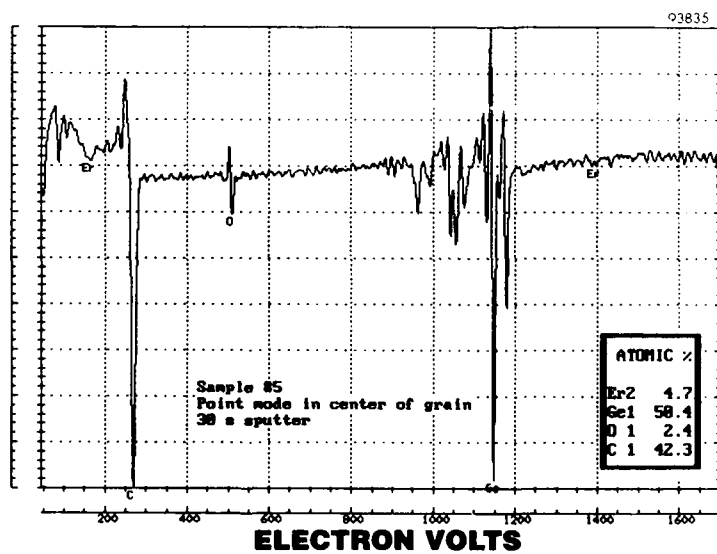


Figure 5 Auger spectroscopy of erbium doped germanium film deposited from $\text{Er}(\text{Cp})_3$, showing excess carbon contamination.

The Auger Spectroscopy data in Figure 5 is from a doped germanium film. Deposition parameters were 825°C at a carrier flow rate of 100 sccm for the erbium source, 20 sccm for the germanium source kept at -5°C, at a pressure of 75 torr and total flow (balance hydrogen) of 5 slpm. In accord with the known instability of elemental carbon at higher temperatures, it was postulated that such conditions would reduce the carbon in the film. As shown in Figure 5, however, nearly stoichiometric germanium-carbide was deposited with a few percent erbium doping. Although the composition of the Auger data was not calibrated, it does not change our conclusion, this is a poor source to use for MOCVD with our conditions.

The difference with the erbium amide compound is shown by the Auger spectroscopy data in Figure 6. Initial tests with the amide at 150°C source temperature produced no visible deposits at substrate temperatures of 400 and 600°C. The source temperature was raised to 175°C (see Figure 3) and a thin (4 nm) film was formed on a silica coated wafer. Analysis of the as-received surface is shown in Figure 6. Sputter cleaning would have removed this film. The carbon content observed is typical of atmospheric contamination of any sample not cleaned by sputtering. The silica on the surface indicates that the deposition is of an island growth nature, and complete coverage has not been reached yet. These erbium compounds react with oxygen at low temperatures, and accidental exposure contaminated the amide source and prevented further work.

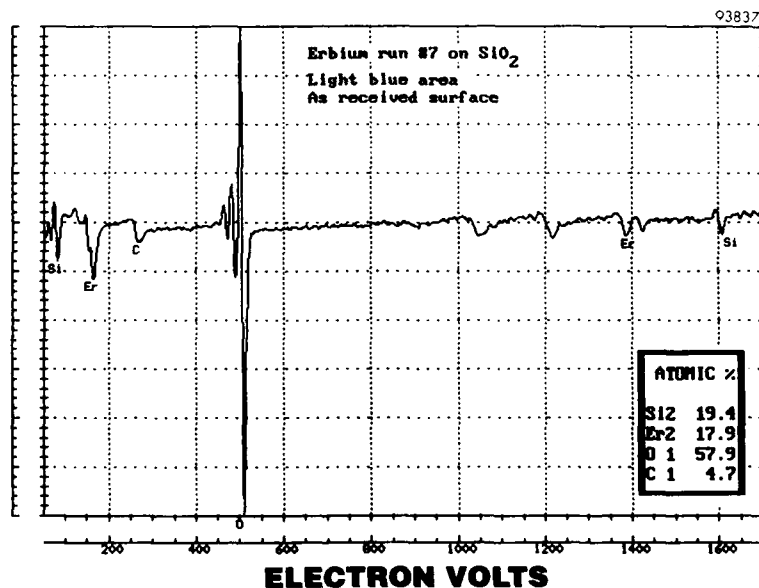


Figure 6 Auger spectroscopy of erbium film deposited from the amide compound showing significant decrease (possible zero without atmospheric contamination) in carbon content.

CONCLUSIONS

For our conditions, the amide compound decomposed with little trace of silicon, nitrogen, or carbon contamination. It may be preferred as a source for MOCVD doping of GaAs compared to the cyclopentadienyl compound, which left large amounts of carbon in the film with, or without, semiconducting metalorganics present.

Carbon contamination in MOCVD grown GaAs films using cyclopentadienyl compounds for doping was also reported by Y.Li *et al.*, [this volume], while no carbon contamination was reported by F. Scholtz [this volume]. Chemical reactions in the presence of arsine, as opposed to TBA, may be the critical difference.

REFERENCES

1. T. Beyattou, D. Seghier, G. Guillot, R. Moncorge, P. Galtier, and M.N. Charasse, *Appl. Phys. Lett.*, **60**, 350 (1992).
2. V.A. Kasatkin *et al.*, *Sov. Phys. Semicond.*, **12**, 974 (1979).
3. A.G. Dimitriev *et al.*, *Sov. Phys. Semicond.*, **17**, 1201 (1983).
4. G.S. Pomrenke *et al.*, *J. Appl. Phys.*, **59**, 601 (1986).
5. K. Uwai *et al.*, *Appl. Phys. Lett.*, **50**, 977 (1987).
6. H. Nakagome *et al.*, *Appl. Phys. Lett.*, **53**, 1726 (1988).
7. M. Tamiguchi *et al.*, *Appl. Phys. Lett.*, **58**, 2930 (1991).
8. A.J. Neuhalfen and B.W. Wessels, *Appl. Phys. Lett.*, **59**, 2317 (1991).
9. W.S. Rees, Jr., D.M. Green, W. Hesse, T.J. Anderson and B. Pathangey, in Chemical Perspectives of Microelectronic Materials, ed. C.R. Abernathy *et al.* (*Mat. Res. Soc. Proc.* **262**, Pittsburgh, PA, 1993), p.63.
10. D.C. Bradley, J.S. Ghotra and F.A. Hart, *J. Chem. Soc. Dalton* **1973**, 1021.

PRASEODYMIUM DIOXIDE DOPING OF $\text{In}_{1-x}\text{Ga}_x\text{As}_y\text{P}_{1-y}$ EPILAYER GROWN WITH LIQUID PHASE EPITAXY

KARI T. HJELT*, MARKKU A. SOPANEN*, HARRI K. LIPSAANEN*, TURKKA O. TUOMI* AND STANISLAV HASENÖHRL**

*Optoelectronics Laboratory, Helsinki University of Technology, SF-02150 Espoo, Finland

**Institute of Electrical Engineering, Slovak Academy of Sciences, Dúbravská Cesta 9, 842 39 Bratislava, Slovakia.

ABSTRACT

Praseodymium dioxide (PrO_2)-doped $\text{In}_{0.69}\text{Ga}_{0.31}\text{As}_{0.67}\text{P}_{0.33}$ layers are grown on semi-insulating InP substrates with liquid-phase epitaxy. The PrO_2 doping of the growth solution varies from 0 to 0.32 wt %. The quaternary $\text{In}_{0.69}\text{Ga}_{0.31}\text{As}_{0.67}\text{P}_{0.33}$ layer composition determined with two-crystal X-ray diffraction and photoreflectance is found to be independent of the PrO_2 concentration in the melt. The photoluminescence spectra measured at 12 K show both exciton and donor-acceptor peaks, the magnitudes of which depend on the PrO_2 doping. The carrier concentration of the n-type quaternary layer decreases and the mobility increases with increasing PrO_2 concentration and reaches the values of $8.3 \cdot 10^{15} \text{ cm}^{-3}$ and $7300 \text{ cm}^2/\text{Vs}$, respectively, at about 0.1 wt% at 77 K. The experiments show that PrO_2 has an impurity gettering effect in the growth process.

INTRODUCTION

InGaAsP quaternary compounds are widely used in various kinds of semiconductor laser and detector structures. Impurities such as sulphur, silicon and residual doping elements make the fabrication of high purity III-V epitaxial layers difficult with liquid-phase epitaxy (LPE).

Rare-earth elements (REEs) are chemically highly reactive and form easily oxides and other compounds. This property is used for the gettering of residual impurities from LPE growth solutions [1-6]. It is of great interest to study the impurity gettering properties of the rare earth elements. However, due to their great chemical activity the REEs require very careful handling and it is practically impossible to load them to the epitaxial boat unoxidized. The growth process is therefore not reproducible. The REE oxides show a similar chemical reactivity to the residual impurities in the growth solution as the pure REEs [1]. They are stable in air and their handling is easy.

It has been shown that praseodymium dioxide PrO_2 acts as a gettering dopant in the LPE growth of InGaAs layers [1]. In this paper we will report about the first evidence of donor gettering by PrO_2 in the InGaAsP layers.

EXPERIMENTAL

Lattice matched quaternary layers were grown with LPE on an iron doped, semi-insulating indium phosphide substrate. PrO_2 powder was added to the melt containing 14 mg of GaAs and 75 mg of InAs in one gram of indium. The growth melt was then homogenized at the temperature of 663°C for two hours. The graphite boat was subsequently loaded with the InP substrate, and 39 mg of InP were put on top of the melt constituents. During the next process cycle the melt was heated to 656°C , at which temperature it was kept for one hour to reach the equilibrium. Immediately before the substrate was moved underneath the quaternary melt a surface layer having a thickness of $5 \mu\text{m}$ was removed by etching with indium at 640°C for

three seconds. The quaternary layer was grown at 640 °C when the temperature was lowered from 656 °C at a constant rate of 0.6 °C/min. The growth of the InGaAsP layer took 3 min 20 s at a descending temperature from 640 °C to 638 °C. The thickness of the grown layers was typically 1.8 μm . The layer composition was $\text{In}_{0.69}\text{Ga}_{0.31}\text{As}_{0.67}\text{P}_{0.33}$, which has the emission wavelength of 1.3 μm at 300 K.

Photoluminescence (PL), photorefectance (PR), x-ray diffraction and Hall measurements were carried out to characterize the grown layers. Photoluminescence (PL) spectra were measured at 12 K and 295 K. Excitation was made by an Ar^+ -ion laser in the wavelength of 488 nm. Laser power was about 25 W/cm^2 . No correction was made for the optical response of the monochromator or detector.

It is well known that the growth history of the LPE equipment has some effect on the grown layers. A few growth cycles using the same initial constituents are needed until reproducible results are obtained. Two sets of samples were grown in this way with the same LPE reactor.

RESULTS

Carrier concentration and mobility

All quaternary layers were lattice matched to the InP substrate. The relative change of the lattice constant $\Delta a/a$ in the layers measured using double crystal X-ray diffractometry varied from $-8.0 \cdot 10^{-5}$ to $-2.1 \cdot 10^{-3}$. Layers with larger lattice mismatch than $4 \cdot 10^{-4}$ were discarded.

Hall measurements showed that all the grown layers were n-type. Figure 1 and Figure 2 show the carrier concentration and carrier mobility at 77 K as a function of the PrO_2 amount in the growth solution, respectively. The carrier concentration decreases from $2 \cdot 10^{17}$ to $8 \cdot 10^{15} \text{ cm}^{-3}$ and the mobility increases from 4000 to 7400 cm^2/Vs when the PrO_2 amount in the solution increases from 0 to 0.15 wt %. At higher dopant levels from 0.15 to 0.32 wt % the carrier concentration and mobility do not change anymore. Further adding of PrO_2 does not have any clear effect to the electrical properties of the grown layers. These results suggest that PrO_2 is not incorporated in the grown layers. It is worth mentioning that the layers were never p-type at any doping of PrO_2 .

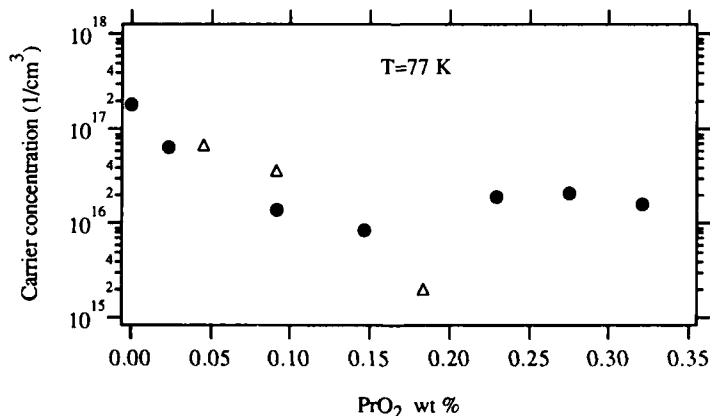


Fig 1. Electron concentration of the PrO_2 -doped InGaAsP-grown layers at 77 K as a function of the PrO_2 wt % in the growth melt. First set of samples is marked with triangles (Δ) and the second one with solid circles (\bullet).

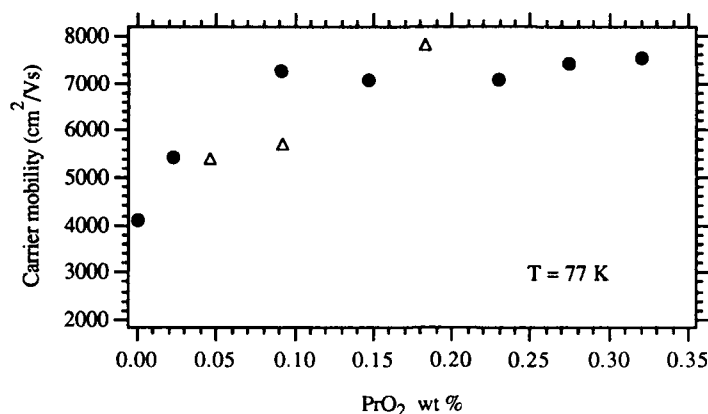


Fig. 2. Electron mobility of the PrO₂-doped InGaAsP layers at 77 K as a function of the PrO₂ wt % in the growth melt. First set of samples is marked with triangles (Δ) and the second one with solid circles (●).

Properties studied by photoluminescence and photoreflectance

Figure 3 shows the PL spectra of five samples, the PrO₂ doping of which ranges from 0 to 0.32 wt%. At 295 K all the samples exhibit only one PL emission band at 0.93 eV (1.33 μm) due to band-to-band recombination. At 12 K the shape of the PL spectrum depends on the amount of the PrO₂ in the growth solution. Lightly doped samples show two or three separate peaks, two of which are thought to result from a near band-gap transition at about 0.98 eV and conduction band to acceptor transition at about 0.96 eV. The low intensity peak at 0.93 eV can be seen in a few lightly doped samples only and it is assumed to be a phonon replica of the 0.96 eV peak.

The general trend is that the band-edge emission increases and the donor-acceptor radiative recombination decreases with increasing the amount of PrO₂ from 0 to 0.15 wt%. Lai and Chang [5] have observed a similar effect in InGaP layers doped with pure praseodymium. It is interesting to notice that the further increase of the PrO₂ doping from 0.15 to 0.32 wt% seems to have an opposite effect to the relative magnitudes of the two peaks.

The width of the PL spectra at 295 K decreases from 50 meV down to 36 meV with the increase of the PrO₂ amount, which is attributed to the decreased amount of impurities in the layers due to PrO₂ gettering.

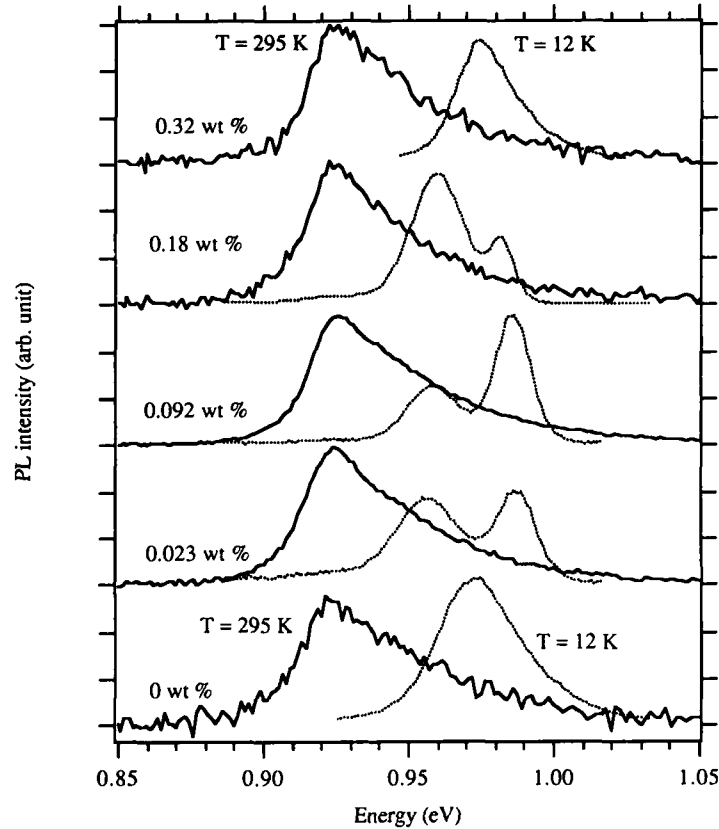


Fig. 3. PL spectra measured at 295 K (full line) and at 12 K (dotted line) of five InGaAsP samples grown with different amounts of praseodymium dioxide in the growth melt.

The band gap of the quaternary layers was determined from the photoreflectance (PR) measurement made at 150 K. Figure 4 shows PR spectra of six samples having been grown with PrO_2 amounts ranging from 0 to 0.32 wt% in solution. The relative PR signal levels are shown on the left side of each spectrum in Figure 4. The band gap was determined by a computer simulation based on the theory of electoreflectance. The temperature shift of the band gap was taken into account to obtain the gap at room temperature.

We found correlation between the PL and PR signal and the doping amount of praseodymium dioxide. There is a clear maximum in the PL and PR signal levels at about 0.1 wt% of PrO_2 in the growth melt. This can be seen also in Figure 3 in which the signal-to-noise ratio in the PL spectra clearly depends on the concentration of the PrO_2 .

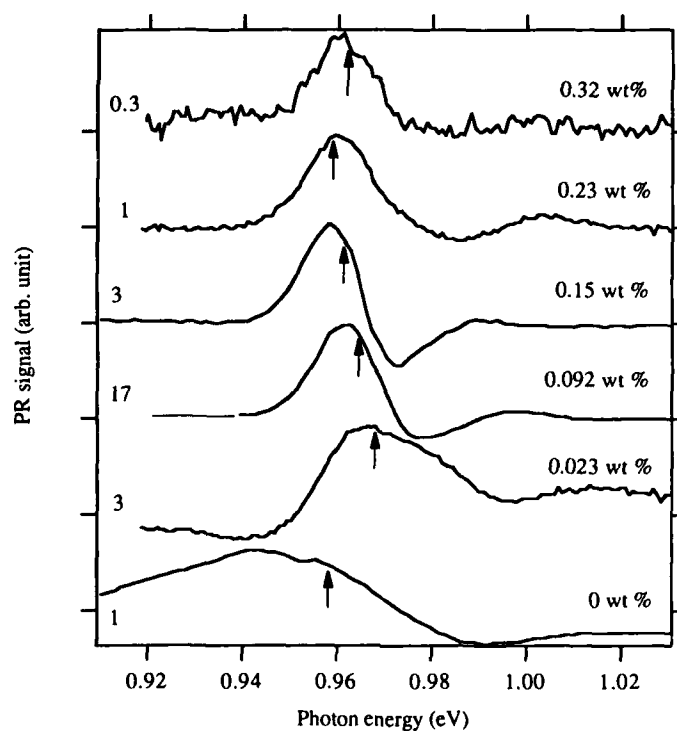


Fig. 4. Photoreflectance spectra measured at 150 K of six InGaAsP samples grown with different amount of PrO_2 in the growth melt. The calculated band gap energy is indicated with an arrow. The relative PR signal levels are shown on the left side of the spectra. Short horizontal lines mark the zero level of the signal for each spectrum.

The composition of the grown InGaAsP-layers was calculated from the x-ray diffraction and PR data using the equations of Kuphal [7]. Figure 5 shows the solid composition of the $\text{In}_{1-x}\text{Ga}_x\text{As}_y\text{P}_{1-y}$ -layers as a function of the PrO_2 amount in the growth melt. The composition was found to be independent of the PrO_2 amount.

DISCUSSION

The results from the PL and PR measurements supplemented with those of the X-ray diffraction studies clearly show that the solid composition of the $\text{In}_{1-x}\text{Ga}_x\text{As}_y\text{P}_{1-y}$ layers does not depend at all on the amount of PrO_2 added to the growth melt. This suggests that the concentration of praseodymium in the grown layers is so small that it does not cause any significant change in the lattice constant. The results also show that PrO_2 has a behavior different from that of Er as a dopant in the InGaAsP growth [6].

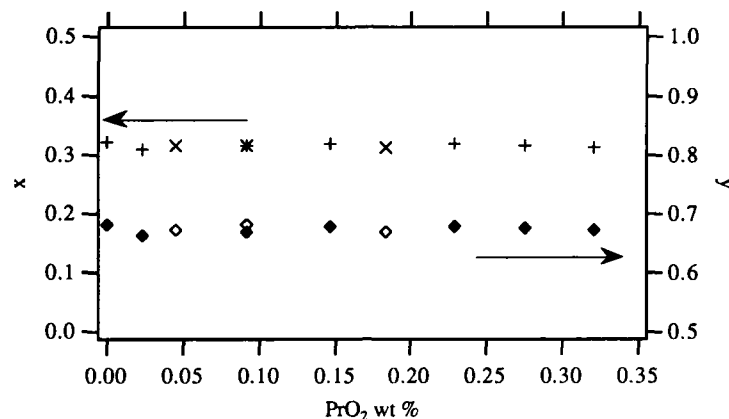


Fig. 5. Solid composition of the $\text{In}_{1-x}\text{Ga}_x\text{As}_y\text{P}_{1-y}$ -layers as a function of the PrO_2 amount in the melt. The atomic fraction of gallium (x) is marked with X for the first set of samples and with + for the second one. The atomic fraction of arsenic (y) is marked with open squares (first set) and solid squares (second set).

Praseodymium is thought to act as an acceptor in InGaP and InGaAs layers [1,5] and high amount in the growth solution should lead to either p-type layers or reduced carrier concentrations. Because no p-type layers were grown even at high doping levels, there seems to be a mechanism that prevents praseodymium from being incorporated into the grown layers. Novák et al. [1] have observed that PrO_2 doping of InGaAs-layers results in p-type layers, which is thought to be caused by the incorporation of praseodymium into the grown layers where it acts as an acceptor. Praseodymium does not seem to form microparticles with phosphorus or arsenic because the solid composition does not change with increasing PrO_2 concentration in the melt.

Both PL and PR signal intensities depend strongly on the doping concentration. It was found that about 0.1 wt % of PrO_2 in the growth melt results in improved optical and electrical properties, which indicates that PrO_2 has an impurity gettering effect in the LPE growth process.

References

1. J. Novák, S. Hasenöhrl, M. Kuliffayová and J. Oswald, *J. Crystal Growth* **110**, 862-866 (1991).
2. N. T. Bagraev, L. S. Vlasenko, K. A. Gatsoev, A.T. Gorelenko, A. V. Kamanin, V. V. Mamutin, B. V. Pushnyi, V. K. Tibilov, Yu. P. Tolparov, and A. E. Shubin, *Sov. Phys. Semicond.* **18** (1), 49-50 (1984).
3. L. F. Zakharenkov, V. F. Masterov, and O. D. Khokhryakova, *Sov. Phys. Semicond.* **21** (2), 211-212 (1987).
4. M. Wu and C. Chiu, *J. Appl. Phys.* **73** (1), 468-470 (1993).
5. M. Z. Lai, L. B. Chang, *J. Appl. Phys.* **72** (4), 1312-1315 (1992).
6. M. Wu, E. Chen, T. Chin and Y. Tu, *J. Appl. Phys.* **71** (1), 456-461 (1992).
7. E. Kuphal, *J. Crystal Growth* **67**, 441-457 (1984).

RARE-EARTHS APPLICATIONS IN III-V CRYSTAL GROWTH TECHNOLOGY.

LEO ZAKHARENKOV

St. Petersburg State Technical University, Experimental Physics Dept.,
Polytechnicheskaya St., 29, St. Petersburg, 195251, Russia.

The problem of manufacturing high purity semiconductor materials with super high electron mobility is among important, though technologically difficult ones.

Traditional with regard to III-V compounds this problem has been solved using the following technique :

- the choice of alternative crucible material;
- the application of high purity initial materials;
- oxygen doping for shallow donors removal;
- isoelectronic doping (e.g. bismuth).

We can also mention other attractive directions in this sphere of activity, such as secondary methods of influence upon the crystals grown - heat treatment and purification by radiation methods, the latter ones still wanting being explored.

From the late 70's we have been carrying out the investigations of the rare-earths (RE) influence upon the electrical characteristics of InP, and later - of GaAs.

In this work submitted are the results of comprehensive investigation of RE applications in bulk III-V crystal growth technology with the aim of purification and heavy doping of the crystals.

Growth technology.

InP and GaAs are chosen as the objects of investigation. Single crystals were grown by standard Czochralskii technique in the crystal puller with HF heating. RE doping was done while the material was being synthesized or RE was introduced into the charge during the crystal growth.

InP polycrystalline charge was synthesized by double-temperature technique in SiO_2 or BN crucibles without B_2O_3 using.

GaAs was synthesized by direct alloying of Ga and As in BN and RED/SiO_2 crucibles, As/Ga+As ratio being 0.53.

In all experiments we used high purity starting materials : Ga, As of 6N purity grade, Ga of 7N and RE distillates of 99.95%.

Some results have been obtained with the InP crystals grown from nonstoichiometric melts.

Preliminary results.

During the first experiments with the synthesis and crystal growth it became already obvious that SiO_2 crucibles did not suit for these purposes. Chemically active RE deoxidised SiO_2 which caused contamination of a growing crystal with silicon, whereas the RE itself combined with oxygen and acquired inactive state within the crystal.

The process of doping GaAs with ytterbium during the synthesis in BN crucible resulted in the formation of white powder. Its composition consists of 70% YbBO_3 , 15% Yb_2O_3 , 15% YbB_6 . Taking into account that this process was carried out without B_2O_3 we consider this powder to be the product of RE active interaction with the crucible material BN.

We managed to produce a promising, in our opinion, material for crucibles. We have been granted a patent for chemically persistent protective coating onto quartz products. The coating consists of the RE oxides (REO), e.g. ytterbium or dysprosium. Resulting from annealing, the formed intermediate layer of complex chemical compound - RE ortho- or metasilicate - provides for excellent adhesion of the coating to quartz.

The synthesis and crystal growth of InP and GaAs in the coated crucibles have demonstrated the complete absence of interaction between RE and SiO_2 or REO.

We faced another nuisance while doping the melt during the crystal growth. It was caused by the fact of RE interaction with B_2O_3 and RE redistribution between the melt and the B_2O_3 encapsulant.

The measurements of the static magnetic susceptibility of $\text{InP}(\text{Yb}, \text{Er})$ single crystals have indicated that RE concentration in B_2O_3 reaches the value of $\sim 10^{19}$ at/cm³ which naturally decreases its concentration in the solid state.

We managed to eliminate or essentially reduce the above described interaction by doping the melt during the synthesis.

Indium phosphide.

The great bulk of investigations dealing with the influence of RE's on the crystal properties were carried out by our Lab. with respect to indium phosphide.

Investigated were the properties by Hall effect, ESR and Raman scattering of light.

Manufacturing conditions of InP crystals are shown in table I, their characteristics - in table II.

The charge carrier concentration in undoped samples (1 and 2) was $n \sim 2 \cdot 10^{16}$ cm⁻³. Since a single crystal (2) was made of polycrystalline indium phosphide in a quartz crucible, it may be concluded that no new donors have been introduced during crystal growth. More likely, partial compensation of the residual donors occurred in the initial material and this resulted in the observed reduction of the carrier mobility. An attempt to dope with ytterbium directly during crystal growth by adding metallic Yb to the charge gave a negative result (3). This was accompanied by an increase in the electron concentration by almost one order of magnitude resulting from partial deoxidation of the container material.

Doping of a second batch of samples with RE took place during synthesis resulted in significant reduction of residual donor concentration both in synthesized material and single crystals.

According to the ESR data, ytterbium and erbium in the original samples 5 and 7 were present in the form of cubic Yb^{3+} and Er^{3+} centers in concentrations of $5 \cdot 10^{19}$ and $5 \cdot 10^{18}$ at/cm³, respectively. During growth these impurity atoms interacted actively with residual impurities and formed stable chemical compounds. Since the ESR failed to reveal the presence of RE atoms in $\text{InP}(\text{Yb})$ and $\text{InP}(\text{Er})$ single crystals, we concluded that during growth of a single crystal they formed chemical compounds and were removed with the slag (into encapsulant).

Table I.
Manufacturing conditions of InP crystals.

N/N	Dopant	Doping method, rare-earth concentration melt (wt.%)	Crucible material
1.	Undoped	Polycrystalline charge, double-temperature synthesis	SiO ₂
2.	- # -	Single crystal, original charge (1)	SiO ₂
3.	Ytterbium	Yb (0.15) introduced during growth, single-crystal charge (1)	SiO ₂
4.	- # -	Yb (0.5) introduced during synthesis, polycrystalline charge	BN
5.	-	Single crystal, original charge (4)	SiO ₂
6.	Europium	Eu (0.1) introduced during growth of dendritic crystals, forming dopant in a single crystal	Dendritic crystals-BN, single crystals-SiO ₂
7.	Erbium	Er (0.5) introduced during synthesis, single crystal	Synthesis - BN, single crystal-SiO ₂
8.	Undoped	Polycrystalline charge, double-temperature synthesis	RED/SiO ₂
9.	- # -	Single crystal, original charge (8)	RED/SiO ₂
10.	Ytterbium	Yb (0.15) introduced during synthesis, polycrystalline charge	RED/SiO ₂
11.	- # -	Single crystal, original charge (10)	RED/SiO ₂

Table II.
Electrical characteristics of InP crystals (300K).

N	1	2	3	4	5	6	7	8	9	10	11
n	3*10 ¹⁶	2*10 ¹⁶	9*10 ¹⁶	(10 ¹⁵)	(10 ¹⁵)	~10 ¹⁶	(10 ¹⁵)	2*10 ¹⁵	3*10 ¹⁵	(10 ¹⁵)	(10 ¹⁵)
M	4300	2200	2000	-	-	4100	-	~5000	~4700	5500	5200

The best results with the semiconductors purification have been achieved when quartz crucibles with RED coating and simultaneous RE doping were used in the process of synthesis (samples 10 and 11).

Gallium Arsenide.

The experience obtained in experimental single crystal growth of high purity InP was transferred to the investigations connected with the manufacturing of Si-GaAs with high electron mobility (more than 6000 cm²*V⁻¹*s⁻¹).

If the concentration of residual shallow impurities in GaAs does not exceed the level of $\sim 10^{15} \text{ cm}^{-3}$, electrical, optical and magnetic properties are determined by native point defects. All of them - vacancies, interstitials, antisites available in the both sublattices - give evidence of electrical activity. Therefore the problem of getting SI-GaAs may be divided into two constituents:

- reduction of residual impurity concentration,
- monitoring of concentration and types of native defects.

The results of the analytical methods show that usual concentrations of shallow donors S, Si_{Ga} and acceptors C, Zn, Si_{As} are $N_d < 2 \cdot 10^{15} \text{ cm}^{-3}$ and $N_a < 5 \cdot 10^{15} \text{ cm}^{-3}$, respectively. Carbon is assumed to be the dominant residual impurity.

We have carried out a series of experiments on GaAs purification by analogy with InP (see table III).

Table III.
Manufacturing conditions of bulk SI-GaAs single crystals.

N sample	Initial materials	Dopant, concentr., wt. %	Manufacturing conditions	Crucible material	Note
1.	Ga - 7N As - 6N	Undoped	Direct synthesis Single crystal growth	BN RED/SiO ₂	
2.	- # -	Yb 0.25	Direct synthesis (Yb) Single crystal growth	BN RED/SiO ₂	
3.	- # -	Yb 0.5	(2)	(2)	
4.	- # -	Yb 0.12	Synth. (1)+Synth. (2)=1:1 Single crystal growth	(2)	Dilution
5.	Ga - 6N As - 6N	Undoped	Direct synthesis Single crystal growth	RED/SiO ₂ RED/SiO ₂	
6.	- # -	Yb 0.1	Direct synthesis (Yb) Single crystal growth	RED/SiO ₂ RED/SiO ₂	

The results of electrical measurements of SI-GaAs crystals are listed in table IV.

Table IV.
Electrical parameters of SI-GaAs single crystals (300K).

N sample	Specific resistance, ρ , Ohm*cm	Charge carrier mobility, $\text{cm}^2 \cdot \text{V}^{-1} \cdot \text{s}^{-1}$	Charge carrier concentration, cm^{-3}
1.	$(0.5 - 1) \cdot 10^7$	3000 - 4500	$(0.5 - 1.0) \cdot 10^7$
2.	$(1 - 3) \cdot 10^8$	5000 - 5700	$(4 - 6) \cdot 10^6$
3.	$\sim 10^8$	< 3000	$\sim 10^7$
4.	$(1 - 3) \cdot 10^8$	5500 - 6500	$(5 - 7) \cdot 10^6$
5.	$(3 - 6) \cdot 10^7$	< 4000	$\sim 10^7$
6.	$\sim 10^8$	> 5500	$5 \cdot 10^6$

As we can see from table IV, with the direct synthesis of undoped material and the subsequent single crystal growth, it is possible to get SI-GaAs with electron mobility less than $4000 \text{ cm}^2 \text{V}^{-1} \text{s}^{-1}$. Deviation of ρ and μ within one ingot is $\sim 20\%$, these parameters changing within the limits of 25-30% from ingot to ingot. Deviations of ρ and μ within one wafer have not been investigated.

Adding ytterbium to the synthesis contributes to the increase of both ρ to the value $\sim 10^8 \text{ Ohm}\cdot\text{cm}$, and μ . In this case the concentration dependence is observed and we think, it reaches the maximum in its mobility value. Variation between ρ and μ decreases both within one ingot and from crystal to crystal up to $\sim 8-12\%$.

Most probably, ytterbium getters residual impurities that can be seen on photoluminescent spectrum (PL) at 77K (fig.1). The spectra have power compositions typical for of semi-insulating samples. Emission in the region of 1.5-1.52 eV is on the whole caused by the recombination of a free exciton or excitons bounded upon shallow donor or acceptor impurities DX, D+X, AX, and by recombination of free hole upon neutral donor Dh, as well. Low-energy spectrum edge 1.48-1.49 eV is formed at the expense of the electron transitions up to the neutral acceptor C, Zn or Si level if it stays at the As site. Carbon seems to be the most likely available residual acceptor of all the set of impurities mentioned above.

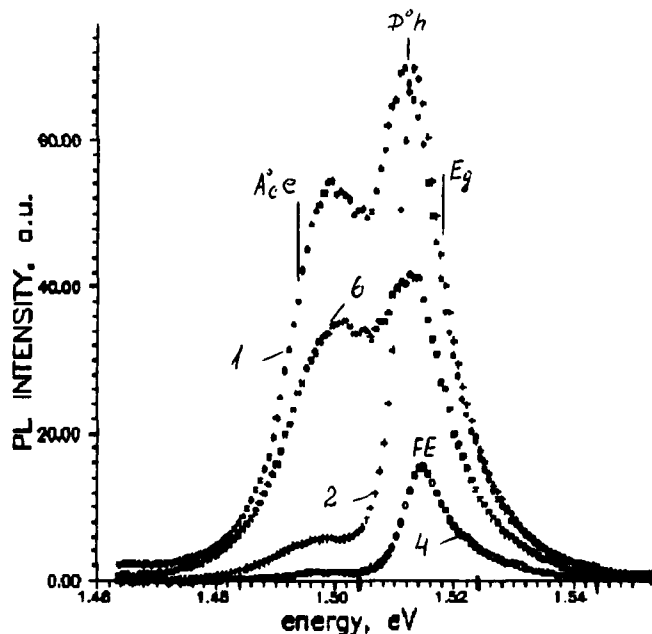


FIG. 1.
The edge photoluminescence
spectra of SI-GaAs single crystals.

In sample 4 with $\mu \sim 6500 \text{ cm}^2 \text{V}^{-1} \text{s}^{-1}$ all emission is concentrated practically in the exciton region, and the exciton zone itself is moved

towards the high energy region, in comparison with the analogous spectrum section of the other three crystals.

More uniform μ distribution along the ingot and the above enumerated features of PL spectrum testify to high purity of sample 4 and lower shallow acceptors concentration.

The state of structure defects was monitored with the help of the optical absorption spectra, their energy quantum ranging from 0.4 to 1.5 eV. The results of the measurements have demonstrated that type EL2 structure defects concentration is the same in all the test specimens, its value being $(1-3) \cdot 10^{16} \text{ cm}^{-3}$.

III-V(RE) single crystals application.

Systematic investigations of semiconductors doped with RE have started little over a decade ago. Nowadays, there are many works published concerning the application of III-V compounds doped with RE.

The current wide interest in RE doped semiconductors is first and foremost due to their optical properties. The sharp lines in the luminescence spectra, resulting from the intracenter f-f transition, in different semiconductors (Si, III-V) make it possible to suggest them as material for solid - state coherent and noncoherent light sources with the wavelength of about 1.0-1.5 microns.

It is vital to have heavily RE doped semiconductors for producing such sources. Furthermore, RE atoms must be located in the substitutional positions of III component sites in the lattice.

As it was exposed during our experiments, the upper RE atoms' concentration has been achieved in InP grown from nonstoichiometric melts.

The maximum registered concentrations of RE atoms at the substitutional positions of indium sites with a nearly cubic environment were $5 \cdot 10^{19} \text{ at/cm}^3$ for Yb^{3+} and $1 \cdot 10^{18} \text{ at/cm}^3$ for Er^{3+} (ESR), while Eu^{2+} concentration reached the value of $2 \cdot 10^{20} \text{ at/cm}^3$ (magnetic susceptibility).

Thus, the fields, where we have achieved the most significant results of RE application in crystal growth technology, are:

- semiconductor materials purification,
- production of protective coating onto quartz crucibles,
- heavily RE doped material for light sources with narrow emission band manufacturing.

The author expresses his gratitude to Eng. E.Vavilov who did the electrical measurements and to Dr. V.Savel'ev who measured the optical spectra.

RARE-EARTH DOPING BY ION IMPLANTATION AND RELATED TECHNIQUES

Ian G. Brown
Lawrence Berkeley Laboratory, University of California, Berkeley, CA 94720

ABSTRACT

Some metal plasma techniques have been developed that provide a convenient means for the doping of semiconductor hosts with rare-earths. These plasma and ion beam tools are based on the application of vacuum arc discharges for the formation of dense rare-earth plasmas which then can be used in a number of ways for doping and otherwise introducing the rare-earths into substrate materials. At the low energy end of the spectrum, the streaming metal plasma can be used for the deposition of thin films, and if more than one plasma source is used then of multilayer structures also. Or by building the vacuum-arc rare-earth plasma generator into an ion source configuration, high current ion beams can be produced for doing high energy ion implantation; alternatively the substrate can be immersed in the streaming rare-earth plasma and by using appropriately phased high voltage substrate pulsing and pulsed plasma generation, plasma immersion ion implantation can be done. Between these two limiting techniques — low energy plasma deposition and high energy ion implantation — a spectrum of hybrid methods can be utilized for rare earth doping. We've made a number of plasma and ion sources of this kind, and we've doped a wide range of substrates with a wide range of rare-earths. For example we've implanted species including Sc, Y, La, Ce, Pr, Nd, Sm, Gd, Dy, Ho, Er and Yb into host materials including Si, GaAs, InP and more. The implantation dose can range from a low of about 10^{13} cm⁻² up to as high as about 10^{17} cm⁻², and the ion energy can be varied from a few tens of eV up to about 200 keV. Here we review these vacuum-arc-based plasma methods for rare-earth doping, describing both the tools and techniques that are available and the applications to which we've put the methods in our laboratory.

INTRODUCTION

A wide range of surface modification techniques have been developed for imparting various exotic and desirable characteristics to material surfaces and for tailoring the structure of surfaces and interfaces. Many of these methods make use of beams of atoms, ions, or neutral plasma [1-4], and the energy range can span many orders of magnitude. Ion implantation is used to energetically inject ions to depths of hundreds or thousands of Angstroms below the surface, and non-equilibrium alloys can be formed that are difficult or impossible to form using standard equilibrium processes. Surface films of a great variety of elements and compounds can be deposited onto the substrate using a low energy flux of neutral or ionized species, and thin film deposition is an advanced technology. An area of investigation that is receiving increasing attention is the synthesis of multilayer structures, with layer thickness being down to just one to several atomic monolayers and layers perhaps forming an ordered two-dimensional crystalline array (superlattices). Many hybrids of these various methods have been investigated, such as ion beam mixing [5] and ion beam assisted deposition (IBAD) [6]. For example a condensible species (eg, metallic) deposited at low energy can be driven into the substrate material by knock-on collisions by energetic ions; this is called recoil implantation, and much progress has been made in a number of means of implementation of this technique.

In conventional ion implantation [7] a beam of energetic ions is directed onto the material to be implanted using an appropriate ion source to form and accelerate the ion beam; additional post-extraction acceleration of the beam may also be applied. The ion source, the beam and the target are located within a high vacuum environment, and the beam trajectory may be up to many meters long. This is of course a technology which has been honed to a fine pitch and applied widely in the semiconductor / ic fabrication industry. In this case the ion beam is mass-analyzed and focused onto the semiconductor wafer, and large areas are implanted by scanning the beam and the wafer. The kind of ion source used almost universally for this kind of

implanter is the Freeman source; other kinds of sources such as Penning sources have also been used. These ion sources do not work ideally for high boiling point metals. From the user's point of view this means that the beam currents obtainable are low and that long irradiation times are needed to accumulate the required implantation dose. We have developed a different kind of ion source, based on the vacuum arc for generation of the metal plasma, which we've used to make a different kind of ion implanter from the 'conventional' (semiconductor implantation) kind, and we've used it to do a very wide range of metal ion implantation, including of most of the rare-earths.

An alternative to the usual method of ion implantation has been developed in recent years [8-13], in which the object to be implanted is immersed in a gaseous plasma of the desired implantation species and repetitively pulse-biased to high negative voltage. A high voltage sheath rapidly forms at the substrate-plasma boundary, and plasma ions are accelerated through the sheath drop and into the substrate, thereby accomplishing implantation into the substrate of plasma ions at an energy determined by the bias voltage. The sheath grows rapidly, expanding into the plasma at approximately the ion acoustic speed in the plasma, and the system would be severely disrupted (eg, high voltage breakdown and plasma depletion) if the substrate were maintained at high voltage. Thus the voltage is pulsed. The process is repeated, ie, repetitively pulsed, until the desired implantation dose is accumulated. This technique has been called plasma source (or plasma immersion) ion implantation (psii or piii), and it has been shown to be an effective tool for semiconductor [11-13] ion implantation. We have taken this technique a step further by combining it with vacuum-arc-produced metal plasma techniques to provide a means for accomplishing similar ends with metal species [14]. We refer to this processing method as metal plasma immersion surface modification.

If one has the plasma wherewithall for creating dense metal plasma streams, thin films and multilayer structures can be formed by depositing onto a substrate that is inserted into the plasma stream. In a way this is a simpler thing to do than implantation, since the plasma generator does not need to be incorporated within an ion source to form the high energy ion beam. We have used our metal plasma production apparatus for synthesizing a number of rare earth films and structures.

In the following we describe how vacuum arcs can be used to form dense rare-earth plasmas that can be used in all the above ways. The plasma guns that we've used and the properties of the plasma are outlined. The vacuum arc ion source embodiments that we've made are also described together with the kinds of rare-earth ion implantation doping that can be done. Examples are presented of some of the implantations that we've done and the films and multilayer structures that we've fabricated using this array of techniques.

RARE-EARTH PLASMA GENERATION

Dense plasmas can be efficiently generated from solid metals by means of a vacuum arc [15]. Vacuum arc plasma sources have been used for the deposition of metallic thin films and for the formation of metallic and TiN coatings by Physical Vapor Deposition (PVD) [16-19]. Industrial arc source deposition equipment is readily available on the market. The vacuum arc is commonly also called a 'cathodic arc', especially when used in a dc mode. Cathodic arc PVD facilities are large pieces of equipment and are designed to apply metallic coatings to large substrate areas; the titanium nitriding of cutting tools and other components in a large batch processing mode is a typical application. In the approach described here, a repetitively pulsed vacuum arc plasma source is used to generate the metal plasma flux.

The plasma is generated from a solid metal cathode by an arc discharge between the cathode and the nearby anode. In much of our work, the arc discharge is driven by a simple L-C pulse line of impedance about 1 Ω and pulse duration about 250 μ s, charged up to several hundred volts with a small, isolated dc power supply. A short, high voltage pulse (~ 10 kV, ~ 5 μ s) applied to a trigger electrode initiates a surface spark discharge between the central cathode and a coaxial trigger electrode. This spark plasma closes the anode-cathode circuit, allowing the main arc discharge to take place. In the vacuum arc, the discharge current is concentrated on the cathode surface at a small number of very intense and tiny "cathode spots", of diameter typically

1 - 10 μm , at which the current density is $\sim 10^8 \text{ Acm}^{-2}$ or more. These local concentrations of very high energy density vaporize and ionize the cathode material which is then ejected away from the cathode in the form of a dense metal plasma plume, not dissimilar to the way in which laser-produced plasmas are created from solid surfaces.

We have studied the properties of the metal plasma generated in this way as part of our vacuum arc ion source program [20-22]. The source works with virtually all the solid metals of the periodic table [23,24] and specifically for the rare earths; we've made plasma from Sc, Y, La, Ce, Pr, Nd, Sm, Gd, Dy, Ho, Er, Tm and Yb. The plasma source is efficient and it can be scaled up. It operates in a high vacuum environment; no support gas is required. We've made a number of different embodiments of vacuum arc plasma gun, from tiny, sub-miniature versions up to large, water-cooled dc versions. A multiple-cathode version has also been made, whereby one can switch from one cathode species to another very simply and without breaking vacuum.

Along with the metal plasma that is generated by the vacuum arc a flux of macroscopic droplets of size typically in the broad range 0.1 - 10 microns is also produced [25-27]. The origin of the macroparticles is at the cathode spots, where they are produced by the intense heating of the cathode material beneath the spot. The amount of molten material formed is less for higher melting point materials, and the macroparticle contamination is observed to be less for cathode materials of higher melting point. For those applications for which the macroparticle generation is severe or for which truly 'macro-free' plasmas are required, a magnetic filter can be used, as has been investigated and described by several workers. One simple configuration is a curved 'magnetic duct' which stops line-of-sight transmission of macroparticles while allowing the transmission of plasma by virtue of an axial magnetic field which ducts the plasma through the filter [28-34].

ION IMPLANTATION

Metal ion beams have traditionally been somewhat more difficult to produce than beams of gaseous ions, because of difficulties in ion source design, and this has been an impedance to the development of metal ion implantation applications. With the development of the vacuum-arc-based ion source [22-22], however, metal ion beams of exceptionally high intensity have become available, providing a means for carrying out a wide range of metal ion implantation. Our implanter makes use of a multi-cathode, broad-beam source version [35,36]. The extractor grids are 10 cm in diameter, and this is thus also the beam maximum initial diameter; the multi-cathode assembly houses 18 separate cathode materials, between which one can switch simply and quickly. In typical operation the source is pulsed at a rate of several tens of pulses per second. For our standard pulse length of 250 μsec , a repetition rate of 40 pps corresponds to a duty cycle of 1%, and the mean beam current is then 1% of the peak (pulse) beam current. Beam extraction voltage is up to 100 kV, corresponding to an ion energy of up to several hundred keV because of the ion charge state multiplicity, and the ion current can be up to several

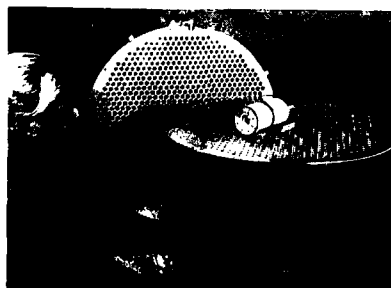


Fig. 1 Broad-beam multi-cathode vacuum arc ion source used for the work described here.

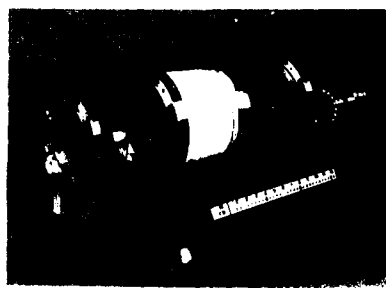


Fig. 2 Other versions of vacuum arc ion source, including a 50-cm diameter extractor and a thumb-sized version.

amperes peak and 10 ma time averaged delivered onto target. A photograph of the partially-disassembled broad-beam, multi-cathode source used for our implantation work is shown in Figure 1. Figure 2 shows some other source embodiments, including our largest and smallest.

Implantation is done in a broad-beam mode, without magnetic analysis of charge-to-mass beam components, and the ion trajectories are line-of-sight from ion source to target. The high ion beam charge density demands a very high degree of space charge neutralization of the beam, and any attempt at magnetic analysis would cause a major perturbation to the neutralizing electrons and disturb or destroy the neutralization, with consequent space charge blow-up and loss of beam. However, the metal ion beam is particularly pure, containing a high fraction of just the wanted metal ion species; this is because the plasma is formed solely from the cathode material where the cathode spots of the vacuum arc are active, and there is no carrier gas. Thus implantation in a non-mass-analyzed mode for many purposes (but not all) poses no problems.

The target to be implanted is introduced into the vessel through an air lock and the turnaround time between target changes can be as short as a matter of minutes. The target is mounted on a water-cooled holder suspended from a vertically moving shaft; the source-to-target distance is 65 cm. A magnetically-suppressed Faraday cup with a 5 cm diameter entrance aperture can be inserted into the beam immediately in front of the target, and the beam current can thus be adjusted prior to implantation and the number of beam pulses required to accumulate the required dose can be calculated.

The ion beam charge state distribution can be measured using a time-of-flight diagnostic. The detector measures the electrical current in the different Q/A (ion charge-to-mass ratio) states and provides a good measurement of the ion composition of the extracted ion beam. The time-of-flight system has been described in more detail elsewhere [37]. Oscillograms of the time-of-flight charge state spectra for Nd and Er beams are shown in Figure 3.



Fig. 3 Time-of-flight charge state spectra for Nd (left) and Er (right) ion beams produced by a vacuum arc ion source. The peaks are the electrical current into a Faraday cup; the major peak corresponds to $Q = 2+$ and the secondary to $Q = 3+$.

Beam is extracted in the broad range 20 - 100 kV, and the maximum voltage at which we have operated is 110 kV. Since the mean ion charge state for the rare-earths is close to 2, the mean energy of the beam ions is about twice the extractor voltage, thus spanning the approximate range 40 - 200 keV.

Ions incident upon the target are implanted to a depth determined by the ion energy and mass and the substrate atomic mass. The ion penetration is a statistical process that occurs via a many-step collision cascade in the substrate. This process has been studied by a number of workers and computer codes have been written by means of which the depth distribution of the implanted ions and many other features of the implantation can be calculated, the most widely known of which is the TRIM code (*Transport and Range of Ions in Matter*) [38], a Monte Carlo approach. In the ideal and simplified low-dose case, the depth distribution can be approximated by a gaussian, and then the mean of the distribution is the "projected range" R_p , and the width (standard deviation of the gaussian) is the "straggling", ΔR_p , of the implanted ion depth profile. For higher implantation doses various effects come into play that cause the

profile to depart from the ideal gaussian shape, such as sputtering away of the surface and previously-implanted material by the incident beam itself. For the parameters that typically apply here, the implantation range is typically a few hundred angstroms and the straggling about one hundred angstroms. An example of a TRIM-calculated prediction of the implantation profile is shown in Figure 4 for the case of Yb implanted into GaAs at a beam energy of 100 keV. Here the range is 289 Å and the straggling 109 Å.

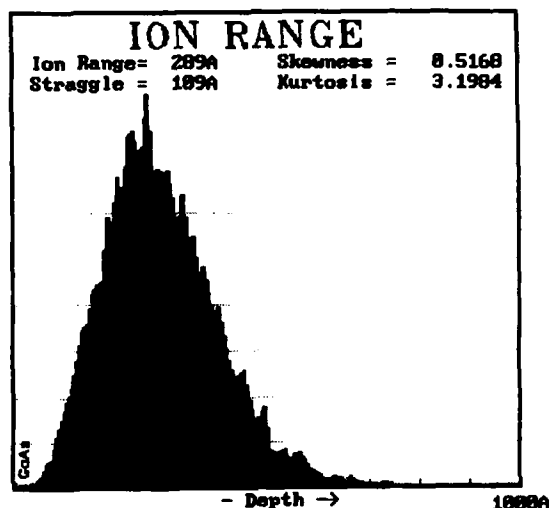


Fig. 4 TRIM-calculated depth profile for Yb implanted into GaAs at 100 keV.

As well as its traditional application for relatively low concentration doping of materials, ion implantation can also be used as a means for synthesizing buried layers such as silicides. In this case the implantation is done at quite high dose, $\sim 10^{17}$ ions/cm², and a post-implantation high temperature anneal is required; substrate heating and annealing by the ion implantation itself is an alternative possibility. We have demonstrated the method by doing iridium ion implantation to form buried IrSi₃ layers; this work has been reported elsewhere [39]

PLASMA DEPOSITION

Whereas in ion implantation the rare-earth species is energetically buried below the surface using high energy ion bombardment, an alternative approach is to allow the rare-earth plasma to deposit on the substrate surface at relatively low energy. In the latter approach the plasma is used "as-is", as a streaming plasma and not as an energetic ion beam, and the tool required is thus a plasma gun rather than an ion source. We have developed and used a number of different kinds of vacuum arc plasma guns and demonstrated their suitability for the growth of metallic thin films of thickness ranging from monolayers to microns. Films of all of the rare-earths can be formed, and by using an array of such guns multilayer structures can be fabricated.

For many applications it may be necessary that the plasma and film be free of the micron-sized macroparticles referred to above. The macroparticles can be removed from the plasma stream by incorporating a bent magnetic duct into the plasma source [34]. One such embodiment that we've made and used is shown in Figure 5. A photograph of plasma passing through a self-supporting duct, so that the plasma flow through the duct can be seen, is shown in Figure 6.

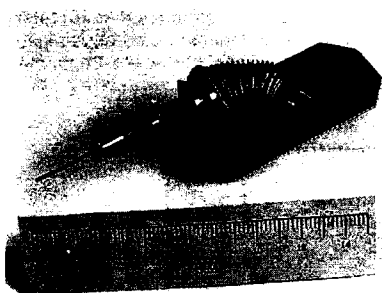


Fig. 5 Micro plasma gun with magnetic duct for filtering of macroparticles from the plasma stream.

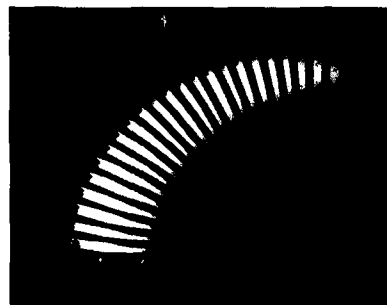


Fig. 6 Self-supporting magnetic duct with plasma streaming through it.

The plasma gun is positioned with the duct exit anywhere from a few to a few tens of centimeters from the substrate onto which deposition is to be formed. The gun is located entirely within the vacuum system, and the embodiment shown in Figure 5 can be baked to high temperature if desired. The instantaneous deposition rate (ie, during the plasma pulse) is typically of order several hundred up to 1000 Å/sec, and the time-averaged rate is ~ 0.01 to 1 Å/sec. Films in the 1 - 100 Å thickness range can be deposited very quickly, and the upper limit for convenient operation of these pulsed microguns is about a micron. Thicker films still can of course be made by scaling up the plasma sources, and dc operation is possible. By biasing the substrate negative by several tens of volts the plasma ion current to the substrate can be measured and related to the film thickness, providing a convenient monitor of the film growth. The bias need not necessarily be maintained throughout the deposition; it is an option to ground (or otherwise bias) the substrate, having determined the film thickness increment per pulse.

Multilayer structures can be synthesized by using two or more nearby plasma guns. The filtered microguns are small and simple and can readily be clustered together. We have also made a (non-filtered) multi-species gun which houses 10 separate cathodes and 6 separate substrates, all of which can be rotated into a desired alignment configuration; this device is shown in Figure 7.

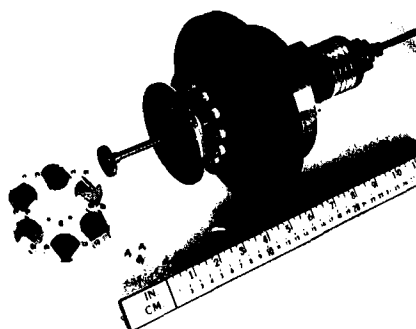


Fig. 7 Multi-cathode plasma gun. Any of 10 separate cathodes and 6 separate substrates can be rotated into place.

We have used these plasma guns for the formation of various kinds of surfaces, including for example monolayers of Re on Pt and Pt on Re for catalytic studies [40], diamond-like carbon films of thickness typically several hundred angstroms, films of a wide range of metals with thickness ranging from up to a micron [41], and some multilayer structures [41,42]. For example, thin films of Y are easily made, and by using two guns with different cathodes we formed an Y/Ti multilayer structure, both on a Si substrate. We've used a number of different diagnostic methods to examine the films deposited, including RBS, SEM, TEM, SIMS and in-situ ESCA. A disadvantage of ex-situ methods is post-deposition oxidation of the film. RBS data of an Y film approximately 0.5μ thick is shown in Figure 8, and of an Y/Ti multilayer structure in Figure 9. The Y film was made from 5,900 pulses of the gun, just under 1 Å/pulse.

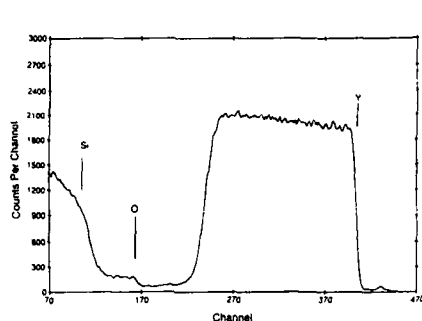


Fig. 8 RBS spectrum of Y film on Si.
Film thickness is about a half-micron.

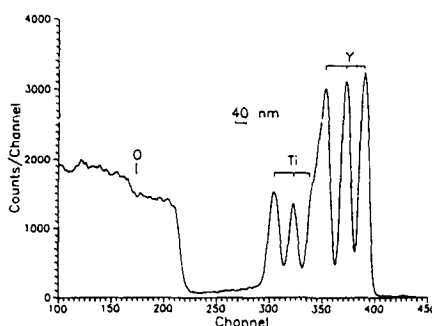


Fig. 9 Y/Ti multilayer structure with layer thickness about 400 Å.

METAL PLASMA IMMERSION ION IMPLANTATION

In the metal plasma immersion surface processing scheme, the substrate is repetitively pulse biased to high negative voltage while it is "immersed" in a metal plasma, so as to create a high voltage sheath at the substrate surface through which the plasma ions fall and are accelerated into the substrate. If the pulse voltage is sufficiently great then the ions acquire significant energy and ion implantation is brought about. This is thus an alternative means of doing ion implantation, that can be convenient in some parameter regimes. During that part of the processing cycle when the substrate pulse voltage is off but the plasma is on, then the metal plasma will deposit onto the substrate at low energy, forming a surface film. Subsequent high voltage substrate bias pulses will cause energetic ion bombardment of this thin (~monolayer) film, in turn causing recoil implantation of the film into the substrate — a thin surface film can be formed which is atomically mixed into the substrate. The method provides a means for doing surface modification and materials synthesis with a range of features and properties that could be valuable in many ways. The method is fundamentally simple and the hardware required is not exotic or difficult to make. We've carried out a number different experiments demonstrating some of the different kinds of surfaces that can be formed by the technique. Each involves the synthesis of a film or multilayer structure that is atomically mixed to the substrate. A review of these experiments and results has been presented elsewhere [14,43].

The atomic mixing that can be produced in this way is indicated in Figure 10, where RBS spectra are shown for two Y films produced side-by-side, one with and one without the pulse biasing feature. Here the Si substrate was repetitively pulse biased with -30 kV, 1μs pulses timed for the maximum of the plasma pulse. The equivalent time-averaged ion implantation current was several tens of microamperes onto the substrate of area several square centimeters. The mean ion charge state of the vacuum-arc-produced yttrium plasma was 2.3 [24], and thus the 30 kV voltage pulse corresponded to a mean ion energy of 70 keV. A second sample was

prepared under identical conditions except that the high voltage implantation pulse was not applied, thus providing a non-implanted sample for comparison. The samples were analyzed by 2.0 MeV He⁺ Rutherford Backscattering Spectrometry (RBS). The RBS resolution is indicated by the Gaussian-shaped profile obtained when pulse biasing is not applied. With pulse biasing the depth profile extends below the surface and has a shape that is qualitatively as expected for a combination of conventional ion implantation, recoil implantation, and surface deposition. A nominal depth of the implanted region (half width of the profile with an ad-hoc correction for the RBS resolution) is approximately 500 Å, which is comparable to the TRIM-calculated [38] range for 70 keV Y into Si of 470 Å. The RBS-measured dose was 1.0×10^{16} atoms/cm², in agreement with the dose expected from the accumulated number of pulses. This simple application of the method thus confirms that the technique works fundamentally as expected.

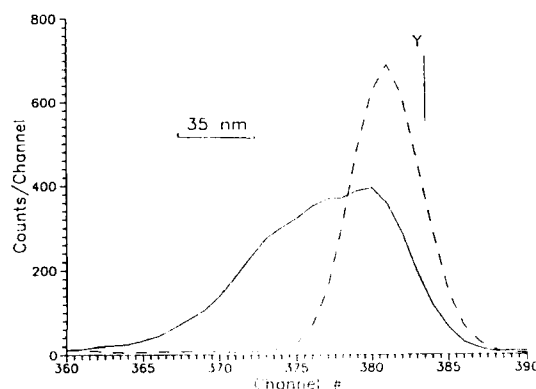


Fig. 10 Rutherford Backscattering spectra for Y into Si. The dashed curve is from the sample without pulse biasing and the solid curve from that with pulse biasing.

Many variations on the metal plasma immersion theme can be concocted. It provides a means of producing very high concentrations of rare-earth metals in the near-surface regions of the chosen substrate. A continuum of modified surfaces can be formed, spanning the conceptual space bounded at one end by plasma-deposited thin films lying entirely on top of the substrate and at the other by high energy ion implantation.

CONCLUSION

Metal plasma production by vacuum arc techniques provides a tool that is eminently suited to the rare-earths. Dense rare-earth plasmas can be created efficiently and simply, and the plasma so formed can be used directly for the synthesis of thin rare-earth films ranging in thickness from sub-monolayer up to about a micron, or the plasma generator can be incorporated within an ion source configuration and high energy rare-earth ion beams produced for doing ion implantation. Ion implantation is a convenient means for doping materials with any of the rare-earths, and layers of thickness up to about 1000 Å and having rare-earth concentration that can be varied over many orders of magnitude can be formed.

ACKNOWLEDGEMENTS

The work described here has been accomplished as a group effort. I am greatly indebted to my scientific colleagues including Drs. André and Simone Anders, Igor Ivanov, Xiang Yao, Kin-Man Yu, and Xavier Godechot. The mechanical design and fabrication of the sources and other equipment was done by a team led by Bob MacGill and including Mike Dickinson and

Bob Wright, and the electrical and electronics support was provided by Jim Galvin, Jan DeVries, Bud Leonard and Mark Rickard. This work was supported by the Electric Power Research Institute under Award RP 2426-27, the Army Research Office and the Office of Naval Research under Contract No. ARO 116-89, and the Department of Energy, Office of Basic Energy Sciences, Advanced Energy Projects, under Contract No. DE-AC03-76SF00098.

REFERENCES

1. See, for instance, "Ion Implantation and Plasma Assisted Processes", edited by R. F. Hochman, H. Solnick-Legg and K. O. Legg, (ASM, Ohio, 1988).
2. "Plasma Processing and Synthesis of Materials", edited by D. Apelian and J. Szekeley, Mat. Res. Soc. Symp. Proc. Vol 98, (MRS, Pittsburgh, 1987).
3. G. Deamaley, Nucl. Instr. and Meth. **B50**, 358 (1990).
4. M. Iwaki, Critical Rev. in Solid State and Mat. Sci., **15**, 473 (1989).
5. L. E. Rehn and P. R. Okamoto, Nucl. Instr. and Meth. **B39**, 104 (1989).
6. G. K. Wolf and W. Ensinger, Nucl. Instr. and Meth. **B59/60**, 173 (1991).
7. See, for instance, the proceedings of conferences such as those on Ion Implantation Technology, and Ion Beam Modification of Materials, in Nucl. Instrum. Methods.
8. J. R. Conrad, J. L. Radtke, R. A. Dodd, F. J. Worzala and N. C. Tran, J. Appl. Phys. **62**, 4591 (1987).
9. J. T. Scheuer, M. Shamim and J. R. Conrad, J. Appl. Phys. **67**, 1241 (1990).
10. J. Teudys, I. J. Donnelly, M. J. Kenny and J. T. A. Pollock, Appl. Phys. Lett. **53**, 2143 (1988).
11. H. Wong, X. Y. Qian, D. Carl, N. W. Cheung, M. A. Lieberman, I. G. Brown and K. M. Yu, Mat. Res. Soc. Symp. Proc. **147**, 91, (MRS, Pittsburgh, 1989).
12. X. Y. Qian, H. Wong, D. Carl, N. W. Cheung, M. A. Lieberman, I. G. Brown and K. M. Yu, 176th Electrochemical Society Meeting, Hollywood, Fla, October 15-20, 1989.
13. X. Y. Qian, M. H. Kiang, J. Huang, D. Carl, N. W. Cheung, M. A. Lieberman, I. G. Brown, K. M. Yu and M. I. Current, Nucl. Instrum. Meth. Phys. Res. **B55**, 888.
14. I. G. Brown, A. Anders, S. Anders, X. Yao, K. M. Yu and I. C. Ivanov, "Plasma Synthesis of Metallic and Composite Thin Films with Atomically Mixed Substrate Bonding", 8th International Conference on Ion Beam Modification of Materials, Heidelberg, Germany, September 7-11, 1992; to be published in Nucl. Instrum. Meth. **B** (1993).
15. See, for instance, J. M. Lafferty, ed., "Vacuum Arcs - Theory and Application", (John Wiley and Sons, New York, 1980).
16. R. L. Boxman, S. Goldsmith, S. Shalev, H. Yaloz and N. Brosh, Thin Solid Films **139**, 41 (1985).
17. D. M. Sanders, "Review of Ion Based Coating Processes Derived from the Cathodic Arc", J. Vac. Sci. Tech. **A7**, 2339 (1989).
18. C. Bergman, in "Ion Plating and Implantation", edited by R. F. Hochman, American Society for Metals, USA, 1986. (Proceedings of the ASM Conference on Applications of Ion Plating and Implantation to Materials, June 3-5, 1985, Atlanta, GA).
19. P. A. Lindfors, loc. cit. [17].
20. I. G. Brown, J. E. Galvin, and R. A. MacGill, Appl. Phys. Lett. **47**, 358 (1985).
21. I. G. Brown, in "The Physics and Technology of Ion Sources", I. G. Brown editor, (Wiley, N.Y., 1989).
22. I. G. Brown, Rev. Sci. Instrum. **63**, 2351 (1992).
23. I. G. Brown, B. Feinberg, and J. E. Galvin, J. Appl. Phys. **63**, 4889 (1988).
24. I. G. Brown and X. Godechot, IEEE Trans. Plasma Sci. **PS-19**, 713 (1991).
25. D. T. Tuma, C. L. Chen and D. K. Davies, J. Appl. Phys. **49**, 3821 (1978).
26. J. E. Daalder, Physica **104C**, 91 (1981).
27. I. I. Aksenov, I. I. Kononov, E. E. Kudryavtseva, V. V. Kunchenko, V. G. Padalka and V. M. Khoroshikh, Sov. Phys. Tech. Phys. **29**(8), 893 (1984).
28. I. I. Aksenov, V. A. Belous, V. G. Padalka and V. M. Khoroshikh, Sov. J. Plasma Phys. **4**(4), 425 (1978).
29. V. A. Osipov, V. G. Padalka, L. P. Sablev and R. I. Stupak, Instrum. and Exp. Techniques **21**(6), 173 (1978).

30. I. I. Aksenov, S. I. Vakula, V. G. Padalka, V. E. Strelitski and V. M. Khoroshikh, *Sov. Phys. Tech. Phys.* **25**(9), 1164, (1980).
31. V. S. Voitsenya, A. G. Gorbanyuk, I. N. Onishchenko and B. G. Safranov, *Sov. Phys. - Tech. Phys.* **9**(2), 221 (1964).
32. I. I. Aksenov, A. N. Belokhovostikov, V. G. Padalka, N. S. Repalov and V. M. Khoroshikh, *Plasma Physics and Controlled Fusion* **28**, 761 (1986).
33. J. Storer, J. E. Galvin and I. G. Brown, *J. Appl. Phys.* **66**, 5245 (1989).
34. S. Anders, A. Anders and I. Brown, submitted for publication in *Appl. Phys. Lett.* (1993).
35. R. A. MacGill, I. G. Brown and J. E. Galvin, *Rev. Sci. Instrum.* **61** (1990) 580.
36. I. G. Brown, J. E. Galvin, R. A. MacGill and F. J. Paoloni, *Rev. Sci. Instrum.* **61** (1990) 577.
37. I. G. Brown, J. E. Galvin, R. A. MacGill and R. T. Wright, *Rev. Sci. Instrum.* **58** (1987) 1589.
38. J. F. Ziegler, J. P. Biersack and U. Littmark, in "The Stopping and Range of Ions in Solids", Vol 1, edited by J. F. Ziegler (Pergamon, N.Y., 1985).
39. K. M. Yu, B. Katz, I. C. Wu and I. G. Brown, "Formation of Iridium Silicide Layer by High Dose Iridium Ion Implantation into Silicon", *Nucl. Instrum. Methods* **B58**, 27 (1991).
40. C. Kim, D. F. Ogletree, M. B. Salmeron, X. Godechot, G. A. Somorjai and I. G. Brown, "Preparation of Monolayers of Re and Pt on Metal Substrates Using a Pulsed Metal Plasma Deposition Source", *Appl. Surface Sci.* **59**, 261 (1992).
41. X. Godechot, M. B. Salmeron, D. F. Ogletree, J. E. Galvin, R. A. MacGill, K. M. Yu and I. G. Brown, "Thin Film Synthesis using Miniature Pulsed Metal Vapor Vacuum Arc Plasma Guns", *Mat. Res. Soc. Symp. Proc.* **190**, 95 (1991).
42. S. Anders, A. Anders, J. Kortright, K. M. Yu, I. G. Brown and I. C. Ivanov, "X-Ray Mirror Production by Vacuum Arc Deposition Techniques", International Conference on Metallurgical Coatings and Thin Films, San Diego, CA, April 1993.
43. I. Brown, in *Plasma Synthesis and Processing of Materials*, K. Upadhy, editor, (TMS, Warrendale, PA, 1993),

GROWTH OF ER DOPED SI FILMS BY ELECTRON CYCLOTRON RESONANCE PLASMA ENHANCED CHEMICAL VAPOR DEPOSITION

JIM L. ROGERS*, WALTER J. VARHUE* and EDWARD ADAMS**

*Dept. of Electrical Engineering, University of Vermont, Burlington, VT 05405

**IBM Corp., Essex Junction, VT. 05452.

ABSTRACT

Thin Si films doped with Er have been grown at low temperature by plasma enhanced chemical vapor deposition. The Er gas source is a sublimed organo-metallic compound fed into the process chamber. High doping concentrations without precipitation are possible because of the low deposition temperatures. The process relies on the beneficial effects of low energy ion bombardment to reduce the growth temperature. The ions as well as reactive chemical species are produced by an electron cyclotron resonance (ECR) plasma stream source. A hydrogen plasma stream is used to perform an in-situ pre-deposition clean to remove oxide from the Si surface. Film crystallinity and impurity concentration are determined by Rutherford backscattering spectrometry.

INTRODUCTION

Silicon is an indirect band gap semiconductor material and therefore is a low efficiency light emitter. This fact limits Si's potential for applications in the optoelectronics area. However, Si is presently the most important semiconductor material for the fabrication of solid state devices. There is a highly developed technology in the design and fabrication of Si integrated circuits for both logic and memory. This is due in part to Si's ability to grow a good thermal oxide as well as its other superior physical properties. Other than its inability to act as an efficient light source, Si is well suited for optoelectronic applications. It is transparent to wavelengths greater than 1.1 μm and can be used to fabricate long wavelength devices and short wavelength optical receivers. Attempts to overcome Si's shortcomings have included the heteroepitaxial growth of III-V direct gap materials such as GaAs¹ and InP on Si substrates. Another approach is to add impurities to the Si lattice which are luminescent. There is considerable interest in the use of rare earth dopants such as Er, Yb, Tm, Pr, Nd and Ho. The Er doped material is of particular interest because its luminescence peak is energetically located near the low loss, low dispersion window for optical fibers at 1.55 μm . The origin of the emission is the internal transition within the 4f states of the Er³⁺ ion. The degenerate 4f electronic states of the ion must be split in the field created by the host lattice to permit the optical transition.

Ennen et al.² have proposed the use of Si:Er for the fabrication of LED's and laser diodes. Attempts have been made to build Si:Er LED's using forward biased pn junctions as the pumping source.³ A sharply structured electroluminescence spectrum at 1.54 μm was observed but the quantum efficiency was too low for device applications. An evaluation of Si:Er material for the fabrication of LED's and other devices was performed by Xie et. al.⁴. It was concluded that Si:Er is not suitable for LED applications because of low emission power resulting from the long spontaneous transition lifetime and the limited solid solubility of Er in Si. However, it could be used in laser applications if an efficient external pumping mechanism could be developed. One of the recommendations for future research was to increase the concentration of Er in the Si material and thus increase the emission intensity for a given pumping process. The concentration of Er in the Si crystal is limited however by its solid solubility. It was also suggested that modification of the micro-environment around the Er impurities may also lead to an improvement in pumping efficiency. If large concentration Er or other rare earth element doped Si can be grown, the potential for electrically pumped lasers and optical amplifiers is greatly increased. This would open up an entirely new field, silicon light emitters for Si based devices.

Previous attempts to incorporate Er in Si have included ion implantation, MBE and MOCVD. Eaglesham et. al.⁵ studied the effect of microstructure on the photoluminescence (PL) of high-energy ion implanted Er in Si. The threshold for precipitation of ErSi_2 at 900 °C was determined to be $1.3 \times 10^{18} \text{ cm}^{-3}$. The 1.54 μm PL intensity however saturated at an Er concentration of only $5.0 \times 10^{17} \text{ cm}^{-3}$. The onset of precipitation in Czochralski grown Si enhanced light emission. Ennen et. al.³ deposited epitaxial Si:Er layers by a modified molecular beam process where the films were simultaneously implanted with 20 KeV Er ions. The resulting material concentration was $5.6 \times 10^{18} \text{ cm}^{-3}$. The samples were then annealed at 900 °C for 30 minutes. The material yielded the characteristic Er emission spectrum for both optical and electronic excitation. Efeoglu et. al.⁶ deposited Si:Er by MBE at 500-700 °C and measured the solid solubility to be $5.0 \times 10^{18} \text{ cm}^{-3}$. The observation of ErSi_2 precipitation began at a concentration of $10^{19} \text{ Er cm}^{-3}$.

Beach et. al.⁷ used UHV/CVD to deposit Si doped with Er with concentrations as high as $8 \times 10^{19} \text{ cm}^{-3}$. The substrate temperature was 650 °C. An organometallic dopant Er source was used, tris-1,1,1,5,5,5-hexafluoro-2,4-pentaedionato erbium (III). It was determined by SIMS that a few atomic percent of C and O contaminants were incorporated into the films.

This paper reports the progress towards the growth of rare earth doped Si by low temperature plasma enhanced chemical vapor deposition (PECVD). The goal of this investigation is to develop a commercially compatible technique to deposit thick, high concentration, precipitation free, rare earth doped semiconductors. The low temperature growth technique proposed is plasma enhanced chemical vapor deposition with an electron cyclotron resonance (ECR) source.

EXPERIMENTAL

The doped Si films were deposited by PECVD using an ECR plasma stream source. A sketch of the system is shown in Fig 1. The chamber is constructed of standard 8 inch diameter stainless steel vacuum flanges with Cu gaskets. The chamber is evacuated with a turbo pump backed by a Roots blower and rotary mechanical pump. Microwave power at 2.45 GHz is supplied to the system through a quartz window. The samples are placed and removed from the reactor through a load-lock chamber. The base vacuum of the system is 3×10^{-9} Torr. The wafer is supported on a SiC coated graphite block, which is radiantly heated from behind by a W filaments.

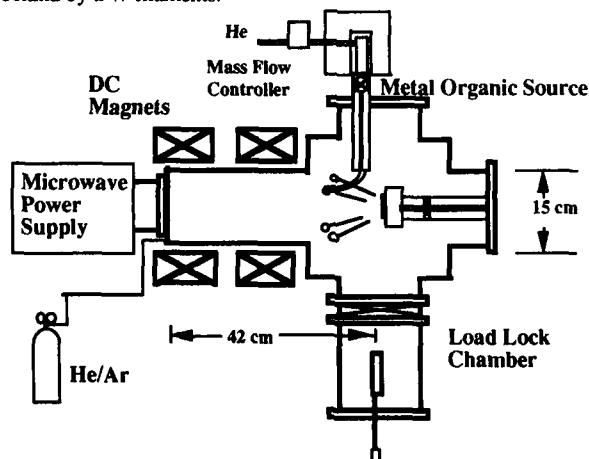


Figure 1. Electron cyclotron resonance deposition system with an organo-metallic dopant source.

The erbium source used was a sublimed organometallic compound, tris (2,2,6,6)-tetramethyl-3,5-heptanedionato erbium), abbreviated as $\text{Er}(\text{thd})_3$. This compound has a vapor pressure of 0.1 mm Hg at 165 °C. The sublimation source chamber consisted of a stainless steel cylinder located inside a standard laboratory oven. The oven was necessary to provide a uniformly heated gas source chamber which prevented the accumulation of the OM compound at cooler spots in the source cylinder. An earlier, more compact version was unacceptable because of a slow drift in the dopant stream composition over time. A He carrier gas flow of 3 sccm is passed through the source cylinder during deposition. The source chamber was operated between 40 °C and 100 °C. The delivery tube connecting the source chamber to the gas ring contained an in-line on-off valve which was heated to 120 °C to prevent condensation. Two gas rings, one for the Er compound and the other for the silane mixture were located 10 cm in front of the substrate. The gas ring was heated by the plasma stream to approximately 150 °C.

The Si films were deposited on (100) oriented Si substrates. The wafers were prepared by a degrease in trichloroethane followed by a rinse in methanol. Just prior to loading the samples in the chamber, the wafers were placed in a HF solution followed by a DI water rinse and finally blown dry with nitrogen. Following pump down, the substrates were plasma cleaned in-situ with a 50% Ar / 50% H_2 discharge for 5 min. Deposition was initiated by changing the gas flow to the resonance chamber and initiating the silane flow (2% silane in He, 10 - 20 sccm) to the substrate region. Three different gas combinations were fed upstream to the resonance chamber during deposition. The three combinations included; pure Ar, pure He and He with 10% Ar added. The chamber pressure was controlled by a Venetian blind throttle valve, between 1.0 and 5.0 mtorr. The substrate temperature in all cases was 375 °C. The microwave power used was varied between 200 and 500 W.

RESULTS AND DISCUSSION

Obtaining good epitaxial material proved to be a challenge in this investigation. Crystal quality was determined through the degree of signal channelling obtained from Rutherford Backscattering Spectrometry. The RBS analysis also gave a quantitative measure of most species contained in the films. For films deposited at low reactor pressure, equal to and below 1 mTorr, measurable Fe or Ni contamination (2 - 5 %) was found. This was a result of sputtering which occurred in the resonance chamber from the stainless steel walls. Upon inspection of the resonance chamber after a number of deposition runs, the entire surface was covered with a Si deposit, with the exception of a 3 cm wide ring located approximately 20 cm from the microwave window. The ECR zone was located between approximately 5 to 9 cm from the microwave window. Plotting the gradient of the magnetic flux density along the length of the resonance chamber revealed the cause of the metallic contamination. Energetic ions from the ECR zone are directed and further accelerated in the diverging magnetic field onto the chamber wall. The threshold for sputtering Fe and Ni is approximately 20 eV. Although the yield is low at these energies, the ionic flux in the ECR chamber is high ($> 50 \text{ mA/cm}^2$).

Before the start of this particular investigation involving the rare earth doping of Si films, epitaxial Ge films had been deposited on both Si and Ge substrates using this system.⁸ What at the time were believed to be slight variations in the reactor geometry, involving the removal of a limiting orifice to heat the gas rings in the plasma stream, contributed to the sputter contamination of the chamber walls which prevented epitaxial growth. Despite these problems, some valuable lessons were learned from this investigation.

The use of the organometallic compound $\text{Er}(\text{thd})_3$ and the plasma enhanced deposition process, was determined to be an efficient means of incorporating Er into the Si thin film material. In conventional MOCVD, the reactor operating pressures are comparatively higher, a few Torr and flow rates in the range of 100 sccm are typical. In these processes it is necessary to have a significantly volatile organo-metallic dopant source to obtain the desired dopant concentration level. Only a small fraction of the doping reagent is eventually incorporated into the depositing film. In the process studied here, reactor operating pressures are low, 0.5 to 5 mTorr, and the required partial pressure of the dopant compound is low. The atomic percent of Er incorporated into the Si film as a function of source temperature is plotted in Figure 2. It was possible to vary the dopant composition from 0.01 to 1.0 atomic percent or (1.0×10^{17} to

$1.0 \times 10^{20} \text{ cm}^{-3}$) for a moderate range of bubbler temperatures. The pressure drop across the supply line was monitored and the net flow of the OM gas was estimated to vary between 0.01 to 0.09 sccm for bubbler temperatures from 40 to 100 °C.

Quantifying the C or O content of the film by RBS is difficult, however it was estimated through modelling the spectra that in the worst case, the concentration was as high as 10 atomic percent. All of the runs performed with the organometallic dopant sources were performed with 500 W microwave power and 1.0 mTorr reactor pressure. With the goal of reducing the C and O concentration in the film, different operating conditions would be chosen. Using a higher operating pressure would reduce the energy and flux of both ionic species and electrons

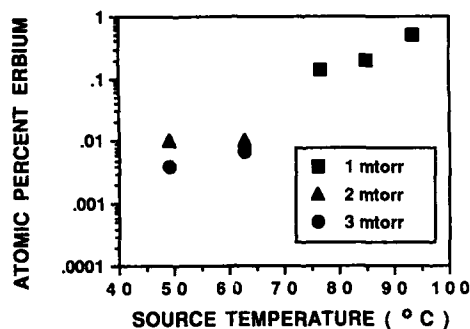


Figure 2. Atomic percent Er incorporated in the film as a function of OM source temperature as measured by RBS. Microwave power used was 500 W.

from the ECR region to the downstream position where the OM source is introduced. Modelling of the ECR discharge has shown that a significant high energy electron tail will extend down into the downstream position if the pressure is low, in the range of 1.0 mTorr. In the case of the OM Er source used here, $\text{Er}(\text{thd})_3$, the six Er-O bonds are the weakest and should be the first to break. The presence of high energy electrons ($> 20 \text{ eV}$), will contribute to the further dissociation of the OM source ligands, producing carbon and oxygen free radical species.

Energetic ion bombardment of the growth surface is an important consideration in the process necessary for low temperature epitaxial growth of Si thin films. Ohmi et. al. have presented results indicating that an ion energy of 25 eV using a sputtered source was optimal for epitaxial Si deposition.⁹ Deposition of epitaxial Si films with an ECR is typically performed with a discharge sustained in the ECR chamber using an inert gas such as He or Ar and with silane fed downstream near the substrate. Two previous investigations using ECR-PECVD obtained epitaxial Si using He^{10} or Ar^{11} as the discharge gas. This choice resulted in significantly different conditions required for epitaxial growth. The use of the more massive Ar ion required higher operating pressures which moderated the ion energy supplied to the surface and reduced atomic displacements in the growing film. In the study with the He discharge gas,¹⁰ lower optimum operating pressures were determined, 0.5 mTorr, indicating that sufficient ionic bombardment of the growing surface is necessary. In our previous studies involving the growth of epitaxial Ge films on both Ge and Si, a He discharge gas was used. Although it was possible to obtain epitaxial films, the He discharge was difficult to strike and the plasma stream was somewhat non-uniform. In the present investigation, three different discharge gas mixtures were tried. Pure He, pure Ar and a mixture of He with 10% Ar. It was observed that the deposition rates for the $\text{He}(10\% \text{ Ar})$ gas mixture were higher than either pure He or Ar as shown in Figure 3 a and b. A large fraction of the silane is dissociated by energy obtained from an excited He or Ar atom, this process is known as the Penning effect. The ionization cross section for Ar is approximately 10 times that of He and it has a lower threshold energy, 15.76 eV compared with 24.53 eV. This explains why the Ar plasma is better behaved, but not why the mixture enhances deposition rate. The long-lived metastable state of

He is more energetic than that of Ar, 19.8 eV compared with 11.55 eV, and this should contribute positively to the use of He as a Penning gas. However, the greatest effect is due to the enhanced transport through diffusion or drift of the lighter He atom to the substrate region. Both diffusion and drift of the excited atoms are inversely proportional to square root of the atomic mass, therefore transport of He is 10 times faster than Ar. The use of the He/Ar gas mixture will likely be useful in other ECR applications.

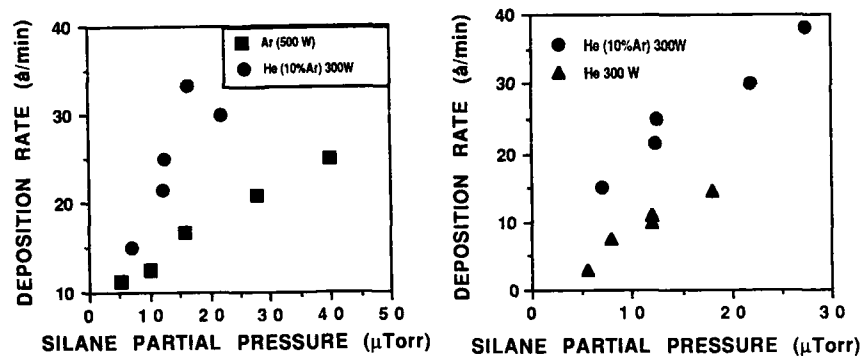


Figure 3a. and 3B. Deposition rate as a function of silane partial pressure for three difference discharge gas gas mixtures. The reactor pressure used in all cases is 3.0 mTorr.

CONCLUSIONS

The use of organo-metallic dopant sources with ECR-PECVD is an effective means of depositing semiconductor films with high dopant concentrations despite the low vapor pressure of the sources. Epitaxial growth of the Si film was not obtained in this investigation due to Fe and Ni contamination which resulted from sputtering of the resonance chamber wall. Care must be taken to eliminate large magnetic field gradients in the resonance chamber. This can be achieved by including a downstream shaping magnet. The choice of inert discharge gases, He or Ar, used in ECR-PECVD has significant effects on the dissociation and deposition rate of films grown in the downstream location. Ar ionizes easily, generating an abundant supply of electrons which results in a stable, easy to strike discharge. He, due to it lighter mass and more energetic metastable state efficiently transfers the discharge energy into the production of reactive species which are the precursors to film growth.

ACKNOWLEDGEMENT

The authors would like to thank the Air Force Office of Scientific Research for their support.

REFERENCES

1. B. Y. Tsaur, J. C. C. Fan, and R. P. Gale, Appl. Phys. Lett. 38 (3) 176 (1981).
2. H. Ennen, J. Schneider, G. Pomrenke and A. Axmann, Appl. Phys. Lett. 43 (10) 943 (1983).
3. H. Ennen, G. Pomrenke, A. Axmann, K. Eisele, W. Haydl and J. Schneider, Appl. Phys. Lett. 46 (4) 381 (1985).
4. Y. H. Xie, E. A. Fitzgerald and Y. J. Mii, J. Appl. Phys. 70 (6) 3223 (1991).
5. D. J. Eaglesham, J. Michel, E. A. Fitzgerald, D. C. Jacobson, J. M. Poate,

- J. L. Benton, A. Polman, Y.H. Xie and L. C. Kimerling, Appl. Phys. Lett. 58 (24) 2797 (1991).
6. H. Efeoglu, J. H. Evans, J. M. Langer, A. R. Peaker, N. L. Rowell, J-P Noel, D. D. Perovic, T. E. Jackman, and D. C. Houghton, Proc. of Mater. Res. Soc. (1991).
 7. D. B. Beach, R. T. Collins, F. K. Legoues and J. O. Chu, MRS Fall Meeting, Symp. E, Boston (1992).
 8. W. J. Varhue, J. M. Carulli, J. Miller and G. Peterson, J. of Appl. Phys. 71 (4) 1949 (1992).
 9. T. Shibata and T. Ohmi, J. of Electronic Mater. 19 (10) 1065 (1990).
 10. D. S. L. Mui, S. F. Fang, and H. Morkoc, Appl. Phys. Lett. 59 (15) 7 1887 (1991).
 11. K. Fukuda, J. Murota, S. Ono, T. Matsuura, H. Uetake and T. Ohmi, Appl. Phys. Lett. 59 (22) 2853 (1991).

ERBIUM DOPED SEMICONDUCTOR THIN FILMS
PREPARED BY RF MAGNETRON SPUTTERING

HONG KOO KIM ^{a)}, CHENG CHUNG LI ^{a)}, XIAO MING FANG ^{b)}, JAMES SOLOMON ^{c)},
GERALD NYKOLAK ^{d)}, AND PHILIPPE C. BECKER ^{d)}

a)University of Pittsburgh, Department of Electrical Engineering, Pittsburgh, PA 15261

b)Microtronics Associates, Pittsburgh, PA 15213

c)University of Dayton, Research Center, OH 45469-0167

d)AT&T, Bell Laboratories, Murray Hill, NJ 07974.

ABSTRACT

Highly Er-doped ($\sim 10^{20}$ atoms/cm³) silicon and silica films were deposited by RF magnetron sputtering. Erbium was doped into the host material by co-sputtering technique. Deposited films (0.5 - 1.2 μm thick) were characterized by photoluminescence (PL), secondary ion mass spectroscopy (SIMS), and fluorescence decay measurements. Er-doped silica glass films show a strong, room-temperature luminescence at 1.54 μm wavelength. In contrast, Er-doped silicon films show a weak luminescence at room temperature. However, a big enhancement in the Er³⁺ luminescence was observed after a proper annealing, for example, 900 °C for 30 to 120 min in air ambient, resulting in the luminescence intensities comparable with that of the Er-doped silica films. This enhancement is attributed to the oxygen incorporation into the Si host film during the annealing, thus forming an Er-doped oxide layer on top of the film. The result suggests that Er-O bonding plays important role in forming optically active erbium ions. Er-doped, three-component silicate glass ($\text{SiO}_2 + \text{Al}_2\text{O}_3 + \text{MgO}$) films were also sputter deposited to investigate the dependence of Er³⁺ luminescence on the host material's composition. Even stronger luminescence was observed from the Er-doped, three component silicate glass films compared with the Er-doped SiO_2 films.

INTRODUCTION

Erbium, when incorporated as a trivalent ion, shows an optical transition at 1.5 μm , coinciding with the low-loss window of standard optical telecommunications silica fiber. Er-doped fiber amplifiers with gain on the order of 30 dB have been reported. So far work has concentrated on fiber devices, but planar waveguide devices are of great interest for integrated optoelectronic circuits. In planar waveguide technology, integration of an optical amplifier on the same substrate with other components, such as semiconductor lasers, modulators, switches, beam steerers, or detectors is attractive. The performance of Er-doped optical amplifiers will be determined mainly by the two fundamental parameters: a lifetime of the metastable state and the amount of active Er³⁺ ions incorporated into the host material. A long lifetime of the metastable state will permit the required high-population inversions to be obtained under steady-state conditions using modest pump powers [1]. It has been reported that lifetimes on the order of 10 ms have been measured with Er-doped silicate glass fibers and Er-implanted silicon dioxide materials. The maximum amount of Er³⁺ ions that can be incorporated into the host material without showing a concentration quenching problem is an important factor in designing Er-doped optical devices. It is estimated that an Er concentration as high as $10^{20} - 10^{21}$ cm⁻³ is necessary for thin film optical amplifiers.

Erbium implantation experiments have been conducted by many groups for various materials such as Si, GaAs, and glass thin films [2,3,4,5]. Polman et al. demonstrated that MeV Er-implantation can be used to incorporate Er at high concentrations (0.1 at. %) with long lifetimes (10 ms) in SiO_2 and Si [4,5]. Although implantation techniques have advantages in that it can control a doping amount accurately while being compatible with thin film processing, it has

certain disadvantages too. The dopant profile by implantation is inherently fixed, normally of Gaussian shape with a certain width. Therefore, achieving an arbitrary profile of doping is extremely difficult, which is an important factor in fabrication of advanced devices with more complicated layer structures. Implantation is also a relatively low-thrput and high-cost process.

In this paper, we report on the sputter deposition of highly Er^{3+} -doped silicate glass thin films. We adopted sputtering technique since a sputtering technique overcomes most of the problems described above and has been widely used for deposition of various optical films.

EXPERIMENTAL

Er-doped SiO_2 films were deposited by RF magnetron sputtering. The system was pumped to a 10^{-6} Torr base pressure by a turbomolecular pump backed by a rotary vane pump. A two-inch diameter, $10\ \Omega\text{-cm}$ resistivity, (100) Si target was mechanically clamped to a water-cooled magnetron gun (Kurt J. Lesker's Torus 2C). Narrow stripes of 4N-purity Er plates were put on the Si target surface. Then Er was co-sputtered with a Si target in an Ar/O_2 ambient to deposit Er-doped SiO_2 films. With this method, the Er-concentration can be estimated and adjusted easily since the Er flux will be proportional to the total area of the Er stripes. The Er stripes were put in a radial direction on the Si target surface since the plasma density is radially symmetric on the target surface. Recently, Shmulovich et al. have reported sputter deposition of Er-doped silicate glass film on a silicon substrate showing signal enhancement up to 21 dB at 1.53 μm with 975 nm pumping [6,7]. In their case, an Er-doped sodium-calcium silicate glass target was first prepared with a fixed composition and then sputtered to deposit Er-doped films of similar composition. While the single target method may provide better uniformity of Er concentration in the deposited films, our co-sputtering technique allows easy adjustment of Er-concentration or glass composition. The substrates used in our experiments were (100) Si wafers (p-type; $0.01\ \Omega\text{-cm}$ resistivity) or fused-quartz plates (1 mm thick), and they were cleaned with a standard cleaning procedure. Prior to deposition, the target was presputtered for 5 min in order to remove any contamination. 0.5 - 1.2 μm thick Er-doped SiO_2 films were deposited at a substrate temperature of 350 $^\circ\text{C}$. The following deposition conditions were used for this work: target-substrate distance (1.5 - 2.0 inch), RF power (40 - 80 W), gas pressure (15 - 20 mTorr). The deposited films were anneal treated at 600 - 950 $^\circ\text{C}$ for 30 - 120 min in air ambient.

Photoluminescence spectroscopy was used to study the optical properties of the incorporated Er^{3+} ions. Photoluminescence (PL) measurements were performed at room temperature using the 488 nm line of an Ar^+ laser as a pump source with an excitation power in the range of 75 - 165 mW. Luminescence spectra were detected using a 0.25 m Jarrel-Ash monochromator and a room-temperature InGaAs photodetector. The pump beam was mechanically chopped at 80 Hz and the luminescence signal was collected using a lock-in amplifier. Fluorescence decay measurements were also performed using the 400 mW, 980 nm pump source.

The Er concentration and the host material's composition profile were analyzed by secondary ion mass spectroscopy (SIMS) measurement. A Perkin Elmer 6600 SIMS system was used with 6-keV O_2^+ ions for bombarding. The Er concentration was calibrated with an Al-implanted Si sample. It was assumed that the sensitivity for Er and Al is very similar in a Si host since the two atoms have similar ionization potentials (6.10 eV for Er and 5.99 eV for Al).

RESULTS AND DISCUSSION

Fig. 1a shows a room-temperature PL spectrum of a silica film deposited on a quartz substrate in an Ar/O_2 (95/5) ambient and annealed at 750 $^\circ\text{C}$ for 30 min. The Er-doped silica layer has a thickness of 0.5 μm and is estimated to have mid 10^{19} - 10^{20} Er atoms/ cm^3 . The

spectrum is peaked at $1.54\ \mu\text{m}$ and side peaks are observed at 1.53 and $1.55\ \mu\text{m}$ as shoulders. The wavelength region around $1.54\ \mu\text{m}$ coincides with the wavelength of the $^4I_{13/2} - ^4I_{15/2}$ transitions of Er^{3+} ($4f^1$). The relatively large width of the main peak ($200\ \text{\AA}$ FWHM) is a result of Stark splitting of the excited and ground state in the host field. Background luminescence in the shorter wavelength region is believed to originate from the quartz substrate. This attribution is based on the observation that the Er-doped silica films deposited on a Si substrate do not show any background luminescence. (See Fig.1b.)

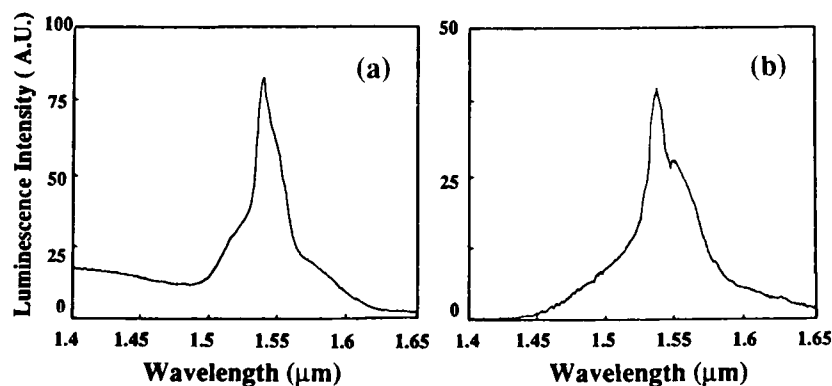


Fig.1 Room-temperature PL spectra of silica films deposited on a quartz substrate (a) and on a silicon substrate (b). Both films were deposited in an Ar/O_2 (95/5) ambient and annealed at $750\ ^\circ\text{C}$ for 30 min.

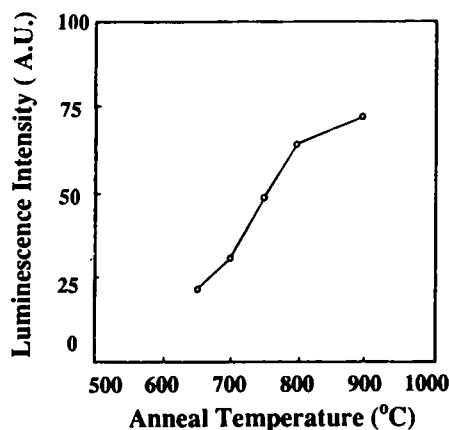


Fig.2 PL peak intensity of Er-doped silica films as a function of anneal temperature

Fig.2 shows temperature dependence of PL peak intensity of Er-doped silica films annealed at different temperatures ranging from 650 to $900\ ^\circ\text{C}$. The PL intensity increases monotonically with the increase of anneal temperature without showing clear saturation behavior in the temperature range used. To investigate further the annealing effects, fluorescence decay measurements were conducted for the $^4I_{13/2} \rightarrow ^4I_{15/2}$ transition. Fig.3a is a decay profile of the Er-doped SiO_2 films annealed at $800\ ^\circ\text{C}$ for 30 min. It shows two slightly different time constants: $1.4\ \text{ms}$ and $1.0\ \text{ms}$. This non-exponential behavior suggests that a nonradiative relaxation process is involved in the fluorescence via defects.

The defects may include voids or grain boundaries, which are usually of significant amount in sputter deposited SiO_2 films. Er to Er interaction may also be involved in this nonexponential decay process due to the high doping of Er.

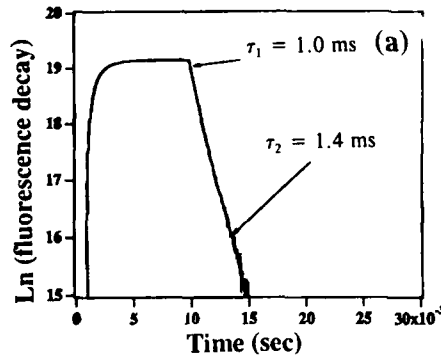


Fig.3b shows the decay times as a function of anneal temperature. The anneal time was fixed at 30 min. The monotonic increase in lifetime with anneal temperature is consistent with the dependence of PL intensity on anneal temperature as shown in Fig.2. This suggests that annealing of network defects might not be completed in this temperature range. This is a big contrast to the Er-implanted SiO_2 films case, where bulk glass plates or a thermally grown oxide films were used and showing saturation in lifetime above 700 °C range [4]. Different nature of defects in glass network is believed to cause this different anneal behavior.

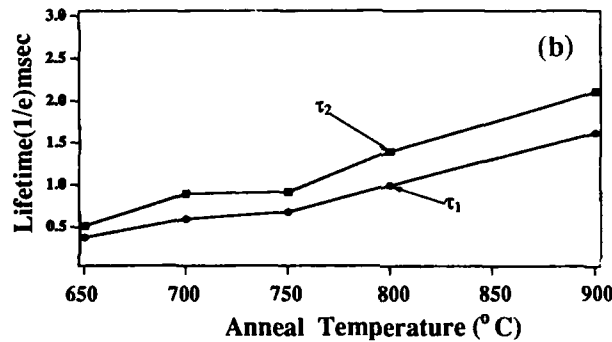


Fig.3 Fluorescence decay profile (a) and decay time constants as a function of anneal temperature (b)

In order to investigate the role of oxygen in the incorporation of Er^{3+} ions, Er was co-sputtered with Si in pure Ar ambient also and then compared with the result of the Er-doped SiO_2 films. The two films were deposited under the same condition except for the ambient gas. Fig.4 shows PL spectra of the Er-doped Si films deposited in pure Ar ambient and annealed in air ambient at different conditions: 800 °C for 30 min, 900 °C for 30 min, and 900 °C for 120 min. The Er-doped Si film does not show strong Er^{3+} luminescence even with 800 °C annealing. This is a big contrast to the case of the Er-doped films deposited under Ar/O_2 ambient. It is interesting to note that Er^{3+} -luminescence peak begins to appear at higher temperature annealing, i.e., 900 °C. This indicates that the high temperature annealing enhances the formation of optically active erbium ions. Annealing of the network defects might be involved in this process as we discussed in the Er-doped silica glass case. However, we attribute this enhancement to the oxidation of Er-doped Si films. Since the sample was annealed in air ambient, oxygen atom might have diffused into the Si host material. Thus Er atoms coordinate with more oxygen atoms, forming Er^{3+} ions. It should also be mentioned that sputter deposited Si films have generally more voids than thermally grown poly Si. Therefore, the diffusivity of oxygen is expected to be high in these sputter deposited Si films.

SIMS analysis was conducted to characterize the amount of oxidation of the Er-doped Si film during the annealing [8]. Fig.5 shows a SIMS profile of the Er-doped Si film annealed at 900 °C for 30 min in air ambient. Taking into account the fact that the calibration process involves a certain amount of ambiguity, we estimate that the film has mid 10^{19} - 10^{20} Er atoms per cm^3 . The oxygen profile shows an increase near the surface. This is believed to be due to the oxidation of Si during the annealing process. The high background level of oxygen across the Si layer is an artifact due to the use of oxygen ions for bombarding the films. Another evidence of the oxidation of the surface layer is the apparent increase of the Si concentration near the surface. The ion yield of Si in oxide materials is generally higher than that in pure silicon

materials. The oxide layer thickness is estimated to be $0.2\text{ }\mu\text{m}$. The diffusivity of oxygen in amorphous Si at this temperature range (above 900°C) makes this diffusion possible. Comparison of the PL intensities of the two samples annealed at 900°C provides another evidence of this diffusion process. The PL intensity is doubled as we anneal four times longer. This result is well matching the square-root relationship between diffusion depth and time in diffusion theory.

Our observation of the enhancement of Er^{3+} luminescence with incorporation of oxygen in the sputter deposited Si host is consistent with the report about the effect of oxygen in Er-implanted Si [9]. In Er-implantation experiments with Si material, it has been found that Er^{3+} luminescence intensity depends on oxygen concentration in Si host, showing almost two order of magnitude stronger luminescence in the presence of oxygen atoms compared with that of pure Si host.

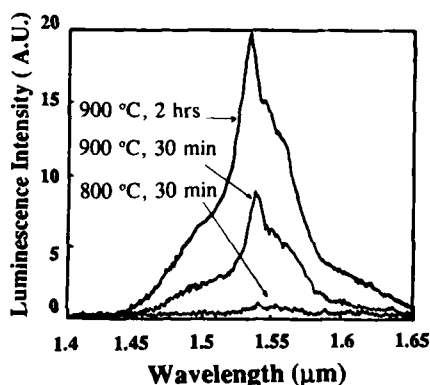


Fig.4 PL spectrum of Er-doped Si films deposited in pure Ar ambient and annealed in air ambient at different temperatures and times

The local chemical environment around Er is believed to be important in determining its optical activity. The $^4I_{13/2} \rightarrow ^4I_{15/2}$ transition in the free atom is dipole forbidden. Only when the crystal field of the host breaks inversion symmetry and mixes states of opposite parity is the transition allowed. Because the magnitude of the crystal field splitting, which determines the transition probability, depends on the symmetry and chemical nature of the ligands bound to Er, it is not surprising that the two local environments leads to very different degrees of optical activity. Therefore, shorter and more ionic Er-O bonds might be associated with more intense Er luminescence relative to the case of Er configured with longer covalent Er-Si bonds [9].

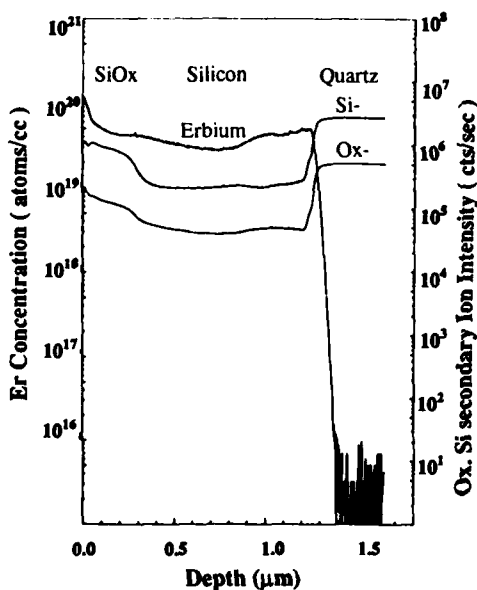


Fig.5 SIMS profile of the Er-doped Si film showing oxidized surface layer

In Er-doped optical fiber materials research, Er-doped silica codoped with Al shows improvements of up to 10 times of

the maximum concentration that can be doped without showing significant quenching effects [1]. The role of Al has been explained in terms of solution chemistry [1]. Al_2O_3 forms a solvation shell around the rare-earth ion and the resultant complex is readily incorporated into the silica network. While Al has been added as a codopant to Er-doped silica fibers, glass composition can be varied tremendously different ways by adding other oxides, called network modifiers. Network modifiers such as Mg change or modify the basic properties of glass, such as index of refraction, thermal expansion, absorption, and melting point.

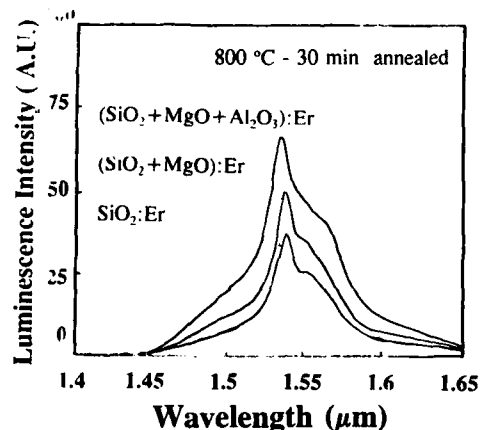


Fig.6 PL spectra of Er-doped silicate glass ($\text{SiO}_2 + \text{Al}_2\text{O}_3 + \text{MgO}$) films

We have conducted sputter deposition of Er-doped silicate glass ($5 \text{ SiO}_2 + 2 \text{ Al}_2\text{O}_3 + 2 \text{ MgO}$) films. Our preliminary results show that the three-component silica-host films show stronger Er^{3+} -luminescence than the pure-silica-host films and require lower anneal temperatures. The results suggest that Al is helping the incorporation of Er^{3+} ions, possibly by reducing any tendency to form erbium clusters. It is also clear that the addition of network modifiers softens the network structure, thus allowing a lower temperature annealing to cure the defects.

ACKNOWLEDGEMENT

The authors are grateful to Professor D. W. Langer for fruitful discussions and to Dr. M. Frost at Evans East for SIMS measurements.

REFERENCES

1. W. J. Miniscalco, *J. of Lightwave Technology*, **9**, 234 (1991).
2. H. Ennen, J. Schneider, G. Pomrenke, and A. Axmann, *Appl. Phys. Lett.*, **43**, 943 (1983).
3. G. S. Pomrenke, H. Ennen, and W. Haydl, *J. Appl. Phys.*, **59**, 601 (1986).
4. A. Polman, D. C. Jacobson, D. J. Eaglesham, R. C. Kistler, and J. M. Poate, *J. Appl. Phys.*, **70**, 3778 (1991).
5. A. Polman, J. S. Custer, E. Snoeks, and G. N. van den Hoven, *Appl. Phys. Lett.*, **62**, 507 (1993).
6. J. Shmulovich, A. Wong, Y. H. Wong, P. C. Becker, A. J. Bruce, and R. Adar, *Electronics Letters*, **28**, 1181 (1992).
7. J. Shmulovich, Y. H. Wong, G. Nykolak, P. C. Becker, R. Adar, A. Bruce, D. J. Muehlner, G. Adams, and M. Fishteryn, *International Conference on Integrated Optics and Optical Fiber Communication*, Post Deadline Paper PD18-1, San Jose, CA, February 21-26, 1993.
8. H. K. Kim, C. C. Li, and X. M. Fang, submitted to *Appl. Phys. Lett.*, 1993.
9. D. L. Adler, D. C. Jacobson, D. J. Eaglesham, M. A. Marcus, J. L. Benton, J. M. Poate, and P. H. Citrin, *Appl. Phys. Lett.*, **61**, 2181 (1992).

Er-DOPING IN SILICON BY PULSED LASER IRRADIATION

KENSHIRO NAKASHIMA

Nagoya Institute of Technology, Department of Electrical and Computer Engineering,
Showa-ku, Nagoya 466, Japan

ABSTRACT

Erbium ions were successfully doped in silicon by pulsed laser irradiation above the threshold laser energy density. Photoluminescence peaks at 1.54, 1.59 and 1.64 μm from Er-optical centers were observed after annealing of Er-doped samples. The intensity of the 1.54 μm Er-emission band increased upon increase in the laser energy density, and then gradually decreased after reaching the maximum, due to the laser sputtering of the silicon substrate. Oxygen atoms, which were unintentionally codoped with Er-ions, were found to be distributed in the same region as in Er-ions, and were suggested to play roles to activate Er-optical centers. The maximum concentration of Er-ions doped in the solid state regime were estimated to be the order of 10^{18} cm^{-3} by the Rutherford back-scattering measurements.

INTRODUCTION

Rare-earth ions in semiconductors have a potential for development of optoelectronic integration. Especially Er in Si has attracted an attention for its features to emit sharp luminescence (PL) at 1.54 μm under optical excitation or electronic injection. Several methods have been applied to dope Er atoms into Si substrates; ion implantation[1], molecular beam epitaxy [2] and doped crystal growth [3]. In spite of much efforts to realize intense luminescence in high efficiency, none of the methods are successful as yet in obtaining Er-doped Si with high performance.

In this paper a new method using pulsed laser irradiation is described to be applicable for doping Er ions into Si substrates. This method requires only a pulsed laser (a dye laser in this case) with high enough output energy for doping. Laser fluences are restricted not to exceed a critical value to melt Si surface. We, therefore, are concerned in the present experiment with the impurity-doping in the solid state regime. Since the pulsed laser irradiation on commercial grade floating zone (FZ) Si, which contains little amount of oxygen and carbon impurities, is essentially a defect-free process [4], as far as PL and DLTS studies concerned, this doping method does not necessarily require high temperature anneal to remove process-induced defects. In spite of this fact, heat-treatment is necessary for enhancing the PL intensity from Er ions. The PL, the secondary ion mass spectrometry (SIMS) and Rutherford backscattering measurements (RBS) are used to detect Er ions doped and their depth profiles. The PL intensity at 1.54 μm and the amount of doped Er ions are found to be dependent on the fluences of the incident pulsed laser.

EXPERIMENTAL

Samples used are mainly phosphorus-doped floating-zone (FZ) Si of a commercial grade ($15 \Omega\text{cm}$). After cleaning mirror surfaces with a solution of NH_4OH and H_2O_2 , erbium with 4 ninespurity was deposited in a vacuum at 5×10^{-6} Torr. One shot from a pulsed dye laser (wave length; 584nm, pulse width; 500ns) was incident to the Er-deposited sample surface through a quartz window of a cryostat evacuated to 2×10^{-6} Torr. The energy density was ranged from 0 to 2.1 J/cm^2 . After rinsing the sample with 1% HF solution, PL was excited with the laser line at 514 or 488 nm from an Ar ion laser, and detected by a cooled Ge diode. PL was measured mainly at 77K, and at 4.2K when the high resolution detection was required. The annealing in a gold image furnace

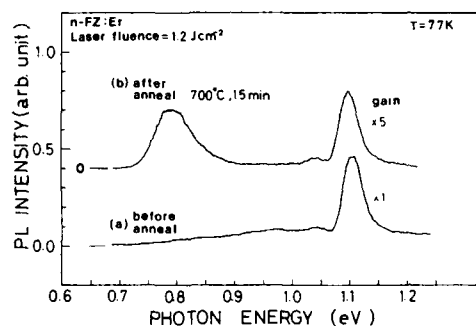


Fig.1 PL-spectra for Er-doped samples (n-type FZ) irradiated with laser fluences of 1.2 J/cm^2 ; (a) before anneal and (b) after anneal at 700°C for 15 min in N_2 -gas ambient.

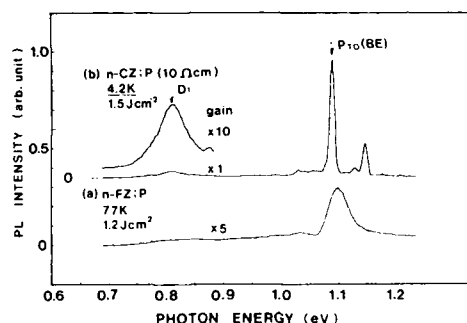


Fig.2 PL-spectra of reference n-type FZ and CZ samples without Er doping; (a) FZ irradiated with 1.2 J/cm^2 laser fluence and annealed at 750°C for 15 min, and (b) CZ irradiated with 1.5 J/cm^2 and annealed at 700°C for 15 min.

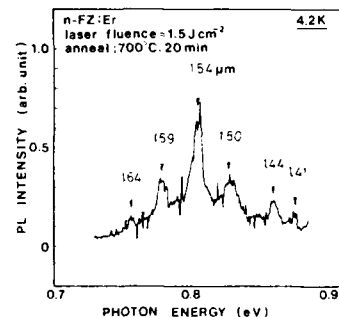


Fig.3 Er-PL spectrum of a sample irradiated with 1.5 J/cm^2 laser fluence. The spectral resolution is 5 nm.

was performed in the nitrogen gas atmosphere. Samples were placed on a Si wafer with a doped-face down to avoid impurity contamination.

RESULTS AND DISCUSSION

Figure 1 shows the PL spectra for Er-doped FZ Si irradiated with laser energy density of 1.2 J/cm^2 , observed at 77K. The band at 1.1 eV comes from the near band edge luminescence. After laser irradiation (Fig.1(a)) the PL spectrum at 0.8 eV due to Er^{3+} is not observable, but it comes up after annealing at 600°C and above as shown in Fig.1(b). The spectrum is not well resolved due to the low resolution of the spectrometer. Almost of all the Er film deposited on the samples is sputtered off by laser irradiation, and the sample is rinsed in 1% HF solution before PL measurements. Er atoms, therefore, were not found on the surface as observed by Auger electron spectrometry (AES). As shown later secondary-ion mass spectroscopy (SIMS) clearly shows in-depth profiles of doped-Er ions. In order to test whether the PL band at 0.8 eV really comes from Er ions, we examined the reference PL spectra from FZ and CZ materials processed without Er-deposition by otherwise the same process adopted for Er-doping. Fig.2(a) shows the result for FZ material after laser irradiation (1.2 J/cm^2) and anneal (700°C , 20 min), observed at 77K. Laser irradiation induces no observable

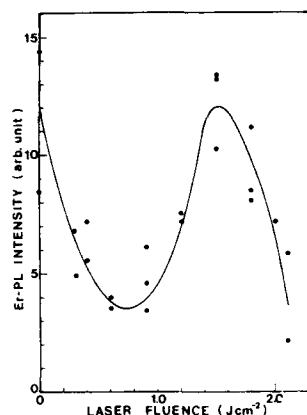


Fig.4 Laser fluence dependence of the Er-related emission line at 0.8 eV. Each sample was annealed at 700 °C for 20 min.

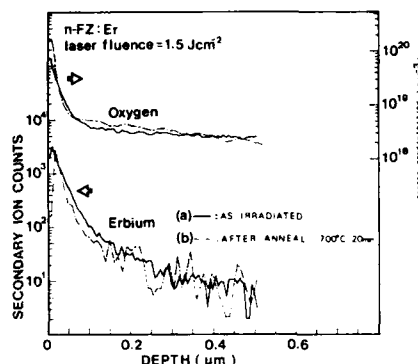


Fig.5 SIMS profiles of Er and O in Er-doped FZ samples subjected to laser irradiation of a fluence 1.5 J/cm²; (a) as irradiated and (b) after anneal at 700 °C for 20 min.

change in PL spectrum. On the other hand, as shown in Fig.2(b), a broad band at 0.8 eV appeared in CZ (p-doped, 10Ωcm) samples processed by almost the same way as that for FZ samples. In this case PL was measured at 4.2K in order to get a well resolved spectrum. The band at 0.8 eV should correspond to the D1 line[5, 6] due to dislocations induced by laser irradiation. Due to this fact we used FZ materials not to confuse the Er³⁺ ion-PL with dislocation-PL. Fig.3 shows a high resolution PL spectrum of a FZ sample irradiated with a 1.5 J/cm² laser energy density and annealed for 20 min at 700°C. Three emission peaks at 1.54, 1.59 and 1.64 μm are likely to correspond to the Er³⁺ ions occupying tetrahedral symmetry (either substitutional or interstitial) in the Si lattice, as suggested by Tang et al.[7] Except for these peaks, three other emission peaks at higher energy side are observed, which possibly reflect the local surroundings involving the Er³⁺ ions.

The PL intensity of various luminescence lines at 4.2K have been measured as a function of excitation power of Ar⁺ ion laser. The intensity of the phonon side band of the bound exciton recombination (P_{70} in Fig.2(b)) shows linear dependence on the excitation power, indicating that excitonic recombination dominates over the emission process.[8] The Er³⁺-PL intensity, I , varies as $I \propto L^{0.5-0.6}$, where L represents the excitation power. Since the PL intensity due to laser-irradiation induced dislocations increases more slowly as an increase in the excitation power, we can clearly find out the PL due to Er³⁺ ions.

Figure 4 shows the PL intensity of the Er-related emission band at 0.8 eV for the samples subjected to irradiation with various laser energy densities and subsequent anneal at 700°C for 20 min. We distinguish between three regions of the laser energy density P ; (1) $P < 0.9$ J/cm², (2) 0.9 J/cm² $< P < 1.6$ J/cm², (3) 1.6 J/cm² $< P < 2.1$ J/cm². The region (1) corresponds to laser-sputtering of the deposited Er-film. Because of the low energy density the Er-film still remains on the sample surface. Erbium-oxides are formed during annealing in the N₂ gas flow, which are also emission sources of the Er-related luminescence. This is assured by AES measurements on the Er-deposited samples which have been annealed in the N₂ gas ambient (700 °C, 20min) without laser pulse irradiation, indicating that Er and O atoms are distributed in the same region of the deposited film. Increasing the laser energy density in this region, the amount of sputtered-off Er atoms increases, and then the decrease in the residual Er-film thickness leads to the decrease in PL intensity.

The region (2) corresponds to Er-doping by laser irradiation, where Er deposited on the surface was not found due to both sputtering and doping of Er as measured by AES.

SIMS measurements on laser-irradiated samples (1.5 J/cm^2 , pre- and post-anneal) clearly show that Er atoms are doped to the depth of about $0.4 \mu\text{m}$ in this case. The results are illustrated in Fig.5. Curves (a) and (b) in Fig.5 represent Er-depth profiles in an as-irradiated and an annealed (700°C , 20 min) sample, respectively. Unfortunately it is not possible to convert secondary ion counts to Er concentration at present. After annealing at 700°C the Er-distribution moves slightly toward the sample surface possibly on account of the small segregation constant. As stated before the laser energy density 1.5 J/cm^2 is not sufficient for melting the sample surface, so that Er atoms are doped in the solid state regime. Figure 5 also shows oxygen in-depth profiles incorporated in the sample at the same time of Er-doping. The origins of oxygen are likely to be erbium oxides involved in the as-deposited Er-film. After annealing an oxygen-profile also shifts toward the surface, and shows a steeper distribution than that before annealing, as if oxygen atoms were attracted by Er ions. The oxygen concentration was evaluated using a standard sample from Charles Evans & Associates. As shown in Fig.1, Er-optical centers become emissive by this annealing process, which probably serves not to anneal out the irradiation-induced defects, but to arrange the surroundings of Er ions.

In the region (3) the sputtering process of the Si substrate competes with the Er-doping process. The former will begin to dominate the whole process with increasing the laser fluence. Therefore the maximum doping efficiency will be expected at some laser energy density in this region. Fig.6 shows an RBS spectrum after a 700°C anneal (20min) of an Er-doped sample with 2.0 J/cm^2 laser irradiation. The Er-profile has a peak concentration at 50 nm from the surface, and is distributed to the depth of about $0.2 \mu\text{m}$, which is consistent with SIMS profiles. The maximum Er concentration has been estimated to be 10^{18} to 10^{19} cm^{-2} from the detection limit of the RBS system. When the laser energy density exceeds a critical value to melt the sample surface (about 2.5 J/cm^2 in this case), another doping event, accompanied by the rapid phase transition from the liquid to solid state, dominates the whole process. Experiments on doping in the liquid phase are continued at present.

As stated before the annealing of samples at 700 to 750°C is a necessary process to get the maximum intensity of the Er-PL at $1.54 \mu\text{m}$. Oxygen atoms are likely to play an important role for enhancing the Er-PL[9,10,11] in also the present experiment. Fig.7 shows the result of isothermal annealing of the Er-PL and the near band edge luminescence (NBL), performed at 700°C . The laser energy density was 1.8 J/cm^2 in this case. After anneal for 60 seconds the NBL was rapidly decreased in the intensity to less than 1% of that before annealing, followed by an appearance of a broad luminescence band at lower photon energy around 0.9 eV . At this moment the Er-PL was scarcely observed. The NBL gradually grows after the subsequent anneal, and

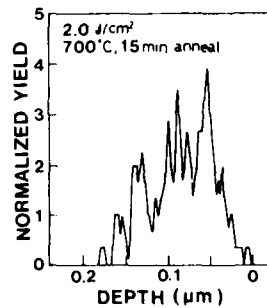


Fig.6 Er portion of RBS spectrum after a 700°C anneal of an Er-doped sample with 2.0 J/cm^2 laser irradiation.

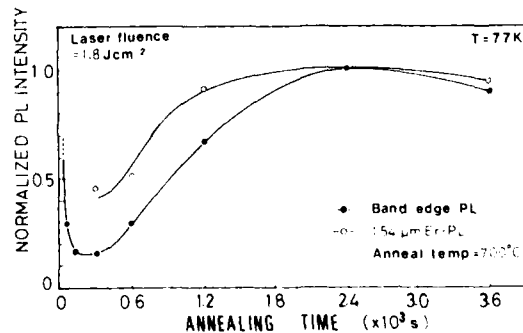


Fig.7 Isothermal annealing curves of both $1.54 \mu\text{m}$ -Er and the near band edge luminescence lines. The sample was irradiated with 1.8 J/cm^2 laser fluence and annealed at 700°C .

reaches the maximum intensity after the 40 min-anneal, passing the minimum at 300 seconds. Even at the maximum, the NBL intensity is only a few percent of that before annealing. The similar annealing behavior of the NBL is observable even at the 500 °C stage. The nonradiative centers, which are probably induced by the migration of oxygen atoms contained or doped in FZ materials, should be responsible for the change in the NBL intensity. It is well known that oxygen atoms become mobile at 450 to 500 °C to form oxygen aggregation. The increase of the Er-PL intensity is almost parallel to the recovery of the NBL. These results together with investigations on oxygen contribution[9,10,11] suggest that the mobile species during annealing, which play roles to enhance the Er-PL, might also be oxygen atoms. In fact oxygen profiles doped by the laser irradiation move toward the surface after anneal at 700 °C, as stated before.

CONCLUSION

The pulsed laser irradiation has been applied for doping Er atoms in silicon, and was found to provide a useful and convenient method to dope Er^{3+} optical centers. We have incorporated about 10^{18} to 10^{19} Er/cm^3 in the region 0.2 μm deep from the surface after 2.0 J/cm^2 laser irradiation. Although this method is a defect-free process, the subsequent annealing was necessary to activate Er^{3+} -centers. SIMS measurements revealed that oxygen atoms were unintentionally doped in the same region as that of the Er^{3+} ion distribution. The Er luminescence grows up in a similar manner to that of the recovery of the near band edge luminescence in both isothermal and isochronal anneals. The migration of oxygen atoms was inferred to be responsible for arranging the surroundings of Er^{3+} optical centers. Efforts to obtain the intense PL at room temperature are necessary for realizing light-emitting diodes, and are under way.

ACKNOWLEDGEMENT

The authors express sincere thanks to Dr. M. Katayama of Nippon denso Co., Ltd for SIMS measurements. This paper was supported in part by a Grant-in-Aid for Scientific Research from the Ministry of Education, Science and Culture.

REFERENCES

1. H. Ennen, J. Schneider, G. Pomrenke, and A. Axmann, *Appl. Phys. Lett.* **43**, 943(1983).
2. H. Ennen, G. Pomrenke, A. Axmann, K. Eisele, W. Haydl, and J. Schneider, *Appl. Phys. Lett.* **46**, 381(1985).
3. V. V. Petrov, V. S. Prosolovich, V. D. Tkachev, G. Tsyrulkevich, and Yu. A. Karpov, *Sov. Phys. Semicond.* **19**, 474(1985).
4. K. Nakashima, *Mater. Sci. Forum* **38-41**, 219(1989).
5. N. S. Minaev, A. V. Mudryi, and V. D. Tkachev, *Sov. Phys. Semicond.* **13**, 233 (1979).
6. R. H. Uebbing, P. Wagner, H. Baumgart, and H. J. Queisser, *Appl. Phys. Lett.* **37**, 1078(1980).
7. Y. S. Tang, Zhang Jingping, K. C. Heasman, and B. J. Sealy, *Solid State. Commun.* **72**, 991(1989).
8. T. Schmidt and K. Lischka, *Phys. Rev.* **B45**, 8989(1992).
9. P. N. Favennec, H. L'Haridon, D. Moutonnet, M. Salvi, and M. Gauniau, *Jpn. J. Appl. Phys.* **29**, L524(1990).
10. J. Michel, J. L. Benton, R. F. Ferrante, D. C. Jacobson, D. J. Eaglesham, E. A. Fitzgerald, Y. H. Xie, J. M. Poate, and L. C. Kimerling, *J. Appl. Phys.* **70**, 2672 (1991).
11. D. A. Adler, D. C. Jacobson, D. J. Eaglesham, M. A. Marcus, J. L. Benton, J. M. Poate, and P. H. Citrin, *Appl. Phys. Lett.* **61**, 2181(1992).

Er³⁺-DOPED SILICON PREPARED BY LASER DOPING

T. ASATSUMA*, P. DODD, J. F. DONEGAN, J. G. LUNNEY, AND
J. HEGARTY

Department of Pure and Applied Physics, Trinity College, Dublin 2, Ireland

* Present address : Corporate Research Laboratories, Sony Corporation, 6-7-35
Kitashinagawa, Shinagawa-Ku, Tokyo, 141, Japan

ABSTRACT

We have carried out an investigation of the laser doping of Si with rare-earth ions. In this technique a silicon surface coated with a thin layer of the rare-earth metal is melted with a pulsed laser, the dopant is mixed in the molten layer, and incorporated in the crystal during regrowth. Er was chosen for the main part of our work as it is the best characterized of the rare-earth ions in Si. Luminescence is observed around 1.54 μ m and is assigned to optical transitions on Er³⁺ ions. This preliminary study shows that this new technique is viable for the production of optically active Er³⁺ in Si.

INTRODUCTION

Silicon has dominated the world of electronic devices for the last 30 years. Despite its indirect bandgap the simplicity of this elemental semiconductor means that Si still accounts for over 95% of all electronic devices. Until recently it was expected that Si would not make a significant contribution to the newer generation optoelectronic devices due to the weak radiative recombination processes at its indirect bandgap. However, the discovery of highly luminescent porous silicon and the incorporation into silicon of luminescent rare-earth ions now places silicon optoelectronics in the forefront of optical materials research.

Rare-earth ions have been very interesting and attractive candidates for laser sources when incorporated into insulating host materials. The characteristics of rare-earth ion emission in insulating hosts are sharp luminescence lines in the visible and near infra-red, whose spectral position and emission intensity are essentially temperature independent. The recent development of diode-laser (semiconductor) pumped Nd:YAG (insulator) lasers with efficiencies of greater than 10% shows the technological importance of the rare-earth ions. A rare-earth doped semiconductor-diode laser would combine the pumping and the emission in the same material structure thereby greatly simplifying these lasers and potentially increasing the overall electrical efficiency much further. In this and other ways, rare-earth ion doped semiconductor materials have tremendous potential¹⁻⁶.

Among the rare-earth ions, Er is interesting because the emission occurs mainly around 1.54 μ m, which is very close to the wavelength of the least transmission loss of silica optical fibre. Therefore there have been several reports on the properties of Er in semiconductor host lattices⁷⁻¹⁵. In those reports, several processes to dope the semiconductor with the rare-earth ion were reported; MBE^{7,8,11}, MOCVD⁹, and ion-implantation followed by annealing^{10,12-15}. To date all of these techniques have failed to produce silicon with significant concentrations of rare-earth ions which can be electrically excited at room temperature. By way of contrast with insulating materials, the characteristics of rare-earth ion emission in silicon and other semiconductor materials are sharp luminescence lines in the visible and near infra-red, whose spectral positions are temperature independent but whose emission intensities under band-to-band excitation are strongly temperature dependent. In the present phase of development, the major effort is now in tackling the doping problem in silicon and other semiconductor materials. The equilibrium solubility of Er in the covalent semiconductors is relatively small, $\sim 10^{18}$ cm⁻³¹³. This is more than two orders of magnitude smaller than in insulating crystals such as YAG. To increase the Er concentration in the semiconductor it is necessary to fabricate the samples under non-equilibrium conditions. In this paper, we report the photoluminescence of Er³⁺ incorporated in the Si host lattice (Si:Er) using such a non-equilibrium technique.

SAMPLE PREPARATION

The Si:Er samples were prepared by a novel laser doping technique which involves two steps: (i) pulsed laser deposition (PLD) of an ultrathin erbium film on a Si substrate and (ii) subsequent laser melt-in of the erbium into the substrate to a predetermined distance. During the laser melt-in step the erbium dopant is mixed with the melted silicon by liquid phase diffusion; and during regrowth the erbium is incorporated in the silicon lattice. As the resolidification process takes place on a sub-microsecond timescale the crystal regrowth process occurs under conditions that are far from thermodynamic equilibrium. Crystallisation front velocities of the order of several m/sec are attainable and result in very large dopant segregation coefficients¹⁶. Laser doping has been shown to produce doping levels significantly higher than the solid solubility limited maximum doping concentrations attainable by processes operating under equilibrium conditions¹⁷.

A series of erbium films were deposited having thicknesses in the range 1 to 31 Å either with or without a capping layer of 50 Å of silicon. The purpose of the overlayer was to investigate the possibility of limiting the oxidation of the deposited layer and also to prevent possible loss of the optically active dopant during the laser melt-in step. The laser melt-in step was monitored by the time resolved reflectometry (TRR) method which is a well established technique for monitoring melt durations in laser melting experiments.^{18,19}

Both n-type (P-doped, 70 Ωcm) and p-type (B-doped, 24 Ωcm) Si were used as starting materials. These materials were used both as the substrate for the deposition and as target sources for the PLD of thin (50 Å) Si overlayers onto some samples. The Si samples were thoroughly cleaned with IPA for 30 minutes in an ultrasonic bath before introduction into the deposition chamber. The Er deposition was performed at a pressure of 10⁻⁶ mbar using an excimer laser operating at 248 nm and 20 ns pulse duration. The peak fluence at the target was approximately 8 J/cm², yielding a deposition rate of 0.2 Å/shot for erbium and 0.15 Å/shot for silicon, as measured by a quartz crystal oscillator thickness monitor.

The melting was performed in air using a second excimer laser (248 nm, 23 ns FWHM). An aperture 0.3 cm² placed in the beam was imaged with a demagnification of 3.2 using a 7.5 cm quartz lens to give a spot size of 0.03 cm². The melt duration of the erbium coated silicon was monitored using TRR. The lens position was adjusted so as to give a melt duration of 100 ns as measured by the HeNe reflectivity. The required fluence was 1.3 J/cm² which agrees well with previous work on excimer laser annealing of uncoated silicon surfaces²⁰. A melt duration of 100 ns corresponds to a melt depth of approximately 400 nm under the conditions we have used¹⁹. From the thickness of the deposited erbium film and taking a melt depth of 400 nm, the erbium dopant concentrations were calculated. Assuming uniform doping, the sample details are given in table I.

The Si:Er samples were placed in a closed-cycle He refrigerator which provides temperatures down to 11 K. Photoluminescence (PL) spectra were taken by excitation with UV, 488, and 476 nm-lines of an Ar⁺ laser. Typical excitation power was around 80 mW at the sample with a focussed spot size of 1.0 mm². Emitted light was focussed into a 1.0 m-spectrometer and then detected by a liquid-nitrogen-cooled Ge detector with a muon filter and a lock-in amplifier.

PHOTOLUMINESCENCE RESULTS

Figure 1 shows the luminescence spectrum of sample Er2 in the near infra-red region. The lines around 1.1 μm are due to the phonon assisted free-exciton transitions. There are two common Si defect bands in the figure, the transition with zero-phonon line at 1.28 μm is the G-line (C_i-C_s pair defect)²² and the line at 1.61 μm is the P line (C-O related) defect²³. The lines around 1.55 μm appear after the erbium deposition and laser annealing steps and are assigned to Er³⁺ transitions. The inset in Fig. 1 show the area around 1.55 μm in more detail.

Sample Name	Substrate	d(Er) Å	d(Si) Å	Er Conc. ($\times 10^{20} \text{ cm}^{-3}$)
Er1	n type	31.0	-	2.5
Er2	n type	31.0	50	2.5
Er3	n type	12.3	-	1
Er4	n type	1.23	50	0.1
Er5	p type	1.23	-	0.1
Er6	p type	1.23	50	0.1
Er7	p type	6.15	-	0.5
Er8	p type	6.15	50	0.5
Er9	p type	12.3	-	1
Er10	p type	12.3	50	1

Table I Parameters for the Si:Er Samples

The results of the annealing studies are summarized in Fig. 2. Spectrum (a) is the same as that in Figure 1, spectrum (b) is from the area of Er2 which was not laser annealed and spectrum (c) is from the sample after oven annealing an Er2 sample which had been previously laser annealed. We observe that the G-line and Er related luminescence spectra are observed only in the laser annealed area, while a broad luminescence band peaking at $1.3 \mu\text{m}$, and the P line luminescence are observed in both the unannealed and laser-annealed 7 sample areas. It is clear that the luminescence lines around $1.55 \mu\text{m}$ are observed only in the laser annealed area of the same sample. This fact clearly indicates the effect of laser annealing. In other words, not only laser deposition of Er but also laser annealing is necessary to produce the luminescent centres.

To confirm our assignment of the luminescence to Er^{3+} transitions, we carried out a measurement of the temperature-dependence of the lines. We find that the luminescence peaks numbered 1-5 in the Fig.1 (inset) do not shift in wavelength up to 100 K while the line marked by an asterisk in the inset, the G-line and P-line systems were observed to shift significantly in the same temperature interval. The intensity of luminescence lines 1-5 decreases by a factor of 6 between 11 K and 100 K under 476 nm excitation. The positions and the decrease in intensity of these lines with temperature are similar to previous results¹⁴. The Er^{3+} -related luminescence is observed in the laser annealed areas for all the samples in Table I. The samples with the thickest Er layer also show the strongest Er^{3+} luminescence. The samples with the Si capping layer of 50Å show luminescence stronger by about a factor of 2 than samples without the capping layer. The luminescence intensity in the $1.1 - 1.8 \mu\text{m}$ region including the Er^{3+} luminescence is found to be twice as strong under 476/488 nm than UV Ar^{+} laser excitation.

DISCUSSION

To date rare-earth doped semiconductors have been an area of active materials research but no optical devices based on them have been achieved to date. The difficulty in doping the semiconductors to the levels achieved in insulating materials and the electrical excitation of the rare-earth ions at room temperature have been identified as the principle problems. In a study of Nd-doped GaP Donegan⁶ showed that coupling of the rare-earth ion to external and band states (necessary for electrical excitation) produced luminescence intensities orders of magnitude higher than in excitation directly into the internal 4f-states. Coupling to band states is not observed in insulating crystals and so only the weak internal excitation is possible. Even so, lasing systems such as Nd:YAG have been developed. This coupling to external states in Nd:GaP was found to be strongly temperature dependent and at room temperature only the internal 4f excitation channel was observed. In all rare-earth doped systems studied to date this large reduction in the excitation efficiency in going from low to room temperature has been observed and gives rise to the large decrease in emission characteristic of rare-earth ion doped semiconductors. The coupling of the rare-earth ions to

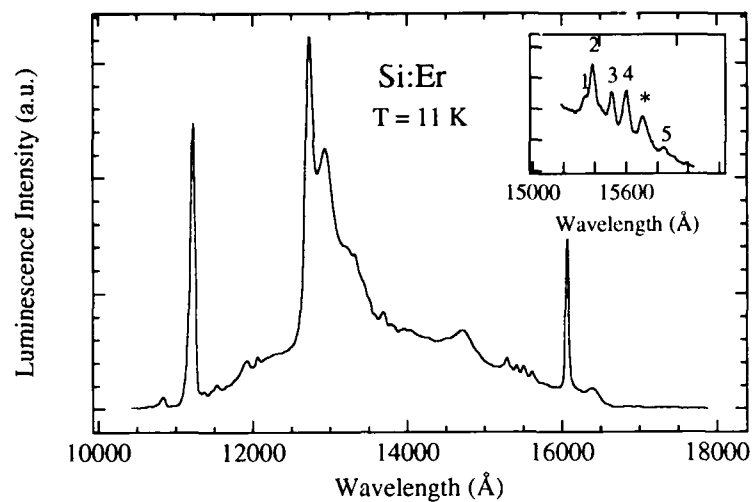


Fig. 1 The luminescence spectrum of sample Er2 using 80 mW of 476 nm laser excitation. The inset shows the Er^{3+} lines in the spectral region around 1.55 μm in more detail.

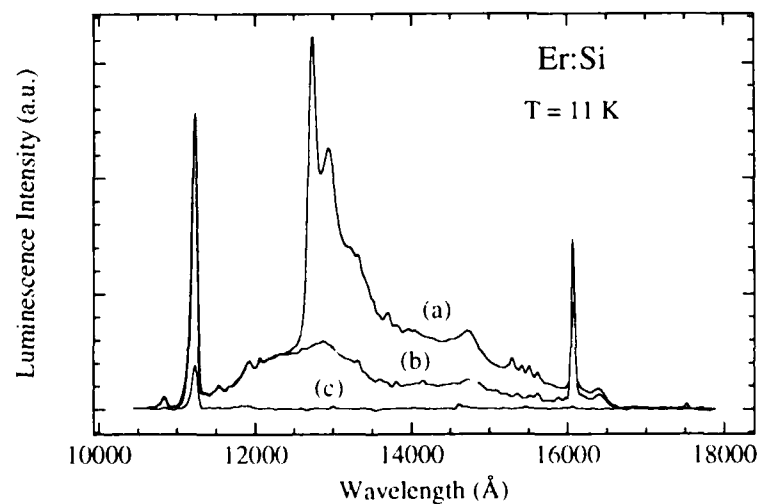


Fig. 2 Luminescence spectra of samples with different annealing conditions: (a) sample Er2 after laser annealing, (b) sample Er2 with Er deposition but without laser annealing and (c) Er2 after laser and oven annealing at 900°C.

the semiconductor states is poorly understood at present. Therefore, the present goal must be to increase the doping levels in rare-earth doped semiconductors and optically pumped systems will probably be the first generation of rare-earth doped semiconductor devices.

Recently, Polman et al.²³ have shown that high concentrations of erbium can be achieved by ion-implantation followed by an annealing stage at 600°C. The Er incorporated substitutionally in this way can then be optically activated by a subsequent heat treatment step at 1000°C. We have adopted a different approach towards the same goal of large erbium concentrations. To date we have produced Si:Er samples that exhibit Er³⁺ luminescence but it is not the dominant luminescent centre in our samples and so further work must be done especially on the physical analysis of the laser doped materials.

The technique of laser doping described above offers a very simple and fast method of producing Er doped Si. The laser melting technique has proven very successful for the incorporation of large dopant concentrations in semiconductors¹⁷. After laser melting, the trapping of the solute by the rapid resolidification process results in the large dopant incorporation²⁴⁻²⁶. This technique shows particular promise for rare-earth doped semiconductors as their equilibrium solubility appears to be quite small¹³.

The annealing and generation of the optically active Er³⁺ ions has not been optimized for these samples as evidenced in Fig. 2. We see that the laser annealing stage is required to generate the Er³⁺ luminescence but a subsequent oven anneal at 900°C results in the complete loss of all the dopant luminescent centres in the original and laser treated samples. Clearly, this oven anneal stage so useful in the production of Er³⁺ centres in ion-implanted Czochralski Si is not effective in our case. We have of course introduced very large concentrations of Er ($> 10^{20} \text{ cm}^{-3}$) into the Si material and as yet we have no information on the physical location of the bulk of the Er which is clearly not optically active after the laser annealing stage. We would expect that for optically active Er³⁺ dopant concentrations of over 10^{20} cm^{-3} that the 1.55 μm luminescence lines would dominate the luminescence spectrum from our samples.

The luminescence lines at 1.54 μm are identified as due to Er³⁺ from their wavelength position and the temperature independence of the wavelength positions. The lines 1-5 in Fig. 1 occur at 1.533, 1.538, 1.551, 1.561 and 1.586 μm , lines 2 and 4 coincide with the lines of Er³⁺ ions in T_d symmetry while the other lines appear to be associated with Er³⁺ sites of lower symmetry¹⁰. As yet we cannot determine the symmetry of the Er³⁺ centres in the laser doped samples. We observed that the Er³⁺ luminescence was stronger in the samples with the Si capping layer. As yet there is no clear explanation for this, it may be possible that some Er is lost during the laser melt-in stage in the uncapped samples.

At this preliminary stage we have been successful in a new doping technique for Er in Si. The advantages of the laser deposition and annealing technique are its simplicity, its speed in producing samples, and the non-equilibrium nature of the doping process. Our plans are to investigate the laser annealing further using a range of melt durations and laser melt shots. Further investigations using sources other than metallic Er will be attempted.

We acknowledge helpful discussions with Ken Jackson at the initial stages of this project.

REFERENCES

- [1] V.V.Petrov, V.S.Prosolov, V.D.Tkachev, Yu A.Karpov, and M.G.Millvidskii, *Phys.Stat.Sol.* **a88**, K141, (1985).
- [2] K.Takahei, Ouyō Butsuri, **60**, 120, (1991) and references therein.
- [3] G.Aszodi, J.Weber, Ch.Uihlein, L.Pu-lin, H.Ennen, U.Kaufmann, J.Schneider, and J.Windscheif, *Phys.Rev.* **B31**, 7767, (1985).
- [4] J.Wagner, H.Ennen, and H.D.Müller, *J.Appl.Phys.* **59**, 1202, (1986).
- [5] H.D.Müller, H.Ennen, J.Schneider, and A.Axmann, *J.Appl.Phys.* **59**, 2210 (1986).
- [6] J.F.Donegan, *Phys.Rev.* **B41**, 10254, (1990).
- [7] H.Ennen, G.Pomernke, A.Axmann, K.Eisele, W.Haydl, and J.Schneider, *Appl.Phys.Lett.* **46**, 381 (1985).
- [8] K.Thonke, H.U.Hermann, and J.Schneider, *J.Phys.C* **21**, 5881, (1988).

- [9] H.Nakagome, K.Uwai, and K.Takahei, Appl.Phys.Lett. **53**, 1726, (1988).
- [10] Y.S.Tang, K.C.Heasman, W.P.Gillin, and B.J.Sealy, Appl.Phys.Lett. **55**, 432, (1989).
- [11] P.Galtier, J.P.Pocholle, M.N.Charasse, B.de Cremoux, J.P.Hirtz, B.Groussin, T.Benyattou, and G.Guillois, Appl. Phys.Lett. **55**, 2105 (1989).
- [12] P.N.Favennec, H.L'Haridon, D.Moutonnet, M.Salvi, and M.Gauneau, Jpn.J.Appl.Phys., **29**, L524, (1990).
- [13] J.L.Benton, J.Michel, L.C.Kimerling, D.C.Jacobson, Y.-H.Xie, D.J.Eaglesham, E.A.Fitzgerald, and J.M.Poate, J.Appl.Phys. **70**, 2667, (1991).
- [14] J.Michel, J.L.Benton, R.F.Ferrante, D.C.Jacobson, D.J.Eaglesham, E.A.Fitzgerald, Y.-H.Xie, J.M.Poate, and L.C.Kimerling, J.Appl.Phys. **70**, 2672, (1991).
- [15] D.J.Eaglesham, J.Michel, E.A.Fitzgerald, D.C.Jacobson, J.M.Poate, J.L.Benton, A.Polman, Y.-H.Xie, and L.C.Kimerling, Appl.Phys.Lett. **58**, 2797, (1991).
- [16] C. W. White in Pulsed Laser Processing of Semiconductors, Semiconductors and Semimetals Vol. **23**, Academic Press, (1984), Chapter 2.
- [17] K. Sugiano and K. Toyoda, Appl.Phys. Lett. **61**, 2817, (1992).
- [18] D.H. Lowndes, and G.E. Jellison in Pulsed Laser Processing of Semiconductors, Semiconductors and Semimetals Vol. **23**, Academic Press, (1984), Chapter 6.
- [19] J. Solis, and C. N. Afonso, J. Appl. Phys., **69**, 4, (1991).
- [20] G.E. Jellison, D.H Lowndes, D.N. Mashburn, and R. F. Wood, Phys. Rev. **B34**, 2407, (1986).
- [21] G.Davies, Phys.Reports **176**, 83, (1989).
- [22] J. Wagner, A. Dörnen and R. Sauer, Mat. Res. Soc. Symp. Proc. Vol. **46**, 453, (Materials Research Society, Pittsburgh) 1985.
- [23] A. Polman, J.S. Custer, E. Snoeks and G.N. van den Hoven, Appl. Phys. Lett. **62**, 507, (1993).
- [24] K.A. Jackson, G.H. Gilmer, and H.J. Leamy, in Laser and Electron Beam Processing of Materials edited by C.W. White and P.S. Peercy, Academic Press (1980), p. 104.
- [25] M.J. Aziz, J. Appl. Phys. **53**, 1158, (1982).
- [26] M.J. Aziz and C.W. White, Phys. Rev. Lett. **57**, 2675, (1986).

**MONOCRYSTAL DISLOCATIONLESS Si:Ge,
GROWN FROM THE MELT WITH Gd IMPURITY.**

Borschensky V.V., Brinkevich D.I., Petrov V.V., Prosolovch V.S.
Byelorussian State University, Department of Physics, Scorina
Avenue, 4, 220080 Minsk, Republic Belarus.

ABSTRACT

The properties of Si grown from the melt having impurities of germanium and gadolinium have been studied by IR-absorption and Hall effect methods. It was stated that Ge and Gd are effective getters for technological impurities of oxygen and carbon in silicon melt. It has been shown that the combined doping by rare earth and isovalent impurities allows to increase the thermostability of dislocationless monocrystals of silicon.

1. INTRODUCTION

It is known that doping of silicon by rare earth elements (REE) increases its thermal and radiation stability [1]. It has been stated earlier that isovalent impurity (IVI) Ge in silicon suppresses generation of thermodonors (TD) introduced at 450 °C [2], but practically does not effect the formation of high temperature thermal donors (HTTD) [3]. Thus the study of the properties of silicon doped simultaneously by the REE and IVI impurities is of great interest.

2. EXPERIMENTAL ASPECTS

In this paper dislocationless n-Si monocrystals grown from the melt involving Ge and Gd impurities by Czochralsky method have been studied. Their resistivity was $\sim 10 \text{ Ohm.cm}$. Concentrations of IVI (N_{Ge}) and REE (N_{Gd}) were measured by the method of neutron-activated analyses. Note that N_{Gd} in all samples was $\leq 10^{13} \text{ cm}^{-3}$, i.e. beyond the limits of detection. Concentration of the interstitial oxygen and carbon in the state of re-

placement was found by the IR bands of absorption at 1106 and 607 cm^{-1} using empirical coefficient of $3,3 \cdot 10^{17}$ and $2,2 \cdot 10^{17}$ cm^{-2} correspondingly. Measurements of Hall effect and conductivity were made in the temperature range of 77-300 K. Thermal treatment (TT) have been made in air at 450 and 650 $^{\circ}\text{C}$ for period to 100 hours.

3. RESULTS AND DISCUSSIONS.

A. Gettering

The results of measurements (Table 1) show that Ge and Gd are getters for oxygen and carbon in the melt and this effect is the most prominent for the latter technological impurity. The noticeable decreases of oxygen concentration in the doped REE and IVI samples were observed only for the lower parts of the ingots. It should be noted that the simultaneous introducing of Ge and Gd into the melt efficiently increased the rate of purifying of monocrystals from C. Gettering effect

Table 1.

Original parameters of silicon ingots.

Ingots	Number of the wafer	$N_{\text{Ge}} \cdot 10^{20}, \text{cm}^{-3}$	$N_{\text{O}} \cdot 10^{17}, \text{cm}^{-3}$	$N_{\text{C}} \cdot 10^{16}, \text{cm}^{-3}$	$N_{\text{TD}}^{\text{G}} \cdot 10^{14}, \text{cm}^{-3}$
Test material	1U	-	8,6	6,7	1,53
	1P	-	6,5	16,0	-
	1L	-	8,3	42,2	-
Si:Ge	2U	1,06	8,7	6,0	0,6
	2P	1,14	6,3	13,5	-
	2L	1,27	7,8	35,3	-
Si:Gd	3U	-	8,6	5,3	0,2
	3P	-	6,4	7,4	-
	3L	-	7,6	13,2	-
Si:Ge,Gd	4U	0,80	8,5	3,3	0,2
	4P	0,87	6,5	5,0	-
	4L	0,94	7,1	7,5	-

(* U,P,L- upper part, middle part, lower part of the ingot, N_{TD}^{G} - concentration of "grown" thermodonors.)

at addition of REE into the melt occurred for background technological impurities of Au, Cu, Na, W [1] as well.

Measurements of the profile of oxygen distribution showed that in all crystals N_O decreased when approaching the edge of the wafer due to evaporation. Introducing of Ge into the melt did not change the radial homogeneity of oxygen distribution: $\Delta N_O/N_O \approx 0,06$ into Si:Ge and test material. Addition of Gd caused its decrease in Si:Gd ($\Delta N_O/N_O \approx 0,12$) and Si:(Ge,Gd) ($\Delta N_O/N_O = 0,30$). Radial distribution of carbon impurity was highly homogeneous ($\Delta N_O/N_O \approx 0,02$).

The effect of IVI and REE described above may be caused by some reasons:

1. Change of coefficients of segregation of oxygen and carbon.
2. Binding of the given impurities in the melt of germanium or REE followed by the formation of the complexes of Z_nO_m and Z_nO_m ($Z = \text{Ge, Gd}$) types, expelled into the melt and precipitated at the bottom of the crucible as a slug.
3. Additional solution of silicon crucible resulted in the increase of the silicon melt by oxygen.

According to [1, 4] and the data given above, mechanisms of gettering in Si:Ge and Si:Gd should differ. For Si:Ge the decrease of the magnitude of segregation of C and O is dominant because germanium did not produce noticeable effect on the solution of the crucible; the formation and precipitation of slugs also did not occur. Introducing of REE into the melt enables the increase of N_O , increasing the solubility of silicon crucible [4]. Lanthanoids, binding oxygen and carbon in the melt prevent their introduction into the growing crystal that enables the gettering effect in Si:Gd. Its increase and decrease of the concentration of germanium in Si:(Ge,Gd), shows the interaction of Ge and Gd impurities in the melt.

B. Thermal Donors

From the analyses of the experimental data (Table 2) one can conclude that Si:Ge, Gd has the increased thermostability as compared to the test material. This effect reveals itself

in all types of TD in the samples cut from the lower parts of ingots as well as that from the upper parts. Kinetic curves of generation of TD and HTTD in this paper are not presented as they are analysed in details in Ref [5,6]. Duration of the used TD was taken sufficient for the formation of TD in maximum concentration but we note the fact stated before [1] that impurity of Gd at the concentrations used in the present paper does not show the noticeable effect on the duration of TD at 450°C and 650°C.

One can explain the specific characteristics of TD accumulation at 450°C by the fact that the impurities of carbon at $N_C \geq 5 \cdot 10^{16} \text{ cm}^{-3}$ [7] and germanium at $N_{Ge} \geq 10^{19} \text{ cm}^{-3}$ [2] essentially suppress the introducing of these defects. Taking all the facts into account one can understand why the concentration of TD was lower in the lower part of the ingot than in the upper part, and the initial rate of introducing (IRI) and the maximal achieved concentration (MAC) of thermodonors had minimal values in Si:Ge, and the maximal - in Si:Gd (Table 2).

Table 2

Initial rates of introducing and maximal achieved concentrations of thermal donors

Number of pea- te	TD				HTTD		
	-		SA		-	HT	SA+HT
						450°C	450°C
						85h	85h
	IRI $\times 10^{-13}$, cm^{-3}/h	MAC $\times 10^{-14}$, cm^{-3}/h	IRI $\times 10^{-13}$, cm^{-3}/h	MAC $\times 10^{-14}$, cm^{-3}/h	MAC $\times 10^{-14}$, cm^{-3}		
1U	11,0	16,57	0,32	6,34	1,62	4,14	5,58
1L	~0,1	2,6	-	~1,0	6,2	8,08	10,80
2U	0,6	2,73	-	<1,0	2,15	4,51	5,06
2L	-	<0,8	-	<1,0	5,1	6,96	7,6
3U	12,0	12,33	0,65	6,24	0,54	1,61	2,34
3L	~0,1	2,4	-	~1,0	2,8	6,04	8,62
4U	3,8	6,28	0,28	3,57	0,56	1,54	1,92
4L	-	<0,8	-	<1,0	0,3	1,10	1,40

The impurities studied at generation of HTTD have another behavior. It is known that carbon stimulates it [6] and Ge even at $N_{\text{Ge}} \approx 10^{20} \text{ cm}^{-3}$ does not show noticeable effect [3]. Thus, gettering effect of REE in the melt (Table 1) causes the lower of accumulation of HTTD in Si:Ge,Gd and Si:Gd.

Stabilizing annealing (SA) at 650°C during 30 min made after the growth of an ingot, suppressed the further generation of TD introduced at 450°C . Its strongest effect revealed itself in the test material (Table 2). Taking into account that the given effect was caused by the annealing of the centers of generation of TD (8), one can come to the conclusion that in Si:Ge their concentration is lower. On the other hand SA caused the increase of the concentration of HTTD at the two-stage TT ($450..650^\circ\text{C}$). The given effect revealed itself most of all in Si:Gd (the increase of MAC was approximately 45%) and in the test material (approximately 35%). SA did not practically show any effect on the samples of Si:Ge and Si:Ge, Gd (Table 2). It is most probable that stabilizing annealing enables the formation of the centers of HTTD generation, and Ge suppresses their generation. These centers are not low temperature TD, because SA, as it has mentioned before, decreases its concentration.

4. CONCLUSION

On the bases of the experimental data presented in this paper one can come to the following conclusions:

- impurities of Ge and Gd are effective getters for technological impurities of oxygen and carbon in the melt of silicon;

- combined doping of REE and IVI allows to increase the thermal stability of dislocationless silicon monocrystals, suitable for semiconductor microelectronics.

R E F E R E N C E S

1. A.G. Dutov, Yu.A. Karpov, V.A. Komar, V.V. Petrov, V.S. Prosolovich, B.M. Turovsky, S.A. Chesnokov, Yu.N. Yankovsky *Izv. AN SSSR. Neorgan.mat.* 25, 1589, (1989).

2. Yu.M. Babitsky, N.I. Gorbacheva, P.M. Grinshtein, M.A. Ilyin, M.G. Milvidsky, B.M. Turovsky. Fiz. Tekhn. Poluprovodn.. **18**, 1309, (1984).
3. D.I. Brinkevich, N.I. Gorbacheva, V.V. Petrov, V.S. Prosolovich, B.M. Turovsky. Izv. AN SSSR. Neorgan. mat. **25**, 1376, (1989).
4. E.P. Bochkarev, V.P. Grishin, Yu.A. Karpov, M.I. Marunina- Properties of doped semiconductors. (Nauka, Moscow, 1977) p.88.
5. W. Kaiser, H.L. Frisch, H. Reiss. Phys. Rev. **112**, 1546, 1958.
6. A. Kanamori, M. Kanamori. J. Appl. Phys. **50**, 8095, (1979).
7. A.R. Bean, R.C. Newman. J. Phys. Chem. Sol. **33**, 255, (1972).
8. V.P. Markevich, L.I. Murin. Phys. Stat. Sol. (a), **111**, K149, (1989).

EPITAXIAL LAYERS Si:(Sn,Yb) PRODUCED BY THE CRYSTALLIZATION FROM THE MELT-SOLUTION ON THE BASIS OF Sn.

D.I.Brinkevich, N.M.Kazuchits, V.V.Petrov.

Department of Physics, Belorussian State University. Minsk, Republic Belarus.

ABSTRACT

Epitaxial layers (EL) Si:Sn doped with Yb in the process of liquid phase epitaxy were studied by optical microscopy and photoluminescence (PL) methods. At low concentration of lanthanoid ($0,01 < N_{Yb} < 0,1$ weight %) the good planarity of the interface and high quality of the surface are detected. At $N_{Yb} > 0,1$ weight % microirregularities are presented.

In EL Si:(Sn, Yb) irradiated by 4,5 MeV-electrons the suppression of the generation of radiation defects, responsible for G- and C-lines of PL, has been found. This effect has been explained within the scope of the model taking into the consideration gettering properties of Yb in reference to the impurities of O and C as deformation fields, attributed to the presence of Sn atoms.

INTRODUCTION

Doping by rare-earth elements (REE) can be used for purposeful control of the properties of semiconductor materials, susceptible to the presence of structural defects [1]. In particular, introducing of REE into monocrystal silicon allows to increase the stability of its main electrophysical parameters to radiation effect [2].

EXPERIMENTAL ASPECTS

The purpose of the given work is to study the processes of defect formation in epitaxial layers (EL) of silicon of n- and p-type conductivity, doped by Yb in the process of crystallization from the melt-solution (M-S) on the Sn basis. EL were

grown in the graphite cassetts with the help of shift technology in the temperature range of 900-1150 °C. Forced cooling of M-S was made with the rate of 0,1..1,0 K .min⁻¹. Concentration of tin (N_{Sn}), according to the neutron-activation analyses made up $(3-6) \cdot 10^{19} \text{ cm}^{-3}$. The content of ytterbium (N_{Yb}) in M-S varied from 0 to 6.0 weight %. Resistivity of EL, found by four probes method, changed from 0,04 to 10 Ohm.cm. The thickness of EL varied in the range from 2 to 20 μ . PL spectra were measured at temperature of 4,2-77 K optical excitation was made by the arc xenon lamp. The impurity content of EL was studied with the help of the local X-ray probe microanalyses with 70 Å resolution. Irradiation by electrons with the energy of 4,2 MeV by fluencies (F_e) $2 \cdot 10^{15}$ - $3 \cdot 10^{17} \text{ cm}^{-2}$ was made at 300 K.

RESULTS AND DISCUSSIONS

Introducing of REE into the melt-solution allows to increase the wetting of the substrate and consequently, to decrease the temperature of the film growth. At low concentrations of Yb in M-S (0,01-0,1%) the grown layers had good planarity of the interface and high quality surface morphology. At the increase of $N_{\text{Yb}} > 0,1\%$ the microroughness was observed on the surface of EL, that is connected with the nonuniformity of the distribution of lanthanoid and with the increased solubility of the substrate on those areas where the content of Yb was high.

The analyses of the data, obtained by the method of the local probe microanalyses, allows to come to the following conclusions:

- Sn in EL was distributed nonuniformly. The local regions ($\sim 50 \mu$) where N_{Sn} reached the values $(8-10) \cdot 10^{19} \text{ cm}^{-3}$ occurred:

- concentration of technological impurities of oxygen N_{O} and carbon N_{C} in EL is 3 times as low than in the substrate. The above impurities were distributed non-uniformly;

- addition of the impurity Yb of the concentration to 0,1 weight% into M-S increases the homogeneity of the distribution of Sn and decreases N_{C} and N_{O} in EL;

-at $N_{Yb} \geq 0.2..0.4$ weight % the mentioned impurity forms in EL the inclusions of the second phase with the dimensions to 10μ . At low N_{Yb} (0.01..0.1 weight %) the inclusions of the second phase were not observed. Precipitation of the second phase at high concentrations REE was attributed to the low values of the effective coefficients of the distribution of lanthanoids in silicon (for Yb - $6 \cdot 10^{-8}$);

-the conditions of the growth (the speed of the cooling (V_c), the temperature of growth (T_g) and so on) substantially influenced the impurity content of EL. The decrease of V_c increased the homogeneity of the impurity distribution. The increase of T_g and the decrease of V_c resulted in the growth of N_c and N_o in EL.

It was stated by the method of optical microscopy combined with the selective etching, that the non-informly distributed growth defects of package and dislocation grouped into the form of the pulled clusters with the width $\sim 50 \mu$ are present in the epitaxial layers. The density of dislocations in the was clusters - $8 \cdot 10^5 \text{ cm}^{-2}$, their average density on the surface $\sim 1 \cdot 10^3 \text{ cm}^{-2}$. Dislocations in Si:Sn,Yb were distributed uniformly, their density ($\sim 2.5 \cdot 10^4 \text{ cm}^{-2}$) was higher, than in the layers being not doped by Yb. The density of the package defects did not exhibit dependency on N_{Yb} . The density of the grooves of etched pits in Si:Sn,Yb monotone increased with the removal from the surface of EL and was as high as $\sim 1 \cdot 10^7 \text{ cm}^{-2}$ in the depth of the substrate.

The typical spectra of PL have the line of the free exciton (FE) and the set of lines, connected with the dislocations (D1-D4) [3]. In the substrate spectra, grinded on the nonoperative side before the epitaxy, FE line is absent, and the dislocation radiation (in D1 region) is considerably more intensive (\sim three times) than in EL. Pre-epitaxial polishing of the "nonoperative" side of the substrates results in the decrease of the intensity of the dislocation lines. Lines of PL connected with the Yb impurity were not detected. The ratio of the intensity of the lines D1 to FE in Yb doped layers was critically higher than in Si:Sn. This is the evidence of the deterioration of the structural perfectness of EL with addition of

Yb with the concentration $> 0,1$ weight % into M-S.

Dislocations are not located at the EL-substrate interface, but "penetrate" the whole substrate. This conclusion is confirmed by the fact that the intensity of dislocation lines of PL practically did not change with moving away from the surface into the depth of the substrate.

As in the dislocation set the radiation in the region D1 dominates, one can come to the conclusion that dislocations were introduced directly in the process of epitaxy at high temperatures ($900...1050^{\circ}\text{C}$), when the centers D3-D4 lines were annealed [4]. This conclusion is confirmed by the fact that in PL spectra of the original plates (before the epitaxy) only the line of the free exciton FE was present, and the dislocation lines did not occur.

After the electron irradiation C- and G- lines of PL exhibited [5]. The values of τ in the EL agreed with the analogous values in the substrate. The intensity of the lines FE and D1-D4 decreased with the growth of Φ_e in the substrates as well as in EL. The given effect can be attributed to the decrease of τ and the "loss" of the dislocations of the recombination activity due to their interaction with the radiation defects (RD). At irradiation $\Phi_e \geq 10^{16} \text{ cm}^{-2}$ in EL spectra the wide structureless band of radiation in the region of $0,75-0,95 \text{ eV}$ (Fig. 1 e) exhibited, its intensity increased with the increase of Φ_e and Sn concentration. It did not occur in the spectra of substrated (Fig. 1 b). The introduction of the Yb impurity into M-S had no substantial effect on its intensity. The obtained results allow to conclude that the given band is connected with the centre caused by the Sn impurity.

Note the main peculiarities of PL spectra of the irradiated structures:

1) Considerable (more than two order) difference in the intensities C- and G- lines (I_c, I_g) for spectra of EL and substrates takes place.

2) The efficiency of introducing of RD into EL depends on the conditions of their obtaining. At the decrease of V_c from $0,25$ to $0,1 \text{ K.min}^{-1}$ or at the increase of T_g from 1173 to 1323 K I_c and I_g increased by the factor of 2.

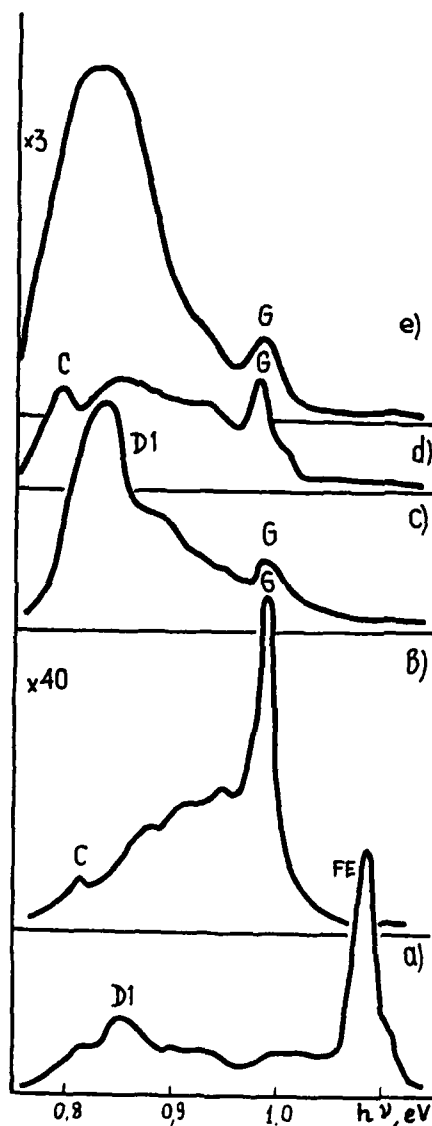


Fig. 1. PL spectra of substrate (b) and EL Si:Sn (a, c-e) P_e, cm^{-2} : 0 (a); $2.5 \cdot 10^{15}$ (b, c) $8 \cdot 10^{15}$ (d); $3 \cdot 10^{16}$ (e).

3) Introducing of Yb impurity into M-S with the concentration 0.1 weight % decreased I_c, I_g as well as the value of their ratio comparing to EL Si:Sn. At the higher values N_{Yb} differences disappeared.

It has been stated before, that G- and C- lines were caused by the inner transitions. The former is connected with the centre, containing carbon, ($C_I - C_S$); the latter one is connected with the complex, consisting of divacancy and the atoms of carbon and oxygen (C-O-W) [5]. The decrease of I_c and I_g in EL as compared to the corresponding values in substrate is caused by the decrease of content of oxygen (N_o) and carbon (N_c) impurities. According to the data, obtained by the method of the local probe microanalysis by the scanning electron microscope "Nanolab-7" the average values run to: in EL- $N_o \approx 1 \cdot 10^{17} \text{ cm}^{-3}$, $N_c \leq 2 \cdot 10^{16} \text{ cm}^{-3}$; in the substrate $N_o \approx 1.2 \cdot 10^{18} \text{ cm}^{-3}$, $N_c = 8 \cdot 10^{16} \text{ cm}^{-3}$.

Besides, when interpreting the results one should take into account effects, connected with the deformation fields, attributed to the interface as well as Sn impurity. The presence of the con-

traction deformations in EL results in the decrease of concentrations of defects of interstitial type and to the increase of the concentration of vacancy complexes [6]. As a result of this, I_g must decrease, I_c -increase, and the I_c/I_g ratio for EL should exceed the corresponding value for the substrate.

The decrease of V_c and the increase of T_g stimulates the processes of diffusion of technological impurities in EL from the container and the substrate, that must lead to the increase of N_c and N_o in EL, and finally, to the increase of concentration of RD with their participation. On the other hand as in the process of epitaxy N_c and N_o do not vary in the substrate, varying of T_g and V_c should not have an impact on the intensity of G- and C-lines in the substrate spectrum.

It should be noted that the Yb impurity has the double influence on the properties of EL. It interact with oxygen and carbon in M-S [2] and prevents their input into EL, that leads to the decrease of I_c and I_g . Besides, Yb atoms, forming additional deformations of compression in Si that enable the increase of I_c/I_g ratio at $N_{Yb} \geq 0,2$ weight %.

REFERENCES

- 1.O.M.Alimov, V.V.Petrov, T.D.Kharchenko and V.Yu.Yavid, Fiz. Tekh. Poluprovodn. **26**, 1914 (1992).
- 2.Yu.A.Karpov, V.V.Petrov, V.S.Prosolovich and V.D.Tkachev, Fiz. Tekh. Poluprovodn. **17**, 1530 (1983)
- 3.N.A.Drozдов, A.A.Patrin, and V.D.Tkachev, Pisma ZhETF, **23**, 651 (1976)
- 4.Yu.A.Oripjan, A.M.Rtishchev and E.A.Steinman, Fiz.tverd.tela, **26**, 1772 (1984)
- 5.L.N.Safronov, Radiation Effects in Semiconductors, (Nauka, Moscow, 1979-in Russian), p.101
- 6.E.V.Solpovjova, G.V.Lazareva, B.M.Leiferov et all, Fiz. Tekh. Poluprovodn. **18**, 1573 (1984)

PART II

Rare Earth Doped Silicon

IC COMPATIBLE PROCESSING OF Si:Er FOR OPTOELECTRONICS

F. Y. G. REN*, J. MICHEL*, Q. SUN-PADUANO*, B. ZHENG*, H. KITAGAWA*¹⁾,
D.C. JACOBSON**, J.M. POATE**, and L. C. KIMERLING*

* MIT, Dept. of Materials Science and Engineering, Cambridge, MA 02139

** AT&T Bell Laboratories, Murray Hill, NJ 07974

ABSTRACT

We have fabricated the first Si:Er LED, operating at 300 K, based on an understanding of the Si-Er-O materials system. Er-doped Si (Si:Er) provides an exciting opportunity for the monolithic integration of Si based opto-electronics. In this paper, Er-Si reactivity, and Er diffusivity and solubility have been studied to establish Si:Er process compatibility with a silicon IC fabline. Er_3Si_5 is the most stable silicid formed; and it can be oxidized into Er_2O_3 at high temperature under any oxidizing conditions. Among Er compounds, Er_2O_3 luminesces and Er_3Si_5 and ErN do not. The diffusivity of Er in Si is low and SIMS analysis yields a diffusivity $D(\text{Er}) \sim 10^{-12} \text{cm}^2/\text{s}$ at 1300 C and $\sim 10^{-15} \text{cm}^2/\text{s}$ at 900 C, and a migration enthalpy of $\Delta H_m(\text{Er}) \sim 4.6 \text{ eV}$. The equilibrium solubility of Er in Si is in the range of 10^{16} cm^{-3} at 1300 C. The Si:Er LED performance is compared with GaAs LEDs to demonstrate its feasibility.

INTRODUCTION

The limiting factors to increased functionality of integrated circuits (ICs) are interconnection density, interconnect driver-related power dissipation and systems bandwidth. The integration of optoelectronic devices for interconnection provides an immediate solution of the above in the form of multiplexed outputs; absence of interconnect line capacitance and resistance; and an unlimited ($\sim 10^{15} \text{ Hz}$) bandwidth capacity. In addition, new capabilities in parallel architectures, immunity from electromagnetic interference and package integration present the opportunity for breakthrough applications. Hence, optical interconnection is a component on every silicon technology roadmap.

The purpose of this research is to create an IC compatible process technology for optical interconnection. We report here a summary of our work on the light emitting diode (LED), optical driver. Rare earth centers emit with a sharp linewidth [1] required for high data rates. For Er:Si, $\Delta\lambda = 0.1 \text{ \AA}$ at 4.2 K and 100 \AA at 300 K [2]. This paper will review our results on Er:Si reactivity, diffusivity and solubility which establish silicon fabline compatibility; and will then describe the first reported room temperature sharp-line electroluminescence at 1.54 \mu m from a silicon LED.

¹⁾ permanent address: Fukuoka Institute of Technology, Dept. Electr. Mat. Engineering, Fukuoka 811-02, Japan

SILICON:ERBIUM REACTIVITY

The phase stability of Si:Er in typical process ambients was determined by the evaporation of pure erbium on etched silicon substrates, followed by heat treatment in controlled ambients.

Figure 1 shows the thin film X-ray diffraction data for vacuum, air and nitrogen ambients. Polycrystalline Er_2O_3 and ErN form easily in air (450 C, 1 h) and N_2 (650 C, 1 h), respectively. In vacuum, a multiphase combination of silicides is often observed with some fraction of Er_2O_3 , unless extreme care is taken. The best condition for single phase silicide formation, Er_3Si_5 , was found to be (450C, 3 h) under a vacuum of 10^{-5} Torr.

The silicide, Er_3Si_5 , is the most stable compound in the series ErSi , ErSi_2 , Er_3Si_5 . The reacted film exhibits a rough morphology on Si(100), but a planar highly textured Er_3Si_5 (001) on Si(111). The lattice mismatch between Er_3Si_5 (001) and Si(111) is small (1.2%) [3], providing a basis for this interface to be low energy. This conclusion was tested by reacting metallic erbium with a substrate of vicinal Si (111), miscut 4° toward $\langle 110 \rangle$ at elevated temperatures. Figure 2 shows a scanning electron micrograph of a cross section of a reacted sample. The lower part of the picture is a schematic of the SEM observations revealing consistency with Si(111) being the terrace interface. We conclude that the formation of an (001) Er_3Si_5 texture and of Si(111) terrace upon heat treatment in vacuum at 1160 C define this interface to be lowest in energy for the Si:Er system.

Heat treatment of Er on SiO_2 in vacuum and Er_3Si_5 in an oxygen containing ambient in the range $450 < T < 1100$ C yields Er_2O_3 . Thus, erbium reacts similar to titanium with respect to silicon [4]. Figure 3 shows the

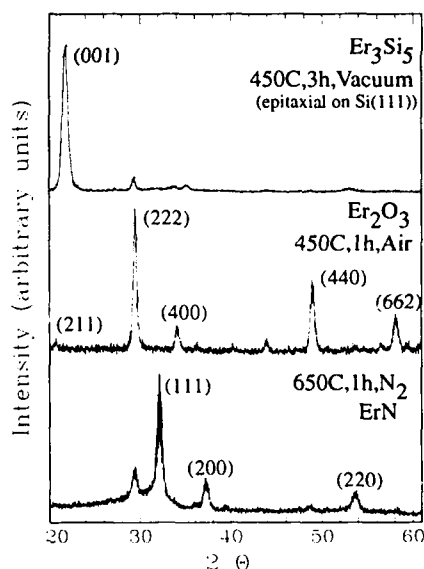


Figure 1. Comparison of X-ray diffraction spectra of the different erbium phases formed during the annealing of Er/Si under different annealing conditions.

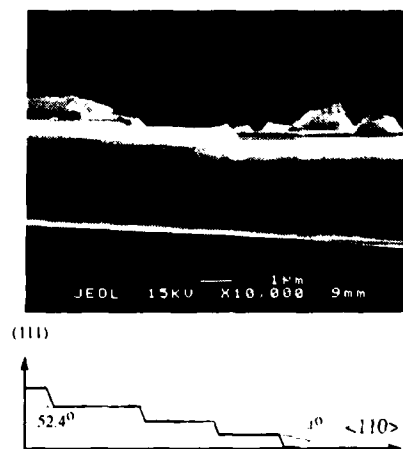


Figure 2. Crosssectional SEM micrograph of a vicinal Si (111) surface

relevant ternary phase diagram for the Er-Si-O system. Er_2O_3 , the dominant phase, will capture the erbium activity under any oxidizing condition.

Of the reaction products Er_2O_3 , Er_3Si_5 and ErN , only Er_2O_3 is optically active with emission at $\lambda=1.54 \mu\text{m}$. We assume that both Er_3Si_5 and ErN are conductive and absorbing. This conclusion is strengthened by the fact that in silicon both O and N provide optically activating ligand fields for erbium.

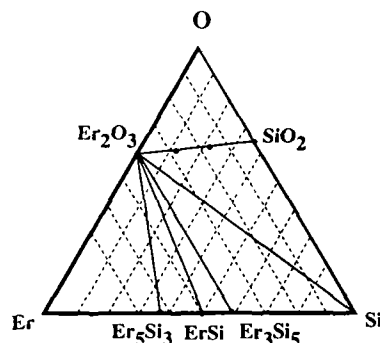


Figure 3. Proposed ternary phase diagram of the Er-Si-O system between 450 C and 1100 C based on X-ray phase identification.

Figure 4 shows a comparison of the optical spectra of Si:Er (900 C, 30 min) compound and poly-crystalline Er_2O_3 (450 C). There are two reproducible differences: 1) the primary emission shifts to shorter wavelengths for Si:Er; and 2) the multiple crystal field split emission bands for Er:Si are absent for Er_2O_3 . This difference is critical in determining whether erbium emission originates in a surface oxide or bulk silicon.

ERBIUM DIFFUSIVITY AND SOLUBILITY IN SILICON

The internal quantum efficiency of Si:Er for light emission is dependent on the dominant role of erbium in the generation-recombination processes in the silicon host. Thus, it is necessary to establish that Er diffusivity is small enough during processing to prohibit cross-contamination of adjacent devices, wafers and process equipment. In addition, a high solubility of Er in Si is desirable because the optical power out is proportional to $[\text{Er}]$ [5]. We describe below the experiments which define these parameters and discuss their consequences.

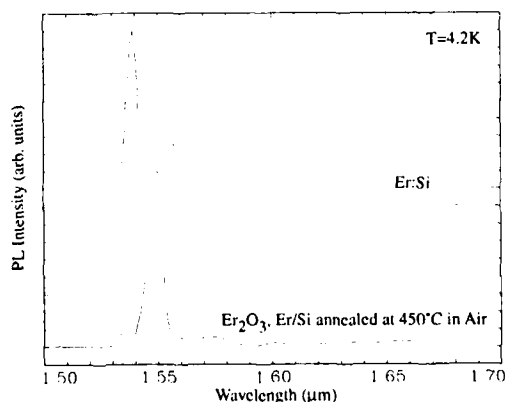


Figure 4. Comparison of photoluminescence spectra of Er_2O_3 and Er:Si.

Figure 5 shows a typical Secondary Ion Mass Spectroscopy (SIMS) profile of Er implanted silicon. The erbium was implanted to a peak concentration of $3 \times 10^{18} \text{ cm}^{-3}$ at an energy of 5.25 MeV. The data, after heat treatment at 850 C, 1/2 hour, represent no change from the as-implanted profile. A subsequent heat treatment of 1300 C, 1 hour, results in contraction of the profile rather than the broadening commonly observed for Group III and V dopants in silicon

(dashed lines). A second aspect of the profile is a constant $[\text{Er}] \sim 10^{16} \text{ cm}^{-3}$ away from the implanted distribution.

The narrowing of the distribution unambiguously connotes precipitation at the peak of the distribution. Thus, the precipitates, as well as the surfaces, act as sinks for the $[\text{Er}]$ to approach its equilibrium solubility. By assuming that complete point defect equilibrium is reached by 1300C, 1 hour, we define the flat portion of the distribution as the solid solubility ($[\text{Er}]_{\text{sol}}$) of Er in Si. Since $[\text{Er}]_{\text{sol}}$ is retrograde at high temperatures, $[\text{Er}]_{\text{max}}$ is somewhat greater than 10^{16} cm^{-3} (to be published). However, $[\text{Er}]_{\text{max}}$ is significantly less than the value of $2 \times 10^{18} \text{ cm}^{-3}$ at 900 C observed as an onset of precipitation by Eaglesham et al. [6].

It is important to note that Eaglesham et al. do not claim to measure solid solubility, but rather the threshold concentration for the onset of precipitation. This threshold may be controlled by either kinetic or equilibrium factors.

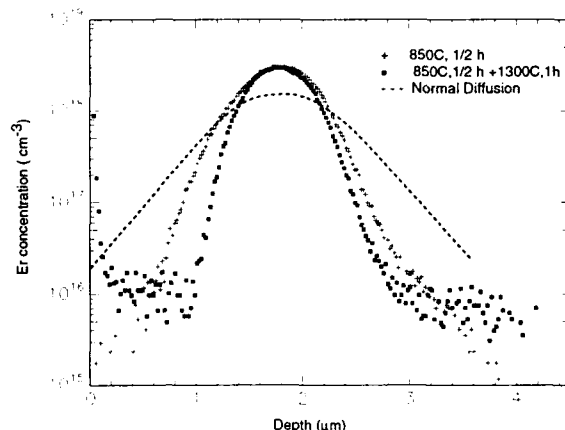


Figure 5. SIMS depth profiles of Er:Si before and after diffusion annealing at 1300 C for 1 h. The dotted line represents an expected normal diffusion profile

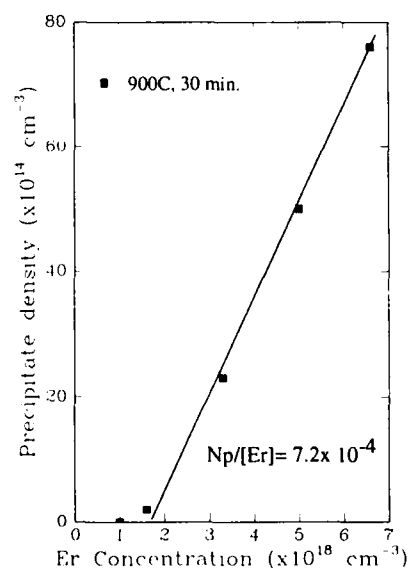


Figure 6. Precipitate density of Si:Er for a 900 C anneal versus $[\text{Er}]$. The line shows a fit using homogeneous nucleation theory

Figure 6 shows our fit (line) of the Eaglesham et al. [6] data (filled squares) to a diffusion limited precipitation model. The data exhibit two key features: an 'incubation' stage of $[Er] \approx 2 \times 10^{18} \text{ cm}^{-3}$ at 900 C, 30 min; and a linear increase in precipitation density with $[Er]$ beyond that concentration. The linear increase with $[Er]$ is consistent with a nucleation limited precipitate density. The incubation stage represents the concentration-dependent, minimum time-at-temperature for Er atoms to associate.

The observed value of 10^{18} cm^{-3} sets a lower limit of the diffusivity $D(Er) > 6 \times 10^{-16} \text{ cm}^2/\text{s}$ at 900 C. Analysis of the SIMS profiles over a wide range of temperatures has yielded a preliminary migration enthalpy, $\Delta H_m(Er) \approx 4.6 \text{ eV}$, and a value of $D(Er) = 10^{-15} \text{ cm}^2/\text{s}$ at 900 C.

Fitting the linearly increasing portion of the data with standard nucleation theory [7] provides a self correcting check for $D(Er)$ and an estimate of the barrier to nucleation F^* . The density of precipitates is given by equations 1(a) and 1(b).

$$N_p \sim \int I(T,t) dt \quad (1a)$$

$$= a_c \left(\frac{2D(Er)}{a_0^2} \right) [Er] t \exp \left[-\frac{F^*}{kT} \right] \quad (1b)$$

where I is the nucleation rate, a_c is a constant taken here as unity, and a_0 is the silicon interlattice distance (2.78 \AA).

The slope of the data $N_p/[Er] \approx 7.2 \times 10^{-4}$ is very sensitive to $D(Er)$ and F^* in the analysis. Using $D(Er) \approx 10^{-15} \text{ cm}^2/\text{s}$, we estimate that approximately 100 hours are required to reach equilibrium at 900 C. A two parameter fit yields $D(Er) = 10^{-15} \text{ cm}^2/\text{s}$ and $F^* = 1.57 \text{ eV}$. The nucleation barrier is similar to values discussed for oxygen precipitation in silicon [8].

The values for $D(Er)$ are similar to those observed for Ge in silicon [9] and $[Er]_{sol}$ is in the range observed for S in silicon [10]. The process relevant conclusions are as follows: 1) Er is a slow diffuser with moderate solubility and should not contaminate during silicon IC processing; 2) implanted erbium can be maintained in a metastable solid solution at concentrations two orders of magnitude higher than its solid solubility.

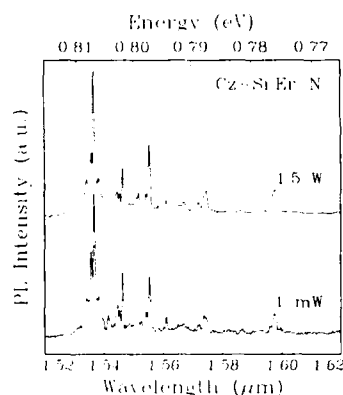


Figure 7. High resolution Si:Er spectra for different excitation powers.

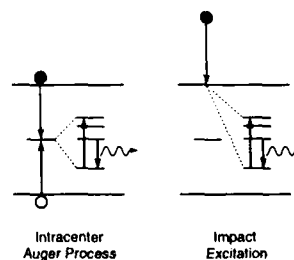


Figure 8. Possible excitation processes for Si:Er

Si:Er LIGHT EMITTING DIODES

Light emission at $\lambda = 1.54 \mu\text{m}$ in the Si:Er materials system comes from relaxation of the $\text{Er}^{3+}(4f^{11})$ first excited state ($^4I_{13/2}$) to the first ground state ($^4I_{15/2}$). The 4f states are "core" states which are decoupled from "valence" states which comprise the valence band, conduction band and impurity gap states. Evidence of this decoupling is given in Figure 7 where the characteristic Si:Er emission spectrum is shown to be independent of pump power. No "hot lines" arise after the standard spectrum is saturated. In the absence of direct coupling to a gap state, excitation of the $4f^{11}$ manifold can only occur through an interactive Auger process or through impact ionization [11] (Figure 8). Impact ionization is relatively inefficient because only very hot electrons with energies greater than 0.8 eV ($1.54 \mu\text{m}$) can contribute. Previous photoluminescence studies based on "back-side" excitation of "front-side" implanted silicon eliminate impact ionization as a necessary mechanism [2].

Recent total energy calculations [12] together with the observed donor activity of Si:Er suggest that Er^{3+} occupies a tetrahedral interstitial site. In addition, high internal quantum efficiencies are only observed when the Er is surrounded by a strongly electronegative ligand field. This requirement arises because the $^4I_{13/2} \rightarrow ^4I_{15/2}$ transition is dipole forbidden in isolated Er^{3+} . The ligand field is required to break the inversion symmetry of the site and to admix states of opposite parity. Crystal field splittings of the emission spectrum are observed whose number depends on the site symmetry and whose magnitude depends on the magnitude of the crystal field. Figure 9 shows the spectral dependence on the ligand field for the roles of oxygen and nitrogen

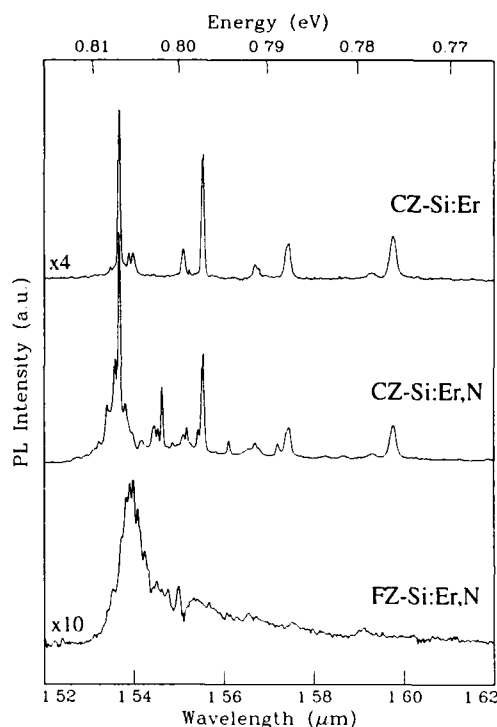


Figure 9. High resolution PL spectra for different co-implanted Si:Er samples.

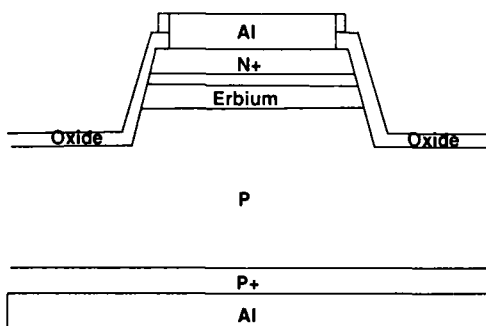


Figure 10. Schematic cross section of the Er:Si LED

(coimplanted with Er).

The process for our LEDs was designed based on the following understanding of the electronic excitation mechanism:

- 1) the Er ligand field determines optical activity,
- 2) oxygen is an effective ligand,
- 3) energy transfer to the f-manifold by Auger mechanism is most likely.

Figure 10 shows a schematic cross sectional cut of the device structure. We have constructed oxide passivated mesa diodes in both surface and edge emitting geometries. The erbium was implanted at an energy of 4.5 MeV together with a range of energies of oxygen co-implants designed to overlap the Er distribution.

Figure 11 shows the 300 K light intensity vs forward bias injection current for a typical diode. The light output saturates, as expected, because of the long excited state lifetime (~ 1 ms) [13] of the Er center. This saturation shows the relative ease of population inversion under electronic injection. The inset confirms that sharp line emission ($\Delta\lambda = 100$ Å) is maintained at 300 K. A comparison with the 100 K spectrum is also shown. At 300 K the intensity is reduced significantly (x50) and a background feature at $\lambda = 1.53$ μm arises (due to dislocations introduced by processing). In the next generation design, carrier confinement schemes and improved process paths should further enhance the impressive results.

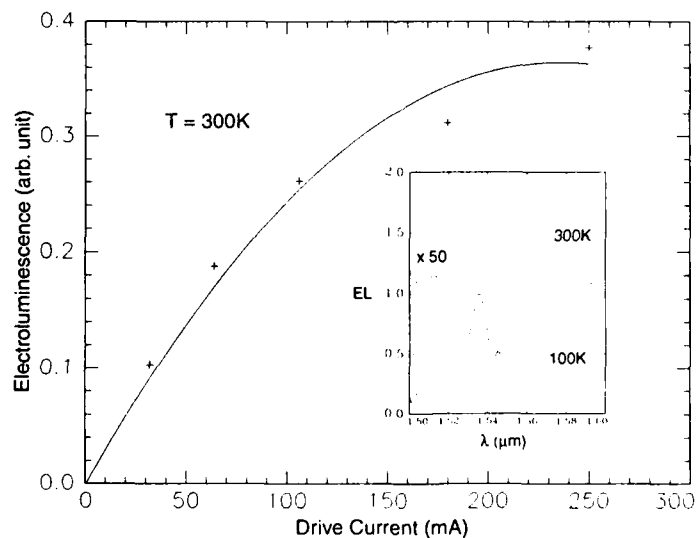


Figure 11. Si:Er LED intensity as function of drive current. The inset shows the EL spectra at 100 K and 300K.

COMPARISON OF Si:Er AND GaAs HOMOJUNCTION LEDs

In conclusion, Table I shows a comparison of the observed silicon LED performance with a GaAs homojunction LED at 77 K. The silicon LED offers significant advantages in the lack of self-absorption and sharper linewidth. With the additional compatibility of off-chip optical amplification at $\lambda = 1.54 \mu\text{m}$, we see no fundamental limits to the introduction of Si:Er LEDs for optoelectronic interconnection.

Table I. LED Performance comparison between GaAs and Er:Si at 77 K

	GaAs	Er:Si
Wavelength (μm)	0.88	1.54
Absorption Coefficient (cm^{-1})	10^4	2
Internal Quantum Efficiency	0.5	0.5
External Quantum Efficiency	1.0%	1.4%
Linewidth (\AA)	1000	100

ACKNOWLEDGEMENTS

The MIT group acknowledges partial support by Rome Laboratories, Hanscom, DARPA and AFOSR under contract F19628-92K-0012, and SRC under contract 92-SP-309.

REFERENCES

- [1] H. Ennen, J. Schneider, G. Pomrenke, and A. Axmann, Appl. Phys. Lett. **43**, 943 (1983).
- [2] J. Michel, J.L. Benton, R.F. Ferrante, D.C. Jacobson, D.J. Eaglesham, E.A. Fitzgerald, Y.-H. Xie, J.M. Poate and L.C. Kimerling, J. Appl. Phys. **70**, 2672 (1991).
- [3] J.A. Knapp and S.T. Picraux, Appl. Phys. Lett. **48**, 466 (1986).
- [4] S.P. Murarka, Silicides for VLSI Applications, (Academic Press, Orlando, 1983), p.142.
- [5] Y.-H. Xie, E.A. Fitzgerald and Y.-J. Mii, J. Appl. Phys. **70**, 3223 (1991).
- [6] D.J. Eaglesham, J. Michel, E.A. Fitzgerald, D.C. Jacobson, J.M. Poate, J.L. Benton, A. Polman, Y.-H. Xie and L.C. Kimerling, Appl. Phys. Lett. **58**, 2797 (1991).
- [7] J.P. Hirth and G.M. Pound, Progress in Materials Science **11** (Macmillan, New York, 1963) p. 15.

- [8] P.E. Freeland, K.A. Jackson, C.W. Lowe, and J.R. Patel, Appl. Phys. Lett. **30**, 31 (1977).
- [9] S.M. Sze, Physics of Semiconductor Devices, 2nd ed. (John Wiley & Sons, New York, 1981) p. 69.
- [10] F.A. Trumbore, Bell Syst. Tech. J. **39**, 205 (1960).
- [11] I.N. Yassievich and L.C. Kimerling, Semicond. Sci. Technol. **7**, 1 (1993).
- [12] M. Lannoo and C. Delerue, (MRS Proceedings) this volume.
- [13] P.B. Klein and G.S. Pomrenke, Electron. Letters **24**, 1503 (1988).

OXYGEN-ENHANCED 1.54 μ m PHOTOLUMINESCENCE OF Er⁺³ IN SILICON

F. ARNAUD D'AVITAYA^{a*}, Y. CAMPIDELLI^a, J.A. CHROBOCZEK^a,
P.N. FAVENNEC^b, H. L'HARIDON^b, D. MOUTONNET^b, AND A. WASIELA^c

^a Centre National d'Etudes des Télécommunications, 38243 Meylan, France,

^b Centre National d'Etudes des Télécommunications, 22301 Lannion, France,

^c Laboratoire de Spectrométrie Physique, Université Joseph Fourier,
38402 St. Martin d'Hères, France.

ABSTRACT

Favennec *et al.* (Jap. J. Appl. Phys. **29**, L524, 1990) reported that the 1.54 μ m photoluminescence of Si implanted with Er⁺³ is activated by oxygen impurities. We observe a significant enhancement in the luminescence in Er-doped silicon epitaxial layers MBE-grown with intentional oxygen contamination. The PL is shown to be a bulk property of the material as it persisted after a partial layer removal by wet etching.

INTRODUCTION

It has been reported by Favennec *et al.* [1] and Michel *et al.* [2] that the photoluminescence (PL) in the 1.54 μ m wave-length region is detectable in Er-implanted silicon crystals solely when the oxygen impurities and the Er⁺³ ions coexist in the Si matrix. This finding has been corroborated in [1] by two sets of experimental data. First a correlation has been established between the intensity of the 1.54 μ m PL in Si:Er and the residual oxygen concentration in Si substrates used for Er implantation. Thus Czochralski-grown Si substrates (known to be oxygen-rich) gave a much stronger PL intensity than the zone-refined crystals or CVD-grown Si layers (almost oxygen-free), after the Er implantation and a subsequent defect annealing. Secondly, a more direct confirmation of the oxygen-induced activation of the 1.54 μ m PL in Si:Er has been furnished by a series of experiments in which Er and O were both implanted into CVD Si epilayers. The layers showed appreciable PL and both elements were found to redistribute during annealing, producing characteristic density peaks in their respective SIMS profiles, occurring at the same depths for Er and O and having comparable amplitudes. This fact has been interpreted [1] as evidence that a part of implanted O ions form optically active Er-O complexes in Si. The hypothesis of the Er-O complex formation has not been directly confirmed so far, although it is consistent with the large crystal-field splitting of the 4f multiplets of the Er⁺³ in the PL spectra [3]. This suggests ionic bonding of the optically-active Er ions embedded in the crystalline lattice. The idea of the oxygen-rare earth complex formation is not new; e.g. Petrov *et al.* [4] used this concept to account for their transport data in Si:Er. Furthermore correlations in SIMS profiles of oxygen and other elements have been reported (cf. e.g. [5]).

In this paper we present further evidence that oxygen impurities activate the PL of Er⁺³ ions in Si. We have studied the PL properties of MBE-grown Si samples, Er-doped during growth. Some of them were prepared with a controlled oxygen contamination. We found that the 1.54 μ m PL is detected only in the samples which contained oxygen. The growth experiments were followed by the PL measurements on samples subjected to etching. They demonstrate that the luminescence comes from the interior of the layers and rule out the possibility of it originating in the surface oxide, or a near-surface region.

SAMPLE PREPARATION

Epitaxial layers of Si were MBE grown maintaining a constant flux of Si and Er, calibrated so as to give the atomic Er concentration of the order of 10¹⁸ cm⁻³. The layers were several kÅ thick and had good overall crystallographic properties. They were smooth, mirror-like, and showed a distinct 7x7 low energy electron diffraction pattern on the (111) surface. The ratio of

intensities for Rutherford back-scattering, measured at the channeling and the randomizing orientations was typically below 10%, indicating a small defect concentration in Si and that the impurities were mainly substitutional. However the transport properties of the layers demonstrated that Er^{+3} cannot be treated as a simple acceptor, providing one hole per atom, although electrical transport in the layers was found to be hole-dominated. We interpreted the Hall data using a single-carrier transport model. The room temperature carrier concentration thus determined in the layers was typically of the order of 10^{15}cm^{-3} , the hole mobility about $25 \text{Vcm}^2 \text{V}^{-1} \text{s}^{-1}$, and the resistivity $75 \Omega \text{cm}$. These values are characteristic of trap-dominated conduction due to residual impurities in a compensated semiconductor. The samples doped with Er alone showed no appreciable PL in the $1.54 \mu\text{m}$ wavelength region, although the near-band gap luminescence was visible at higher laser excitations, with the characteristic electron-hole droplet lines dominating the spectrum at sufficiently low temperatures.

The activation of the PL of Er^{+3} in Si by oxygen implantation described in ref. [1] suggested that the incorporating of oxygen into the MBE layers could lead to a similar effect. In order to introduce oxygen into the layers during the MBE epitaxy, we modified the growth chamber by introducing a capillary enabling the layers to be grown in a jet of gas, and preserving the overall vacuum level in the system at below 10^{-8} Torr. By maintaining the Si and Er flux at the same level as in the preceding set of experiments, conducted without the presence of oxygen, we obtained samples with an atomic Er concentration of about 10^{18}cm^{-3} . Evaluation of the O content was not straightforward. However, from the appearance of a weak signal observable in the vicinity of 500eV in the Auger spectrum taken on the layers *in situ*, it could be evaluated to be above 10^{19}cm^{-3} . The atomic composition of the MBE Si:Er:O samples thus fabricated was, therefore, similar to that of samples prepared by the Er and O co-implantation [1].

Another method we used for incorporating oxygen into Er-doped MBE layers involved amorphous Si:Er layers, grown on cold substrates. The samples were briefly exposed to an ambient atmosphere, in order to trap a small amount of oxygen in the amorphous layer. They were subsequently recrystallized either by rapid thermal annealing (RTA) or by furnace heating under an oxygen-free gas flow. This method of oxygen incorporation into the Er-rich layer does not offer much control of the O content, but was used for convenience and eliminated the necessity of contaminating the MBE chamber with oxygen. As we shall demonstrate below it gave comparable results to the other method.

RESULTS

The PL spectra taken at 1.8K on an Er-implanted Czochralski Si sample and on an Er-doped MBE sample, both containing about 10^{18}Er/cm^3 are compared in Fig. 1. Note that the power of the primary Ar laser beam used for the MBE sample was about 4.5 times higher than that used for the implanted layer and produced only a weak, diffused PL signal in the $1.54 \mu\text{m}$ spectral region. The implanted sample showed a reasonably strong luminescence with a resolved multiplet structure.

A comparison of the PL spectra measured at 77K on the Er-implanted sample (data at 1.8K shown in Fig. 1), and on two MBE-grown samples, containing both Er and O, is made in Fig. 2. The 0202 sample was MBE-grown in the oxygen jet, as described, and the 0602 sample was initially amorphous and recrystallized after exposure to air. The luminescence in MBE samples was easily measurable, but about an order of magnitude weaker than that observed in the Er-implanted sample. A comparison of the PL intensity near the 1.1eV indirect gap of Si with that in the spectral range of Er^{+3} ions (respectively near $1 \mu\text{m}$ and $1.5 \mu\text{m}$) was made. We found that the amplitude ratio of the most prominent peaks in the two spectral regions, measured at the same excitation level, at 1.8K, on the MBE0202 sample, was about 3:1. A separate study was devoted to optimizing the annealing conditions giving the strongest PL signal and the RTA-treatment at about 700°C was found to be optimal. The sample MBE0602 was prepared under these conditions.

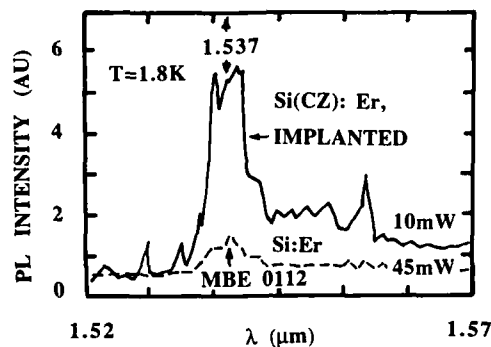


Figure 1
The 1.8K photoluminescence of Er-doped Si.
 The Czochralski-grown Si are known to contain oxygen. The MBE0112 sample was grown without oxygen. Note different excitation power levels used for each sample.

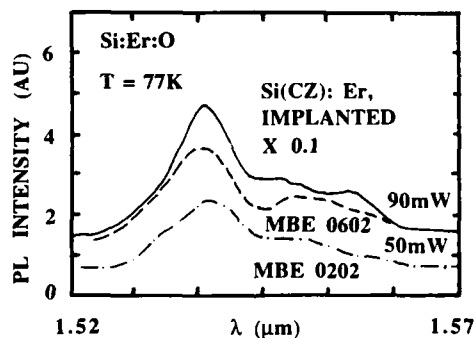


Figure 2
The 77K photoluminescence of Er-doped Si. Samples containing oxygen.
 The Si(CZ) sample as in Fig. 1. The MBE0202 sample was grown in a jet of O_2 and the MBE0602 sample was initially amorphous and recrystallized after exposure to air.

Because Er^{+3} is known to luminesce when embedded in the SiO_2 matrix, we performed a series of experiments involving chemical treatment of the MBE-grown Si:Er:O samples in order to establish whether the PL we observed indeed originated in the doped Si.

First, we compared the luminescence of the samples before and after a dip in 30% HF. The HF etch is known to rapidly attack SiO_2 and to be neutral in relation to Si. An accepted criterion of oxide removal is the absence of wetting of the surface of a sample when dipped in the HF etch. We found that the samples subjected to such a treatment retained their luminescence properties.

Having established that the PL is not associated with the surface native oxide, we used a KOH etch, known to attack Si, in order to check whether the thinning of the doped layer affected the PL or not. We used a 33% KOH solution with a 3:1 isopropanol/methanol mixture as a wetting agent, at 75°C, stirring the solution during the reaction. The thickness of the removed layer was then directly measured. We found that the samples showed no change in the PL intensity after a 50% decrease in the thickness of the initial layer. It is worthwhile noting that the etch rate in the Si:Er:O samples was an order of magnitude higher than in the control samples [(111) zone-refined Si]; they were, respectively equal to about 0.2 $\mu\text{m}/\text{min}$ and 0.03 $\mu\text{m}/\text{min}$. The KOH etch is known to be highly preferential and its etch rate on the (100) surfaces is about an order of magnitude higher than on the (111) planes, where it is primarily used for defect revelation. The increased etch rate in Si samples containing Er and O impurities suggests that the (100) planes were accessible on the nominally (111) surface of the specimens. This implies the presence of defects or steps at the surface.

As the formation of Er precipitates is known to limit the 1.54 μm PL in III/V semiconductors, a few measurements of cathodoluminescence were carried out in order to check the homogeneity of Er^{+3} luminescence in the MBE Er-doped samples. The experiments revealed the presence of areas showing much stronger luminescence than the background. No systematic study has, however been devoted to this problem.

CONCLUSIONS

We found that the luminescence of Er^{+3} ions in Si can be enhanced if oxygen is introduced into Er-doped layers during the MBE growth, or during annealing of amorphous layers, previously exposed to atmospheric oxygen. At liquid He temperatures the PL of Er^{+3} in such samples is found to be 3 to 4 times weaker than the 1.1 eV PL involving the indirect gap of Si. We have shown that the PL is not associated with the surface oxide layer nor with the near-surface oxygen-rich Si strata, but that it is a bulk property of Si:Er:O. This work confirms the previous reports [1,2,6,7] on oxygen activation of the 1.54 μm PL of Er^{+3} ions in Si, detected in Er- and O-implanted samples. It is also consistent with the hypothesis put forward in ref. [1] that the PL might be associated with Er-O complexes in Si. However, we cannot exclude the possibility of the PL originating in regions having high concentrations of Er and O. Non-uniform cathodoluminescence suggests the formation of such regions.

ACKNOWLEDGEMENTS

We thank Annie-Claire Papadopoulou (Centre Nat. d'Etudes. Télécom.-Bagneux) for the cathodoluminescence analysis of our samples.

REFERENCES AND FOOTNOTES

*) present address: Université de Marseille-Luminy, 13288 Marseille, France.

1. P.N. Favennec, H. L'Haridon, D. Muttonet, M. Salvi, and M. Gaunau, *Jap. J. Appl. Phys.* **29**, L524 (1990).
2. J. Michel, J.L. Benton, R.F. Ferrante, D.C. Jacobson, D.J. Eagelesham, E.A. Fitzgerald, Y. H. Xie, I.M. Poate, and L.C. Kimmerling, *J. Appl. Phys.* **70**, 2672 (1991).
3. F. Auzel, p. 59 in SPIE Vol. 1182, *French-Israeli Workshop on Solid State Lasers*, Jerusalem 1988.
4. V.V. Petrov, S.V. Prosolovitch, V.D. Tkachev, Yu. A. Karpov, and M.G. Milvidskii, *Phys. Stat. Solidi A* **88**, K141 (1988).
5. A.E. Von Neida, S.J. Pearton, W.S. Hobson, and C.R. Abernathy, *Appl. Phys. Letters*, **54**, 1540 (1989).
6. D.L. Adler, D.C. Jacobson, D.J. Eagelesham, M.A. Marcus, J.L. Beneton, J.M. Poate, and P.H. Citrin, *Appl. Phys. Letters* **61**, 2181 (1992).
7. M. Efeoglou, J.H. Evans, T.E. Jackman, B. Hamilton, D.C. Houghton, J.M. Langer, A. R. Peaker, D. Perovic, I. Poole, N. Ravel, P.H. Hemment, and C.W. Chan, *Semicond. Sci. Technol.*, **8**, 236 (1993).

This article also appears in *Mat. Res. Soc. Symp. Proc.* Vol 298

HIGH CONCENTRATIONS OF ERBIUM IN CRYSTAL SILICON BY THERMAL OR ION-BEAM-INDUCED EPITAXY OF ERBIUM-IMPLANTED AMORPHOUS SILICON

J. S. Custer, A. Polman, E. Snoeks, and G. N. van den Hoven
FOM Institute for Atomic and Molecular Physics
Kruislaan 407, 1098 SJ Amsterdam, the Netherlands

ABSTRACT

Solid phase epitaxy and ion-beam-induced epitaxial crystallization of Er-doped amorphous Si are used to incorporate high concentrations of Er in crystal Si. During solid phase epitaxy, substantial segregation and trapping of Er is observed, with maximum Er concentrations trapped in single crystal Si of up to $2 \times 10^{20} \text{ cm}^{-3}$. Ion-beam-induced regrowth results in very little segregation, with Er concentrations of more than $5 \times 10^{20} \text{ cm}^{-3}$ achievable. Photoluminescence from the incorporated Er is observed.

INTRODUCTION

There is substantial technological interest in achieving efficient light emission from crystal Si (c-Si). Unfortunately, because of its indirect band gap, Si exhibits very inefficient band-to-band luminescence. Ennen *et al.* have pointed out the potential of rare-earth ions as optical dopants in semiconductors, including Si [1,2]. Rare-earth ions in the correct charge state exhibit luminescent intra-4f transitions, which are shielded from the surroundings by filled outer electron shells. This produces a nearly host-independent luminescent transition. Erbium is of particular interest because Er^{3+} has a transition from the first excited state to the ground state at a wavelength of $1.5 \mu\text{m}$, which is important in optical communication technology. There are three major steps to actually use Er-doped Si. First, high concentrations of Er have to be incorporated in Si. Second, the Er must be made optically active, that is have the $3+$ charge state. Finally, the Er ions must be efficiently pumped by electrical excitation.

In this paper, we will concentrate on the first step, incorporating Er in c-Si. Because the solubility limit of Er in Si is not known, it is not clear *a priori* what concentrations can be easily achieved. By analogy to the transition metals, though, it is likely that the solubility of Er is relatively small ($\sim 10^{14} - 10^{16} \text{ Er/cm}^3$). This concentration is too low to make useful optical devices [3]. We demonstrate here that by using non-equilibrium crystal growth, at least $5 \times 10^{20} \text{ Er/cm}^3$ (1 at.%) can be incorporated in c-Si. This is done by recrystallizing an Er-doped amorphous Si (a-Si) layer on c-Si, using either thermal solid phase epitaxy (SPE) [4] or ion-beam-induced epitaxial crystallization (IBIEC) [5]. Both methods are capable of trapping impurities in c-Si above their solid solubility limits [6-8]. Thermal SPE results in significant segregation and trapping of Er [9,10], with trapped concentrations of up to $2 \times 10^{20} \text{ Er/cm}^3$ achievable. IBIEC at 320°C leads to little segregation and nearly complete trapping of Er at concentrations of at least $5 \times 10^{20} \text{ Er/cm}^3$. Both types of samples exhibit photoluminescence (PL) characteristic of Er, and the PL intensity can be optimized by post-growth anneals.

EXPERIMENT

For the SPE sample, $9 \times 10^{14} \text{ cm}^{-2}$ 250 keV Er was implanted into c-Si. The IBIEC sample was made by a $4.0 \times 10^{15} \text{ cm}^{-2}$ 250 keV Er implant. Both implants were performed with the samples heat sunk to a copper block cooled by liquid nitrogen. The (100) c-Si substrates used in this work were Czochralski-grown and either P doped ($1-1.5 \Omega\text{cm}$) (SPE samples) or B doped ($5-10 \Omega\text{cm}$) (IBIEC samples).

The a-Si thicknesses and Er concentration profiles were measured with Rutherford backscattering spectrometry (RBS) using 2 MeV He and a backscattering angle of 110° was used to increase the depth resolution. Thermal anneals to induced SPE were done in a rapid thermal annealer (RTA) under flowing Ar. The indicated anneal times are measured once the actual anneal temperature was reached. Ion-beam-induced epitaxy was performed by irradiating with $1 \times 10^{17} \text{ cm}^{-2}$

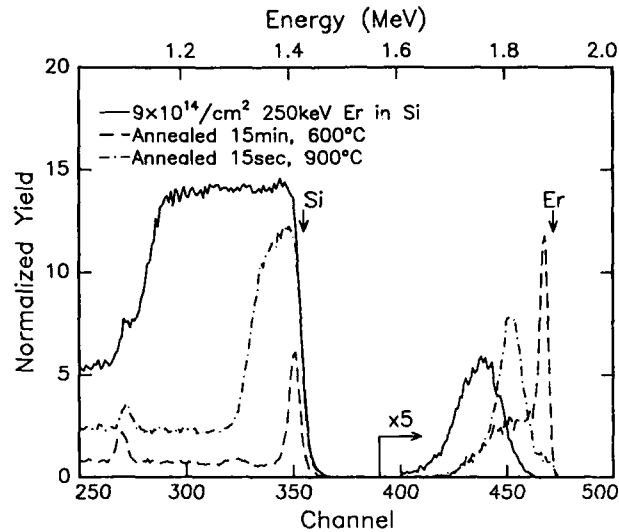


FIG 1. RBS/channeling spectra for samples as-implanted with $9 \times 10^{14}/\text{cm}^2$ 250 keV Er (solid line), which makes a surface amorphous layer, and after annealing either for 15 min at 600°C (dashed line) or for 15 sec at 900°C (dashed-dot line). The Er portions of the spectra are multiplied by a factor of 5.

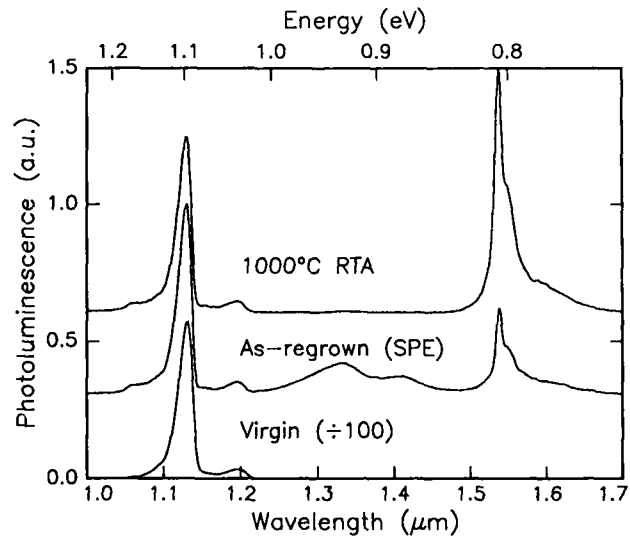


FIG 2. Photoluminescence spectra at 77 K for the $9 \times 10^{14} \text{ Er}/\text{cm}^2$ sample as regrown at 600°C and after a post-regrowth 1000°C RTA anneal. A spectrum for a virgin c-Si wafer is shown for comparison, reduced by a factor of 100.

1 MeV Si with the substrates held at 320°C. The range of the 1 MeV Si, 1.2 μm , is well beyond the a-Si surface layer. After either SPE or IBIEC, samples were annealed in the RTA at up to 1000°C for times up to one minute.

Photoluminescence (PL) spectroscopy was performed using the 514 nm Ar ion laser line as an excitation source (50–250 mW focused into a ~ 0.5 mm diameter spot). The samples were mounted in a vacuum dewar and cooled to liquid nitrogen temperature. The luminescence signal was spectrally analyzed with a 48 cm monochromator and detected with a liquid nitrogen cooled Ge detector. The pump beam was chopped at 10–20 Hz and the Ge detector output was recorded using a lock-in amplifier.

RESULTS

Figure 1 shows RBS/channeling spectra for the 9×10^{14} Er/cm² SPE sample as-implanted and after annealing for either 15 min at 600°C or 15 sec at 900°C. The as-implanted sample has an 160 nm thick a-Si surface layer with a Gaussian Er profile peaked (1.5×10^{20} Er/cm³) at a depth of ≈ 70 nm. After the 600°C anneal, a thin disorder layer ≈ 10 nm thick remains at the surface, but the channeling minimum yield in the regrown layer is $\chi_{\text{min}} < 5\%$, indicating that the crystal quality is good. The Er segregated with 65% of the Er remaining trapped in the regrown crystal at concentrations up to 9×10^{19} Er/cm³. During the 900°C anneal, the initial regrowth is epitaxial, but 60 nm from the surface the quality of the crystal begins to degrade through the introduction of twins [9]. Regrowth of a-Si layers implanted with different Er doses shows that at a given temperature there is a maximum trapped Er concentration above which twins form during growth. This maximum concentration is 2×10^{20} Er/cm³ for SPE at 500°C, 1.2×10^{20} Er/cm³ at 600°C, and only 6×10^{19} Er/cm³ for the 900°C anneals [9,10].

Figure 2 shows PL spectra taken at liquid nitrogen temperature of the 9×10^{14} Er/cm² sample both after regrowth at 600°C and after a subsequent RTA anneal at 1000°C for 15 sec. In addition, the spectrum of a virgin (unimplanted) sample is also shown, with the signal divided by 100. All spectra are offset from each other for clarity. The features near 1.1–1.2 μm are the intrinsic phonon-assisted luminescence from c-Si [11]. In either Er-doped sample, the intrinsic c-Si luminescence is drastically reduced compared with the virgin sample, most likely as a result of reduced carrier lifetimes caused by carrier trapping at remaining structural defects. After SPE, the spectrum shows a feature near 1.55 μm which arises from the Er, as well as a broad band centered around 1.33 μm which corresponds to luminescence from various irradiation-induced defects [11]. Further annealing to 1000°C removes the defect band and increases the strength of the Er signal.

Figure 3 shows RBS/channeling spectra for the 4×10^{15} Er/cm² IBIEC sample as-implanted and after IBIEC with 1×10^{17} /cm² 1 MeV Si at 320°C. The as-implanted sample has a 180 nm thick a-Si layer containing a Gaussian Er profile with a peak concentration of 5×10^{20} Er/cm³. After regrowth, a thin disordered surface region (containing substantial C and O because of the long hot implant) remains on the surface. Behind this layer, the dechanneling yield is $\chi_{\text{min}} = 8\%$, which is normal for IBIEC regrown material [5], but definitely not as good as for the SPE samples. This near-surface dechanneling comes from point defects in the regrown region, not from dislocations or other extended defects. However, starting at ≈ 700 nm from the surface (not seen in this scattering geometry) the dechanneling increases drastically because of a dense network of dislocations from the end-of-range damage of the 1 MeV Si irradiation [12]. The Er profile is barely affected by the IBIEC regrowth, although a little redistribution of Er towards the surface is evident.

Directly after IBIEC growth, the samples exhibit no measurable PL signal. Figure 4 shows PL spectra after post-IBIEC RTA anneals at either 600 or 1000°C for 1 min. The 600°C annealed sample exhibits a small Er-related feature near 1.54 μm . However, it lies on the tail of the large defect-related signal near 1.33 μm . Because the channeling data in Fig. 3 show that the crystal quality is not very good, it is not surprising that there is a substantial amount of defect-related signal in the spectrum.

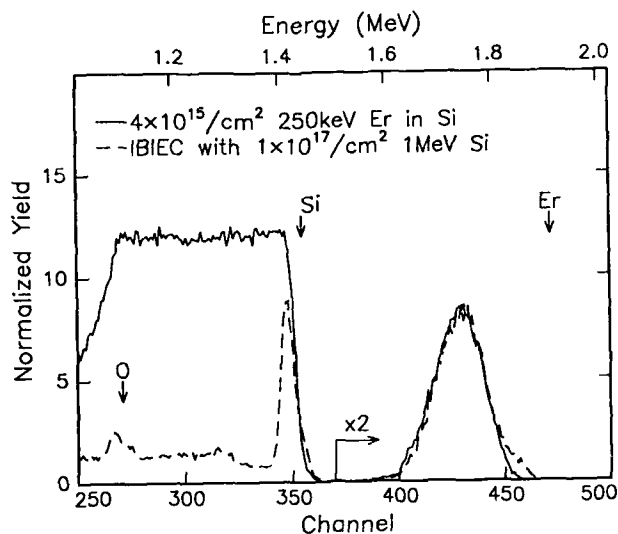


FIG 3. RBS/channeling spectra for the $4 \times 10^{15}/\text{cm}^2$ 250 keV Er sample as-implanted (solid line) and after IBIEC growth with $1 \times 10^{17}/\text{cm}^2$ 1 MeV Si at 320°C (dashed line). The Er portion of the spectrum has been multiplied by 2. Very little redistribution of Er is seen.

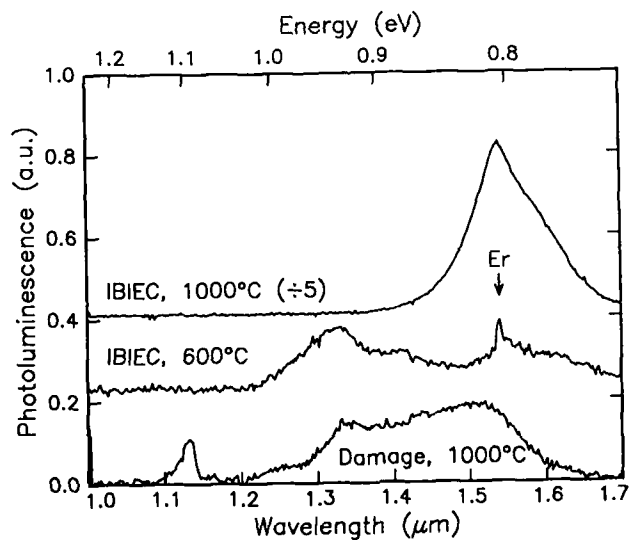


FIG 4. Photoluminescence spectra at 77 K for the IBIEC sample after RTA anneals at 600 and 1000°C. The spectrum of the 1000°C annealed sample has been divided by a factor of 5. The PL spectrum for low-dose Si-implanted Si after annealing at 1000°C also shown.

After annealing at 1000°C, the PL spectrum changes dramatically. The defect band near 1.3 μm disappears, as it does in the SPE sample. Instead, a large, broad feature centered near 1.5 μm appears, which appears very different from the Er signal in the 600°C annealed sample, or in the SPE samples. The question is if this signal is related to the Er at all. We believe that the majority of this signal is *not* from Er, but instead from implantation damage [11]. For comparison, a PL spectrum of a c-Si sample that has been lightly damaged ($2 \times 10^{14}/\text{cm}^2$ 1 MeV Si) and annealed at 1000°C is also shown in Fig. 4. This implant and annealing treatment will result in the formation of dislocations [13]. This sample exhibits the defect band near 1.3 μm (also observed for lower temperature anneals where dislocations are not formed), as well as a second band near 1.5 μm that is similar to what is observed for the IBIEC-regrown sample. Since this sample contains no Er, this signal is clearly not related to Er, and comes most likely from dislocation-related centers [11]. Since IBIEC results in a very high density of dislocations near the end-of-range of the 1 MeV Si, and the probe depth for the 514 nm pump light encompasses this region, the occurrence of this signal is not surprising.

CONCLUSIONS

Thermal SPE of Er-doped a-Si results in significant segregation and trapping of Er at the moving interface. In this way, up to 2×10^{20} Er/cm³ can be incorporated in c-Si. Post-regrowth RTA anneals can be used to increase the photoluminescence from the Er, and eliminate the defect-related PL. IBIEC of Er-doped a-Si results in trapping of at least 5×10^{20} Er/cm³ in c-Si. Again, post-regrowth RTA anneals can be used to increase the PL signal. However, very little of the IBIEC-trapped Er is optically active compared with the SPE samples, and the PL response after high temperature anneals is dominated by the crystal damage inherent to the IBIEC process. Although we have solved the first problem, incorporating high concentrations of Er in c-Si, it appears that either the optical activation or excitation steps are limiting the photoluminescence response of the material.

This work is part of the research program of the Foundation for Fundamental Research on Matter (FOM) and was made possible by financial support from the Dutch Organization for the Advancement of Pure Research (NWO), the Organization for Technical Research (STW), and the Innovative Research Program (IOP Electro-Optics).

REFERENCES

1. H. Ennen, J. Schneider, G. Pomrenke, and A. Axmann, *Appl. Phys. Lett.* **43**, 943 (1983).
2. H. Ennen, G. Pomrenke, A. Axmann, K. Eisele, W. Haydl, and J. Schneider, *Appl. Phys. Lett.* **46**, 381 (1985).
3. Y.-H. Xie, E. A. Fitzgerald, and Y. J. Mii, *J. Appl. Phys.* **70**, 3223 (1991).
4. G. L. Olson and J. A. Roth, *Mater. Sci. Rep.* **3**, 1 (1988).
5. F. Priolo and E. Rimini, *Mater. Sci. Rep.* **5**, 319 (1990).
6. S. U. Campisano, J. M. Gibson, and J. M. Poate, *Appl. Phys. Lett.* **46**, 580 (1985).
7. F. Priolo, J. L. Batstone, J. M. Poate, J. Linnros, D. C. Jacobson, and Michael O. Thompson, *Appl. Phys. Lett.* **52**, 1043 (1988).
8. J. S. Custer, Michael O. Thompson, D. C. Jacobson, and J. M. Poate, *Phys. Rev. B* **44**, 8774 (1991).
9. A. Polman, J. S. Custer, E. Snoeks, and G. N. van den Hoven, *Appl. Phys. Lett.* **62**, 507 (1993).
10. A. Polman, J. S. Custer, E. Snoeks, and G. N. van den Hoven, *Nucl. Instr. and Meth. B*, in press.
11. G. Davies, *Physics Reports* **176**, 83 (1989).
12. R. G. Elliman, J. S. Williams, W. L. Brown, A. Leiberich, D. M. Maher, and R. V. Knoell, *Nucl. Instrum. Methods* **B19/20**, 435 (1987).
13. R. J. Schreutelkamp, J. S. Custer, J. R. Liefting, W. X. Lu, and F. W. Saris, *Mater. Sci. Rep.* **6**, 275 (1991).

This article also appears in *Mat. Res. Soc. Symp. Proc.* Vol 298

OPTICAL DIRECT AND INDIRECT EXCITATION OF Er^{3+} IONS IN SILICON

A. Majima*, S. Uekusa*, K. Ootake*, K. Abe*, and M. Kumagai**

*Meiji University, Kawasaki, Kanagawa, 214 Japan.

**Kanagawa High-Technology Foundation, Kawasaki, Kanagawa, 214 Japan.

ABSTRACT

Optical direct and indirect excitation of erbium (Er) ions in silicon substrates was performed in order to investigate the high efficiency of Er^{3+} -related $1.54\mu\text{m}$ emission ($^4\text{I}_{13/2} \rightarrow ^4\text{I}_{15/2}$) for direct excitation that is not concerned with the indirect band gap and low quantum efficiency of a Si host. The samples were prepared by ion-implantation or thermal diffusion methods. In each sample, photoluminescence (PL) showed the peaks originating from $^4\text{I}_{13/2} \rightarrow ^4\text{I}_{15/2}$ of Er^{3+} ions.

In Er thermally diffused samples, optical excitation for energy level $^4\text{I}_{11/2}$ of Er^{3+} ions was successfully effected by photoluminescence excitation spectroscopy (PLE). The PLE spectra consisted six peaks (963.1nm, 965.0nm, 976.1nm, 978.9nm and 980.9nm) which were caused by direct excitation ($^4\text{I}_{15/2} \rightarrow ^4\text{I}_{11/2}$) of Er^{3+} ions. The emission directly excited is about 2 times more intense than the indirectly excited emission. The six peaks originating from the splitting of the $^4\text{I}_{11/2}$ levels meant that Er^{3+} ions were in the sites of noncubic symmetry. The samples prepared by Er ion-implantation did not show the effect.

INTRODUCTION

A emission in Si is weak because of the its indirect band gap, and the applications of Si have been limited to electrical devices and light absorbing devices. With development of optoelectronic integrated circuits (OEICs), it has been necessary to fabricate light emitting devices in/on Si substrate. In recent years an increasing amount of research has been focused on the realization of III-V/Si-structure OEICs. However, for systems of GaAs light-emitting devices on Si, there is a high lattice mismatch of about 4%. On the other hand, electroluminescence and photoluminescence from rare-earth ions incorporated into III-V compound semiconductors and silicon have been studied because of the sharp and temperature-independent emission due to intra-4f-shell transition of rare-earth ion [1-8]. Especially the $1.54\mu\text{m}$ luminescence peak from Er^{3+} ions have been attracted increasing attention because the wavelength is corresponding to minimum absorption of silica fibers. For the Si:Er system, Er^{3+} -related $1.54\mu\text{m}$ emission is weak, and it is hard to observe the emission at room temperature until now. However, It was reported that the Er doped amorphous silicon prepared from rf-sputtering technique showed Er^{3+} -related emission at room temperature [1]. Recent studies revealed that impurities (B, C, O, N and F) codoped in Si:Er enhance Er^{3+} -related emission [2]. This is due to the fact

that these impurities increase the number of optically activated Er^{3+} ions. In this work, Er^{3+} ions were excited by direct and indirect excitation in order to investigate the Er^{3+} -related emission for direct excitation that is not concerned with the indirect band gap and low quantum efficiency of a Si host.

EXPERIMENTAL

In Er ion implantation, boron (B)-doped p-type CZ Si wafers were used. Er^{+} ions were implanted at room temperature at energy of 2MeV to a dose of $1 \times 10^{13} \text{cm}^{-2}$. To avoid the channeling effect, samples were inclined 7° with respect to ion beam. After ion implantation, annealing was performed at a temperature of 900°C for 30 min. For Er-diffused samples, undoped n-type FZ Si substrates were used as starting materials. Er and Si were deposited on the substrates about 700Å thickness in vacuum (10^{-8} torr). Subsequently, the samples were kept at 600°C for 10 hours in vacuum (10^{-7} torr).

Photoluminescence (PL) spectra were measured by using an argon ion (Ar^{+}) laser (514.5nm or 488nm) and a tunable Ti:sapphire laser as the excitation light sources. PLE spectra were performed by using the Ti:sapphire laser over the wavelength range of $\lambda=780 - 1000\text{nm}$. The PL and PLE spectra are recorded by a 1-m double monochromator and a cooled Ge detector and analyzed using a conventional lock-in technique. PL and PLE spectra were measured as a function of excitation power or temperature.

RESULTS AND DISCUSSION

Typical low temperature PL spectrum at 10K of Er-implanted CZ Si is shown in Fig. 1. The emissions located at $1.5\mu\text{m}$ region were caused by the transition $^4\text{I}_{13/2} \rightarrow ^4\text{I}_{15/2}$ of Er^{3+} ion. The five PL peaks were assigned to the crystal fields splitting of the $^4\text{I}_{15/2}$ ground state into five levels. This shows that the Er^{3+} ion is surrounded by a crystal field of cubic symmetry [3]. The inset of Fig.1 shows the excitation power dependence of Er^{3+} -related emission intensity as well as band-edge emission. The sample was excited with an Ar^{+} ion laser using the 514.5nm line which is near the excited state $^2\text{H}_{11/2}$ of Er^{3+} ion, and 488nm laser line. No difference in PL intensity was observed between the two laser lines. The full widths at half maximum (FWHMs) of lines of Er^{3+} -related PLE spectra are very narrow (as shown in Fig. 2), therefore the direct excitation to $^2\text{H}_{11/2}$ seems to be difficult. The excitation of the Er^{3+} ions is due to energy transfer from the recombination of electron-hole pairs in the Si host. The Er^{3+} -related emission intensity shows weak dependence against excitation intensity in comparison to GaAs:Er (Bantien *et al*) [4]. We assume that the efficiency of energy transfer to Er^{3+} ions is very low, or a small number of Er^{3+} ions exists in Si host. No Er^{3+} -related PLE spectra ($^4\text{I}_{15/2} \rightarrow ^4\text{I}_{11/2}$) was observed over the wavelength range of $\lambda=960 - 990\text{nm}$.

Figure 2 shows the typical low temperature PL spectrum at 10K of Er-diffused FZ Si. Five prominent peaks with other weak emissions were observed around $1.549\mu\text{m}$. This spectrum is very similar to the GaAs:Er

prepared by liquid phase epitaxy (LPE) [4] and thermal diffusion [5], but different from those in ion-implanted Si:Er [6] and molecular beam epitaxy (MBE)-grown Si:Er [7]. This fact suggests that the semiconductors such as Er doped GaAs and Si under equilibrium growth show same Er^{3+} -related spectra. The inset of Fig. 2 shows the PLE spectrum of Er^{3+} -related PL for the Er thermally diffused sample. The PL intensity of Er^{3+} was detected at the $1.549\mu\text{m}$ line. The spectrum consisted of six sharp peaks (963.1nm, 965.0nm, 976.1nm, 978.9nm and 980.9nm) that were caused by the direct excitation ($4\text{I}_{15/2} \rightarrow 4\text{I}_{11/2}$) of Er^{3+} ion. This fact indicates that Er^{3+} -related emission is enhanced by direct excitation. The six peaks originating from the splitting of the $4\text{I}_{11/2}$ level meant that Er^{3+} ions were in the site of noncubic symmetry. When Er^{3+} ion is in a site of cubic symmetry, $4\text{I}_{11/2}$ state splits into four levels. Single-crystal X-ray diffraction was carried out to investigate crystal structure and revealed that surface of Si did not have the diamond structure. Therefore the Er diffused samples might have amorphous-like structure with a lower absorption coefficient than crystal Si.

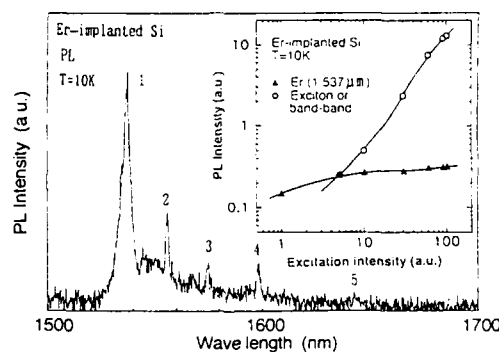


Fig. 1. PL spectrum of Er-implanted CZ Si. Inset shows excitation power dependence of Er^{3+} -related emission ($1.537\mu\text{m}$ line) intensity.

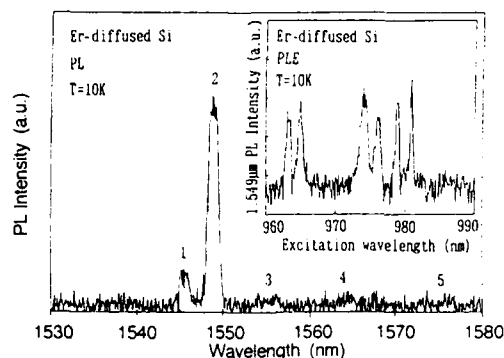


Fig. 2. PL spectrum of Er thermally diffused FZ Si. Inset shows PLE spectrum of Er^{3+} -related emission ($1.549\mu\text{m}$ line) intensity.

Figure 3 shows the PLE spectra of the Er center in thermal diffused sample (20mol% Er in the Si powder), where the PLE spectra was obtained by monitoring the main PL peak ($\lambda_{PL}=1.549\mu\text{m}$) intensity. Figure 3 (a) and (b) show the spectrum under different excitation power. Under low excitation power as shown in Fig.3 (a), six PLE lines in the $0.98\mu\text{m}$ region ($^4I_{15/2} \rightarrow ^4I_{11/2}$) and three weak lines in the $0.80\mu\text{m}$ region ($^4I_{15/2} \rightarrow ^4I_{9/2}$) were observed. As shown in Fig. 2, these thermal diffused samples, the Er center is surrounded by a crystal field of noncubic symmetry. If the Er center is surrounded by a crystal field of noncubic symmetry, five PLE lines in $0.80\mu\text{m}$ region are expected. We assume that other two lines in this region are hidden behind base line, i.e., indirect excitation-related emission since the absorption coefficient of Si in $0.80\mu\text{m}$ region is an order higher than in $0.98\mu\text{m}$ region. For that reason, under high excitation power [Fig. 3 (b)], the base line intensity of PLE spectrum in $0.80\mu\text{m}$ region was increased, on the other hand, the PLE spectrum in $0.98\mu\text{m}$ region is very similar to that under low excitation. In $0.98\mu\text{m}$ region, the lines on long-wavelength side tend to intense, but it is not clear that it is caused by absorption coefficient of Si host.

Figure 4 shows the excitation power dependence of Er^{3+} -related PL peak ($\lambda_{PL}=1.549\mu\text{m}$). The optical direct excitation ($\lambda_{ex}=980.9\text{nm}$) and indirect excitation ($\lambda_{ex}=970.0\text{nm}$) were performed, respectively. The emission directly excited is always about 2 times more intense than the indirectly excited emission in each excitation power, but does not show

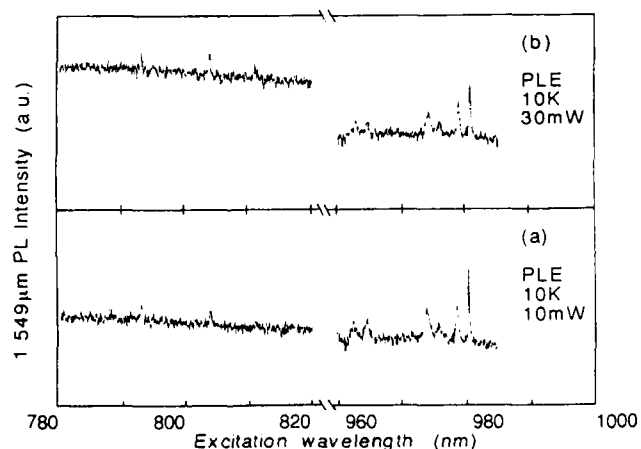


Fig. 3. PLE spectra of Er-thermally diffused FZ Si (Er: 20 mol% powder) taken at two different excitation power: (a) 10mW excitation; (b) 30mW excitation. The Er^{3+} -related PL was detected at the $1.549\mu\text{m}$ line.

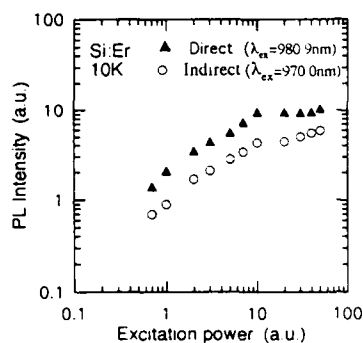


Fig. 4. Excitation power dependence of Er^{3+} -related PL peak ($\lambda_{\text{PL}}=1.549\mu\text{m}$).

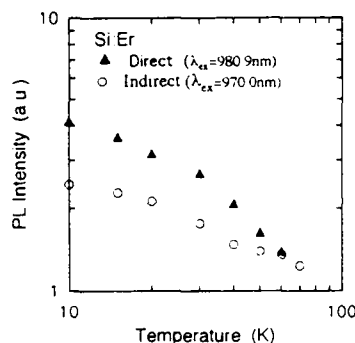


Fig. 5. Temperature dependence of Er^{3+} -related PL peak ($\lambda_{\text{PL}}=1.549\mu\text{m}$).

strong dependence on the excitation power. This indicates that the Er^{3+} ion is well excited by optical direct excitation, however, when the excitation energy is above the energy gap (E_g) of Si host, this efficient excitation is disturbed by absorption coefficient of host material even if the absorption coefficient was considerable low.

Figure 5 shows temperature dependence of the PL peak intensity ($\lambda_{\text{PL}}=1.549\mu\text{m}$) of direct excitation ($\lambda_{\text{ex}}=980.9\text{nm}$) and indirect excitation ($\lambda_{\text{ex}}=970.0\text{nm}$). These two intensities decrease with increasing temperature, and at a temperature of around 60K the direct excitation peaks were hidden behind the indirect excitation-related emission. We expected that the directly excited PL does not depend more on temperature than indirectly excited, however, the Er-related intensity was hardly observed about at 100K. It was reported that Er^{3+} ions excited directly by impact excitation (without energy transfer from the recombination of electron-hole pairs), the emission intensity decreases very slowly with increasing temperature [8]. This reason is assumed that the excitation does not depend on nonradiative process (e.g., Auger recombination) which increases with increasing temperature. In our case, the emission intensity decreases rapidly because the absorption coefficient of Si host in $0.98\mu\text{m}$ region increases with increasing temperature. In the region, the absorption coefficient of Si varies critically with excitation wavelength, and temperature.

CONCLUSION

In summary, the optical direct and indirect excitation of Er^{3+} ions in Si was performed to investigate the high efficiency of Er^{3+} -related emission. The excitation wavelength was chosen to be equal to the excited states of Er^{3+} ion, which is above bandgap-energy of Si host. For the samples prepared by ion-implantation, no difference in Er^{3+} -related PL intensity was observed between two laser lines, 488nm and 514.5nm. For the samples prepared by thermal diffusion, optical excitation for energy level

$^4I_{11/2}$ of Er^{3+} ions was successfully effected by photoluminescence excitation spectroscopy. This effect was caused by low absorption coefficient of Si host.

ACKNOWLEDGMENTS

This work is supported in part by a Grant-in-Aid for Scientific Research from the Ministry of Education, Science and Culture, Japan.

REFERENCES

- [1] T. Oestereich, C. Swiatkowski, and I. Broser, *Appl. Phys. Lett.* **56**, 446 (1990).
- [2] J. Michel, J. L. Benton, R. F. Ferrante, D. C. Jacobson, D. J. Eaglesham, E. A. Fitzgerald, Y.-H. Xie, J. M. Poate, and L. C. Kimerling, *J. Appl. Phys.* **70**, 2672 (1991).
- [3] Y. S. Tang, K. C. Heasman, W. P. Gillin, and B. J. Sealy, *Appl. Phys. Lett.* **55**, 432 (1989).
- [4] F. Bantien, E. Bauser, and J. Weber, *J. Appl. Phys.* **61**, 2803 (1987).
- [5] Xinwei Zhao, Kazuhiko Hirakawa, and Toshiaki Ikoma, *Appl. Phys. Lett.* **54**, 712 (1989).
- [6] H. Ennen, J. Schneider, G. Pomrenke, and A. Axmann, *Appl. Phys. Lett.* **43**, 943 (1983).
- [7] H. Ennen, G. Pomrenke, A. Axmann, K. Eisele, W. Haydl, and J. Schneider, *Appl. Phys. Lett.* **46**, 381 (1985).
- [8] Hideo Isshiki, Riichiro Saito, Tadamasa Kimura, and Toshiaki Ikoma, *J. Appl. Phys.* **70**, 6993 (1991).

EFFECT OF THE Er^{3+} CONCENTRATION ON THE LUMINESCENCE OF $\text{Ca}_{1-x}\text{Er}_x\text{F}_{2+x}$ THIN FILMS EPITAXIALLY GROWN ON Si(100)

A.S. BARRIERE, S. RAOUX, P.N. FAVENNEC*, H. L'HARIDON** and D. MOUTONNET**

LEMME, Univ. Bordeaux I, 351 c. de la Libération, 33405 Talence, France.

*CNET/DIR/SAS, **CNET/LAB/OCM, France Télécom, 2 route de Tregastel, BP 40, 22301 Lannion, France.

ABSTRACT

$\text{Ca}_{1-x}\text{Er}_x\text{F}_{2+x}$ thin films, with a substitution rate, x , varying from 1 to 20%, were deposited on Si(100) substrates by sublimation of high purity solid solution powders under ultra-high-vacuum. Rutherford backscattering studies have shown that the films have the composition of the initial solid solution powders, are quite homogeneous and are epitaxially grown on the substrates.

The optical properties of these films were studied by means of cathodoluminescence and photoluminescence. At room temperature, the emissions due to the de-excitations from the $^4\text{S}_{3/2}$, $^4\text{F}_{9/2}$, $^4\text{I}_{11/2}$ and $^4\text{I}_{13/2}$ excited levels to the $^4\text{I}_{15/2}$ ground state of Er^{3+} ($4f^{11}$) ions are easily detected ($\lambda = 0.548, 0.66, 0.98$ and $1.53 \mu\text{m}$).

The strong $1.53 \mu\text{m}$ infrared luminescence, which presents evident potential applications for optical communications, is maximum for an erbium substitution rate included between 15 and 17%. These Er concentrations are three or four orders of magnitude greater than the optimum ones in the case of Er-doped semiconductors, which are close to 10^{18} cm^{-3} . In the visible range, the luminescences are also important. They allow us to detect high energy ion or electron beams. However their maximum efficiencies were observed for a relatively low erbium concentration, close to 1%. These different behaviours are explained by the cross relaxation phenomena, which depopulate the higher levels to the benefit of the $^4\text{I}_{13/2} \rightarrow ^4\text{I}_{15/2}$ transition.

The energy distribution of the Stark sublevels of the $^4\text{I}_{15/2}$ state, which results from crystal field splitting, was deduced from a photoluminescence study at 2K. The obtained results show that the environment of the luminescent centres does not change with the erbium concentration.

At last, it must be noted that the refractive index of the layers increases with the erbium concentration, leading to the realization of optical guides. Consequently opto-electronic components could be developed from such erbium doped heterostructures.

INTRODUCTION

Rare earth (RE) elements have partially filled $4f$ shells, which are well screened by outer closed orbitals $5s^2$ and $5p^6$. Consequently, the intrashell transitions of $4f$ electrons give rise to identical sharp emission spectra in various host materials [1]. Among RE, erbium, which has a luminescence peak centered at $1.53 \mu\text{m}$ (0.811 eV), which lies within the spectral range for minimum absorption in silica-based optical fibers, seems to be particularly attractive [2,3].

In other respects, it is well known that calcium fluoride (CaF_2) thin films, can be epitaxially grown on silicon substrates. Indeed the crystalline structure of CaF_2 (fcc fluorine) is very similar to that of Si (fcc diamond) and its lattice parameter (5.462 \AA) is close to that of silicon (5.431 \AA) [4]. Moreover it must be noticed that the solubility limit of ErF_3 in CaF_2 is very large (40%) [5].

These considerations led us to study the growth of $\text{Ca}_{1-x}\text{Er}_x\text{F}_{2+x}$ thin films under ultrahigh vacuum (UHV) on Si(100) substrates, x varying from 1% to 20% and the optical

properties of the obtained structures. In this case the host material seems to be very attractive to have a strong luminescence intensity. It presents a wide gap ($E_g = 11.9$ eV) [6], the low phonon energy in this material can enhance the probabilities of photonic de-excitations, compared with another matrix, and the solid solution thin films can be grown with a high degree of crystal quality and purity.

The texture, structure and composition of the obtained layers were respectively studied by means of scanning electron microscopy (SEM), X-ray diffraction (DX) and nuclear analysis. Their optical properties were deduced from cathodoluminescence (CL) and photoluminescence (PL) measurements, performed from room temperature (RT) to 2K.

GROWTH AND CHARACTERIZATION

Thin films of $\text{Ca}_{1-x}\text{Er}_x\text{F}_{2+x}$ were grown on Si(100) substrates, classically cleaned (degreasing, etching (1min in hot HNO_3), de-oxidization (HF-ethanol, 10%)) under a dry nitrogen atmosphere, before outgassed at 800°C under vacuum. The initial solid solution powders, prepared by direct synthesis of binary fluorides (CaF_2 and ErF_3) at 1150°C and controlled from X-ray diffraction [7], were evaporated under UHV at 1250°C from platinum crucibles. The growth rate was 0.1 nm s^{-1} and the temperature of the substrates was 550°C . The thicknesses of the films did not exceed $1.5 \mu\text{m}$.

A SEM study of the structures showed that for high erbium substitution rates the thin film surfaces are rugged, while, for x lower than 17%, the surfaces are smooth. For such Er concentrations, the X-ray diffraction patterns showed that the layers are crystallized. Only one diffraction peak was revealed indicating that the (100) planes of the fluoride are parallel to the substrate [7].

The composition of the layers was mainly deduced from Rutherford backscattering (RBS) of $2 \text{ MeV } ^4\text{He}^+$ particles. This technique and equipment are described in Ref. 8. The scattering angle in the laboratory coordinates was $\theta_L = 160^\circ$. The surface barrier detector has a resolution of 13.5 keV , checked with a ^{241}Am source. The experimental equipment allows us to record the RBS spectra of single crystal targets under either random or channeling conditions [9,10]. For classical RBS investigations the spot of the incident beam was typically 1 mm^2 . It can be reduced to $1.5 \times 1.5 \mu\text{m}^2$, using a nuclear microprobe, to study the spatial distribution of the basic components at the surface of the samples. During the measurements, the pressure in the analysis chamber was lower than 10^{-7} Torr and the samples remained at room temperature.

For example, RBS spectra, random (α) and aligned (β), of a 130 nm thick $\text{Ca}_{0.9}\text{Er}_{0.1}\text{F}_{2.1}$ thin film, deposited on a Si(100) substrate at 550°C are presented in fig. 1-a. The peaks occurring at 1.873 , 1.355 and 0.873 MeV correspond, respectively, to

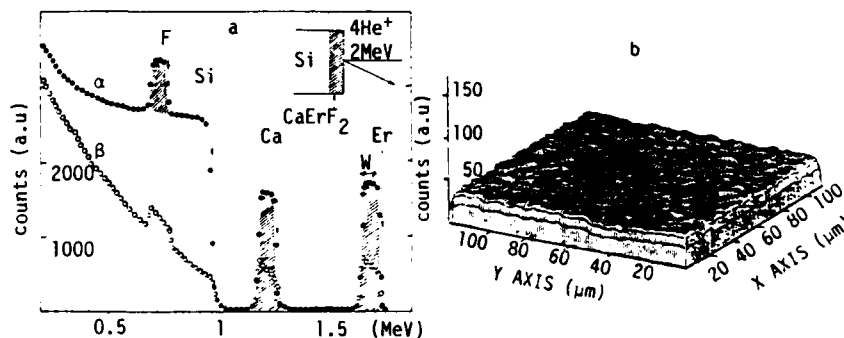


Fig. 1. (a) RBS spectra (α) random and (β) aligned of a 130 nm thick $\text{Ca}_{0.9}\text{Er}_{0.1}\text{F}_{2.1}/\text{Si}(100)$ structure; (b) surface distribution of erbium on a $120 \times 120 \mu\text{m}^2$ area of the fluoride layers.

erbium, calcium and fluorine of the layer. The global atomic concentration ratio of the different basic components, calculated from a comparison of the areas of RBS peaks, correspond well (whatever the theoretical substitution rate, x_{th} , varying from 1 to 20% to $N(F)/N(Ca) = (2+x_{th})/(1-x_{th})$ and $N(Er)/N(Ca) = x_{th}/(1-x_{th})$). No significant impurity, in particular oxygen, was revealed in the bulk of the layers with this analysis technique, even if the films are deposited on light substrates as carbon. Moreover, no heavy impurities were detected from particulate induced X-ray emission (PIXE) studies.

To establish the in depth concentration profiles $N(F)/N(Ca)$ and $N(Er)/N(Ca)$, thin films of increasing thicknesses were grown on silicon substrates and the areas of RBS peaks of the different components were compared. In all cases, the atomic concentration ratios were found to be close to the expected theoretical values. The surface distribution of erbium atoms was studied by using the nuclear microprobe previously mentioned. Spectrum b in Fig. 1 was obtained on the basis of an energy window, W , corresponding to the erbium response, on the RBS pattern (fig. 1-a). It illustrates the surface distribution of this element on a $120 \times 120 \mu m^2$ sample area and shows that its content does not vary significantly in the different points of the studied structure.

The measure of the ratio H_A/H_R of the heights of two spectra taken in the near-surface region for aligned and random orientations, referred to as the minimum yield χ_{min} , allows us to estimate the quality of the epitaxy of a deposited thin film at the surface of a single-crystal substrate [11,12]. The random (α) and aligned (β) spectra of the structure previously studied are reported in fig. 1-a. They show that a channeling of the incident particles with the (100) axis of the substrate is observed in the fluoride layer. Therefore, an epitaxy of the solid solution thin films on Si(100) seems to be obtained. However, near the external surface of the structure χ_{min} has not been found lower than 25%, although the relative mismatch between the solid solution and the silicon substrate does not exceed 1.3% at room temperature. Such an observation could be partially due to the presence of supplementary F ions in interstitial sites of these materials.

OPTICAL PROPERTIES

The energy distribution of the $4f^{11}$ levels of Er^{3+} ions in CaF_2 environment was deduced from optical absorption measurements, performed at RT on the solid solution powders, by using a Varian-Cary 2415 spectrometer. Among the most intensive absorptions we have noted those corresponding to the transitions between the $^4I_{15/2}$ ground state and the $^4F_{7/2}$ and $^2H_{11/2}$ excited levels ($\lambda = 484$ and 517 nm). Consequently the 488 and 514.5 nm lines of an Ar^+ ion laser were chosen as excitation source for PL studies. The CL spectra were taken on a JEOL 840 scanning electron (SEM). The beam parameters were : 10 keV, 10 nA, focussed on $2.5 \times 2.5 \mu m^2$. For photon detection a cooled GaAs photo-multiplier and a cooled germanium detector were used in the visible and the near-infrared ranges, respectively.

For example, the PL and CL spectra of a 240 nm-thick $Ca_{0.87}Er_{0.13}F_{2.13}$ epitaxial layer on a Si(100) substrate, performed at RT, are presented in Fig. 2 (full and dashed lines respectively). They show that in the visible range, the $^4S_{3/2}$ and $^4F_{9/2} \rightarrow ^4I_{15/2}$ transitions ($\lambda = 533$ and 650 nm) and in the near-infrared domain the $^4I_{11/2}$ and $^4I_{13/2} \rightarrow ^4I_{15/2}$ transitions ($\lambda = 980$ and 1530 nm) give strong light emissions. It is interesting to note that, in a good agreement with the nuclear micro-probe analysis, previously mentioned, the SEM-CL spectra show that the luminescence is homogeneous in all points of the surface of the layers. Moreover, in this case, we have remarked that the luminescence intensity at RT is only 30% reduced compared to that observed at 10K.

In the following we will only present some PL observations. First, we have reported in fig. 3, the evolution of the $^4S_{3/2} \rightarrow ^4I_{15/2}$, $^4F_{9/2} \rightarrow ^4I_{15/2}$ and $^4I_{13/2} \rightarrow ^4I_{15/2}$ PL intensities as a function of the erbium substitution rate, x , in $Ca_{1-x}Er_xF_{2+x}$ thin films grown on Si(100) substrates. Each experimental point corresponds to the integrated surface

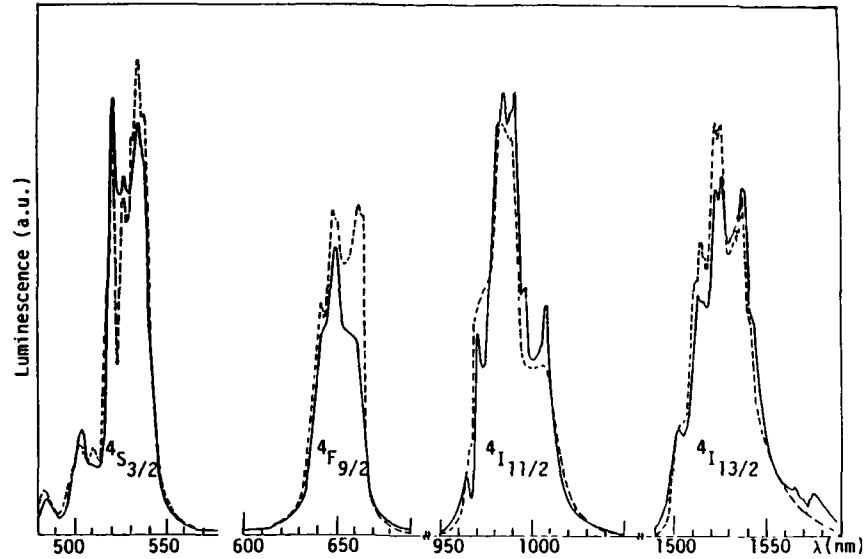


Fig. 2 - PL (full lines) and CL (dashed lines) of a $\text{Ca}_{0.87}\text{Er}_{0.13}\text{F}_{2.13}/\text{Si}(100)$ structure at RT.

of the observed peaks. In the visible range, the PL intensity continuously decreases from $x = 1\%$ to $x = 20\%$, while for the $1.53 \mu\text{m}$ transitions, the higher PL intensities have been found for x varying from 15% to 17%. These different behaviours are controlled by the cross relaxation phenomena which depopulate the higher states while the $^4\text{I}_{13/2}$ levels is enriched.

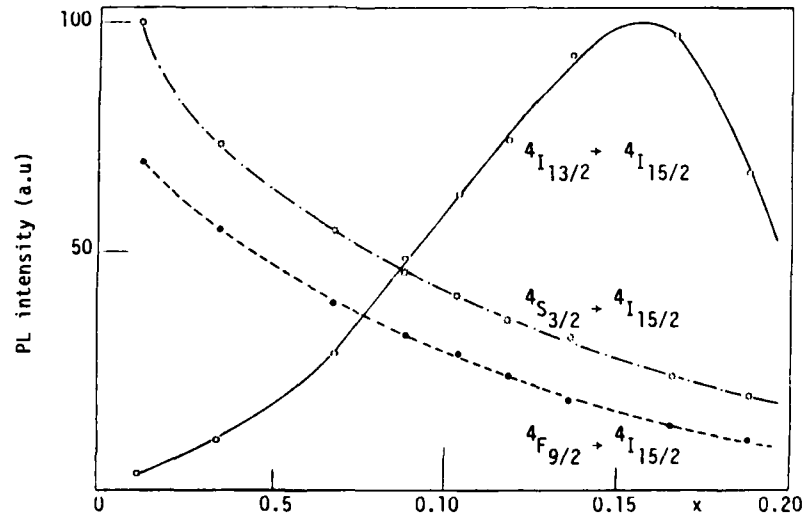


Fig. 3 - $1.53 \mu\text{m}$ and visible PL intensities, at RT, as a function of the erbium concentration, in $\text{Ca}_{1-x}\text{Er}_x\text{F}_{2+x}$ thin films grown on $\text{Si}(100)$.

Such results seem very attractive since, in these solid solution thin films, the maximum of the 1.53 μm PL intensity is obtained for an erbium concentration of three order of magnitude greater than in the case of erbium-doped classical semiconductors (Si, GaAs, InP. ...).

The crystal field splitting (Stark effect) of the $^4I_{15/2}$ ground state was studied by means of PL measurements, performed at 2K, as a function of the erbium substitution rate, x . In fig. 4 are represented the PL spectra of three $\text{Ca}_{1-x}\text{Er}_x\text{F}_2+\text{x}/\text{InP}(100)$ structures. The mixed, full and dashed lines, correspond respectively to $x = 4, 6$ and 15%.

For low erbium concentrations, five principal lines occur on the spectra, labelled 1, 2, 3, 4 and 5. This could be in agreement with a crystal field of cubic symmetry, as present at a Ca substitutional site in the CaF_2 lattice, for which the free ion spin-orbit $^4I_{15/2}$ states of Er^{3+} ($4f^{11}$) split into five Kramers doublet states [13].

In other respects, we can remark that for $x \leq 4\%$, the most intensive luminescence peak, labelled 5 in fig. 4, corresponds to transitions from the back sublevel of the $^4I_{13/2}$ excited state to the lower sublevel of the $^4I_{15/2}$ fundamental state ($\lambda = 1.518 \mu\text{m}$, 818 meV). For $x = 6\%$ the same PL peaks, pointed out at the same energies, are observed, but their relative intensities are changed. The most intensive one corresponds now to that which is labelled 3, in fig. 4 ($\lambda = 1.543 \mu\text{m}$, 804 meV). At last, for high erbium concentrations ($x = 15\%$), the peak 5, in fig. 4, has completely disappeared, but the energies of the other lines remain constante. The most

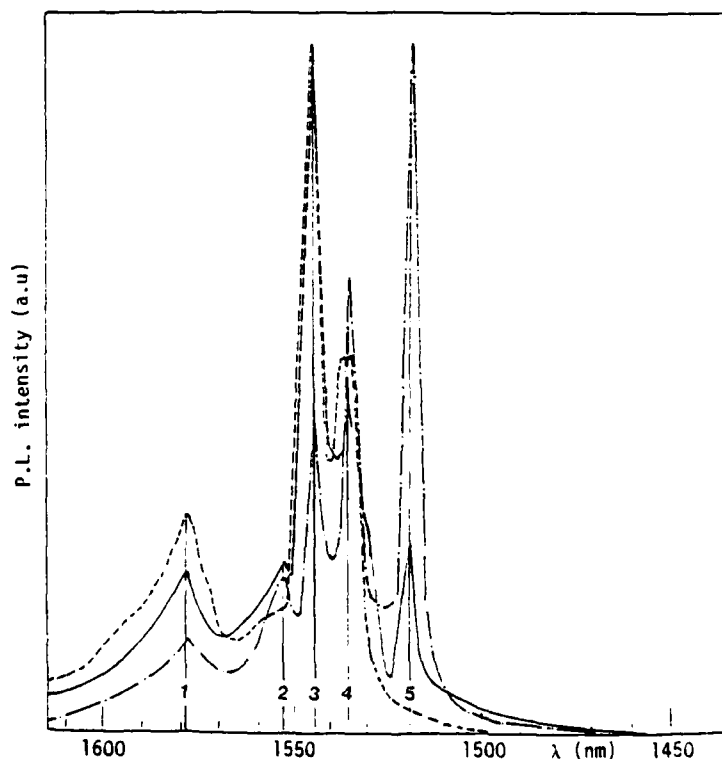


Fig. 4 - 1.53 μm PL spectra of $\text{Ca}_{1-x}\text{Er}_x\text{F}_2+\text{x}/\text{Si}(100)$ structures, performed at 2K. Mixed, full and dashed lines correspond to $x = 4, 6$ and 15%.

intensive luminescence corresponds again to a de-excitation on the third fundamental sublevel. These results show that the environment of the luminescent sites remains unchanged when x increases. On the other hand the evolution of the different line intensities as a function of the erbium substitution rate can be interpreted in terms of a reabsorption of the emitted light corresponding to the de-excitation on the ground sublevel of the $^4I_{15/2}$ state, due to the strong Er-Er coupling at high erbium concentration.

At last we must report that an ellipsometric study, performed at RT, on $Ca_{1-x}Er_xF_{2+x}$ thin films has shown that the refractive index, n , of the layers increases with the erbium substitution rate. For 1.3 and 0.6328 μm incident radiations, n increases from 1.425 to 1.466 and from 1.470 to 1.497, respectively, when x varies from 4% to 19%.

CONCLUSION

We have shown that homogeneous $Ca_{1-x}Er_xF_{2+x}$ thin films can be grown on Si(100) substrates with a high degree of crystal quality and purity. CL and PL studies showed that these films present strong luminescences, at room temperature, in the visible and the near-infrared spectral domains, corresponding to intra-4f-shell transitions of Er^{3+} ($4f^{11}$) ions. The $^4I_{13/2} \rightarrow ^4I_{15/2}$ (1.53 μm) transition, which lies within the spectral range for minimum absorption in silica-based optical fibers, presents evident potential applications for optical communications. Its maximum of luminescence intensity has been found for an erbium substitution rate as high as 16%. The emissions in the visible range can be used, in particular, to visualize the spot of high energy electron or ion beams. At last, we report that the evolution of the refractive index of the layers as a function of the erbium concentration can lead to the realization of plane optical guides [14].

REFERENCES

- [1] P.N. Favenec, H. L'Haridon, M. Salvi, D. Moutonnet and Y. Le Guillou, *Electron. Lett.* 25 (1989) 719.
- [2] W.F. Krupke and I.B. Gruber, *J. Chem. Phys.* 39 (1963) 1024.
- [3] W.F. Krupke and I.B. Gruber, *J. Chem. Phys.* 41 (1964) 1225.
- [4] T. Asano and H. Ishiura, *Thin Solid Films*, 93 (1982) 143.
- [5] B.P. Sobolev and P.P. Fedorov, *J. Less Com. Metals*, 60 (1978) 33.
- [6] A.S. Barrière, G. Couturier, G. Gevers, J. Grannec, H. Ricard and C. Sribi, *Surf. Science*, 168 (1986) 688.
- [7] A.S. Barrière, B. Mombelli, B. Porté, S. Raoux, H. Guégan, M. Reau, H. L'Haridon and D. Moutonnet, *J. Appl. Phys.* 73 (3) (1993) 1.
- [8] G. Gevers, A.S. Barrière, J. Grannec, L. Lozano and B. Blanchard, *Phys. Stat. Solidi*, A81 (1984) 105.
- [9] W.K. Chu, J.W. Mayer and M.A. Nicolet, *Backscattering Spectrometry*, (Acad., N.Y. 1976) p 223.
- [10] A.S. Barrière, A. Elfajri, H. Guégan, B. Mombelli and S. Raoux, *J. Appl. Phys.* 71 (1992) 709.
- [11] J.H. Barret, *Phys. Rev. B* 3 (1971) 1527.
- [12] D.S. Gemmel, *Rev. Mod. Phys.* 46 (1974) 129.
- [13] H. Ennen and J. Schneider, "Luminescence of rare earth ions in III-V semiconductors" 13th I.C.D.S., Colorado, 1984.
- [14] P.N. Favenec, H. L'Haridon, D. Moutonnet, A.S. Barrière, S. Raoux and B. Mombelli - Patent Nr 92403099.2, nov. 18 (1992).

CORRELATION OF ELECTRICAL, STRUCTURAL, AND OPTICAL PROPERTIES OF ERBIUM IN SILICON

J. L. Benton, D. J. Eaglesham, M. Almonte, P. H. Citrin, M. A. Marcus, D. L. Adler, D. C. Jacobson and J. M. Poate
AT&T Bell Laboratories, Murray Hill, New Jersey 07974

ABSTRACT

An understanding of the electrical, structural, and optical properties of Er in Si is necessary to evaluate this system as an opto-electronic material. Extended x-ray absorption fine structure, EXAFS, measurements of Er-implanted Si show that the optically active impurity complex is Er surrounded by an O cage of 6 atoms. The Er photoluminescence intensity is a square root function of excitation power, while the free exciton intensity increases linearly. The square root dependence of the 1.54 μm -intensity is independent of measurement temperature and independent of co-implanted species. Ion-implantation of Er in Si introduces donor activity, but spreading resistance carrier concentration profiles indicate that these donors do not effect the optical activity of the Er.

INTRODUCTION

The interest in erbium doping of silicon is an outgrowth of the successful materials science which resulted in the new generation of lightwave communications based on Er-doped fibers and fiber amplifiers. Lightwave networks employing Er doped components offer a new technology with the potential for powerful communications services. It is a natural scientific step, therefore, to introduce Er into silicon in an attempt to invent a compatible silicon optoelectronic device. Light from Si, especially at 1.54 μm , is an important scientific advance, but further work in this area should be measured against technological benchmarks.

A careful evaluation of materials parameters has suggested that the erbium-silicon system is not well suited for light emitting diodes, amplifiers or modulators, and that the best chance for its commercial success will reside in lasers.^[1] Achievement of a laser based on electroluminescence of Er in Si requires increasing the impurity incorporation beyond the measured solid solubility of $1 \times 10^{18} \text{ cm}^{-3}$ and demands, as well, an understanding of the excitation mechanism of the Er defect. With advances on these two fronts, it might be possible to create and maintain the inverted population necessary for stimulated emission.

The results presented in this study add some understanding to the issue of Er excitation. The extended x-ray absorption fine-structure (EXAFS) experiments indicate that the optically active Er defect in Si is a complex of Er and six oxygen atoms. The Er luminescence exhibits a square-root function of excitation laser power. This result eliminates exciton bonding as the rate limiting step and suggests that either a back-transfer mechanism or Auger process limits the efficiency of the Er emission. Previous work^[2] established that high energy ion implantation of Er into Si introduced donor activity. Although the donor concentration correlates with the Er photoluminescence intensity, this paper shows that the donor defects are not involved in the excitation process.

EXPERIMENTAL PROCEDURE

Er^+ ions were implanted into room-temperature n- and p-type silicon at energies of 0.2 to 5.25 MeV. The concentration of oxygen in the samples was varied by using float zoned (FZ) Si, with $[\text{O}] \approx 1 \times 10^{16} \text{ cm}^{-3}$, Czochralski-grown (CZ) Si, with $[\text{O}] \approx 1 \times 10^{18} \text{ cm}^{-3}$, and Si implanted with additional oxygen to doses as high as $1 \times 10^{19} \text{ cm}^{-3}$. Post-implantation heat treatments were performed in vacuum at temperatures ranging between 900-1350°C.

The donor activity associated with the implanted Er was monitored by four standard measurements, room-temperature Hall effect, spreading resistance probe (SRP), capacitance-voltage (C-V) profiling, and deep level transient spectroscopy (DLTS).^[2] The 514 nm line of an argon ion laser at a power of 400 mW excited the Er photoluminescence (PL) which was detected with a LN₂ cooled germanium detector. The PL spectra were generated with a 0.75-m Spex monochromator.

Multiple Er ion implants were used to prepare samples for EXAFS measurements, which produced an Er concentration of approximately $5 \times 10^{17} \text{ cm}^{-3}$ uniformly distributed from the silicon sample surface to a depth of $\sim 2 \mu\text{m}$. Er L₃-edge EXAFS data were obtained with fluorescence-yield detection at the National Synchrotron Light Source. All x-ray absorption measurements were obtained from samples at 50K. Bulk standard compounds of ErSi₂ and Er₂O₃ were used as references in the determination of coordination numbers and bond lengths.

RESULTS

Local Structure of Optically Active Er

The microscopic structure of the optically active Er species in Si was resolved by EXAFS experiments. Er incorporation in Si is limited by precipitation, with the solid solubility of approximately $1 \times 10^{18} \text{ cm}^{-3}$ at 900°C. The Er precipitates, which have a ErSi₂ structure, are found in both FZ and CZ silicon and are not the source of the 1.54 μm luminescence.^[3] The presence of oxygen impurities in the CZ silicon increases the Er luminescence intensity by more than two orders of magnitude compared with FZ material.^[4] Therefore, both CZ and FZ silicon Er-implanted substrates were measured by EXAFS along with bulk compounds of ErSi₂ and Er₂O₃.^[5]

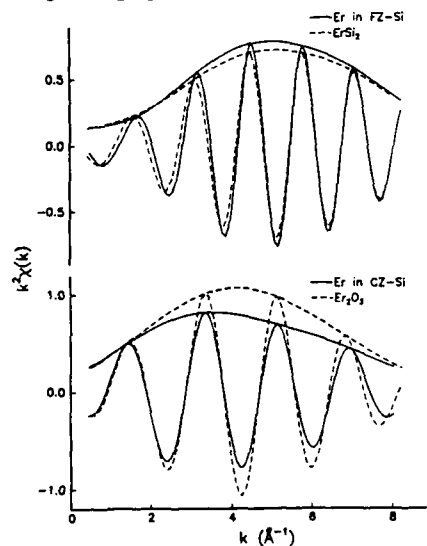


Figure 1. Filtered, back-transformed EXAFS data from first neighbor shells of Er implanted into FZ Si (top data) and Er in CZ Si (bottom data). Comparison with reference samples of erbium and Er silicide show that the optically active Er is surrounded by 6 oxygen atoms.

The filtered EXAFS data are shown in Figure 1. Analysis of the amplitude functions in each pair of spectra identify both the type and number of nearest neighbor atoms surrounding the absorbing Er atoms. The local environment of Er in FZ Si closely resembles the 12 Si atoms in ErSi₂, and the first coordination shell of atoms surrounding Er in CZ Si resembles the 6 oxygen atoms in Er₂O₃. The frequency information in Figure 1 allows the average distance between

absorbing Er and its nearest neighbors to be determined, giving for Er-O, 2.25 \AA and for Er-Si, 3.0 \AA . Since the EXAFS experiments indicate that greater than 80% of the incorporated Er is measured in the CZ and FZ samples, it is clear that the local environment around the Er determines its optical activity.

Excitation Mechanism of Er Luminescence

The excitation dependence of a PL line measured as a function of laser power was examined to give an indication of the excitation mechanism.^[6] Figure 2 shows the excitation laser-power dependence of both the Er signal at $1.54\text{ }\mu\text{m}$ and the free exciton signal at $1.23\text{ }\mu\text{m}$ in the same boron-doped Si sample. The laser power was held constant at 400 mW and the excitation level was reduced by insertion of neutral density filters. The free exciton intensity is linear in power for all measured temperatures, as expected. The Er signal intensity, however, exhibits a square-root dependence on excitation power, which eliminates exciton bonding as the rate limiting step for the Er photoluminescence. The data at 10K, 40K, 60K, and 80K, presented in Figure 2, illustrate that the square-root function is independent of temperature. Additional measurements indicate that this function is also independent of co-implanted species.

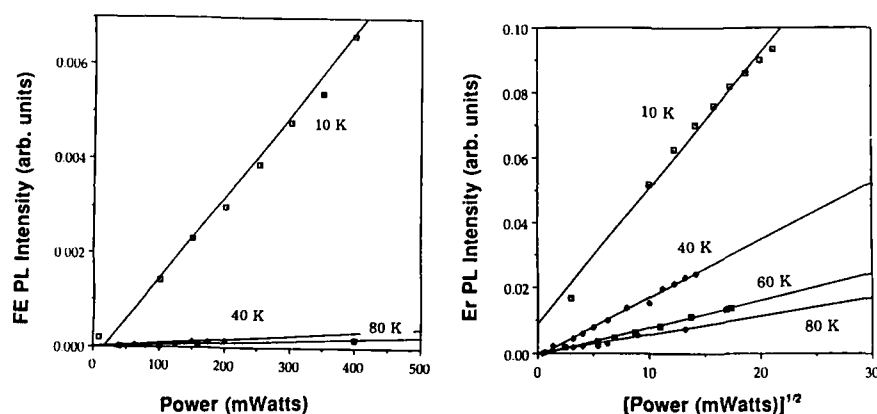


Figure 2.
Excitation power dependence of the free exciton (FE) luminescence is linear in laser power at measurement temperatures of 10K, 40K, and 80K. The $1.54\text{ }\mu\text{m}$ Er photoluminescence (PL) intensity varies as the square root of excitation laser power.

This square-root dependence of Er PL intensity could result from a three-level excitation mechanism or it could indicate the presence of an alternate nonradiative deexcitation mechanism. Back transfer mechanisms have been proposed for Er luminescence in InP and evidence has been presented for localized Auger quenching.^{[7] [8]} In MBE Si:Er, the PL intensity was also reported to be sublinear with excitation power.^[9]

Electrical Activity of Er in Si

Determination of the optimal annealing conditions for Er implantation into Si were made by monitoring the PL intensity at $1.54\text{ }\mu\text{m}$ as a function of heat treatment temperature and time. The process was optimized at 900°C for 30 minutes.^[4] Deep level transient spectroscopy (DLTS) of ion-implanted Er in n-type Si at low doses ($10^{14} - 10^{16}\text{ cm}^{-3}$) detected 9 levels

related to Er, and carrier concentration profiling by C-V measurements and spreading resistance probe (SRP) correlated the presence of donors with the implanted Er concentration.^[2] This excess donor concentration increased with increasing Er concentration and reached a maximum at approximately $4 \times 10^{16} \text{ cm}^{-3}$, as shown in Figure 3. C-V profiling determined the donor concentrations related to low doses of Er, and SRP and Hall effect measurements recorded the mobile carrier concentrations at higher ion-implantation doses. Since the Er luminescence intensity showed a similar relationship to the implanted Er dose (open circles in Figure 3), it was suggested that these donor states might provide the pathway for excitation of the Er.^[2] Further investigation of the electrical activity of the Er:Si system indicates that this is not the case.

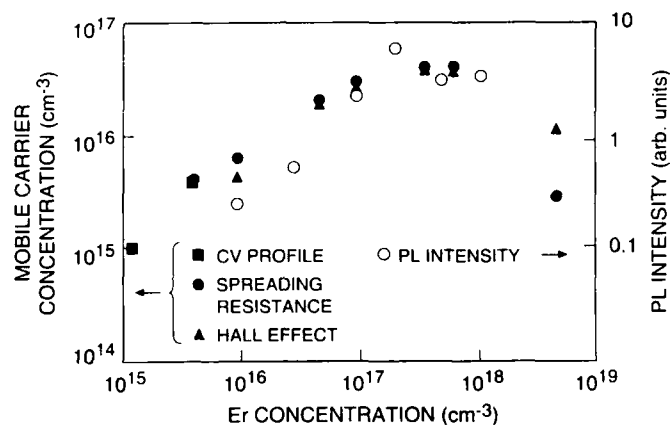


Figure 3. Excess donor concentration, as measured by C-V profiling, SRP, and Hall effect, plotted as a function of implanted Er ion concentration in CZ, n-type Si (left axis). Corresponding $1.54 \mu\text{m}$ PL intensity is included for comparison.

The samples represented in Figure 4 were given a series of 500 keV implants at $7 \times 10^{17} \text{ cm}^{-3}$, each followed by a heat treatment at 900°C for 30 min, totaling a dose of $2.1 \times 10^{18} \text{ cm}^{-3}$. Both FZ and CZ, boron doped silicon was monitored. The donors introduced by the Er implantation compensated the material and the dip in the SRP profiles at $0.66 \mu\text{m}$ marks the p-n junction. The maximum donor concentration is approximately three times greater in the oxygen-rich CZ material, consistent with previous results.^[2] However, the Er PL signal is a factor of 30 greater in the CZ sample. Both samples were processed and measured concurrently. The presence of high concentrations of Er-related donors in silicon is not sufficient for efficient luminescence. The data in Figure 4 prove that the Er-related donors alone do not produce luminescence at $1.54 \mu\text{m}$, and the data in Figure 5 prove that these donors are not even necessary for the PL production. Spreading resistance carrier concentration profiles were measured on boron doped FZ silicon after three different sets of implant and annealing conditions. The profiles represented by the dashed and dashed-dotted lines are similar and show no evidence of donor activity. The first sample (dashed line) received a 5.25 MeV Er dose of $7 \times 10^{17} \text{ cm}^{-3}$ followed by a vacuum anneal at 1100°C for 30 min; the second sample (dotted-dashed line) received an additional oxygen implant, $2 \times 10^{18} \text{ cm}^{-3}$ and subsequent thermal treatment of 1100°C for 30 min. The additional co-implantation of oxygen increased the Er luminescence intensity by two orders of magnitude. The third sample (solid line) received the identical Er and O implants as the second sample, but only the final anneal was given. The carrier concentration profile for this case shows donor compensation of the boron dopant, a p-n junction at $2 \mu\text{m}$, and a maximum donor

concentration of $4 \times 10^{15} \text{ cm}^{-3}$. The Er PL intensity was the same for the two samples containing both Er and O ion implants. The Er related donors are not providing the pathway for the energy transfer necessary to excite the Er luminescence.

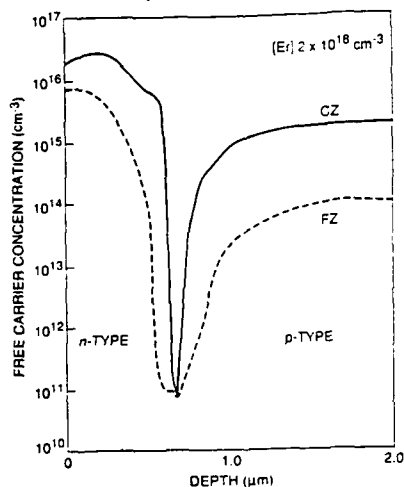


Figure 4. Spreading resistance profiles converted to free carrier concentrations of $2 \times 10^{18} \text{ cm}^{-3}$ Er ions implanted into both CZ and FZ p-type Si at 500 keV. Donors are created in both samples but only the Si with high oxygen concentration has an intense Er PL signal.

The initial impetus for these experiments, represented in Figures 4 and 5, was that proper choice of processing might reduce the implantation damage and thus allow the formation of greater concentrations of the Er-O complexes, which would increase the luminescence intensity. However, up to 10 sequential implants and anneals at 900°C at doses of both $3 \times 10^{17} \text{ cm}^{-3}$ and $7 \times 10^{17} \text{ cm}^{-3}$ yielded the same Er PL intensities to within a factor of three.

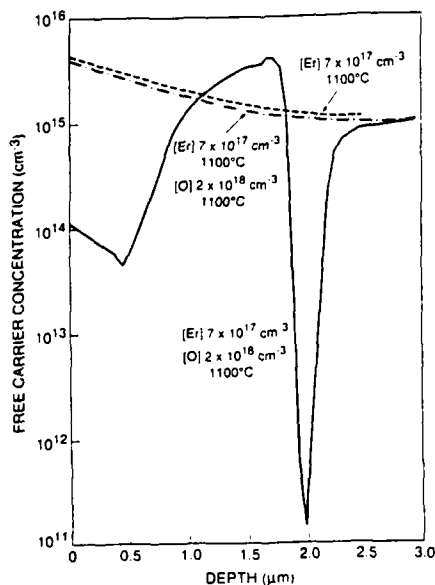


Figure 5. Free carrier concentration profiles measured by SRP in p-type, FZ silicon. Er ion-implantation alone gives the dashed data with no evidence of donor formation and low $1.54 \mu\text{m}$ PL intensity. After co-implantation of O (dashed-dotted data), the PL intensity increases by two orders of magnitude but the electrical activity remains constant. The solid line shows the formation of a p-n junction at $2 \mu\text{m}$.

CONCLUSIONS

Erbium is an effective "microscopic getter" of oxygen in silicon, forming optically active point defects of Er surrounded by six oxygen atoms. A complete understanding of the excitation mechanism of the Er 1.54 μm luminescence in Si requires an investigation of the electrical activity of these Er-O defects. Ion-implanted Er introduces a related donor in both n-type and p-type Si with the electrical activity saturating at $4 \times 10^{16} \text{cm}^{-3}$. These donor-related defects recover, however, under proper annealing conditions without effecting the Er photoluminescence intensity. The PL intensity of the Er signal is proportional to the square root of the excitation laser power. This power dependence suggests that a three-level system or a back-transfer mechanism controls the Er luminescence efficiency.

REFERENCES

1. Y. H. Xie, E. A. Fitzgerald and Y. J. Mii *J. Appl. Phys.* **70**(6), 3223 (1991).
2. J. L. Benton, J. Michel, L. C. Kimerling, D. C. Jacobson, Y. H. Xie, D. J. Eaglesham, E. A. Fitzgerald and J. M. Poate, *J. Appl. Phys.* **70** (5), 2667 (1991).
3. D. J. Eaglesham, J. Michel, E.A. Fitzgerald, D.C. Jacobson, J. M. Poate, J. L. Benton, A. Polman, Y. H. Xie and L. C. Kimerling, *Appl. Phys. Lett.* **58**, 2797 (1991).
4. J. Michel, J. L. Benton, R. F. Ferrante, D. C. Jacobson, D. J. Eaglesham, E. A. Fitzgerald, Y. H. Xie, J. M. Poate and L. C. Kimerling, *J. Appl. Phys.* **70** 2672 (1991).
5. D. L. Adler, D. C. Jacobson, D. J. Eaglesham, M. A. Marcus, J. L. Benton, J. M. Poate, and P. H. Citrin, *Appl. Phys. Lett.* **61** (18) 2181 (1991).
6. J. Weber, W. Schmid and R. Sauer *Phys. Rev. B*, **21**, (6) 2401 (1980).
7. A. Taguchi, M. Taniguchi and K. Takahei, *Appl. Phys. Lett.*, **60**, 5604 (1991).
8. B.J. Heijmink Liesert, M. Godlewski, T. Gregorkiewicz, and C. A. J. Ammerlaan, *Appl. Phys. Lett.*, **59** (25) 3279 (1991).
9. H. Efeoglu, J. H. Evans, J. M Langer, A. R. Peaker, N. L. Rowell, J-P Noel, D. D. Perovic, T.E. Jackman and D. C. Houghton *Mat. Res. Soc. Symp. Proc.* **220**, 367 (1991).

Er Luminescence in Si:

A Critical Balance between Optical Activity and Pumping Efficiency

S. Coffa^(a), F. Priolo^(a), G. Franzó^(a), V. Bellani^(b), A. Carnera^(c) and C. Spinella^(d)

^(a)Dipartimento di Fisica, Università di Catania, Corso Italia 57, I95129 Catania (Italy)

^(b)Dipartimento di Fisica 'A. Volta', Università di Pavia, Via Bassi 6, I27100 Pavia (Italy)

^(c)Dipartimento di Fisica, Università di Padova, Via F. Marzolo 8, I35131 Padova (Italy)

^(d)IMETEM - CNR, Corso Italia 57, I95129 Catania (Italy)

ABSTRACT

The several processes required to achieve Er luminescence in Si are investigated. In particular, the role of Er - O interactions to obtain the incorporation of high Er concentrations, electrically and optically active, in crystalline Si is investigated. It is found that a large enhancement in the electrical activation of Er (up to three orders of magnitude) is obtained by co-implanting Er with O at 573 K or at 77 K. However, the introduction of high concentrations of active Er in Si is not sufficient to obtain a large enhancement in the luminescence since an efficient pumping of the optically active sites is also required. The optical efficiency of this sample has been studied by photoluminescence. It is seen that an enhancement by a factor of ~ 5 with respect to literature data is obtained. Moreover studies on the luminescence intensity as a function of the pump power gave important information on the mechanisms underlying Er luminescence in Si and its competing phenomena. These data are presented and discussed.

INTRODUCTION

The use of silicon in optoelectronics is severely hampered by the indirect bandgap of this material. However, being silicon the semiconductor with the most mature technology, a large effort has been devoted to the realization of silicon - based optoelectronic devices^{1,2}. It has been demonstrated^{3,4} that the introduction of rare earth atoms has noticeable potentiality. In fact, it is possible to have light emission from the intra-4f transitions of these elements. In particular the transition $I_{13/2} \rightarrow I_{15/2}$ of Er ions produces light emission at 1.54 μm which is of particular interest in the communication technology because the losses in optical fibers have a minimum at this wavelength.

The process of Er luminescence in Si is a phenomenon which involves different but equally important steps. First Er has to be incorporated at high concentrations in Si without the formation of precipitates. Second, it has to be incorporated in its optically active 3^+ state. Finally the rate of pumping of the levels involved in the transition has to be as efficient as possible.

The incorporation of Er in Si is limited by the formation of precipitates which occurs⁵ when the Er concentration exceeds $10^{18}/\text{cm}^3$. Moreover it is observed that only a small fraction of Er atoms is optically active, i.e. in the 3^+ state. This fraction can be largely increased^{6,7} by the presence of O. Indeed it is much higher in Czochralski grown (CZ) Si (which has an O content of $\sim 10^{18}/\text{cm}^3$) than in float zone (FZ) Si (in which the oxygen concentration is $\sim 10^{16}/\text{cm}^3$). The presence of O also modifies the electrical properties of Er in Si. In fact it has been shown⁸ that Er in c-Si behaves as a donor and that the maximum donor concentration obtained for a fixed Er content is much higher in CZ than in FZ Si. These similarities suggest that electrical and optical activations of Er in Si can indeed be correlated, i.e. the Er donor behavior might be associated with the Er^{3+} state. The pumping of Er levels is thought to occur through the recombination of e-h pairs⁹ at the Er atoms. Therefore this pumping is strongly dependent on those processes, such as recombination at crystallographic defects or at surface, which cause a reduction in the e-h

pairs population. It is then mandatory that the optically active sites must be introduced in a good quality crystal.

In this paper we show that high concentrations of active Er atoms (up to $10^{19}/\text{cm}^3$) can be incorporated in c-Si by co-implanting Er and O at 573 K or 77 K. While the crystal quality after annealing is quite poor for the 573 K implanted samples, an almost defect free c-Si is obtained by epitaxial regrowth of the amorphous layer produced by the Er and O implants at 77 K. Measurements of the photoluminescence intensity as a function of the pump power demonstrate that the limiting step in obtaining high luminescence yield is the efficient pumping of the active sites.

EXPERIMENTAL

Erbium and oxygen ions were co-implanted in both CZ (2 Ωcm) and FZ (250 Ωcm) n-type (100) Si substrates at 573 K or 77 K. For the hot implants, in which amorphization of the layer was avoided, Er was implanted at an energy of 5 MeV and in the dose range $4 \times 10^{13} - 6 \times 10^{15}/\text{cm}^2$. Some of the samples were co-implanted with oxygen in the energy range 1.1 - 1.8 MeV and in the dose range $1 \times 10^{13} - 7 \times 10^{16}/\text{cm}^2$. Multiple implants of oxygen were performed in order to obtain almost constant concentration profiles of $1 \times 10^{17} - 2.5 \times 10^{21}/\text{cm}^3$ in the region implanted with Er. After implantation samples were annealed at 900 $^\circ\text{C}$ for 30 sec in N_2 atmosphere.

For liquid nitrogen implants, in which a 2.3 μm thick amorphous Si (a-Si) layer was produced, six different Er implants in the energy range 0.5 - 5 MeV and in the dose range $8 \times 10^{13} - 9 \times 10^{14}/\text{cm}^2$ were used to obtain an almost constant Er concentration of $1 \times 10^{19}/\text{cm}^3$ between 0.3 and 2 μm . Some of the samples were subsequently implanted with multiple O implants in the energy range 0.15 - 1.4 MeV and in the dose range $1.5 \times 10^{15} - 3.1 \times 10^{15}/\text{cm}^2$ to obtain an almost constant concentration of $10^{20}/\text{cm}^3$ in the Er doped region. After implantation samples were annealed in a vacuum furnace at 620 $^\circ\text{C}$ for 3 hrs to induce the epitaxial regrowth of the amorphous layer and were then treated by rapid thermal annealing (RTA) at 900 $^\circ\text{C}$ for 30 sec to activate both electrically and optically the implanted erbium.

The impurity profiles (both before and after annealing) were measured by Secondary Ion Mass Spectroscopy (SIMS) using a CAMECA IMS-4f instrument. The electrically active Er concentration was measured by spreading resistance (SR) analyses. Samples for SR were bevelled at an angle of 34 $^\circ$ and the data were converted into carrier concentration through a code by Berkowitz and Lux¹⁰. Structural characterization of the samples was performed by TEM in the cross sectional configuration using a 200 kV JEOL 2010 microscope. Photoluminescence spectra were obtained by pumping with a Kr ion laser tuned at a wavelength of 530.9 nm. The pump power on the samples was varied in the range $10^{-2} - 10^3$ mW. During the measurements samples were introduced into a cryostat whose temperature could be continuously varied between 3 K and 300 K. The detection apparatus consisted of a lock-in system, a 1402 Spex double spectrometer and a liquid nitrogen cooled Ge detector and resulted in an overall resolution of 15 \AA .

RESULTS AND DISCUSSION

In fig.1 the O (dashed line) and Er (continuous line) SIMS profiles of an as implanted FZ Si sample are reported. These profiles refer to a 5 MeV - $1 \times 10^{15} \text{Er}/\text{cm}^2$ implantation at 573 K followed by a multiple oxygen implant to obtain an almost flat oxygen profile with a concentration of $\sim 8 \times 10^{19}/\text{cm}^3$ in the region doped with Er. As a matter of fact the Er profile has a peak at $\sim 1.6 \mu\text{m}$ with a concentration of $\sim 1 \times 10^{19}/\text{cm}^3$ and matches perfectly with the oxygen profile. This sample was subsequently annealed at 900 $^\circ\text{C}$ for 30 sec and analyzed by spreading resistance. The thermal treatment does not change the as-implanted profiles at all (SIMS not shown). However a strong activation of the

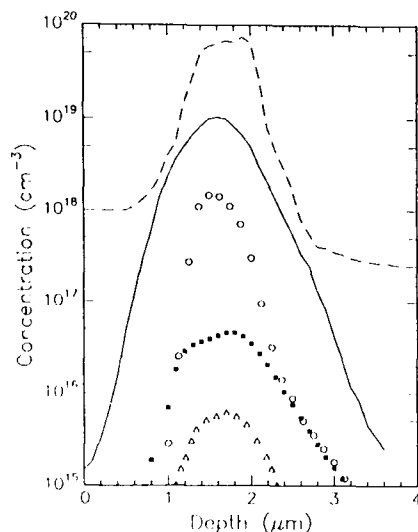


Fig. 1: SIMS profile of Er (—) for a 5 MeV- 1×10^{15} Er/cm² implant. The SR electrical profile of this Er implant in FZ Si (Δ), CZ Si (\blacksquare) and O-doped Si (\circ) are also reported. The O SIMS profile in this last sample is also shown (---).

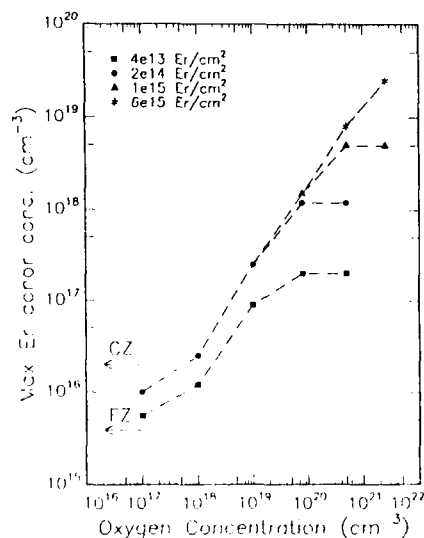


Fig. 2: Maximum Er donor concentration vs oxygen concentration for several Er implants. Data were obtained by SR.

implanted Er is observed. This is also shown in fig.1 where the donors concentration, as obtained by SR, for 5 MeV - 1×10^{15} Er/cm² implanted in FZ (triangles), CZ (squares) and oxygen doped Si at a concentration of 8×10^{19} /cm³ (circles) are compared. The maximum donor concentration introduced by Er is 6×10^{15} /cm³ in FZ Si and increases to 5×10^{16} /cm³ in CZ-Si. Similar effects have been previously observed by Benton *et al.*⁴ who showed that in CZ-Si (where oxygen is present at a concentration of 1×10^{18} /cm³) Er activation is higher than in FZ-Si (with $\sim 1 \times 10^{16}$ O/cm³). It is however particularly interesting to observe that a further increase of the oxygen concentration (to 8×10^{19} /cm³) produces a further strong enhancement in the electrical activation which reaches a peak of $\sim 1.5 \times 10^{18}$ /cm³. In this case $\sim 15\%$ of the implanted Er is electrically active. Oxygen then seems to play a key role on the electrical activation of Er.

We have therefore performed several Er implants (all at 573 K, at 5 MeV and at different doses) and several oxygen implants (at different concentrations) in order to obtain samples having several different combinations in the concentrations of these two elements. The samples were annealed in RTA and analyzed by SR. These data are summarized in fig.2 where we report the peak donor concentration introduced by the Er atoms as a function of the oxygen concentration. Data for samples implanted at different Er doses are compared. Data for implants in FZ and CZ-Si (without any further intentional O doping) are also reported. Samples of Er implanted in FZ and CZ-Si have donor concentrations of $\sim 6 \times 10^{15}$ /cm³ and $\sim 2 - 5 \times 10^{16}$ /cm³ which are nearly independent of the Er dose (above 4×10^{13} Er/cm²). This means that Er activation is limited by the lack of oxygen atoms. At 4×10^{13} Er/cm² by increasing the oxygen content also the donor concentration increases and saturates at a value of 2×10^{17} /cm³ at an oxygen concentration of $\sim 1 \times 10^{20}$ /cm³. At this point the Er activation is $\sim 50\%$. A further increase in the

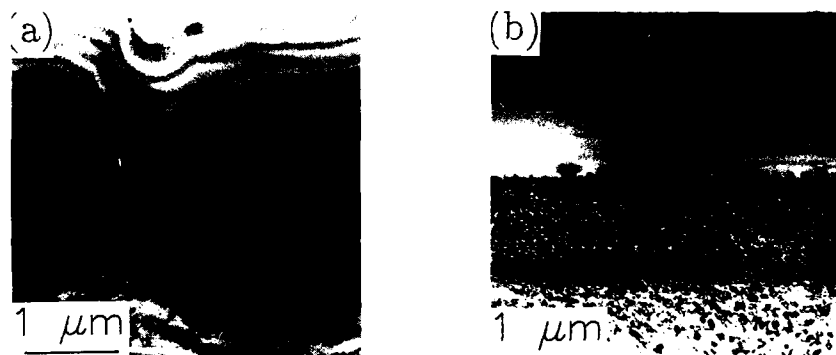


Fig.3: Cross sectional TEM images of 5 MeV Er hot implants at $1 \times 10^{15}/\text{cm}^2$ (a) and $6 \times 10^{15}/\text{cm}^2$ (b) after 900°C -30 sec.

oxygen content does not produce any further electrical activation. This means that at this stage electrical activation is limited by the presence of Er atoms. By increasing the Er dose to $2 \times 10^{14}/\text{cm}^2$ the donor concentration increases to $1 \times 10^{18}/\text{cm}^3$ and saturates again at an oxygen concentration of $5 \times 10^{20}/\text{cm}^3$. A further increase of the Er dose produces a consequent increase in the donor concentration which reaches a maximum value of $2 \times 10^{19}/\text{cm}^3$ for an Er dose of $6 \times 10^{15}/\text{cm}^2$ and an oxygen concentration of $2.5 \times 10^{21}/\text{cm}^3$. This electrical activation of Er in Si is almost three orders of magnitude above the maximum value reported in the literature⁴ and demonstrates that huge amounts of electrically active Er atoms can be incorporated in Si crystals provided that the oxygen concentration is increased as well. The crystal quality, however, rapidly deteriorates increasing the Er fluence in these hot implants. This is evident in the TEM of fig.3. Fig.3a is a cross sectional analysis of a sample implanted with $1 \times 10^{15}\text{Er}/\text{cm}^2$ and with an oxygen concentration of $8 \times 10^{19}/\text{cm}^3$ (after the RTA treatment). A band of precipitates, similar to those reported by Eaglesham *et al.*⁵, is present at a depth of $\sim 1.7\mu\text{m}$. These precipitates strongly increase in number when the Er dose is increased to $6 \times 10^{15}/\text{cm}^2$ (fig.3b). It is really interesting to note that, in spite of the formation of precipitates, a huge amount of Er atoms is still able to link with oxygen and becomes electrically active. As a matter of fact the amount of electrically active Er can be as high as an order of magnitude above its solid solubility! Of course damage and precipitation will induce several competitive phenomena which hamper further Er activation. This is clear by observing that the number of oxygen atoms needed to produce an electrically active Er atom increases with the Er donor concentration (see fig.2). At low donor concentrations ($\sim 10^{16}/\text{cm}^3$) 10 oxygen atoms are enough to produce a donor while ~ 120 O atoms are necessary for an Er donor concentration of $2 \times 10^{19}/\text{cm}^3$. This is a clear effect of competitive processes, such as oxygen precipitation, which are more effective in presence of damage.

The presence of a high concentration of defects and precipitates in the material will strongly inhibit the pumping of the active sites. In order to achieve the incorporation of a high concentration of electrically and optically active Er atoms in a good quality crystal Si we have followed a different approach. Er and O were co-implanted at 77 K to obtain almost constant profiles at a ratio 1:10. These implants also produce a $2.3\mu\text{m}$ thick amorphous layer. A thermal process at 620°C for 3 hrs produced the epitaxial regrowth of this layer. Fig.4 shows the Er and O SIMS profiles taken before and after the

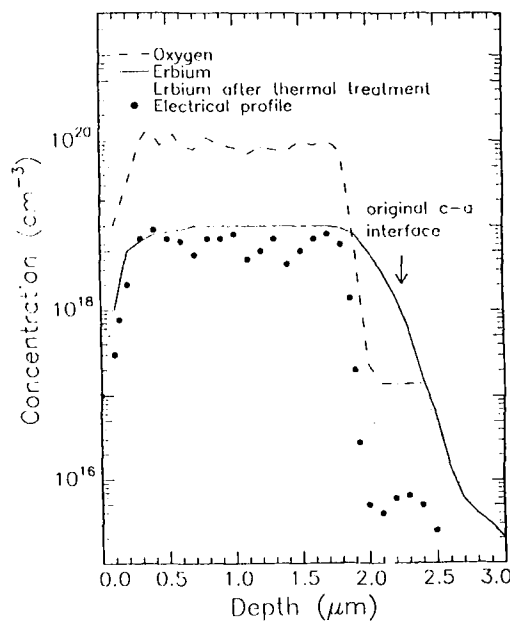


Fig.4: SIMS profiles of multiple Er and O implants at 77 K before and after annealing at 620 °C-3 hrs. The Er electrical profile after 900 °C-30 sec is also shown.

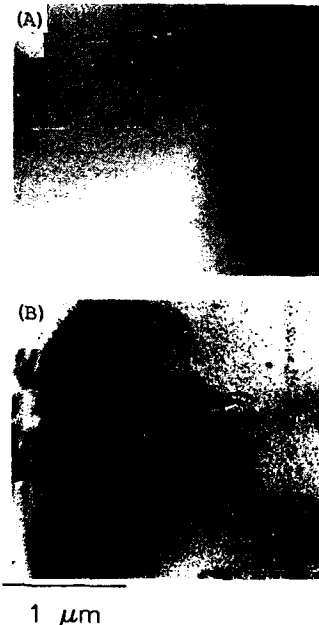


Fig.5: Cross sectional TEM pictures of the sample in fig.4 before (a) and after annealing (b).

annealing process. During annealing the O profile remains unmodified at a constant value of $\sim 10^{20}/\text{cm}^3$ between 0.3 and 1.8 μm . On the other hand the Er profile changes upon annealing. A peak of Er is segregated at $\sim 2.3 \mu\text{m}$, which is where the end of range defects are probably left. Moreover, in the region between 2.3 and 1.8 μm Er has been swept by the moving c-a interface. As soon as Er enters the O-doped region this redistribution however stopped. A clear Er peak is indeed observed at 1.8 μm (which is due to the Er coming from the deeper region) and after that the Er profile is almost unchanged. This redistribution is attributed to segregation processes occurring at the moving c-a interface^{11,12}. This process depends on both interface velocity and Er diffusivity. Oxygen is known to retard the c-a interface velocity¹³ and to reduce Er diffusivity through the formation of Er-O complexes¹⁴. Therefore the segregation process abruptly changes when the c-a interface enters the O-doped region and Er remains trapped in the regrowing crystal. In the same figure the depth distribution of electrically active Er atoms after a further annealing at 900°C for 30 sec is also reported (●). A donor concentration of $\sim 8 \times 10^{18}/\text{cm}^3$ flat between 0.3 and 1.8 μm is present, demonstrating that most of the Er is electrically active. Note that only ~ 10 oxygen atoms are necessary in this case to produce an Er donor.

In fig.5 cross sectional TEM images of both as-implanted and annealed samples are shown. Fig. 5a shows the as-implanted sample in which a 2.3 μm thick continuous a-Si layer is clearly present. After annealing this layer is transformed into a good quality single crystal (fig. 5b). A band of dislocation loops is present at the end of range (corresponding to

the Er peak in SIMS) and for the rest a good crystal with a few threading dislocations traversing the whole film is observed. It is noticeable that a huge amount of active Er has been incorporated in such a layer. Epitaxial regrowth occurred in spite of the presence of oxygen. As a matter of fact oxygen played a crucial positive role in stabilizing the Er thus allowing crystallization. In fact, epitaxial regrowth of a sample which did not contain O occurred for only ~ 800 nm and then the interface broke up with the formation of a heavily twinned material. This suggests that the Er redistribution (occurring in absence of O) makes the c-a interface unstable and twin formation soon occurs.

Incorporating a high concentration of Er in a good quality c-Si is a promising step towards the achievement of high luminescence intensities. In fact, if electrical and optical activations are indeed correlated it is expected that the concentration of optically active Er atoms in our sample must be quite high. We have therefore performed photoluminescence measurements on the sample prepared by solid phase epitaxy. For the sake of comparison these measurements were also performed on a reference sample. This sample was produced by Er implantation at 5 MeV to a fluence of $4 \times 10^{13}/\text{cm}^2$. It contains about the maximum amount of active Er that can be introduced before the onset of precipitation and/or the formation of a continuous amorphous layer. Therefore it represents one of the best samples which can be produced by the procedures so far reported in the literature⁶.

The photoluminescence spectra at 3 K for these two samples are reported in Fig. 6. For these spectra a pump power of 120 mW was used. The intensity is about a factor of three higher for the epitaxially regrown sample than for the reference sample. However, the estimation of the ratio between the number of optically active sites in the two samples is not an easy task. Photoluminescence intensity, in fact, depends not only on the total number of optically active sites but also on the pumping efficiency for these sites and on the balance between radiative and non radiative decay of the excited atoms. These two last steps are critically dependent on the crystal quality. In particular the pumping occurs through the recombination of e-h pairs at the Er atoms. It is therefore affected by those processes, such as recombination at defects and/or at the surface, which reduce the concentration of e-h pairs. A hint on which process really limits the pumping efficiency may be obtained by measuring the photoluminescence intensity as a function of pump power at different temperatures. The results obtained for the two samples are reported in fig.7 at 3 K (a) and 140 K (b). Note that the vertical scale is different in the two cases. For the reference sample (Er in CZ, circles) the photoluminescence intensity increases with pump power and eventually saturates. However, both the saturation level and the pump power at which saturation occurs strongly depend on temperature. The existence of a saturation suggests that all the Er atoms are excited. Therefore the factor limiting the luminescence yield is not the excitation due to the lack of e-h pairs but the Er content. The difference in the saturation level at different temperatures is clearly due to a difference in the radiative lifetime of the excited Er atoms. The temperature dependence of the pump power at which saturation occurs indicates, instead, that the pumping efficiency of the Er atoms reduces with increasing temperature. This is due both to a reduced lifetime of the excited state through alternative non-radiative paths and to the fact that the number of e-h recombination events, not ending with the excitation of an Er atom, increases with temperature. Recombination of e-h pairs in Si can occur through Auger mechanisms, both interband and impurity-mediated, through exciton recombination, via deep traps or at surface states¹⁵. While Auger mechanisms are almost temperature-independent, the efficiency of deep traps and surface states strongly increase with temperature thus reducing the e-h pairs population. Therefore in order to obtain the same number of excitation events higher and higher powers are required as the temperature increases.

In fig.7 the data of the regrown sample are also reported (triangles). At all temperatures the luminescence intensity increases with the pump power but saturation is not achieved in the explored power range. This indicates that in all cases only a fraction of the Er atoms is excited and the limiting step for higher luminescence is then the ef-

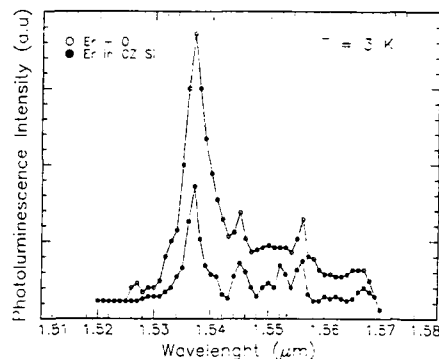


Fig. 6: Photoluminescence spectra at 3 K of the epitaxially regrown sample (○) and of a reference sample (●).

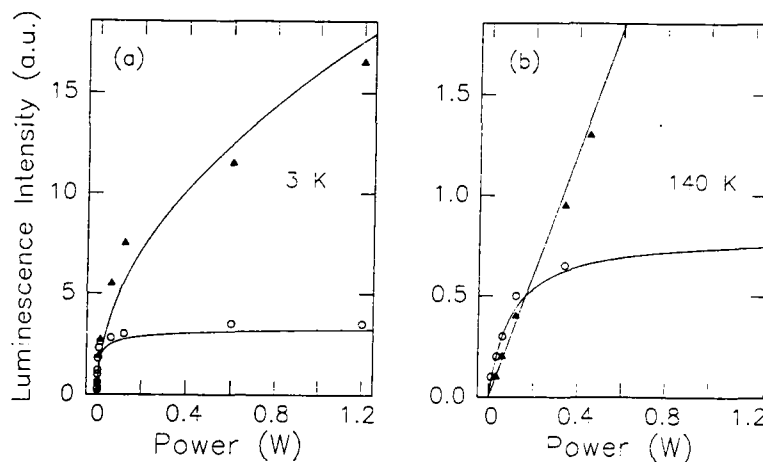


Fig. 7: Luminescence intensity vs pump power for the epitaxially regrown sample (▲) and a reference (○) sample. Data are shown at 3 K (a) and 140 K (b).

ficient pumping of the optically active sites. While a strong effort has been devoted in achieving the incorporation of high concentrations of optically active sites in Si, the major role of pumping efficiency in determining the luminescence yield has been probably not completely recognized. Several features of the curves in fig.7 are noteworthy. The intensity increases less than linearly at 3 K while a linear increase is observed at 140 K. The sublinear dependence at low temperatures is present also in the reference sample in the region well before saturation (this feature is not evident from fig.7 due to the x-scale). Therefore sub-linear and linear behaviors are not peculiar of the regrown sample but are determined by the different mechanisms which control the e-h pair population at the different temperatures. In particular, recombination through excitons is known to be very efficient at low temperatures¹⁶ while recombination at deep traps prevails at higher temperatures. Moreover at low pump powers (before saturation in the reference sample) the luminescence intensity is quite similar for the two samples. Large differences are instead observed at high pump powers, as the reference intensity saturates while that of the O-doped sample continuously increases. This confirms that, when the Er concentration is sufficiently high, the process of luminescence is completely controlled by the number of excitation events and not by the number of optically active sites.

CONCLUSIONS

In conclusion, we have shown that high concentrations of electrically and optically active Er atoms in Si can be achieved by co-implanting Er and O. In particular solid phase epitaxial regrowth of Er and O co-implanted amorphous Si layers results in the incorporation of a high active Er concentration ($\sim 8 \times 10^{18}/\text{cm}^3$) in a good quality c-Si. Photoluminescence of these samples has been measured and compared with that of a standard reference sample. In particular photoluminescence measurements as a function of the pump power gave important information on the mechanisms producing luminescence and on those limiting it. It has been shown that luminescence can be limited by either the number of optically active sites or by the pumping efficiency.

ACKNOWLEDGEMENTS

We wish to thank J.L. Staehli of the Ecole Polytechnique Federale de Lausanne (Switzerland) for the use of his photoluminescence apparatus. Thanks are also due to A. Giuffrida, A. Marino and S. Pannitteri for the expert technical assistance. This work has been supported in part by GNSM-CNR.

REFERENCES

1. A.M. Glass, *Science* **235**, 1003 (1987)
2. Y. H. Xie, E. A. Fitzgerald and Y. J. Mii, *J. Appl. Phys.* **70**, 3223 (1991)
3. H. Ennen, J. Schneider, G. Pomrenke and A. Axmann, *Appl. Phys. Lett.* **43**, 943 (1983)
4. H. Ennen, G. Pomrenke, A. Axmann, W. Haydl and J. Schneider, *Appl. Phys. Lett.* **46**, 381 (1985)
5. D.J. Eaglesham, J. Michel, E. A. Fitzgerald, D.C. Jacobson, J.M. Poate, J.L. Benton, A. Polman, Y.H. Xie and L.C. Kimerling, *Appl. Phys. Lett.* **58**, 2797 (1991)
6. J. Michel, J.L. Benton, R.I. Ferrante, D.C. Jacobson, D.J. Eaglesham, E.A. Fitzgerald, Y.H. Xie, J.M. Poate and L.C. Kimerling, *J. Appl. Phys.* **70**, 2672 (1991)
7. P.N. Favennec, H. L'Haridon, D. Moutonnet, M. Salvi and M. Gauneau, *Jpn. J. Appl. Phys.* **29**, L521 (1990)
8. J.L. Benton, J. Michel, L.C. Kimerling, D.C. Jacobson, Y.H. Xie, D.C. Eaglesham, E. A. Fitzgerald and J.M. Poate, *J. Appl. Phys.* **70**, 2667 (1991)
9. S. Schmitt-Rink, C.M. Varna and A.F.J. Levi, *Phys. Rev. Lett.* **66**, 2782 (1991)
10. H.L. Berkowitz and R.A. Lux, *J. Electrochem. Soc.* **18**, 1137 (1981)
11. A. Polman, J.S. Custer, E. Snoeks and G.N. Van Den Hoven, *Appl. Phys. Lett.* **62**, 507 (1993)
12. J.M. Poate, J. Linnros, F. Priolo, D.C. Jacobson, J.L. Batstone, M.O. Thompson, *Phys. Rev. Lett.* **60**, 1322 (1988)
13. E.F. Kennedy, L. Csepregi, J.W. Mayer and T.W. Sigmund, *J. Appl. Phys.* **48**, 4241 (1977)
14. F. Priolo, S. Coffa, G. Franzó, C. Spinella, A. Carnera, V. Bellani, to be published
15. for a review see for example: *Solid State Electronics* **21**, Numbers 11/12 (1978)
16. W. Schmid, *Solid State Electronics* **21**, 1285 (1978); W. Schmid, *Phys. Stat. Sol. B* **84**, 529 (1977)

1.54 μm PHOTOLUMINESCENCE OF ERBIUM IMPLANTED HYDROGENATED AMORPHOUS SILICON

M. Kechouane, N. Beldi, T. Mohammed-Brahim
 Lab "Les Couches Minces", USTBH, Institut de Physique, BP 32, el alia, ALGER,
 ALGERIE
 H. L'Haridon, M. Salvi, M. Gauneau
 FRANCE TELECOM/CNET, LAB OCM, BP 40, 22301 LANNION, FRANCE
 P.N. Favennec FRANCE TELECOM/CNET, SAS, BP 40, 22301 LANNION, FRANCE

ABSTRACT

The luminescence of erbium implanted in hydrogenated amorphous silicon (a-Si : H) is presented. For the first time an intense and relatively sharp luminescence at 1.54 μm is observed in a-Si : H, using implanted erbium. The Er^+ emission intensity strongly depends on the hydrogen film content and on the measurement temperature. A direct correlation between the optical gap energy of the semiconductor and the hydrogen film content is observed.

INTRODUCTION

In the last few years, erbium doping of III-V compounds semiconductors and silicon was extensively studied [1, 3]. Great effort on various semiconductor materials was made to detect the luminescence of erbium, introduced in the host matrix by doping or ion implantation [3-5]. The erbium luminescence at 1.54 μm , associated with $^4\text{I}_{13/2} \rightarrow ^4\text{I}_{15/2}$ transitions in the 4f shells of Er^{3+} ions, was found to be independent of the host material, nor on both its temperature and the band gap energy of the semiconductor [3]. A wide band-gap is necessary to obtain an intense room temperature emission. Thus, hydrogenated amorphous silicon appears as an alternative material insofar as it offers the semiconductor properties necessary for industrial and electro-optical applications. Research effort on this material is greatly motivated by the interest of improving solar cells efficiency; A recent study (6) has shown for the first time an erbium luminescence in hydrogenated amorphous silicon, using erbium as a dopant. In this study the erbium ions are introduced by the ion implantation technique and this paper deals with the erbium luminescence in implanted hydrogenated amorphous silicon. In particular, the intensity variation of the erbium emission with the hydrogen film content is studied.

EXPERIMENTAL

Samples preparation

Undoped a-Si : H films were prepared, using a high rate dc sputtering system. The target and the substrate holder were in parallel plate configuration, at a distance set to 33 mm. The sputtering target, bonded to a wafer cooled copper backing plate, was a 76 mm diameter disk of high purity undoped silicon (99.99995 %). An electrical resistance is used to heat the substrate holder, the temperature being measured and controlled with a type k thermocouple fixed on the substrate holder. Prior to sputtering, the chamber was pumped out and then heated to about 100°C to degas it to a pressure less than 10^{-4} Pa. A gas mixture of hydrogen and argon of 5N purity was introduced directly in the plasma region. The conditions of the deposition were chosen so as to obtain samples with good electrical characteristics ; typical conditions were :

deposition temperature: T_d - 280°C
 power : P - 180 W
 Argon pressure : P_{Ar} - 0.93 Pa

The hydrogen content C_H was varied by changing the hydrogen flow in the discharge chamber. Films with various thicknesses were deposited on two kinds of substrates : fused quartz plates and crystalline silicon. The optical parameters (thickness and gap) were determined from the transmission measurements in the 0.4 μm - 2.5 μm range. Implantation of erbium ions was carried out at room temperature, using a beam 7° off the normal of the sample surface and at an energy of 330 keV. Doses were varied from 10^{13} to $10^{15} \text{Er}^+ \text{cm}^{-2}$. After implantation the samples were annealed at 600°C for 15 s, under high purity oxygen flowing. An argon laser source (0.4880 μm line) was used to excite the luminescence and a liquid nitrogen-cooled germanium detector to detect the signal. For measurements at 77 K, the samples were directly immersed in liquid nitrogen.

RESULTS AND DISCUSSIONS

After erbium implantation in hydrogenated amorphous silicon and annealing, an intense and sharply luminescence spectrum was measured around 1.54 μm . Fig. 1 shows typical spectra in the 1.5 μm - 1.6 μm range, recorded at 77 K and at room temperature (R.T). The decrease of the peak intensity, from 77 K to R.T, is around a factor of 40. As far as we know, this is the first experimental evidence of erbium luminescence in implanted a-Si : H.

Fig. 2 shows a comparison at 77K of the luminescence spectrum of erbium implanted into crystalline silicon at 300 keV with a dose of 10^{13}cm^{-2} and the luminescence spectrum in a-Si : H with the same dose and energy. It may be seen that the luminescence peak in a-Si : H is higher and broader than that in c : Si. The broadness is due to the amorphous nature of our material. In addition, the PL spectra have the same luminescence line at 1.536 μm , ; however a second luminescence line at 1.545 μm is observed in the a-Si : H spectrum.

Table 1 summarizes the results of SIMS (Secondary Ion Mass Spectroscopy) and transmission measurements made on various samples in order to determine the hydrogen content C_H and the optical gap energy of the semiconductor, respectively E_g , the optical gap, was deduced from the linear relation between $(\alpha h\nu)^{1/2}$ and $h\nu$, where α and ν represent respectively the absorption coefficient and the frequency of light.

Sample	C_H %	E_g (eV)
K ₁	7	1.68
K ₂	18	1.79
K ₃	7	1.64
K ₄	2	1.53

Table 1 : Hydrogen content C_H and optical gap energy in various a-Si : H substrates

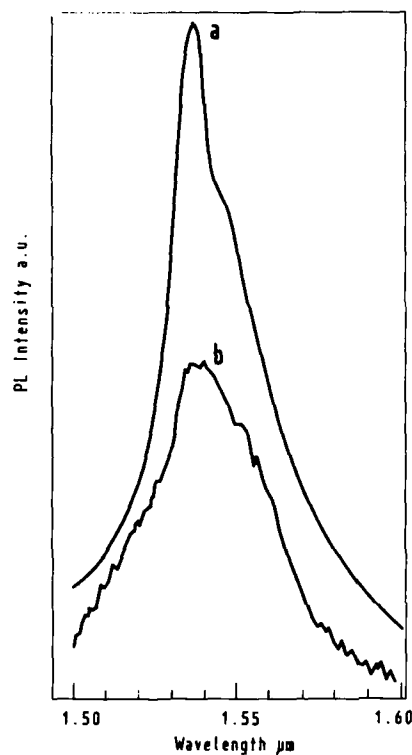


Fig. 1 : PL spectra for erbium implanted a-Si:H (sample K1) (energy : 300 keV dose : 10^{14} Er cm^{-2} , annealing : 850°C 15s)
a : spectrum at 77K
b : spectrum at room temperature

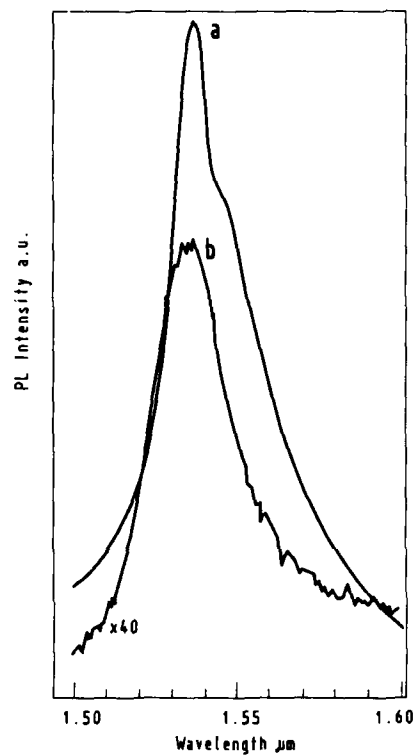


Fig.2 : a) PL spectrum for erbium implanted a-Si:H compared to b) PL spectrum for erbium implanted crystalline silicon (dose : 10^{13} Er+ cm^{-2} , energy : 300 keV, annealing 900°C 30 min)

A recent study showed that, with the same samples studied by E.R.D (Elastic Recoil Detection and transmission measurement), the optical gap E_g increases linearly when C_H varies from 5 to 15 % (Fig. 3). This linear behaviour may be described by : $E_g(\text{eV}) = (0.014 * C_H + 1.55)$.

Favennec et al [3] showed that there is a direct correlation between the efficiency of optical centres induced by the implanted erbium element and the band gap energy. Thus in order to increase the luminescence intensity versus temperature, the band gap energy may be adjusted by varying the hydrogen content in the a-Si : H films.

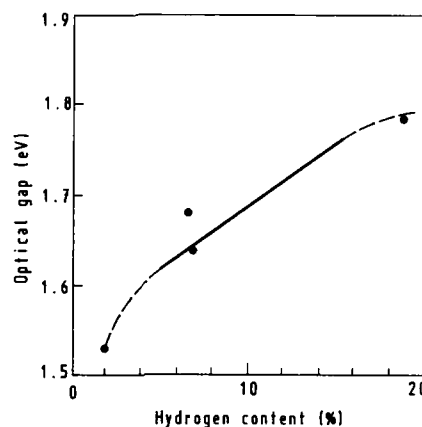


Fig. 3 : Optical gap variation with hydrogen film content ; full line : obtained from transmission and ERD measurements in Ref. (7)

In conclusion ion implantation seems a very attractive technology to introduce erbium impurities into a-Si : H. An intense luminescence is observed at 1.54 μm , even at room temperature. By increasing the hydrogen content from 5 to 15 % in the a-Si : H films, it may be possible to adjust the optical gap energy value from 1.62 to 1.76 eV, and so to increase the luminescence intensity at room temperature. These results offer new possibilities for applications to optical devices, using wide gap a-Si : H films.

References

- [1] H. Ennen, J. Schneider, G. Pomrenke and A. Axman
Appl. Phys. Lett. 43, 943 (1983)
- [2] P.S. Whitney, K. Uwai, H. Nagagome and K. Takakei,
Electron. Lett. 24, 740 (1988)
- [3] P.N. Favenec, H. L'Haridon, M. Salvi, D. Moutonnet and Y. Le Guillou
Electron. Lett. 25, 718 (1989)
- [4] C. Rochaix, A. Rolland, P.N. Favenec, B. Lambert, A. Le Corre, H. L'Haridon
and M. Salvi
Jap. J. of Appl. Phys., 27 L 2348 (1988)
- [5] G. Pomrenke, H. Ennen and W. Haydl
J. Appl. Phys. 59, 610 (1986)
- [6] T. Oestereich, G. Swiatkowski and I. Broser
Appl. Phys. Lett., 56, 446 (1990)
- [7] N. Beldi, A. Rahal, D. Hamouli, M. Aouchier, T. Mohammed-Brahim,
D. Mencaraglia, Z. Djebour, Chahed and Y. Bouizem
Proceedings of the 11th European Photovoltaic Conference, Montreux
(Switzerland), October 1992

PART III

**Optical, Electrical and
Structural Properties**

ELECTRONIC PROPERTIES AND THEIR RELATIONS TO OPTICAL PROPERTIES IN RARE EARTH DOPED III-V SEMICONDUCTORS

AKIHITO TAGUCHI*, KENICHIRO TAKAHEI*, AND JYOJI NAKATA**

*NTT Basic Research Labs., Musashino-shi, Tokyo, JAPAN

**NTT LSI Labs., Atsugi-shi, Kanagawa, JAPAN.

ABSTRACT

We discuss the energy transfer mechanism between rare-earth 4f-shells and III-V semiconductor hosts. For Yb-doped InP, we have proposed an excitation and relaxation model, which explains experimental results for the electronic and optical properties. The Yb 4f-shell is excited by a recombination of an electron and a hole at an electron trap formed by Yb, which is located near the bottom of the conduction band of InP. At high temperatures, the relaxation energy of the Yb 4f-shell is back transferred as a host electron-hole pair, resulting in Yb luminescence quenching. We have found that Er-doped GaAs samples grown by metalorganic chemical vapor deposition contain as much C as Er. Rutherford back scattering and electronic property measurement results suggested that most of the Er atoms form complexes with C atoms, and these complexes are not electrically active. Such samples showed complicated Er 4f-shell luminescence spectra. To obtain a simple Er luminescence spectrum with a high peak intensity, O was intentionally doped with Er. Er-O complexes seemed to be formed in GaAs and these are responsible for simple and strong 4f-shell luminescence.

INTRODUCTION

Rare-earth (RE) doped III-V semiconductors are attractive materials, because they have the potential to combine the advantages of optical properties of RE³⁺ ions and the advantages of electronic properties of semiconductor hosts. In the early 1980's, RE 4f-shell luminescence was reported for various combinations of RE's and III-V hosts synthesized by melt growth and ion implantation.[1] Optical properties have been widely studied, but the luminescence efficiency is still low and the intensity rapidly decreases at high temperatures. At room temperature, RE 4f-shell luminescence has been observed for a few materials such as GaAs:Er[2], GaP:Nd,[3] and GaInP:Tm.[4] To increase the efficiency and to obtain strong luminescence at room temperature, it is necessary to clarify the energy transfer mechanism between RE 4f-shells and semiconductor hosts. The electronic properties of the RE ions in III-V semiconductor hosts are important in the energy transfer mechanism. However, few studies have been carried out on these properties compared with studies on the optical properties. The electronic properties of Yb-doped InP have been most extensively studied and are well understood.[5,6] In the next section, we discuss the energy transfer mechanism between the Yb 4f-shell and InP host based on the electronic and optical properties. We show that the Yb-related electron trap level in the band gap plays an important role in the energy transfer processes.

Another problem in III-V:RE materials is that the RE 4f-shell spectrum generally depends on the sample preparation method. For Er-doped GaAs, it has been reported that the Er luminescence spectra for the samples grown by molecular beam epitaxy (MBE)[7] and metalorganic chemical vapor deposition (MOCVD)[8] strongly depend on growth conditions. The spectra for the samples synthesized by ion implantation also depend on the annealing conditions.[9] It is necessary to control the site of the RE ion in the host to obtain sharp and strong luminescence from RE 4f-shells. Recently, we found that C is doped with Er when samples are grown by MOCVD. The Er and C atoms seem to form complexes in the GaAs host, which are not electrically active. The samples showed complicated Er 4f-shell luminescence spectra depending on the growth conditions. To obtain a simple Er spectrum, we intentionally doped O. The spectrum was changed dramatically. The GaAs:Er,O samples showed simple Er luminescence spectra, suggesting selective formation of a specific Er luminescence center.

Yb-DOPED InP

Yb-doped InP has been widely used to investigate the excitation and relaxation mechanism of the RE 4f-shells in the semiconductor hosts, because of the two characteristic features of this material. One is that the photoluminescence (PL) spectrum of the Yb^{3+} 4f-shell does not depend on sample preparation methods such as ion implantation,[10] liquid phase epitaxy,[11] and MOCVD.[12] The other is that the Yb^{3+} 4f-shell has only one excited state. Yb is considered to substitute for In in InP, since Zeeman spectroscopy measurements[13] showed that the Yb luminescence center has the tetragonal symmetry.

Electronic properties

Since Yb-doped InP samples synthesized from molten solution tend to show *p*-type conductivity,[11] it was assumed that Yb is an acceptor impurity in the InP host. However, MOCVD-grown InP:Yb samples were highly resistive or showed *n*-type conductivity,[5] indicating that Yb is not an acceptor impurity. Deep level transient spectroscopy (DLTS) measurements on the MOCVD-grown samples showed that a very shallow level is formed by the Yb-doping.[5] Its energy position is in the band gap of the InP host at 30 meV below the bottom of the conduction band. The same level was observed by temperature dependent Hall effect measurements.[5] For samples grown by liquid phase epitaxy (LPE), the same level was observed.[6] The relation of the free electron density and Hall mobility at 77 K indicates that this level is not a conventional donor but acts as a scattering center. At low temperatures, this level captures an electron. At higher temperatures, the captured electron is thermally activated to the conduction band, since the energy position is close to the bottom of the conduction band. We call this trap an acceptor-like electron (AE) trap. Concentration of the AE trap estimated by DLTS agreed with the Yb concentration in the epitaxial layers estimated by secondary ion mass spectroscopy (SIMS).[5] Hence, it is likely that Yb forms the AE trap.

The Yb 4f-shell luminescence is due to the intra-4f-shell transition of the 3+ charged state (Yb^{3+}). However, it has been suggested that an Yb ion may take the 2+ charged state (Yb^{2+}) in the InP host.[10,11] Electron paramagnetic resonance measurement, however, revealed that the Yb ions are in the Yb^{3+} states even in *n*-type InP host.[14] This means that the AE trap with an electron is in the Yb^{3+} state. Therefore, the electron captured by the AE trap is located outside the 4f-shell. The AE trap is considered to be an isoelectronic trap. The difference in electron affinity between Yb and In, and local stress around the Yb ion must be the origin of the attractive force on electrons.

Excitation and Quenching mechanisms

Various mechanisms have been proposed as the excitation mechanism of the Yb 4f-shell in the InP host: energy transfer from donor-acceptor pairs or from exciton[15] and impact excitation by hot carriers[11]. In these mechanisms, the electronic properties of Yb was not taken account. Another energy transfer mechanism has been proposed by assuming *p*-type behavior of Yb.[11] However, this assumption conflicts with the electronic properties described above.

We have proposed an excitation mechanism based on the AE trap.[16] Figure 1 shows a configurational coordinate model of our excitation mechanism. The horizontal axis is the lattice distortion around Yb and the vertical axis is the total energy of the 4f-shell electrons, host carriers, and lattice distortion. E_g is the band gap of InP, and E_t is the energy between the AE trap and the bottom of the conduction band. The ground state of the system is expressed by (1). A free electron and a free hole are produced by host excitation, and the system is activated to state (2). The AE trap captures an electron from the conduction band. In state (3), the trap is negatively charged and attracts holes by Coulomb force because of the trapped electron. Subsequently, recombination of the electron and a hole occurs at the AE trap. A part of the recombination energy is transferred to the Yb 4f-shell, resulting in the excitation of the shell. This state is expressed by (4). The excited 4f-shell relaxes radiatively by emitting a photon with energy E_{fl} . The energy transfer process from the electron-hole pair to the Yb 4f-shell is likely to be an Auger process. Since the AE trap is isoelectronic, the captured electron

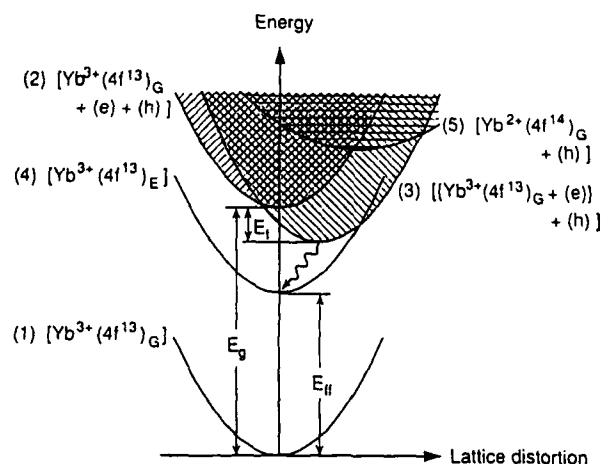


FIG. 1 Configurational coordinate model of our excitation mechanism.

should be closely localized near the Yb ion causing a strong interaction between the 4f-shell and the electron-hole pair. Hence, the efficiency of this energy transfer is expected to be high.

Our proposed mechanism is also consistent with the temperature dependence of the Yb 4f-shell luminescence. Figure 2 shows the temperature dependences of the Yb PL intensity and the free electron concentration for two samples.[17] The AE trap concentrations are 4×10^{16} and $4 \times 10^{15} \text{ cm}^{-3}$ for MO1 and MO2, respectively. The two samples have similar free electron concentrations ($2 \times 10^{16} \text{ cm}^{-3}$) at room temperature, which is almost the same as the shallow donor concentrations, since almost all shallow donors are ionized at that temperature.

In MO1, the PL intensity is almost constant up to about 70 K, and then decreases as temperature increases. In MO2, the intensity monotonically decreases with increase in temperature. Below 70 K, the PL intensities of the two samples show different temperature dependence. The difference can be explained by the difference in the electronic properties of the samples. It has been reported that the photoluminescence time-decay (PL-TD) curve shows an initial fast nonexponential decay followed by a slower exponential decay in samples with a higher shallow donor concentration than the AE trap concentration.[16] The nonexponential fast decay was explained as follows. After the excitation of the 4f-shell by the electron-hole recombination, the AE trap becomes empty. Such empty trap may capture an electron again from distant shallow donors. These re-trapped electrons cause 4f-shell quenching, since the electron can be excited into the conduction band receiving the relaxation energy of the 4f-shell by the localized Auger process. This process modifies the PL-TD properties and reduces the PL intensity. This mechanism would be effective in a sample with higher shallow donor concentration than the AE trap concentration. Hence, the PL intensity decrease observed below 70 K in MO2 is due to this mechanism. This process is less efficient in MO1, since the shallow donor concentration is smaller than the AE trap concentration in this sample.

Above 100 K, the PL intensities of the two samples rapidly decrease. Since at these temperatures the PL spectrum becomes broad and hot lines appear, the intensity estimation includes some experimental error. However, the activation energy of this PL intensity decrease is estimated to be about 150 meV for both samples. Hence, this quenching does not depend on the relative magnitude of the AE trap concentration and the shallow donor concentration. The estimated activation energy is almost the same as the previously reported activation energies for p-type and semi-insulating samples.[6,10,11] Because an activation energy of the 4f-shell decay time was the same as that of the PL intensity,[10,11] the quenching must be due to de-excitation of the excited 4f-shell and

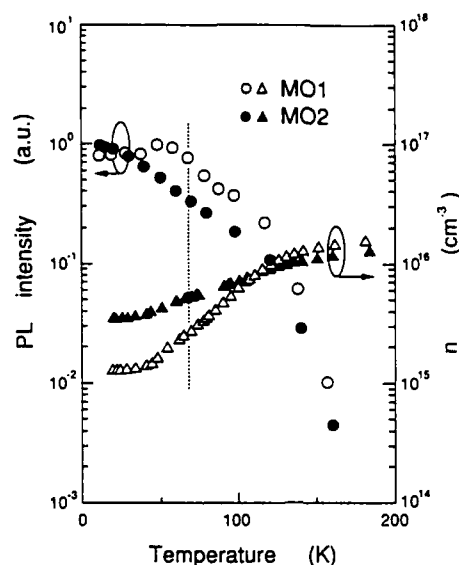


FIG. 2 Temperature dependences of Yb 4f-shell PL intensity and free electron concentration for two InP:Yb samples.

universal to Yb-doped InP samples. In the excitation process, the recombination energy of the electron-hole pair is about 1.42 (the band gap energy) - 0.03 (the depth of the AE trap) = 1.39 eV, since binding energy of the electron-hole pair is expected to be only a few meV.[18] To excite the Yb³⁺ 4f-shell, the energy needs to be nearly equal to the 4f-shell luminescence energy, 1.24 eV. Therefore, there is an energy mismatch between the recombination and the excitation energies, which is 1.39 - 1.24 = 0.15 eV. This energy mismatch is nearly equal to the activation energy of the quenching. This energy coincidence suggests that the quenching is due to the energy-back transfer mechanism. This mechanism was first proposed for RE-doped II-VI materials,[19] but has not been verified. The energy-back transfer is the reverse process to the excitation process: the relaxation energy of the Yb 4f-shell is back transferred to the host, producing an electron-hole pair.

In InP:Yb, we have confirmed the back-transfer mechanism by investigating the properties of the band-edge PL.[17,20] Figure 3 shows the temperature dependence of the band-edge luminescence intensities of the Yb-doped and undoped InP samples. The PL intensity of the undoped InP sample decreases monotonically as temperature increases. In contrast, the PL intensities of the two Yb-doped InP samples show some increases at around 140 K. Moreover, the amount of the increase is larger in MO1 than in MO2. MO1 has larger AE trap concentration than MO2. Therefore, the intensity increase is caused by the presence of Yb. Figure 4 shows PL-TD curves of the band-edge PL for MO1 measured at 51 and 110 K. For comparison, the PL-TD curve of the Yb 4f-shell PL for the same sample measured at 110 K is also shown. At 51 K, at which the quenching is not observed, the band-edge PL-TD shows fast decay. The decay time of the band-edge luminescence is expected to be of the order of nanoseconds or less, so the observed decay curve represents the time response of the measurement system. At 110 K, at which the quenching occurs, the decay curve includes a slow decay component. The time constant of the slow decay part looks similar to that of the Yb 4f-shell luminescence. Since the PL spectra of the Yb-doped and undoped InP samples at the band edge were the same at 110 K, the slow component is not due to an additional recombination process of the electron-hole pair but due to the increase in the number of the electron-hole pairs, whose recombination energy corresponds to this wavelength region. The slow component was observed between 100 and 120 K. In this temperature range, the decay time of the slow component of the band-edge PL is the same as that of the Yb 4f-shell PL.[20]

These results directly verify the energy back-transfer. In the back-transfer process,

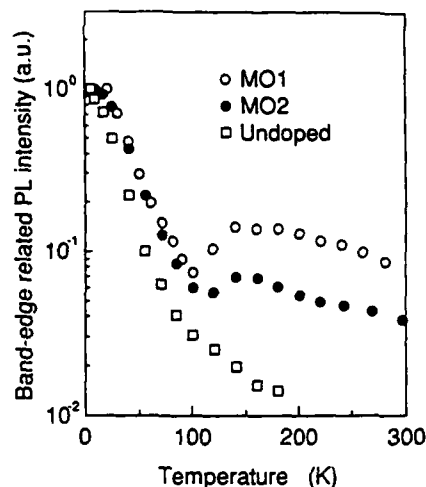


FIG. 3 Temperature dependence of band-edge related PL intensity for undoped and Yb-doped InP samples.

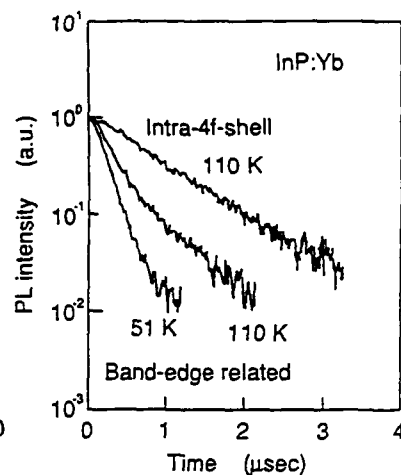


FIG. 4 Time-decay curves of band-edge related PL and Yb 4f-shell PL.

the relaxation energy of the Yb 4f-shell is used to produce the electron-hole pair in the InP host. At temperatures where the back-transfer occurs, the electron-hole pair easily dissociates, since the binding energy of the pair is small[18] and the energy position of the AE trap is close to the bottom of the conduction band. Some of the dissociated electrons and holes recombine radiatively, resulting in the band-edge luminescence. Therefore, the back-transfer mechanism increases the band-edge PL intensity as shown in Fig. 3. Since the rate of the electron-hole pair dissociation and the recombination of carriers are much larger than that of the energy transfer from the excited 4f-shell to the host, the energy transfer process is the rate determining process of the band-edge luminescence due to the back-transfer. Therefore, the slow component of the band-edge luminescence is nearly the same as the decay rate of the 4f-shell luminescence, as shown in Fig. 4.

Zn-doped InP:Yb

The proposed excitation model and the back-transfer quenching model are based on the experimental results for *n*-type InP:Yb samples. The model does not depend on the conduction type. It was reported, however, that the Yb luminescence intensity in a *p*-type InP host starts to decrease at a lower temperature than that in an *n*-type host.[11,10] This feature can not be explained by the proposed model. To investigate the optical properties of *p*-type InP:Yb, we doped Zn with Yb into InP hosts by MOCVD.

Figure 5 compares the high resolution Yb 4f-shell spectra of Yb-doped (*n*-type) and Yb- and Zn-doped (*p*-type) samples at 4 K.[21] Signal-to-noise ratio is worse in the *p*-type sample due to the weak PL intensity, but the spectra are essentially the same in *n*-type and *p*-type hosts. The 4f-shell luminescence spectrum depends on the crystal field, which is determined by the local atomic configuration. Hence, the identical spectra indicate that the atomic configuration is the same. So the Yb atom is located at the In site even in the *p*-type host.

Although the Yb center is the same as in an *n*-type host, the Yb 4f-shell PL intensity for the InP:Yb,Zn sample starts to decrease at about 40 K, which is lower than that in the *n*-type host. The activation energy of this quenching was estimated to be about 40 meV. Allowing for experimental error, this activation energy is nearly equal to the previously reported values, 50 and 33 meV.[11,18] Hence, it seems that the low temperature quench-

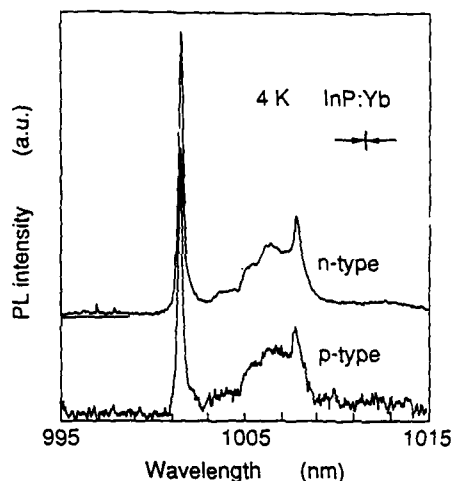


FIG. 5 High resolution spectra of the Yb 4f-shell PL at 4 K for Yb-doped (n-type) and Yb- and Zn-doped (p-type) InP samples.

ing of the Yb 4f-shell PL is universal in p-type samples. At 53 K, at which the quenching occurs, the 4f-shell PL-TD curves shows fast nonexponential decay. In LPE-grown p-type InP:Yb samples, the nonexponential nature of the 4f-shell luminescence was also reported.[18] Therefore, the intensity quenching must be due to the de-excitation of the excited 4f-shell and it is characteristic for the p-type samples. However, the mechanism is not clear yet.

The dependence of the band-edge PL intensity on temperature was also investigated for the p-type samples. The results are shown in Fig. 6. The PL intensity of the Zn-doped sample monotonically decreases as the temperature increases. The PL intensities of the two Yb- and Zn-doped samples have shoulders at around 100 K. This feature is the same as that of the n-type samples as shown in Fig. 3. Therefore, energy back-transfer also occurs in the p-type InP:Yb samples, supporting the proposed energy transfer mechanism.

Figure 7 shows a schematic description of the energy transfer mechanism. The excitation process and the energy back-transfer process are universal processes in InP:Yb materials. The important point is that Yb forms an electron trap level. Due to this feature, the trapped electron is located close to the Yb ion. This causes strong interactions between the electron and the 4f-shell, which results in an efficient 4f-shell excitation. Since the excitation and the energy back-transfer processes do not require other impurities except for Yb itself, this mechanism may be applied to other RE-doped semiconductors.

Er-DOPED GaAs

Er-doped GaAs is another widely studied III-V:RE material. The Er 4f-shell luminescence appears at around 1.54 μm , corresponding to the minimum energy loss wavelength range of silica based optical fibers. The Er 4f-shell luminescence spectrum generally has many luminescence lines, indicating that many kinds of Er luminescence centers are formed in one sample. Because of this complexity, the electronic properties of Er in a GaAs host, nor the excitation and relaxation mechanisms are understood. Some features of this material are discussed in the following.

Er-C coupling in GaAs samples grown by MOCVD

Recently, SIMS measurement revealed that the Er-doped GaAs samples grown by MOCVD unintentionally contain C. Figure 8 shows a typical SIMS depth profile of a

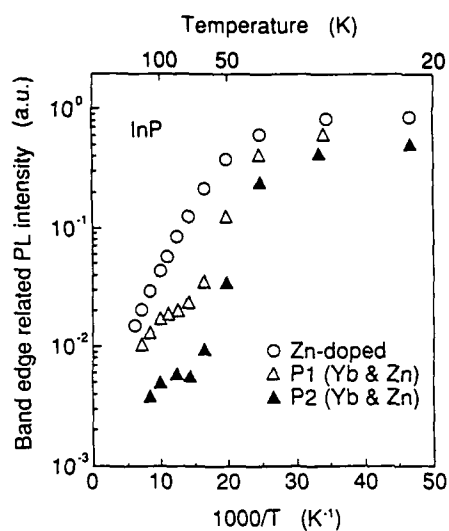


FIG. 6 Temperature dependence of band-edge related PL intensity for Zn-doped InP and Yb- and Zn-doped InP samples.

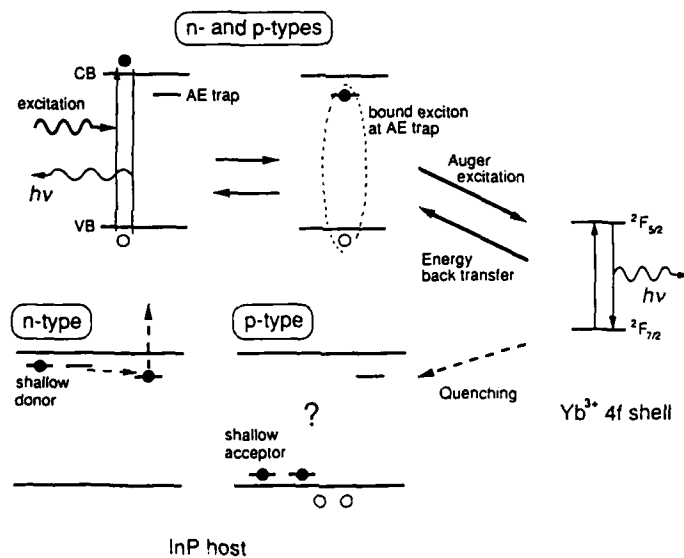


FIG. 7 Schematic diagram of energy transfer between Yb 4f-shell and InP host.

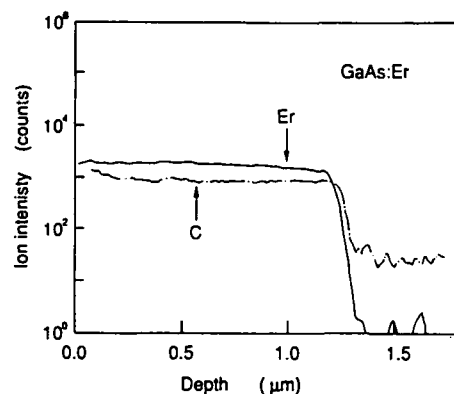


FIG. 8 SIMS depth profile of Er and C for MOCVD-grown GaAs:Er samples.

GaAs:Er sample. The Er profile is flat in the growth direction. The figure shows that C is also doped in the epitaxial layers with the same depth profile as that of Er. The coincidence of the depth profile for Er and C suggests a strong correlation between Er and C. It was found that samples grown under different growth conditions also contain C. The C concentrations are estimated to be equal to, or somewhat larger than the Er concentration. C must come from the source gas. SIMS measurements were also carried out for undoped GaAs samples grown by MOCVD, but C was not detected. The incorporation C along with Er is characteristic to this material. In Yb-doped InP samples, C has not been detected.

Since C is known to be an acceptor impurity in GaAs, the MOCVD-grown GaAs:Er samples are expected to show *p*-type conductivity. However, all samples showed *n*-type conductivity. The free electron concentrations of the samples at room temperature are shown in Fig. 9 as a function of the Er concentration. The electron concentrations are nearly the same for all samples, not depending on the Er concentration. They are almost the background level in the present MOCVD apparatus. Therefore, the Er nor C emits free carriers. The electron concentrations must be determined by the residual impurities. It seems that the Er and C in the epitaxial layer form complexes, which are electrically inactive.

To investigate the Er lattice location in GaAs host, Rutherford back scattering (RBS) channeling measurement was carried out.[22] The results are shown in Fig. 10. The broad spectra are due to the GaAs host while the separated peaks in the high energy region are due to the Er. The $\langle 110 \rangle$ spectrum of Er ions is higher than that of the 45°

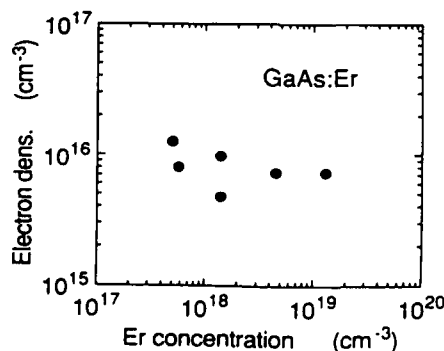


FIG. 9 Free electron density at room temperature for GaAs:Er samples.

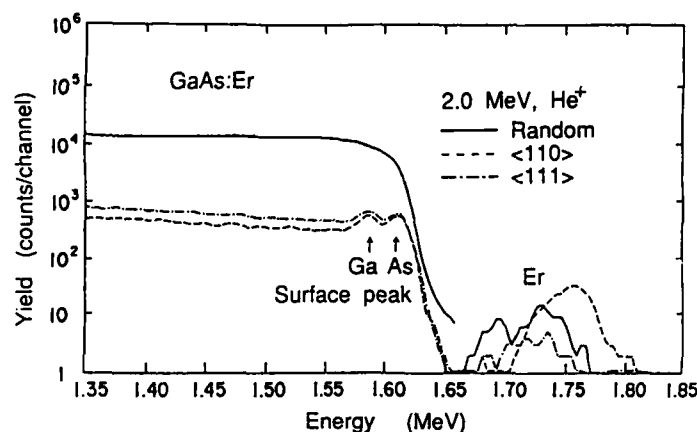


FIG. 10 RBS channeling spectra for MOCVD-grown GaAs:Er.

random spectrum, whereas the peak height of the $\langle 111 \rangle$ is lower than that of the random spectrum. This is direct evidence that Er ions occupy an interstitial site in the $\langle 110 \rangle$ channel, i.e., tetrahedral interstitial site.[23] Detailed analysis of the RBS data showed that Er ions occupy a somewhat displaced tetrahedral interstitial site. This suggests that native defect or impurities may be located near the Er site. This is consistent with the coupling of Er and C inferred from the SIMS measurements and electronic measurements.

PL measurements of these samples were performed at 4 K. The spectra showed complicated structures with more than 16 luminescence lines, indicating that many kinds of Er luminescence centers are present. The PL spectra depend on the growth conditions. These results suggest that the dominant Er-C complex may not be an efficient luminescence center.

O co-doping effect

It was reported that O co-implantation with Er enhances Er 4f-shell luminescence in Si[24,25] and AlGaAs.[26] We doped O with Er into GaAs hosts by MOCVD.[27] The O co-doping dramatically changes the Er 4f-shell luminescence spectrum. The complicated Er luminescence of the Er-doped GaAs sample, shown in Fig. 11(a), becomes simple by O co-doping as can be seen in Figs. 11(b) and 11(c). The samples of Figs. 11(a) and 11(b) have the same Er concentration, $2 \times 10^{17} \text{ cm}^{-3}$. The two samples were grown under the same condition except for the O co-doping. The peak intensity of the strongest luminescence line of the O co-doped sample, Fig. 11(b), is more than five times larger than that of the sample without O co-doping, Fig. 11(a). An exact estimation of the peak intensity is difficult because the strongest line of the co-doped sample is too narrow to be resolved. The total PL intensity between 1.5 μm and 1.6 μm , including a broad background luminescence in Fig. 11(a), was about 20% larger for the co-doped sample. The spectrum shown in Fig. 11(b) is composed of two groups denoted by N and F. The wavelengths of the N lines are the same as those of the previously reported lines for the MOCVD-grown sample.[8] The wavelengths of the sharp luminescence lines reported for the MBE-grown sample[7] are different from those of the N lines, but the same as those of the F lines shown in Fig. 11(b). The atomic configurations of the N and F centers must be different, because the wavelengths of the luminescence lines are different. The relative intensities of the lines denoted by N are the same in all samples measured, indicating that one kind of Er center emits these lines. In a sample with a larger Er concentration, $1.5 \times 10^{18} \text{ cm}^{-3}$, the F lines disappear as shown in Fig. 11(c). The O co-doping enhances the luminescence from the N center, suggesting that one kind of Er center is selectively

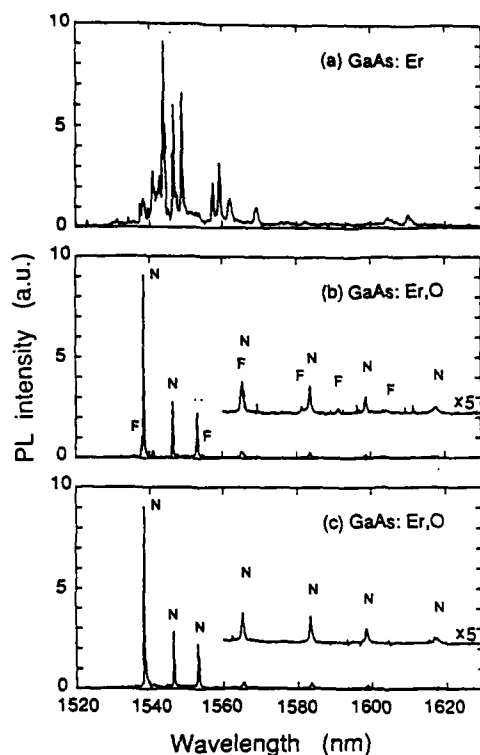


FIG. 11 Er 4f-shell PL spectra for (a) GaAs:Er sample, and (b), (c) GaAs:Er,O samples.

formed by the O co-doping.

Figure 12(a) shows the results of SIMS measurements for the Er-doped GaAs sample with O co-doping. The depth profile of O is the same as that of Er, showing a strong correlation. Although the Er-doped GaAs sample without O co-doping shows a clear relation between Er and C as shown in Fig. 7, the relation between Er and C is not clear in Fig. 12(a) due to the decrease in C concentration. A GaAs sample without Er was grown in an atmosphere containing the same amount of O concentration as that in the growth of the GaAs:Er,O samples. The results of SIMS for such sample are shown in Fig. 12(b). The arrow shows the interface between the substrate and the epitaxially grown layers. Both O and C are background levels throughout the epitaxial layers. Therefore, a high concentration of O is incorporated only when Er is doped. It seems that O forms complexes with Er in GaAs layers. Such complexes must be responsible for the simple Er 4f-shell luminescence shown in Fig. 11(c).

The GaAs:Er,O samples show *n*-type conductivity. The energy transfer mechanism for this material is under study.

SUMMARY

The energy transfer mechanism between the Yb³⁺ 4f-shell and InP host has been clarified by investigating both the electronic and optical properties. The 4f-shell is excited by the recombination of the electron-hole pair at the trap formed by Yb. It was found that the energy back-transfer mechanism is the dominant quenching mechanism at high temperatures. This is the reverse process of the excitation process: the relaxation energy of the 4f-shell is used to produce the electron-hole pair in the host. In both excitation

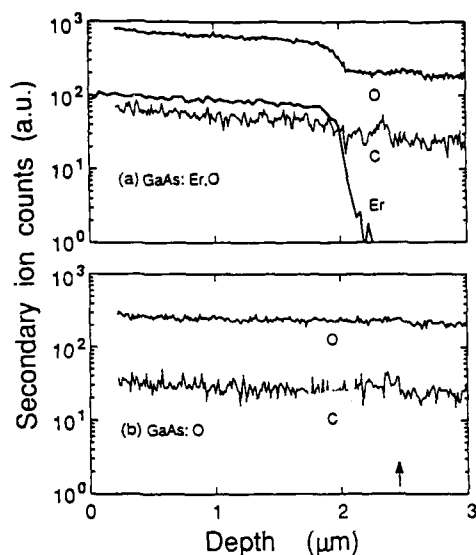


FIG. 12 SIMS measurement results for (a) GaAs:Er,O sample, and (b) GaAs:O sample.

and quenching processes, the Yb-related trap plays the dominant role. The proposed energy transfer mechanism may be applied to other RE-doped semiconductors, since this mechanism requires no other impurities other than the RE.

We found that the MOCVD-grown GaAs:Er samples always unintentionally contain C. Er and C seem to form complexes, which are not electrically active. Many kinds of Er luminescence centers were formed in such samples. We also found that the Er 4f-shell luminescence spectrum is greatly affected by O co-doping. The Er 4f-shell PL spectrum becomes very sharp and much simpler. A strong correlation between Er and O was observed, suggesting formation of Er-O complexes. Such complexes must be responsible for the sharp and simple Er 4f-shell luminescence spectrum.

ACKNOWLEDGEMENTS

The authors thank Dr. S. J. Chan for his valuable discussion. They are also grateful to Dr. T. Kimura, Dr. Y. Horikoshi, and Dr. H. Kanbe for their helpful suggestions during the work.

REFERENCES

- [1] H. Ennen and J. Schneider, *J. Electron. Mater.* **14A**, 115(1985).
- [2] R. S. Smith, H. D. Müller, H. Ennen, P. Wennickers, and M. Maier, *Appl. Phys. Lett.* **50**, 49(1987); P. Galtier, M. N. Charasse, J. Chazelas, A. M. Huber, C. Grattapain, J. Siejka, and J. P. Hirtz, *Proc. Int. Symp. GaAs and Related Compounds*, Atlanta, Georgia, 1988. *Int. Phys. Conf. Ser.* **96**, 61.
- [3] K. Takahei and H. Nakagome, *Proc. Int. Symp. GaAs and Related Compounds*, Karuizawa, Japan, 1989. *Int. Phys. Conf. Ser.* **106**, 913; *J. Appl. Phys.* **72**, 3674(1992).

- [4] K. Pressel, J. Weber, C. Hiller, D. Ottenwälder, W. Kürner, A. Dörnen, F. Sholtz, K. Locke, D. Wiedmann, and F. Cordeddu, *Appl. Phys. Lett.* **61**, 560(1992).
- [5] P. S. Whitney, K. Uwai, H. Nakagome, and K. Takahei, *Appl. Phys. Lett.* **53**, 2074(1988).
- [6] B. Lambert, A. Le Corre, Y. Toudic, C. Lhomer, G. Grandpierre, and M. Gauneau, *J. Phys.: Condens. Matter* **2**, 479(1990).
- [7] H. Ennen, J. Wagner, H. D. Müller, and R. S. Smith, *J. Appl. Phys.* **61**, 4877(1987).
- [8] H. Nakagome, K. Uwai, and K. Takahei, *Appl. Phys. Lett.* **53**, 1726(1988); K. Takahei, P. S. Whitney, and K. Uwai, *J. Appl. Phys.* **65**, 1257(1989).
- [9] G. S. Pomrenke, H. Ennen, and W. Haydl, *J. Appl. Phys.* **59**, 601(1986).
- [10] P. B. Klein, *Solid State Commun.* **65**, 1097(1988).
- [11] W. Köber and A. Hangleiter, *Appl. Phys. Lett.* **52**, 114(1988).
- [12] K. Uwai, H. Nakagome, and K. Takahei, *Appl. Phys. Lett.* **50**, 988(1987).
- [13] G. Aszodi, J. Weber, Ch. Uihlein, L. Pu-lin, H. Ennen, U. Kaufmann, J. Schneider, and J. Windscheif, *Phys. Rev. B* **31**, 7767(1985).
- [14] B. Lambert, Y. Toudic, G. Grandpierre, and A. Le Corre, *Electron. Lett.* **24**, 1446(1988).
- [15] V. A. Kasatkin and V. P. Savel'ev, *Sov. Phys. Semicond.* **18**, 1022(1984).
- [16] K. Takahei, A. Taguchi, H. Nakagome, K. Uwai, and P. S. Whitney, *J. Appl. Phys.* **66**, 4941(1989).
- [17] A. Taguchi, H. Nakagome, and K. Takahei, *J. Appl. Phys.*, **70**, 5604(1991).
- [18] K. Thonke, K. Pressel, G. Bohnert, A. Stapor, J. Weber, M. Moser, A. Molassioti, A. Hangleiter, and F. Scholz, *Semicond. Sci. Technol.* **5**, 1124(1990).
- [19] R. Boyn, *Phys. Status Solidi (b)* **148**, 11(1988).
- [20] A. Taguchi, M. Taniguchi, and K. Takahei, *Appl. Phys. Lett.* **60**, 965(1992).
- [21] A. Taguchi and K. Takahei, *Materials Science Forum* **117-118**, 303(1993).
- [22] J. Nakata, M. Taniguchi, and K. Takahei, *Appl. Phys. Lett.*, **61**, 2665(1992).
- [23] W. K. Chu, J. W. Mayer, and M. A. Nicolet, *Backscattering Spectrometry* (Academic, New York, 1978).
- [24] P. N. Favennec, H.L'Haridon, D. Moutonnet, M. Salvi, and M. Gauneau, *Jpn. J. Appl. Phys.* **29**, L524(1990).
- [25] J. Michel, J. L. Benton, R. F. Ferrante, D. C. Jacobson, D. J. Eaglesham, E. A. Fitzgerald, Y. -H. Xie, J. M. Poate, and L. C. Kimerling, *J. Appl. Phys.* **70**, 2672(1991).
- [26] J. E. Colon, D. W. Elsaesser, Y. K. Yeo, and R. L. Hengehold, *Mater. Res. Soc. Proc.* **37**, Boston, 499(1992).
- [27] K. Takahei and A. Taguchi, *submitted to J. Appl. Phys.*

Effects of Ytterbium Addition on Liquid Phase Epitaxial Growth of InGaAs/InP Heterostructures

A. DAVIS, H.M. DAUPLAISE, J.P. LORENZO, G.O. RAMSEYER*, AND
J. A. HERRIGAN

Rome Laboratory

Hanscom Air Force Base, MA 01731

*Griffiss Air Force Base, NY 13441

ABSTRACT

We have investigated the effects of Yb addition to melts used for the growth of InGaAs/InP heterostructures by liquid phase epitaxy. Our results indicate that impurities in the Yb play an important role in determining the changes in electrical properties observed in the epilayers after Yb treatment of the melt. We have examined samples using double-crystal x-ray diffractometry, photoluminescence, Hall/van der Pauw measurements, and secondary-ion mass spectroscopy. After Yb treatment, the residual carrier concentrations of the epilayers were reduced by more than one order of magnitude and the samples luminesced more strongly; while the lattice matching and crystal quality of the epilayers were not measurably affected by the Yb. There was a smaller-than-expected increase in the 77K mobility and a marked increase in the compensation ratio of the epilayers grown after the addition of Yb to the melt. We believe the Yb is both acting as a scavenging agent in the melt, combining with impurities that otherwise would have been incorporated in the epilayers, and introducing deep level impurities of its own, which are incorporated into the grown layers.

INTRODUCTION

Past studies of rare-earth doping of semiconductors have focused primarily on the 4f-4f emission line of the dopant, the wavelength of which is generally independent of the host material. Rare-earth luminescence has been seen in III-V layers grown by liquid phase epitaxy (LPE), metalorganic chemical vapor deposition (MOCVD), and molecular beam epitaxy (MBE) [1-3]. The addition of rare-earth elements to epitaxial growth sources has also been reported to dramatically improve the electrical properties of the resulting epilayers [4-7]. A reduction in residual carrier concentration was also observed after rare-earth addition to bulk InP crystals grown by liquid-encapsulated Czochralski [8].

The addition of small amounts of rare-earth elements to LPE growth melts has been shown to reduce the length of the bakeouts that have typically been required to obtain residual carrier concentrations sufficiently low to fabricate usable optoelectronic devices [4]. We have investigated the results of ytterbium addition to LPE melts used to grow InGaAs/InP heterostructures. The resulting epilayers were examined by double-crystal x-ray diffractometry (DCXRD), photoluminescence (PL), Hall/van der Pauw measurements, and secondary-ion mass spectroscopy (SIMS). We have compared samples grown before and after rare-earth addition to the melt. Our results indicate that impurities present in the Yb play a critical role in the observed electrical phenomena.

EXPERIMENTAL

The InGaAs layers were grown in a low-mass LPE system consisting of a sliding, high-density graphite boat, as shown in Figure 1, situated in a quartz tube with a purified (palladium-diffused) hydrogen ambient flowing throughout growth runs. The sliding furnace is resistively-heated, with a gold-coated pyrex outer tube. The complete system is shown in Figure 2.

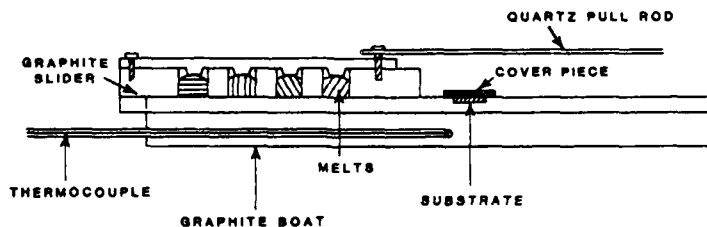


Figure 1. The sliding graphite boat used to grow all layers.

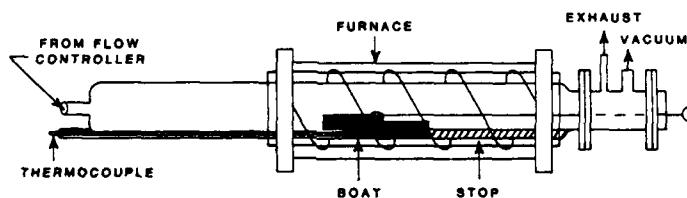


Figure 2. Layout of liquid phase epitaxial growth system.

The melts were prepared from a 5 gram slug of 7N indium and the appropriate amounts of undoped InAs, and either undoped or Cr-doped GaAs for lattice-matched growth at a chosen temperature [9]. The growth temperature was varied slightly, but was usually at or slightly below 631°C. Ytterbium of 99.9% purity was used for rare-earth addition studies. Because the rare-earth elements tend to be both difficult to separate and highly reactive, it is difficult to obtain ultra-high purity rare-earth elements. The substrates were semi-insulating (Fe-doped) InP squares, approximately 8 mm to a side. Some substrates were degreased in trichloroethylene, acetone, and methanol, then blown dry with nitrogen prior to any other treatment. All substrates were etched in 0.5% bromine in 2-propanol, then rinsed in methanol and blown dry immediately prior to being loaded into the LPE system. The system was evacuated to <10 millitorr, then backfilled and flushed with purified hydrogen for one hour prior to heating. In order to minimize the dissociation of phosphorus from the substrate during prebake, the substrates were protected by a sacrificial proximity cap of InP, either undoped or n^+ (Sn-doped), separated from the substrate by a gap of approximately 25 μm . Neither surface degreasing nor lack thereof, type of GaAs used in the melt, nor type of proximity cap used was shown to have any measurable effect on the ultimate quality of the InGaAs layers. Before the first growth from a given melt, each melt was baked in purified hydrogen for 24 hours

at 721°C. As a part of each individual growth run, the solution was prebaked at 665°C for 30 minutes, then quickly cooled to 640°C, where it was held for 10 minutes. Then the system was cooled approximately 1°C/minute, with growth initiated at the pre-determined temperature.

Initially, the Yb had a dark coating on it. Therefore some of the Yb was etched in dilute hydrochloric acid before being added to the melt. When this treatment was not shown to have any measurable impact on the ultimate quality of the epilayers grown from the melt, it was discontinued. Yb was added to selected melts by placing it on top of the re-frozen melt and baking at 731°C overnight. For some melts, the Yb was included with the GaAs and InAs under the In slug before the initial molten solution was made. The molten solution was agitated by hand, but a slag was clearly visible on top of the melt. This slag formation has been attributed to reaction of the rare earth with residual impurities in the melt [5]. It has been reported that even minute amounts of oxygen will oxidize Yb [6]. We have no facilities to isolate the Yb from air before placing it into the system. Therefore some oxidation of the rare earth is inevitable. It is noteworthy that the amount of slag visible on top of the melt was directly related to the amount of Yb added to the melt. The quantity of the slag was much too great for it to be attributed exclusively to compounds of Yb and residual impurities. We therefore believe that the bulk of the slag can be attributed to insoluble compounds of Yb, probably oxides, present when the Yb was added to the system. It is also likely that the slag includes undissolved Yb, particularly after large amounts of Yb have been added to the melt.

Double-crystal x-ray diffraction measurements were performed on a Bede Precision Double Axis Diffractometer Model 150, using K_{α} radiation and a first crystal of (001) InP. Rocking curves were measured for symmetric (004) reflections to yield the lattice mismatch and thus the composition of the epitaxial layers. The full width at half maximum (FWHM) of the rocking curve peaks provided a measure of the layer quality.

Photoluminescence (PL) data was taken at room temperature, 77K, and 4K, with an incident laser power ranging from 7mW/cm² to 550 mW/cm². A fiber-optic cable was used to deliver the 5145Å argon laser signal to the sample and transmit the observed photoluminescence to a Spex fl spectrometer. The slit width was varied from 100 µm to 1 mm, depending on the intensity of the light luminesced by the sample. A liquid nitrogen-cooled Ge detector was used to collect the PL signal from the spectrometer. The samples were held in place by a small clamp on a copper holder at the end of the fiber-optic cable. A minimum of pressure was applied to the sample to keep it in place during immersion in liquid nitrogen and liquid helium, which were used for 77K and 4K measurements, respectively.

SIMS analysis was performed on a Perkin Elmer PHI 3500 Secondary Ion Mass Spectrometer attached to a PHI 600 Scanning Auger Microprobe. An oxygen beam from a duoplasmatron ion source was used for sample depth profiling. The use of an oxygen beam prevents us from examining the oxygen content of the epilayers and the melts. An argon beam was used to sputter the Yb source, but it was not used on any samples or melts. The sputtered areas were approximately 2 mm x 2 mm, with the detector gated at 50% so that only secondary ions sputtered from the bottoms of the sputtering craters were analyzed. The signal intensities for some elements were converted to atomic concentrations with sensitivity factors developed by Leta [10]. The atomic concentration of As was assumed to be 50% in each epilayer. A sample of InP

implanted with a known dose of Yb was used as a reference to determine the atomic concentration of Yb in the grown epilayers.

Hall effect measurements were made using the van der Pauw technique. The ohmic contacts on the corners of the sample were indium, annealed by rapid thermal processing. A rotatable 3380 G permanent magnet and a Keithley Model 7065 Hall Effect Card were used for the Hall measurements.

RESULTS AND DISCUSSION

The alloy concentrations and strain were determined by double-crystal x-ray diffractometry (DCXRD). The composition thus determined was used to find the resulting bandgap using the relation developed by Goetz *et al.* [11]:

$$E_g(x) \big|_{2K} = 0.4105 + 0.6337x + 0.475x^2 \quad (1)$$

Excellent lattice matching was consistently achieved in samples grown at the temperature for which the melt ingredients were chosen. We measured $\Delta a/a$ as low as 39ppm, and were consistently able to achieve $\Delta a/a$ of less than 10^{-4} . The DCXRD spectrum of a sample grown at 631°C with approximately 5×10^{-5} mole fraction of Yb added to the melt is shown in Figure 3. Note that the addition of Yb to the melt also had no effect on optimum growth temperature. There have been reports of rare-earth addition deleteriously affecting crystal quality [5]. This effect was attributed to incorporation of the larger rare-earth atoms into the III-V lattice. We have seen no such effect, indicating either that the Yb is not distorting the InGaAs crystal structure or that the Yb is not being incorporated into the InGaAs at all.

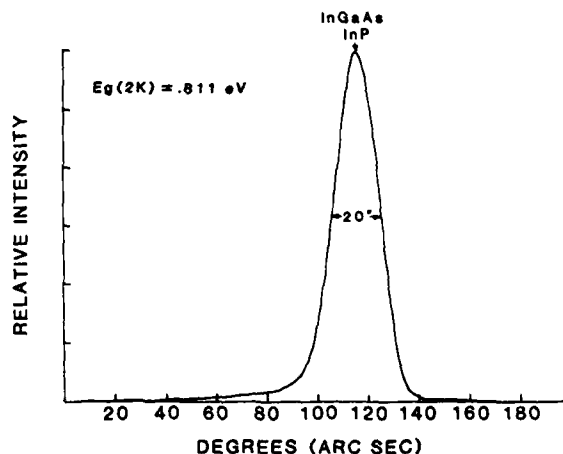


Figure 3. Double-crystal x-ray spectrum of sample with Yb added to the melt.

A representative 4K PL spectrum taken at several optical input powers from a sample grown with no Yb added to the melt is shown in Figure 4(a). The power designated by 1X corresponds to a laser output power of 7 mW/cm². There

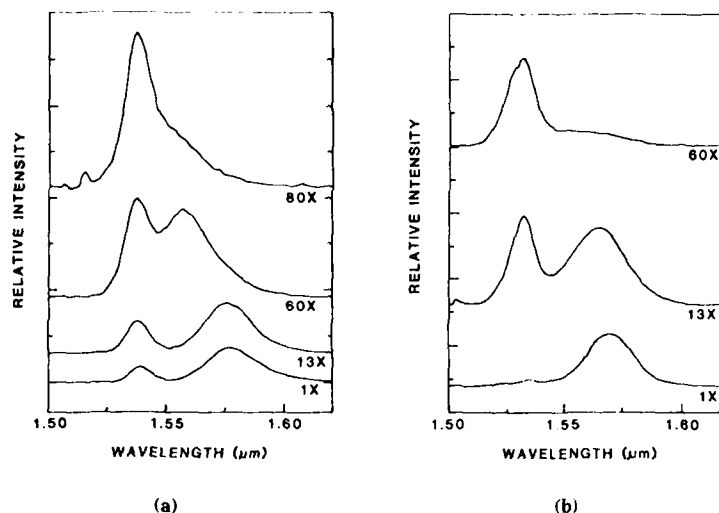


Figure 4. PL spectrum of sample grown (a) before the addition of Yb to the melt, and (b) after the addition of Yb to the melt.

is a peak 2 meV (38\AA) below the bandgap, and a second peak at an energy 18 meV (347\AA) below that of the first peak. Note that as the laser power is increased, the peak near the bandedge increases superlinearly with increasing pump power. At high pump powers it dominates the peak at the lower energy. This lower energy peak increases linearly with pump power. It also shifts to higher energies with increasing laser power, indicating that it is a donor-to-acceptor peak. The superlinear behavior of the bandedge peak indicates it is due to either a bound or free exciton. The fact that the donor-to-acceptor peak is located approximately 18 meV from the exciton peak leads us to believe that the acceptor is carbon. A graphite-boat system like the one we employ is constantly shedding carbon into the melt and some incorporation would not be surprising.

The PL spectrum of a sample grown after Yb was added to the melt was taken at several optical input powers and is shown in Figure 4(b). No luminescence peaks were visible outside the range of wavelengths shown in Figure 4(b). The laser power corresponding to 1X is identical to the power corresponding to 1X in Figure 4(a). A large 4f-4f emission peak at $1.0\text{ }\mu\text{m}$ is normally seen after Yb has been added to LPE melts of other III-V compounds [6,12]. We do not expect to observe strong Yb luminescence in InGaAs, since $1.0\text{ }\mu\text{m}$ light would be strongly absorbed by the crystal. Therefore the absence of any Yb emission lines in the PL spectra is not proof of a lack of Yb in the epilayers. If Yb is being incorporated into the epilayers, we would expect the distribution to be such that enough Yb is present within an absorption length of the surface to be able to see at least some emission at $1.0\text{ }\mu\text{m}$. Although we have observed the Yb 4f intracenter transition from Yb-implanted InP, there was no evidence of Yb luminescence in any of our InGaAs films. Secondary-ion mass spectroscopy (SIMS) analysis did not detect the presence of Yb in any epilayers grown with a

mole fraction of less than 5×10^{-4} Yb added to the melt. It has been reported that LPE GaAs grown after erbium is added to the melt luminesces at the characteristic wavelength of Er only after high-temperature annealing [13]. We observed no Yb luminescence even after rapid thermal annealing of our samples.

For identical laser power densities, we see that the sample in Figure 4(b), grown from the Yb-doped melt, requires less optical pumping for the acceptor peak to become saturated, perhaps indicating that the Yb is scavenging this particular acceptor impurity, in addition to donor impurities. Note that the presence of deep level traps added by the incorporation of Yb impurities will not be detected by PL.

Figure 5 is a plot of the free carrier concentration ($N_D - N_A$) at 300K of the samples from a representative melt. The x-axis represents the samples in the sequence in which they were grown. Each arrow represents the addition of more Yb to the melt. Note the immediate decrease in $N_D - N_A$ after the addition of a mole fraction of 3×10^{-5} Yb following the growth of Sample 6. Another decrease is seen after the Yb additions following the growths of Samples 9 and 11. It is likely that the Yb added after Samples 10 and 12 needed longer bakeouts to dissolve, thus accounting for the delay in the reduction of the free carrier concentrations.

In other melts, with lower initial $N_D - N_A$, we have seen a tendency for the free carrier concentrations to increase with each successive growth. This phenomenon has been attributed to chemical reduction of the silica tube by hydrogen [14]. We probably don't see this effect in the data in Figure 5 because the initial residual impurity concentration is so high. The addition of Yb to those cleaner melts not only immediately decreases $N_D - N_A$ by an order of magnitude; it greatly reduces the rate of increase with successive growths.

As expected, the 300K Hall mobility of the samples shown in Figure 5 (not plotted) increased slightly, from approximately $7000 \text{ cm}^2/\text{Vsec}$ to approximately $9000 \text{ cm}^2/\text{Vsec}$, after the addition of Yb caused a decrease in $N_D - N_A$. This is consistent with the increase in 300K mobility predicted by theory for a comparable decrease in free carrier concentration [15].

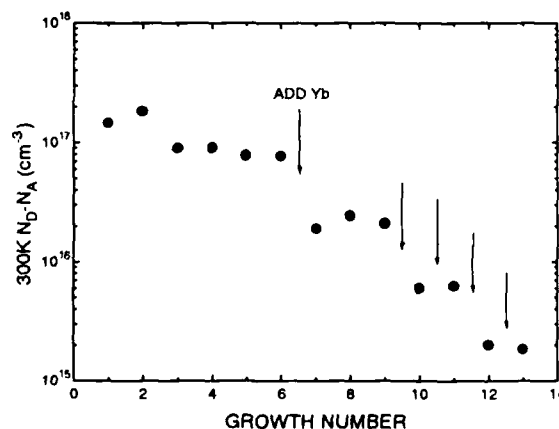


Figure 5. 300K free carrier concentration vs. sequential sample number.

Figure 6 is a plot of the 77K Hall mobility *vs.* the free carrier concentration of the same samples. The theoretical line is a linear approximation of the curve calculated by Takeda for a compensation ratio of 1 (*i.e.*, $N_A=0$), which is nearly linear in this region. The circles represent samples grown before the addition of Yb to the melt, the triangles represent samples grown after the Yb addition. Clearly, the increase in μ_{77} is significantly less than that predicted by theory. At 77K the dominant mechanism limiting mobility is ionized-impurity scattering, which would initially seem to indicate that the addition of Yb to the melt has added shallow impurities to the layers that are suppressing the mobility at 77K.

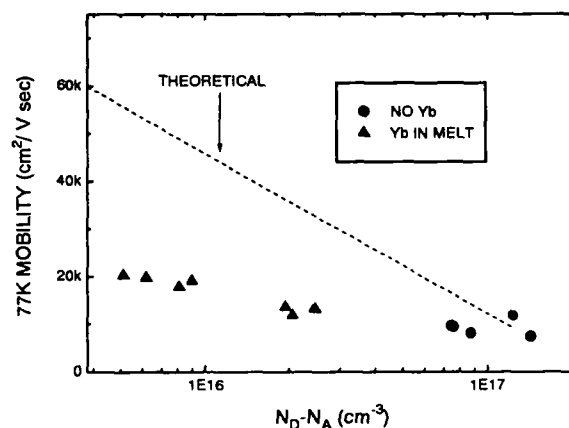


Figure 6. 77K mobility *vs.* free carrier concentration.

Figures 7 and 8 are plots of μ *vs.* the free carrier concentration at 300K and 77K, respectively. The solid lines represent Takeda's theoretical values at selected compensation ratios. The dashed lines in Figure 8 represent an extrapolation of Takeda's data, taking into account the change in curvature that begins to appear in this region. It is clear from Figure 7 that the compensation ratio at 300K increases dramatically after Yb addition to the melt, as indicated by the open circles. In Figure 8 it is clear that there is only a small increase in 77K compensation ratio. We conclude that the addition of Yb to the melt also adds deep level impurities that are being incorporated in the epilayers. These deep level impurities are at least partially ionized at 300K, thereby increasing the compensation ratio. At 77K, the deep levels are frozen out, so they do not affect the compensation ratio.

Previous work on rare-earth doping of InP and InGaAs resulted in *n*-type material, even when large mole fractions of rare earths were used [4]. Körber *et al.* have shown that the addition of increasing amounts of Yb to their InP melts results in *p*-type epilayers at a mole fraction greater than 2.5×10^{-5} [6]. It has been suggested that the type conversion effect seen with rare-earth dopants has more to do with shallow acceptor impurities in the rare-earth than with the rare-earth element itself [12]. We believe compensation may also play a role in this type conversion.

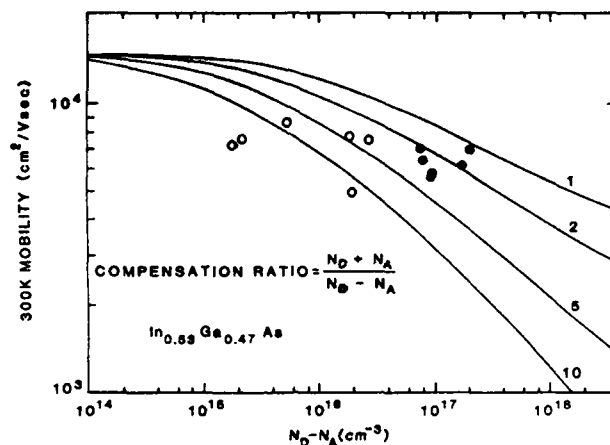


Figure 7. Compensation ratio at 300K.

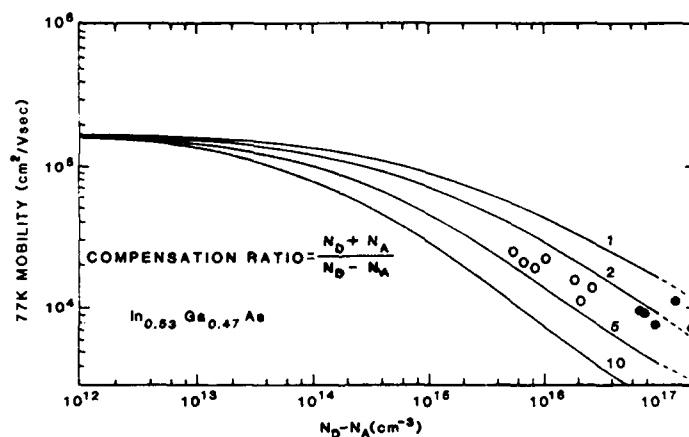


Figure 8. Compensation ratio at 77K.

In order to determine exactly what Yb addition to the melt is doing to the epilayers grown from the melt, we calculated the donor and acceptor concentrations of the samples from this melt. Figure 9 is a plot of the donor concentration at both 300K and 77K vs. sequential sample number. The donor and acceptor concentrations were calculated after determining the compensation ratio of each sample from the theoretical values in Figure 7. Note that N_D decreases noticeably after each of the first two Yb additions. There is no consistent difference between the 300K and 77K values. The corresponding values of N_A are plotted in Figure 10. Before any addition of Yb to the melt, there appears to be a gradual decrease in N_A , without any clear trend between the 300K and 77K

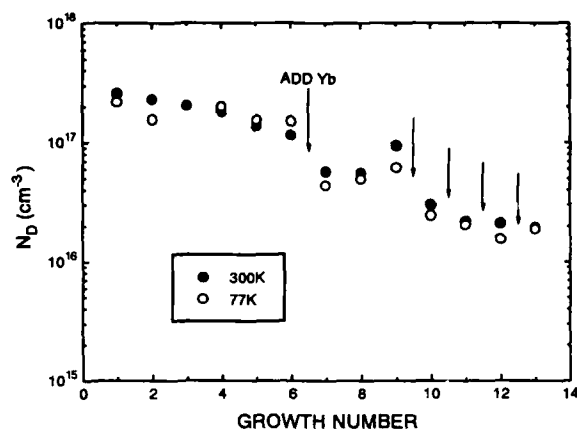


Figure 9. Donor concentration vs. sequential growth number.

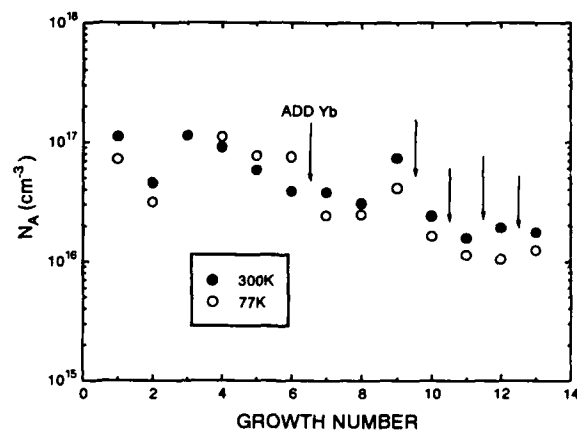


Figure 10. Acceptor concentration vs. sequential growth number.

values. After the first Yb addition, the acceptor density at 77K is slightly, but consistently, lower than the 300K density. This indicates that along with the Yb we have also introduced a deep-level acceptor that is ionized at 300K, but is freezing out at 77K. We do not believe that we are merely seeing deep levels that were already present in the layers grown from melts with no Yb added, because we see a similar effect even in melts where N_A is 10^{15} . It does appear, however, that the Yb is getting the acceptor that was initially found in the melt; a finding that is consistent with our PL measurements. Since Yb is known to form compounds with carbon, this is further evidence that we have carbon contamination in our system initially [4].

Figure 11 is a plot of the compensation ratios of the samples at both 300K and 77K *vs.* sequential sample number. The formula for the compensation ratio is indicated on the plot. Note that the increase in the compensation ratio at 77K is gradual, while there is a dramatic increase in 300K compensation ratio upon the addition of Yb to the melt. This plot makes it clearer that we are adding some type of deep level, active at 300K but inactive at 77K, along with the Yb.

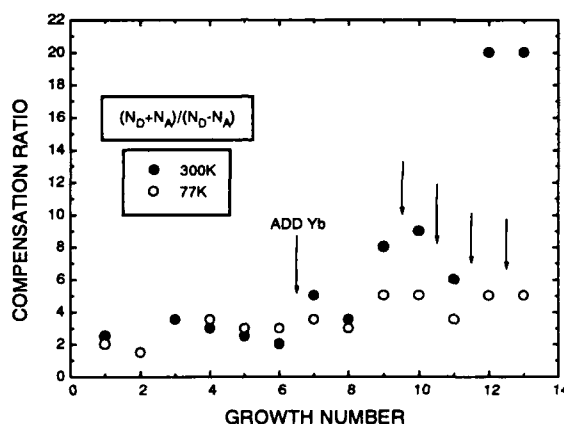


Figure 11. Compensation ratio *vs.* sequential sample number.

SIMS analysis of the Yb source detected many impurities, including Fe, Cr, Si, and Mg. A complete list of impurities found in the Yb at a level above the detection limit of the SIMS system is shown in Table I.

Table I. Impurities present in Yb dopant.

Li	Mg	Cr	C	F
Na	Ca	Mo	Si	Cl
K	Y	Sm	O	Br
	Al	Fe		

Fe concentrations in samples grown after Yb addition to the melt were higher than for those samples grown with no rare-earth addition. Fe incorporation leads to the possibility of donor compensation from deep level traps as a mechanism for the reduction in free carrier concentration after the addition of Yb to the melt. The residual impurity concentration in our undoped InGaAs is usually about 10^{16} *n*-type. Because silicon is present throughout our growth system, and because it is detected in our epilayers by SIMS, we believe it to be the dominant *n*-type impurity. While Si can act as either a donor or acceptor, it is widely known to act primarily as a donor in InGaAs.

A typical SIMS scan of a sample prepared with 5×10^{-5} Yb added to the melt is shown in Figure 12. Note that the relative intensities have not yet been corrected for elemental and instrumental sensitivities. It is known that Fe and Cr will congregate at a growth front and the abrupt end to growth caused by the

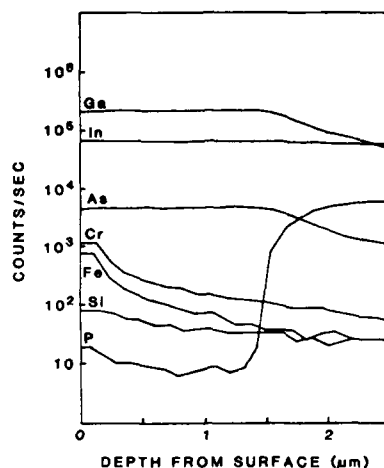


Figure 12. SIMS plot of atomic concentrations in an InGaAs layer on InP with 5×10^{-6} Yb mole fraction added to the melt.

removal of the melt at the end of a run would explain the upward trend in the concentration of these elements toward the surface. Also, the presence of surface oxides will enhance the detected signal of those oxidized elements at the surface. SIMS analysis of a melt found most of the Yb present at the top of the melt, with a small amount at the bottom and none at the center. For samples grown from a melt with a mole fraction of more than 5×10^{-4} Yb, the atomic concentration of Yb found in the epilayer was at or near the SIMS detection limit. The levels of Yb, if any, in samples grown with a mole fraction of Yb in the melt of less than 5×10^{-4} were always below the SIMS detection limit of approximately 10^{16} .

CONCLUSIONS

We have grown LPE InGaAs on InP and tested samples grown both with and without Yb added to the melt. The addition of Yb to the growth melts was not a factor in the ultimate crystal quality, as determined by DCXRD, with very good lattice matching possible both before and after Yb addition. Qualitatively, PL shows stronger luminescence for samples grown from Yb-doped melts. PL analysis shows no optical evidence of Yb incorporation in any samples. SIMS analysis indicates Yb incorporation for only those films grown from melts with Yb mole fractions larger than 5×10^{-4} added. Fe incorporation into the grown epilayers is also detected by SIMS, but we are not yet able to quantitatively analyze the levels of this impurity. Hall/van der Pauw analysis indicates that samples grown from melts to which Yb has been added have sharply reduced donor concentrations and slightly reduced acceptor concentrations. The lightly Yb-doped melts consistently yield *n*-type samples with reduced free carrier concentrations; a large enough Yb addition inconsistently yields *p*-type samples. Addition of Yb to the melt consistently increases the compensation ratio by several times.

We believe the ytterbium is acting as a scavenging agent in the melt, tying up n -type impurities, most likely Si, and p -type impurities, probably carbon. We also believe that impurities introduced with the Yb are an important factor contributing to the reduction in background carrier concentration and the type conversion others have seen. We believe the impurities are predominantly deep-level traps that compensate donors until, if enough Yb is added, acceptors prevail. It is likely that the smaller-than-expected increase in 77K mobilities following Yb treatment is a direct result of the increase in compensation ratio brought about by the inclusion of these traps in our epilayers.

ACKNOWLEDGMENTS

We thank K. Vaccaro of Rome Laboratory and T.E. Crumbaker of Tufts University for helpful discussions on numerous topics and W. Waters of Rome Laboratory for technical assistance.

REFERENCES

- [1] L.F. Zakharenkov, V.A. Kasatkin, F.P. Kesamanly, B. E. Samorukov, and M.A. Sokolova, *Sov. Phys. Semicond.* **15**, 946 (1981).
- [2] K. Uwai, H. Nakagome, and K. Takahei, *Appl. Phys. Lett.* **50**, 977 (1987).
- [3] R.S. Smith, H.D. Müller, H. Ennen, P. Wennekers, and M. Maier, *Appl. Phys. Lett.* **50**, 49 (1987).
- [4] N.T. Bagraev, L.S. Vlasenko, K.A. Gatsoev, A.T. Gorelenok, A.V. Kamanin, V.V. Mamutin, B.V. Pushnyi, V.K. Tibilov, Y.P. Tolparov, and A.E. Shubin, *Sov. Phys. Semicond.* **18**, 49 (1984).
- [5] S.I. Larikov, A.I. Petrov, O.V. Rychkova, and A.É. Yunovich, *Sov. Tech. Phys. Lett.* **12**, 135 (1986).
- [6] W. Körber, J. Weber, A. Hangleiter, K.W. Benz, H. Ennen, and H.D. Müller, *J. Crystal Growth* **79**, 741 (1986).
- [7] A.T. Gorelenok, V.G. Gruzlov, R. Kumar, V.V. Mamutin, T.A. Polyanskaya, I.G. Savel'ev, and Y. V. Schmartsev, *Sov. Phys. Semicond.* **22**, 21 (1988).
- [8] L.F. Zakharenkov, V.F. Masterov, and O.D. Khokhryakova, *Sov. Phys. Semicond.* **21**, 211 (1987).
- [9] J.J. Hseih, *IEEE J. Quantum Electr.* **QE-17**, 118 (1981).
- [10] D.P. Leta and G.H. Morrison, *Anal. Chem.* **52**, 514 (1980).
- [11] K.H. Goetz, D. Bimberg, H. Jürgensen, J. Selders, A.V. Solomonov, G.F. Glinskii, and M. Razeghi, *J. Appl. Phys.* **54**, 4543 (1983).
- [12] W.H. Haydl, H.D. Müller, H. Ennen, W. Körber, and K.W. Benz, *Appl. Phys. Lett.* **46**, 870 (1985).
- [13] F. Bantien, E. Bauser, and J. Weber, *J. Appl. Phys.* **61**, 2803 (1987).
- [14] S. Kondo, T. Amano, and H. Nagai, *Jpn. J. Appl. Phys.* **26**, 1997 (1987).
- [15] Y. Takeda in *GaInAsP Alloy Semiconductors*, edited by T.P. Pearsall, John Wiley & Sons, New York (1982).

ELECTRICAL AND OPTICAL PROPERTIES OF Yb, Er doped GaAs

T. BENYATTOU*, D. SEGHER*, G. BRÉMOND*, S. MONEGER*, A. KALBOUSSI*, G. MARRAKCHI* AND G. GUILLOT*, C. LHOMER***, B. LAMBERT**, Y. TOUDIC** AND A. LE CORRE**

*INSA de Lyon, Bât 502, LPM URA CNRS 358, 20 Av Albert Einstein 69621 Villeurbanne Cédex France

**CNET/LAB/OMC/MPA, 22301 Lannion, France

ABSTRACT

In this paper we report results from electrical and optical measurements carried out on GaAs:Yb, Er.

For GaAs:Yb electrical experiments such as photoconductivity (PC) and Photo Induced Current Transient Spectroscopy (PICTS) show that there is a level at 0.65eV related to Yb. This explains why no Yb³⁺ photoluminescence (PL) emission is detected, the recombination energy of the trapped excitons is too low ($\approx 0.6\text{eV}$) to excite the Yb³⁺ internal transition ($\approx 1.24\text{eV}$). We also present results on Er doped GaAs materials. From PL experiments we deduce an estimate of 10^{-19}cm^2 for the stimulated emission cross section. By PICTS and PC, we have evidenced a trap at 0.67eV related to Er ions in GaAs. And we think that in this case, the rare earth ions are excited via formation of bound excitons.

INTRODUCTION

Rare earth (RE) doped III-V materials are very attractive for new emitting device applications such as lasers and LEDs [1-6]. In this case, the emission is no more based on band to band recombination but on the internal emission of the doping ions. Among them, Er³⁺ is very promising because of its 1.54 μm emission which is well adapted to silica based optical fiber telecommunication. However, electrical properties of these systems are not fully understood as well as their relations to the optical activity of the RE impurity. In order to improve our understanding of the RE excitation mechanism, we have carried out photoluminescence (PL), photo-induced current spectroscopy (PICTS), and photoconductivity (PC) measurements on Er, Yb doped GaAs materials.

EXPERIMENTAL

Yb-doped GaAs epitaxial layers have been successfully obtained by the gas MBE technique at Centre National d'Etude des Télécommunications. A gaseous source (AsH_3) was used to obtain the V element and a solid source to obtain the RE element (Yb). A 1.2 μm thick layer was grown on a semi-insulating GaAs substrate with a growth rate of about $1\text{ }\mu\text{m h}^{-1}$. Yb concentration measured by Secondary Ion Mass Spectroscopy (SIMS) in the layer was found to be $2 \times 10^{17}\text{ cm}^{-3}$. SIMS analysis also indicated the poor quality of the Yb source (4N) since metallic impurities such as Si, Ca, and Mg were detected in the sample with concentrations below 10^{16} cm^{-3} . At room temperature the sample is semi-insulating. Details concerning the growth technique are reported elsewhere [7].

Er-doped GaAs samples have been grown in the Laboratoire Central de Recherche de THOMSON-CSF, by MBE. All details concerning the growth technique are reported in the reference [8].

The PL measurements were carried out using a 5145 Å line of argon ion laser with a power of 200 mW focused on a 150 μm diameter spot. The PL signal was detected with a 0.64 m HRS2 JOBIN YVON monochromator and a Ge photodetector cooled down to 77 K.

For PC experiments which consist in measuring the variation of conductivity versus the excitation wavelength, a continuously tunable source of excitation, which consist of a quartz Wolfram halogen lamp of 150 W has been used. The light is dispersed by a 0.64 m monochromator and focused in a 1 mm by 0.6 mm spot size, with excitation density up to 3 mW/cm^2 . To detect the photocurrent, we have used a current voltage converter with a gain ranging from 10^3 to 10^{11} V/A .

In PICTS experiments, a voltage was applied between two coplanar AuGe/Ni ohmic contacts situated on the sample surface. Electron-hole pairs were generated by a light pulse. After removal of the optical pulse at $t=0$, a rapid decrease in the current due to the recombination of free photocarriers is observed followed by a slower current transient owing to the thermally stimulated release of carriers from the traps. The current transient is sampled at two points with time delays of t_1 and t_2 and the difference $i(t_1) - i(t_2)$ is plotted as a function of temperature. It can be shown that the current transient is given by:

$$i(t) = KN_T e_n \exp(-e_n t) \quad (1)$$

K is a constant depending on the applied electric field, and the illuminated surface located between the two ohmic contacts. N_T and e_n represent the trap concentration and the thermal emission rate respectively.

Both electron and hole traps produce current transients which result in positive PICTS peaks making difficulties in determining the nature of traps. Details concerning this characterisation technique are reported by C. Hurtes et al [9].

The optical excitation was given by a light emitting diode at 1.3 eV whose optical pulse delay and excitation frequency are 140 ms and 0.8 Hz respectively. A bias of 8 V has been applied to the sample.

RESULTS

PL spectrum recorded at 6K from Yb doped GaAs shows no feature near $1 \mu\text{m}$ related to the $2F_{7/2} \rightarrow 2F_{5/2}$ Yb $^{3+}$ internal transition whereas for GaAs : Er an emission near $1.54 \mu\text{m}$ is clearly seen (fig.1).

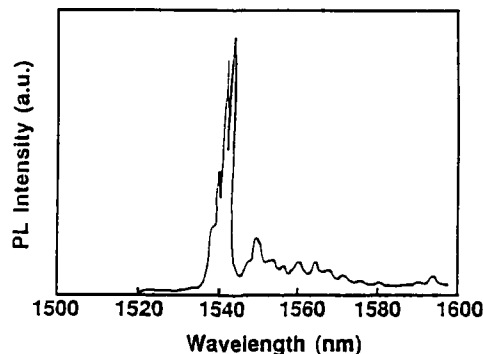


Figure 1. PL spectrum of the transition $4I_{13/2} \rightarrow 4I_{15/2}$ of Er^{3+} ion in GaAs recorded at 6 K.

This emission is typical of the $4I_{13/2} \rightarrow 4I_{15/2}$ internal Er^{3+} transition. The emission lifetime is around 1 msec.

Concerning the electrical activity we have noticed that for both GaAs : Yb and GaAs : Er doped material are semi-insulating. However SIMS measurements have shown that several donors such as Si and S are present in the epitaxial layers with a concentration of the order of 10^{16} cm^{-3} . To check if the RE ions are responsible for the semi-insulating character of these layers we have performed PICTS experiments.

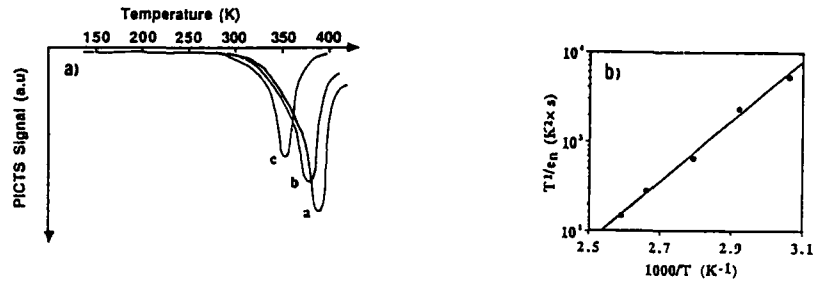


Figure 2. a) PICTS spectra at different rate windows of the Yb doped GaAs:

$\tau_n = 1000 \text{ s}^{-1}$ (a), 500 s^{-1} (b), 200 s^{-1} (c)

b) Arrhenius plot for the observed electron trap related to Yb in GaAs.

In figure 2a) the PICTS spectra recorded at high temperature are reported. An intense and clearly resolved peak appears near 380K. From the Arrhenius plot shown in figure 2b), we have deduced the following values for the activation energy E_t and capture cross section $\sigma_{\tau_{\text{trap}}}$:

$$E_t = 0.65 \pm 0.02 \text{ eV}$$

$$\sigma_{\tau_{\text{trap}}} = 5 \times 10^{-15} \text{ cm}^2$$

These results are in good agreement with those reported by Taguchi et al. [10] on n type Yb doped GaAs. Using DLTS experiments, the authors observed a peak at high temperature and estimated its activation energy between 0.5 and 0.6 eV. If we assume that Yb doping is responsible for the semi-insulating character of an n-type layer, we deduce that the 0.65 eV level is an electron trap.

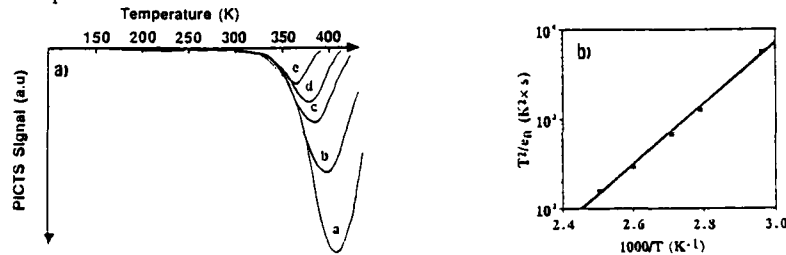


Figure 3. a) PICTS spectra at different rate windows of the Er doped GaAs :

$\tau_n = 1000 \text{ s}^{-1}$ (a), 500 s^{-1} (b), 200 s^{-1} (c), 100 s^{-1} (d), 20 s^{-1} (e)

b) Arrhenius plot for the observed electron trap related to Er in GaAs.

The PICTS spectra of GaAs : Er present also an intense peak around 400K (cf. fig 3a). From the Arrhenius plot we deduce the following values for the activation energy E_t and the capture cross section σ_{trap} :

$$E_t = 0.67 \pm 0.02 \text{ eV}$$

$$\sigma_{trap} = 1 \times 10^{-14} \text{ cm}^2$$

Because of the similitude with GaAs : Yb we suppose that this level is directly related to Erbium ions and is an electron trap.

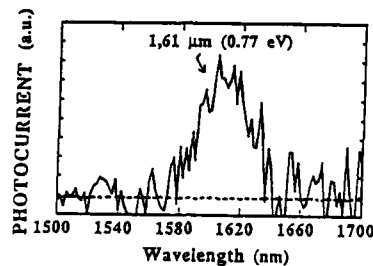


Figure 4. PC spectrum for Yb doped GaAs at 300 K. The horizontal line corresponds to undoped material.

To confirm these results we have performed photoconductivity measurements (PC) at 300K. In figure 4, we can see the PC spectrum of an undoped and Yb doped GaAs. Whereas no peak is seen below the GaAs gap (1.42 eV) for the undoped sample, the Yb doped one exhibits a peak at 0.77 eV. This energy corresponds exactly to the difference between the GaAs band gap (1.42 eV) and the activation energy of the electron trap (0.65 eV). Thus, we conclude that the PC signal originates from this electron trap.

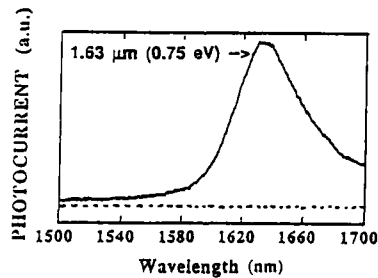


Figure 5. PC spectrum for Er doped GaAs at 300 K. The horizontal line corresponds to undoped material.

A similar behavior is found for GaAs : Er. An intense peak at 0.76 eV detected in PC experiment at 300K (cf. fig 5). In this case also the PC transition corresponds to the difference between GaAs band gap and the electron trap activation energy (0.67 eV). Therefore we attribute the PC signal to the center detected in PICTS experiments.

DISCUSSION

We have shown in previous paper [6, 10] that Yb ions behave as an isoelectronic trap in InP. Using admittance, spectroscopy we have evidenced an electron trap 30 meV below the conduction band and a hole trap 50 meV above the valence band. Because of the larger ionic radius and electronegativity difference with the substituting ion a potential that can trap both types of carriers is created. However, the Yb ion remains in the 3+ state. In this state the excitation occurs via the formation of bound excitons on these traps and energy transfer to the Yb ions [11, 12]. The transfer process is very effective because the bound exciton energy is close to the internal Yb³⁺ transition one. Within this framework we try to analyse the results obtained on GaAs : Er, Yb.

For the Yb doped GaAs, most of the papers reports an absence of Yb luminescence [2,12]. However, Ennen et al [14] have observed it in ion implanted materials. This luminescence is very weak and is may be related to an Yb complex. Our results also, show the absence of such luminescence. This could be easily explained if we assume the same excitation mechanism as the one proposed for InP : Yb³⁺. PICTS experiments on GaAs : Yb have shown that Yb create an electron trap 0.65 eV below the conduction band and these results have been confirmed by PC experiments. It is reasonable to assume that Yb behave like an isoelectronic trap. The bound exciton energy are expected to be too low (≈ 0.77 eV) to transfer their energy to Yb³⁺ ions (≈ 1.2 eV).

In contrast, the Erbium luminescence is detected in GaAs. An electron trap at 0.67 eV below the conduction band is detected. Here also we assume that the Erbium ion create an isovalent trap. In this case, the bound exciton energy (≈ 0.75 eV) is close enough to the Erbium internal transition (0.8 eV) to allow the energy transfer. These results confirm our PL excitation model. The PL lifetime of 1 ms indicates that the ion recombination is quite insensitive to the crystal host. From this value an estimate of 10^{-19} cm² for the stimulated emission cross section has been deduced [15]. This means a gain of 10^{-1} cm⁻¹ for the highest doping level (10^{18} cm⁻³) achieved without any layer degradation. Therefore it is not realistic to expect laser operation for such system.

CONCLUSION

Optical and electrical measurements have been carried out on GaAs : Yb, Er. The rare earth internal PL transition has been detected only for GaAs : Er. PICTS measurements have shown that Yb and Er ions introduce an electron trap at 0.65 eV and 0.67 eV from the conduction band, respectively. With PC experiments the corresponding transitions from the valence band have been observed. All these results confirm the PL model where the excitation occurs via the formation of bound excitons at the rare earth centers. For Yb, the bound exciton energy is too low to excite its internal transition. This explains the absence of Yb photoluminescence in GaAs. Whereas for Er ions, the bound exciton energy is close enough to the Er internal transition to allow the PL excitation. The long lifetime and the low value of the stimulated emission cross section lead us to think that these systems are not well suited for laser application.

REFERENCES

1. T. Benyamou, D. Seghier, G. Guillot, R. Moncorgé, P. Galtier, and M. N. Charasse, *Appl. Phys. Lett.* **58**, 2132(1991).
2. A. Kozanecki, and R. Groezschel, *J. Appl. Phys.* **64**, 3315(1988).

3. P.B. Klein, Solid State Commun. 65, 1097(1988).
4. T. Benyattou, D. Seghier, G. Guillot, P. Galtier, M.N. Charasse, and R. Moncorgé, in Impurities, Defects, and Diffusion in Semiconductors: Bulk and Layered Structures, edited by D. J. Woford, J. Bernhole, and E. E. Haller (MRS, Pittsburgh, PA, 1990), Vol. 163, pp.69-74.
5. K. Thonke, K. Pressel, G. Bohnert, A. Stapor, J. Weber, M. Moser, A. Malassioti, A. Hangleiter, and F. Scholtz, Semicond. Sci. Technol. 5, 1124(1990).
6. D. Seghier, T. Benyattou, G. Bremond, F. Ducroquet, J. J. Marchand, and G. Guillot published in the proceedings of the 16th International Conference on Defects in Semiconductors, Bethlehem (USA), 1991.
7. B. Lambert, Y. Toudic, G. Grandpierre, A. Rupert, and A. Le Corre, Electron. Lett. 24, 1447(1988).
8. P. Galtier, J.P. Pocholle, M.N. Charasse, T. Benyattou, G. Guillot, B. de Cremoux, and J.P. Hirtz, Appl. Phys. Conden. Matter 2, 479(1990).
9. C. Hurtes, M. Boulou, A. Mitonnesu, and D. Bois, Appl. Phys. Lett. 32, 821(1978).
10. A. Taguchi, H. Nakagome, and K. Takahei, J. Appl. Phys. 68, 3390(1990).
11. D. Seghier, T. Benyattou, G. Bremond, F. Ducroquet, J. Gregoire, G. Guillot, C. Lhomer, B. Lambert, Y. Toudic, A. Le Corre, Appl. Phys. Lett. 60, 983(1992).
12. P.S. Whitney, K. Uwai, H. Nakagome and K. Takahei, App. Phys. Lett. 53, 2074(1988).
13. J. Raczhska, K. Frone, J.M. Langer, A. Lemanska and A. Stapor, Appl. Phys. Lett. 53, 761(1988).
14. H. Eenen, U. Kaufmann, G. Pomrenke, J. Windscheif, and A. Axmann, J. Cryst. Growth 64, 165(1983).
15. T. Benyattou, D. Seghier, G. Guillot, R. Moncorgé, P. Galtier, and M. N. Charasse, Appl. Phys. Lett. 60, 350(1992).

LUMINESCENCE STUDY OF THE INTRA-4f EMISSIONS FROM GaAs:(Er+O) AND Al_xGa_{1-x}As:(Er+O)

JOSE E. COLON*, DAVID W. ELSAESSER*, YUNG KEE YEO*, ROBERT L.
HENGEHOLD*, and GERNOT S. POMRENKE**

*Air Force Institute of Technology, Wright-Patterson Air Force Base, OH 45433

**Air Force Office of Scientific Research, Bolling Air Force Base, Washington, D.C. 20332

ABSTRACT

A systematic photoluminescence study of erbium and oxygen co-implantation into GaAs and Al_xGa_{1-x}As with $x = 0.1, 0.2, 0.3$, and 0.4 was carried out. The addition of oxygen greatly enhanced the Er emission intensity from Al_xGa_{1-x}As:Er while the O and Er co-doping into GaAs rather made the Er emission intensity decrease from that of the GaAs:Er. The Er emission intensity from Al_xGa_{1-x}As:(Er+O) generally increases with increasing Al mole fraction and O dose up to $1 \times 10^{15}/\text{cm}^2$, but it does not depend much on the substrate conductivity.

INTRODUCTION

Recently, the study of rare-earth doped III-V semiconductors has attracted considerable attention due to their possible use in optoelectronic device applications. In particular, erbium doped semiconductors exhibit various sharp emissions around $1.54 \mu\text{m}$ [1-4] due to transitions between the crystal field split states $^4I_{13/2}$ and $^4I_{15/2}$ of Er^{3+} . However, to date, the observed emissions have been very weak, thus making impractical the fabrication of light emitting devices based on these materials. One possible solution to this problem might be the addition of a second dopant to enhance the intra-4f emissions as is done, for example, in II-VI compounds [5]. In the case of Er-doped III-V semiconductors, some authors [6,7] have suggested that the Er^{3+} emissions might in fact originate from some type of Er-O complex. Also, for Er-doped Si it has been reported that the addition of O enhanced the Er^{3+} emissions [8,9]. In order to determine the effect of oxygen on the Er^{3+} emissions from III-V semiconductors, a systematic study of Er and O co-doping into GaAs and Al_xGa_{1-x}As with $x = 0.1, 0.2, 0.3$, and 0.4 was carried out as a function of Er and O doses, Al mole fraction, and substrate conductivity. The results are reported here.

EXPERIMENT

Er-ion implantation was done at room temperature at an ion energy of 1 MeV with a dose of either 10^{13} or $5 \times 10^{13}/\text{cm}^2$. Subsequently, oxygen was implanted with various doses at an ion energy of 110 keV, which yielded the same projected range as that of the Er distributions ($\sim 0.18 \mu\text{m}$). Substrates used were liquid encapsulated Czochralski grown semi-insulating (SI)

GaAs, metalorganic chemical vapor deposition (MOCVD) grown undoped AlGaAs, and Si or Zn doped MOCVD grown GaAs and $\text{Al}_{0.29}\text{Ga}_{0.71}\text{As}$ layers. Following implantation, the samples were annealed using the rapid thermal annealing (RTA) technique. Photoluminescence (PL) was excited with the 488 nm Ar-ion laser line, dispersed with a 3/4-m spectrometer using a 1.25 μm blazed grating, and detected with a liquid nitrogen cooled Ge detector.

RESULTS AND DISCUSSION

The Er emissions from undoped Si-GaAs, Si-doped GaAs, and Zn-doped GaAs samples co-implanted with Er and O were studied as a function of O dose. The effect of O co-doping on the Er^{3+} emissions is illustrated in figure 1, which shows the low temperature PL spectra obtained from GaAs:(Er+O) samples implanted with Er at a dose of $10^{13}/\text{cm}^2$ and implanted with O at different doses. Following ion implantation, the samples were annealed at 750 °C for 15 seconds. The arrows shown in the figure indicate the zero luminescence level

for each spectrum. The oxygen co-doped samples show essentially the same emission structure as the sample implanted with Er alone. In all cases, the main Er^{3+} emission occurs near 1.538 μm which can be attributed to the transition between the crystal field split states of $^4\text{I}_{13/2}$ and $^4\text{I}_{15/2}$. As shown in the figure, the PL intensity of the main Er^{3+} emission from the sample co-implanted with O at a dose of $5.3 \times 10^{12} \text{ cm}^{-2}$ is at least three times weaker than that from the control sample implanted with Er alone. A stronger emission can be observed from the sample implanted with an O dose of $1.7 \times 10^{13} \text{ cm}^{-2}$, but the sample implanted with the O dose of $3.4 \times 10^{13} \text{ cm}^{-2}$ shows much weaker emissions than the control sample. Although some differences were observed among the various GaAs:(Er+O) samples studied, the overall results indicate that oxygen co-implantation into GaAs:Er generally resulted in weaker Er^{3+} emissions than those from the sample implanted with Er alone.

We have also investigated the effect of oxygen co-doping on the Er^{3+} emissions for the Si-doped n-type GaAs and Zn-doped p-type samples as a function of O doses. All these samples

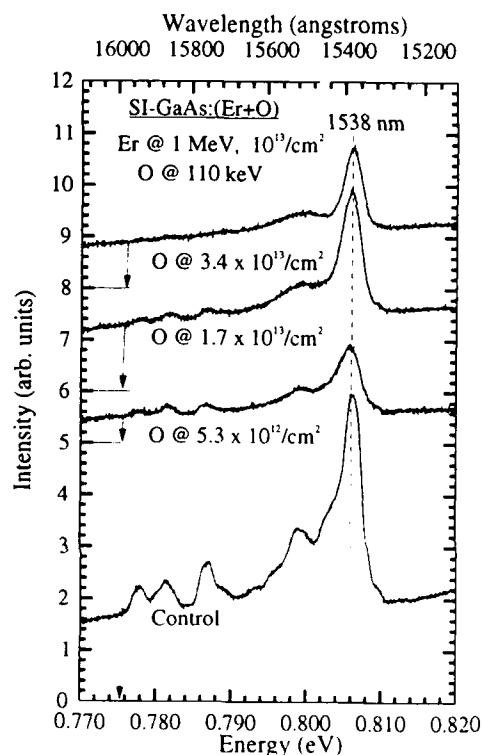


Figure 1 Photoluminescence of GaAs:(Er+O) samples annealed at 750 °C for 15 seconds for various O doses

showed a similar trend in emission structure and intensity variation as the Si-GaAs:(Er+O) samples. Therefore, the results discussed above for the SI samples are also representative of those obtained for all samples of different substrate conductivity type.

Some authors have proposed that the luminescence normally observed from GaAs:Er originates from some type of Er-O complex [6,7]. This seems to be the case in Si:Er [8,9]. However, although it is certainly possible that Er and O might form some type of complex in GaAs, such complexes do not seem to give rise to the intra-4f emissions as witnessed by the decrease in the emission intensity upon O co-doping.

The results obtained for the $\text{Al}_{0.1}\text{Ga}_{0.9}\text{As}:(\text{Er}+\text{O})$ samples were significantly different from those obtained for GaAs:(Er+O). Although all the Er^{3+} emission peak intensities were not affected in the same way, O co-doping dramatically increased the Er^{3+} emission intensity from that of the control sample doped with Er alone. The low temperature PL for $x = 0.1$, 0.2, 0.3, and 0.4 as well as $x = 0.29$ samples with n- and p-type conductivity was studied as a function of O dose. In all cases an increase in the Er^{3+} emission intensity was observed as the O dose was increased.

The enhancement of the emission intensity upon O and Er co-doping is illustrated in figure 2 for the undoped $\text{Al}_{0.1}\text{Ga}_{0.9}\text{As}$ substrate. In this case, the Er dose was $5 \times 10^{13}/\text{cm}^2$ while the O doses were 10^{13} , 10^{14} , and $10^{15}/\text{cm}^2$, respectively. In general, the emission spectrum of the control sample implanted with Er alone varied as both the aluminum mole fraction x and the annealing conditions were changed. In the case shown in figure 2, the PL spectrum of the $x = 0.1$ control sample implanted with Er alone is dominated by three emission peaks at 1536 (peak A), 1541 (Peak D), and 1552 nm. Note that, on O co-implantation at $10^{13}/\text{cm}^2$, the intensity of the peak D increased approximately threefold from that of the sample implanted with Er alone, while the intensity of the peak A increased only by a small factor. However, the strongest emission from the sample co-implanted with an O dose of $10^{14}/\text{cm}^2$ occurs at 1.538 μm (peak B), and it is approximately seven times more intense than the strongest emission from the sample implanted with Er alone. The sample implanted with an O dose of $10^{15}/\text{cm}^2$ showed a further increase in the emission intensity of the peak B, resulting in an

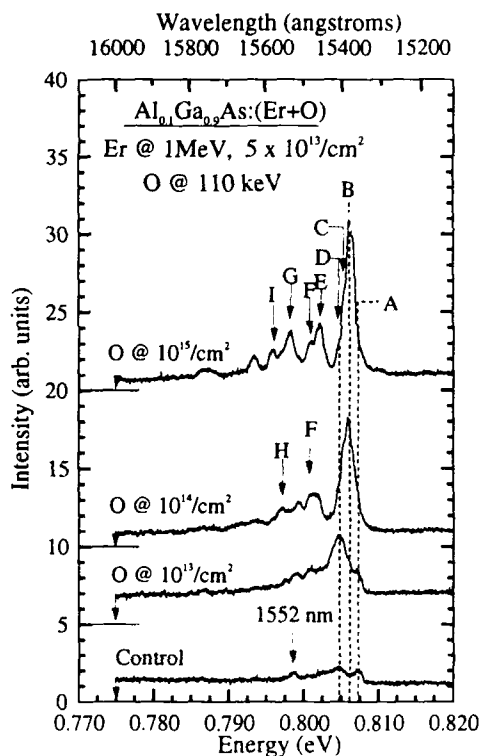
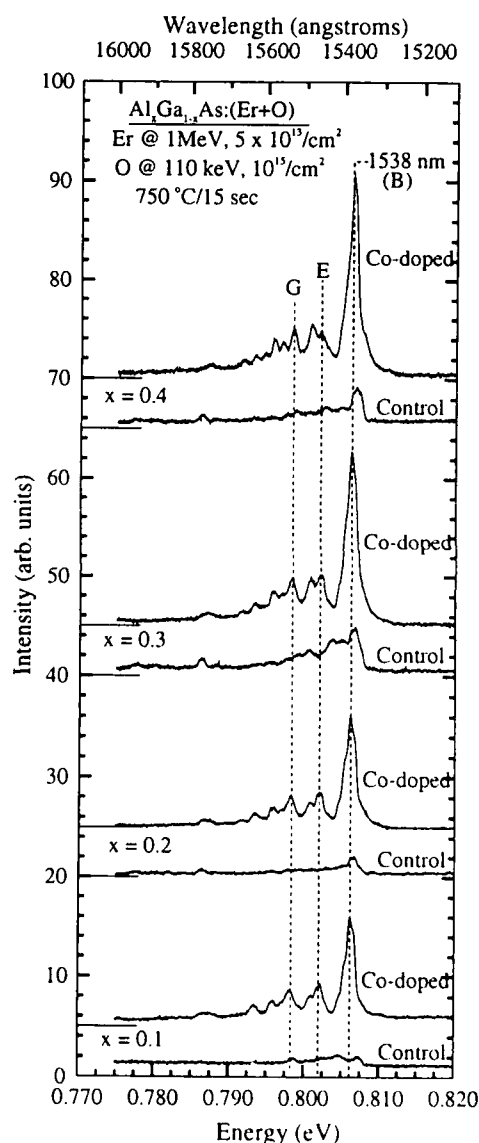


Figure 2 Photoluminescence spectra of $\text{Al}_{0.1}\text{Ga}_{0.9}\text{As}:(\text{Er}+\text{O})$ annealed at 750 °C for 15 sec for various O doses

It is interesting to note that although the PL spectra of the samples implanted with Er alone showed an emission intensity and peak structures which were dependent on both x and the annealing temperature, all the samples co-implanted with the highest O dose of $10^{15}/\text{cm}^2$ showed essentially the same emissions, independent of x , as illustrated by the spectra shown in figure 3. However, it should be noted that the emission intensity of the $1.538\text{ }\mu\text{m}$ peak for the oxygen co-doped sample increased with increasing x value, although the enhancement factor of the peak intensity for the given x value did not increase correspondingly. This is because the control samples implanted with Er alone also showed somewhat stronger emissions for higher x values.

Figure 3 Photoluminescence spectra of $\text{Al}_x\text{Ga}_{1-x}\text{As}:(\text{Er}+\text{O})$ and control samples as a function of x



enhancement of the PL intensity. It is possible that the optimum O dose will vary with x value and Er dose. All the results presented here are for the samples annealed at 750 °C for 15 seconds. It has also been found that the emission intensity of the 1.538 μm peak increased with increasing annealing temperature [10], showing the strongest emission intensity for an 850 °C anneal for an Er dose of $5 \times 10^{13}/\text{cm}^2$. Therefore a further enhancement of the Er^{3+} emissions can be obtained upon O co-doping than is reported here.

Finally, the effect of the PL intensity on the O and Er co-doping into $\text{Al}_x\text{Ga}_{1-x}\text{As}$ has also been investigated as a function of the conductivity type of the AlGaAs substrates. This would be important both from the point of view of fundamental physics as well as future applications. It has been found that essentially the same trend of spectral variation was observed as a function of O dose, with very little difference being observed as a function of substrate conductivity, although somewhat stronger emission was observed in the peak intensity of the p-type sample as can be seen from figure 4. By carefully examining the spectra shown in figure 4, it can be seen that there are some differences in emission structures for the control samples having different substrate conductivity. However, the oxygen co-doped samples implanted at the highest dose of $10^{15}/\text{cm}^2$ show essentially the same emission structures independent of the substrate conductivity.

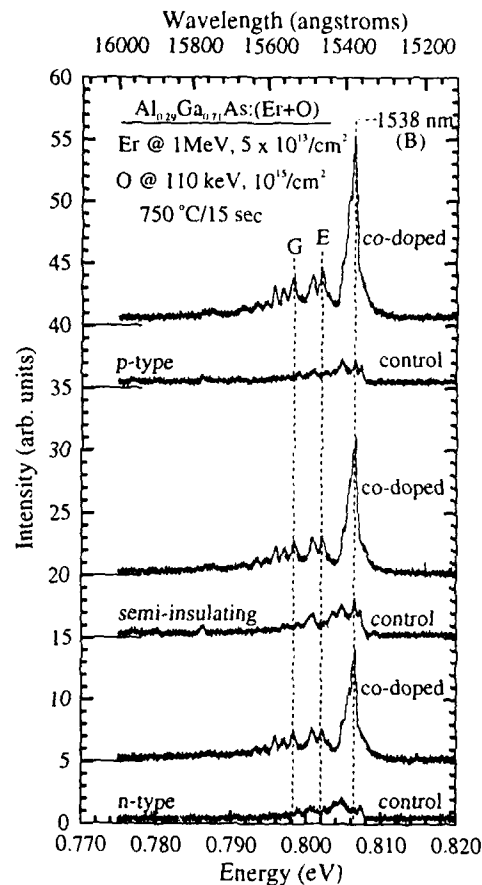


Figure 4 Photoluminescence spectra of $\text{Al}_{0.29}\text{Ga}_{0.71}\text{As}:(\text{Er}+\text{O})$ for different substrate conductivity type

CONCLUSIONS

Low temperature photoluminescence studies of Er and O co-implanted into GaAs and $\text{Al}_x\text{Ga}_{1-x}\text{As}$ with $x = 0.1, 0.2, 0.3$, and 0.4 have shown that the Er^{3+} emissions from $\text{Al}_x\text{Ga}_{1-x}\text{As}:(\text{Er}+\text{O})$ samples are enhanced significantly upon O co-doping from those of the samples doped with Er alone, but the Er^{3+} emissions from $\text{GaAs}:(\text{Er}+\text{O})$ actually decreased in the emission intensity upon O co-doping compared to those from GaAs doped with Er alone. A possible explanation for the observed behavior is that the emissions from the co-doped samples originate from some type of complex involving not only Er and O but also Al. This $\text{Er}+\text{Al}+\text{O}$ complex may be a more efficient emitter than other Er-related centers. The fact that the Er^{3+} emissions from GaAs:Er are not enhanced upon O co-doping and that the PL intensity of the $1.538\text{ }\mu\text{m}$ emission from $\text{Al}_x\text{Ga}_{1-x}\text{As}:(\text{Er}+\text{O})$ increases with increasing x value seem to favor this interpretation. It has been observed that the Er^{3+} emission intensity of the $1.538\text{ }\mu\text{m}$ peak for the Er and O co-doped $\text{Al}_x\text{Ga}_{1-x}\text{As}$ increased significantly with increasing x value and O dose, whereas the Er^{3+} emission intensity of the $\text{Al}_x\text{Ga}_{1-x}\text{As}$ samples implanted with Er alone did not increase much at all as the x value increased. It has also been found that the Er^{3+} emission intensities and peak structures for the Er and O co-doped $\text{Al}_x\text{Ga}_{1-x}\text{As}$ samples do not depend on the substrate conductivity type, as is also generally true for the $\text{Al}_x\text{Ga}_{1-x}\text{As}$ samples doped with Er alone.

REFERENCES

1. H. Ennen and J. Schneider in Thirteenth International Conference on Defects in Semiconductors, edited by L. C. Kimerling and J. M. Parsey Jr. (1989), pp. 115-127.
2. C. Rochaix, A. Rolland, P. N. Favennec, B. Lambert, A. Le Corre, H. L'Harridon, and M. Salvi, *Jap. J. Appl. Phys.* **27** (12), L2348-L2350 (1988).
3. P. N. Favennec, H. L'Harridon, M. Salvi, D. Moutonnet, and Y. Le Gillou, *Electr. Lett.* **25** (11), 718-719 (1989).
4. H. Nakagome, K. Uwai, and K. Takahei, *Appl. Phys. Lett.*, **53** (8), 1726-1728 (1988).
5. R. Boyn, *phys. stat. sol. (b)*, **148** (11), 11-47 (1988).
6. F. Auzel, A. M. Jean-Louis, Y. Toudic, *J. Appl. Phys.* **66** (8), 3952-3955 (1989).
7. P. Galtier, T. Benyattou, J. P. Pocholle, C. N. Charasse, G. Guillot, and J. P. Hirtz, in GaAs and Related Compounds, 1989, pp. 327-332.
8. P. N. Favennec, H. L'Harridon, D. Moutonnet, M. Salvi, and M. Gaunneau, *Jap. J. Appl. Phys.* **29** (4), L524-L526 (1990).
9. J. L. Benton, J. Michel, L. C. Kimerling, D. C. Jacobson, Y. -H Xie, D. J. Eaglesham, E. A. Fitzgerald, and J. M. Poate, *J. Appl. Phys.* **70** (5), 2667-2671 (1991).
10. J. E. Colón, D. W. Elsaesser, Y. K. Yeo, R. L. Hengehold, and G. S. Pomrenke 1993 (To be published).

LATTICE LOCATION AND PHOTOLUMINESCENCE OF Er IN GaAs AND Al_{0.5}Ga_{0.5}As

E. ALVES¹, M.F. DA SILVA¹, A. A. MELO², J.C. SOARES², G.N. VAN DEN HOVEN³,
A. POLMAN³, K.R. EVANS,⁴ AND C.R. JONES⁴

¹ Departamento de Física, ICEN/LNETI, Estrada Nacional n° 10, 2685, Sacavém, Portugal

² Centro de Física Nuclear da Universidade de Lisboa, Av. Prof. Gama Pinto 2, 1699, Lisboa
Codex, Portugal

³ FOM-Institute for Atomic and Molecular Physics, Kruislaan 407, 1098 SJ Amsterdam, The
Netherlands

⁴ Wright Laboratory, Solid State Electronics Directorate (WL/ELRA) Wright - Patterson Air
Force Base, OHIO 45433 - 6543, USA

ABSTRACT

Epitaxial Er-doped GaAs and Al_{0.5}Ga_{0.5}As films, 1.6 μm thick, grown by MBE on (100) GaAs substrates at 560 °C, with Er concentrations in the range 9×10^{17} to $2 \times 10^{20} \text{ cm}^{-3}$ were studied with RBS/channeling and photoluminescence techniques. Angular scans in the $\langle 110 \rangle$ and $\langle 111 \rangle$ axial and (111) planar directions indicate that the Er atoms in GaAs are located on interstitial sites. In Al_{0.5}Ga_{0.5}As doped with $5 \times 10^{19} \text{ Er cm}^{-3}$, 70% of the Er atoms are on positions slightly displaced from the interstitial site, the rest presumably substitutional. In Al_{0.5}Ga_{0.5}As doped with $9 \times 10^{17} \text{ Er cm}^{-3}$, more than 88% of the Er atoms are on substitutional sites.

Photoluminescence around 1.54 μm is observed at room-temperature in Er-doped Al_{0.5}Ga_{0.5}As. Both the low and highly Er-doped samples show similar luminescence intensities; the luminescence lifetimes are on the order of 1 ms. The Er-doped GaAs does not show any measurable signal at room-temperature. Correlation of the luminescence data to the Er lattice location suggests that only substitutional Er in AlGaAs is in the luminescent trivalent state.

I. INTRODUCTION

Optical doping of semiconductors with Er has recently become of interest due to the Er³⁺ intra-4f transitions around 1.54 μm , a standard telecommunications wavelength. Different techniques, including ion implantation and molecular beam epitaxy (MBE), have been used to dope Si as well as III-V semiconductors with Er [1-10]. Many of these materials exhibit Er-related luminescence, but in nearly all cases the local structure around the Er, and the Er lattice site are unknown.

In the present work the lattice sites of Er in epitaxially grown Al_{0.5}Ga_{0.5}As and GaAs is determined for different Er concentrations using Rutherford backscattering spectrometry (RBS)/channeling techniques. Also, the Er luminescence around 1.5 μm is measured for these materials. The correlation between optical data and channeling measurements suggests that Er only luminesces when it is substitutionally located in the lattice.

II. EXPERIMENTAL DETAILS

Epitaxial layers of Er-doped Al_{0.5}Ga_{0.5}As and GaAs were grown by MBE on semi-insulating (100) GaAs at a substrate temperature of 560 °C. Two Al_{0.5}Ga_{0.5}As layers with Er concentrations of 9×10^{17} and $5 \times 10^{19} \text{ cm}^{-3}$ and one GaAs layer with a concentration of $2 \times 10^{20} \text{ cm}^{-3}$ were prepared. The layer thickness was about 1.6 μm in each case.

The RBS/channeling analysis was done using a collimated beam of 1.6 MeV He⁺ using the 2 MV Van de Graaff accelerator at LNETI [11]. The backscattered alpha particles were

detected with two surface barrier solid state detectors placed at 160° and 180° with respect to the beam direction, and having energy resolutions of 14 and 18 keV, respectively. The pressure in the vacuum chamber during the measurements was 8×10^{-8} mbar. The angular scans were done using a two-axis goniometer. In order to reduce the damage by beam irradiation and to increase the sensitivity for Er, the beam current was kept below 1 nA on a spot of 0.4 mm^2 . Each measurement was done on a fresh spot to ensure that radiation effects would not influence the results. Computer simulations were performed to model the angular scans and determine the Er lattice sites in each sample [12].

Luminescence measurements were performed using the 514.5 nm line of an Ar ion laser as a pump source. The absorption depth of the light at this wavelength is approximately 100 nm for GaAs [13]. The pump beam was mechanically chopped at a frequency of 12 Hz. The samples were mounted in a cryostat, and the sample temperature was varied between 77 K and room-temperature. The luminescence was spectrally analysed using a 48 cm single-grating monochromator and detected with a liquid-nitrogen cooled Ge-detector. A lock-in amplifier was used to measure the signal. Time-resolved luminescence measurements were performed by measuring the decay of the luminescence signal after pumping to steady-state, and switching off the pump beam mechanically. The decay curves were measured using an oscilloscope and digitizing camera system, and averaged 300 times.

III - RESULTS

a) RBS/channeling

Figure 1 shows the random and aligned spectra for the $\langle 110 \rangle$ and $\langle 111 \rangle$ axial directions of the AlGaAs sample doped with $5 \times 10^{19} \text{ Er cm}^{-3}$. The minimum backscattering yields (χ_{\min}) for Ga and As are 3.8% and 4.5% in the $\langle 110 \rangle$ and $\langle 111 \rangle$ axial directions, respectively, against 3.0% and 3.8% found for a virgin GaAs substrate. These results show good crystalline quality in the films despite the high Er concentration. The corresponding results for GaAs:Er are presented in Fig. 2.

Figure 1 shows a difference in Er yield for the two channeling directions in AlGaAs. In the $\langle 111 \rangle$ direction the Er yield in the AlGaAs case reduces like that of Ga and As, but in the $\langle 110 \rangle$ direction the yield is higher than the random height and a modulated behaviour in depth is observed. The same behaviour is observed in Fig. 2 for GaAs, but less pronounced. These effects may be explained by a large fraction of Er occupying interstitial lattice sites at or near the centre of the $\langle 110 \rangle$ channel.

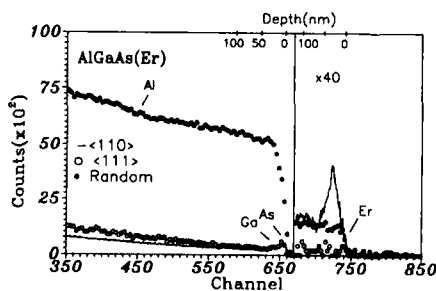


Fig. 1 - Random and aligned 1.6 MeV He⁺ RBS spectra of Er-doped Al_{0.5}Ga_{0.5}As. The Er concentration is $5 \times 10^{19} \text{ cm}^{-3}$.

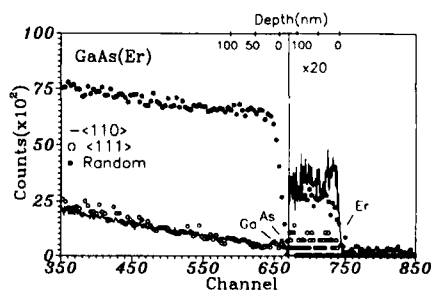


Fig. 2 - The same as Fig. 1 for GaAs: Er. The Er concentration is $2 \times 10^{20} \text{ cm}^{-3}$.

Due to the wavy trajectories of the channeled particles [14] the backscattering yield will increase when the particles cross the center of the channel. The depth of the peak in backscattering yield may be estimated from the relation derived by Van Vliet [15]:

$$\lambda/4 = \pi p_{ch}^2 / (3n)^{1/2} c \alpha \psi_1$$

where λ is the wavelength of the channeled particles, n the number of atomic strings bordering the channel, p_{ch} the distance from a string to the center of the channel, c a constant taken as $\sqrt{3}$, α the screening distance, and ψ_1 the Lindhard characteristic angle. From this equation a value of 375 Å for the first maximum in GaAs was derived using parameters obtained from ref. 15. This is close to the value of 300 Å observed experimentally. Taking into account the structure of the crystal, the only site which is both shadowed along the $\langle 111 \rangle$ axis and near the middle of the $\langle 110 \rangle$ channel is the tetrahedral interstitial site [16]. From these results we can conclude that Er mainly occupies the tetrahedral interstitial site.

In order to get quantitative information about the Er lattice location in AlGaAs and GaAs, detailed angular scans were performed in the $\langle 110 \rangle$ and $\langle 111 \rangle$ axial and (111) planar directions as shown in Fig. 3. The host and Er yields correspond to identical depths of 100 nm from the surface in all the scans. The scan for the $\langle 110 \rangle$ axis was done along the (110) plane and shows a flux peak in the middle of the channel in both AlGaAs and GaAs. The Er channeling dip in the $\langle 111 \rangle$ direction overlaps with that of the GaAs host atoms. It is slightly narrower in the case of the AlGaAs matrix. In the (111) plane a broad and pronounced flux peak of Er is observed for GaAs. The corresponding peak for AlGaAs is less pronounced.

The results of the simulations, also shown in Fig. 3, reproduce the experimental data using a thermal vibration amplitude of 0.10 Å for Ga and As and 0.12 Å for Al. These values

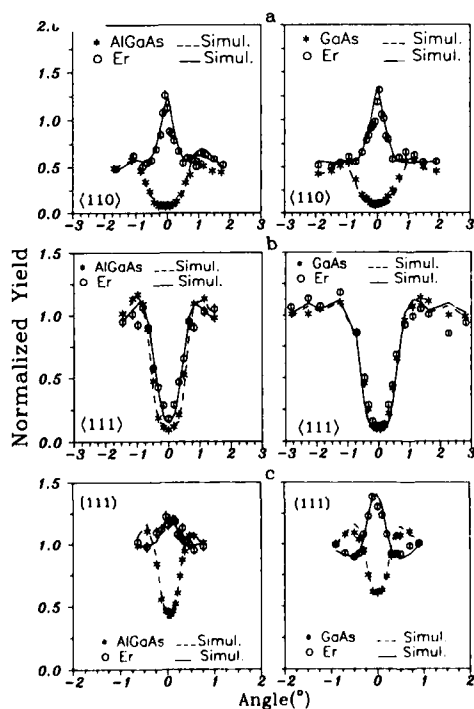


Fig. 3 - Angular scans for Al_{0.5}Ga_{0.5}As:Er ($5 \times 10^{19} \text{ cm}^{-3}$) and GaAs:Er ($2 \times 10^{20} \text{ cm}^{-3}$). a) $\langle 110 \rangle$ direction along the (110) plane; b) $\langle 111 \rangle$ direction; c) (111) plane. The continuous and dashed curves are results of the Monte Carlo simulation.

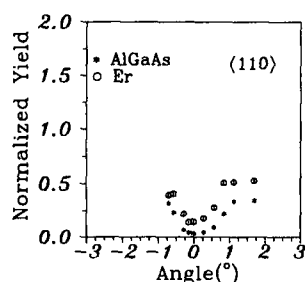


Fig. 4 - Angular scan for $\text{Al}_{0.5}\text{Ga}_{0.5}\text{As}:\text{Er}$ with $9 \times 10^{17} \text{ Er cm}^{-3}$. $\langle 110 \rangle$ axis along the $(\bar{1}\bar{1}0)$ plane as Fig. 3a.

are in agreement with the results of Dygo et. al. [17]. To compensate for the fact that the measured χ_{\min} is about 5% higher than the theoretical one, we have introduced a random fraction of 5% in the simulations for both GaAs and AlGaAs. From this analysis it follows that at least 95% of the Er atoms in GaAs are on tetrahedral interstitial lattice sites. Note the good agreement between the experimental and simulated angular scans. For the highly doped AlGaAs sample ($5 \times 10^{19} \text{ Er cm}^{-3}$) best agreement between the measured and calculated angular scans was obtained by assuming two fractions of Er occupying different sites: a 25% substitutional fraction and a fraction of 70% on a site with an averaged displacement of 0.35 \AA from the ideal tetrahedral interstitial position. Although the fits are not sensitive to the direction of the displacement, following the similar case of Te in GaAs [18], we have assumed an Er displacement along the $\langle 111 \rangle$ axis towards the nearest neighbour tetrahedral site. The observed shift may be related to the fact that the smaller Al atoms (covalent radius = 1.18 \AA) that occupy the Ga sublattice (Ga covalent radius = 1.26 \AA) cause a slight lattice distortion.

Channeling spectra for the AlGaAs sample with the lower Er concentration ($9 \times 10^{17} \text{ cm}^{-3}$) show a quite different result. Although the same χ_{\min} value is observed in the $\langle 111 \rangle$ and $\langle \bar{1}\bar{1}0 \rangle$ directions for both the Er and host atoms, indicating that Er substitutes either Ga or As atoms. Figure 4 shows an angular scan for this AlGaAs sample. This scan was performed along the (110) plane as in Fig. 3. In contrast to the angular scan for the highly doped AlGaAs sample no flux peaking is observed for the Er. From a comparison of the Er and the AlGaAs yields it follows that more than 88% of the Er atoms are substitutionally located in the matrix.

b) Luminescence measurements

Figure 5 shows the room-temperature luminescence spectra of the $\text{Al}_{0.5}\text{Ga}_{0.5}\text{As}$ films doped with $9 \times 10^{17} \text{ Er cm}^{-3}$ (solid line) and $5 \times 10^{19} \text{ cm}^{-3}$ (dashed line). The luminescence spectra are peaked at $\lambda = 1.54 \mu\text{m}$, characteristic of transitions between the $^4I_{13/2}$ and $^4I_{15/2}$ manifolds in Er^{3+} . Note that the luminescence from the low-concentration sample is more intense than that from the sample with 50 times more Er. The Er-doped GaAs film does not exhibit any room-temperature luminescence. This is in agreement with earlier work on liquid phase epitaxy grown GaAs:Er [4,8].

Figure 6 shows the luminescence spectra measured at 77 K for the Er-doped AlGaAs samples. The spectra are much more asymmetric than those in Fig. 5 as a result of the disappearance of "hot lines" from the luminescence of higher levels in the first excited manifold of Er^{3+} . The integrated luminescence intensity at 77 K is approximately 15 times larger than a room-temperature.

Luminescence decay measurements were done on the Er-doped AlGaAs samples held at 77 K. In each case the decay is single-exponential, with lifetimes of $\tau = 1.24 \text{ ms}$ and $\tau = 0.84 \text{ ms}$

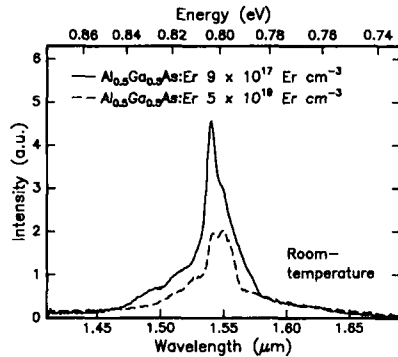


Fig. 5 - Room-temperature luminescence spectra for MBE grown $\text{Al}_{0.5}\text{Ga}_{0.5}\text{As}$ films doped with 9×10^{17} and $5 \times 10^{19} \text{ Er cm}^{-3}$. The luminescence was excited using the 514.5 nm line of an Ar ion laser at 120 mW as a pump source. The spectral resolution is 6 nm.

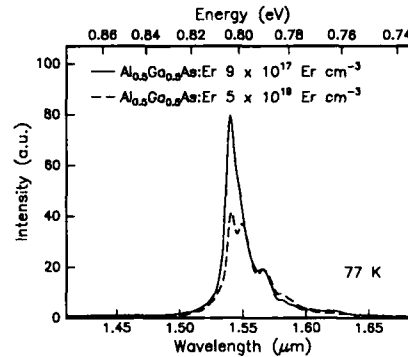


Fig. 6 - The same as Fig. 5 but now measured at 77 K.

for the 9×10^{17} and the $5 \times 10^{19} \text{ Er cm}^{-3}$ doped samples, respectively. It is interesting to note that the ratio in lifetimes for the two concentrations is similar to the ratio in luminescence intensities. The luminescence intensity (I) is related to the lifetime (τ) by

$$I \propto N W_{\text{rad}}/W = N W_{\text{rad}} \tau$$

where W_{rad} and W are the radiative and total radiative decay rates respectively, and N the number of active Er ions. W includes both radiative (W_{rad}) and non-radiative (W_{nr}) components: $W = W_{\text{rad}} + W_{\text{nr}}$. The luminescence intensity and lifetime data shown above indicate that $I \propto \tau$. Assuming that W_{rad} is constant, this implies that the number of optically active Er ions is the same for the low and high concentration AlGaAs samples. The decrease in lifetime upon increasing the Er concentration from $9 \times 10^{17} \text{ Er cm}^{-3}$ to $5 \times 10^{19} \text{ Er cm}^{-3}$ may be caused by the incorporation of defects during MBE due to the high Er concentration. Such defects can act as non-radiative decay centres.

Heating the samples to room-temperature decreases the lifetime to approximately 0.8 ms for the low Er concentration AlGaAs sample. This dependence compares well to values reported earlier [2], which show a decrease from 1.1 ms around 77 K to approximately 0.7 ms at room-temperature, which is attributed to thermally activated deexcitation of Er^{3+} .

IV - DISCUSSION

The RBS/channeling data show that for a low concentration of Er ($9 \times 10^{17} \text{ cm}^{-3}$) in AlGaAs all Er is substitutionally located. For more than an order of magnitude higher Er concentration ($5 \times 10^{19} \text{ cm}^{-3}$), 70% of the Er occupies slightly displaced tetrahedral interstitial positions, the remaining 30% presumably being substitutional. In GaAs doped with a high Er concentration ($2 \times 10^{20} \text{ cm}^{-3}$) all Er is interstitial. Both low and high doped AlGaAs samples show similar luminescence intensities, both at 77 K and room-temperature, with lifetimes around 1 ms. No room-temperature emission is observed for highly-doped GaAs:Er.

Several conclusions may be drawn from the results presented above. First of all, the absence of luminescence for the highly Er-doped GaAs sample indicates that interstitial Er is not in the optically active trivalent state in GaAs. Secondly, in $\text{Al}_{0.5}\text{Ga}_{0.5}\text{As}$, Er can be

incorporated substitutionally and Er-related luminescence is observed. Increasing the Er concentration from 9×10^{17} to $5 \times 10^{19} \text{ cm}^{-3}$ results mainly in the addition of interstitial Er in AlGaAs. However, this does not lead to additional luminescence intensity, suggesting that only substitutional Er is optically active in AlGaAs. Moreover, there seems to be a limit to the concentration of optically active substitutional Er, since the low and highly doped AlGaAs samples show similar luminescence intensities. This limit may be associated with lattice strain or defects related to the high Er concentration.

In summary, room-temperature Er luminescence in AlGaAs is observed when Er resides on substitutional sites in the lattice. Optimal luminescence is achieved for a low Er concentration of $9 \times 10^{17} \text{ cm}^{-3}$. More measurements are necessary to study the precise dependence of the luminescence properties on Er concentration and the role of defect incorporation.

Acknowledgements

This work was partially supported by AFOSR (USA) Luso American Foundation (Lisbon) and JNICT under contract n° PMCT/C/MPF/511/90. Thanks are due to Luís Rebouta for help in the installation of the simulation code. Work at the FOM-Institute was part of the research program of the Foundation for Fundamental Research on Matter (FOM), and was made possible by financial support from the Dutch Organisation for the Advancement of Pure Research (NWO), the Stichting Technische Wetenschappen (STW), and the IC Technology Program (IOP Electro-Optics) of the Ministry of Economic Affairs.

References

- [1] A. Polman, J. S. Custer, E. Snoeks, and G. N. van den Hoven, *Appl. Phys. Lett.* 62 (1993) 507.
- [2] T. Benyattou, D. Seghier, G. Guillot, R. Moncorge, P. Galtier, and M. N. Charasse, *Appl. Phys. Lett.* 60 (1992) 350 and 58 (1991) 2132.
- [3] P. B. Klein, F. G. Moore, and H. B. Dietrich, *Appl. Phys. Lett.* 58 (1991) 502.
- [4] F. Bantien, E. Bauser and J. Weber, *J. Appl. Phys.* 61 (1987) 2803.
- [5] A. Kozanecki and R. Gröetzchel, *J. Appl. Phys.* 64 (1988) 3315.
- [6] A. Kozanecki and R. Gröetzchel, *J. Appl. Phys.* 68 (1990) 517.
- [7] A. Kozanecki, M. Chan, C. Jeynes, B. Sealy and K. Homewood, *Solid State Commun.* 78 (1991) 763.
- [8] Gernot S. Pomrenke, H. Ennen and W. Haydl, *J. Appl. Phys.* 59 (1986) 601.
- [9] H. Ennen, J. Wagner, H.D. Muller and P.S. Smith, *J. Appl. Phys.* 61 (1987) 4877.
- [10] Kenichiro Takahei, Peter S. Whitney, Hiroshi Nakagome and Kunihiro Uwai, *J. Appl. Phys.* 65 (1989) 1257.
- [11] M.F. da Silva, M.R. da Silva, E. Alves, A. Melo, J.C. Soares, P.M.J. Winand and R. Vianden, in *Surface Engineering*, NATO Advanced Study Institute, Ed. R. Kossowsky and S.C. Singhal, Martinus Nijhoff Publisher (1984) pg. 74.
- [12] L. Rebouta, M. F. da Silva, J. C. Soares, P. J. M. Smulders, D. O. Boerma, and F. Agullo-Lopez, *Phys. Rev. B* in press.
- [13] H. Melchior, in *Laser Handbook*, Vol. 1, edited by F. T. Arecchi and E. O. Schulz-Dubois (North-Holland, Amsterdam, 1972) pp. 725-835.
- [14] J. Lindhard, K. Dan. Vidensk. Selsk. Mat. Fys. Medd. 34 (1965) No. 14.
- [15] D. Van Vliet, *Rad. Effects* 10 (1971) 137.
- [16] J.W. Mayer and E. Rimini, *Ion Beam Handbook for Material Analysis* (Academic Press, New York, 1977).
- [17] A. Dygo and A. Turos, *Phys. Rev. B* 40 (1989) 7704.
- [18] P.J.M. Smulders, D.O. Boerma and M. Shaanan, *Nucl. Inst. and Meth. B* 45 (1990) 450.

OPTICAL ACTIVATION OF ION IMPLANTED RARE-EARTHS

P. N. FAVENNEC*, H. L'HARIDON**, D. MOUTONNET**,
M. SALVI** AND M. GAUNEAU**

*France Telecom, CNET, DIR/SAS, B.P. 40, F-22301 LANNION

**France Telecom, CNET, LAB/OCM, B.P. 40, F-22301 LANNION

ABSTRACT

A review of the main results concerning the ion implantation of the rare-earth elements is given.

To obtain the best optical activation of rare-earths, we attempt to optimize the implantation (energy, dose) and annealing (temperature, duration) conditions. The studied materials are Si, II-VI binaries (ZnTe, CdS), III-V binaries (GaAs, InP), III-V ternaries (GaAlAs, GaInAs) and III-V quaternaries (GaInAsP).

1 - INTRODUCTION

The semiconductor rare-earth (RE) element system exhibits some interesting properties that are of potential importance for nowadays semiconductor technology. One of the main characteristic features of rare-earth ions is the partially filled inner 4f shell where the f electrons are screened by the closed 5s² and 5p⁶ shells. As a consequence, the characteristic sharp transitions of these electrons are highly insensitive to their environment, giving rise to a :

- sharp luminescence even at relatively high temperatures,
- photon energy of their luminescence independant of host semiconductor materials and temperature.

Optical properties of rare-earth impurities in silicon, in III-V materials and II-VI semiconductors have recently attracted much attention. Rare-earth doped materials belong to a new class of materials for optic or optoelectronic devices. Incorporation of erbium into a semiconductor is of particular interest as the 1.54 μm Er³⁺ emission is applicable to the low-loss region of silica-based optical fibers. Erbium emission from various semiconductors have been the subject of numerous investigations [1 to 10]. The rare-earth ytterbium, neodymium, thulium... have also been studied [11 to 14].

In this paper, the optical activation of rare-earth elements, mainly erbium, implanted in various semiconductors, is presented. The ion implantation is recognized as a most useful tool in fabricating devices.

2 - CHEMICAL IN-DEPTH PROFILES

In order to apply this technique to devices, it is necessary to know the chemical distribution of implanted impurities in the target materials. In the process of ion implantation, atoms of the desired rare-earth element are ionized and accelerated to high velocity. After the energetic ion comes to rest and equilibrium has occurred, the implanted atoms can be in a position in which they

serve to change the optical properties of the host material. Factors such as the ion energy, ion species and target density influence the range distribution. For the determination of the chemical in-depth profiles, SIMS is the most popular technique used ; this existing fact is due to the combination of high sensitivity, acceptable quantitativity, and good depth and lateral resolution.

The rare-earth elements are high mass (from $M = 140$ for cesium to $M = 174$ for lutetium). When high mass elements are implanted in implantors having low mass resolving powers, several isotopes can be implanted simultaneously ; the example given here in figure 1 is that of erbium for which the three isotopes ^{166}Er , ^{167}Er and ^{168}Er were registered during the SIMS analysis. The total dose as measured during the implantation were 10^{14} erbium atoms- cm^{-2} , it corresponds to the sum of the three species and, if only one isotope is monitored during the SIMS analysis, the measured signal is equal to the dose multiplied by the virtual abundance of that species registered ; in the present case the virtual abundance of say ^{166}Er was 60 % (true value should be 100 %, and the true dose which had to be taken into account for SIMS calibration was $10^{14} \times 0.6$ (for a 10^{14}cm^{-2} implantation) ; neglecting this experimental fact would have induced a 40 % error in the erbium concentration.

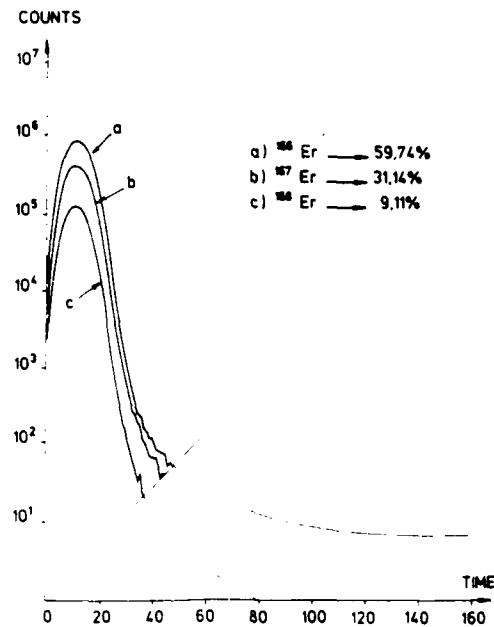
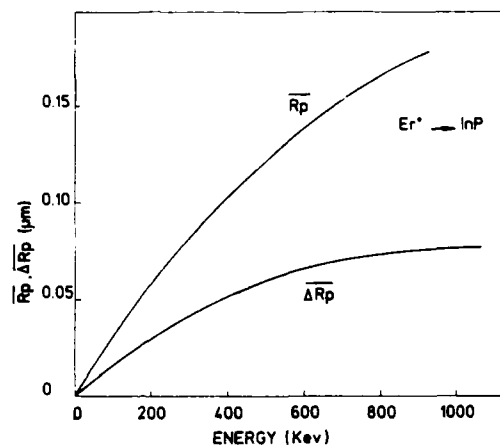


Figure 1 : SIMS profiles for erbium implanted in InP. Three isotopes of erbium were simultaneously implanted at 400 keV. The dose as measured during the implantation corresponds to the sum of the three species concentrations.

In the figure 2, we show some as-implanted erbium profiles in InGaAs, the energy was 400 keV, the doses were 10^{13} , 10^{14} and 6×10^{14} erbium- cm^{-2} . The concentration scale was corrected to have the correct erbium concentration [15].

For the determination of the projected ranges and the stragglings, several profiles at different energies are necessary. As an example we show on the figure 3 some as-implanted erbium profiles. The dose was 10^{14} erbium-cm $^{-2}$, the energies were 130 keV, 400 keV and 800 keV. These profiles are near gaussian.



Energy (KeV)	20	40	60	80	100	120	140	160	200	250	300	350	400	500	600	700	800	900	1000
$\overline{R_p}$ (μm)	0.008	0.015	0.021	0.027	0.033	0.038	0.044	0.050	0.059	0.071	0.082	0.092	0.102	0.120	0.137	0.152	0.165	0.176	0.184
ΔR_p (μm)	0.040	0.075	0.011	0.015	0.018	0.021	0.024	0.027	0.032	0.037	0.042	0.046	0.051	0.058	0.063	0.070	0.073	0.076	0.077

Figure 2 : Variations of the projected range and the straggling for erbium implanted in InP. The table gives the experimental values from 20 keV to 1 000 keV.

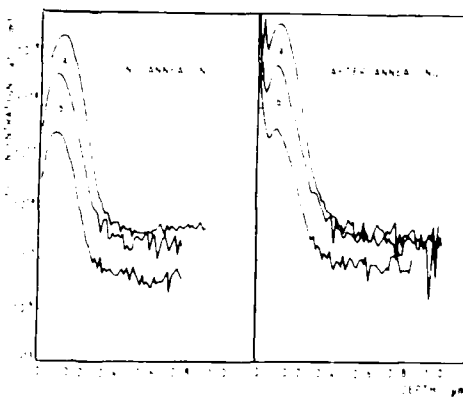


Figure 3 : Erbium profiles in InGaAs. The energy was 400 keV. The doses were (a) 6×10^{14} Er-cm $^{-2}$, (b) 10^{14} and (c) 10^{13} ; on the left, as-implanted; on the right, annealed at 700°C, 10 s.

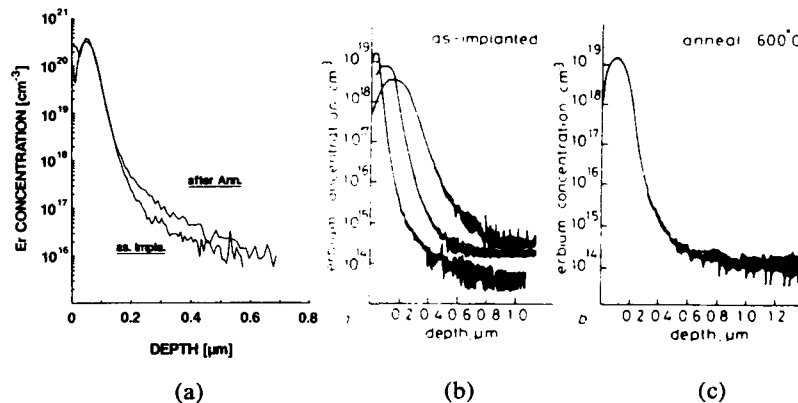


Figure 4 : Erbium profiles in InP (a) 150 keV to a dose of $7.10^{14} \text{ Er}^+\text{cm}^{-2}$, before and after a 20 hours long annealing at 600°C, after Issiki et al [16], (b) 130 keV, 400 keV and 800 keV at a dose of $10^{14} \text{ Er}^+\text{cm}^{-2}$ (c) 400 keV to a dose of $2 \times 10^{14} \text{ Er}^+\text{cm}^{-2}$ and after annealing at 600°C for 10 minutes.

We present in the figure 4 the variation of the projected range and the standard deviation as a function of the incident energy. The values are deduced from SIMS profiles. The curves and tables are presented for InP. The same values are found for ytterbium and erbium ions. From the experimental values, it can be stressed that for the most energies usable in the ion implantation technique, the projected range can be approximated as being a linear function of the incident energy. It can be evaluated as following :

$$R_p(\mu\text{m}) = 2.10^{-4} E (\text{keV}) \pm 20 \%$$

After these values for InP (density d_{InP} and projected range $R_p)_{\text{InP}}$, for other materials (density d) the variation of the projected range ($R_p)_i$) follows approximatively the relation :

$$R_p)_i = \frac{d}{d_{\text{InP}}} R_p)_{\text{InP}}$$

All rare-earth elements are heavy, so these imputities can only be implanted near the surface.

For the activation of the implanted impurities in the matrix, the materials are annealed at high temperature. So, it is useful to know the behavior of the implanted chemical profiles (diffusion and redistribution) after annealing. In figures 5 and 6, we present some annealed in-depth profiles in InP [4, 16] and InGaAs [17]. After annealing, these erbium profiles are very slightly modified, they are very close to those obtained for as-implanted samples. Towards the surface, according to the implanted dose, a slight redistribution of erbium can be noted, it could be due to the implantation damage. Towards the bulk, we have never detected an erbium diffusion, beyond the projected range, the in-depth distribution is nearly unchanged, the diffusion coefficient, for GaInAs at

700°C, should be smaller than $10^{-18} \text{ cm}^2 \cdot \text{s}^{-1}$. The erbium impurity in Si, GaAs, InP, InGaAs, etc... has a very small diffusion coefficient, if any. We have observed the same behavior for ytterbium impurity.

Anyway, after implantation and annealing, the in-depth chemical analyses have proven that the erbium impurities are really present near the material surface and then the optical properties (photoluminescence, cathodoluminescence, electroluminescence...) concern really the material layer containing erbium impurities.

3 - OPTICAL ACTIVATION IN InP

Figure 5 shows typical spectra for a semi-insulating substrate implanted at $10^{14} \text{ Er}^+ \cdot \text{cm}^{-2}$ for an energy of 400 keV and annealed at 700°C for 600 sec. In figure 5a, we show the 1.7 K spectrum. We observe a sharply structured luminescence spectrum centered around 1.536 μm . The peak width at half-maximum is 2.2 meV. For this same sample, at 77 K, we have also a strong emission centered at 1.536 μm and the peak width at half-maximum is 7 meV (Fig. 5b). At room temperature, we have also detected an emission at 1.536 μm and the peak width at half-maximum was 16 meV (Fig. 5b). This emission at 1.536 μm is independent of the temperature of the host substrate and it is due to an intrashell transition of Er 4f electrons.

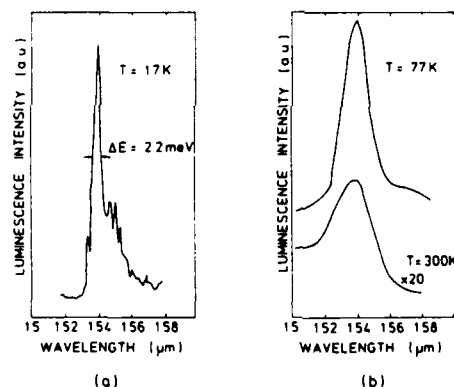


Figure 5 : Photoluminescence spectra for Er-implanted semi-insulating InP (energy : 400 keV ; dose : $10^{14} \text{ Er}^+ \cdot \text{cm}^{-2}$, annealing temperature : 700°C, annealing time : 600 sec). a) 1.7 K b) 77 K and 300 K

The photoluminescence intensity of the 77 K erbium emission (at 1.536 μm) was measured for a range of annealing times and temperatures. It is plotted in Fig. 6 as a function of annealing time for a temperature of 700°C. From 3 sec to 600 sec, the photoluminescence intensity of the 1.536 μm peak is constant. We have verified that the implanted and unannealed samples did not luminesce. So, during the very early stage of annealing, the "optical activation" (and recrystallisation?) occurs. Unfortunately, it appears difficult to anneal reproducibly with a duration smaller than 3 sec. But, it is useful to note that the optical activation of erbium occurs during a very short time of annealing.

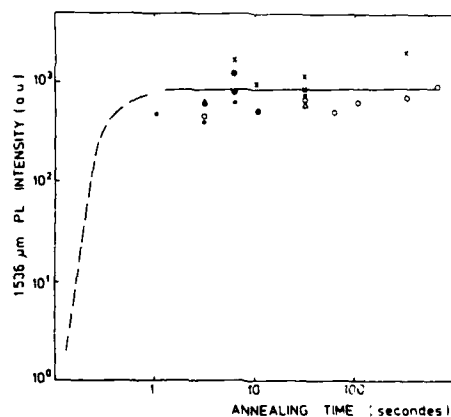


Figure 6 : 1.536 μm photoluminescence intensity, at 77 K, as a function of the annealing time (Energy: 400 keV; annealing temperature 700°C). The doses were varying from 10^{13} to 6×10^{13} erbium- cm^{-2} . The InP substrates were n-type or semi-insulating.

For these experimental conditions ($E = 400$ keV, dose $> 2 \times 10^{12}$ $\text{Er}^+ \cdot \text{cm}^{-2}$), the surface was amorphised. After an annealing at 700°C, the reordering of erbium-implanted layer occurred for times smaller than 3 seconds: the amorphous layer has completely disappeared as detected by RBS measurements. So, during the very early stage of annealing, the recrystallisation and the optical activation of erbium occurred.

The variation of the 1.536 μm photoluminescence intensity at 77 K, as a function of annealing temperature is shown in the Fig. 7, for two annealing times (10 sec and 600 sec). For low annealing temperatures ($T < 550^\circ\text{C}$), the erbium implanted InP layers do not luminesce. From 500°C, an erbium luminescence appears, it becomes more intense when the annealing temperature is increasing. When the annealing time is short, typically 10 sec or less, an anneal at a temperature higher than 700°C and up to 900°C does not improve the photoluminescence intensity. But, if the annealing time is long, typically 600 sec, the Er peak intensity decreases when the temperature is increased, it became unobservable at 800°C. This decrease could be due to a degradation of the InP surface during the long thermal annealing or a diffusion of some impurities from the bulk towards the surface which could induce an annihilation of the properties of erbium luminescence. These experimental results demonstrate that the "optical activation" of erbium is complete for a temperature of 650°C and for very short times.

The variation of the luminescence intensity at 1.536 μm as a function of the erbium concentration introduced in the substrate is shown on the figure 8. For low doses, the erbium peak is undetectable, it appears for a dose of 10^{12} $\text{Er}^+ \cdot \text{cm}^{-2}$. Then, it increases and the intensity was strong for the dose around 10^{14} $\text{Er}^+ \cdot \text{cm}^{-2}$. Above, the photoluminescence intensity decreases and it becomes unobservable for a dose of 10^{15} $\text{Er}^+ \cdot \text{cm}^{-2}$.

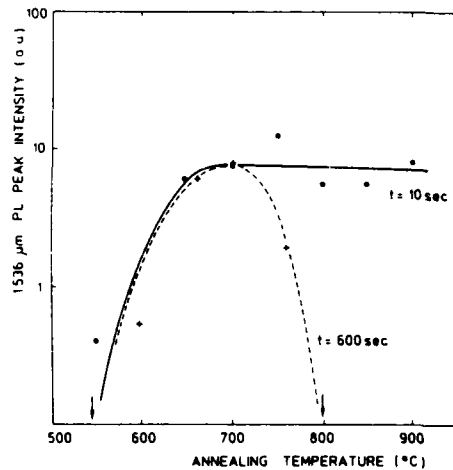


Figure 7 : 1.536 μm photoluminescence intensity at 77 K as a function of the annealing temperature for undoped n-type InP samples. Energy : 400 keV, dose : $6 \times 10^{13} \text{ Er}^+ \cdot \text{cm}^{-2}$. Full line : annealing time is 10 sec. Dotted line : annealing time is 600 sec.

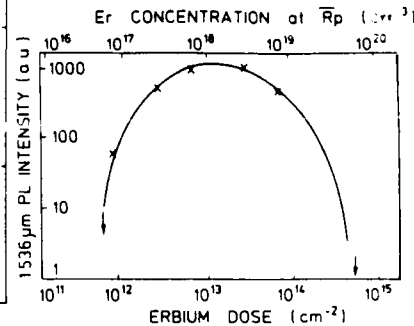


Figure 8 : 1.536 μm photoluminescence intensity at 77 K as a function of the erbium dose (and the erbium concentration at R_p). The samples were annealed at 700°C for 6 sec.

4 - OPTICAL ACTIVATION

Figure 9 shows typical PL spectra at 77 K for different III-V materials implanted at $10^{14} \text{ Er}^+ \cdot \text{cm}^{-2}$ with an energy of 330 keV. For these three spectra, the main emission at 77 K is centered at the same wavelength whatever the substrate is. So, the emission energy corresponds to the intracenter transition in Er^{3+} . In addition, the PL spectra in GaAs reveal that the Er-related luminescence is about 200 times more intense than the band-edge emission.

Next, we studied the erbium dose dependence of the 77 K PL spectra of 300 keV erbium implanted GaAs from 5×10^{12} to $5 \times 10^{14} \text{ Er}^+ \cdot \text{cm}^{-2}$ (Figure 10). The erbium related luminescence peak intensity was strong whatever the dose was. Even at low dose, that is $5 \times 10^{12} \text{ Er}^+ \cdot \text{cm}^{-2}$ which corresponds to a maximum concentration of $1.5 \times 10^{17} \text{ Er}^+ \cdot \text{cm}^{-3}$ at R_p , the 1.54 μm intensity is strong. For very high doses, the PL intensity decreases. This decrease could be due to an absorption induced by some unannealed bombardment damage.

The study of the temperature dependence of the PL spectra of Er-implanted III-V materials showed that the energy of the erbium related line is constant. In figure 11, the temperature dependence of the Er-related PL intensity from 77 K to 300 K is shown for GaAs. The intensity of this line decreases when the temperature increases. The linewidth of the Er^{3+} related band is temperature independent, within our experimental resolution. This fact suggests that the 4f intracenter transitions in Er implanted material, as diffused Er, are not coupled with phonons in the crystal.

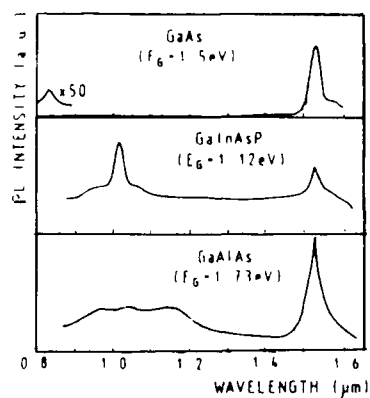


Figure 9 : PL spectra at 77 K after an Er implantation ($\phi = 10^{14} \text{ Er}^+ \text{ cm}^{-2}$) and an annealing. (a) GaAs ($E_G = 1.5 \text{ eV}$) (b) GaInAsP ($E_G = 1.12 \text{ eV}$) (c) GaAlAs ($E_G = 1.73 \text{ eV}$).

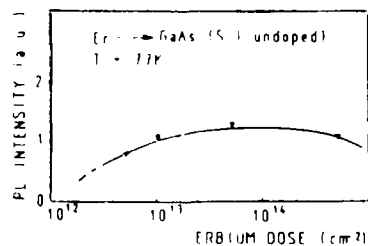


Figure 10 : 1.54 μm photoluminescence intensity versus the erbium dose, at 77 K for GaAs.

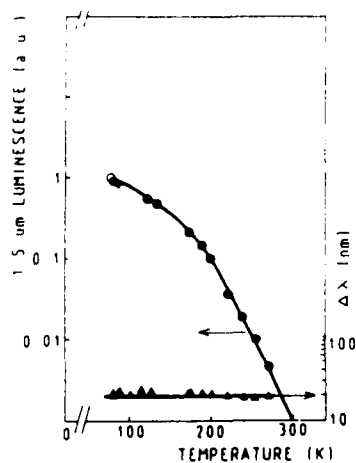


Figure 11 : 1.54 μm PL intensity and linewidth in GaAs versus the sample temperature. Erbium was implanted at 330 keV with a dose of $10^{14} \text{ Er}^+ \text{ cm}^{-2}$. The annealing temperature and the time were 840°C and 10 sec.

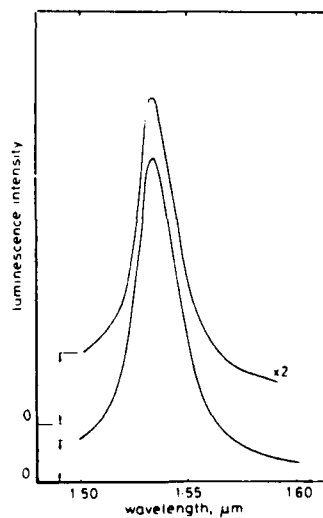


Figure 12 : Room temperature photoluminescence spectra in erbium implanted ZnTe and CdS.

5 - OPTICAL ACTIVATION OF ERBIUM IN VARIOUS SEMICONDUCTORS

Figure 12 shows PL spectra for erbium implanted II-VI semiconductors. These PL spectra are performed at room temperature. For ZnTe ($E_G = 2.26$ eV) and CdS ($E_G = 2.42$ eV), the RT emission is intense. The emission wavelength is always $1.536 \mu\text{m}$ and is independent of the band gap energy of the host material. The greatest intensity is detected with CdS: the CdS bandgap energy is higher than the ZnTe bandgap energy.

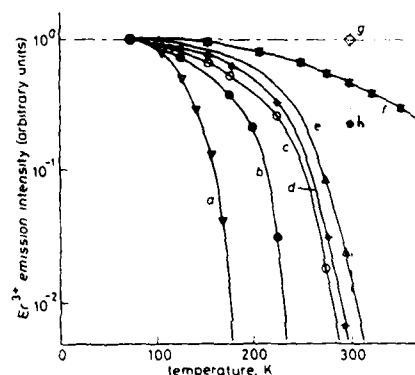


Figure 13 : Er^{3+} emission intensity against host semiconductor temperature. Materials are implanted with Er ions : $E = 330$ keV, $\phi = 10^{13} \text{ Er}^+ \text{ cm}^{-2}$. E_G values are given at room temperature

- (a) $\text{Ga}_{0.38}\text{In}_{0.62}\text{As}_{0.84}\text{P}_{0.12}$ ($E_G = 0.807$ eV)
- (b) Si ($E_G = 1.12$ eV)
- (c) InP ($E_G = 1.27$ eV)
- (d) GaAs ($E_G = 1.43$ eV)
- (e) $\text{Al}_{0.17}\text{Ga}_{0.83}\text{As}$ ($E_G = 1.67$ eV)
- (f) ZnTe ($E_G = 2.26$ eV)
- (g) CdS ($E_G = 2.42$ eV)
- (h) a-Si : H ($E_G = 1.8$ eV)

Variations of the Er^{3+} emission intensity against temperature are given in Fig. 13 for various semiconductors. At low temperatures (77 K), all Er-doped semiconductors having a bandgap energy higher than 0.805 eV corresponding to the intrashell transition energy of Er 4f electrons, present an emission peak centered at $1.54 \mu\text{m}$. The intensity is approximately the same for any semiconductor. However, at higher temperature, the Er emission wavelength remains constant and the intensity depends strongly on the nature of the host semiconductor. The shape of variation curve is identical for all semiconductors. We observe that the narrower the bandgap, the weaker the intensity. The decrease is particularly steep in $\text{Ga}_{0.38}\text{In}_{0.62}\text{As}_{0.84}\text{P}_{0.12}$ ($x = 0.38$, $y = 0.84$, $E_G = 0.807$) where the bandgap energy is the nearest of Er emission energy. Beyond 175 K, the Er^{3+} emission is no longer detectable. The temperature of Er^{3+} emission detection varies with the material. We also observe an increase in the limit temperature of Er emission as the bandgap energy increases.

At room temperature, the Er^{3+} emission cannot be detected in materials such as $\text{Ga}_{1-x}\text{In}_x\text{As}_{1-y}\text{P}_y$ ($E_G = 0.807$) and silicon. It can be detected in the other material but it is very weak in InP and GaAs , weak in $\text{Al}_x\text{Ga}_{1-x}\text{As}$ ($E_G = 1.67$ eV) and intense in a-Si:H [19] and ZnTe and CdS . The greater the bandgap energy of the semiconductor, the more intense the Er^{3+} emission. This is particularly pronounced for II-VI semiconductors. For ZnTe ($E_G = 2.226$ eV), the Er luminescence intensity is only 2 times weaker at RT than at 77 K. And for temperature increasing up to 400 the intensity decrease is quite slow. These results show that there is a direct correlation between the efficiency of optical centres induced by the implanted Er element and the bandgap energy of the host material.

6 - OPTICAL ACTIVATION OF Er^{3+} IMPLANTED IN SILICON BY OXYGEN IMPURITIES

Table 1 summarizes the results of PL measurements made from various Si samples implanted with erbium. The substrates were: (i) Czochralski grown (CZ) (100) and (111) orientated substrates of n or p type, (ii) floating zone grown (FZ) (100) and (111) oriented crystals of n or p type and (iii) Si epitaxial n^+ type layers grown by chemical vapor deposition (CVD) on silicon substrates.

The wafer orientation or the substrate type had no noticeable effects on the PL intensity. The emission peak due to erbium impurities is centered at $1.54 \mu\text{m}$. The maximum intensity (++) is found in Er^+ implanted CZ samples. In FZ refined crystals, the intensity is lower (+) and almost non-existent in CVD layers (-). The second line of Table 1 gives the estimated oxygen concentration in the host material. The existence of a correlation between the intensity of the PL and the oxygen level strongly suggests that the oxygen plays an important role in the optical activation of erbium impurity and then enhances the $1.54 \mu\text{m}$ luminescence of the Er^{3+} .

In order to confirm this hypothesis, oxygen ions were implanted into CVD layers of n-type Si (10^{15} cm^{-2}) previously implanted with Er (10^{13} cm^{-2}). Almost flat oxygen profiles from the surface down to the 3000 \AA depth were obtained by multiple oxygen implantations. The total oxygen doses varied from 10^{12} to 10^{15} cm^{-2} .

Si growth method	CZ	FZ	CVD layer
1.54 μm PL	++	+	-
Residual oxygen concentrations cm^{-3}	10^{18}	10^{13} - 10^{17}	$< 10^{15}$

Table 1 : Luminescence and residual concentration in various Er implanted substrate ($\phi = 10^{13} \text{ Er}^+ \text{ cm}^{-2}$, $E \approx 330 \text{ keV}$)

Before oxygen implantation, the PL intensity at $1.54 \mu\text{m}$ is very local, and it increases considerably after oxygen implantation. The variation of Er^{3+} PL intensity versus oxygen dose for CVD layers on n-type silicon is shown in the figure 14. The PL intensity increases with the dose up to 10^{13} cm^{-2} , from 10^{13} to $3 \times 10^{13} \text{ cm}^{-2}$ the luminescence is the highest, then the intensity decreases as the dose increases.

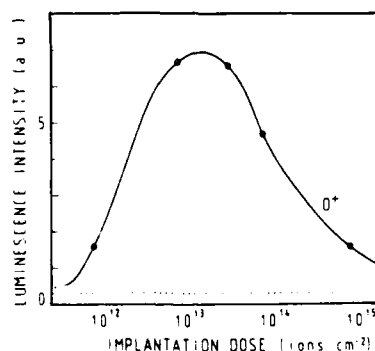


Figure 14 : Er^{3+} luminescence intensity as a function of O^+ implantation dose. The dashed line corresponds to the Er^{3+} implantation alone, the PL signal is undetectable. The $1.54 \mu\text{m}$ PL is the greatest at an oxygen concentration of about 10^{13} ions $\cdot \text{cm}^{-2}$. The erbium dose was $10^{13} \text{ Er}^+ \cdot \text{cm}^{-2}$.

Codoping with oxygen and erbium of silicon layers grown by MBE gives some similar results [19].

In addition, the Er and O chemical in-depth are correlated [21]. The formation of Er^+O complexes is strongly suggested [7, 21, 22]. It is consistent with a large crystal-field splitting of the 4f multiplets known in Si and other semiconductors. All these facts indicate that Er^+O complexes act as luminescence centres for the $I^{13/2} \rightarrow I^{15/2}$ transitions in the 4f shell of Er^{3+} ion involved in the $1.54 \mu\text{m}$ PL.

7 - SOME ORIENTATIONS

For optical or optoelectronic applications, it is necessary to have an intense room temperature emission at a wavelength stable with the temperature, a thick R.E. doped layer and an easy adaptability to the classical semiconductor technologies (Si, GaAs...). It has been shown that :

- a - To obtain an intense R.T. emission, a wide-gap host material must be used [7, 20, 23].
- b - Whatever the doping process (ion implantation and epitaxy growth) of host materials, the maximum of luminescence intensity is observed for a relatively low erbium concentration, close to $10^{18} \cdot \text{cm}^{-3}$. Higher erbium concentrations are necessary to have a higher optical center concentration (as an example, see Raoux's paper [23] on $\text{Ca}_{1-x}\text{Er}_x\text{F}_{2+x}$ layers).
- c - $1.54 \mu\text{m}$ PL of Er^{3+} ions in silicon can be activated by oxygen (in Er-doped silica, the $1.54 \mu\text{m}$ fluorescence is intense at RT). The formation of Er^+O complexes is strongly suggested to enhance the optical activation of erbium [21, 22]. We suggest that erbium can be also activated by another oxidant impurities, fluor for examples.

- d - For optical waveguides, a R.E.-doped layer thickness of some microns is necessary. Ion implantation does not permit to have a thick layer doped with erbium (or other R.E. impurities). Is it possible to have an enhancement of the diffusion coefficient assisted by defects or by impurity redistribution? Some indications have been given by Ikoma et al [18] and by Kechouane et al [22].

BIBLIOGRAPHY

1. H. Ennen, J. Schneider, G.S. Pompenke and A. Axmann, Appl. Phys. Lett. **43**, 943 (1983)
2. G.S. Pomrenke, H. Ennen and W. Haydl, J. Appl. Phys. **59**, 610 (1986)
3. W.T. Tsang and R.A. Logan, Appl. Phys. Lett. **49**, 1686 (1986)
4. P.N. Favennec, H. L'Haridon, A. Le Corre, M. Salvi and M. Gauneau, Electron. Lett. **23**, 684 (1987)
5. R.S. Smith, H.D. Muller, H. Ennen, P. Wennekers and M. Maier, Appl. Phys. Lett. **50**, 49 (1987)
6. H. Ennen, J. Wagner, H.D. Muller and R.D. Smith, J. Appl. Phys. **61**, 4807 (1987)
7. P.N. Favennec, H. L'Haridon, M. Salvi, D. Moutonnet and Y. Le Guillou, Electron. Lett. **25**, 718 (1989)
8. J. Michel, J.L. Benton, R.F. Ferrante, D.C. Jacobson, D.J. Eaglesham, E.A. Fitzgerald, Y.H. Xie, J.M. Poate and L.C. Kimerling, J. Appl. Phys. **70**, 2672 (1991)
9. H. Nakagome, K. Takahei and Y. Homma, J. Cryst. Growth **85**, 345 (1987)
10. R. Saito and T. Kimura, Phys. Rev. B **46**, 1423 (1992)
11. W.H. Haydl, H.D. Muller, H. Ennen, W. Korber and K.W. Benz, Appl. Phys. Lett. **46**, 870 (1989)
12. H. L'Haridon, D. Moutonnet, Y. Toudic, M. Salvi and P.N. Favennec, SPIE **1144**, 428 (1989)
13. G.S. Pomrenke, E. Silkowski, J.E. Colon, D.J. Topp, Y.K. Yeo and R.L. Hengehold, J. Appl. Phys. **71**, 1919 (1992)
14. A.J. Neuhaufen and B.W. Wessels, Appl. Phys. Lett. **59**, 2317 (1991)
15. P.N. Favennec, M. Gauneau, M. Salvi, Solid St. Phen. **1**, 377 (1988)
16. H. Isshiki, R. Saito, T. Kimura, I. Ikoma, J. Appl. Phys. **70**, 6993 (1991)
17. P.N. Favennec, H. L'Haridon, D. Moutonnet, M. Salvi, M. Gauneau and A.C. Papadopoulos, Inst. Phys. Conf. Ser **106**, 333 (1989)
18. X. Zhao, K. Hirakawa and T. Ikoma, Appl. Phys. Lett. **54**, 712 (1989)

19. F. Arnaud D'Avitaya, Y. Campidelli, J.A. Chroboczek, P.N. Favennec, H. L'Haridon, D. Moutonnet and A. Wasiela, this conference
20. M. Kechouane, N. Beldi, T. Mohamed-Brahim, H. L'Haridon, M. Salvi, M. Gauneau and P.N. Favennec, this conference
21. P.N. Favennec, H. L'Haridon, D. Moutonnet, M. Salvi and M. Gauneau, Jap. J. Appl. Phys. **29**, 524 (1990)
22. M. Kechouane, H. L'Haridon, M. Salvi, P.N. Favennec, D. Moutonnet, M. Gauneau and J.P. Mercier, Electron. Lett. **26**, 1067 (1990)
23. S. Raoux, A.S. Barrière, P.N. Favennec, H. L'Haridon, D. Moutonnet, this conference

LUMINESCENCE OF Tm^{3+} IN GALLIUM ARSENIDE GROWN BY METAL-ORGANIC VAPOR PHASE EPITAXY

ACHIM DÖRNEN, KLAUS PRESSEL*, CHRISTOPH HILLER, DIETER HAASE, JÜRGEN WEBER,** and FERDINAND SCHOLZ

4. Physikalisches Institut, Universität Stuttgart, D-W-7000 Stuttgart 80, Box 80 11 40, Federal Republic of Germany

*now with: Institut für Halbleiterphysik, D O-1200 Frankfurt/Oder, Walter-Korsing-Str. 2, Federal Republic of Germany

**now with: ALCATEL-SEL Research Center, ZFZ1 WO, Lorenzstr. 10, D W-7000 Stuttgart 40, Federal Republic of Germany

ABSTRACT

We investigate the excitation mechanism of the characteristic 4f luminescence $^3H_5 \rightarrow ^3H_6$ of Tm^{3+} in GaAs by photoluminescence excitation spectroscopy. This luminescence transition is also used to study the incorporation of thulium into the GaAs lattice by angular dependent Zeeman spectroscopy.

INTRODUCTION

When thulium is introduced into various host crystals a characteristic 4f luminescence at $1.2 \mu\text{m}$ (1.0 eV) and $1.9 \mu\text{m}$ (0.68 eV) can be observed [1]. This emission is due to the Tm^{3+} charge state. The Tm^{3+} ion has a $4f^{12}$ electron configuration. By spin orbit coupling the electronic ground state ($L = 5, S = 1$) is threefold split into the 3H_6 , 3H_4 , and 3H_5 levels. The latter two are separated from the 3H_6 ground state by 0.68 and 1.0 eV, respectively. In III-V semiconductors each level is additionally split by the tetrahedral crystal field, when the ion occupies a simple substitutional lattice site. The electric dipole transitions $^3H_5 \rightarrow ^3H_6$ and $^3H_4 \rightarrow ^3H_6$ then give rise to both luminescence bands. The luminescence of Tm^{3+} in III-V semiconductors has recently been observed after Tm implantation by G. Pomrenke and coworkers [2, 3] and after doping during metal-organic vapor phase epitaxy (MOVPE) by K. Pressel et al. [4].

The intention of the present work is to investigate the lattice site on which Tm is incorporated into GaAs. For this purpose angular dependent Zeeman measurements on the $^3H_5 \rightarrow ^3H_6$ 1.0 eV luminescence were carried out. Another topic of the present study focusses on the excitation mechanism and the excitation efficiency of the characteristic 4f luminescence transitions $^3H_5 \rightarrow ^3H_6$ at 1 eV.

EXPERIMENTAL

For photoluminescence measurements the samples were excited by the 647 nm line of a krypton-ion laser. The light was dispersed with a 3/4m Spex grating monochromator and detected by a high sensitive Northcoast germanium detector. When high sensitivity was required a BOMEM DA3.01 Fourier spectrometer was used instead of the grating monochromator. Photoluminescence excitation (PLE) spectra were recorded by using a Titanium/sapphire laser which is tunable from 1100 to 700 nm wavelength. All PLE spectra were corrected for the spectral response of the laser. Zeeman measurements were carried out with a 3/4m Spex grating monochromator. Magnetic fields up to 7.5 T could be applied with a split-coil magnet, allowing measurements in Voigt and Faraday configuration (perpendicular and parallel to the magnetic field), respectively.

The samples were grown by MOVPE using $\text{Tris(isopropylcyclopentadienyl)Tm}$ as a doping source. The growth procedure is described elsewhere [5, 6]. A GaAs sample implanted with Tm was kindly supplied by G. Pomrenke (Air Force Office of Scientific Re-

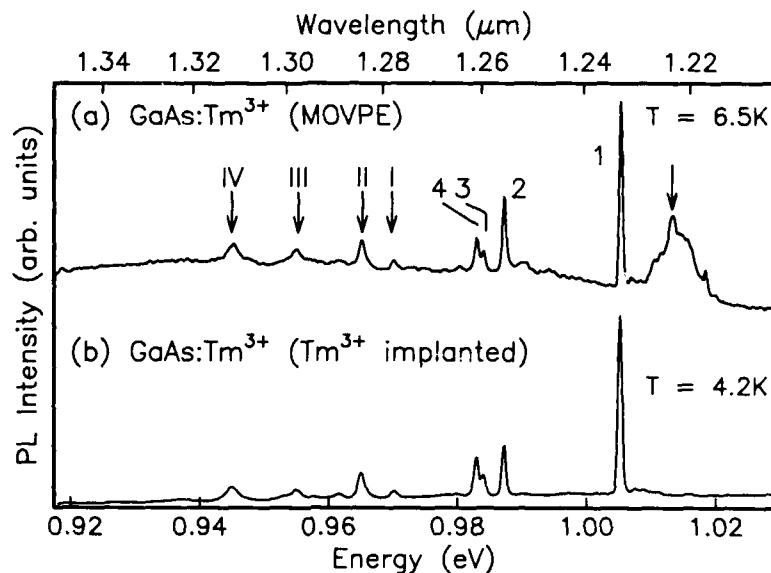


Figure 1: Luminescence spectra of the $^3H_5 \rightarrow ^3H_6$ transition of Tm^{3+} . (a) The sample was doped during MOVPE growth; (b) the sample was implanted with Tm.

search, Bolling AFB, DC). The implantation dose was $5 \cdot 10^{13} \text{ cm}^{-2}/390 \text{ keV}$. To reduce the implantation damage the sample was annealed at 750°C for 10 minutes.

PHOTOLUMINESCENCE MEASUREMENTS

Figure 1 shows the $^3H_5 \rightarrow ^3H_6$ luminescence spectra of two Tm-doped GaAs samples. For spectrum (a) the Tm ion was introduced during the MOVPE growth process, while the other sample was doped by implantation of Tm. The details of the spectra have been observed recently [3, 4]. Line 1 is due to a zero-phonon transition between the crystal field states of 3H_5 and 3H_6 . The identification of the other lines between 1.00 and 0.94 eV partly to LO phonon replica, higher excited crystal field states of the 3H_6 level, and to possible Tm-related complexes remained unclear.

The line spectra shown in Fig. 1 are superimposed on a spectroscopically broad background which is stronger in the MOVPE sample compared to the ion implanted sample. The line 2 is strongly temperature dependent. This line emerges stronger in the upper spectrum since the temperature was a little higher compared to spectrum (b). The halfwidth of the lines for both samples is less than $40 \mu\text{eV}$. The only difference between both samples is a broad feature peaking at 1.015 eV which only shows up in the MOVPE grown sample. Except this feature both line spectra are identical. This strongly suggests that all the lines 1 to IV belong to the same defect center. Thus, optically active Tm is mainly present in one specific center irrespective whether it is introduced by implantation or during the MOVPE growth process.

When line 1 is completely resolved a fourfold fine structure shows up, as already shown in Ref. [4]. In Fig. 2 this fine structure is depicted for two different temperatures. The components of the fourfold fine structure show different thermalization behavior. Over a certain temperature range the lines 1a and 1b stay constant while line 1c and 1d increase with raising temperature. It follows from the different thermalization behavior that both

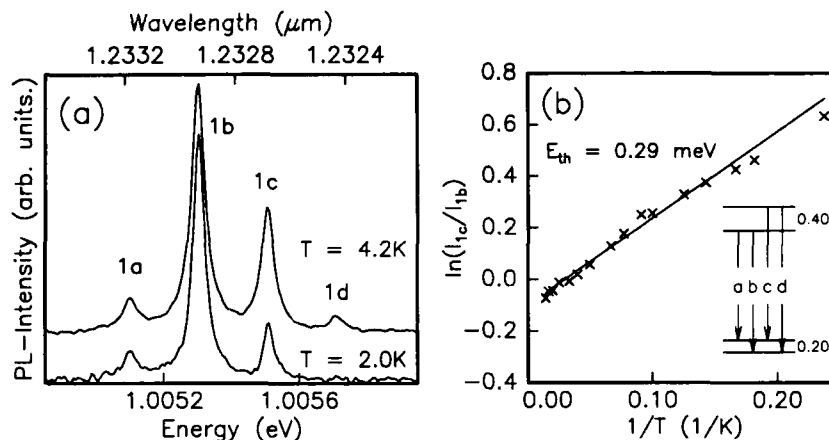


Figure 2: (a) Thermalization of the fine structure of line 1. Lines 1c and 1d increase with temperature, while lines 1a and 1b remain constant. (b) Arrhenius-diagram of the intensity ratio I_c/I_b . The level scheme shows the fine structure of line 1 (Energies given in meV).

ground state and excited state are twofold split. A level scheme is shown in the inset of Fig. 2. For a quantitative analysis the spectra were decomposed by fitting lines 1b and 1c to gaussian curves [lines 1a and 1d are too weak for an analysis and were omitted]. From the Arrhenius-type diagram [Fig. 2(b)] we compute an activation energy of $0.29 \pm .05 \text{ meV}$ from the intensity ratio I_c/I_b . This value deviates slightly from the expected 0.4 meV of the upper state splitting.

Theoretically, much more lines than found in line 1 are expected for Tm^{3+} occupying a simple substitutional lattice site in a tetrahedral environment. According to group theoretical considerations at low temperatures up to five lines should be observable from the lowest excited state to the 3H_6 levels [7, 8]. A part of the transitions may be among the lines 2 to IV. Higher excited states of 3H_5 are not thermally populated and the 3H_6 levels may be lifetime broadened by phonon scattering, so that they do not contribute to the luminescence spectrum. The fine structure of line 1 hints to an even lower symmetry of the defect studied here. The Zeeman measurement presented below evidences a considerable contribution of a crystal field with a symmetry lower than T_d .

ZEEMAN MEASUREMENTS ON LINE 1

The Zeeman measurements on the fine structure of line 1 presented here were carried out at the Tm-implanted sample. The sample had a [001] surface. When the angular dependence was recorded the magnetic field was always kept in the (1 $\bar{1}$ 0) plane. With an angular scan of 90° it was possible to cover the three important crystallographic directions [001], [111], and [110]. The measurements shown in Fig. 3 were carried out in Voigt configuration.

To each line of the fine structure a Zeeman component can be found which does not shift when the field is applied parallel to the [001] and the [011] direction, respectively. Another set of two components can be identified which are Zeeman active and show only little non-linearities for fields below 1 Tesla. One line shifts to higher energies and the other line moves to lower energies.

The angular dependence of the Zeeman effect is highly anisotropic. Due to the limited linewidth probably the lines are not fully resolved or detected. Despite this lack it is clear

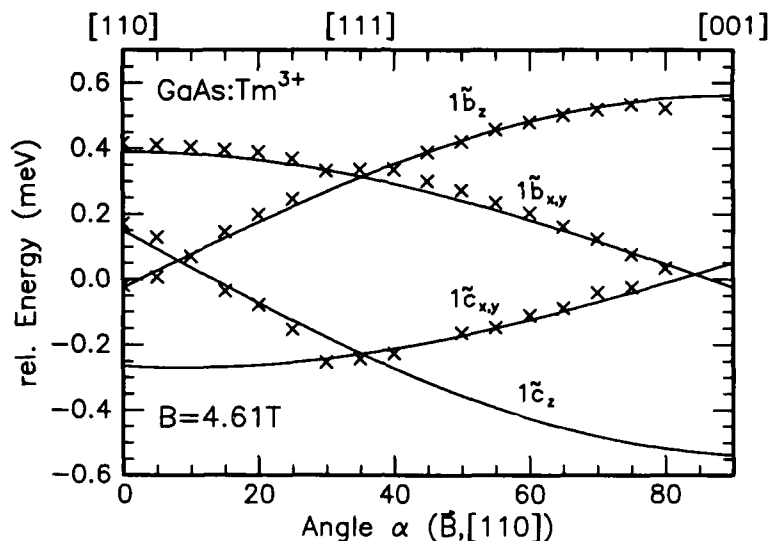


Figure 3: Zeeman effect of the fine structure of line 1. The Zeeman effect measured at constant field is plotted versus the angle between magnetic field and $[110]$ direction.

that the responsible defect has an axial symmetry and the several lines observed can only be explained by lifting the orientational degeneracy due to the applied magnetic field. Since the coincidence of Zeeman components occurs when the magnetic field is parallel to the $[111]$ direction, the actual center symmetry must be at least tetragonal (D_{2d} , $[001]$ -axial). Additionally, for the excited state and the ground state only g_z is non-zero while g_x and g_y vanish. The lines drawn in Fig. 3 have been modeled assuming a g -tensor of this type for the excited state and ground state. From the measured data a value $\Delta g = 2.1$ is found.

The Zeeman lines $1b_z$ and $1c_z$ as given in Fig. 3 originate from the center with the symmetry axis along $[001]$. The other lines $1b_{x,y}$ and $1c_{x,y}$ originate from centers with their symmetry axis along $[010]$ and $[100]$, respectively. The highly anisotropic g -tensor obtained here reflects the strong axial component of the crystal field which is active in the defect center. A similar case was reported previously for the $1.55 \mu\text{m}$ luminescence of Er^{3+} in GaAs [9]. According to crystal field theory the ground state of the 3H_6 in tetrahedral coordination should be either a Γ_2 or a Γ_3 level [8]. These states show no first order Zeeman splitting. Further lowering of the symmetry down to D_{2d} also does not yield states which are Zeeman-active in first order. The lowest 3H_5 sublevels should be Γ_5 or Γ_4 [8]. In the axial D_{2d} symmetry these states are split further into levels which are not Zeeman-active in first order, too. These circumstances may be responsible for the weak non-linearities found in the field dependence.

Though the Zeeman effect of line 1 is not completely resolved up to now it is clear that the defect center has at least axial symmetry D_{2d} (tetragonal). Better resolution is required to reveal completely the Zeeman effect of Tm^{3+} in GaAs. Measurements, which use the resolution power of the Fourier spectrometer, are in progress.

PHOTOLUMINESCENCE EXCITATION

To analyze the excitation mechanism of the 1.0 eV luminescence the PLE was measured on the most prominent feature of this transition, line 1. In Fig. 4(a) the PLE spectra of

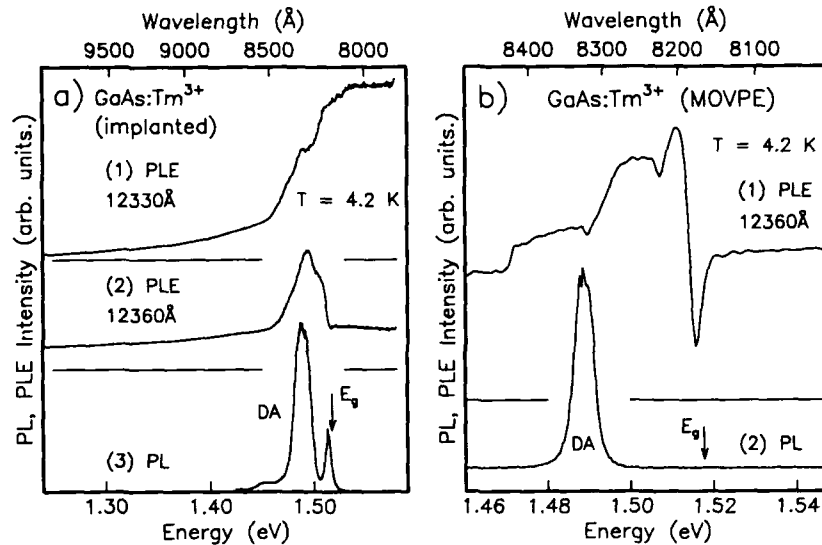


Figure 4: (a) PLE and PL of the Tm^{3+} -implanted sample. The PLE was monitored on line 1 (1) and on the background (2). The PL was performed using the 647 nm line of a Kr^{+} -ion laser (3). (b) PLE and PL of the Tm^{3+} -doped MOVPE sample. The PLE was monitored on the background of the line spectrum.

the Tm -implanted sample are displayed. Since the sharp line spectrum is superimposed on a spectroscopically broad background, the monitor wavelength was first set to the background ($1.236 \mu\text{m}$) [spectrum (2)]. Then the PLE spectrum of line 1 was recorded ($1.233 \mu\text{m}$). Spectrum (1) is the difference between the spectra taken at the monitor wavelength of $1.233 \mu\text{m}$ and $1.236 \mu\text{m}$. For comparison spectrum (3) shows the near-band-edge luminescence of the (unresolved) donor and acceptor bound excitons and the donor-acceptor (DA) recombination band.

As the most important fact the line spectrum seems to be pumped by another mechanism than the background. The PLE signal of the $1.233\text{-}\mu\text{m}$ line has its maximum for above band-gap excitation and drops down when the excitation energy is lower than the band gap energy. A tail extends down to a threshold of 1.26 eV . Differently, the PLE signal of the background spectrum is weak as long as the excitation energy exceeds the band gap. The PLE maximum is close to the peak of the DA recombination band. At energies below 1.46 eV the PLE signal decreases slowly without any further structure. No onset is observable down to the lower tuning limit of the titanium/sapphire laser (1.22 eV).

The PLE signal for the MOVPE-grown sample is more complicated. Line 1 is harder to observe since it is weaker and the background mentioned above provides a much larger contribution than in the implanted sample. Line 1 shows roughly the same trend as in the Tm -implanted sample. Fig. 4 (b) shows the PLE response at the spectroscopic position of the background. A strong dip occurs exactly at the position of the excitonic luminescence. Obviously the bound excitons generated by the pump light contribute mainly to non-radiative recombination channels. In the PL spectrum only the DA recombination band appears in the near-band-edge region. The excitonic luminescence seems to be suppressed by unintentional dopants, which act as efficient recombination centers.

Thus, we conclude that the ${}^3H_5 \rightarrow {}^3H_6$ emission is most efficiently pumped by the capture of excitons. This is in accordance with previous results on the characteristic $4f$ luminescence of $\text{InP}:\text{Yb}^{3+}$ at 1.23 eV [9]. Results from recent optically detected micro-

wave induced impact ionization experiments on the Yb^{3+} luminescence support this view [10]. For the background luminescence the importance of electrically active defects, which are introduced together with Tm, is evidenced by the sample dependent spectral shape of the PLE signal. Presently it is unclear whether the background is directly correlated to Tm^{3+} or not.

CONCLUSION

We have studied the excitation behavior of the characteristic $^3H_5 \rightarrow ^3H_6$ luminescence of Tm^{3+} in GaAs at 1.0 eV. We find that irrespective whether thulium is incorporated by implantation or during MOVPE growth, the Tm^{3+} ion is present mainly in one dominant optically active modification. Zeeman measurements revealed that the Tm^{3+} ion occupies a site of tetragonal symmetry (D_{2d}), which could be due to a distortion from the simple substitutional site to the [001] direction. The luminescence can be excited most efficiently by above band-gap excitation. The excitation of the Tm^{3+} -related background depends strongly on the doping process.

We thank M. H. Pilkuhn for his steady interest in our work. For supplying several Tm-implanted samples we are grateful to G. Pomrenke. We appreciate the technical support of our colleague B. Kaufmann. This work was supported by the *Deutsche Forschungsgemeinschaft* under contract no. Pi/71-23.

REFERENCES

1. S. Hufner, *Optical Spectra of Transparent Rare Earth Compounds* (Academic, New York, 1978) p. 4.
2. G. S. Pomrenke, Y. K. Yeo, and R. L. Hengehold, in *Long-wavelength semiconductor devices, materials, and processes*, edited by A. Katz, R. Biefeld, R. Gunshor, and R. J. Malik, (Mat. Res. Soc. Proc. **216**, Pittsburgh, PA, 1991) pp. 415-420.
3. G. S. Pomrenke, E. Silkowski, J. E. Colon, D.J. Topp, Y. K. Yeo, R. L. Hengehold, J. App. Phys. **71**, 1919 (1992).
4. K. Pressel, J. Weber, C. Hiller, D. Ottenwälder, W. Kürner, A. Dörnen, F. Scholz, K. Locke, D. Wiedmann, and F. Cordeddu, Appl. Phys. Lett. **61**, 560 (1992).
5. F. Scholz, J. Weber, D. Ottenwälder, K. Pressel, A. Dörnen, K. Locke, F. Cordeddu, and D. Wiedmann, J. Crystal Growth **124**, 470 (1992).
6. F. Scholz et al., this conference.
7. G. F. Koster, J. O. Dimmock, R. G. Wheeler, H. Statz, *Properties of the Thirty-Two Point Groups*, M.I.T. Press, Cambridge/MA, 1963).
8. K. R. Lea, M. J. M. Leask, W. P. Wolf, J. Phys. Chem. Solids **23**, 1381 (1962).
9. K. Thonke, K. Pressel, G. Bohnert, A. Stapor, J. Weber, M. Moser, A. Molassioti, A. Hangleiter, and F. Scholz, Semicond. Sci. Technol. **5**, 1124 (1990).
10. B. J. H. Liesert, M. Godlewski, A. Stapor, T. Gregorkiewicz, C. A. J. Ammerlaan, J. Weber, M. Moser, and F. Scholz, Appl. Phys. Lett. **58**, 2237 (1991).
11. K. Thonke, H. U. Hermann, and J. Schneider, J. Phys. C: Solid State Phys. **21**, 5881 (1988).

OPTICAL ACTIVITY OF Yb³⁺ IN MeV ION-IMPLANTED InP.

S. Uekusa*, A. Majima*, H. Katsumata*, Y. Noyori*, and M. Kumagai**

*Meiji University, Kawasaki, Kanagawa, 214 Japan

**Kanagawa High-Technology Foundation, Kawasaki, Kanagawa, 214 Japan.

ABSTRACT

For the evaluation of an implanted layer, photoluminescence (PL) and photoluminescence excitation (PLE) measurements, which are nondestructive and sensitive methods for identifying impurities and defects, were performed. Yb³⁺-related sharp luminescence was observed at a wavelength of 1002nm, due to the transitions which occurred between the spin-orbit levels $^2F_{5/2} \rightarrow ^2F_{7/2}$ of Yb³⁺ (4f¹³). Most efficient luminescence of Yb³⁺ was achieved at an excitation wavelength of around 880nm. The luminescence intensity of this peak (Yb³⁺) decreased with an increase in annealing temperature. Since the peak has not been observed for good samples in crystallinity, it may indicate that new, efficient energy transfer processes to rare-earth ions occur through the defect energy level. Especially, for the sample annealed at 600°C, Yb-related luminescence intensity excited by the photon energy below the band gap is about 3 times larger than that of excited by the photon energy above the band gap.

INTRODUCTION

The optical behavior of rare-earth (RE)-doped III-V compound semiconductors, such as GaAs and InP, has been attractive because of its sharp and temperature-independent emission due to intra-4f-shell transition of RE [1]. These features are very important in optoelectronic device applications, e.g., light-emitting diodes and laser diodes. Among the RE ions in III-V compounds, Yb-doped InP has been one of the most extensively studied materials in studies of the luminescence mechanism [2], because this material has two characteristic properties. For one thing an energy level scheme of the Yb-4f-shell is simple with only one excited state, for another Yb intra-4f-shell luminescence spectrum does not depend on the sample preparation methods: This luminescence spectrum has been observed in samples grown by liquid phase epitaxy (LPE) [3], metal-organic chemical vapor phase epitaxy (MOCVD) [4], molecular beam epitaxy (MBE) [5], as well as ion implanted samples [6][7]. This suggests that the Yb atoms occupy only one type of lattice site in InP. Zeeman effect measurements have revealed that the Yb³⁺ in InP is in a site of Td symmetry, probably substituting indium [8].

Whitney et al. [9] have observed that Yb forms an acceptor-like electron trap (AE trap) level at 30meV below the bottom of the conduction band. According to their proposed excitation model, the Yb-4f-shell is excited by an Auger-type transfer of energy from the recombining electron-hole pair at the AE trap. On the other hand, Kasatkin et al. [10] and Körber et al. [3] have proposed that the Yb-4f-shell is excited by the energy released through the recombination of donor-acceptor pair, and either by direct capture of an exciton or impact excitation by hot carriers, respectively.

In this work we investigated the annealing temperature dependence of photoluminescence excitation (PLE) and photoluminescence (PL) spectra of 2MeV Yb-implanted InP in order to clarify the influence of defects on Yb intra-4f-shell luminescence. The PLE spectra of Yb-related luminescence in InP annealed at temperatures ranging from 600°C to 650°C exhibited a novel peak at an excitation wavelength of around 880nm. This peak is most efficient luminescence of Yb^{3+} , increasing by approximately three times PL intensity for the above band gap excitation. A. Kozanecki et al. [11] have observed similar peak for PLE spectra of Yb-related luminescence in $\text{InP}_{0.93}\text{As}_{0.07}$. On the other hand, for InP:Yb samples grown by MOCVD method, the novel peak located at an excitation wavelength of around 880nm has not been observed [12]. Taking into consideration these matters, optical activity of Yb^{3+} in MeV ion-implanted InP is discussed based on experimental results.

EXPERIMENTAL PROCEDURE

Undoped LEC n-type (100) InP ($n=4.5 \times 10^{15}/\text{cm}^3$) was implanted with 2MeV Yb ions to a dose of $1 \times 10^{13}/\text{cm}^2$ at room temperature. The projected range (R_p) and Yb density at R_p are estimated at 400nm and $3 \times 10^{17}/\text{cm}^3$, respectively. After implantation, the samples were annealed at high temperatures, from 350°C to 750°C, for 15min with a face-to-face technique in a high-purity argon atmosphere. PL spectra were measured by using the 860nm line of a tunable Ti:Al₂O₃ laser as an exciting-light source. PLE spectra of Yb-related luminescence monitored at a wavelength of 1008nm line were measured by using a tunable (850nm~1000nm) Ti:Al₂O₃ laser as an exciting-light source. The luminescence was dispersed by a 1m double-grating monochromator, and it was detected with a liquid-nitrogen-cooled Ge p-i-n photodiode.

RESULTS AND DISCUSSION

Figure 1 shows the PL spectrum of 2MeV Yb-implanted InP sample, subsequently annealed at 600°C. The PL spectrum exhibits two intense peaks [Yb-related ($\text{Yb1}=1002\text{nm}$, $\text{Yb2}=1008\text{nm}$) and EDA (900nm)]. The sharply structured Yb-related luminescence is assigned to the intra 4f-4f transition $^2F_{5/2} \rightarrow ^2F_{7/2}$ of Yb^{3+} ($4f^{13}$). EDA corresponds to the energy of the donor-acceptor-recombination-related PL peak.

In order to optimize the luminescence intensity of Yb^{3+} , we investigated its annealing temperature dependence. Figure 2 shows the annealing temperature dependence of PL intensity of each peak. It is found that the recrystallization required to induce the optical activation tends to occur at annealing temperature of around 550°C. The Yb-related luminescence intensities remain constant at 600°C and above. On the other hand, the luminescence intensity of EDA, which is affected by crystallinity of host material, reaches the maximum at 550°C and then decreases with an increase in annealing temperature, though defects introduced by implantation should be removed with an increase in annealing temperature. This fact suggests that the recombination energy of EDA transfers to the Yb-4f-shell by an Auger effect, and gives rise to the luminescence of Yb^{3+} .

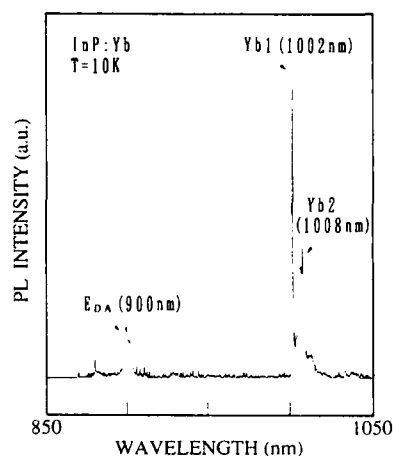


Figure 1. PL spectrum of 2MeV Yb-implanted InP, subsequently annealed at 600°C for 15min.

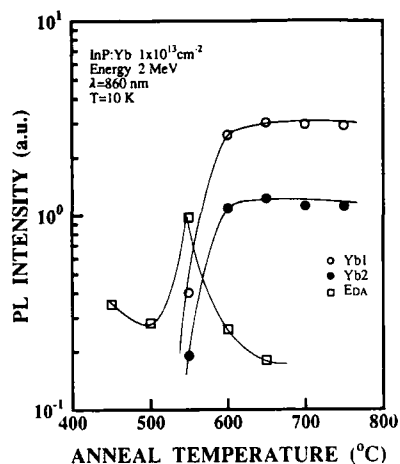


Figure 2. Annealing temperature dependence of PL intensity of each peak.

Figure 3 shows the annealing temperature dependence of PLE spectra of Yb-related luminescence (monitor:Yb2) at 10K. PLE spectra of Yb-related luminescence depend strongly on the annealing temperature and consist of four characteristic peaks [A=875nm (1.417eV), B=880nm (1.409eV), C=890nm (1.393eV), and D=877.5nm (1.413eV)]. The sharp peak A was observed for the samples annealed at 700°C and 750°C. This peak A results from the transition related to the band edge exciton. In the PLE spectra for the samples annealed at 700°C and 750°C, Yb-related luminescence intensity suddenly decreases below the band gap energy. This suggests that the Yb-related luminescence arises due to the energy transition from the host material to the Yb intra-4f-shell. The PLE spectrum feature for the sample annealed at 750°C has been also observed for the InP:Yb samples grown by MOCVD[12] or LPE methods, which can provide the high crystalline quality samples. As a consequence, we suspect that the defects introduced by implantation were almost removed through the annealing treatment at 750°C. Novel peaks, B,D were observed for the first time for InP:Yb samples. Especially, for the sample annealed at 600°C, Yb-related luminescence intensity excited by the photon energy below the band gap is about 3 times larger than that excited by the photon energy above the band gap. The luminescence intensity of the peak B decreases with an increase in annealing temperature. Hence, this may indicate that new, efficient energy transfer processes to rare-earth ions occur through the defect energy levels. These peaks, B,D have not been ever reported for InP:Yb samples, but A.Kozanecki et al. [11] have reported a peak similar to peak B for $\text{InP}_{0.93}\text{As}_{0.07}\text{:Yb}$ samples. The peak arises when the Yb intra-4f-shell luminescence is most efficiently excited with the laser wavelength tuned to an Yb-impurity level located at a depth of $28 \pm 2\text{meV}$ in the band gap, which is assigned to an Yb- P_3As complex. The energy of broad peak C, which has been also reported by K.Takahei et al.[12] and K.Thonke et al.[13], is clearly higher than that of the donor-acceptor-recombination-related PL peak. This peak C has been interpreted by K.Takahei et al. [12] as energy transfer between either valence band and AE traps-related states or acceptor level and conduction band.

In order to investigate about the peak B and the peak D in detail, we measured the annealing temperature dependence of PLE spectra of the donor-acceptor-recombination-related luminescence monitored at a wavelength of 900nm line. The results are shown in Fig.4. In the PLE spectrum for undoped InP sample, luminescence intensity reaches a maximum at a wavelength of 877.5nm and then decreases rapidly with a decrease in photon energy. This fact is due to the decrease of absorption coefficient for InP as the energy of excitation wavelength becomes lower energy than the band gap energy. In the PLE spectra for the samples annealed at temperatures ranging from 350°C to 650°C, peak d appears at a wavelength of 877.5nm. On the contrary, the luminescence intensity excited by the photon energy above the band gap is very weak in comparison with the luminescence intensity excited by the photon energy below the band gap. This fact suggests that the defect levels make it difficult to occur the energy transfer from the host material to donor-acceptor pairs. Peak b located at a wavelength of 880nm starts to appear with an increase in annealing temperature, and the luminescence intensity of this peak becomes dominant as compared to that of the peak d for the samples annealed at 700°C and 750°C. Similar tendency was observed in the case of PLE spectra of Yb-related luminescence, too. Therefore, we suppose that the peak b and the peak d shown in Fig.4 correspond to the peak B and the peak D shown in Fig.3, for the excitation processes, respectively.

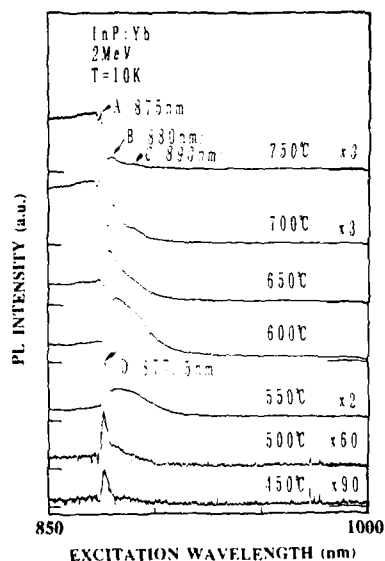


Figure 3. Annealing temperature dependence of PLE spectra of Yb-related luminescence (monitor: 1008nm line).

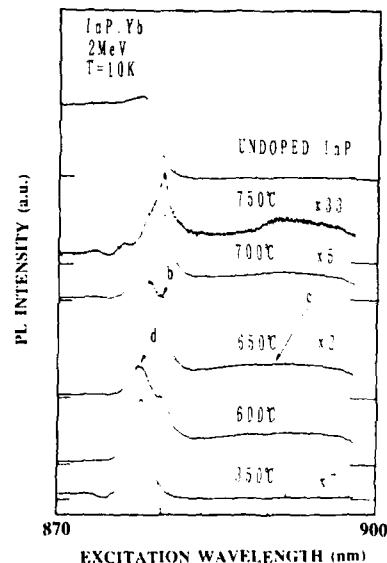


Figure 4. Annealing temperature dependence of PLE spectra of donor-acceptor pair luminescence (monitor: 900nm line).

Figure 5 shows the annealing temperature dependence of Yb-related (Yb2) luminescence vs inverse temperature. It is found that the high temperature annealing treatment suppresses the thermal quenching. In particular, it makes a significant difference between 650°C and 700°C. Since there is a significant difference between 650°C and 700°C in the case of PLE spectra of Yb-related luminescence, we consider that the defects in the host material are removed well between these temperatures.

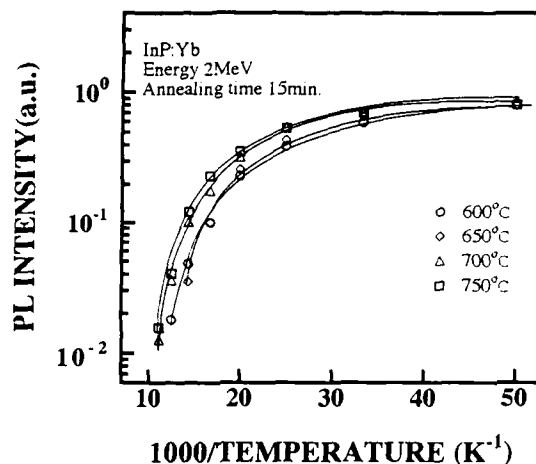


Figure 5. Annealing temperature dependence of Yb-related luminescence vs inverse temperature.

CONCLUSION

It was found that the recrystallization required to induce the optical activation of Yb³⁺ tends to occur at the annealing temperature of around 550°C. Furthermore, high efficient Yb-related luminescence at the excitation wavelength below the band-gap energy was observed due to the defects inside InP. The defect energy levels are considered to be located at a constant distance of about 4~8meV from the band gap. The PLE spectra of Yb-related luminescence and donor-acceptor-recombination-related luminescence depend strongly on the annealing temperature, and in both cases the emission peak with lower energy becomes dominant with an increase in annealing temperature. This indicates that both Yb-4f-shell and donor acceptor pairs are excited by energy transfer from the same levels, which are defect energy levels introduced by ion-implantation. Lastly, we confirmed the thermal quenching of Yb-related luminescence depends on the crystallinity of the host material.

ACKNOWLEDGMENTS

This work is supported in part by a Grant-in-Aid for Scientific Research from the Ministry of Education and Culture, Japan

REFERENCES

- (1) H. Ennen and J. Schneider, in: Proc. 13th Intern. Conf. on Defects in semiconductors, Coronado, CA (Metallurgical Society of AIME, New York, 1985) 115.
- (2) Akihito Taguchi, Hiroshi Nakagome, and Kenichiro Takahei, J. Appl. Phys. **70**, 5604 (1991).
- (3) W. Körber and A. Hangleiter, Appl. Phys. Lett. **52**, 114 (1988).
- (4) H. Nakagome, K. Uwai, and K. Takahei, Appl. Phys. Lett. **53**, 1726 (1988).
- (5) R. S. Smith, H. D. Müller, H. Ennen, P. Wennekers, and M. Maier, Appl. Phys. Lett. **50**, 49 (1987).
- (6) H. Ennen, G. Pomrenke, and A. Axmann, J. Appl. Phys. **57**, 2182 (1985).
- (7) A. Kozanecki and R. Groetzschel, J. Appl. Phys. **68**, 517 (1990).
- (8) G. Aszodi, J. Weber, Ch. Uhleihn, L. Pu-Lin, H. Ennen, U. Kaufmann, J. Schneider, and J. Windscheiff, Phys. Rev. **B31**, 7767 (1985).
- (9) P. S. Whitney, K. Uwai, H. Nakagome, and K. Takahei, Appl. Phys. Lett. **53**, 2074 (1988).
- (10) V. A. Kasatkin and V. P. Savel'ev, Sov. Phys. Semicond. **18**, 1022 (1985).
- (11) A. Kozanecki, K. Karpinska, and Z. Kalinski, Appl. Phys. Lett. **62**, 84 (1993).
- (12) K. Takahei, A. Taguchi, H. Nakagome, K. Uwai, and P. S. Whitney, J. Appl. Phys. **66**, 4941 (1989).
- (13) K. Thonke, K. Pressel, G. Bohnert, A. Stapor, J. Weber, M. Moser, A. Molassioti, A. Hangleiter, and F. Scholz, Semicond. Sci. Technol. **5**, 1124 (1990).

PREPARATION AND PROPERTIES OF GALLIUM PHOSPHIDE DOPED BY RARE-EARTH ELEMENTS

SERGEI L. PYSHKIN* AND ALBERTO ANEDDA**

*Institute of Applied Physics, Academy of Sciences, Academy Str.5, 277028 Kishinev, Moldova

**Department of Physics, University of Cagliari, Ospedale Str. 72, I-09124 Cagliari, Italy

ABSTRACT

GaP single crystals have been grown from 5at.% solution of P in Ga with (0.01-0.1)at.% of La, Sm or Gd as dopants. Electric properties, photoconductivity and luminescence of the crystals have been investigated by standard methods.

Energy levels of impurities, mobility and concentration of current carriers have been determined in wide temperature region. It was shown that nitrogen (N) and other uncontrolled impurities present in the crystals due to some peculiarities of crystal growth. The intrinsic RE impurity luminescent spectra can be seen only together with spectra of excitons bounded on N traps. The evaluation of quantum efficiency for RE impurity made on the base of luminescence decay measurements gives the value close to 1. The interpretation of GaP:RE luminescence spectra is presented as intrashell transitions activated by bound exciton recombination as well as D-A and D-valency band transitions between some contaminating impurity (donor) and RE element (acceptor).

INTRODUCTION

The results on luminescence of GaP doped by elements of II (acceptors) and VI (donors), III and V (isoelectronic traps) groups demonstrate the unique properties of this semiconductor which are useful for development of basic models of irradiational recombination mechanisms through bound excitons and donor-acceptor pairs. It should be noted that the set of possible irradiational transitions as well as other prospective properties of GaP can not be realized completely on the base of the mentioned above dopants. Indeed, the quantum efficiency of the GaP light emitting diodes is very low up to now due to the non-radiational thermal processes as well as due to the low degradation parameters. It is obvious, that for GaP and other broad-band semiconductors the best impurities are those which create the irradiational transitions effective up to the room temperature. The most interesting are the intrashell transitions in Rare-Earth (RE) elements which are well screened from the influence of crystal field and temperature. The electronic states of some of these elements (Sm, for instance) are very well match with the band structure of GaP as well as with bound exciton states in this material.

A laser system in which the centers of recombination and activators are uniformly intermixed in a crystal matrix was proposed by Bell in 1963 [1]. In such a system the recombination of non-equilibrium electron-hole pairs creates photons which are effectively absorbed by the activation centers. In semiconductors with indirect band gap, such as GaP, the irradiational transitions between valency and conduction bands are suppressed, so the efficiency of activator excitation could be as high as 100%. It was especially interesting to investigate the luminescence and the other properties of GaP:N:RE system because GaP reveals a stimulated emission through bound excitonic states [2] and can be doped simultaneously with nitrogen by some Rare-Earth elements [3].

EXPERIMENTAL DETAILS

GaP:RE single crystals have been obtained by the method of slow cooling, diluted solution of P in Ga. Optical quality silica tubes and pure components (95at.% of Ga, appr.5at.% of P and appr.0.01at.% of RE element) were chosen for the crystal preparation. All the crystals except RE element contained up to 10^{17} cm^{-3} of the nitrogen (N).

Perfect platelet crystals have been taken for the investigation by standard methods of conductivity and the Hall effect in 80-750K temperature interval using ohmic contacts to the samples and the magnetic field up to 1T.

The luminescence spectra were obtained using the double-photon excitation by a Q-switched Ruby laser (the photon energy - 1.78eV, the pulse duration - 35ns and the light intensity - up to $10^{27} \text{ cm}^{-2} \text{ s}^{-1}$). Such kind of excitation supplies an uniform bulk pumping of the sample with the non-equilibrium electron-hole concentration up to 10^{16} cm^{-3} [4]. A grating monochromator, a PMT, a boxcar-integrator and a X-Y recorder have been used for registration of the luminescence spectra.

RESULTS

Fig.1 and Fig.2 show the temperature dependences of the normalized Fermi level (η) and the Hall coefficient (R) respectively. An extraction from these measurements is presented in Table I.

Table I. Some properties of GaP:RE

Sample	Type of conductivity	Concentration of carriers, cm^{-3}	Mobility, $\mu = [R \cdot T]$, $\text{cm}^2 \text{ V}^{-1} \text{ s}^{-1}$
GaP:N:Sm	p	$(1-2)10^{17}$	80-170
GaP:N:Gd	p	$(1-5)10^{18}$	10-90
GaP:N:La	p	$(5-6)10^{18}$	30

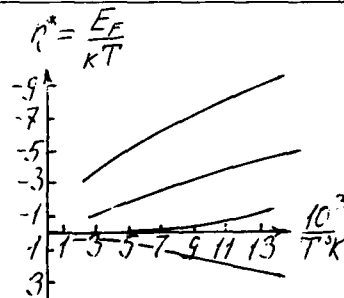


Fig.1. The normalized Fermi level-temperature relationship.
1. GaP:N:Sm. 2. GaP:N:Gd,
 $p = (1-2)10^{18} \text{ cm}^{-3}$. 3. GaP:N:Gd,
 $p = (3-5)10^{18} \text{ cm}^{-3}$. 4. GaP:N:La.

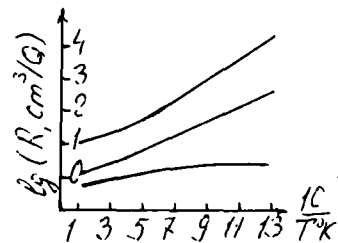


Fig.2. The Hall coefficient-temperature relationship.
1. GaP:N:Sm. 2. GaP:N:Gd, 3. GaP:N:La

The normalized Fermi level η^* was obtained from the equation:

$$p = N_v F_{1/2}(\eta^*) \quad (1)$$

where N_v - the density of states in valency band and $F_{1/2}(\eta^*)$ - the Fermi-Dirac integral tabulated in [5]. Fig.1 shows that GaP:N:Gd crystals having the hole concentration $\text{appr. } 5 \times 10^{18} \text{ cm}^{-3}$ (300K) are close to degeneration, GaP:N:La crystals are degenerated while the hole behavior in GaP:N:Sm can be described in framework of classic statistics. The activation energies of acceptors determined as the slope of the dependence:

$$\lg(RT^{3/4}) \sim F(1/T), \quad (2)$$

where R - the Hall coefficient, are 0.11eV and 0.15 eV for GaP:N:Sm, 0.07eV for GaP:N:Gd. Due to the hole degeneration in GaP:N:La the impurity activation energy can not be determined.

These data demonstrate that GaP doped by Sm, Gd or La has p-type of conductivity, the hole mobility considerably depends on the level of the dopant concentration and the activation energies are different for the doping elements.

The investigation of the spectral distribution of photoconductivity gives some additional information about band-to-band and impurity transitions, while the induced impurity photoconductivity promotes to a clear establishment of the transitions between impurity states. Particularly, an additional acceptor level with the activation energy of $\text{appr. } 0.25\text{eV}$ has been discovered by this method.

GaP:N:Gd as well as GaP:N:La excited by low intense light sources did not have any remarkable luminescence except a broad luminescence band centered at 1.9eV. The same broad band presents also in GaP:N:Sm but this sample develops also a set of characteristic luminescence lines at 1.96-2.25 eV (see Fig.3).

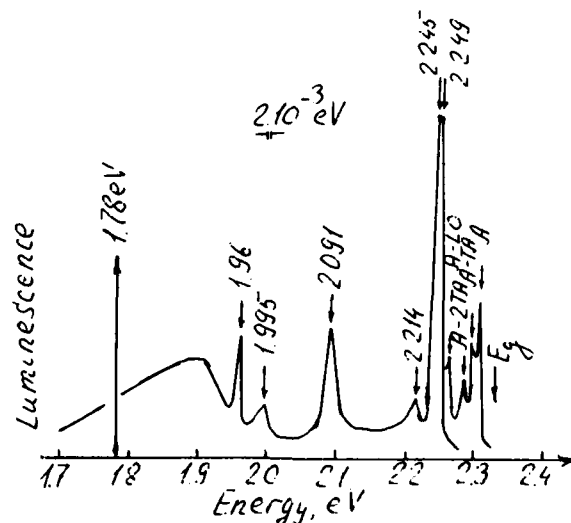


Fig.3. The luminescence spectrum of GaP:N:Sm at 300K. The position of the excitation line at 1.78eV is indicated by the vertical line. The intensity of the A-line and its phonon replica is increased by factor 5.

Fig.3 shows that the luminescence spectrum of GaP:N:Sm consists of the bound exciton lines (A, A-TA, A-2TA and A-LO) at 2.26-2.31 eV (GaP:N system, see [6]) as well as it contains the new lines at 1.96, 1.995, 2.091, 2.214, 2.245 and 2.249 eV [7] and the above noted broad band centered at 1.9eV. Note that the intensity of the GaP:N lines (the no-phonon line and its phonon replica; excitons, bound to N impurity atoms) is two order less than in undoped by Sm impurity GaP:N with the same N concentration measured under the same level of double-photon excitation. One can see from Fig.3 that not all of 6 new lines have the equal shape. For instance, the low intense lines at 1.995 and 2.214 eV have the shape like to phonon replica, while the other 4 lines are symmetrical and narrow. The double line at 2.25eV is splitting at 4.2K into 5 narrow lines with the halfwidth less than 1meV (Fig.4).

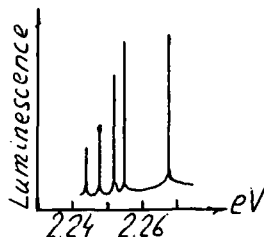


Fig.4. A part of GaP:N:Sm. spectrum at 4.2K

The radiative life time τ , measured in the region 1.95-2.25eV on the luminescence decay at 77.3K is less than 50ns. It corresponds to the oscillator strength:

$$f = mc^3/8\pi^2 e^2 \nu^2 \tau \approx 10^{-1} - 10^{-2} \quad (3)$$

at the quantum efficiency which is nearly equal to 0.1-1.0. On the other hand for the broad band centered at 1.9eV the parameter τ is equal to a few seconds at 77.3K or tens of seconds at 4.2K.

DISCUSSION

The results presented in the recent paper reveal several novel aspects of GaP properties: (1) new acceptor levels obeyed to Gd (0.07eV) and Sm (0.1, 0.15 and 0.25eV), (2) broad luminescence band at 1.9eV for GaP:N:Sm and analogical broad bands for the other GaP:RE and (3) mechanism of irradiational recombination in GaP through N isoelectronic traps and RE impurities uniformly intermixed in the crystal.

Energy of activation

It should be noted that all of the RE elements have 2 electrons in outer shell, so they act in GaP, substituting the host P atoms, as acceptors. These elements at high temperature of melting solution are very chemically active, therefore they intensively interact with the walls of the silica tube during the crystal growth process. As a result of such an interaction some uncontrolled impurities such as Si (0.08eV), O (0.40eV), S (0.13eV) can dope additionally GaP crystals. Of course, it is a disadvantage of the growth method but another method which could produce GaP crystals with an intense characteristic luminescence of RE impurity is yet unknown. Therefore the intrinsic RE element impurity luminescence could be seen only on the background of the broad luminescence band originating from donor-acceptor recombination between the states of uncontrolled impurities or intrinsic GaP bands and RE elements acting as acceptors.

Broad luminescence band at 1.9eV

The band with unusually large halfwidth is constantly present in doped

GaP. We suppose, that the position of the band as well as its halfwidth can be explained in framework of multi-phonon theory applicated to the cases of donor-acceptor and impurity-band recombination [8]. It seems that the main contribution in the band formation gives the donor levels creating by O and S and the deep acceptor level of Sm (0.25eV). The expression for activation energy of an impurity level taking into account both the polaron and the condensation effects according to the disturbance theory is:

$$J_s = -E_s^0 - 1/2 \chi q_{\chi s}^2 \hbar \omega - 1/2 \phi Q_{\phi s} \hbar \omega_s, \quad (4)$$

where $q_{\chi s}$, $Q_{\phi s}$ - the steady-state magnitudes of acoustic and optic vibration magnitudes, E_s^0 - the activation energy of a hydrogen-like impurity center having Z^* effective charge. For the case of GaP this equation has the following simple form:

$$J_s = (4.55 Z^{*2} - 0.61 Z^* - 5.1 Z^{*3}) \quad (5)$$

Substituting into the eq.(4) the known magnitudes of Z^* of the above noted uncontrolled impurities one can obtain their activation energies. Then, the position of the band in the spectrum is:

$$\hbar \omega_{\max}^{\text{lum}} = E_g - (J_1 + J_2) - [(\delta \Omega^{\text{opt}})^2 / 8 \ln 2 \hbar \omega_{\text{opt}} + (\delta \Omega^{\text{ac}})^2 / 8 \ln 2 \hbar \omega_{\text{ac}}], \quad (6)$$

where E_g - the energy gap; J_1 , J_2 - the activation energies of donors and acceptors; ω_{ac} , ω_{opt} - the mean frequencies of acoustic and optic phonons in GaP and $\delta \Omega^{\text{opt}}$, $\delta \Omega^{\text{ac}}$ - the halfwidth of luminescence band at electron interaction with optical and acoustic phonons. The expressions for the halfwidth of the luminescence band have the form:

$$\Sigma \delta \Omega = [(\delta \Omega^{\text{ac}})^2 + (\delta \Omega^{\text{opt}})^2]^{1/2}, \quad (7)$$

$$\delta \Omega^{\text{ac}} = 2 \hbar [2 \ln(2 d^2 \mu^4 e^8 Z^{*4} / 3 \pi \hbar^9 \epsilon^4 v_1 \rho)]^{1/2}; \quad (8)$$

$$\delta \Omega^{\text{opt}} = 2 \hbar \omega_{\text{opt}} [5 Z^* \mu e^4 / 8 \hbar^3 \epsilon \omega_{\text{opt}} (1/\hbar^2 - 1/\epsilon) \ln 2]^{1/2}, \quad (9)$$

where $\mu=0.35m$ - the electron effective mass, $d=55\text{eV}$ [9] - the deformation potential, $\epsilon=10.18$ [10] - the static dielectric constant, $n=2.9$ [11] - the refraction index, $v_1 = 6 \times 10^5 \text{ cm/s}$ [12] - the longitudinal sound velocity, $\rho = 4.13 \text{ Gr/cm}^3$ [13] the specific crystal density. Substituting into the eqs.(7-9) the respective magnitudes of Z^* as well the other parameters one can obtain for the cases of simultaneous recombination between deep donors (O) - valency band and S (donor, 0.13eV) - Sm (acceptor, 0.25eV) the total halfwidth $\Sigma \delta \Omega \approx 0.2\text{eV}$ that coincides with the experimental data.

Recombination mechanisms through N traps and Sm

It is known that in GaP non-equilibrium electron-hole pairs recombine mainly through the bound exciton states created by N isoelectronic traps substituting P in the crystal lattice. Indeed, the cross-section of the bound exciton creation, determined by us from the experiments on thermal quenching of radiation, is anomalously large, namely, it is equal to $10^{-12} - 10^{-13} \text{ cm}^2$ [14]. Photons with the energy 2.26-2.32eV, irradiated in the bound exciton annihilation (the no-phonon line A and its phonon replica), at the presence in the crystal matrix of Sm impurity must be effectively absorbed by the latter, because this element has an intense absorption band at

the region $\geq 2.2\text{eV}$ which is transparent for GaP. Then this absorbed energy will be re-emitted by Sm ion electronic states in the region of 1.8-2.2eV[15].

GaP:N:Sm system reveals a very intense luminescence at a high quantum efficiency in the region of Sm ion electronic states (probably, 4f-shells of Sm^{3+}) and two order less luminescence intensity of bound excitons (comparing with GaP:N crystals having the same N concentration at the same excitation level). One can suppose that the excitation transfer from the recombination centers (N) to the activators (Sm) takes place at the double-photon light absorption. Note that at bulk double-photon absorption with a low absorption coefficient ($10^{-3}\text{-}1\text{cm}^{-1}$ at $10^{24}\text{-}10^{27}\text{cm}^{-2}\text{s}^{-1}$ of light intensity) can be actual also the direct excitation of activators through the absorption bands of Sm ions at 3.6eV that corresponds to the energy of two Ruby laser photons.

SUMMARY

In conclusion, we have extended investigations of GaP, doped by RE elements. Even under bad growth conditions provoking contamination of crystals by uncontrolled impurities due to an interaction of chemically active melt solution with the walls of a silica tube it is possible to establish some characteristic properties of RE elements in GaP. Reviewing various explanation for irradiational recombination in GaP:N:Sm, we propose that it originates from donor(S)-acceptor(Sm) and deep donor(O)-valency band transitions (the broad band at 1.9eV) as well as from intrashell transitions in Sm ions activated by bound exciton annihilation.

ACKNOWLEDGEMENTS

It is pleasure to thank Professor V.A.Kovarsky for many interesting discussions on multi-phonon theory as well as Dr.V.Budyanu and Dr.A.Mura for their help in the experiments.

REFERENCES

1. R.Bell, J.Appl.Phys.34, 1563 (1963)
2. S.L.Pyshkin, DAN SSSR 219, No.6, 1345 (1974), [Sov.Doklady 219 (1974)]
3. S.L.Pyshkin et al. Fiz. Tekn. Poluprovodn. 1, 1013 (1967), [Sov. Phys. Semicond. 1 (1967)]
4. B.M.Ashkinadze, S.L.Pyshkin et al. Fiz. Tekn. poluprovodn. 1, 1017 (1967) [Sov. Phys. Semicond. 1 (1967)]
5. McDougall and E.Stoner, Phil. Trans. R. Soc. A237, 67 (1938)
6. S.L.Pyshkin et al., Opto-Electronics 2, 245 (1970)
7. S.L.Pyshkin, Fiz. Tekn. Poluprovodn. 8, 1397 (1974), [Sov. Phys. Semicond. 8 (1974)]
8. V.A.Kovarsky and S.L.Pyshkin, Bull. Mold. Ac. Scie. 12, 63 (1968)
9. E.Haga and H.Kimura, J. Phys. Soc. Jap. 19, No.5, 658 (1964)
10. D.A.Kleinman and W.G.Spitzer, Phys. Rev. 118, 110 (1960)
11. F.Oswald, Z. Naturforsch. 10A, 927 (1957)
12. D.A.Kleinman, Phys. Rev. 118, 118 (1960)
13. P.Aigrain and M.Balkanski in Selected Constants Relative to Semicond. (Pergamon, New York, 1961)
14. B.M.Ashkinadze, I.P.Kretsu, S.L.Pyshkin et al. Fiz. Tverd. Tela, 10, 3681 (1968), [Sov. Phys. Solid State, 10 (1968)]
15. P.Goerlich, H.Karras, G.Koetitz and R.Leman, Phys. stat. sol. 5, No.3, 454 (1964)

ESR OF RARE EARTH IMPURITIES (Dy^{3+} , Er^{3+} , Yb^{3+}) IN THE NARROW GAP SEMICONDUCTOR PbTe .

A.M. GENNARO*, G.B. MARTINS*, C. RETTORI *, G.E. BARBERIS* and C.Y. AN**

*Instituto de Física, UNICAMP, CP 6165, 13081, Campinas (SP), Brazil

**Instituto Nacional de Pesquisas Espaciais, INPE, CP 5125, 12201, São José dos Campos (SP), Brazil.

ABSTRACT

Electron Spin Resonance experiments of several diluted rare-earths (Dy^{3+} , Er^{3+} , Yb^{3+}) in the narrow gap semiconductor PbTe show ground states appropriated with a cubic crystal field splitting of the lowest multiplet (\bar{J}). The data permits the determination of the sign and ratio of the cubic crystal field parameters $A_4 \langle r^4 \rangle$ and $A_6 \langle r^6 \rangle$. These results suggest that the rare-earths substitute the Pb^{2+} ions and that the crystal field is mainly associated to an octahedron of Te^{2-} ions. The observed ESR spectra also show lower symmetry sites probably associated with nearest neighbor Pb^{2+} vacancies.

I - INTRODUCTION

Electron Spin Resonance (ESR) studies of non-S state rare-earths (RE) in many insulating [1-5] and metallic hosts [6-16] have been already a subject of extensive studies during the last few decades. However, only few works were reported in semiconducting hosts [17-20]. The semiconducting materials have many properties intermediate between those of insulators and metals. Recently, investigations of the possibility of the electrical excitation of internal 4f-4f emission have been undertaken with promising results [21]. All the trivalent and divalent RE have states in the visible or infrared except S-state ions (Gd^{3+} and Eu^{2+}) whose gaps are well into the ultraviolet. Although PbTe is not a candidate for studying optical properties of RE due to its narrow gap (0.19 eV at 4 K) [22], the systematic study of ESR of diluted RE has considerable interest with respect to magnetic and transport properties as well as interaction between localized and mobile spins [23]. This work will describe results of the dopants Dy^{3+} ($6\text{H}_{15/2}$ ground state), Er^{3+} ($4\text{I}_{15/2}$) and Yb^{3+} ($2\text{F}_{7/2}$) in PbTe .

II - EXPERIMENTAL

Single crystals were stoichiometrically prepared from Pb and Te with nominal purity of 99.9999% and from rare earths of 99.9%. The synthesis of the master alloy ($\text{Pb}_{1-x}\text{RE}_x$)Te ($x=0.005$) was carried out in a quartz ampoule evacuated at 5×10^{-6} Torr that was kept at temperature of 950°C during 24 hours. A rapid cooling was performed to avoid an inhomogeneous distribution of the magnetic impurities. The Bridgman method was used to grow the single crystals, (NaCl structure $a_0=6.46$ Å) which were oriented in the [110] direction using the Laue method and then cut and polished in the form of prisms of approximate dimensions of $(15 \times 2.5 \times 2.5)\text{mm}^3$.

X-band ($\nu = 9$ GHz) ESR measurements were performed in a conventional Varian E-15 spectrometer using a tail liquid helium cryostat adapted to a TE_{102} cavity, allowing the sample temperature to be varied from 1.6 to 4.2 K. The magnetic field was always rotated in the (110) plane of the sample. We took care to keep the microwave power and modulation frequency low enough to avoid saturation and time dependent effects. Similarly to $\text{Pb}_{1-x}\text{Gd}_x\text{Te}$ [24] we observed, at low temperatures ($T \approx 2\text{K}$), high microwave power ($P_{\mu\lambda} > 1\text{mw}$) and high modulation frequency ($f_{\text{mod}} > 1\text{KHz}$), an out-of-phase ESR signal. This out-of-phase signal,

which has approximately the same intensity than the in-phase one, is being at the moment a subject of investigation in our group.

Hall effect measurements in undoped samples at 77 K showed p-type conductivity, probably due to Pb vacancies [25, 26], carrier concentration $n_p = 10^{10} \text{ cm}^{-3}$, Hall mobility $m_H = 12000 \text{ cm}^2 (\text{V.s})^{-1}$ and Hall resistivity $r_H = 3 \times 10^{-4} \text{ W cm}$.

Since the electrical conductivity of PbTe is relatively high even at low temperatures [27], we expect skin depth effects. Dysonian ESR lineshape, characteristic of conducting materials, were observed in all cases [28]. Thus, the observed spectra come from magnetic ions within the skin depth ($\approx 10 \mu$) which may be seriously affected by the mechanical polishing procedure. To avoid the effect of possible lattice distortions, an electrochemical etching was performed, which removed several microns of the damaged sample surface. Except for 10-40 % narrower lines, the ESR spectra were not affected by the etching. This indicated that the lattice distortions produced by the mechanical cut and polishing of the crystal surfaces will not be relevant for our analysis.

III - RESULTS AND ANALYSIS

1. $\text{Pb}_{1-x}\text{Er}_x\text{Te}$

Fig. 1 shows the ESR spectra of Er^{3+} in PbTe for the magnetic field along the [100], [111] and [110] directions. We attribute the intense line to the ^{166}Er ($I=0$) isotope, and the satellites to the hyperfine structure of the ^{167}Er ($I=7/2$) isotope with natural abundance of 23%. This identification is based on the good agreement obtained between the relative line intensities and isotopes natural abundance. Also the hyperfine constant estimated for various orientations ($^{167}\text{A} = 75 \pm 2 \text{ gauss}$) agrees with that obtained for ^{167}Er in other cubic materials (29, 30). The temperature dependence of the ESR intensity between 4.2 and 1.6K showed that the spectra correspond to transitions within the ground state multiplet. No temperature dependence of the linewidth was observed in this interval. Fig. 2 shows the angular dependence of the g-value in the (110) plane, obtained from the intense line ($I=0$) after Dysonian lineshape analysis [28]. For magnetic field orientations around the [111] direction, the spectra show a complicated broadening, splitting and also new hyperfine lines. A set of extra low field ($<1500\text{G}$) lines showing lower symmetry features, were also observed, indicating the presence of lower symmetry Er^{3+} ion sites. At the moment all these effects are subject of separated studies

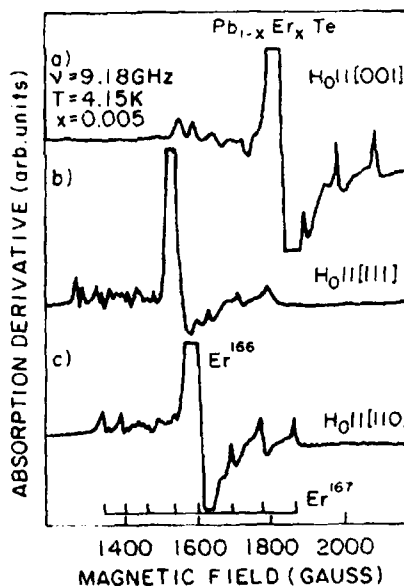


Fig. 1- ESR spectra of the most intense line of Er^{3+} in PbTe, along the principal cubic axes. (a) = [001], b = [111], c = [110]

The crystal field Hamiltonian for a non-S RE ion in cubic symmetry can be written [32]

$$\hat{H}_{CF} = B_4[O_4^0(\vec{J}) + 5O_4^4(\vec{J})] + B_6[O_6^0(\vec{J}) - 21O_6^4(\vec{J})] \quad (1)$$

where the $O_n^m(\vec{J})$ are the Stevens' operators, and $B_4 = \beta_J A_4 \langle r^4 \rangle$, $B_6 = \gamma_J A_6 \langle r^6 \rangle$, where β_J , γ_J are reduced matrix elements [32] and $A_4 \langle r^4 \rangle$, $A_6 \langle r^6 \rangle$ are the fourth- and sixth-order crystal field parameters. Following Lea et al. [32] the parameters W and x are defined as

$$B_4 F(4) = Wx \quad (2a)$$

$$B_6 F(6) = W(1 - |x|) \quad (-1 < x < 1) \quad (2b)$$

$F(4)$, $F(6)$ are numerical factors tabulated in [32]. W is proportional to the overall crystal field splitting for the given J multiplet while x depends on the ratio of the fourth- and sixth-order crystal field parameters.

In the case of Er^{3+} the crystal field splits the ground state multiplet, $J = 15/2$, into three quartets (Γ_i , $i = 1, 2, 3$) and two doublets (Γ_6 and Γ_7). The crystal field ground state and the level ordering are determined by the sign and magnitude of $A_4 \langle r^4 \rangle$ and $A_6 \langle r^6 \rangle$. The wave functions and the energy levels, as a function of x , for the $4f$ configurations are tabulated in [32]. When the decomposition of a given J multiplet contains more than one Γ_8 , these states are anisotropic in the presence of an external magnetic field. This anisotropy

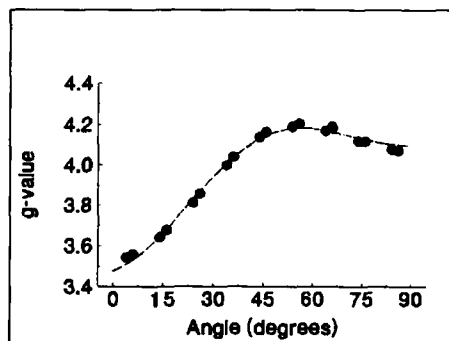


Fig. 2- g-value anisotropy of the strong resonance ($l=0$) shown in Fig. 1. The magnetic field is rotated in the (110) plane. The dashed line is the best fit of the calculation (see text) to the experimental data

was studied by Ayant et al. [33], in the spirit of the effective spin Hamiltonian of the ground Γ_8 quartet, neglecting admixtures between different crystal field states via magnetic field. Alternatively, we preferred to consider the whole $J = 15/2$ multiplet, and, including the Zeeman effect and eq. (1), performing a complete diagonalization of the 16×16 matrix. The experimental g -values were fit to the energy difference between the obtained lower levels, using a minimization program for non-linear parameters to perform the calculation. Fitting parameters were g_J , x and W . As can be seen in fig. 2, we got very good agreement between the theory and the experimental data. The value obtained for W , positive, give us a minimum value of 100 K for the overall crystal field splitting. The fitting becomes insensitive to increases of W . We obtain $x = 0.65 \pm 0.005$ and $g_J = 1.18 \pm 0.005$, which shows the well-known reduction in the Landé parameter, generally attributed to covalency effects [3]. We obtain from this fitting both A_4 and A_6 positive, and the ratio $A_4 \langle r^4 \rangle / A_6 \langle r^6 \rangle = 20.0 \pm 0.5$, that will be used below.

2 $\text{Pb}_{1-x}\text{Dy}_x\text{Te}$

Figure 3 shows the ESR spectrum of Dy^{3+} in PbTe at 4.2K with the magnetic field along the $[111]$ direction. The most intense resonance corresponds to ^{164}Dy ($I=0$) isotope and the satellites or hyperfine structure can be clearly assigned, as indicated in the figure, to the ^{163}Dy ($I=5/2$) and ^{161}Dy ($I=5/2$) isotopes, with hyperfine constants $^{163}A=84.5 \pm 1$ gauss and $^{161}A=59.4 \pm 1$ gauss respectively. Fig. 4 shows the angular variation of the g-value for the main line ($I=0$) extracted after a Dyson lineshape analysis. The linewidth was anisotropic and temperature independent between 4.2 and 1.8K. The temperature dependence of the intensity indicated that the observed spectra correspond to the ground state.

Assuming that A_4 and A_6 are mainly determined by the host crystal field and $\langle r^4 \rangle$ and $\langle r^6 \rangle$ does not change much for different RE impurities [34], we can estimate the x value for Dy^{3+} from the x value extracted for Er^{3+} . Using eq. (2) together with the tabulated values of β_J , γ_J , $F(4)$ and $F(6)$ [32], we obtain $x(\text{Dy}^{3+}) = -0.82$. Looking at the plots of ref. [32], we see that for Dy^{3+} , $J=15/2$, and $W > 0$, a Γ_6 ground state with an isotropic g-value of 6.667 is expected in the case

of an isolated Γ_6 . Nevertheless the experimental results, shown in fig. 4, indicate that the g-value is anisotropic. The anisotropy expected by the simple admixture of the Γ_6 ground state with the next Γ_8 excited state via the Zeeman terms is opposite to that found in our experiments. However preliminary calculations, including distortions along the $[110]$ directions, seems to account for the observed g-value anisotropy. This analysis will be a subject of a forthcoming communication. The observed anisotropic behavior of the linewidth is also an indication that the Dy^{3+} spectra, as much as the Er^{3+} spectra, reveal the presence of a distribution of distortions in PbTe:RE .

3. $\text{Pb}_{1-x}\text{Yb}_x\text{Te}$

Figure 5 shows the ESR spectrum of Yb^{3+} in PbTe at 4.2K with the magnetic field along the $[111]$ direction. The strong resonance corresponds to ^{170}Yb ($I=0$) isotope and the satellites or hyperfine structure can be assigned, as indicated in the figure, to the ^{171}Yb ($I=1/2$) and ^{173}Yb ($I=5/2$) isotopes with hyperfine constants $^{171}A = 580 \pm 10$ gauss and $^{173}A = 186 \pm 5$

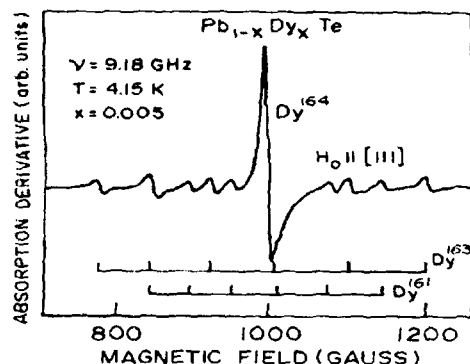


Fig. 3- ESR spectrum of Dy^{3+} in PbTe

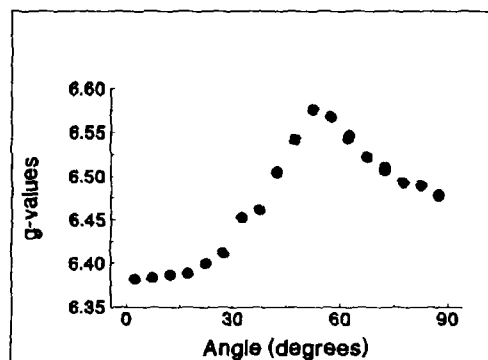


Fig. 4- g-value anisotropy of the strong ($I=0$) resonance shown in Fig. 3. The magnetic field was rotated in the (110) plane

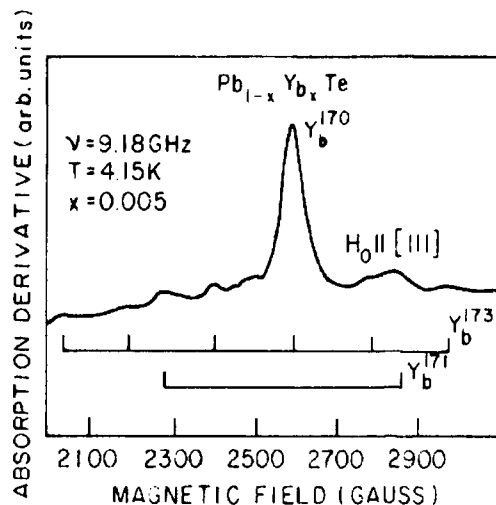


Fig. 5 - ESR spectra of Yb^{3+} in PbTe .

close to that obtained in our experiments. Again the observed difference can be attributed to covalency effects, usually larger for Yb^{3+} [1,3]. The observed anisotropy of the linewidth, although smaller in magnitude than that found for Dy^{3+} , is again an indication for the presence of a distribution of distortions in PbTe:REs .

IV - CONCLUSIONS

In summary our ESR measurements conclude that the REs substitute the Pb^{2+} ions in PbTe . The results indicate the presence of cubic and lower symmetry sites. For the cubic sites the sign of the crystal field parameters agree with that predicted by the point charge model for an octahedral coordination of negative charges. Preliminary analysis seems to indicate that crystal distortions along the [110] directions can account for all the low symmetry features. These distortions may be associated to Pb^{2+} vacancies. The data and analysis for the lower symmetry sites will be a subject of a future publication.

Acknowledgment.

The authors acknowledge Prof. Alvin Kiel, for interesting suggestions and critically reading the manuscript.

REFERENCES

1. W. Low and R.S. Rubins, Phys. Rev. **131**, 2527 (1963).
2. R.W. Bierig and M.J. Weber, Phys. Rev. **132**, 164 (1963).
3. D. Descamps and Y. Merle D Aubigne, Phys. Letters **8**, 5 (1964).
4. A. Wasiela and Y. Merle D Aubigne, Phys. Stat. Solidi (b) **47**, 663 (1971).
5. R.W. Reynolds, Y. Chen, L.A. Boatner and M.M. Abraham, Phys. Rev. Letters **29**, 18 (1972).
6. D. Davidov, R. Orbach, L.J. Tao and E.P. Chock, Phys. Letters **34A**, 379 (1971).

gauss respectively. The g-value of the main resonance ($I=0$) was found to be isotropic with value of 2.54 ± 0.05 . The linewidth was found to be anisotropic. Both, the g-value and the linewidth were obtained from a Dyson [28] analysis of the resonance lineshape.

Assuming again that $A_4 < r^4 >$ and $A_6 < r^6 >$ does not depend much on the REs and using eq.(2) together with the tabulated values of β_j , γ_j , F(4) and F(6) for Yb^{3+} ($J=7/2$), we found $x = -0.91$. This value lead to an isotropic Γ_6 ground state according to the scheme levels given by Lea et al. [32]. The theoretical g-value for an isolated $\Gamma_6(J=7/2)$ is 2.667, very

7. L.J. Tao, D. Davidov, R. Orbach and E.P. Chock, Phys. Rev. **B4**, 5 (1971).
8. D. Davidov, R. Orbach, C. Rettori, L.J. Tao and E.P. Chock, Phys. Rev. Letters **28**, 490 (1972).
9. R.A.B. Devine and W. Zingg, Solid State Comm. **11**, 233 (1972).
10. C. Rettori, D. Davidov, A. Dixon, K. Baberschke, E.P. Chock and R. Orbach, Phys. Rev. **B8**, 3563 (1973).
11. D. Davidov, E. Bucher, L.W. Rupp Jr, L. Longinotti and C. Rettori, Phys. Rev. **B9**, 2879 (1974).
12. D. Davidov, V. Zevin, J.M. Bloch and C. Rettori, Solid State. Comm. **17**, 1279 (1975).
13. R. Levin, D. Davidov, C. Rettori, J.F. Suassuna and D. Shaltiel, J. Phys. F: Metal Phys. **7**, 703 (1977).
14. G.E. Barberis, D. Davidov, J.P. Donoso, F.G. Gandra, C. Rettori and J.F. Suassuna, Solid State Comm. **28**, 427 (1978).
15. J.M. Bloch, D. Davidov and C. Rettori, J. Mag. Mag. Materials **25**, 271 (1982).
16. S.E. Barnes, Adv. Phys. **30**, 801 (1981).
17. J.D. Kingsley and M. Aven, Phys. Rev. **155**, 235 (1967).
18. V.A. Kasatkin, V.F. Masterov, V.V. Romanov, B.E. Samorukov and K.F. Shtel makh, Sov. Phys. Semicond. **16**, 106 (1982).
19. V.F. Masterov, K.F. Shtel makh and L.F. Zakharenkov, Sov. Phys. Semicond. **21**, 223 (1987).
20. M. Baeumler, J. Schneider, F. Kohl and E. Tomzig, J. Phys. C: Solid State Phys. **20**, L963 (1987).
21. P.B. Klein, F.G. Moore and H.B. Dietrich, Appl. Phys. Letters **58**, 502 (1991).
22. D.R. Lovett, in "Semimetals and narrow gap semiconductors" (Pion Ltd., London, 1977).
23. Diluted Magnetic (Semimagnetic) Semiconductors. R.L. Aggarwal, J.K. Furdyna and S. von Molnar. MRS Symposia Proceed. **89**, (1987).
24. M. Bartkowski, D.J. Northcott, J.M. Park and A.H. Reddoch, Solid State Comm. **56**, 659 (1985).
25. J. Parada and G.W. Pratt jr., Phys. Rev. Lett. **22**, 180 (1969).
26. Semiconductors and Semimetals. Willardson and Beer 5, T.C. Harman.
27. R.S. Allgaier and W.W. Scanlon, Phys. Rev. **111**, 1029 (1958).
28. F.J. Dyson, Phys. Rev. **98**, 349 (1955).
29. E. Belorizky, Y. Ayant, D. Descamps and Y. Merle D Aubigne, J. de Physique **27**, 313 (1966).
30. R.A.B. Devine and J.M. Moret, Phys. Letters **41A**, 11, (1972).
31. V. Zevin, D. Shaltiel and W. Zingg, Phys. Rev. **B16**, 1902 (1977).
32. K.R. Lea, M.J.M. Leask and W.P. Wolf, J. Phys. Chem. Solids **23**, 138 (1962).
33. A. J. Freeman and R.E. Watson, Phys. Rev. **127**, 2058 (1962).

CORRELATION OF THE LOCATION IN CRYSTAL LATTICE AND OPTICAL ACTIVITY OF THE Yb IMPURITY IN III-V COMPOUNDS

ADRIAN KOZANECKI

Institute of Physics, Polish Academy of Sciences, Al.Lotnikow 32/46,
02-668 Warsaw, Poland

ABSTRACT

Rutherford backscattering (RBS) and channeling measurements have been applied to study lattice location of the Yb atoms implanted into III-V compounds. It has been found that the Yb atoms locate in the lattice positions only in InP and its alloys with Ga and As, while in gallium compounds the substitutional fraction of Yb atoms could not be detected. The intra-4f-shell luminescence of the Yb^{3+} ions in different crystalline matrices have been studied. It has been shown that the ability of efficient excitation of the atomic-like luminescence of Yb^{3+} ions is associated with their substitutional location in the lattice. The intracentre emission from substitutionally located Yb^{3+} ions may serve as a probe of the local alloy disorder in GaInP and InPAs crystals.

INTRODUCTION

Semiconducting materials doped with rare earth (RE) impurities have attracted much attention for their possible application in optoelectronic devices [1,2]. It is expected that sharp, temperature stable, atomic-like emission originating in electronic transitions within the 4f-shell of REs, excited by minority carrier injection, will be utilized in these devices.

The excitation of the 4f-electron shell of REs in semiconductors having moderate energy gap values, as GaAs or InP, is almost always accomplished by the energy transfer of recombining charge carriers, either free or trapped at the impurities, to the 4f-electron shell. Therefore, the energy levels in the band gap associated with lanthanide ions ought to be identified. A primary information indispensable for such identification is atomic structure of the RE-related centres and, in particular, the location of RE ions in crystalline lattice. Another important issue is the possibility of participation of other chemical impurities, (as i.e. oxygen), in RE-related complexes, which can play a role of luminescence activators [3,4].

In spite of intense technological effort in growing the high quality RE-doped semiconductors exhibiting sharp atomic-like spectra of the REs, there is not too much information on the local configuration of atoms around the lanthanide ions. At least several factors may badly influence the quality of RE-doped III-V compounds. One of them is the well known high chemical activity of REs, in particular their notorious affinity to oxygen. Another serious problem is associated with a possible 6-fold coordination of lanthanide atoms in their complexes with As and P. Stoichiometric compounds of REs with As and P (pnictides) are of a cubic NaCl-type structure [5], while the substitutional position in zincblende-type crystals is 4-fold coordinated. Even if the lattice constants of pnictides and those of III-V semiconductors are equal, the bond lengths between atoms in III-V compounds are shorter of at least of 15% than in pnictides. Moreover, the bond angles are different, and the RE-As (P) bonds are much stronger than bonds between host atoms in semiconductors. It suggests that ones the RE-As or RE-P complexes, typical of pnictides, were formed, they may remain stable and resistant to thermal decomposition. The existence of such complexes will lead to large lattice distortion, which may limit excitation efficiency of the intra-4f-shell luminescence by i.e. nonradiative energy transfer from recombining charge carriers or excitons [6,7]. It also seems that the RE atoms involved in such 6-fold coordinated

complexes would tend to locate nonsubstitutionally in zincblende-type lattices.

The simplest and very reliable experimental method of finding the location of an atom heavier than host atoms in crystal is Rutherford backscattering (RBS) and channeling. In this work lattice location of the Yb atoms in III-V compounds have been studied. Intra-4f-shell luminescence of Yb^{3+} has been examined to investigate an interdependence between optical activity and location of the Yb atoms in crystalline lattices.

EXPERIMENT

Implantations of Yb^+ ions were performed into a variety of $\langle 100 \rangle$ oriented semiconductors: InP, GaAs, liquid phase epitaxy grown layers of lattice-matched $\text{Ga}_{0.5}\text{In}_{0.5}\text{P/GaAs}$, and $\text{Al}_{0.35}\text{Ga}_{0.65}\text{As/GaAs}$, and into $\langle 111 \rangle$ oriented GaP. The samples were implanted at room temperature (RT) in a misoriented direction (7° tilt angle between the surface normal and the ion beam) at an energy of 150 keV, and a dose of 10^{15} cm^{-2} . Some implantations were performed at 250°C to avoid amorphization. After implantations the samples were covered with a SiO_2 protective layer and then furnace annealed up to 700-1000°C, dependent on the material.

InPAs:Yb (a 0.1% mole fraction of Yb) and GaInP mixed crystals were grown by the synthesized solute diffusion (SSD) method. $\text{Ga}_{0.5}\text{In}_{0.5}\text{P}$ crystals were nominally undoped, so the Yb impurity was introduced by implantation at the energy of 150 keV at room temperature.

Random Rutherford backscattering, $\langle 100 \rangle$ and $\langle 111 \rangle$ axial channeling spectra were measured using the 1.7 MeV He^+ ions. The backscattered particles were detected at an angle of 170°. The ratio of the channeling/random backscattering yields was taken as a rough estimation of the interstitial fraction of the Yb atoms.

Photoluminescence (PL) spectra were measured to monitor optical activity of the implanted Yb ions in all as-grown materials, and after each annealing step in case of implanted samples. PL was excited with the 488 nm line of an argon laser and detected with a liquid nitrogen cooled S1 cathode photomultiplier (EMI 9684B) and recorded utilizing a standard lock-in technique.

RESULTS

The ytterbium impurity profiles in the implanted InP, GaInP and GaP as measured using RBS/channeling are presented in Figs.1-3, respectively. An overview of the Yb profiles shows that the highest substitutional fraction of the Yb atoms exists in InP (50% - $8 \cdot 10^{19} \text{ cm}^{-3}$), while in GaP the concentration of substitutional Yb (if any) cannot be distinguished [8]. It can also be seen that as a result of annealing the Yb atoms in RT implanted GaP diffuse towards the surface.

The situation in GaInP (Fig.2) is apparently intermediate between InP (Fig.1) and GaP (Fig.3), and the substitutional concentration of Yb in a 50% alloy has roughly been estimated for $2 \cdot 10^{19} \text{ cm}^{-3}$.

The RBS/channeling measurements performed on GaAs, AlGaAs and GaAsP showed that the Yb atoms were almost exclusively located at nonsubstitutional positions [9], (within the limitations of ion beam analysis techniques).

A strong Yb-related luminescence was observed in the implanted InP [10,11] and GaInP crystals [11]. The PL spectra of Yb^{3+} for selected compositions of GaInP alloys have been presented in Fig.4. It can be seen that the Yb spectra consist of two independent emissions, which have

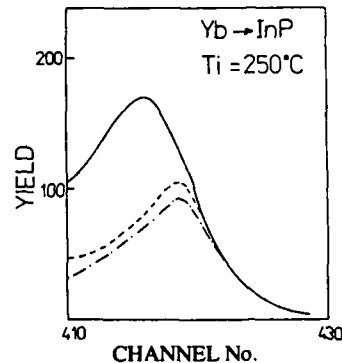


Fig.1. Yb profiles in InP: Random (—), and $\langle 100 \rangle$ axial for as implanted sample (---) and annealed at 700°C (-.-.).

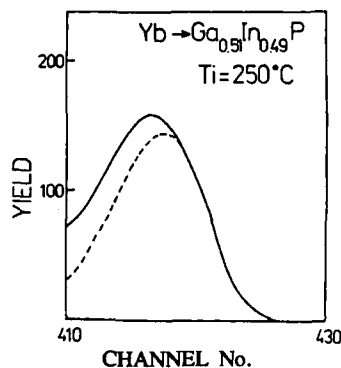


Fig. 2. Yb profiles in GaInP implanted at 250°C and annealed at 850°C: random (solid line) and <100> axial (broken line).

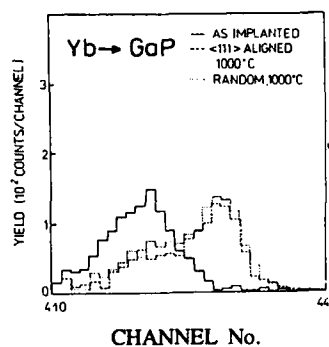


Fig. 3. Yb profiles in RT implanted GaP.

been ascribed to two different Yb-centres: a cubic Yb-P₄, and an axial one - Yb-P₄In₁₁Ga [11]. Interestingly, the energy difference ($\approx 9 \text{ cm}^{-1}$) between the new PL lines, labeled B and C, appeared to be independent of alloy composition. It was proposed [11] that the B and C lines are due to electron transition from the lowest lying level in the $^2F_{5/2}$ excited state of Yb³⁺, and the Γ_8 level in the $^4F_{7/2}$ ground state, split into two components by uniaxial strain caused by the Ga-In substitution in the second coordination sphere around the Yb³⁺ ion. Following this interpretation it can be

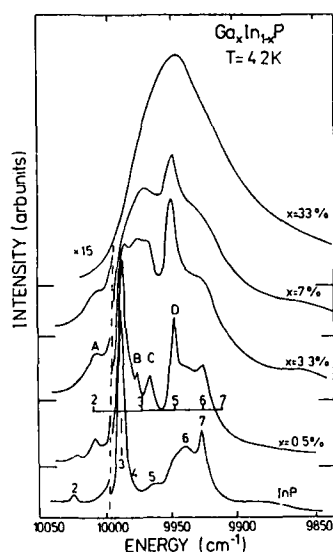


Fig. 4. PL spectra of Yb³⁺ in RT implanted and annealed at 850°C GaInP alloys.

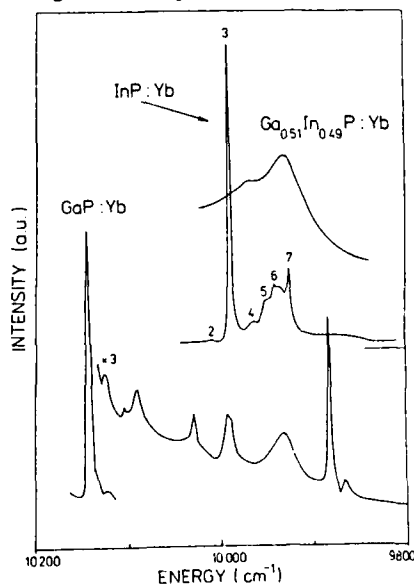


Fig. 5. PL spectra of Yb³⁺ in InP, GaP and GaInP (50% In contents).

concluded that the local strain around the Yb ion is independent of alloy composition. In fact, the nearest environment of the substitutional Yb^{3+} ion (Yb-P_4) remains unchanged in the full range of GaP-InP compositions. Such behavior of the strain could be expected on the basis of the well known results of Mikkelsen and Boyce [12], proving that the bond lengths in ternary alloys is almost independent of alloy composition.

In Fig.5 the PL spectra of Yb^{3+} in the implanted InP, $\text{Ga}_{0.5}\text{In}_{0.5}\text{P}$ and in as-grown GaP:Yb have been presented. It can be seen that the spectrum for a 50% alloy follows the trend in the behavior of Yb-related luminescence in GaInP (Fig.4), for compositions lower than 33%. In particular, no change in the transition energy of Yb^{3+} between 33% and 50% alloy have been observed. It indicates that alloy disorder in these materials contributes mostly to broadening of the PL lines. The constant emission energy suggests also that, in the first approximation, there is no change in the local electric field in $\text{Yb-P}_{12-n}\text{Ga}_n$ complexes.

The PL spectrum of Yb^{3+} in SSD-grown GaP (Fig.5) is shifted to higher energies. The PL intensity is two orders of magnitude lower than in InP. The spectrum differs from that presented by Masterov *et al.* [13], but the spectrum same as in Fig.5, was also observed by us in Yb-implanted GaP. It suggests that in as-grown as well as in implanted GaP the Yb luminescent centres have identical structure. A very weak intensity of PL in comparison with InP suggests that PL originates either in a very low concentration of the centres, or the energy transfer is ineffective.

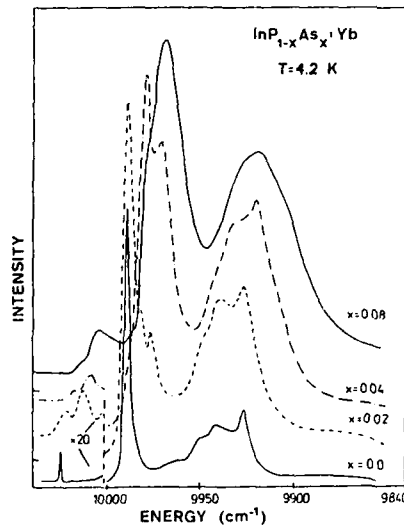


Fig.6. PL spectra of Yb^{3+} in InPAs alloys.

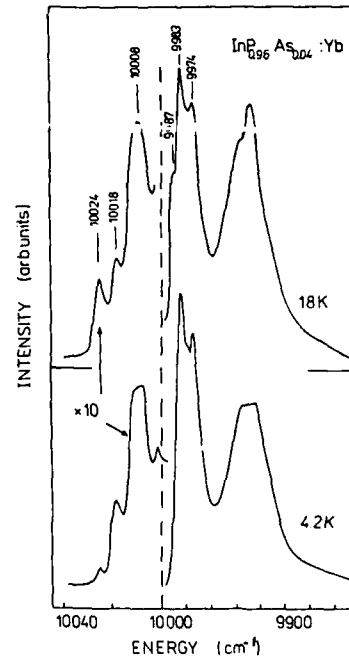


Fig.7. PL spectra of Yb^{3+} at 4.2 and 18 K in a 4% InPAs alloy.

Dependence of the Yb^{3+} PL on crystal composition has also been observed for InPAs alloys (Fig.6). Similarly to the situation observed in GaInP:Yb crystals, the spectra of Yb^{3+} appeared to be extremely sensitive to isovalent doping with arsenic. Adding arsenic to InP results in new luminescence transitions (Fig.6). For the lowest As contents (2%) a weak doublet appeared on the low energy side of the luminescence at 9987 cm^{-1} , ascribed to $\Gamma_8-\Gamma_8$ transition of Yb^{3+} ions located in undistorted Yb-P_4 tetrahedra.

The intensity of new lines becomes dominant already for a 4% arsenic admixture. In contrast with the behavior of the Yb PL in GaInP, here, new luminescence shifts to lower energies with the increase of As concentration.

The PL spectra in InPAs can be attributed as originating in two centres: a cubic Yb-P_4 , and an axial one $\text{Yb-P}_3\text{As}$. According to findings of Mikkelsen and Boyce [12] the lattice constant of mixed sublattice follows the Vegard's law, so the volume of the distorted $\text{Yb-P}_3\text{As}$ tetrahedron increases with

the As contents. As a consequence of this local expansion the electric field acting upon the Yb^{3+} ion decreases leading to a small shift of the PL energy, in agreement with observations (Fig.6).

To support the two centre interpretation of the Yb-related spectra the temperature dependence of luminescence has been measured. The results for a 4% and 7% As contents have been presented in Fig.7 and 8, respectively. The most pronounced difference in the spectra at $T > 4.2$ is a remarkable intensity enhancement of the PL lines at 10024 and 9987 cm^{-1} , which are due to the emission from the Yb^{3+} ions in regular Yb-P_4 centres. In general, the Yb-related PL has not been observed in gallium compounds at all or it was very weak, as in the case of GaAsP [9] and GaP (Fig.5). This kind of behavior has recently been confirmed by Takahei *et al.*[14], who have not found any Yb-related emission even in MOCVD grown GaAs:Yb.

DISCUSSION

The compositional dependence of Yb PL in InP-based alloys suggests that in spite of screening by the outer $5s^2$ and $5p^6$ closed electron shells, the 4f- electron function is affected by the presence of Ga and As atoms in the mixed sublattices. Isoelectronic impurities added to a binary compound change the interatomic distances in the common sublattice, while keeping the bond lengths almost unchanged [12]. As a result the common sublattice suffers significant bond angle distortion. Local distortions around impurities modify the intensity and symmetry of the electric field acting upon Yb atoms which causes Stark splittings of the 4f-electron energy level of the Yb^{3+} ion located at the lattice site. Distortions lower the T_d symmetry of the regular Yb-P_4 centre either to C_{3v} in case of $\text{Yb-P}_3\text{As}$ complex, or to C_4 in case of $\text{Yb-P}_4\text{-In}_{11}\text{Ga}$. As a consequence of different symmetries the Yb PL-spectra in GaInP and InPAs alloys differ, as it has clearly been demonstrated in Figs.4 and 6. In our opinion, different sensitivity of the Yb luminescence to cationic and anionic disorder, allows to discard the possibility that

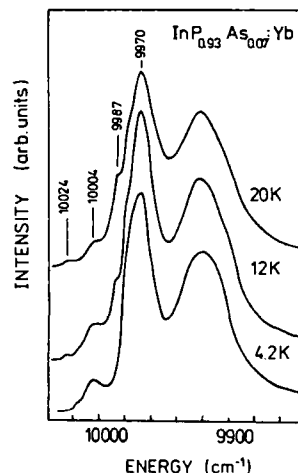


Fig.8. Temperature dependence of Yb PL in a 7% InPAs alloy.

Yb PL originates in complexes of Yb with unidentified impurities. It also supports strongly the conclusion that the Yb atoms are located substitutionally in crystalline lattices of the InP-based alloys.

According to the results obtained in this work it can be suggested that the possibility of activation of the Yb intra-4f-shell luminescence is associated with the substitutional location of the Yb^{3+} ions in the lattice. Size matching of the Yb^{3+} and In^{3+} ions is one of the reasons, which make the Yb-In substitution possible. The admixture of ligand wave function to the 4f-electron wave function (covalency effects), found by Aszodi *et al.* [15], should also be favorable for substitutional location of the Yb atoms, because of the $\langle 111 \rangle$ directional character of the covalent bonds. Moreover, covalency effects relax the parity selection rule thus making parity forbidden dipole transitions in the 4f-shell possible.

Absence of the intra-4f-shell luminescence of Yb^{3+} in gallium compounds seems to be associated with nonsubstitutional location of the Yb atoms in the lattices. Size mismatch between Yb^{3+} and Ga^{3+} ions may prevent incorporation of RE atoms into the lattice positions. However, more studies are necessary to answer the question whether optical inactivity of Yb in gallium compounds is related to atomic structure of the Yb-complexes, or depends on the nature of Yb-As bonding.

ACKNOWLEDGEMENT

The author appreciates dr. Z.Kalinski for providing the SSD-grown materials, and dr R.Groetzschel for a help in performing RBS measurements.

REFERENCES

1. L.C.Kimerling, MRS Bull.16, 42 (1991).
2. I.Hayshi, in Solid State Devices and Materials, Extended Abstracts of the 1992 Intern. Conf.Solid State Dev. Mat.,Tsukuba 1992, (Business Centre for Academic Societies, Japan, Tokyo 1992), p.10.
3. P.N.Favennec, H.L'Haridon, D.Moutonnet, M.Salvi, and M.Gauneau, Jap.J.Appl.Phys. 29, L524 (1990).
4. D.L.Adler, D.C.Jacobson, D.J.Eaglesham, M.A.Marcus, J.L.Benton, J.M.Poate, and P.H.Citrin, Appl.Phys.Lett.61, 2181 (1992).
5. P.Villars, and L.D.Calvert, in Pearson's Handbook of Crystallographic Data for Intermetallic Phases, American Society of Metals, Metal Park, Ohio (1985).
6. K.Takahei, A.Taguchi, H.Nakagome, K.Uwai, and P.S.Whitney, J.Appl.Phys.66,4941 (1989).
7. K.Thonke, K.Pressel, G.Bohnert, A.Stapor, J.Weber, M.Moser, A.Molassioti, A.Hangleiter, and F.Scholz, Semicond. Sci. Technol. 5, 1124 (1990).
8. A.Kozanecki, and R.Groetzschel, J.Appl.Phys.64, 3315 (1988).
9. A.Kozanecki, and R.Groetzschel, J.Appl.Phys.68, 517 (1990).
10. H.Ennen, U.Kaufmann, G.Pomrenke, J.Schneider, J.Windscheiff, A.Axmann, J.Cryst.Growth 64, 165 (1983).
11. A.Kozanecki, Z.Kalinski, J.Raczynska, and J.M.Langer, J.Appl.Phys.66, 3202 (1990).
12. J.C.Mikkelsen, Jr. and J.B.Boyce, Phys.Rev.B28, 7130 (1983).
13. V.F.Masterov, V.V.Romanov, and K.F.Shtelmakh, Sov.Phys.Solid State 25, 824 (1983).
14. A.Taguchi, H.Nakagome, and K.Takahei, J.Appl.Phys.68, 3390 (1990).
15. G.Aszodi, J.Weber, Ch.Uhleihn, L.Pu-Lin, H.Ennen, U.Kaufmann, J.Schneider, and J.Windscheiff, Phys.Rev.B31, 7767 (1985).

Tm DOPING OF LEAD TELLURIDE

LUDMILA I. RYABOVA AND MARINA E. TAMM
Moscow State University, 119899, Moscow, Russia

ABSTRACT

Doping with the rare earth elements is widely used for the improvement of parameters of the PbTe-based lasers. It has been found that Tm is a donor in PbTe, and the solubility of TmTe in PbTe does not exceed 7 - 8 mol %. Electron concentration in obtained PbTe(Tm) crystals reaches $4 \cdot 10^{20} \text{ cm}^{-3}$ and depends on Tm content and on deviation from stoichiometry. The analysis of the magnetoresistance oscillation picture shows no variation of the energy spectrum parameters for Tm contents less than 1 at.%. The g-factor does not change as well. This may be due to a rather small exchange interaction between Tm atom, which is magnetic in both +2 and +3 valence states, and band electrons. The experimental data for PbTe(Tm) are compared with the properties of semimagnetic PbTe(Cr) with quite the same electron concentration value.

INTRODUCTION

The rare earth metals (REM) are widely used as dopants for the modification of lead telluride properties. It is possible to attribute them to two groups. The first group includes all REM excepting Eu, Sm, Yb and Tm. The metals forming that group appear to be in 3^+ valence state in their monote tellurides which are found to be metals. In lead telluride they act as donors. Being characterized by low diffusion coefficients these elements have some advantages for the creating of multilayers based on PbTe with minimal thickness of each transition layer. Four excepted elements may be included into the second group. Their monote tellurides are semiconductors with 2^+ valence state of the metals. It was expected that in PbTe they will be neutral impurities and their solid solutions with lead telluride will be characterized by variable energy gap [1-3]. This suggestion was proved for Eu and Sm. The investigation of Tm doped lead telluride has been performed to complete the information concerning REM as dopants.

EXPERIMENTAL

Tm solubility in PbTe along the cross-section PbTe-TmTe and the melting temperature of the alloys in the composition range 0 - 13 mol% TmTe have been investigated. The mixture of lead telluride with Tm monote telluride was used as a growth melt. Synthesis of TmTe was performed using a three staged technology described in paper [4]. As grown TmTe has been a single phase crystal with a parameter of the cubic lattice $a = (6.33 \pm 0.03) \text{ \AA}$.

PbTe single crystals used as a component of the growing melt were p-type with hole concentration $p \sim 1.2 \cdot 10^{18} \text{ cm}^{-3}$. The alloyed polycrystalline $\text{Pb}_{1-x}\text{Tm}_x\text{Te}$ samples were annealed at $T = 750 \text{ C}$ during 120 hours. It has been determined with the help of X-ray diffraction analysis that the solubility of TmTe in PbTe does not exceed 7 - 8 mol%.

PbTe(Tm) single crystals were grown by the directed crystallization (DC) of the melt and by the vapour-liquid-solid (VLS) mechanism. All of the samples were n-type. The electric

parameters of the samples are represented in the table. Tm content was determined using of chemical analytic measurements with accuracy 10 %.

The characteristics of the investigated samples. $T = 4.2$ K.

N	Growth method	Composition of the melt	C_{Tm} , weight %	n , cm^{-3}	μ , cm^2/Vs
1	DC	95%PbTe+5%TmTe	3	$4 \cdot 10^{20}$	100
2	VLS	the same	0.8	$1.6 \cdot 10^{19}$	$4.4 \cdot 10^4$
3	VLS	85%PbTe+10%TmTe+5%Te	2.8	$1 \cdot 10^{19}$	$1.0 \cdot 10^4$
4	VLS+anneal	the same	2.8	$3 \cdot 10^{18}$	$1.3 \cdot 10^4$

It can be seen from the table, that at the same composition of the growth melt Tm concentration C_{Tm} appears to be significantly higher in DC crystals than in VLS ones.

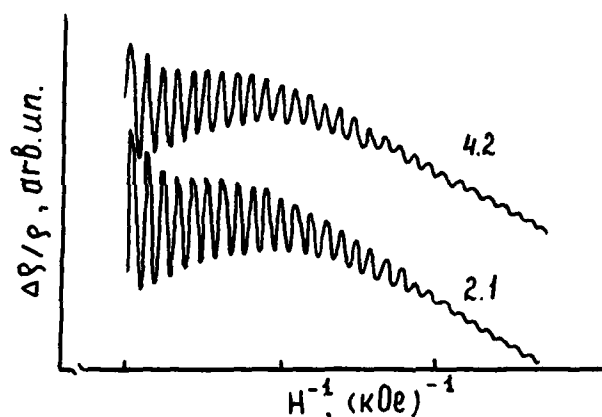


Fig.1. The view of the oscillations of magnetoresistance $\partial\rho/\partial H(H)$ for PbTe(Tm) sample N 2. $H \parallel \langle 100 \rangle$. Figures at the curves point the temperature in K.

For the sample N 2 the view of Shubnikov - de Haas (SH) oscillations is shown in Fig.1. The curves are recorded in the orientation of the magnetic field $H \parallel \langle 100 \rangle$ with the accuracy 0.1° , that corresponds to the equivalent position of the Fermi ellipsoids in PbTe relatively to the vector H . The position of the sample has been correlated with the help of a special turning device using the method described in paper [5]. The electron concentration n was calculated using the experimentally determined period of the oscillations in the reversed magnetic field. The obtained $n \sim 1.4 \cdot 10^{19} cm^{-3}$ is close to the value of the Hall concentration represented in the table. The effective mass of the electrons $m_{100}^* \sim 7.7 \cdot 10^{-2} m_0$ was determined from the temperature dependence of the oscillations amplitude. The m_{100}^* value have been also calculated using the parameters for undoped PbTe (the anisotropy coefficient $\alpha = 3.3$; matrix element $v = 0.25 \cdot 10^8 cm/s$). The obtained value $m_{100}^* \sim 8.4 \cdot 10^{-2} m_0$ practically coincides with the experimental one assuming the

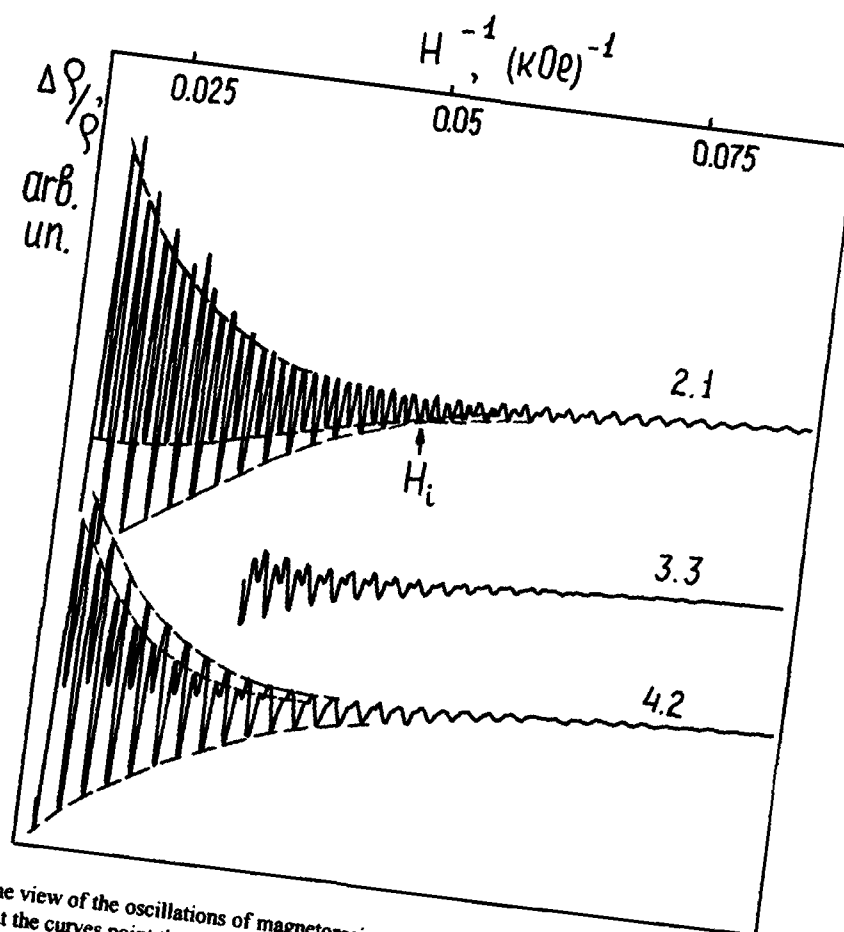


Fig.2. The view of the oscillations of magnetoresistance for PbTe(Cr) sample. $H \parallel \langle 100 \rangle$. Figures at the curves point the temperature in K.

precision ~ 15%. It gives rise to the conclusion that the parameters of energy spectrum of PbTe do not vary significantly at least at $C_{Tm} < 1$ at.%. It seems interesting to compare the obtained data for PbTe(Tm) with the results for PbTe(Cr) [5]. In undoped lead telluride the electron concentration does not exceed $6 \cdot 10^{18} \text{ cm}^{-3}$. Cr doping as well as Tm one results in n increase up to $(1.3 - 1.5) \cdot 10^{19} \text{ cm}^{-3}$ inside the homogeneous region. Comparing the oscillation curves for the samples PbTe(Tm) (Fig.1) and PbTe(Cr) (Fig.2) with close Fermi energies $E_F \sim 100 \text{ meV}$ one can see the significant difference. In PbTe(Cr) crystals a distinct spin splitting of Landau levels has been observed. A characteristic feature of these curves is that at some definite value of magnetic field $H = H_i$ the frequency of SH oscillations is doubled. The H_i value diminishes with a temperature rise. That effect is connected with the change of g -factor value in the magnetic field induced by the magnetic impurity. However, the absence of the features pointing on the magnetic character of Tm impurity in PbTe in the SH oscillations cannot be

considered as a real provement of its nonmagnetic behaviour. It may be attributed to the difficulties in the registration of spin splitting due to the broadening of Landau levels. For the specially annealed sample N 4 grown from nonstoicheometric melt with hihger Tm content the spin splitted SH oscillations have been recorded. But no visible dependence of g-factor on the magnetic field was observed.

Summerizing the experimental data Tm in PbTe may be characterized as a donor impurity which allows to increase the electron concentration up to $\sim 10^{20} \text{ cm}^{-3}$. Oppositely to PbTe(Cr) the saturation region on the dependence of n on C_{Tm} was not found. The effect of Fermi level pinning was not observed. We have not registrate any influence of Tm on the SH oscillation curves pointing on the magnetic interaction of Tm atoms with free electrons. It proves the conclusion of the authors of paper [6] about small value of the exchange integral for the interaction of free electrons in the conduction band with the magnetic moments of impurity atoms in lead telluride.

References

1. D.L.Partin, J.Appl.Phys. **57**, 1997 (1985).
2. M.Averocs, B.A.Lombos and C.Fac, Phys.St.Sol. **131**, 759 (1985).
3. A.Krost, B.Harbecke, R.Faymonville, H.Schlegel, and E.Faunter, J.Phys.C:Sol.St.Phys. **18**, 2119 (1985).
4. E.I.Yarembash and A.A.Eliseev, The rare earth elements chalcocenes, (Moscow, 1975), p.258.
5. B.A.Akimov, P.V.Verteletski, V.P.Zlomanov, L.I.Ryabova and O.I.Tananaeva, Fiz.Tekhn.Poluprov. **23**, 244 (1989).
6. I.I.Zasavitski and A.V.Sazonov, Fiz.Tverd.Tela **30**, 1669 (1988)

THE EFFECT OF RARE-EARTH ELEMENTS ON THE ENTROPY OF RADIATION DEFECTS IONIZATION IN n-TYPE Ge

V.V. PETROV, T.D. KHARCHENKO, V.YU. YAVID
Byelarusian State University, Physics Department, Minsk,
Republic Belarus'.

ABSTRACT

The analyses of the processes of radiation defect formation in germanium doped with phosphorus in the presence of rare-earth element neodymium and without it has been carried out. It has been shown that the presence of neodymium in n-Ge results in the change of enthalpy and entropy of the major radiation defect ionization (complex with the level being near $E_a - 0.20$ eV). The change of enthalpy by 0.03-0.04 eV as well as more than six fold increase of entropy of the complex ionization in Ge:Nd has been stated to be connected with the local deformation of the lattice around defect formed in the process of irradiation.

INTRODUCTION

Great interest aroused lately to the production of semiconductor crystals with sufficiently low content of the background technological impurities was caused by the possibility of the improvement of operating characteristics of the devices, i. e. IR- and ionizing radiations detectors. One of the most perspective methods of purification resides in the introduction into the melt the impurities, being effective intrinsic getters. Lanthanoids may be attributed to them in case of Ge and Si [1-4]. It has been shown [5-7], that the increase of the extent of purifying of silicon crystals with the help of rare-earth elements (REE) has the determined effect on the processes of thermal and radiation defect formation. It should be expected that crystals of germanium, another basic material of semiconductor, must have the analogous properties. However, at present, there is no information about the features of radiation defect formation in germanium having REE.

The purpose of the present paper is to find the main radiation defects (RD) and determine their parameters in germanium of n-type conductivity grown in the presence of neodymium.

EXPERIMENTAL RESULTS

Crystals were grown by the method of pulling from the melt containing $(3-35) \times 10^{-4}$ mass % Nd and $(1.5-17) \times 10^{-7}$ mass % P. Doping by phosphorus was made by introducing of orthophosphate neodymium and neodymium into the melt. All crystals had electron conductivity which, according to the measurement of temperature dependencies of the charge carriers concentration (TDCCC) in the range of 10-300 K, was determined by the impurity atoms of phosphorus, introducing the level of $E_c - 0.012$ eV into the forbidden zone. Concentration of the electrons of conductivity for different crystals and the location of the sample in the ingot varied in the range of $2 \times 10^{13} - 2 \times 10^{15} \text{ cm}^{-3}$. The mobility at room temperature was equal to $3900 \pm 100 \text{ cm}^2 \times (\text{V} \times \text{s})^{-1}$, and the lifetime of the minority charge carriers was $(2.5-3) \times 10^{-4} \text{ s}$. Oxygen content was less than $5 \times 10^{15} \text{ cm}^{-3}$.

The samples were irradiated by ^{60}Co γ - rays at temperature not higher than 295 K. The intensity of the γ - rays flow was 300 roentgen/s. The irradiation was made until the beginning of n - p conversion of conductivity. Temperature dependencies of the concentration of electrons of conductivity (n) were measured in the range of 77 - 320 K.

The analyses of the curves $n = f(10^3/T)$ showed that irrespective of the presence of lanthanoid in the crystals of germanium the effect of ^{60}Co γ - rays results in the removal of electrons from the zone of conductivity and to the formation of radiation defects with the energy of activation of the level near $E_c - 0.20$ eV [8]. The rate of the removal of electrons (278 K) and introducing RD with the level $E_c - 0.20$ eV also did not depend on the presence of neodymium and had the following values correspondingly: $(4.0 \pm 0.5) \times 10^{-4} \text{ cm}^{-1}$ and $(1.1 \pm 0.2) \times 10^{-4} \text{ cm}^{-1}$.

In spite of the similar character of the processes of radiation defect formation in Ge:(Nd,P) and test crystals from TDCCC for all groups of the studied samples it follows that the energy of activation of the defect with the level near $E_c - 0.20$ eV in germanium with Nd was approximately 0.03 eV lower than in the test crystals. The possible reason of the observed effect lies in the fact that as a result of the radiation of Ge:(Nd,P) another defect with the level of $E_c - 0.17$ eV is formed, i. e. the complex with another components involving, for

example, the impurity of Nd. However, in this case the change of the rate of introducing of centers must take place, that does not agree with the obtained results.

DISCUSSION

For the more precise determining of the value of displacement of the main RD level in the forbidden zone the differential analyses of the free-charge-carrier concentration was used [9], according to which the location of the levels and the concentration of the defects are found from the dependence:

$$-kT \frac{dn}{dE_f} = \sum_i N_i \frac{\partial f(E_i - E_f)}{\partial \left(\frac{E_f}{kT} \right)} \left(1 + \frac{E_i - E_f}{kT} \frac{d(kT)}{dE_f} \right), \quad (1)$$

where

$$\frac{\partial f(E_i - E_f)}{\partial \left(\frac{E_f}{kT} \right)} = \frac{1}{4} \cosh^2 \left\{ \frac{\ln g_{effi}}{2} + \frac{E_i - E_f}{2kT} \right\}, \quad (2)$$

E_f - Fermi level, E_i - the location of the level in the forbidden zone, g_{effi} - effective factor of degeneration, N_i - concentration of i-type defects.

The typical dependencies - $kT(dn/dE_f) = f(E_f)$ for Ge:(Nd,P) and test crystals are shown in the Figure. One can see from its analyses that not only the difference in the location of maxima takes place, but the change of value of the half-width of the bands. According to (1) and (2) [10]

$$\Delta E_f = 3.5 kT_{max} - k(T_2 - T_1) \ln(g_{eff}), \quad (3)$$

where T_1 and T_2 is the temperature in the points, corresponding $E_{f1} = E_{fmax} - \Delta E_f/2$ and $E_{f2} = E_{fmax} + \Delta E_f/2$. It follows from [3] that ΔE is determined by the effective factor of degeneration g_{eff} , directly connected with the entropy of the defects ionization:

$$\Delta S = k \ln(g_{eff}). \quad (4)$$

In its turn the quantity ΔS together with enthalpy ΔH determine the free energy of ionization ΔE [11]

$$\Delta E = \Delta H - T\Delta S. \quad (5)$$

The calculation of the dependencies $kT(dn/dE_f) = f(E_f)$ was made to find the accurate values of the parameter of RD by the

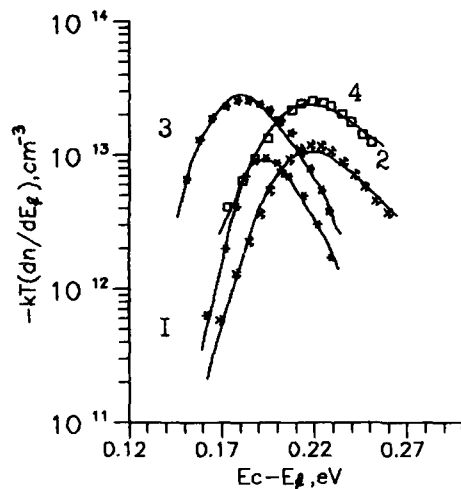


Figure: Function $kT(dn/dE_f)$ of the location of Fermi level in the forbidden zone for n-type germanium with Nd(1,3) irradiated by γ -rays ^{60}Co and the test crystal (2,4). $\phi \times 10^{-17}$, cm^{-2} : 1,2 - 3.5; 3,4 - 10.0. Continuous lines - calculation.

least-squares method with the help of the expressions (1) - (5). The results were presented in the Figure (continuous lines) and the parameters of the centers in the Table.

Table: Values of enthalpy of ionization ΔH , entropy of ionization ΔS , half-width of the band ΔE_f in Ge:(Nd,P) and in the test crystals irradiated by ^{60}Co γ - rays.

Curve	Material	n_0, cm^{-3}	$\Delta H, \text{eV}$	$\Delta S, \text{k}$	g_{eff}	$\Delta E_f, kT_{max}$
1	Ge:Nd,P	$1.79 \cdot 10^{14}$	0.265	4.63	103	2.31
2	test cryst.	$2.21 \cdot 10^{14}$	0.234	0.69	1.99	3.5
3	Ge:Nd,P	$1.12 \cdot 10^{15}$	0.271	4.76	117	2.44
4	test cryst.	$1.01 \cdot 10^{15}$	0.231	0.67	1.95	3.5

From the Table one can see that irrespective of the concentration of the main doping impurity, the presence of neodymium in the melt on the stage of the growing of Ge crystals causes the noticeable change of the parameters of the main radiation defects, i.e. - entropy and enthalpy of ionization.

Ionization entropy has two addends [11]. The first one is attributed to the factor of electron degeneration of the level of $\Delta S = k \ln(g)$. As it is seen from the Table, in germanium without REE $g \approx 2$. The second addend was attributed to the fact that the electron transitions can be followed by the change of the rigidity of the binding of defect with the crystal lattice.

The change of the force constants between the center and its neighbours caused by the change of the connections results in the change of the vibrational entropy of a crystal ΔS [12].

Naturally, one can suggest, that the change of the entropy of ionization at the change of the charge state RD was primarily due to the vibrational entropy of the center. As it was found, one or two vacancies and the atom of donor impurity [8,13] might be involved into the radiation defects in n-Ge with the level situated near $E_g - 0.20$ eV. Photoelectric spectroscopy of Ge:P irradiated by ^{60}Co γ - rays showed [14] that the point radiation defects are placed not homogeneously, but located mainly in the vicinity of the donors of the fifth group, taking strictly determined locations in the crystal lattice relatively the atoms of impurities. The observed fine structure of the spectra of photoexcitation of phosphorus was caused by the presence of the primary RD in the second- the third coordination spheres of the impurity atom, affecting mainly the central-cellular part of its potential. Under these conditions there exists the real possibility of the formation of electrically active complex, consisting of the atom of phosphorus and one or some primary radiation defects, being in the close vicinity. When it is suggested that the vacancy is involved into the compound of the studied complex, then the large value of ΔS shows, that the atoms nearest to it, involving the atom of phosphorus, move to the vacancy, so that each of them goes far from its nearest neighbors and the connection with them becomes loose. In its turn the presence of the atom of rare earth element near it facilitates the efficient loosening of the binding of the atom of phosphorus and the vacancy.

Study of Ge:(Nd,P) by the method of the secondary ion mass-spectroscopy showed that the content of the Nd atoms in the crystals did not exceed $1 \times 10^6 \text{ cm}^{-3}$. It is evident that in such concentration atoms of REE homogeneously distributed on the crystals cannot cause the noticeable deformation of the lattice. Thus, it is naturally to suggest that the atoms of Nd are situated near phosphorus. Actually, from the analyses of the profiles of distribution of electrically active phosphorus along the generating range of the Ge:(Nd,P) ingots grown under the identical conditions of mixing, for the given impurity the numerical values of the equilibrium segregation coefficient

$K_0 = (3.9 \pm 1.6) \times 10^{-2}$ and diffusion coefficient in the germanium melt $D = (1.58 \pm 0.15) \times 10^{-6} \text{ cm}^2/\text{s}$. The analyses was made according to Burton-Prim-Slichter theory [15]. The found value of the coefficient of diffusion in the liquid phase considerably differs from the value D for shallow donors in the germanium melt, which is usually in the range of 10^{-4} - $10^{-5} \text{ cm}^2/\text{s}$ [16]. One can suggest that the low values of D (and, consequently, K_0) comparing to the crystals, without REE, are caused not by the migration of the isolated phosphorus atoms, - in the melt, but by diffusion of the molecules of neodymium orthophosphate having considerably greater sizes, with the following activation of phosphorus on solid-liquid interphase, atoms of Nd in Ge crystals can be placed in the immediate vicinity of the phosphorus atom.

CONCLUSIONS

Thus, the impurity atoms of REE in germanium, revealing no the electrical activity, cause the local deformation of the lattice around the point radiation defects during the process of radiation, that has the determining effect on their microscopic parameters, i.e. enthalpy and entropy of ionization.

ACKNOWLEDGMENT

The author express their acknowledgement to O.M. Alimov for his assistance in the doping of germanium crystals by lanthanoids.

REFERENCES

1. A.R.Salmanov, G.I.Aleksandrova, G.I.Voronkova et. al., *Izv. Akad. Nauk SSSR, Ser.Neorg. Mater.* **14**, 85 (1978).
2. E.O.Movchan, M.M.Bondar, *Ukrain. Fiz. Zh.* **8**, 496 (1963).
3. D.I.Levinzon, G.V.Sachkov, Yu.M.Smirmov, V.A.Sher shel, *Izv. Akad. Nauk SSSR, Ser.Neorg. Mater.* **4**, 280 (1968).
4. N.I.Baransky, V.V.Badakov, D.I.Levinzon, *Izv. Akad. Nauk SSSR, Ser.Neorg. Mater.* **3**, 1259 (1967).
5. J.Mandelkorn, L.Schwartz, J.Broder, H.Kautz, R.Ulman, J. *Appl. Phys.* **35**, 2258 (1964).
6. V.V.Petrov, V.S.Prosolovich, G.S.Tsyrukovich, Yu.A.Karpov, *Izv. Akad. Nauk SSSR, Ser.Neorg. Mater.* **23**, 1386 (1987).
7. Yu.A.Karpov, V.V.Mazurenko, V.V.Petrov, V.S.Prosolovich, V.D.Tkachev, *Fiz. Tekh. Poluprovodn.* **18**, 368 (1984).

8. T.V.Mashovets, V.V Emtsev, S.N.Abdurakhmanova, Fiz. Tekh. Poluprovodn. 8, 96 (1974).
9. H.J.Hoffmann, Appl. Phys. 19, 307 (1979).
10. L.F.Makarenko, V.P.Markevich, L.I.Murin, Fiz. Tekh. Poluprovodn. 19, 1935 (1985).
11. J.Bourgoin, M.Lannoo, Point Defects in Semiconductors II. Experimental aspects, (Springer-Verlag, Berlin, Heidelberg, New York, 1983), p.174.
12. V.V.Voronkov, Fiz. Tekh. Poluprovodn. 5, 920 (1971).
13. V.D.Tkachev, V.I.Urenev, Fiz. Tekh. Poluprovodn. 5, 1516 (1971).
14. V.G.Golubev, V.I.Ivanov-Omsky, G.I.Kropotov, Fiz. Tverd. Tela, 24, 3410 (1982).
15. J.A.Burton, R.C.Prim, W.P.Slichter, J. Chem. Phys. 21, 1987 (1953).
16. H.Kodera, Japan J. Appl. Phys. 2, 212, (1963).

PART IV

Excitation Mechanisms

EXCITATION AND DE-EXCITATION MECHANISMS OF RARE-EARTH IONS IN III-V COMPOUNDS: OPTICALLY DETECTED MICROWAVE-INDUCED IMPACT IONIZATION OF Yb DOPANT IN InP

T. GREGORKIEWICZ*, B.J. HEIJMINK LIESERT*, I. TSIMPERIDIS*,
I. de MAAT-GERSDORF*, C.A.J. AMMERLAAN*, M. GODLEWSKI**,
AND F. SCHOLZ***

*Van der Waals - Zeeman Laboratorium, Universiteit van Amsterdam, Valckenierstraat 65-67, NL-1018 XE Amsterdam, The Netherlands,

** Institute of Physics, Polish Academy of Sciences, Al. Lotników 32/46, PL-06-668 Warszawa, Poland.

*** 4 Physikalisches Institut, Universität Stuttgart, Pfaffenwaldring 57, D-7000 Stuttgart 80, Germany.

ABSTRACT

The excitation mechanisms of rare-earth dopants in III-V semiconductors are being reviewed. The discussion is focused on ytterbium-doped InP crystals for which a particularly large amount of experimental data has been gathered. Here, the results obtained recently by optically detected microwave-induced impact ionization are being examined in detail. On the basis of the experimental findings it is argued that the intrashell luminescence is excited by an intermediate state involving binding of an exciton. Direct evidence for the existence of such a state, of pseudoacceptor type, will be given. The nonradiative recombination channel responsible for the fast decay of Yb luminescence will also be discussed and, for the first time, evidence for an Auger process will be presented. It will also be shown that the nonradiative channel may be effectively blocked by impact ionization of a participating carrier.

INTRODUCTION

Over the past decades, many investigations have been devoted to the optical properties of rare-earth (RE) ions (lanthanides) in ionic solids such as wide-gap sulfides (ZnS, CaS) and garnet oxides (Y_2O_3 , $\text{Y}_3\text{Al}_5\text{O}_{12}$). In these hosts the 4f ions exhibit strong visible and near-infrared luminescence. They find applications in laser materials such as YAG : Nd^{3+} . Rare-earth-activated sulfides have the advantage of obtaining multicolor devices due to internal 4f-shell transitions of RE^{3+} ions. In recent years, also RE-doped III-V semiconductors have been intensively studied because of their possible applications in opto-electronic devices. The characteristic feature of the electronic structure of RE elements in solids is the presence of incompletely filled 4f-core orbitals, surrounded by closed 5s² and 5p⁶ shells. The 4f electrons are thus effectively screened and are only weakly affected by their crystalline environment. As a consequence, rare-earth ions in solids may show sharp luminescence spectra arising from atomic-like, intra-4f-shell transitions. Semiconductor lasers based on these materials have a well defined lasing wavelength which, due to rare-earth-related internal transitions, is relatively insensitive to ambient temperature and almost independent of the III-V host material.

ELECTRICAL AND OPTICAL PROPERTIES OF Yb IN InP

The most extensively studied rare-earth-doped III-V semiconductor is ytterbium-doped InP (InP:Yb). The electron configuration of the free Yb atom is $[\text{Xe}]4f^{14}6s^2$. The

core configuration of the $3+$ charge state, being the stable one (in InP) and responsible for the luminescence, is unclear. Besides the two $6s^2$ electrons participating in bonding, a third electron from the $4f$ shell is involved. Two possible configurations arise: either one electron is missing directly from the $4f$ shell ($4f^{13}$ configuration), or the $4f$ orbitals hybridize with those of the host, the bound hole being partly localized on the $4f$ core and partly on the bonds (linear combination of Yb^{2+} and Yb^{3+} configurations) [1].

Also, despite the large number of studies, a controversy exists on the electrical and optical behavior of ytterbium in InP. Körber *et al.* [2] observed p -type conductivity in InP:Yb grown by liquid phase epitaxy (LPE), with Yb concentrations exceeding the residual donor concentration. From temperature dependent Hall-effect measurements they found an acceptor level located at about 45 meV above the valence band (VB), which they ascribed to the Yb^{3+}/Yb^{2+} transition. Indeed, cluster calculations by Hemstreet [1] predicted a single acceptor state as the Yb ground state with a hole binding energy of approximately 0.26 eV.

In contrast to this, Yb-doped InP grown by metalorganic chemical vapor deposition (MOCVD) showed n -type conductivity [3, 4], even for Yb concentrations much higher than those obtained in LPE-grown material. Synthesized InP:Yb epilayers were also found to be n type [5]. Whitney *et al.* [3], using Hall-effect and deep-level transient spectroscopy (DLTS) data, proposed that ytterbium introduces an acceptor-like level at about 30 meV below the conduction band (CB). These authors suggested that this level would be related to the Yb^{3+}/Yb^{2+} acceptor level. However, electron paramagnetic resonance (EPR) measurements [6] provide some evidence that it is not possible to locate the Yb^{3+}/Yb^{2+} level in the InP band gap since both neutral shallow donors (at $\approx E_{CB} - 7$ meV) and Yb in its $3+$ charge state could be detected simultaneously, even in n -type samples. Although InP crystals studied in this case were not very homogeneous and therefore the EPR results have to be treated with some caution, the observed p -type conductivity of LPE Yb-doped InP is unlikely to be due to Yb ions acting as acceptor impurities in InP, as proposed by Körber *et al.* [2]. It is more likely to result from unintentional co-doping with shallow acceptors (Zn, Mg, Ca), present as residual contaminants in the Yb metallic source [7].

It seems now to be rather generally accepted that Yb introduces an acceptor-like electron trap AE (pseudoacceptor) which can capture an electron at a level of about 30 meV below the conduction band and a hole trap DH at $E_{VB} + 30$ -40 meV. The capture of an additional carrier does not lead to a change of the ytterbium charge state which remains Yb^{3+} (in ionic notation) [3, 5, 8, 9]. To explain this pseudoacceptor (or donor) behavior it was proposed that Yb in InP acts as an isoelectronic trap with a short-range attractive potential either due to a lattice distortion around the Yb site or to a difference in electron affinities of Yb and In [3, 9].

Yb-related photoluminescence (PL) is well known to occur near $1.0 \mu m$, being due to intra- $4f$ -shell transitions of trivalent $Yb^{3+}(4f^{13})$ ions substituting on In sites. These transitions are forbidden as electric dipole transitions. They become possible when the crystal field as experienced by the RE ion, lacks a center of symmetry. As a result, the wavefunction is of mixed parity and the PL intensity is determined by the small admixture of opposite parity.

Most likely due to a wide spread of materials used for PL studies, the dominant Yb photoluminescence excitation (PLE) mechanism was until very recently not understood. Several mechanisms were proposed to account for all features of Yb PL and PLE spectra, especially with respect to their temperature dependencies.

- (a) Kasatkin and co-workers [10, 11] proposed that in their melt-grown crystals Yb^{3+} PL is induced via an energy transfer from donor-acceptor pair (DAP) recombination to Yb ions, leading to Yb^{3+} core states excitation. (The excess energy is transferred in

an Auger-type process to an additionally bound particle residing on a neighboring acceptor or donor.) In fact, some evidence for such an energy transfer was found for heavily doped samples [9].

- (b) Körber and Hangleiter [12], assuming that Yb behaves as a shallow acceptor, concluded that Yb 4f-shell excitation proceeds by direct capture of free excitons or by impact excitation by hot carriers.
- (c) Takahei *et al.* [9] proposed an Yb-related DAP \rightarrow Yb energy transfer mechanism, in which the Yb itself, acting as an acceptor-like electron trap, donates an electron which then interacts with a hole in the valence band or at neutral acceptors. This mechanism is expected to be effective for samples in which the average distance between Yb traps and neutral acceptors is relatively small. Indeed, some evidence for this could be found in highly Yb-doped samples [9] and also in *p*-type LPE samples [12] with high acceptor concentration.
- (d) Thonke *et al.* [8] could explain the majority of their data by assuming that Yb acts as an isoelectronic trap which binds an exciton. Yb intra-4f-shell emission is then induced via an impurity (defect) Auger recombination [13] by an energy transfer from this bound exciton (BE) excited state to Yb 4f-core orbitals resulting in nonradiative BE recombination and 4f-shell excitation. Such a PLE process has been previously proven to be very efficient for rare-earth intrashell emissions in ZnS [14, 15].
- (e) Finally, Lhomer *et al.* [16] suggested that upon laser excitation an Yb BE is formed with both its constituents being captured at relatively deep trapping levels. On the basis of temperature dependent Hall-effect measurements the appropriate energies were determined as $E_{CB} - 30$ meV and $E_{VB} + 40$ meV for the electron and hole trap, respectively. The BE would then decay nonradiatively and excite the Yb ion generating intrashell PL.

Exciton binding is expected to occur for neutral RE ions (and their complexes) which have their $3+/2+$ ionization level within the forbidden gap [13, 17], or which do not change their charge state from $3+$ to $2+$ but have one of their excited states in the energy gap [13]. The latter is the case for Yb in InP. The RE ion in its $3+$ charge state is an isovalent (isoelectronic) dopant when substituting for the cation in the III-V compound. Such centers may introduce a short-range attractive potential for one type of free carriers. Once the first carrier is localized, the second one is trapped by the long-range attractive Coulomb potential of the first carrier, thus forming a RE-bound exciton.

Although in view of the available information the excitation mechanism intermediated by BE appears to be the most probable one, it has never actually been confirmed by experiment. So far the most convincing evidence for the participation of excitons in inducing Yb PL comes from Thonke *et al.* [8]. In this study it has been observed that the characteristic $1\mu\text{m}$ PL of ytterbium could be excited with subband energy corresponding to that of free excitons in InP while, at the same time, no photocurrent could be detected indicating no generation of free carriers. Here we present a study of the Yb excitation mechanism by means of microwave-induced impact ionization spectroscopy. We will show that although the excitation process can proceed in a variety of ways depending on the impurities present and the actual concentrations ratio between ytterbium ions and shallow dopants, the dominant PLE mechanism at low temperatures is the one in which the Yb BE state is the intermediating one. We will also show that the DAP \rightarrow Yb energy transfer mechanism (a) is inefficient and can be rejected.

PRELIMINARIES: MICROWAVE-INDUCED IMPACT IONIZATION

The microwave-induced impact ionization technique is in principle based on the phenomenon of cyclotron resonance. If a semiconductor is placed in an external magnetic field, free carriers travel along helical orbits about the axis of the magnetic field B . The angular rotation frequency is:

$$\omega_c = \pm \frac{eB}{m^*}, \quad (1)$$

where m^* is the electron, light-hole, or heavy-hole effective mass. Resonant absorption from a rf electric field perpendicular to the static magnetic field occurs when the radiating frequency is equal to the cyclotron frequency $\nu_c = \omega_c/2\pi$. Electrons and holes spiralize in opposite sense, which is reflected by the \pm sign in Eqn. (1). Since its first observation in semiconductors in 1953, the technique of cyclotron resonance (CR) has been successfully applied to probe conduction or valence band parameters for a given semiconductor near the band edges [18]. In order to observe cyclotron resonance, the following condition has to be fulfilled:

$$\omega_c \tau \geq 1. \quad (2)$$

Here, τ is the average time between collisions of carriers with lattice imperfections such as phonons and impurity atoms. Eqn. (2) states that CR will occur if the electron (or hole) can complete one or more revolutions between collisions. For the cyclotron frequency to be larger than the collision frequency, it is generally necessary to work with high-purity samples at liquid-helium temperature to reduce both impurity and phonon scattering as much as possible. Application of higher radiating frequencies relaxes these requirements. Under the conditions of pure samples and low temperatures the number of free carriers available in thermal equilibrium to participate in CR may be so small that, e.g., photoexcitation is necessary to create them. Indeed, it is possible to detect CR on both types of carriers under optical excitation using above-gap light.

If $\omega_c \tau < 1$, free carriers will be nonresonantly heated by the electric part of the microwave field. At low temperatures ($k_B T \ll E_x$, with E_x the exciton binding energy) and in the absence of an external electric field, few free carriers are energetic enough to dissociate (ionize) excitons by collisions (impact): in this situation of thermal equilibrium each exciton ionization process is balanced by a corresponding formation process. The microwave electric field accelerates (photoexcited) free carriers, thus increasing the number of carriers which have an energy sufficient to impact ionize excitons. The detailed balance between exciton ionization and formation is changed, the impact-ionization rate being significantly increased by the electric-field-induced carrier heating. A critical microwave field exists [19] at which the impact-ionization rate starts to predominate both exciton recombination and ionization by phonon absorption, which is the dominant ionization process in thermal equilibrium [20].

At microwave electric fields larger than the critical value, the exciton concentration sharply drops with a simultaneous avalanche increase in the free-carrier density. This can be observed optically by recording the change of exciton-related luminescence when the microwave power is increased. (The microwave power P_μ is related to the microwave electric field E via $P_\mu \propto E^2$.) By combining the application of microwave power with the PL technique, the different contributions from deep or shallow bound excitons (BE's) and free excitons (FE's) can be separated in the impact-ionization process. This makes optical detection of microwave-induced impact ionization (ODMII) a very powerful technique. It is quite similar to ODCR, in which also the influence of microwaves on PL is studied: ODCR monitors PL changes under cyclotron resonance, whereas ODMII records nonresonant changes, when the CR condition is not fulfilled. The characteristic feature of

ODMII is the existence of a critical value (threshold) of the microwave electric field and thus the microwave power, above which PL intensity changes are observed. This critical value in turn depends on the type of exciton and on the sample purity.

By varying the applied electric field, the relative concentration of free carriers and excitons will be changed, as well as the free-carrier lifetime and the recombination probabilities of the different emissions. Impact ionization of FE's and BE's (which have fast Auger recombination rates) blocks an efficient nonradiative recombination channel and drastically increases the carrier lifetime. This may promote recombination via deeper centers such as isoelectronic bound excitons (IBE's), donor-acceptor pairs (DAP's), and also free-to-bound recombination. It is even possible to enhance deeper emissions which are not seen in the absence of an electric field. In the past the ODMII technique has been successfully applied to defect studies in silicon and GaAs. Weman *et al.* [21] reported the enhancement of a new broad emission band of unknown origin around 1 eV in *n*-type Si, which had never been observed before. For sufficiently high microwave powers the spectral dependence of their broad ODMR background signal showed an increase of both this new 1 eV band and IBE recombination lines together with a decrease of BE recombination at neutral phosphorus donors. Also, Wang *et al.* [22] reported that in high-purity epitaxial GaAs layers the shallow BE and DAP luminescence was quenched in the high-microwave-power case, while the FB emission was enhanced. These results are a clear fingerprint of the impact ionization mechanism: above a critical value of the microwave power shallower emissions are quenched, simultaneously enhancing deeper and/or less probable recombination channels. Moreover, they allow for direct verification which is the mechanism responsible for the common nonresonant background in ODMR studies. Impact ionization by "hot" (accelerated) free carriers affects shallow recombination channels and leads to large changes of relevant PL intensities. In the range of $\omega_c \tau < 1$, this results in damped cyclotron resonance of free carriers which is observed as the nonresonant background in an optically detected magnetic resonance spectrum.

EXPERIMENTALS

The samples used in this study were kindly provided by dr. F. Scholz of the Universität Stuttgart, Germany. They were grown by metalorganic chemical vapor deposition (MOCVD). In the MOCVD-growth process zone-refined trimethylindium - triethylphosphine ($\text{Me}_3\text{InPET}_3$), phosphine, and tri(methyl-cyclopentadienyl)ytterbium ($\text{Yb}(\text{MeCp})_3$) were used as the In, P, and Yb sources, respectively. More details on the growth process can be found elsewhere [4, 23]. The epitaxial InP:Yb layer was grown on a semi-insulating Fe-doped InP substrate; the layer thickness was 3 μm . The samples exhibited *n*-type conductivity with a carrier concentration of $n = 10^{15} - 10^{16} \text{ cm}^{-3}$ at 300 K. The total Yb concentration, as determined by secondary-ion mass spectroscopy (SIMS), was in the $10^{17} - 10^{19} \text{ cm}^{-3}$ range.

Experiments were performed at 2.1 K using a cw Ar^+ -ion laser operating at 514.5 nm to excite the sample. The luminescence was dispersed by a high-resolution 1.5 m F/12 monochromator (Jobin-Yvon THR-1500) with a 600 grooves/mm grating blazed at 1.5 μm , and detected by a liquid-nitrogen-cooled Ge detector (North-Coast EO-817). Impact ionization measurements were performed at 35 GHz using a split-coil superconducting magnet (Oxford Instruments Spectromag 4). Samples were mounted in a cylindrical TE_{001} cavity with slits for optical access. Microwaves, supplied by a Gunn-oscillator, were on-off modulated with a *p-i-n* diode, typically at 730 Hz. Changes of total PL intensity were monitored setting the monochromator to zeroth order.

PHOTOLUMINESCENCE AND IMPACT IONIZATION RESULTS

Fig.1 presents PL spectra of two of the samples used in the present study. As can be seen both spectra are rather similar with approximately the same intensity of Yb PL. Both spectra differ considerably only in the band-edge luminescence. For sample #KS 185 - Fig.1(a) - this band consists of three components at 1417.5 meV, 1387.5 meV, and 1344.6 meV, attributed to free exciton (FE)/donor-bound exciton (DBE) recombination, donor-acceptor pair (DAP) recombination and its LO phonon replica, respectively [24, 25, 26]. The total intensity of this sub-edge band exceeds the Yb PL. For the second sample #KS 175 - Fig.1(b) - the intensity of band-edge PL is very small and amounts only to $\approx 1\%$ of the Yb PL. As can be seen in the insert of the figure the band consists of three peaks at 1419.3 meV, 1410.9 meV, and ≈ 1380 meV, which can be identified as FE, DBE, and DAP recombinations, respectively.

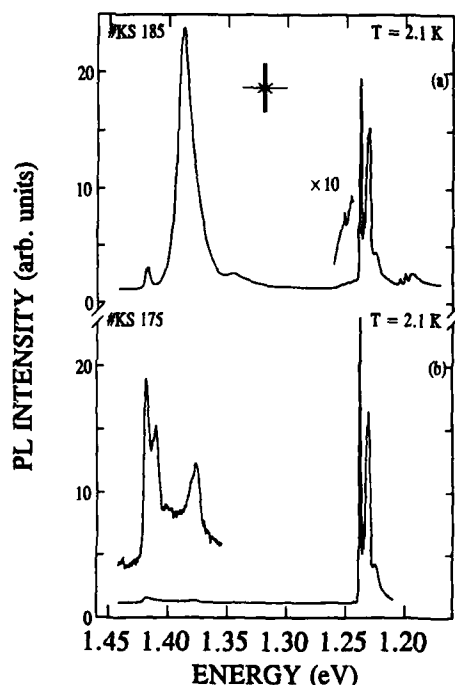


Figure 1: Photoluminescence (PL) spectra of InP:Yb samples used in this study: (a) #KS 185 and (b) #KS 175. The spectra are recorded at 2.1 K under Ar^+ ($\lambda=514.5$ nm)-excitation.

For both samples a second group of lines is observed at 1248.6 meV, 1242.5 meV, 1238.1 meV, and 1230.7 meV. This characteristic luminescence was first reported by Zakharenkov *et al.* [27] and is ascribed to $4f$ -to- $4f$ -shell transitions between the spin-orbit levels $^2F_{5/2}$ and $^2F_{7/2}$ of $\text{Yb}^{3+}(4f^{13})$ split by the crystalline electric field experienced by the Yb_{In} . Since, as discussed before, the $4f$ electrons are screened by the outer-lying closed $5s^25p^6$ shells, the crystal-field splitting of the $^2F_{5/2}$ and $^2F_{7/2}$ levels is rather small as compared to the spin-orbit splitting. Thus the identical spectrum is observed in all InP:Yb samples irrespective of the growth method: LPE, MOCVD, and ion implantation.

The introduction of a magnetic field B , by setting it to 0.5 T, causes no change of photoluminescence. The PL intensity can be influenced by a simultaneous introduction of microwave power. For sample #KS 185 this is illustrated in Fig.2; in this case a 5-6 %

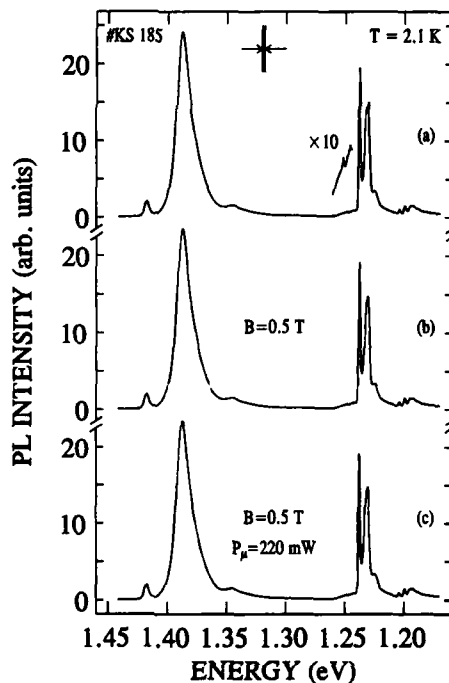


Figure 2: Photoluminescence (PL) spectrum of InP:Yb sample #KS 185 measured at 2.1 K under Ar^+ ($\lambda=514.5$ nm)-excitation (a) without magnetic field B and microwave power P_μ , (b) with $B=0.5$ T and $P_\mu=0$ mW, and (c) with $B=0.5$ T and $P_\mu=220$ mW. The identification of particular PL lines is discussed in the text.

decrease of the overall PL intensity can be noted. Careful analysis of the spectra reveals that the change of PL intensity is different for three different recombination transitions. Whereas the intensity of the FE, DBE and DAP PL is reduced, the Yb^{3+} -related PL intensity is slightly enhanced (by $\approx 1\%$ for both samples). This could be monitored more directly by recording the change of PL intensity while scanning through the luminescence. In this way we could also establish the influence of both P_μ and B on PL intensity. A characteristic example of the spectral dependence of impact ionization, as measured for sample #KS 175 with constant laser excitation and on-off modulated microwave power of 200 mW, is depicted in Fig.3. A relatively high microwave chopping frequency was used (730 Hz) in order to minimize the influence of the so-called bolometric effect on PL intensity; it has been observed before that lattice heating by hot carriers dominates the PL changes for low P_μ chopping frequencies [21]. At high chopping frequencies the dominant mechanism for the PL changes measured in phase with chopped microwaves may be due to impact ionization of excitons and shallow centers by free carriers heated nonresonantly by microwave power.

Relative changes of the PL intensities for $B = 0.5$ T and for different values of P_μ are shown in Figs.4(a) and 4(b) for samples #KS 185 and #KS 175, respectively. ODMII spectra were measured from the maximum power of 220 mW (0 dB attenuation) for #KS 185 and 200 mW for #KS 175 - down, in steps of 2 dB. Data shown in this figure are in fact consistent with the impact ionization mechanism of microwave-induced PL intensity changes. As expected for this mechanism, a threshold dependence on P_μ is observed [21, 28].

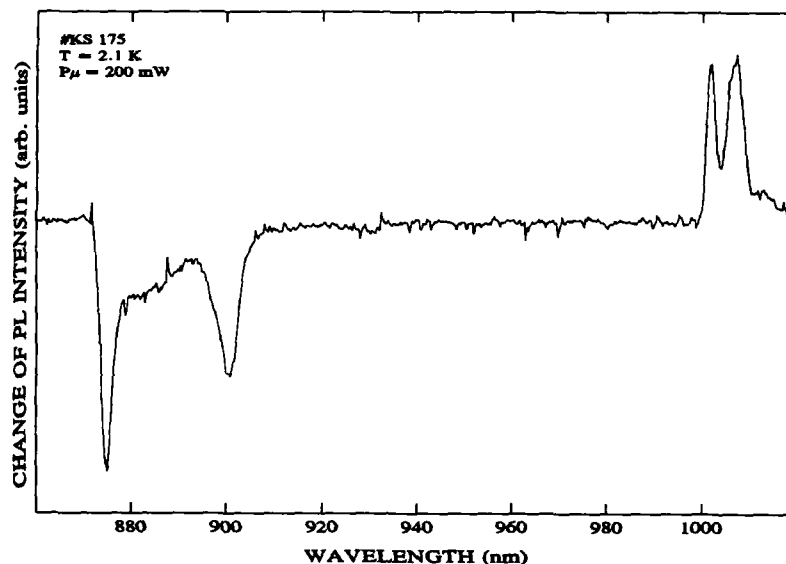


Figure 3: Spectral dependence of impact ionization as measured for sample #KS 175 at 2.1 K and with $B=0.5$ T using 50 mW of constant laser excitation power. The PL signal was detected in phase with the applied microwave power of 200 mW, on-off modulated at 730 Hz.

In view of absolute intensities, the actual threshold values for DBE and DAP transitions could only be determined for the #KS 185 sample; in this case they were found to be 2.2 mW and 5.5 mW, respectively. However, the general behavior of these two bands is similar for both samples. The only difference is that, while in #KS 185 both signals could be quenched by a few percent only, in #KS 175 the band-edge emission could be reduced by more than 50%. In contrast to this, the observed increase of the Yb^{3+} PL differs considerably between the two samples. For #KS 185 it starts to show some saturation for the maximum value of the microwave power; for #KS 175 ytterbium luminescence shows a clear local maximum at ≈ 80 mW followed by a sharp increase for still higher powers.

DISCUSSION

As discussed in the preliminary section the application of a microwave field increases the temperature of laser-excited free carriers. Upon the increase of microwave power, free carriers first reach energies sufficient for DBE impact ionization. As a result the DBE recombination is reduced. For still higher power - $P_\mu > 5.5$ mW for sample #KS 185 - the energy of carriers is large enough to impact ionize shallow donors in InP reducing also the efficiency of DAP recombination. Analyzing this part of the $I_{\text{PL}}(P_\mu)$ dependence we can immediately reject the possibility of a $\text{DAP} \rightarrow \text{Yb}$ energy transfer being the dominant channel for Yb^{3+} PLE in our samples, as proposed by Kasatkin and Savel'ev [10]. They used melt-grown crystals presumably containing a relatively high concentration of residual

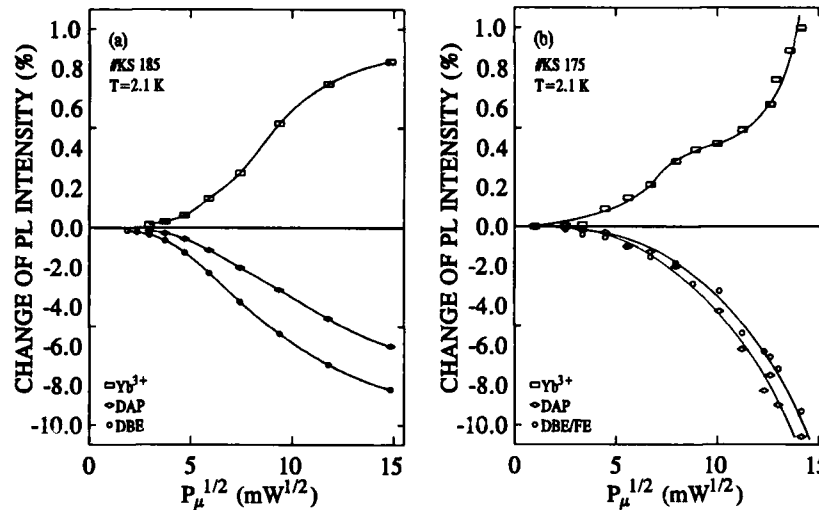


Figure 4: Relative changes of PL intensity (%) versus the square root of applied microwave power chopped at 730 Hz for FE/DBE and DAP recombinations and Yb^{3+} intra-4f-shell emission for sample (a) #KS 185 and (b) #KS 175 (note an enlarged vertical scale for clarity). The experiment was performed at 2.1 K with $B=0.5$ T and constant Ar^+ laser excitation power of 50 mW. The experimental error margin has been indicated. The lines are drawn to guide the eye only.

impurities. Once the DAP transition becomes less effective, Yb^{3+} PL is enhanced – see Fig.4 – being clearly inconsistent with a $\text{DAP} \rightarrow \text{Yb}$ PLE mechanism.

Retrapping of electrons impact ionized from shallow donors should enhance the recombination via a competing electron trap. Indeed, the Yb^{3+} PL starts to be enhanced at the same threshold value of P_μ which leads to DAP quenching, suggesting that electrons ionized from shallow donors are somehow retrapped by Yb^{3+} centres. At the same time electron trapping cannot proceed via the Yb^{2+} level, as suggested previously [29], since this level is not localized in the forbidden gap of InP [6]. Capture thus occurs without a simultaneous change of the ytterbium charge state, via an acceptor-like Yb trap state as discussed in Refs. [3], [6], [8], and [9]. Since it is very unlikely that, in our experiment, trapped electrons recombine with holes on acceptors giving rise to DAP-like transitions, we therefore conclude that upon electron capture, Yb^{3+} transforms to some intermediate state of relatively shallow character.

For higher P_μ the increase of the Yb^{3+} PL does not follow the decrease of the DBE and the DAP transitions. This is especially evident for sample #KS 175, Fig.4(b), where saturation of Yb PL intensity change, in some cases observed even as a local maximum, is found for $P_\mu \approx 80$ mW. Since impact ionization of Yb^{3+} core states is not expected in InP, such an effect must be due to impact ionization (dissociation) of the relatively shallow state intermediating Yb^{3+} excitation. Such an effect is fully consistent with a mechanism of exciton binding by isoelectronic Yb^{3+} centers. Yb^{3+} PL is then excited due to nonradiative recombination of such a BE state (impurity Auger recombination).

Although isoelectronic centres have charge neutrality with respect to the lattice, they can give rise to a short-range potential which creates a bound state for either an electron or hole [30]. The second particle is subsequently bound by the resulting long-range Coulomb potential. The carrier which is primarily bound by Yb can be either an electron [3, 8, 9] or a hole [8]. By combining DLTS and SIMS measurements, Whitney *et al.* [3] determined that the electrically identified acceptor-like electron trap at $\approx E_{CB} - 30$ meV is related to the Yb impurity. Also, Takahei *et al.* [9] could explain their Yb PLE and time-resolved PL data by assuming that Yb ions form electron trap states. From their data Thonke *et al.* [8] could hardly distinguish between the two complementary isoelectronic trap models, although some weak arguments in favor of the pseudodonor model, in which a hole is captured first in a local potential, were given. In either case, carrier capture does not necessarily lead to a change of the charge state of Yb itself; it means that the charge state of the complete cluster of an Yb atom with its phosphorus neighbors can be altered.

In our experiment the ordering of the onset values for impact ionization of FE/DBE and DAP recombinations agrees well with the ordering of DBE and shallow donors levels in InP, i.e. >4 meV and ≈ 7 meV, respectively. For a pseudodonor model of the Yb BE system the electron is captured in a long-range Coulomb field and its ionization energy is then expected to be close to the EMT value, which for InP is 7.31 meV [31]. Since our experimental data show that the saturation of Yb PL occurs for (much) higher powers than the threshold value for impact ionization of shallow donors we take this as an experimental support in favor of a pseudoacceptor model with an electron being captured first, most probably at a deep acceptor-like trap at ≈ 30 meV below the conduction band. (For InP the effective mass of a hole is considerably bigger than that of an electron and thus higher power is needed for its impact ionization.) It should be added here that the impact ionization process is expected to be more effective for sample #KS 175 than for #KS 185 due to lower intensity of band-edge PL. One should note that, as soon as impurities become ionized, the threshold values for impact ionization are no longer linear in microwave power. Ionized impurities (donors) cause a drastic increase in the scattering cross section of nonresonantly heated carriers, thus greatly increasing the microwave power necessary to achieve conditions for impact ionization of centers.

Finally, we will address the increase of Yb PL which, for higher values of microwave power, follows its temporary saturation; this can be observed for sample #KS 175 in Fig.4(b). For this we notice that reported decay time constants of Yb^{3+} PL are of the order of ≈ 10 μs , [8, 12, 29, 9], which is two orders of magnitude faster than the decay of parity-forbidden intra-4f-shell transitions, which are expected to decay in milliseconds, as indeed observed for rare-earth ions in insulating hosts [32]. This large discrepancy is indicative of an efficient nonradiative recombination channel competing with the radiative decay. Takahei *et al.* [9] proposed that the Yb^{3+} decay time may be controlled by a nonradiative two-center Auger-type process involving Yb^{3+} in its excited state and an occupied shallow donor. Yb^{3+} decays due to an energy transfer from Yb to the nearby occupied donor resulting in ionization of this donor. An alternative mechanism assumes that, similarly to Yb^{3+} in the ground state, also the ytterbium ion in its excited state forms an acceptor-like electron trap. An electron localized on excited Yb could then take part in nonradiative recombination. In our opinion, the results depicted in Fig.4(b) present the first experimental fingerprint of such a process: upon increasing the microwave power a particle intermediating the process is impact ionized, which effectively blocks the nonradiative recombination channel. This effect strongly enhances radiative recombination of an excited Yb^{3+} ion clearly overcoming the earlier mentioned opposite effect of dissociation of Yb BE. (It should be noted here that the impact ionization of Yb BE is not expected to be very effective; the fact that it is the deepest of three radiative

recombination mechanisms taking place in the studied material, and that the binding field is of Coulombic, i.e., extended character, will lead to an efficient recapture of the impact-ionized holes by electrons bound to AE trap of ytterbium. On the other hand, the electron participating in the nonradiative Auger recombination of the BE is trapped in a local potential and, as such, can be effectively ionized.) At the same time, our data argue against the two-center Auger process involving shallow donors, the impact ionization of which observed for a relatively small microwave power does not result in any enhancement of YB PL.

CONCLUSIONS

Concluding, it has been shown that the dominant PLE mechanism of the $\text{Yb}^{3+}(4f^{13})$ -related emission is due to the impurity Auger recombination. Ytterbium in InP binds an exciton which intermediates Yb core states excitation. Impact ionization data of this BE system indicate that the system is of a pseudoacceptor type with the electron being localized first, at a considerably deeper level. Our data also indicate that an Auger-type process, most probably involving an additional carrier localized by the ytterbium ion in an excited state, may be responsible for the fast nonexponential decay of the Yb^{3+} emission, as suggested previously by Takahei *et al.* [9]. It is shown that the nonradiative recombination channel can be effectively blocked by impact ionization. The latter observation is of particular importance in view of potential applications of rare-earth-doped III-V compounds for light-emitting devices.

References

- [1] L.A. Hemstreet in *Proceedings of the XIV International Conference on Defects in Semiconductors*, Vols. 10-12 of *Materials Science Forum*, edited by H.J. von Bardeleben (Trans Tech Publications, Aedermannsdorf, Switzerland, 1986), p. 85.
- [2] W. Körber, J. Weber, A. Hangleiter, K.W. Benz, H. Ennen, and H.D. Müller, *J. Cryst. Growth* **79**, 741 (1986).
- [3] P.S. Whitney, K. Uwai, H. Nakagome, and K. Takahei, *Appl. Phys. Lett.* **53**, 2074 (1988).
- [4] J. Weber, A. Molassioti, M. Moser, A. Stapor, F. Scholz, G. Hörcher, A. Forchel, A. Hammel, G. Laube, and J. Weidlein, *Appl. Phys. Lett.* **53**, 2525 (1988).
- [5] B. Lambert, A. Le Corre, Y. Toudic, C. Lhomer, G. Grandpierre, and M. Gauneau, *J. Phys.: Condens. Matter* **2**, 479 (1990).
- [6] B. Lambert, Y. Toudic, G. Grandpierre, A. Rupert, and A. Le Corre, *Electron. Lett.* **24**, 1446 (1988).
- [7] H. Nakagome, K. Takahei, and Y. Homma, *J. Cryst. Growth* **85**, 345 (1987).
- [8] K. Thonke, K. Pressel, G. Bohnert, A. Stapor, J. Weber, M. Moser, A. Molassioti, A. Hangleiter, and F. Scholz, *Semicond. Sci. Technol.* **5**, 1124 (1990).
- [9] K. Takahei, A. Taguchi, H. Nakagome, K. Uwai, and P.S. Whitney, *J. Appl. Phys.* **66**, 4941 (1989).
- [10] V.A. Kasatkin and V.P. Savel'ev, *Sov. Phys.-Semicond.* **18**, 1022 (1984).

- [11] V.A. Kasatkin, A.A. Lavrent'ev, and P.A. Rodnyi, *Sov. Phys.-Semicond.* **19**, 221 (1985).
- [12] W. Körber and A. Hangleiter, *Appl. Phys. Lett.* **52**, 114 (1988).
- [13] D.J. Robbins and P.J. Dean, *Adv. Phys.* **27**, 499 (1978).
- [14] H. Przybylińska, K. Świątek, A. Stapor, A. Suchocki, and M. Godlewski, *Phys. Rev. B* **40**, 1748 (1989).
- [15] K. Świątek and M. Godlewski, *Appl. Phys. Lett.* **56**, 2192 (1990).
- [16] C. Lhomer, B. Lambert, Y. Toudic, A. Le Corre, M. Gauneau, F. Clérot, and B. Sermage, *Semicond. Sci. Technol.* **6**, 916 (1991).
- [17] K. Świątek, A. Suchocki, and M. Godlewski, *Appl. Phys. Lett.* **56**, 195 (1990).
- [18] For a review on cyclotron resonance, see: B. Lax, *J. Magn. Magn. Mater.* **11**, 1 (1979).
- [19] D.L. Smith, D.S. Pan, and T.C. McGill, *Phys. Rev. B* **12**, 4360 (1975).
- [20] A.A. Lipnik, *Sov. Phys.-Solid State* **3**, 1683 (1962).
- [21] H. Weman, M. Godlewski, and B. Monemar, *Phys. Rev. B* **38**, 12525 (1988).
- [22] F.P. Wang, B. Monemar, and M. Ahlström, *Phys. Rev. B* **39**, 11195 (1989).
- [23] G. Laube, U. Kohler, J. Weidlein, F. Scholz, K. Streubel, R.J. Dieter, N. Karl, and M. Gerdon, *J. Cryst. Growth* **93**, 45 (1988).
- [24] B.J. Heijmink Liesert, M. Godlewski, A. Stapor, T. Gregorkiewicz, C.A.J. Ammerlaan, J. Weber, M. Moser, and F. Scholz, *Appl. Phys. Lett.* **58**, 2237 (1991).
- [25] J.U. Fischbach, G. Benz, N. Stath, M.H. Pilkuhn, and K.W. Benz, *Solid State Commun.* **11**, 721 (1972).
- [26] J.U. Fischbach, G. Benz, N. Stath, and M.H. Pilkuhn, *Solid State Commun.* **11**, 725 (1972).
- [27] L.F. Zakharenkov, V.A. Kasatkin, F.P. Kesamanly, B.E. Samorukov, and M.A. Sokolova, *Sov. Phys.-Semicond.* **15**, 946 (1981).
- [28] M. Godlewski, H. Weman, F.P. Wang, B. Monemar, W.M. Chen, and Q.X. Zhao, in *Defects in Electronic Materials*, edited by M. Stavola, S.J. Pearton, and G. Davies (Materials Research Society, Pittsburgh, 1988), Vol. 104, p. 117.
- [29] P.B. Klein, *Solid State Commun.* **65**, 1097 (1988).
- [30] J.J. Hopfield, D.G. Thomas, and R.T. Lynch, *Phys. Rev. Lett.* **17**, 312 (1966).
- [31] Landolt-Börnstein, *Numerical Data and Functional Relationships in Science and Technology*, edited by M. Schulz (Springer, Berlin, 1989), Vol. III/22b, p. 670.
- [32] B. Di Bartolo, *Optical Interactions in Solids* (Wiley, New York, 1968), p. 521.

ANNEALING STUDIES OF Er-IMPLANTED GaAs AND THE EXCITATION MECHANISM OF Er IN GaAs

D. W. Elsaesser*, J. E. Colon*, Y. K. Yeo*, R. L. Hengehold*, and G. S. Pomrenke**

*Air Force Institute of Technology, Wright-Patterson AFB, Oh 45433

**Air Force Office of Scientific Research, Bolling AFB, DC 20332

ABSTRACT

Electrical and optical measurements were performed on p-type GaAs implanted with 10^{13} Er ions/cm² at an energy of 1 MeV. The samples were annealed at 650, 750, 850, or 900 °C for 15 seconds using the rapid thermal annealing technique. Although annealing at 650 °C was insufficient to recover measureable electrical conductivity in the implanted region, Er³⁺ 4f-4f emissions were still observed. Annealing at 750 °C produced a large concentration of hole traps at $E_V + 360$ meV, and the most intense Er-related emissions at 1.54 μ m. The two higher annealing temperatures returned the implanted region to the conductivity of the substrate but resulted in weak Er-related emissions. Two distinct Er-related centers were found, and they are believed to be the cause of the intense and weak emissions, an Er-interstitial and Er substituting for Ga, respectively.

INTRODUCTION

Rare earth (RE) atoms are being investigated as dopants in III-V semiconductors due to their sharp intra-4f-shell emissions which, unlike band-edge emissions, have line-widths and energies that are largely independent of crystal host and temperature. The RE atom Er is of particular interest because the weakly crystal-field split transition from the first excited state to the ground state of the Er³⁺ 4f¹¹ shell, $^4I_{13/2} \rightarrow ^4I_{15/2}$, has a wavelength of 1.54 μ m which is near the minimum in attenuation for silica-based optical fibers. Thus, RE-doped and especially Er-doped semiconductors have applications in optoelectronics. In order to realize the most efficient devices, an understanding of RE-luminescence excitation and quenching mechanisms must be achieved.

A model for the excitation and de-excitation mechanisms of the 4f shell of a RE atom in a III-V semiconductor material has been recently proposed for Yb in InP by Takahei et al. [1]. Their model relies heavily on the earlier reports by Whitney et al. [2] of an isolated Yb on In substitutional giving rise to a 30 meV isoelectronic electron trap. This center binds an exciton, which recombines and nonradiatively transfers its energy to the Yb³⁺ 4f shell. Although GaAs has a similar band gap energy to InP, the relatively strong Yb³⁺ intra-4f-shell luminescence observed in InP is conspicuously absent in Yb-doped GaAs. This has been attributed to the apparent formation of Yb-related deep electron traps between 0.5 and 0.7 eV below the conduction band [3], and thus it may not be energetically possible to excite the Yb³⁺ 4f shell. Therefore, the RE-related electron or hole trap levels introduced into the III-V band gap may play a crucial role in the excitation and de-excitation mechanisms of RE³⁺ 4f shells.

The predominant mechanism for the excitation of the Er³⁺ 4f shell in GaAs has been somewhat more difficult to identify. This is related to generally weaker Er³⁺ intra-4f-shell emissions and the fact that, unlike Yb in InP, Er seems to form two or more centers in GaAs [4]. Previously we have reported that Er doping of n-type GaAs introduced hole traps [1,5]. In this paper, we report on the occurrence of these Er-related centers and other deep centers in Er-implanted p-type GaAs. Specifically, a study of the electrical and optical properties of Er-implanted GaAs as a function of annealing temperature will be presented and used as a basis for a discussion of the excitation Er³⁺ intra-4f-shell emissions in Er-implanted GaAs.

ANNEALING STUDY

Er was implanted at an energy of 1 MeV with a fluence of $10^{13}/\text{cm}^2$ into a $3\text{ }\mu\text{m}$ thick Zn-doped MOCVD grown GaAs layer, with $p = 4 \times 10^{16}\text{ cm}^{-3}$. The samples were then rapid thermal annealed at 650, 750, 850, or 900 °C for 15 seconds in flowing N_2 gas. Band-edge and Er-related photoluminescence (PL) measurements were performed at 4 K, with 488 nm excitation provided by an Ar^+ -ion laser. The emissions were dispersed with a 3/4-m spectrometer and detected with a liquid-nitrogen cooled Ge-detector. Capacitance voltage (CV) carrier profiles and deep level transient spectroscopy (DLTS) measurements were performed on Schottky diodes fabricated using sequential Ti/Au evaporation for the Schottky contact and Au/Zn/Au evaporation for the ohmic contact to the underlying p-layer, which was obtained by etching approximately $1\text{ }\mu\text{m}$ to remove the implanted region.

Figures 1 and 2 show CV carrier profiles and photoluminescence obtained from the Er-implanted GaAs, respectively, as a function of annealing temperature. Figure 1 also shows a typical atomic Er distribution as measured by secondary ion mass spectrometry (SIMS) for Er implantation at the present energy and fluence in GaAs. For the 650 °C anneal, the CV carrier profile begins at about $0.7\text{ }\mu\text{m}$, with no applied bias. Furthermore, slight forward biasing was not effective in probing the implanted region. This is undoubtedly due to the high degree of damage remaining after the anneal. For this sample, the implanted region is probably still in a nearly amorphous state. Nevertheless, Er-related emissions are still measurable, as indicated in Fig. 2 by the small peak observed near $1.54\text{ }\mu\text{m}$.

After annealing at 750 °C, the electrical and optical properties of the implanted layer changed drastically. While we were not able to obtain reliable CV carrier profiles for this annealing temperature, DLTS measurements revealed a large concentration of hole traps, located approximately 360 meV above the valence band, $E_V + 360\text{ meV}$, which has been previously reported in Er-implanted GaAs by Colon et al. [1]. The presence of this center

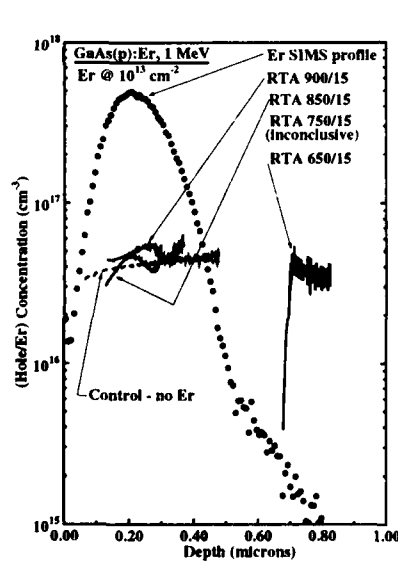


Fig. 1. CV hole carrier profiles for p-type GaAs implanted with Er at an energy of 1 MeV with a fluence of $10^{13}/\text{cm}^2$, and rapid thermal annealed at various temperatures.

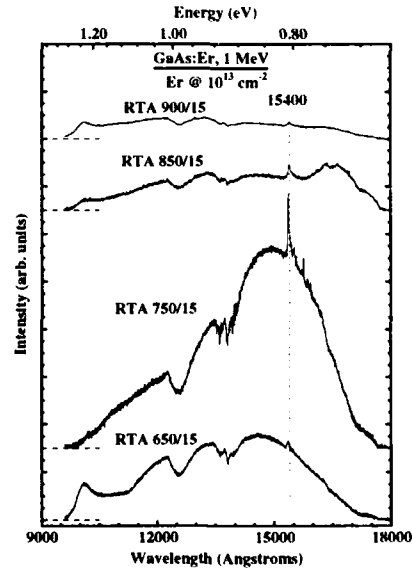


Fig. 2. Photoluminescence of p-type GaAs implanted with Er as a function of annealing temperature, showing Er-related emissions near $1.54\text{ }\mu\text{m}$.

coincides with a large enhancement of the Er^{3+} intra-4f-shell emissions in the $1.54\text{ }\mu\text{m}$ region, as shown in Fig. 2. This spectrum also exhibits a very broad and intense background emission. However, it should be noted that the spectra are not corrected for the response of the grating and detector, and so their shape is to a large extent determined by that response. Our first thought was to attribute these broad emissions to recombinations at unannealed damage-related centers. However, evidence observed to the contrary is presented in Fig. 3, which shows the different RE-related emissions from semi-insulating GaAs implanted with Pr, Nd or Er, with the implant energies, fluences, and annealing conditions listed in the figure. The peak at $1.66\text{ }\mu\text{m}$ observed for the Pr- and Nd-implanted GaAs is the second order band-edge emissions, which were blocked by a $1\text{ }\mu\text{m}$ long-pass filter for the Er-implanted sample. The RE-related emissions from GaAs:Pr ($^1\text{G}_4 \rightarrow ^3\text{H}_5$) and GaAs:Nd ($^4\text{F}_{3/2} \rightarrow ^4\text{I}_{11/2}$) were not accompanied by the broad emission at this annealing temperature, nor any other annealing temperatures between 700 and $825\text{ }^\circ\text{C}$.

We would expect the Pr implantation and especially the Nd implantation to produce a similar amount of crystal damage as encountered in the Er-implanted sample. Furthermore, the annealing behavior of implantation damage-related centers should not strongly depend upon the chemical nature of the RE ion. Therefore, the broad emission, which we have consistently observed in n-type, p-type, and undoped GaAs implanted with Er, is possibly due to the recombination at Er-related deep centers in the band gap.

Annealing Er-implanted GaAs at the higher temperatures of 850 and $900\text{ }^\circ\text{C}$ caused the hole concentration of the implanted region to return to the value of the substrate, as shown in Fig. 1. Furthermore, DLTS measurements indicated a drastic decrease in the concentration of the deep hole traps. The decrease in the concentration of this deep center is also accompanied by a decrease in the intensity of the Er-related emissions as well as the intensity of the broad band.

Another annealing trend is illustrated in Fig. 4, which shows the spectra from Fig. 2 in the much narrower spectral range of 1.5 and $1.6\text{ }\mu\text{m}$. There is a definite shift in the dominant peak position from $1.537\text{ }\mu\text{m}$ for annealing at 650 and $750\text{ }^\circ\text{C}$ to $1.540\text{ }\mu\text{m}$ for annealing at 850 and $900\text{ }^\circ\text{C}$. This indicates that different Er centers are dominating the emissions for low and high annealing temperatures.

Near-band-edge PL measurements were also performed on each annealed sample, as shown in Fig. 5. The increasing intensity of the free-to-bound recombination at 1.49 eV with annealing temperature indicates the annealing of implantation-induced defects. An emission at

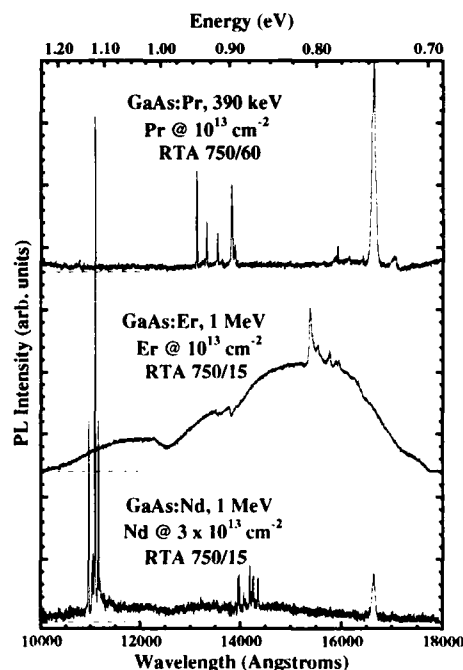


Fig. 3. Photoluminescence of Nd, Er, and Pr-implanted GaAs, at the energies and fluences shown in the figure. Each sample exhibits the sharp intra-4f emissions. However, the broad emission is only observed for the Er-implanted sample.

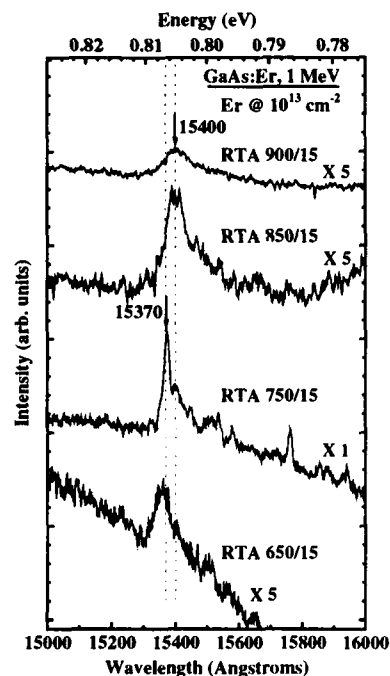


Fig. 4. PL measurements of Er-implanted p-type GaAs, as a function of annealing temperature, showing that two distinct centers are formed.

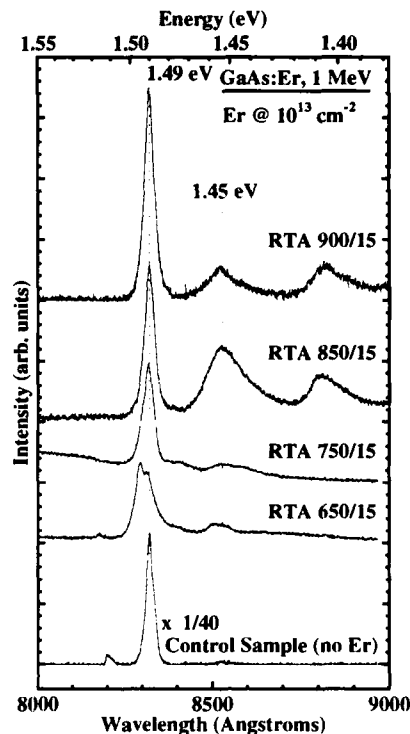


Fig. 5. Near-band-edge PL of Er-implanted p-type GaAs as a function of annealing temperature

1.45 eV is also present. A similar emission has been reported by Yu et al. [6], who also performed temperature-dependent Hall effect measurements, and attributed this emission to recombination at the Ga-antisite defect.

DISCUSSION

The annealing study presented above is complementary to three previous annealing studies performed on Er-implanted GaAs. The first study was performed by Pomrenke et al. [7], who performed PL measurements on Er-implanted GaAs after annealing with a strip heater or after conventional furnace annealing. They found that annealing with the strip heater produced the most intense Er^{3+} 4f-4f emissions, which increased sharply in intensity between the annealing temperatures of 700 °C and 800 °C, and decreased for higher temperature anneals. Their furnace annealed samples exhibited the same annealing trend, but with a much broader maximum in the Er^{3+} 4f-4f emission intensity vs. annealing temperature, with the peak occurring between 625 and 700 °C.

Kozanecki et al. [8] implanted Er in GaAs and performed Rutherford back scattering (RBS) and PL measurements after rapid thermal annealing at temperatures between 700 and 1000 °C. They found that for the lower annealing temperatures, the Er^{3+} intra-4f-shell emissions were relatively intense, and RBS measurements indicated a large concentration of

interstitial Er. However, after annealing at 1000 °C, the Er-related emissions were extinguished, and only less than 3% of the Er atoms occupied interstitial positions. This leads us to conclude that the hole trap near 360 meV above the valence band, which has a large concentration for the lower to intermediate annealing temperatures, is associated with an interstitial Er atom, which exhibits relatively intense 4f-4f emissions. On the other hand, the concentration of substitutional Er increased as the annealing temperature increased, with the Er probably substituting for the Ga atom, i.e., forming the Er_{Ga} center. This is consistent with the observed shift in the dominant peak of the Er^{3+} intra-4f-shell emissions from 1.537 to 1.540 μm , as the annealing temperature increases. Furthermore, we have previously reported the occurrence of a 35 meV hole trap in lightly Er-doped MBE-grown GaAs [5]. Due to the shallow nature of this level, we had assigned it to the Er_{Ga} center, which produced an isoelectronic hole trap. Thus, the Er_{Ga} centers are probably responsible for the relatively weak Er^{3+} intra-4f-shell emissions centered at 1.540 μm .

Klein et al. [1] used conventional furnace annealing on 1 to 1.5 μm layers with a uniform Er concentration of $5 \times 10^{17} \text{ cm}^{-3}$, produced by Er implantation at multiple ion energies up to 5 MeV. Their measurements revealed four distinct Er centers formed in Er-implanted GaAs. Three of these centers have a peak in Er-related PL intensity for annealing between 700 °C and 750 °C, which falls off sharply at higher annealing temperatures. The fourth center gives much weaker Er-related luminescence, but its intensity gradually increased with annealing temperature, and peaked near 800 °C. Based upon the current results and those of Kozanecki, this luminescence probably arises from the Er_{Ga} center. On the other hand, one of the three centers giving the relatively intense Er-related emissions probably corresponds to interstitial Er. The two remaining Er centers reported by Klein may be related to complexes of Er with unannealed damage-related or other defects. For instance, Klein et al. also reported a thermal activation energy of 65 meV as a temperature quenching mechanism for certain Er emissions. This value is quite close to the first acceptor level of the Ga_{As} defect at 77 meV, which has been observed in the present study. Thus, one such Er complex might involve the Ga antisite defect. Furthermore, the broad and intense band observed for Er-implanted GaAs and not for Pr- or Nd-implanted GaAs is possibly related to recombination at one or more of the three Er-related centers which are prevalent for annealing below 800 °C, since Fig. 2 shows that this band is significantly diminished for higher annealing temperatures.

In contrast to the case of InP:Yb , where the Yb_{In} center has been associated with strong Yb^{3+} 4f-4f luminescence, it has been found that the Er_{Ga} center in GaAs:Er is associated with relatively weak Er^{3+} 4f-4f luminescence. This may be due to the small (large) imbalance between the band gap energy and RE^{3+} 4f excitation energy in the former (latter) case. The first excited state of the Yb^{3+} 4f shell ($^4\text{F}_{7/2}$) is 1.2 eV above the ground state ($^4\text{F}_{9/2}$), which is close to the 1.4 eV band gap energy of InP. However, the first excited state of the Er^{3+} 4f shell ($^4\text{I}_{13/2}$) is only 0.8 eV above the ground state ($^4\text{I}_{15/2}$), or slightly more than half of the 1.52 eV GaAs band gap energy. Thus, in the case of GaAs:Er , energy transfer from a bound exciton to the Er^{3+} 4f shell seems unfeasible without the presence of a third particle to carry away the excess energy.

Such an Auger assisted process for the isolated Er_{Ga} may occur as follows. At low temperatures the isoelectronic level associated with the Er_{Ga} center would be unoccupied (occupied with a hole). This center may bind an exciton, which transfers its recombination energy to the excitation of the 4f shell with the remainder exciting the trapped hole deep into the valence band. However, as temperature increases, this center will be more likely to be occupied. In this case, a bound exciton would not have sufficient energy to excite the Er^{3+} 4f shell and simultaneously lift the electron occupying this level to the conduction band. In fact, Klein et al. [1] have also observed a thermal activation energy of 36 meV for temperature quenching of the Er^{3+} 4f-4f emissions in Er-doped MBE-grown GaAs, adding credence to

these proposed excitation/quenching mechanisms for Er^{3+} 4f shell in GaAs. On the other hand, the energy mismatch is significantly lowered for an Er-interstitial center located at $E_V + 360$ meV. Thus, the same excitation mechanism proposed for the Er_{Ga} center may now be much more energetically efficient for the interstitial Er center, explaining the more intense Er^{3+} intra-4f-shell luminescence observed when the concentration of these centers dominate. The stronger RE luminescence may also be accounted for by additional excitation pathways available for the interstitial Er center. For instance, an incident photon may simultaneously transfer a valence band electron to an unoccupied 360 meV level at the interstitial Er center and simultaneously excite the Er^{3+} 4f shell. Such a process would have a threshold energy of $1.16 (= 0.8 + 0.36)$ eV. In fact, we have previously reported even stronger Er^{3+} 4f-4f luminescence with below band gap excitation, which extends to energies much lower than the energies of band-edge transitions, such as, donor-acceptor pairs [1].

SUMMARY

CV and PL measurements have shown that Er forms at least two centers with very different annealing behavior in Er-implanted GaAs. The first center is dominant at lower annealing temperatures, reaching a maximum concentration for a rapid thermal anneal at 750°C . This center, which gives the most intense Er^{3+} intra-4f-shell emissions centered at $1.537\ \mu\text{m}$, is probably related to an Er interstitial which is believed to introduce a hole trap at roughly $E_V + 360$ meV. The second center, which gives much weaker Er-related emissions centered at $1.540\ \mu\text{m}$, occurs at higher annealing temperatures (850°C and above) and is believed to be related to the Er_{Ga} center. A comparison with the previous studies of Yb-doped III-V semiconductors indicates that an energy level position of the RE-related deep center in the band gap seems to be a critical parameter determining the excitation efficiency of the RE^{3+} 4f shells.

REFERENCES

1. K. Takahei and A. Taguchi in *Defects in Semiconductors 16*, edited by G. Davies, G. Deleo, and M. Stavola (Trans Tech Publications Ltd, Zürich, 1992), pp. 641-652; P. Klein, G. Moore, and H. Dietrich, *ibid.*, pp. 665-670; J. Colon, D. Elsaesser, Y. Yeo, R. Hengehold, and G. Pomrenke, *ibid.*, pp. 671-676
2. P. Whitney, K. Uwai, H. Nakagome, and K. Takahei, *Appl. Phys. Lett.* **53**, 2074 (1988)
3. A. Taguchi, H. Nakagome, and K. Takahei, *J. Appl. Phys.* **68**, 3390 (1990)
4. K. Evans, E. Taylor, C. Stutz, D. Elsaesser, J. Colon, Y. Yeo, R. Hengehold, and J. Solomon, *J. Vac. Sci. B* **10**, 870 (1992)
5. D. Elsaesser, J. Colon, Y. Yeo, R. Hengehold, K. Evans and J. Solomon, Proceedings of MBE-VII, to be published in *J. Crystal Growth*
6. P. Yu, W. Mitchel, M. Mier, S. Li, and W. Lang, *Appl. Phys. Lett.* **6**, 532 (1982)
7. G. Pomrenke, H. Ennen, and W. Haydl, *J. Appl. Phys.* **59**, 601 (1986)
8. A. Kozanekci, M. Chan, C. Jeynes, B. Sealy, and K. Homewood, *Solid-State Communications* **78**, 763 (1991)

PHOTOLUMINESCENCE STUDY OF ENERGY TRANSFER PROCESSES IN ERBIUM DOPED $\text{Al}_x\text{Ga}_{1-x}\text{As}$ GROWN BY MBE

TONG ZHANG, J. SUN*, N.V. EDWARDS*, D.E. MOXEY*, R.M. KOLBAS* AND P.J. CALDWELL**

Department of Materials Science and Engineering

*Department of Electrical and Computer Engineering, North Carolina State University, Raleigh, NC 27695-7911

**Martin Marietta, 1450 S. Rolling Rd., Baltimore, MD 21227-3898

ABSTRACT

Sharp photoluminescence from the intra-4f shell of Er^{3+} is observed from erbium doped $\text{Al}_x\text{Ga}_{1-x}\text{As}$ ($0 \leq x \leq 1$) grown by molecular beam epitaxy. The intensity of the luminescence from the erbium is strongly dependent on the aluminum composition with a maximum at $x \approx 0.6$. We will present a model that explains the variation in intensity based on the energy transfer coupling efficiency between the host semiconductor and the optically active erbium ions. The coupling efficiency is dominated by the alignment or misalignment of the erbium energy levels with the energy bands of the host semiconductor and by the excess carrier lifetime in the host. The data and model, which are presented here for the first time, are consistent with our previous work on the effects of co-doping with Be or Si and with other workers' measurements of thermal quenching in rare earth doped semiconductors.

INTRODUCTION

Erbium doped semiconductors have received a lot of attention in the past few years because of their potential use in temperature-stable near-infrared light emitters. The intra-4f shell transition from an excited state ($^4\text{I}_{13/2}$) to the ground state ($^4\text{I}_{15/2}$) of the trivalent erbium ion, Er^{3+} , results in sharp luminescence near $1.5\mu\text{m}$ with little dependence on the host material and temperature. Such intra-4f shell transitions in a host semiconductor can be activated by either photoexcitation or electronic excitation. Electronic excitation is the most attractive for practical device operation.

Erbium doped III-V compounds have been prepared by liquid phase epitaxy, ion implantation, metalorganic chemical vapor deposition and molecular beam epitaxy (MBE) [1, 2]. Photoluminescence (PL) near $1.54\mu\text{m}$ at 77K and room temperature has been observed by several research groups. However, the manner by which the erbium ions are excited by the host semiconductor has not been resolved. Identification of these excitation mechanisms is of great importance for the growth and design of practical light emitting devices.

We report the growth by MBE and photoluminescence characterization of erbium doped $\text{Al}_x\text{Ga}_{1-x}\text{As}$ ($0 \leq x \leq 1$). The Er^{3+} luminescence intensity is strongly dependent on the aluminum composition. A model is proposed to explain this variation, which is based on the energy transfer coupling efficiency between the host semiconductor and the optically active erbium ions.

EXPERIMENTAL METHODS

The samples reported here were all grown by MBE in a Varian 360 at 500°C . The $1.3\mu\text{m}$ thick epilayers were grown on (100)-oriented semi-insulating GaAs substrates at a growth rate of approximately $1\mu\text{m}$ per hour and a beam flux equivalent pressure ratio $\text{V/III} \approx 10$. Various doping concentrations were obtained by using a source of 4N's purity metallic erbium at an effusion cell temperature ranging from 700°C to 1100°C . An erbium doping concentration of $1 \times 10^{18}\text{cm}^{-3}$ was achieved at an effusion cell temperature of 820°C as measured by Secondary Ion Mass Spectrometry (SIMS). A series of $\text{Al}_x\text{Ga}_{1-x}\text{As}$ samples ($0 \leq x \leq 1$) were grown at substrate temperatures from 380°C to 640°C with various erbium concentrations. The aluminum composition was determined by photoluminescence for $x \leq 0.4$ and by Double Crystal X-Ray Diffraction (DXRD) for $x > 0.4$. The highest intensity

photoluminescence (77K) spectra were obtained from $\text{Al}_x\text{Ga}_{1-x}\text{As:Er}$ samples grown at 500 °C with a doping concentration of $\sim 1 \times 10^{18} \text{cm}^{-3}$. At lower or higher doping concentrations a reduction of PL intensity was observed, and a poor surface morphology resulted from very high doping concentrations. This paper focuses on the series of $\text{Al}_x\text{Ga}_{1-x}\text{As}$ samples grown at 500 °C with an erbium doping concentration of $1 \times 10^{18} \text{cm}^{-3}$.

Photoexcitation was provided by the 5145 Å line of a cavity-dumped argon ion laser (8ns pulses at 3.8 MHz repetition rate) with an average power of 50 mW. The continuous wave (CW) photoluminescence experiments were carried out using the 3511 Å line (50mW) from an argon ion laser or the 6328 Å line (1mW) from a He-Ne laser. The PL signal was detected with a 0.6 m monochromator and a liquid nitrogen cooled Ge photodetector using an optical chopper (at a frequency of 200 Hz) and a lock-in amplifier.

RESULTS AND DISCUSSION

A PL spectrum at 77K from an erbium doped $\text{Al}_{0.4}\text{Ga}_{0.6}\text{As}$ sample is shown in Fig. 1. The emission lines near 1.54 μm and the one at 0.98 μm correspond to the electron intra-4f transitions $^4I_{13/2} \rightarrow ^4I_{15/2}$ and $^4I_{11/2} \rightarrow ^4I_{15/2}$, respectively. The insert illustrates the principal energy manifolds and the splitting of these levels for an Er^{3+} . The 1.54 μm emission line was also observed in the room temperature PL spectrum from this sample. Note that the 0.98 μm emission peak from the transition $^4I_{11/2} \rightarrow ^4I_{15/2}$ is more than one order of magnitude weaker than the other lines. The predominant transition was the $^4I_{13/2} \rightarrow ^4I_{15/2}$ emission near 1.54 μm for all of the aluminum alloy compositions and erbium doping concentrations measured except when co-doped with silicon.

The samples reported in this paper were all grown at the same substrate temperature ($T_s = 500$ °C) with an identical erbium doping flux. We observed, as have other researchers [3, 4], that there is an order of magnitude difference in the Er^{3+} related emission intensity between samples of $\text{Al}_{0.4}\text{Ga}_{0.6}\text{As:Er}$ and GaAs:Er . We propose that the presence of aluminum enhances the activation of erbium atoms resulting in a larger number of optically active Er^{3+} centers in the material and/or that certain aluminum compositions enhance the energy transfer from the host semiconductor to the Er^{3+} centers.

The experimental results revealed that the emission intensity at 1.56 and 1.54 μm changes with aluminum composition x as shown in Fig. 2 (77K). There exist a maximum intensity at $x=0.6$ and possibly a shoulder at $x=0.43$ for both emission lines. Note that a substantial increase in intensity occurs in the crossover region of the direct and indirect

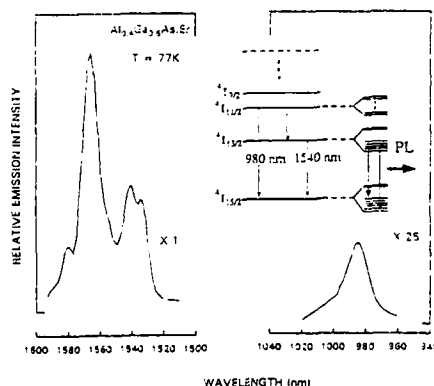


Fig. 1. 77K photoluminescence from $\text{Al}_{0.4}\text{Ga}_{0.6}\text{As:Er}$ grown at 500 °C with an Er doping concentration of $1 \times 10^{18} \text{cm}^{-3}$.

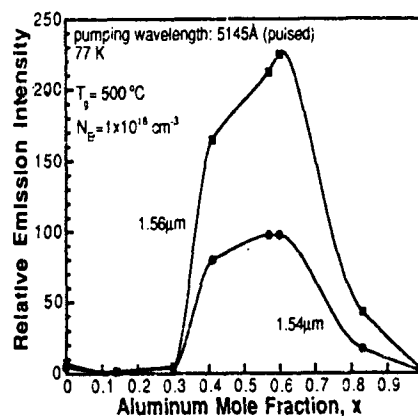


Fig. 2. Emission intensity versus $\text{Al}_x\text{Ga}_{1-x}\text{As}$ alloy composition x , using pulsed photoexcitation ($h\nu = 2.41 \text{eV}$).

bandgap ($0.4 < x < 0.5$). It should be pointed out that good structural and optical quality of the host material is essential in order to perform these measurements.

In an erbium doped semiconductor, the trivalent erbium ions could be excited by two different energy transfer mechanisms. One energy transfer mechanism (photon process) is via photons in which a photon is generated by a radiative recombination event in the host material and is subsequently absorbed by an Er^{3+} center. In this case it is not necessary for the energy levels of the Er^{3+} center and the band edges of the host to be aligned. The second mechanism (electronic process) is via carrier capture by the Er^{3+} center acting as a deep electron trapping level. In this case the energy levels contributing to the emission must reside within the band gap of the host material or within a few kT of the host band edges to successfully capture a carrier (electron or hole). A theoretical discussion of both electron-hole pair excitation (photon process) and non-equilibrium electron excitation (electronic process) was given by Schmitt-Rink *et al.* [5]. In our study the electronic process is a better predictor of the experimental results. For example, as shown in Fig. 2, a relatively strong erbium-related emission was measured in the high aluminum composition region ($x > 0.43$). In this indirect band-to-band transition region, very little or no radiative electron-hole recombination is available to generate photons which are needed to excite the erbium ions according to the photon process.

Considering the effect of the aluminum composition on the emission intensity, as shown in Fig. 2, we propose that there are two possible excitation processes contributing to the electronic energy transfer. One process involves the capture of the excess electrons from the conduction band and the excitation of the Er^{3+} centers through nonradiative channels, where they subsequently contribute to the radiative transitions from $^4\text{I}_{13/2}$ to $^4\text{I}_{15/2}$. Because of the long luminescence decay lifetime of transitions from $^4\text{I}_{13/2}$ to $^4\text{I}_{15/2}$ (measured to be $\sim 600\mu\text{s}$) and from $^4\text{I}_{11/2}$ to $^4\text{I}_{13/2}$ (reported to be $\sim 260\mu\text{s}$) [6] compared to the much shorter excess carrier recombination lifetime (a few nanoseconds) in the Γ conduction band, the predominant transition is Γ band-related recombination when $\text{Al}_x\text{Ga}_{1-x}\text{As}$ host is direct gap ($x < 0.4$). This process results in a very weak erbium related emission intensity near $1.54\mu\text{m}$ because the fast band-to-band radiative recombination rapidly depletes the excess carriers. However, in the Γ -X band crossover region ($0.4 < x < 0.5$), the long-lived excess carriers [7-9] have a greater probability to excite Er^{3+} centers, which results in a much higher energy transfer efficiency from the excess electrons in the conduction band (Γ , X and L) to the Er^{3+} centers.

For the second Er^{3+} excitation process, the maximum intensity at $x=0.6$ is attributed to the conduction band(s) ($E_g^\Gamma=2.28\text{eV}$, $E_g^L=2.20\text{eV}$ and $E_g^X=2.10\text{eV}$) coupling to the $^4\text{S}_{3/2}$ energy level of Er^{3+} (where $\Delta E[^4\text{S}_{3/2} \rightarrow ^4\text{I}_{15/2}] = 2.28\text{eV}$) and to the Er^{3+} ground level, $^4\text{I}_{15/2}$, which is within a few kT of the valence band. The alignment of these energy levels should greatly enhance the energy transfer efficiency from the host to the erbium ions. This energy transfer coupling mechanism is based on the vacuum referred binding energy (VRBE) model [10, 11]. This model exploits a general trend in the binding energy of deep trapping levels in semiconductors and it enables one to predict the approximate location of unknown deep levels in binary crystals and ternary alloys from knowledge of the photothreshold and the energy band edge in related semiconductors. In addition, thermal quenching experiments on erbium doped InGaP revealed that the erbium-related trapping level is independent of the host band edge or composition and is only referenced to the vacuum level [12]. The thermal quenching data indicate that the erbium related trapping level is located approximately 4.4 eV below the vacuum level. The valence band maximum and conduction band minimum relative to the vacuum level can be calculated as a function of aluminum composition and temperature [13], assuming the electron affinity χ_e is a linear function of aluminum composition at 77K for $\text{Al}_x\text{Ga}_{1-x}\text{As}$, using $\chi_e=4.07-1.07x$ (for $x \leq 0.45$) and $\chi_e=3.64-0.14x$ (for $0.45 < x \leq 1.0$) [14]. Hence the valence band maxima and conduction band (Γ , X and L) minima are plotted as a function of the aluminum composition at 77K as shown in Fig. 3. Some of the Er^{3+} energy levels are located in the band gap of the $\text{Al}_x\text{Ga}_{1-x}\text{As}$ at $x=0.6$ and $x=0.4$.

It is not yet known which specific manifold energy level is the so called erbium-related trapping level inside the band gap. Because of the different shapes of the absorption and emission spectra, the cross-section is far from identical for absorption and emission between the same two manifolds. The manifold $^4\text{I}_{13/2}$ has a large emission cross-section for (solely) erbium doped semiconductors but it does not necessarily have a large absorption cross-section. It would appear that the $^4\text{I}_{11/2}$ level or the $^4\text{S}_{3/2}$ level, are the most probable carrier trapping

levels not only because of their large reported absorption cross section in erbium doped ionic crystals and optical fibers [15-17] but also because of the shorter luminescence decay lifetimes of these levels. Furthermore, the transition probabilities for absorption and emission are dependent on the local crystal field. More experimental study is necessary to prove the validity of the assumption that the $^4I_{11/2}$ level or some other energy levels close to it are the trapping level(s). Due to the short excess carrier lifetime, the excited excess carriers at this metastable level will decay rapidly to either the $^4I_{13/2}$ level, nonradiatively, or to the ground level $^4I_{15/2}$, radiatively, (which is observed in our PL spectra). This is one of the reasons that the trapping level, i.e., $^4I_{11/2}$, is assumed to be approximately 4.4eV below the vacuum level as shown in Fig. 3. Another reason for supporting the electronic process in the energy transfer is that the one-electron energy states of the 4f electrons of Er^{3+} and Yb^{3+} ions in semiconductors have been calculated on the basis of a self-consistent, local-density-functional DV-X α cluster calculation [18, 19]. The calculated results show that the one-electron energy level (Fermi level) of a cluster of GaAs:Er lies approximately 0.9eV below the Γ conduction band edge. Our above assumption closely agrees with this cluster calculation result.

Note the close alignment of the ground manifold $^4I_{15/2}$ with the valence band edge and the $^4S_{3/2}$ manifold with the Γ conduction band edge for $x=0.6$ in Fig. 3. The energy transfer efficiency from the host to the erbium ions can be greatly increased when the energy band edges of the host material couple to the appropriate Er^{3+} energy levels. Accordingly, the drastic decrease in emission intensity at higher aluminum compositions is the result of little or no energy level coupling as the energy levels go out of alignment.

It is well known that direct band absorption is stronger than indirect band absorption in semiconductors. Fig. 4 and Fig. 5 show the same trend as in Fig. 2, but under continuous wave

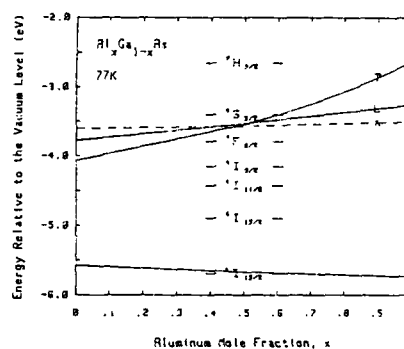


Fig. 3. The manifold energy levels of Er^{3+} in $\text{Al}_x\text{Ga}_{1-x}\text{As}$ ($x=0.4$ and $x=0.6$) at 77K referenced to the vacuum level ($E=0\text{eV}$).

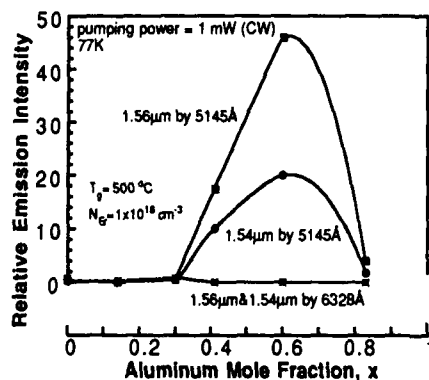


Fig. 4. Emission intensity versus $\text{Al}_x\text{Ga}_{1-x}\text{As}$ alloy composition x , using CW photoexcitation with photon energies of 1.96eV and 2.41eV.

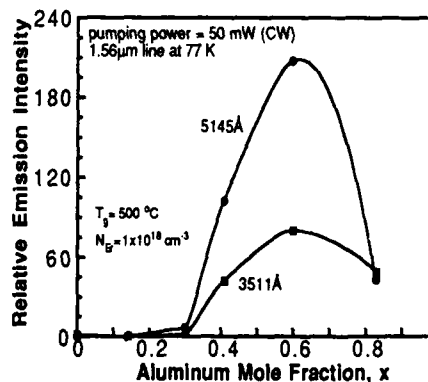


Fig. 5. Note the strong dependence of the $1.56\mu\text{m}$ emission intensity on the Al composition for CW photoexcited with photon energies of 2.41eV and 3.53eV.

(CW) photoexcitation with photons of energy 1.96eV (6328Å), 2.41eV (5145Å) and 3.53eV (3511Å). There is no band-to-band absorption using 1.96eV photons in the samples with aluminum compositions $x \geq 0.4$, since the photon energy is lower than the Γ -, L - or X -band gaps. As a result, no erbium related emission was observed because there is a lack of excess carriers to excite the Er^{3+} centers. However, very weak erbium-related emission was observed only from those of $x < 0.4$ ($E_g < 2.0\text{eV}$) under the same photoexcitation condition.

For the case of 3.53eV photon excitation (Fig. 5), the excitation photon energy is always larger than the Γ -, L - and X -band gaps from $x=0$ to $x=1$. The same trend as that in Fig. 3 is clearly observed. The decrease in energy transfer efficiency for $x > 0.8$ is not due to a reduction in the absorption (electron-hole pair generation) in the host material. The 1.5μm emission intensity is controlled by the energy transfer efficiency as well as the number of optically active Er^{3+} centers in the host material. Compared to 2.41eV (5145Å) photons, the weaker emission intensity at both 1.56μm and 1.54μm using 3.53eV (3511Å) photons is probably due to the high absorption coefficient for high energy photons. Such a large absorption produces most of the carriers near the sample surface and away from the bulk of the Er^{3+} centers, where surface recombination depletes the excess carriers more rapidly.

The proposed energy transfer mechanism can also explain the effects of co-doping with beryllium or silicon in $\text{Al}_{0.4}\text{Ga}_{0.6}\text{As:Er}$ [20]. The Be co-doped sample was grown at 500 °C with an erbium doping concentration of $\sim 1 \times 10^{18}\text{cm}^{-3}$. The hole concentration was determined to be $9 \times 10^{17}\text{cm}^{-3}$ by van der Pauw Hall measurement. The PL spectrum from this sample at 77K is plotted in the upper portion of Fig. 6. The PL from an $\text{Al}_{0.4}\text{Ga}_{0.6}\text{As:Er}$ control sample is shown for comparison in the lower half of Fig. 6. Interestingly, there is one emission peak at 1.54μm (none at 1.56μm) with a comparable intensity to that from the erbium doped control sample. A high resolution PL spectrum from the same sample is shown under the regular PL peak envelope. The change in the emission spectra is a result of successfully eliminating or suppressing the other transitions without sacrificing the 1.54μm emission intensity or line width. It would appear that the acceptor levels or acceptor related defect levels, due to the Be doping, couple to the some/all of the energy levels comprising the $^4I_{15/2}$ ground state and thereby alter the depopulation rate of these levels.

A Si co-doped $\text{Al}_{0.4}\text{Ga}_{0.6}\text{As:Er}$ sample grown at 500 °C with an erbium doping concentration of $1 \times 10^{18}\text{cm}^{-3}$ and an electron concentration of $3 \times 10^{16}\text{cm}^{-3}$ exhibits strong emission at 0.98μm as shown in Fig. 7. The emission at 0.98μm is more than one order magnitude stronger than the erbium doped control sample and is stronger than the 1.56μm and 1.54μm emission lines. On the basis of the energy level coupling mechanism, this observed effect may be the result of the donor levels coupling to the $^4F_{9/2}$ energy levels or/and

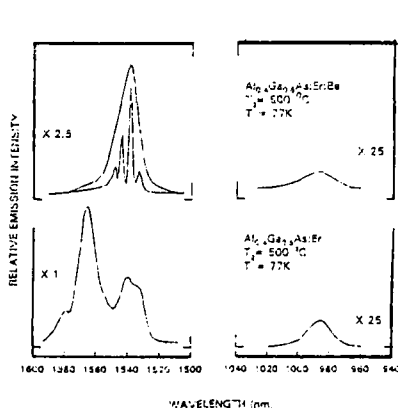


Fig. 6. Comparison of p -type $\text{Al}_{0.4}\text{Ga}_{0.6}\text{As:Er:Be}$ and undoped $\text{Al}_{0.4}\text{Ga}_{0.6}\text{As:Er}$ at 77K.

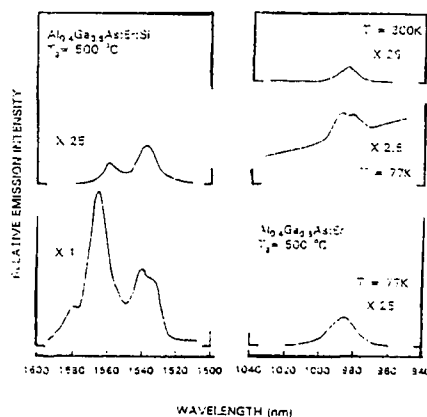


Fig. 7. Comparison of n -type $\text{Al}_{0.4}\text{Ga}_{0.6}\text{As:Er:Si}$ and undoped $\text{Al}_{0.4}\text{Ga}_{0.6}\text{As:Er}$ at 77K.

the donor related defect levels coupling to the $^4I_{11/2}$ manifold of Er^{3+} , which greatly enhances the $^4I_{11/2} \rightarrow ^4I_{15/2}$ radiative transition. In this case the depopulation rate of the ground levels does not change. As a result, this enhancement is such that the 0.98 μ m emission could be detected at temperatures up to room temperature as shown at the top of Fig. 7. This is the first report of room temperature emission at 0.98 μ m from an erbium doped semiconductor.

CONCLUSIONS

Sharp photoluminescence near 1.54 μ m has been achieved at 77K and 300K by erbium doping in GaAs and AlGaAs. The presence of aluminum greatly enhances the erbium-related emission intensity as a result of improved activation of the Er^{3+} ions and enhanced energy transfer between the host semiconductor and the Er^{3+} ions. The proposed model explains the strong dependence of the Er-related emission intensity on the host aluminum composition. We have shown that the energy coupling efficiency can be altered by the alignment and misalignment of the Er^{3+} energy levels with the energy bands (or dopant levels) of the host, or by the excess carrier lifetime in the host.

ACKNOWLEDGMENTS

This work was supported by Martin Marietta Corp. and the NSF Center for Advanced Electronic Materials Processing at NCSU. The authors would like to thank Capt. D. W. Elsaesser from AFIT and Dr. K. R. Evans from WL/ELRA at Wright-Patterson Air Force Base for kindly sending us an erbium doped calibration sample.

REFERENCES

1. R.S. Smith, H.D. Müller, H. Ennen, P. Wennekers and M. Maier, Appl. Phys. Lett. 50, 49 (1987).
2. P. Galtier, J.P. Pocholle, M.N. Charasse, B. de Cremoux and J.P. Hirtz, Appl. Phys. Lett. 55, 2105 (1989).
3. P. Galtier, M.N. Charasse, J. Chazelas, A.M. Huber, C. Grattépalin, J. Siejka and J.P. Hirtz, Inst. Phys. Conf. Ser. No. 96: Chapt. 2, 61 (1989).
4. P. Galtier, T. Benyattou, J.P. Pocholle, M.N. Charasse, G. Guillot and J.P. Hirtz, Inst. Phys. Conf. Ser. No. 106: Chapt. 5, 327 (1990).
5. S. Schmitt-Rink, C.M. Varma and A.F.J. Levi, Phys. Rev. Lett. 66, 2782 (1991).
6. T. Benyattou, D. Seghier, G. Guillot, R. Moncorge, P. Galtier and M.N. Charasse, Appl. Phys. Lett. 58, 2132 (1991).
7. R. Sanfady, A.R.E. Cohen and R.A. Logan, J. Appl. Phys. 59, 780 (1986).
8. H. Kalt, A.L. Smirl and R.F. Boggess, J. Appl. Phys. 65, 294 (1989).
9. K. Bohnert, H. Kalt, A.L. Smirl, D.P. Norwood, T.F. Boggess and I.J. D'Haenens, Phys. Rev. Lett. 60, 37 (1988).
10. M.J. Caldas, A. Fazio and A. Zunger, Appl. Phys. Lett. 45, 671 (1984).
11. L. Ledebo and B.K. Ridley, J. Phys. C, 15, L961 (1982).
12. A.J. Neuhaufen and B.W. Wessel, Appl. Phys. Lett. 60, 2657 (1992).
13. H.C. Casey and M.B. Panish, *Heterostructure Lasers*, Part A, (Academic Press, CA, 1978), pp. 187-194.
14. S. Wang, *Fundamentals of Semiconductor Theory and Device Physics*, (Prentice-Hall, NJ, 1989), pp. 522.
15. A.A. Kaminski, *Laser Crystals*, Springer Ser. in Optical Sci., Vol. 14, (Springer-Verlag, Berlin, 1990), pp. 116-318.
16. Y. Mita, T. Yoshida, T. Yagami and S. Shionaga, J. Appl. Phys. 71, 938 (1992).
17. R.J. Mears and S.R. Baker, Opt. and Quant. Elect. 24, 517 (1992).
18. R. Saito and T. Kimura, Phys. Rev. B, 46, 1423 (1992).
19. L.A. Hemstreet, Mat. Sci. Forum, Vol. 10-12, 85 (1986).
20. T. Zhang, Y. Hwang, J. Sun, N.V. Edwards, R.M. Kolbas and P.J. Caldwell, 1992 Elect. Mat. Conf. MIT, Cambridge, MA June 1992. Paper submitted to J. Elect. Mat.

LUMINESCENCE PROPERTIES OF YB-DOPED INP

H. J. Lozykowski, A. K. Alshawa, Ohio University, Athens, Ohio. G. Pomrenke AFOSR /NE Bolling AFB, Washington, D.C., and I. Brown, Lawrence Berkeley Laboratory, University of California at Berkeley.

ABSTRACT

The photoluminescence, time resolved spectra and kinetics of Yb implanted InP samples are studied under pulsed and CW excitations (above and below band-gap) at different temperatures and excitation intensity. The photoluminescence intensity and decay time as a function of temperature is explained by a proposed new quenching mechanism involving Fe ion. The rise and decay times depend on excitation intensity. The above experimental facts was explained using the kinetics model developed by H.J. Lozykowski [2]. The numerically simulated luminescence rise and decay times show a good quantitative agreement with experiment, over a wide range of generation rates. The electric field InP:Yb photoluminescence quenching was investigated and reported for the first time.

INTRODUCTION

There has been increasing interest in rare earth doped semiconductor compound because of their potential for light emitting device applications. Beside the application aspect, the rare earth impurities are of great interest from the scientific point of view. Scientific interest is related to the uniqueness of optical and electrical properties of rare earth impurities in semiconductor hosts. Among rare earth ions are those that upon replacing the element from column III in III-V compounds that are isovalent, concerning outer electrons of RE^{+3} ions, create isoelectronic traps in III-V semiconductors. This conclusion is supported by the fact that the atomic covalent radii (ionic RE^{+3}) for all rare earth are bigger than atomic radii of Ga and In that they replace [2]. Pauling's electronegativity of rare earth elements is in the range of 1.1-1.25, and is smaller than Ga (1.81) and In (1.78) for which it substitutes. The rare earth isovalent traps (REI-trap) that we can call isoelectronic "structured" impurities [1,2] possess the unfilled 4f core shell. The structured luminescence arises from intra-configurational f-f transitions in the core of the isoelectronic "structured" impurities. Ytterbium in InP replaces indium on a substitutional site [3] and acts as an isoelectronic trap. It was originally proposed by Whitney et al [4] and confirmed by others [5a,b] that the Yb ion creates an electron trap at 30 meV below the bottom of conduction band. Recently, admittance spectroscopy [5b] was used to identify the electrical activity of Yb in n and p type InP. It was found that Yb in InP creates a hole trap at 50 meV above the valence band, and an electron trap at 29 meV below the conduction band.

SAMPLES AND MEASUREMENT RESULTS

The InP material was produced from Fe-doped, semi-insulating iron doped InP. Samples D and E were implanted using a novel high current metal ion implantation facility in which a metal vapor vacuum arc (MEVVA) ion source is used. The Yb was implanted with mean ion energy ≈ 140 keV and the dose $(5-10) \times 10^{13}$ ion/cm² (peak at ~ 370 Å from the surface, concentration 1.8×10^{19} cm⁻³). Sample D and E were annealed for 10 minutes at 600 °C and 680 °C, respectively. Sample C was implanted using ion beam energy of 1 MeV and dose of 3×10^{13} ion/cm² (peak at 1960 Å from the surface, concentration 1.46×10^{18} cm⁻³). The sample was annealed at 650 °C for 15 minutes.

The photoluminescence spectra of InP:Yb (sample C) shown in Fig.1 was recorded at 8.5 K. The emission intensity of sample C is the highest of the three samples. The spectrum of each sample consists of one sharp peak at 1001 nm and broader overlapping peaks at 1005.5 nm and 1007 nm corresponding to the $^2F_{5/2} - ^2F_{7/2}$ transitions. The inset of

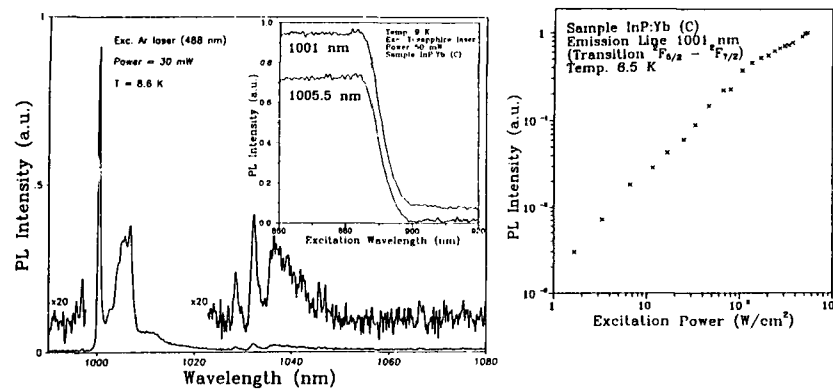


Fig. 1 PL Spectra of InP:Yb (sample C) The inset shows the excitation spectra.
Fig. 2 The PL intensity of InP:Yb (at 1001 nm) as a function of excitation power.

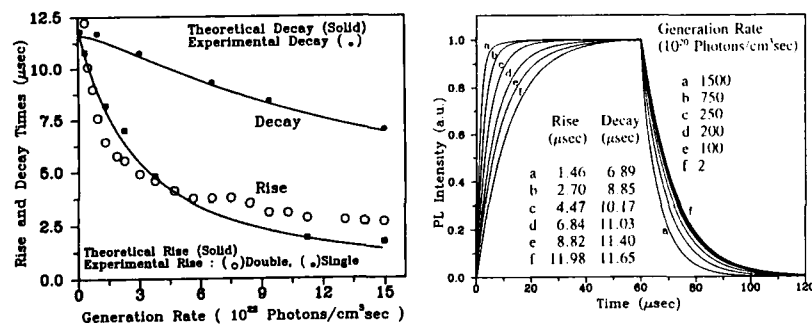


Fig. 3 The computed luminescence rise and decay for different generation rates.

Fig. 4 The calc. and experimental rise and decay times as functions of the generation rate.

Fig. 1 shows the excitation spectra recorded at emission lines 1001 nm and 1005.5 nm. In Fig. 2, the intensity of 1001 nm peak was measured as a function of the excitation power. The PL kinetics measurements were investigated at different excitation intensities and temperatures. The experiment shows that the rise and decay times are function of excitation intensity. The above experimental facts were explained using the kinetics model developed by H.J. Lozykowski [2]. To adequately describe the kinetics of the energy transfer from the host to REI-trap, the buildup and decay kinetics of rare earth luminescence (as the function of excitation intensity), we have to consider six separate states of the REI-trap (for details see [2]). The energy transfer processes occur through: a) transfer of energy from the bound exciton on REI-trap to the core states, and b) by Auger mechanism where the recombination energy of the bound electron with free hole is transferred nonradiatively to the core states. If the initial and final states are not resonant (in both mechanisms), the energy mismatch must be accommodated by emission or absorption of phonons [1,6]. In SI InP:Yb the kinetics are described by a set of differential equations which were solved assuming low temperature. That is, terms explicitly dependent on temperature were ignored, and only trapping, transferring and recombination transitions were considered. The numerical solution of the differential equations was obtained by repeating the numerical calculations for different generation rates. Fig. 3 shows the computed luminescence rise and decay as a

function of the generation rate. In Fig. 4, the solid lines are the computed rise and decay times (the experimental data are imposed on the computed curve). The circles shown in Fig. 4 represent the experimental rise times obtained from fitting to single exponential function. The squares stand for the rise times of the dominant component of the experimental data fitted to double exponential function. The dots represent the experimental decay times of the dominant component of the double exponential fitting. The numerically simulated luminescence rise and decay measurements show a good quantitative agreement with experiment over a wide range of generation rates.

The time resolved spectra (TR, Fig. 5) was recorded at temperatures 8.5K, 20K and 40K for different time delays from 0.0 to 30 μ s (for 8.5 K) and from 0.0 μ s to 25 μ s for temperatures 20K and 40K. The time resolved emission spectra of the main peak at 1001nm (I_1) shows changes in the emission line width and also slight change in the position of the peak. The positions and the widths of the emission lines recorded at long time after the excitation pulse were changed compared to those measured just after the excitation pulse. The excitation energy seems to move within the regular Yb^{3+} and slightly distorted ion system, and also between Yb^{3+} and other accidental impurities where the energy is dissipated nonradiatively. At this point it is reasonable to introduce the hypothesis of energy transfer from Yb^{3+} to iron or other accidental impurities. The energy transfer process from Yb^{3+} to Fe ions is attributed for thermal quenching of the ytterbium luminescence intensity and decay time decrease with temperature increase. Crystals used in our investigation were semi-insulating InP doped with Fe (concentration $> 2 \times 10^{16} \text{ cm}^{-3}$) and implanted with Yb. Iron is a common contaminant in MOCVD Yb doped InP semiconductor. Uwai et al. [7] presented the SIMS analysis of MOCVD grown InP:Yb $^{3+}$ that showed a flat ytterbium incorporation profile for a total Yb $^{3+}$ concentration of about $6 \times 10^{18} \text{ cm}^{-3}$. The SIMS spectra also reveals significant amounts (10^{16} cm^{-3} or higher) of Fe and Mn, elements that were not present in undoped layers, and which probably appear from contaminated ytterbium [$\text{Yb}(\text{C}_2\text{H}_5)_3$] source. Also Williams[8], found an evidence for impurities such as Fe and Mn which, did not appear in undoped samples. The iron contamination of InP:Yb is probably very common to most of the investigated samples in literature.

The excellent review of optical properties of iron doped InP (absorption, photoluminescence, photoconductivity and photoluminescence excitation spectra) was recently published by S. Bishop[9]. The first level scheme of Fe $^{3+}$ ion in InP was proposed by Stauss et al [10] to explain the photo quenching spectra of Fe $^{3+}$ ESR signal with onset at 0.75 eV,

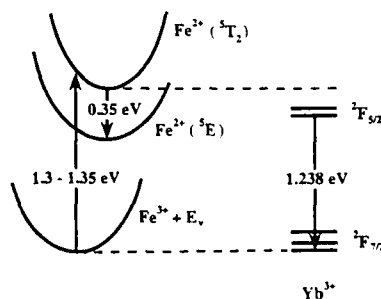
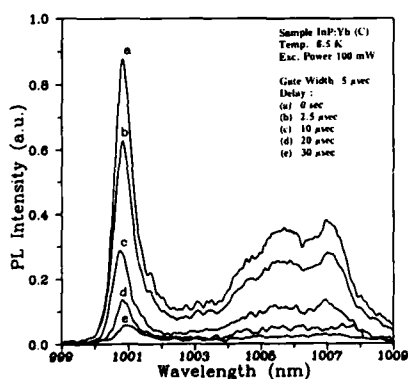


Fig. 5 Time-resolved spectra of InP:Yb, sample(C), for different time delays.

Fig. 6 The energy levels schemes for Yb^{3+} and ($\text{Fe}^{3+} - \text{Fe}^{2+}$) in SI InP.

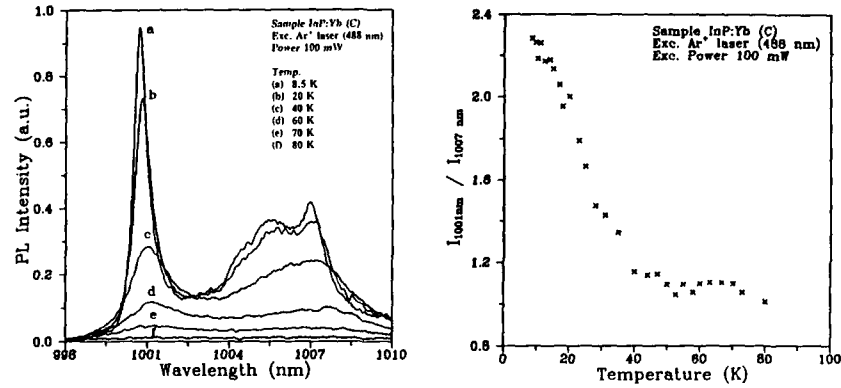


Fig. 7 Temperature dependance of the PL spectra of InP:Yb in the range 8.5 K-80 K.

Fig. 8 The intensity ratio of the emission lines 1001 nm to 1005.5 nm.

a shoulder near 1.13 eV, and maximum between 1.2 eV and 1.4 eV. These thresholds (at 0.75 eV and 1.13 eV) were attributed to direct transfer of electrons from the valence band to Fe^{3+} which converts it to the ground state of Fe^{2+} (^5E) or to excited state of Fe^{2+} ($^5\text{T}_2$) respectively. Bishop [11] and Leyral [12] observed the photoluminescence of Fe^{2+} (^5E) at 0.35 eV by extrinsic excitation (PLE) peaking at the excitation energy between 1.3 eV and 1.35 eV. In conclusion according to Bishop et al. [11] the extrinsic excitation of the Fe^{2+} ($^5\text{T}_2$) photoluminescence is attributed to a ligand-to-metal charge transfer transition in which a valence electron from an adjacent phosphorus atom is transferred to a Fe^{3+} ion, creating an Fe^{2+} in the excited $^5\text{T}_2$ state. The energy levels scheme for Yb^{3+} ($4f^{13}$ in cubic symmetry T_d) and schematic configuration coordinate diagram for the (Fe^{3+} - Fe^{2+}) in SI InP is shown in Fig. 6. Furthermore, the energy levels schemes show the 0.35 eV luminescence attributed to the Fe intracenter transition ($^5\text{T}_2 \rightarrow ^5\text{E}$), and energy transfer from Yb^{3+} to Fe^{3+} via the $^2\text{F}_{5/2}$ state of Yb ion. Excitation of Fe^{2+} photoluminescence at 0.35 eV is due to an electron capture by Fe^{3+} giving a Fe^{2+} in the excited $^5\text{T}_2$ state which, relaxes radiatively to the ^5E (Fe^{2+} ground state). The structured infrared (0.35 eV) PL emission attributed to transition $^5\text{T}_2 \rightarrow ^5\text{E}$ exhibits exponential decay. At 10 K the decay time constant for semi-insulating sample is 8.8 μs , and for n type sample is 10.5 μs which corresponds to the lifetime of the $^5\text{T}_2$ excited state [13]. The lifetime of $^5\text{T}_2$ excited state decreased quickly with increasing temperature, and at 50 K it is 6.6 μs . The Yb^{3+} ($^2\text{F}_{5/2} \rightarrow ^2\text{F}_{7/2}$) emission occurs in the region 1.229-1.242 eV and overlaps the broad extrinsic absorption band of Fe^{3+} , a requirement for efficient energy transfer. The quenching of Yb^{3+} characteristic PL (integrated) emission intensity and the decay time was investigated as a function of temperature. Fig. 7 shows the photoluminescence spectra of InP:Yb as a function of the temperature in the range 8.5 - 80 K. Fig. 8 shows the ratio of the integrated intensity I_1 (area under peak at 1001 nm) to the integrated intensity I_2 (area under broad peak at 1007 nm) as a function of temperature for sample C. The ratio decreases from 2.3 at 8.6 K to about 1.15 at 40 K and remains constant till 80 K. Figure 9 shows that the Yb^{3+} PL integrated intensity as a function of temperature remains approximately constant between 8.6 and 55 K, above which it decreases rapidly with further increase of temperature. The experimental data (for 1001 nm peak) was fitted to equation shown in Fig. 9 and plotted with theoretical fitting (solid line) using parameters $E_A \approx 100$ meV, $E_b \approx 7.57$ meV, $a=0.9$, $b=1.66 \times 10^{11}$ and $c=11.25$. The experimental data are well fitted and explained by the above simple model in which the excited Yb^{3+} ions lose their energy via the $^2\text{F}_{5/2}$ to the $^5\text{T}_2$ of Fe^{2+} ion (quenching trap). Activation energy $E_A \approx 100$ meV obtained from the experimental data is in good agreement with the gap between

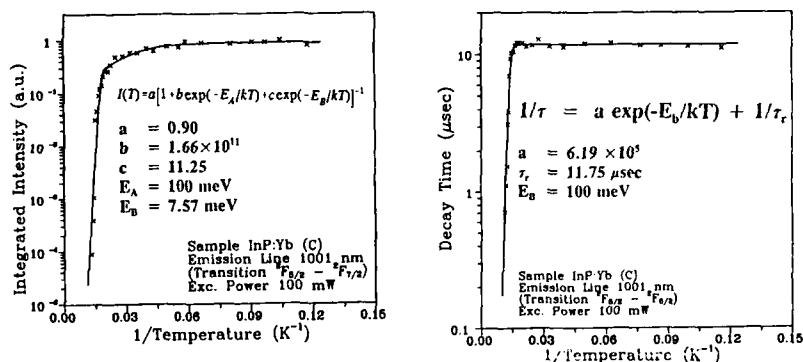


Fig. 9 A fit of the PL intensity of InP:Yb versus temperature.

Fig. 10 A fit of the experimental decay times versus temperature.

the $^2F_{5/2}$ upper Stark level of Yb^{3+} and the excited level 5T_2 of Fe^{2+} . The energy of the excited Fe^{2+} (5T_2) ion is lost via the $^5T_2 \rightarrow ^5E$ photon or multiphonon emissions. A similar simple model describes the relaxation rate $R_r = 1/\tau$ (decay time) of the Yb^{3+} luminescence as a function of temperature shown in Fig. 10. The relaxation rate ($1/\tau$) as a function of temperature is given by the equation shown in Fig. 10 where the activation energy $E_B = 100$ meV, is approximately the separation between $^2F_{5/2}$ (Yb^{3+}) and 5T_2 levels, and $a = 6.19 \times 10^5 \text{ sec}^{-1}$. The $\tau_r = 11.75 \mu\text{sec}$ is the decay time of Yb^{3+} at very low temperature. The lifetime of 5T_2 (Fe^{3+}) excited state decreased quickly with increasing temperature and at 50 K it is $6.6 \mu\text{s}$ [13]. At all temperatures investigated, the Fe^{2+} (5T_2) lifetime is shorter than the Yb^{3+} lifetime, therefore Fe^{2+} is appropriate to serve as an energy sink for Yb^{3+} excitation. As mentioned above, the energy transferred from Yb^{3+} to Fe^{3+} ion is lost via the $^5T_2 \rightarrow ^5E$ (0.35 eV) photon (or multiphonon) emission. The temperature dependence of the PL intensity of the $^5T_2 \rightarrow ^5E$ transition should show some increase at the temperature where the Yb^{3+} ($^2F_{5/2} \rightarrow ^2F_{7/2}$) emission intensity drastically decreases (experiment in progress). If the outcome of the experiment will be positive it will give an additional direct proof of the proposed new quenching mechanism.

The width of the emission line 1001 nm as a function of temperature is shown in Fig. 11. The line shape in the temperature range 9-80 K is described by a convolution of a Lorentzian and Gaussian functions (the Voigt contour). The emission line is homogeneously broadened with the Lorentzian as the dominant component ($\sim 90\%$) of the line shape. The width of the experimental homogeneous component as a function of temperature is plotted together with theoretical curve using the equation shown in Fig. 12. The equation in Fig. 12 is typical for a single-phonon relaxation process with absorption of a phonon of energy ΔE . The fitting parameters are: $\Delta E = 5.976$ meV is the energy difference between the level 5 and 4 [3], $a = 0.65$ meV and $b = 11.44$. The estimated energy $\Delta E = 5.976$ meV is close to the TA zone boundary phonons energy $\text{TA(L)} = 6.82 \text{ meV}$ ($\text{TA(X)} = 8.478 \text{ meV}$), in InP [14].

The effect of the electric field on the PL of InP:Yb was studied for the first time. To perform this experiment, a semi-transparent gold electrode (100 Å) was deposited on the implanted surface of InP, a second thick gold electrode (500 Å) was deposited on the opposite side of the sample. Figure 12 shows the quenching of PL of Yb^{3+} emission as a function of the applied electric field at both polarities. Assuming uniform absorption, the excitation photons are absorbed within the surface layer where a strong electric field exists. The quenching of PL of Yb^{3+} can be explained by two possible mechanisms: (1) exciton

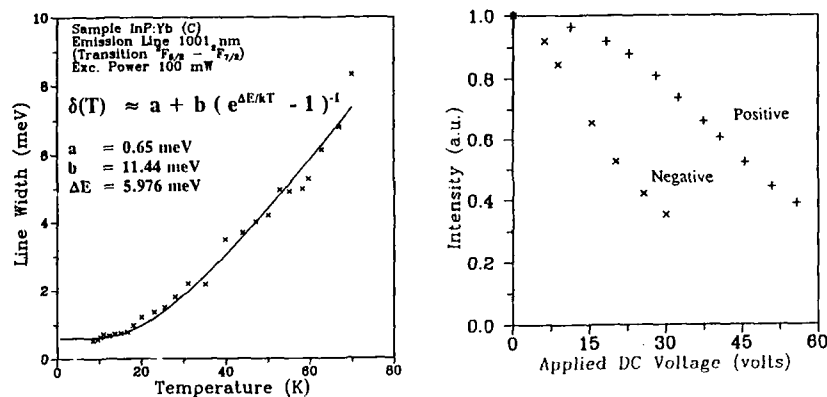


Fig. 11 The temperature dependance of the line width of the emission line 1001 nm.

Fig. 12 The PL intensity of InP:Yb as a function of the applied DC voltage.

bound to the isoelectronic trap dissociation by hot electron impact ionization or (2) swept of electrons or holes to the Au-InP interface where they will recombine nonradiatively.

The authors from Ohio University acknowledge the support by AFOSR grant No. 90-0322

REFERENCES :

- [1] D. J. Robbins and P. J. Dean, Adv. in Physics, 27 (4), 499, (1978) and references
- [2] H.J. Lozykowski, Phys. Rev. (in press)
- [3] J. Wagner, J. Windscheif, and H. Ennen, Phys. Rev. B, 30, 6230, (1984)
- [4] P. S. Vitney, K. Uwai, H. Nakagome, and K. Takahei, Appl. Phys. Lett., 21, 2074, (1988)
- [5a] D. Seghier, T. Benyattou, G. Bremond, F. Ducroquet, J. Gregoire, G. Guillot, C. Lhomer, B. Lambert, Y. Toudic, and A. Le Corre, Appl. Phys. Lett. 60, 983, (1992),
- [5b] B. Lambert, A. Le Corre, Y. Toudic, C. Lhomer, G. Grandpierre and M. Gauneau, J. Phys. Condens. Mater. 2, 479, (1990).
- [6] T. Holstein, S. K. Lyo, and R. Orbach, Excitation in Disorder Systems, in Laser Spectroscopy of Solids, edited by W. M. Yen and P. M. Selzer, Springer-Verlag, Berlin, 1981, p.39.
- [7] K. Uwai, H. Nakagome, and K. Takahei, Appl. Phys. Lett., 50, 977, (1987)
- [8] D.M. Williams and B.W. Wessels Appl. Phys. Lett., 56, 566, (1990)
- [9] S. Bishop, Iron Impurity Centers in III-V Semiconductors in Deep Centers in Semiconductors A State-of-the-Art Approach, Second Edition, Edited by S.T. Pantelides, Gordon and Breach Science Publishers, Philadelphia 1992.
- [10] G. H. Stauss, J. J. Krebs, and R. L. Henry, Phys. Rev. B 16, 974, (1977)
- [11] S. G. Bishop, P. B. Klein, R. L. Henry, and McCombe, in G. J. Rees (Editor) Semi-Insulating III-V Materials, (Shiva, Orpington, 1980), p. 161.
- [12] P. Leyral, G. Bremond, A. Nouailhat, and G. Guillot, J. of Lum., 24/25, 245, (1981).
- [13] P. B. Klein, J. E. Furneaux, and R. L. Henry, Phys. Rev. B 29, 1947, (1984).
- [14] P. H. Borchers, G. F. Alfrey, D. H. Saunderson, and A. D. B. Woods, J. Phys. C : Solid State Phys., 8, 2022, (1975).

EXCITATION OF THE 4f-4f EMISSION OF DONOR-TYPE RARE-EARTH CENTERS THROUGH DONOR-ACCEPTOR PAIR STATES (ZnS:TM)

K. LÖBE*, R. BOYN** AND H. ZIMMERMANN**

*Fritz-Haber-Institut der Max-Planck-Gesellschaft, Berlin, FRG

**Humboldt-Universität, Fachbereich Physik, Berlin, FRG

Abstract

Energy transfer from donor-acceptor pair states is known to be an efficient excitation channel for 4f-4f emission, especially if the rare-earth centers themselves are the relevant donors. Information on this type of mechanism can be obtained in the case when it is possible to observe, parallel to the 4f-4f emission, luminescence arising from radiative deexcitation of the pairs.

We have found these two kinds of emission, under electron-beam excitation, in ZnS:Tm crystals which, according to earlier site-selective studies performed by us, contain predominantly donor-type rare-earth centers. Characteristic differences between the two kinds of emission are found in the dependence of intensities on pumping rate; these arise from partial blocking of the energy transfer due to depopulation of the 4f ground levels. By quantitative studies of the correlation between those intensities we demonstrate that the same types of initial states are involved in the energy transfer and the pair transitions.

1. Introduction

It is well known that the 4f-4f luminescence of rare-earth (RE) centers in semiconductors can be rather efficiently excited through energy transfer from donor-acceptor pair (DAP) states [1,2], especially if these centers themselves are the relevant donors [3,4]. Such a situation is expected for RE's incorporated on metal sites in the II-VI materials. Information on that excitation mechanism can be obtained if it is possible to observe, parallel to the 4f-4f emission, luminescence arising from the radiative deexcitation of the pairs. The latter type of luminescence should become enhanced at high pumping rates at which the DAP to 4f energy transfer becomes partly blocked due to depopulation of the 4f ground state. We have observed those two kinds of emission for ZnS:Tm bulk crystals containing "donor-type" [3] Tm centers. A more detailed discussion of these phenomena including similar data for ZnS:Sm will be published elsewhere [5].

2. Spectra

Fig. 1 shows the cathodoluminescence spectrum of a ZnS:Tm crystal (grown by the high-pressure Bridgman technique) extending from the range of ${}^1G_4 \rightarrow {}^3H_6$ to that of excitonic transitions. The band about 29000 cm^{-1} , which is found to exhibit LO phonon structure and to shift toward higher energy with increasing electron-beam current (J), is obviously due to DAP transitions ("edge emission" [6]). We emphasize that this type of band was found only for ZnS:Tm samples containing two kinds of centers which we believe to have donor character [3]. For the sample of Fig. 1 these centers are the dominant ones. This is demonstrated in Fig. 2: The upper part shows the ${}^1G_4 \rightarrow {}^3H_6$ spectrum at higher resolution (photoluminescence under 514.5 nm Ar^+ laser excitation); in the two

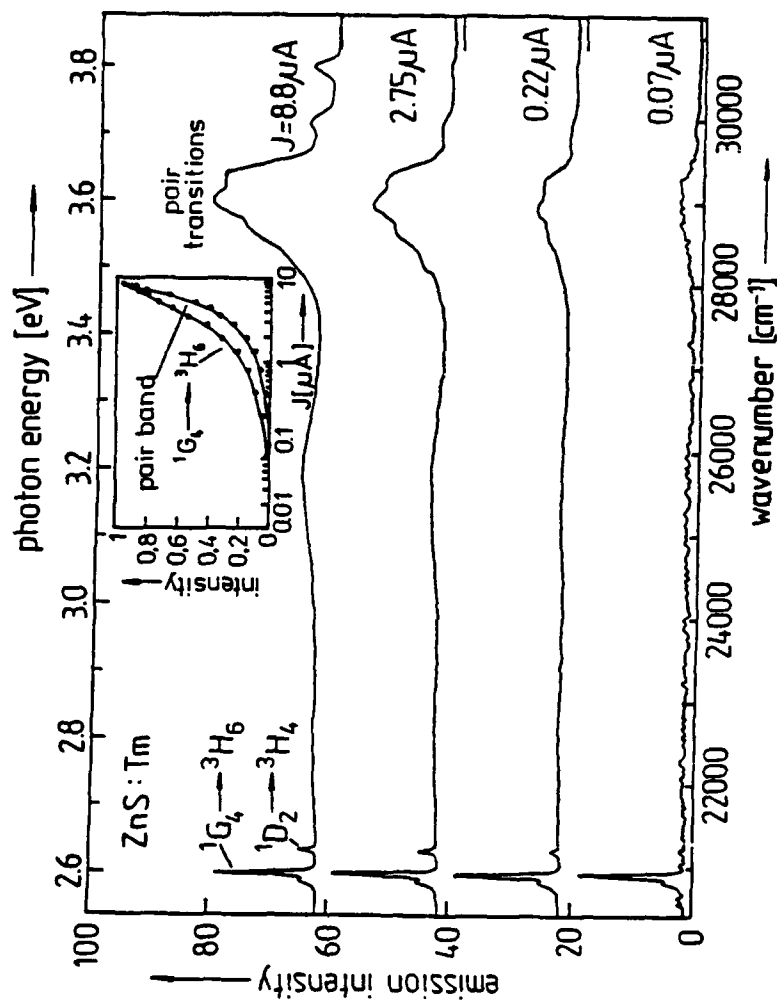


Fig. 1. Cathodoluminescence spectra at various electron beam currents normalized to the $1G_4 \rightarrow 3H_6$ line intensities ($T = 5K$, electron energy 20 keV)

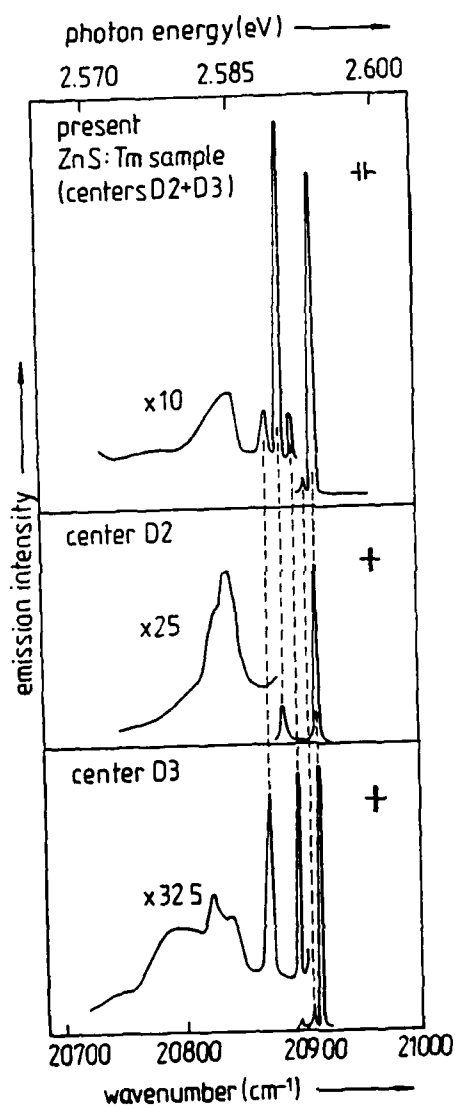


Fig. 2. Top part: ${}^1G_4 \rightarrow {}^3H_6$ photoluminescence spectrum (514.5 nm Ar^+ excitation). Lower part: Site-selective (i.e. dye-laser 4f-4f excited) spectra of the dominant donor-type centers D2 and D3 ($T = 5$ K)

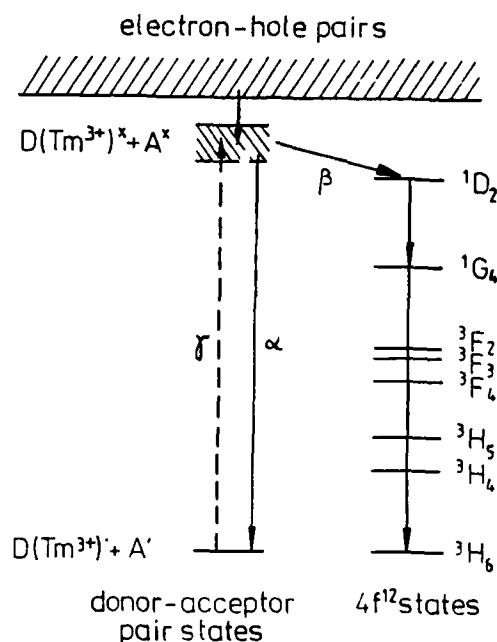


Fig. 3. Transition scheme for the excitation of the $1G_4 \rightarrow 3H_6$ emission through DAP states

lower parts we present corresponding site-selective (i.e. dye-laser 4f-4f excited) spectra of those two centers termed D2 and D3. These results suggest that the relevant donors are just those Tm centers.

Clearly the intensity of the DAP band grows faster with increasing J than that of the $1G_4 \rightarrow 3H_6$ lines (to which the spectra in Fig. 1 are normalized), and this is thought to be due to the $3H_6$ depopulation effect.

In Fig. 3 we present a model for the excitation and emission transitions occurring under electron beam pumping. This model involves, in particular, energy transfer from the pair states to the $1D_2$ excited 4f state (about 27000 to 28000 cm^{-1} above the $3H_6$ ground state), which is followed by relaxation to $1G_4$, the initial state of the observed 4f-4f emission. (The occupation of $1D_2$ manifests itself by emission transitions starting from this level, e.g. $1D_2 \rightarrow 3H_4$; see Fig. 1.) Two further checks of this model have been made:

i) In the optical excitation spectrum of the $1G_4 \rightarrow 3H_6$ emission there is a pronounced peak which can be attributed to transition γ , i.e. the transition inverse to the DAP radiative deexcitation (α) [5].

ii) We find a quantitative correlation of the DAP and 4f emission intensities as predicted from Fig. 3 (see section 3).

3. Correlation of emission intensities (see [5] for details)

From kinetic considerations we predict that the ratio of intensities (I)

$$\rho = I(^1G_4 \rightarrow ^3H_6) / I(\text{DAP}) \quad (1)$$

should decrease linearly when plotted against $I(^1G_4 \rightarrow ^3H_6)$:

$$\rho = \rho_0 [1 - \text{const } I(^1G_4 \rightarrow ^3H_6)] \quad (2)$$

with

$$\rho_0 = \frac{\beta}{\alpha} \cdot \frac{\mu(^1D_2 \rightarrow ^1G_4)}{\mu_{\text{total}}(^1D_2)} \cdot \frac{\mu(^1G_4 \rightarrow ^3H_6)}{\mu_{\text{total}}(^1G_4)} \quad (3)$$

where the μ 's are 4f deexcitation probabilities and α and β are quantities [5] characterizing the elementary processes which are indicated by these letters in Fig.3.

Fig.4 shows that, apart from a narrow range at small pumping rates, such a behaviour is really found in experiment. Those deviations are thought to arise from direct feeding of 1G_4 through another channel which saturates as the pumping rate grows. An extrapolation of the linear part to $I(^1G_4 \rightarrow ^3H_6) = 0$ yields the value $\rho_0 = 0.35$. We have estimated the second and third factors in (3) from Judd-Ofelt data obtained for Tm^{3+} in other hosts [7,8]. This leads to $\beta/\alpha \approx 100$, which seems to be a reasonable result [5]. There is evidence that at the pumping rates employed the majority of Tm donors are neutralized (i.e. the donor states are occupied by electrons).

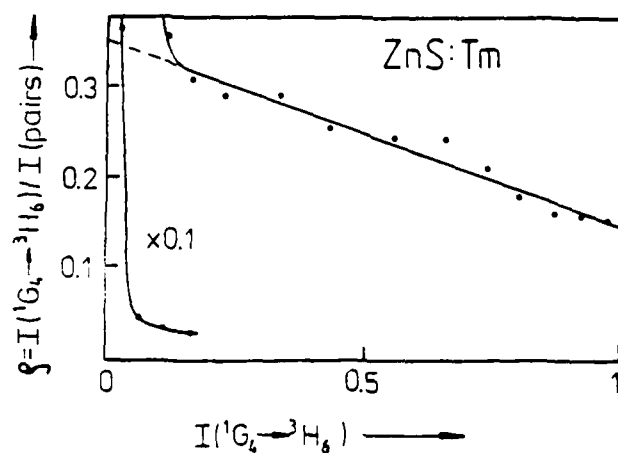


Fig. 4. Correlation of the $^1G_4 \rightarrow ^3H_6$ and DAP cathodoluminescence intensities

Acknowledgements

The authors are much indebted to Prof. H. J. Schulz (Fritz-Haber-Institut der Max-Planck-Gesellschaft, Berlin) for enabling the cathodoluminescence measurements to be performed in his laboratory, and to Dr. M. Kanis and Prof. M. J. Kozielski (Warsaw) for growing ZnS:Tm crystals.

References

- [1] R. Boyn, *phys. stat. sol. (b)* **148**, 11 (1988)
- [2] K. Swiatek, A. Suchocki, and M. Godlewski, *Appl. Phys. Letters* **57**, 40 (1990)
- [3] H. Zimmermann and R. Boyn, *phys. stat. sol. (b)* **139**, 533 (1987)
- [4] J. Shaffer and F. Williams, *phys. stat. sol.* **38**, 657 (1970)
- [5] K. Löbe, R. Boyn, and H. Zimmermann, *J. Phys. Condensed Matter*, to be published
- [6] E. F. Gross and L. G. Suslina, *Fiz. Tverd. Tela* **8**, 872 (1966)
- [7] W. F. Krupke, *Phys. Rev.* **145**, 325 (1966)
- [8] M. J. Weber, T.E. Varitomos, and B. H. Matsinger, *Phys. Rev. B* **8**, 47 (1973)

Eu AND Yb EXCITATION MECHANISMS IN ZnS, CaS, SrS AND InP

M. GODLEWSKI¹, K. ŚWIĄTEK^{1,2}, AND B. MONEMAR²

¹Institute of Physics, Polish Academy of Sciences,
02-668 Warsaw, Al. Lotników 32/46, Poland

²Dept. of Physics and Measurement Technology
Linköping University, Linköping, Sweden

ABSTRACT

The role of the excitonic excitation mechanism of the rare earth (RE) intra-shell emission is discussed. Two cases are analyzed. For Yb ion in InP 4f-4f emission of Yb³⁺ is induced by energy transfer from bound exciton state to the RE core state. For Eu in CaS and SrS RE emission is induced by carrier trapping directly to the excited state of Eu²⁺ ion. Also in this case the intermediate excitonic state may participate in RE excitation, as suggested by some experimental results.

INTRODUCTION

Rare earth (RE) activated II-VI (ZnS, CaS, SrS) and III-V (InP, GaAs) compounds belong to the perspective optoelectronic materials. They may find an application as light emitting diodes or laser diodes (InP, GaAs) [1] or as thin film electroluminescence devices (ZnS, SrS and CaS) [2]. The major hindrance for wider application of RE activated compounds was too low emission excitation efficiency. Recently new excitation mechanism was revealed. The impact ionization mechanism [3] and exciton related mechanism [4] were concluded for some of the RE ions. The latter mechanism will be discussed for the Yb ion in InP and Eu ion in three wide band gap II-VI compounds ZnS, SrS and CaS.

EXPERIMENTAL

The InP:Yb samples studied were grown by either MOCVD method (*n*-type) or by LPE method (*p*-type). They were kindly supplied to us by prof. F. Scholtz (Stuttgart University) and dr. K. Fronc (Institute of Physics, Warsaw).

Wide band gap CaS and SrS samples doped with Eu were grown by the ALE method and were kindly supplied by profs. L. Niinistö and M. Leskelä from Helsinki Technical University and Helsinki University.

Optically detected cyclotron resonance (ODCR) experiments were performed on a converted Bruker 200D-SRC X-band spectrometer. The sample was mounted in an Oxford Instruments ESR 10 He gas flow cryostat. PL was excited with the 514.5 nm line of an Ar⁺ argon laser and detected with a cooled North Coast EO817 Ge detector. PL, for the ODCR-PL study, was dispersed with a 0.25m Jobin - Yvon monochromator.

Photoluminescence (PL) of Eu doped CaS and SrS was excited with the Inova 200 argon laser, dispersed with the GDM 1000 double grating monochromator, and was detected with the S1 EMI photomultiplier and the Stanford Research SR530 lock-in amplifier. The samples were mounted in Leybold close cycle cryogenic refrigerator.

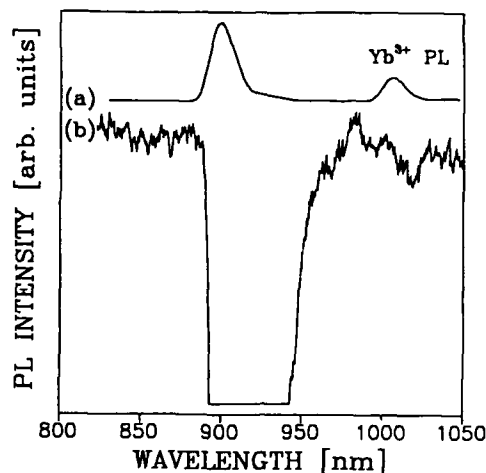


Figure 1: Low resolution photoluminescence (PL) spectra (a) of InP:Yb samples under substrate excitation. Besides DAP emission at 900 nm, Yb^{3+} intra-ion emission is observed indicating energy transfer link between substrate and Yb doped layer. In (b) the spectral dependence of microwave induced impact ionization is shown. The spectrum was measured with on-off modulated microwaves at 6.25 kHz, 200 mW microwave power and magnetic field set at 0.05T.

EXCITONIC MECHANISM OF RE EXCITATION

The feasibility of the new, exciton related, RE excitation mechanism was proved for the first time from our previous studies of Yb doped ZnS [5]. In the process RE ion is excited via energy transfer from RE bound exciton [6], i.e., exciton (carrier) binding is the first step in RE excitation. This requires that the RE ion localizes free carrier. When RE ion is charged in respect to the host, carrier is localized by a long range Coulomb attractive potential. More complex situation occurs when RE ion is neutral. Then carrier binding is by virtue of the short range attractive potential. The nature of such potential was explained by Thomas [7] who related carrier binding by the isoelectronic centers to the difference in electronegativities of the ion and host atom it replaces and stress built into the lattice by doping. For the RE ions we expect that polarization of the external 5s5p shells also may contribute to the binding potential. The type of the carrier (electron or hole) localized by the RE ion depends on the details of the binding potential. A simple intuitive model may allow us to predict if it is electron or hole [8]. If RE ion in its neutral charge state introduces an energy level into the band gap of the host material, it is expected to have a short range hole attractive potential. The short range hole attractive potential is also expected for those RE ions that have only unfilled atomic levels located within the band gap of the material. This is due to the higher order interactions admixing the ground state of the ion to the excited band gap state. On the other hand, if only the negatively charged ion introduces an energy level into the band gap, the center may localize an electron by a short range potential.

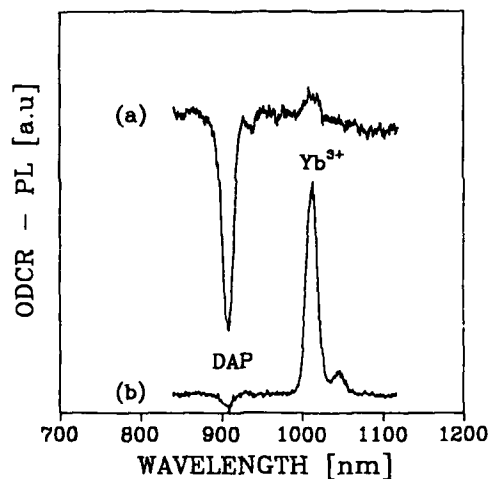


Figure 2: The spectral dependence of microwave induced impact ionization of "shallow" DAP emission in InP. The spectrum was measured with on-off modulated microwaves at 6.25 kHz, 200 mW microwave power and magnetic field set at 0.05 T. Sample (a) contained some unidentified deep traps.

The above model correctly described our previous experimental results for the Yb ion in the ZnS [5]. Here it will be used to verify the excitation mechanism of the Yb^{3+} emission in the InP lattice.

CARRIER BINDING IN InP:Yb

InP:Yb belongs to the most studied systems in which it was proposed that RE emission is induced by energy transfer from RE bound exciton [9]. Thonke *et al.*, could not distinguish between two possible scenarios - Yb binds first electron and then, by the long range Coulomb potential, hole, or Yb binds hole and then electron [9]. Previous DLTS experiments of Whitney *et al.* [10] suggest that the first scenario was more likely. In this work we report the results of the ODCR experiments that with recent ODCR studies [11] strongly favor the first scenario of carrier binding by Yb ion.

The theoretical calculations of Delerue and Lannoo [12] and experimental results of Lambert *et al.* [13] proved that $2+$ charge state of Yb is not stable in the InP. The Yb^{2+} ground state is degenerate with continuum of the CB states [12]. Yb^{3+} has only one excited state close spaced (about 1.25 eV) from its ground state. Thus, it is rather not expected that unfilled excited state of Yb^{3+} introduces energy level to the forbidden gap of InP. This means that the model describing carrier binding by the short range potential cannot be applied. Formally, none of the cases discussed in above model occurs. We expected, however, that proximity of the Yb^{2+} ground state energy level to the edge of the CB favors electron binding scenarios.

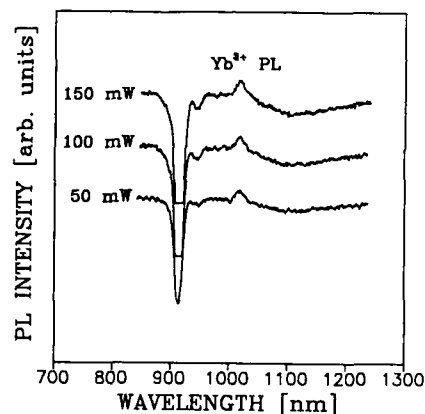


Figure 3: The light excitation intensity dependence of microwave induced impact ionization of "shallow" DAP emission in InP and of Yb^{3+} emission enhancement. The spectrum was measured with on-off modulated microwaves at 6.25 kHz, 200 mW microwave power and magnetic field set at 0.05T.

To verify such scenarios for carrier binding by Yb ion we performed the ODCR experiments for three different InP:Yb samples. The relative efficiencies of electron trapping by Yb and common shallow dopants in InP are compared for LPE-grown *p*-type crystals and two MOCVD-grown *n*-type layers with similar Yb concentration. One MOCVD sample contained increased concentration of deep electron traps. In the experiment the PL changes were measured caused by the imposed large microwave power above the threshold power for the shallow state impact ionization. Impact ionization mechanism of the PL deactivation was proved from our recent ODCR studies [14].

No effect of the applied microwave power on Yb^{3+} 4f-4f emission was observed in the *p*-type LPE sample. Electrons impact ionized from shallow centers preferably recombine with holes on acceptors. Their trapping rate by Yb ions must be very small. We expect that Yb excitation mechanism described by Kasatkin *et al.* [15] correctly describes Yb excitation mechanism then. Yb emission is induced via energy transfer from recombining donor - acceptor pairs (DAPs) and excitonic mechanism is inefficient.

A very small effect occurred for the experiment performed under laser excitation from the substrate side (Fig.1). Even though Yb^{3+} emission was observed under such excitation (indicating energy transfer link between substrate and layer) application of microwave power had a minimum effect on Yb^{3+} PL. Strong deactivation of the InP edge emission occurring in the substrate was not followed by Yb PL enhancement since spatial separation between emitting Yb ions and substrate generated free carriers. Fact that Yb^{3+} center was fed by energy transfer from substrate resulted in Yb PL deactivation following impact

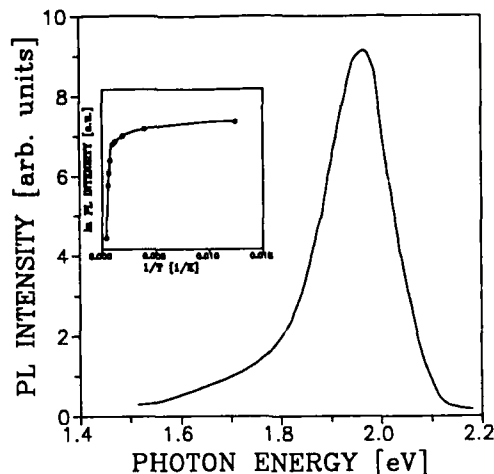


Figure 4: The photoluminescence and temperature dependence of Eu^{2+} emission in SrS thin film under Eu ionization excitation.

ionization of shallow donors. Strong deactivation of "edge" DAP process reduces efficiency of Yb feeding and a small decrease of the Yb^{3+} PL was observed.

Fig.2 shows response to the microwave power of PL spectra of two MOCVD samples of a very similar Yb concentration but with an increased deep center concentration for sample (a). Experiment was performed under layer excitation with microwave power set at 200 mW. Whereas a large enhancement of the Yb^{3+} PL occurs under impact ionization of shallow centers for sample (b), a presence of the electron trap rapidly reduces Yb^{3+} PL enhancement for sample (a). This fact with the results obtained for the *p*-type sample strongly indicate electron binding by Yb^{3+} ion in the InP lattice.

Fig.3 shows the response of the PL spectrum to the applied microwaves for the sample excited from the layer side for three different excitation intensities. With increasing laser power relative intensity of "edge" and Yb emission is changed. For increased laser powers when impact ionization of shallow centers results in appearance of large number of free carriers enhancement of the Yb PL is rapidly reduced. The possible explanation of this otherwise strange observation is based on our recent observation of a new nonradiative recombination of the excited Yb ions in presence of free carriers. The process, discussed separately on this conference [16], includes nonradiative decay of Yb^{3+} ion due to an energy transfer to externally bound free carrier. Thus, carrier binding by Yb^{3+} ion, causing bound exciton formation, may, for the excited Yb^{3+} ion, result in a very efficient Yb^{3+} nonradiative decay [16].

EXCITONIC PROCESSES FOR Eu IN CaS AND SrS

In our previous studies we have found that Eu emission in ZnS is of localized bound exciton nature [17]. Electron ionized from Eu^{2+} is trapped forming charge transfer state of Eu

ion. Energy of this state is too low for Eu^{2+} intra-ion excitation. The increased band gap widths of CaS and SrS results in different Eu emission [18]. Electron ionized from Eu ion to the conduction band (CB) is trapped back to the $4f^65d^1$ excited state of Eu^{2+} ion, which is followed by intra-ion emission. Back transfer of electron from excited state of Eu to the CB results in deactivation of the Eu^{2+} emission at increased temperatures. Such deactivation is depicted in Fig.4 presenting the temperature dependence of Eu emission in SrS:Eu thin film. These data indicate that at low temperature Eu^{2+} emission is deactivated due to a process characterized by a small activation energy. Similar activation energy was determined from the temperature dependence of the PL decay time. These results suggest that the excitonic delocalized state may participate in carrier trapping also for Eu ion. Recently similar results we have obtained for the Eu ion in CaS thin films.

ACKNOWLEDGEMENT

This work was partly supported by the research contract no. 2 0469 91 01 of the KBN

REFERENCES

- [1] K. Takahei and A. Taguchi, Materials Science Forum **83-87**, ed. G. Davies, G.G. DeLeo, and M. Stavola (Trans Tech Publications) p. 641 (1992)
- [2] M. Leskelä and L. Niinistö, Mater. Chem. Phys. **31**, 7 (1992)
- [3] K.Świątek, A.Suchocki, and M.Godlewski, Appl. Phys. Lett. **56**, 195 (1990)
- [4] M.Godlewski and K.Świątek, J. Crystal Growth **117**, 634 (1992)
- [5] H. Przybylińska, K. Świątek, A. Stąpor, A. Suchocki, and M. Godlewski, Phys. Rev. **B40**, 1748 (1989)
- [6] D.J. Robbins and P.J. Dean, Advan. Phys. **27**, 499 (1978)
- [7] D.G. Thomas, J. Phys. Soc. Japan (Supplement) **21**, 265 (1966)
- [8] M. Godlewski, Acta Phys. Polonica (in press)
- [9] K. Thonke, K. Pressel, G. Bohnert, A. Stąpor, J. Weber, M. Moser, A. Molassioti, A. Hangleiter, and F. Scholz, Semicond. Sci. Technol. **5**, 1124 (1990)
- [10] P.S. Whitney, K. Uwai, H. Nakagome, and K. Takahei, Appl. Phys. Lett. **21**, 2074 (1988)
- [11] B.J. Heijmink Liesert, M. Godlewski, A. Stąpor, T. Gregorkiewicz, C.A.J. Ammerlaan, J. Weber, M. Moser, and F. Scholz, Appl. Phys. Lett. **58**, 2237 (1991)
- [12] C. Delerue and M. Lannoo, Phys. Rev. Letters **67**, 3006 (1991)
- [13] B. Lambert, A. Le Corre, Y. Toudic, C. Lhomer, G. Grandpierre, and M. Gauneau, J. Phys.: Condens. Matter **2**, 479 (1990)
- [14] M. Godlewski, H. Weman, F.P. Wang, B. Monemar, W.M. Chen, and Q.X. Zhao, in *Defects in Electronic Materials*, ed. by M. Stavola, S.J. Pearton and G. Davies. Mat. Res. Symp. Proc. Vol. **104**, 117 (1988)
- [15] V.A.Kasatkin and V.P.Savel'ev, Sov. Phys.-Semicond. **18**, 1022 (1984)
- [16] T. Gregorkiewicz, B.J. Heijmink Liesert, I. Tsimperidis, I. de Maat Gersdorf, C.A.J. Ammerlaan and M. Godlewski, this conference
- [17] K. Świątek, M. Godlewski, and D. Hommel, Phys. Rev. **B42**, 3628 (1990)
- [18] K. Świątek, M. Godlewski, D. Hommel, M. Leskelä, L. Niinistö, E. Nykanen, P. Soininen, and M. Tiitta, Acta Polytechn. Scand. Ser. Appl. Phys. **170**, 237 (1990)

Luminescence Properties of Yb- and Nd- Implanted CdS

A. K. Alshawwa, H. J. Lozykowski, T. Li, Ohio University, Department of Electrical and Computer Engineering, Athens, OH. ; and I. Brown, University of California, Berkeley, Lawrence Berkeley Laboratory, Berkeley, CA

ABSTRACT

The photoluminescence (PL) and time resolved spectra of Nd- and Yb-implanted CdS samples are studied under pulsed and CW excitations using Ar⁺ ion laser for different excitation intensities and temperature (9 - 300 K). The samples were annealed under different conditions using the thermal-pulse method. For CdS:Nd, the PL spectra was recorded in the range 890-930 nm (transitions $^4F_{3/2} \rightarrow ^4I_{9/2}$) and for CdS:Yb it was recorded in the range 985 - 1010 nm (transitions $^2F_{5/2} \rightarrow ^2F_{7/2}$). The Rise time and decay time were studied for both CdS:Nd and CdS:Yb at different emission lines as a function of temperature and excitation power.

INTRODUCTION

The photoluminescence properties of rare earth (RE) ions in II-VI semiconductor compounds have been of interest for many years. The light emission due to radiative transitions in the partially occupied 4f shell of RE³⁺ ions in the form of lines and narrow bands is the basis for numerous applications such as solid state lasers. Beside the application aspect, the rare earth impurities are of great interest from scientific point of view. Scientific interest is related to the uniqueness of optical and electrical properties of rare earth impurities in semiconductor hosts. It is well known that the rare earth luminescence depends very little on the nature of the host and the temperature. The 4f orbits of rare earth ions incorporated in semiconductors are so deeply buried within the electronic shell that the energy levels of the 4f configuration are only slightly perturbed compared to free ion energy levels. The electronic structure of the rare earth luminescence centers and their electrical activities, as well as their indirect photoluminescence excitation mechanisms are still not well understood. The luminescence of rare earth doped cadmium sulphide has been reported by many researchers[1-4]. The attempt was to explain the mechanisms of exciting the RE³⁺ in CdS. In [1], Kingsley and et al, proposed that the energy is transferred from luminescence centers (in his case, copper) to the rare earth ions. Anderson [2] proposed that the transfer of energy is due to the electronic transition between donor-acceptor levels. In this paper, we report the luminescence properties of Nd³⁺ and Yb³⁺ implanted in CdS. Time resolved spectra was recorded for Nd³⁺ and Yb³⁺ in the ranges 890-930 nm (transitions $^4F_{3/2} \rightarrow ^4I_{9/2}$) and 985-1010 nm (transitions $^2F_{5/2} \rightarrow ^2F_{7/2}$), respectively. The term assignments for these transitions are obtained from [5]. The PL spectra was investigated at different temperatures in the range 8.5 - 300 K. Rise time and decay time processes were also studied as a function of temperature and excitation intensity.

SAMPLES AND MEASUREMENT

The implantation of Yb and Nd was performed with an unconventional technique using a new kind of high current metal ion source. The implantation dosage was $7.5 \times 10^{13} \text{ cm}^{-2}$ and the mean ion energy was 150 keV for Nd and 140 keV for Yb. In the CdS:Nd sample, the concentration of Nd is $1.31 \times 10^{19} \text{ cm}^{-3}$ and the peak -to-surface depth is 412 Å. For Yb, the concentration is $1.38 \times 10^{19} \text{ cm}^{-3}$ and the peak-to-surface depth is 390 Å. Both samples were annealed at 900 °C for 15 seconds using a Thermal-Heat-Pulse method. The photoluminescence (PL) was excited by the 488 nm line from a argon ion laser (Laser Ionics Model 553A). The pulsed excitation for time resolved spectra (TRS) was obtained by

acousto-optic light modulator (IntraAction Model AOM-125). The samples were mounted on a cold finger cooled by a close-cycle helium cryostat down to 8.5 K. The emission was dispersed by a Jarrel Ash Model 78-490, 0.75 M, scanning monochromator equipped with a 1180 grooves/mm grating. The detecting electronics consists of a Hamamatsu R632-01 photomultiplier with spectral response extended to IR region. The signal from the photomultiplier is amplified by a fast preamplifier and then fed to a dual-channel gated photon counting system controlled by a computer, which also control the scanning monochromator. The photoluminescence kinetics (rise and decay) were measured with exceptional accuracy using Turbo-Multi Channel Scaler (Turbo-MCS, EG&G Ortec) which offers a wide range of channel dwell times (minimum 5ns), with no deadtime between channels.

RESULTS AND DISCUSSION

The Photoluminescence spectra of CdS:Nd and CdS:Yb was recorded at 8.5 K in the spectral range 895 - 930 nm (1.385-1.335 eV) and 985-1010 nm (1.26-1.225 eV), respectively. For CdS:Nd, the spectrum consists of about nine sharp peaks corresponding to the transitions between Stark levels $^4F_{3/2} - ^4I_{9/2}$. The PL spectrum of CdS:Yb consists of six sharp peaks around 988 nm (1.255 eV) and two broader peaks at 995.6 nm (1.245 eV)

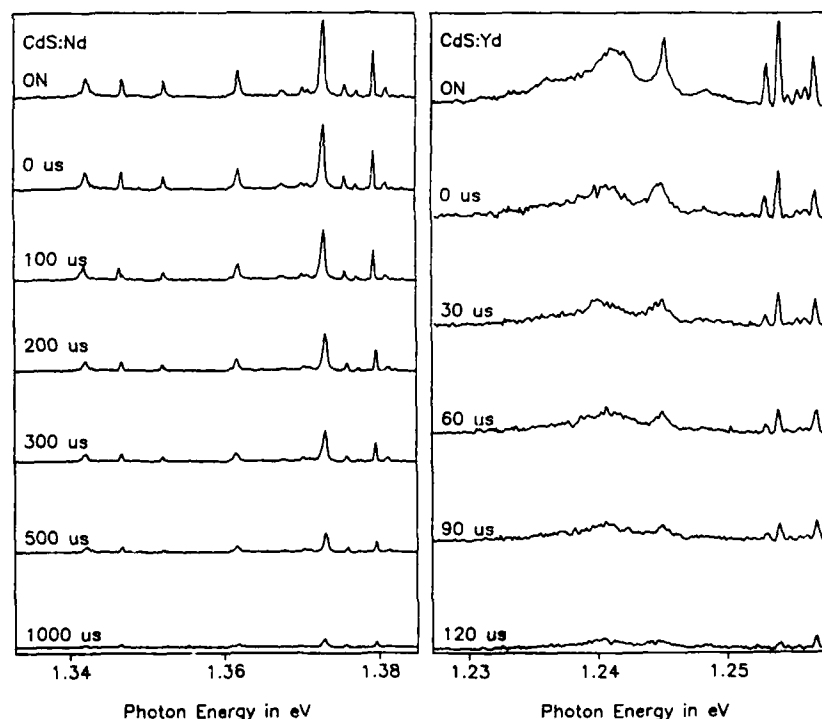


Figure 1. The Time Resolved Spectra (TRS) of (a) CdS:Nd and (b) CdS:Yb at $T=8.6$ K. The gate widths are $100 \mu\text{sec}$. The delays are as indicated in each spectrum. The spectra labeled ON are measured with gate and excitation pulse overlapped.

and 998.8 nm (1.241 eV). The Yb^{3+} emission peaks correspond to the $^2F_{5/2} - ^2F_{7/2}$ transitions. The time resolved spectra were recorded at 8.6 K for different delay times from 0 to 1000 μsec for Nd and from 0 to 120 μsec for Yb as shown in figure 1. For CdS:Nd, the intensity of all emission lines decreased with delay uniformly. In the case of CdS:Yb the intensities of the emission lines at 986 nm (1.257 eV), 995.6 nm (1.245 eV) and 998.8 nm (1.241 eV) decreased slower than the other lines.

The PL spectra were investigated as a function of temperature in the range 8.5 - 300 K for Nd and 8.5- 150 K for Yb. In figure 2a, the intensity of all lines of CdS:Nd stayed fairly constant from 8.5 to 35 K then fell down until no emission was observed after 100 K.

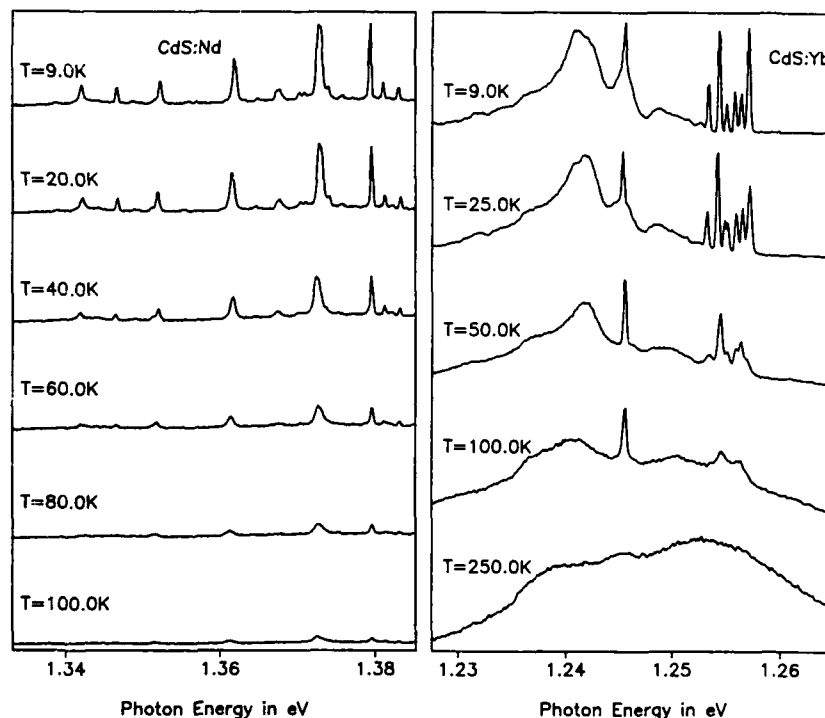


Figure 2. Temperature dependence of the PL spectra of (a) CdS:Nd and (b) CdS:Yb excited by Ar^+ laser at 488 nm with 80 mW power.

The integrated intensity of the emission line 903 nm (1.372 eV) is plotted versus temperature as shown in figure 3a. From figure 2b, the PL intensity of Yb sharp emission peaks decreases with the temperature increase until 40 K and started to increase with temperature until it reached a maximum at around 55 K. Then started to decrease with further increase in temperature. This behavior is clear from figure 3b where the integrated intensity of the emission line 995.6 nm (1.245 eV) is plotted as a function of temperature. Another observation is that with the increase of temperature, the sharp peaks evolved into one broad emission band at the same range of wavelength.

In figure 3a the decay characteristic of the $\text{Nd}^{3+} {}^4F_{3/2}$ integrated emission intensity is shown. The experimental data of the temperature dependence (at peak 903 nm) was fitted to the relationship:

$$I(T) = I(0) \left[1 + A_1 e^{-\frac{E_1}{kT}} \right]^{-1} \quad (1)$$

The experimental result is plotted with theoretical fitting (solid line) using the parameters $E_1 = 72.4$ meV, $I(0) = 0.99$ and $A_1 = 3.5 \times 10^4$.

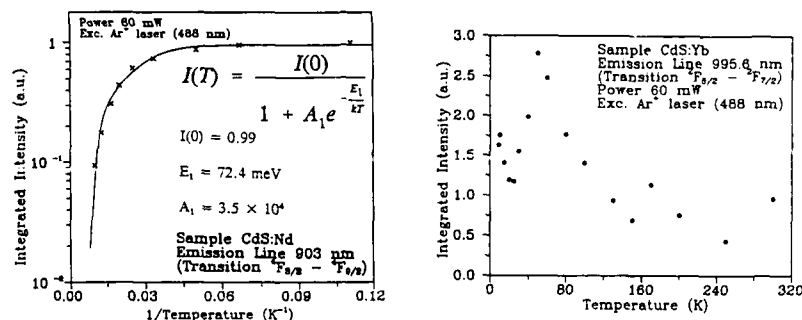


Figure 3. PL integrated intensity of (a) CdS:Nd at emission line 903 nm and (b) CdS:Yb at emission line 995.6 nm versus temperature. For (a) CdS:Nd the solid line is a fit to the experimental data using the relation discussed in the text.

The widths of the Nd emission line at 903 nm (1.372 eV) and Yb emission line at 995.6 nm (1.245 eV) as functions of temperature are shown in figure 4. The line shapes of both samples were described by a Gaussian (inhomogeneously broadened) function in the forementioned temperature range. The experimental line widths for both Nd and Yb as functions of temperature shown in figure 4 (a & b, respectively) are plotted together with the theoretical curves using equation :

$$\delta(T) \approx a + b \left(e^{\frac{\Delta E}{kT}} - 1 \right)^{-1} \quad (2)$$

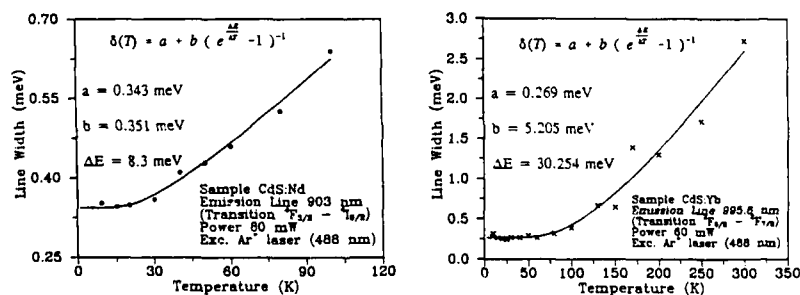


Figure 4. The temperature dependence of line widths of (a) CdS:Nd at 903 nm and (b) CdS:Yb at 995.6 nm.

The authors from Ohio University acknowledge the support by AFOSR grant No. 90-0322

For Nd, $\Delta E = 8.3$ meV, $a = 0.343$ meV and $b = 0.351$ meV, and for Yb, $\Delta E = 30.254$ meV, $a = 0.269$ meV and $b = 5.205$ meV. The above equation describing the width of the emission line as a function of temperature, is typical for a single-phonon relaxation process with absorption of a phonon of energy $\Delta E = 8.3$ meV ($E_{TA} = 9.0$ meV in CdS) for Nd, and $\Delta E = 30.254$ meV ($E_{TO} = 30.0$ meV in CdS) for Yb.

The rise time and decay time of Nd and Yb were investigated as functions of temperature and excitation power. Figure 5 shows the decay time of Nd at emission peak 903 nm (1.372 eV) as a function of temperature.

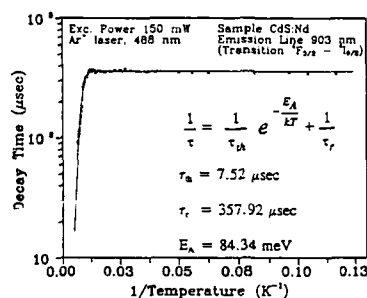


Figure 5. A fit (solid line) of the time decay CdS:Nd at emission line 903 nm to the experimental data (crosses) as a function of temperature.

The decay time remains constant around 357 μsec from 8.6 to 50 K and after it falls down below 100 μsec at 100 K. The decay time, τ , as a function of temperature is given by the equation

$$\frac{1}{\tau} = \frac{1}{\tau_{th}} e^{-\frac{E_A}{kT}} + \frac{1}{\tau_r} \quad (3)$$

where $E_A = 84.34$ meV, $\tau_{th} = 7.52$ μsec and $\tau_r = 357.92$ μsec where τ_r is the decay time at very low temperature. The activation energy $E_A = 84.34$ meV is close to the activation energy $E_i = 72.4$ meV obtained from the decay characteristics of the integrated intensity as a function of temperature. For Yb, the decay time of the emission line 995.6 nm (1.245 eV) decreased constant around 90 μsec for the entire range of temperature of 8.6 - 100 K.

In figure 6, The rise times of both Nd and Yb, were studied as functions of excitation power in the range 1 - 400 W/cm². The rise time of Nd at 903 nm (1.372 eV) decreased from 556 μsec to 300 μsec as the excitation power was increased from 1 W/cm² to 400 W/cm² as shown in figure 6a. For Yb (figure 6b), the rise time at 988.2 nm (1.254 eV) decreased from 97 μsec to 23.5 μsec as the excitation power was increased from 1 W/cm² to 400 W/cm². The rise time decrease with the excitation power increase indicates that the mechanism of exciting the RE is indirect.

The PL intensities of CdS:Nd (at emission line 903 nm) and CdS:Yb (at emission line 988.2 nm) were recorded at different excitation powers in the range 1-400 W/cm². From figure 7, we can see that the intensities increase linearly with the excitation power until 100 W/cm² and then start to saturate.

In order to interpret our results more thoroughly and provide explanations for the energy transfer and kinetics processes, more investigation is needed, such as polarization measurements, excitation spectra, and the electroluminescence.

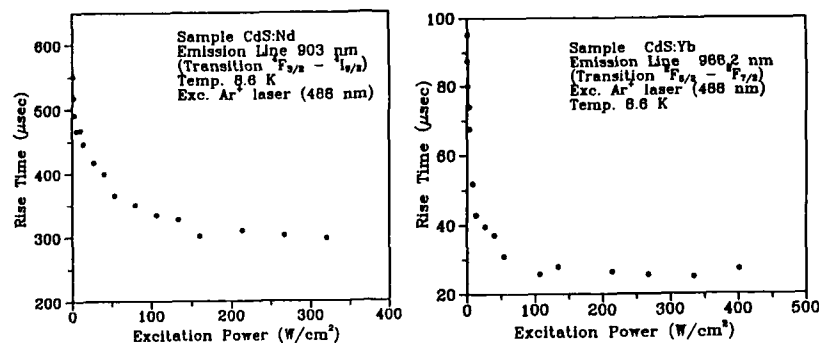


Figure 6. The rise times of (a) CdS:Nd at 903 nm and (b) CdS:Yb at 988.2 nm as functions of the laser excitation power.

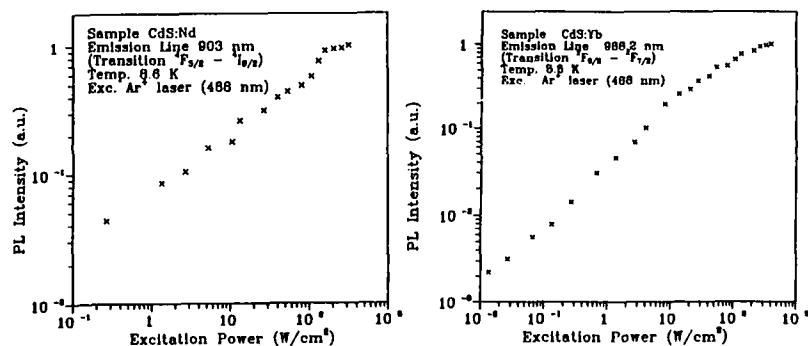


Figure 7. The PL intensities of (a) CdS:Nd at 903 nm and (b) CdS:Yb at 988.2 nm as functions of the laser excitation power

REFERENCE

- [1] J. D. Kingsley, J. S. Prener, and M. Aven, Phys. Rev. Letters 14, 136 (1964)
- [2] W. W. Anderson, J. Chem. Phys. 44, 3283 (1966)
- [3] J. Apperson, W. E. Lamb, and B. Lunn, Infrared Phys. 8, 241 (1968)
- [4] J. Apperson, G. F. J. Garlick, W. E. Lamb, and B. Lunn, Phys. Stat. Sol. 34, 537 (1969)
- [5] G. H. Dieke and H. M. Crosswhite, Appl. Optics 2, 675 (1963)

ELECTRICALLY PUMPED RARE EARTH DOPED SEMICONDUCTOR LASERS

JACQUES I. PANKOVE AND ROBERT J. FEUERSTEIN
Optoelectronic Computing Systems Center
Department of Electrical and Computer Engineering
University of Colorado, Boulder, CO 80309-0425

ABSTRACT

The interest in rare earth (RE) elements as luminescent centers is due to the narrowness and stability of the luminescent transitions. In this paper we review the mechanisms that can be used to electrically excite rare earth impurities in semiconductors: pair recombination energy exchange and impact excitation. The different means of providing energetic electrons for impact excitation are also discussed. We also propose a possible explanation for the temperature dependence of photoluminescence in silicon.

INTRODUCTION

The interest in rare earth (RE) elements as luminescent centers is due to the narrowness and stability of the luminescent transitions. These transitions are sharp because they involve atomic levels, unlike the bands of levels involved in the luminescence of semiconductors. A great number of luminescent lines from IR through visible can be generated by RE atoms.

Rare earths of the lanthanide series have three outer electrons that are used in bonding to neighboring atoms. These outer electrons residing near the neighboring atoms give an ionic character to the RE, essentially putting it in the 3^+ state. The electrons of the next or inner shell are the ones involved in the luminescence process. These inner electrons are decoupled from the adjacent atoms. Their transitions are localized processes that are not influenced by the host atoms. These transitions are characteristic of the RE element only; however, they can be perturbed slightly by local fields. Hence, one obtains nearly the same emission wavelength (1.54 μm) from Er regardless of whether it is inside glass, Si, GaAs, or any other host. Furthermore, the energy levels of the rare earth form a system independent of the energy levels of the host material. One cannot say that the ground state is in the energy gap of the host crystal or in its valence or conduction bands.

In this paper we shall consider only the rare earth erbium, since it is the most widely used RE element, the main practical application being optical communication via optical fibers, where the minimum absorption coincides with the most efficient emission at 1.54 μm . In addition to the low loss, optical fibers also exhibit a low spectral dispersion at this wavelength.

First the scheme of energy levels will be described and the transitions discussed, then the excitation mechanisms will be considered. We shall compare the merits and disadvantages of optical and electrical pumping. The various means for electrical excitation will be explored. The role of the host and of co-dopant atoms will be presented, leading to a new hypothesis about the excitation mechanism. Experimental results and calculations will be compared to test the model. Finally, our experimental approach to electrical pumping will be described.

EXCITATION MECHANISMS

Direct Optical Excitation

The absorption of a photon of energy equal to the separation between an excited state and the ground state will lift the electron from the ground state to the excited state. The capture cross section for optical pumping of Er^{3+} has been evaluated as $\approx 5 \times 10^{-21} \text{ cm}^2$ [1] at about 1480 nm.

Pair Recombination

When an electron-hole pair in the host material recombines, the released energy may excite the RE electron from the ground state to the excited state (Figure 1). This process

would be most efficient if the emitted energy matches the excitation energy--a resonant process. The energy exchange between the recombining pair and the RE may be mediated by photons or by an Auger-like process.

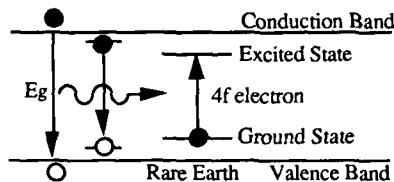


Figure 1. Excitation by pair recombination.

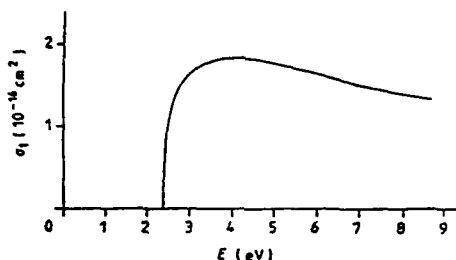


Figure 2. Electron energy dependence of the cross section for excitation of Er to the $^2H_{11/2}$ level from the ground state (from ref. 2).

Impact Excitation

The RE can also be excited by an energetic, or "hot," electron. This is referred to as "impact excitation." As shown in Figure 2, the energy dependence of the cross-section for impact excitation can be higher than $1 \times 10^{-16} \text{ cm}^2$ [2]. This is more than four orders of magnitude larger than the optical cross-section for the erbium atom considered here.

WHY ELECTRICAL PUMPING?

Er-doped fiber lasers consist of meter-long optical glass fibers containing on the order of $10^{20} \text{ Er atoms/cm}^3$. These are pumped optically, which requires laser diodes or other lasers as well as dichroic couplers. Such fiber lasers are bulky and expensive.

Injection lasers made of quaternary III-V alloys can be made to emit at $1.5 \mu\text{m}$. They are extremely small and much less expensive than the Er-doped fiber lasers, although coupling to the optical fiber may be costly. The main weakness of the injection laser is its low spectral stability: the operating wavelength shifts with temperature or power, adding to system complexity and cost. Recently, Ge quantum wells in Si have been proposed as sources of $1.5 \mu\text{m}$ [3], but this approach too would suffer from spectral instability. In contrast, the Er luminescence is spectrally invariant. Hence, it is attractive to explore the possibility of electrically pumping an Er laser electrically.

ELECTRICAL ACTIVATION OF RARE EARTH ATOMS

There are two feasible methods:

1. Injection-induced luminescence - If the RE is present in a pn junction, it is conceivable that pair recombination could excite the RE by energy exchange. However, over the last decade, all reported attempts at producing RE luminescence at a forward-biased pn junction have resulted in weak emission. It is only at this symposium that Kimmerling [4] reported successful $1.54 \mu\text{m}$ luminescence from a forward-biased pn junction in Si:Er operated at 77 K with a 6% efficiency.

2. Impact-excited luminescence -

- a) **Cathodoluminescence**, the most efficient way of causing luminescence, is not elegant for our purpose since it requires high voltage and vacuum packaging.

- b) In **AC electroluminescence (EL)**, widely used in flat panel displays, light emission from luminescent centers is due to impact excitation. The hot electron may directly impact the RE or it may produce electron hole pairs in the host material. The pair

recombination then exchanges energy with the RE. ZnS:Mn,Er has been used to demonstrate this effect [2]. Also, electroluminescence in ZnS:TbF₃ has been studied [5]. However, AC EL is not very efficient because the hot carriers can suffer many collisions before acquiring enough energy to produce a useful impact excitation.

c) **DC electroluminescence in GaN**, a wide bandgap semiconductor, has been shown to result from the impact excitation of occupied Zn acceptor levels [6]. Luminescence results from another electron from the conduction band making a radiative transition to the acceptor. In this case, one could add Er to the GaN and look for the characteristic Er emissions commingled with the visible luminescence of Zn. We are trying this approach with GaN LEDs in which the In electrode has been removed to allow Er implantation (Figure 3). After annealing the implantation-induced damage, the In electrode is replaced and the EL examined. Our results to date have been insignificant due to inadequate annealing.

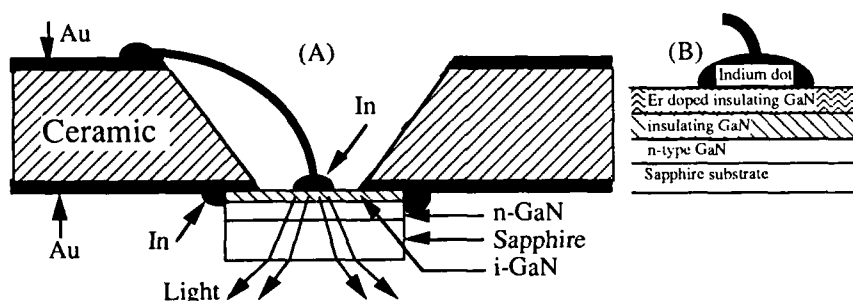


Figure 3. GaN electroluminescent device(A), with Er implant (B).

d) **Hot electron tunneling** consists of introducing the electron into the host material with at least enough kinetic energy to cause luminescence. This is achieved by using a thin dielectric between a metal electrode and the RE-doped host (Figure 4). When a strong enough voltage is applied to allow tunneling of electrons at the metal Fermi level into the host material, the applied voltage must correspond to at least the threshold kinetic energy for impact excitation (Fig. 4 inset). Although this threshold value has not been determined for the RE, it is about 2.5 eV for Mn in ZnS, while the energy for pair creation in ZnS is 9 eV. This process of tunneling hot electron impact-excited luminescence has been demonstrated in ZnS:Mn [7]. DC luminescence was obtained with applied voltages in the range of 10-25 V. In contrast, flat-panel AC EL requires applied voltages on the order of 200 ± 50 V, hence we are planning to test this mode of excitation in Er-doped semiconductors.

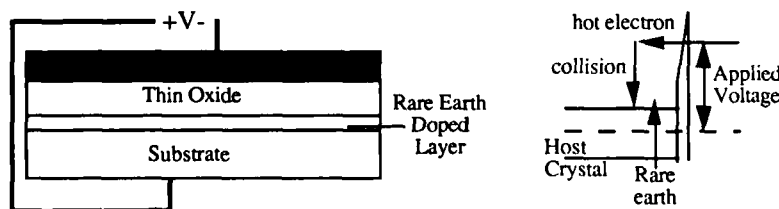


Figure 4. Tunneling structure for electrical impact excitation.

TEMPERATURE DEPENDENCE OF OPTICALLY PUMPED Er LUMINESCENCE

Favennec et al. [8] have shown that the luminescence efficiency of optically pumped Er decreases rapidly with increasing temperatures, as shown in Figure 5. Furthermore, the data

show that wider bandgap hosts maintain high luminescence efficiency to higher temperatures. Thus CdS, with a gap of 2.5 eV, maintains the same efficiency as at 77 K, at least to room temperature. This is why we are encouraged to use GaN (energy of 3.4 eV) as a host material for Er.

Isshiki et al. [9] in searching for an explanation of the thermal quenching of Er in InP proposed that Auger recombination acts as a non-radiative relaxation channel for the excited Er atoms. Taking the opposite tack, we propose that the energy available for pumping the Er ions decreases with rising temperature due to the decrease of the energy gap. This reduces the available energy from trapping or recombination processes. In silicon there is a 50 meV decrease from 0 to 300 K and in GaAs there is a 100 meV drop in the energy gap for the same temperature range [10].

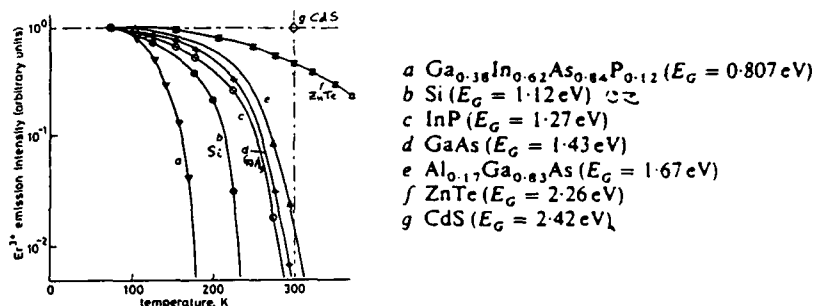


Figure 5. Temperature behavior of Er in semiconductors (from ref. 8).

Erbium in Silicon

Several studies of oxygen co-doping in Si:Er reveal a strong enhancement of the Er luminescence. We propose that the observed mechanism is a resonant excitation of Er by energy exchange with the energy released by a conduction band (CB) electron ending at the deep oxygen acceptor 0.35 eV [11] above the valence band. The energy available from this transition, $\geq 0.82 \text{ eV}$ at $T \leq 77 \text{ K}$ matches the excitation energy of Er and can produce a $1.54 \mu\text{m}$ photon. If this interpretation is correct, the energy available from the CB- $\text{O}_{\text{acceptor}}$ transition would vary like the energy gap of Si--the acceptor state, being derived from the valence band (VB) of Si, moves rigidly with the VB.

Consider the absorption spectrum of Er (Figure 6). The largest peak accessible to IR excitation occurs at 1540 nm. The CB- $\text{O}_{\text{acceptor}}$ transition occurs at an energy corresponding to 1500 nm and shifts to longer wavelengths as the temperature increases. As T increases, the exciting transition moves to "wavelengths" greater than 1500 nm, and eventually where the Er absorption decreases rapidly. The reduction of the recombination energy available to pump the Er would be responsible for the decreased Er luminescence. A calculation of this process leads to a Gaussian intensity dependence that is proportional to

$$\text{Light Power} \propto \text{Exp} \left\{ - \left[\frac{0.000473T^2}{636+T} \right]^2 \right\}$$

where the coefficients 33 meV and 200 are adjustable fitting parameters and the other parameters are the temperature dependence of the silicon energy gap. A comparison of this theoretical evaluation and the experimental results of Favennec et al. is shown in Figure 7.

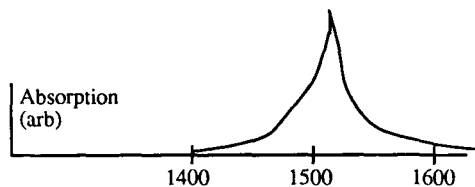


Figure 6. Absorption spectrum of Erbium.

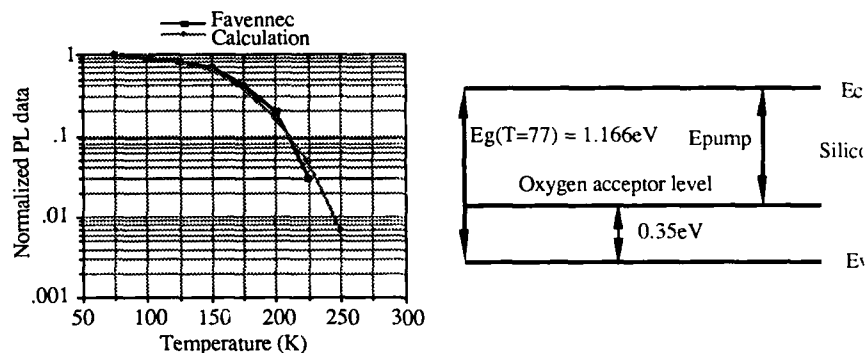


Figure 7. Favenne data for Oxygen and theory. Energy levels corresponding to above model.

PROPOSED EXPERIMENTAL APPROACH TO ELECTRICAL PUMPING OF Si:Er

We are making rib waveguides in Si by reactive ion etching. The Si is Er-doped by ion implantation and either ion beam annealed by S. P. Withrow at Oak Ridge National Laboratory or rapid thermal annealed. The purpose of using a rib waveguide rather than optically pumping the surface of the Si:Er wafer and collecting the luminescence from that surface is that the rib waveguide will collect all the radiation emitted within its confines and channel it to one end where a detector can measure the total light generated in the waveguide (after facet reflectance is taken into account). Depending on the structure (Figure 8), a single mode guide can be made by using a heavily doped Si substrate to create a small drop in refractive index, or a lower loss multimode guide can be made by implanting oxygen to form a large drop in refractive index. Note that oxygen-doped Si, such as Czochralsky-grown Si, will be used to take advantage of the oxygen luminescence enhancing effect of oxygen.

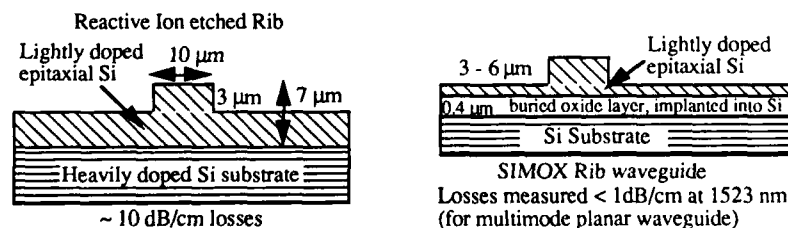


Figure 8. Rib waveguide structures in Si on Si and epitaxial Si grown over oxygen implanted Si. (see Ref. 12 for SIMOX waveguide)

Some rib waveguides will be made in Si:Er wafers that contain a pn junction so that we may test both injection luminescence and impact-excited luminescence using reverse bias to operate the junction in the avalanche mode. Thus, it will be possible to compare the relative merits of optical pumping, injection pumping, and impact excitation.

Another structure (Figure 4) incorporating a thin dielectric will be used to test the hot electron impact excitation mechanism. All the tests with Si:Er will be performed at 77 K.

CONCLUSION

The relationship of the rare earth energy levels to those of the host material was discussed. We have described the techniques of electrical excitation for rare earths in semiconductors and compared the optical and electrical cross sections. We have also proposed a thermal quenching mechanism based on decreasing pumping efficiency with increasing temperature. Device structures for measuring luminescence were described.

ACKNOWLEDGEMENTS

We would like to thank Lt. Col. Gernot Pomrenke and the AFOSR for their support (contract number F49620-92-J0162). We would also like to thank Dr. Stephen Withrow of Oak Ridge National Laboratory for performing the implantation of erbium into silicon. Measurements were also made in the OCS Metrology Laboratory funded by the Keck Foundation.

REFERENCES

- [1] S.A. Payne, L.L. Chase, L.K. Smith, *IEEE J. Quantum Elect.* **28**(11), 2619 (1992).
- [2] J.Yu, Y. Shen, X. Xu, B. Luo, G. Zhong, in *Electroluminescence*, Eds. S. Shionoya and H. Kobayashi, Springer Verlag Proceedings in Physics **38**, p. 24 (1989).
- [3] See Symposium B, Spring 93 MRS meeting: Silicon-based Optoelectronic Materials, MRS Proceedings, Vol. 298, especially papers B2.4 and B2.5.
- [4] L.C. Kimerling, Spring 1993 MRS meeting proceeding, Vol 301, paper E2.1.
- [5] J.I. Pankove, M.A. Lampert, J.J. Hanak and J.E. Berkeyheiser, *RCA Review* **38**, 443 (1977).
- [6] J.I. Pankove and M.A. Lampert, *Phys. Rev. Lett.* **33**, 361 (1974).
- [7] J.I. Pankove, *Journal of Luminescence* **40&41**, 97 (1988).
- [8] P.N. Favenec, H. L'Haridon, M. Salvi, D. Moutonnet, Y. LeGuillon, *Electronics Letters* **25**(11), 718 (1989).
- [9] H. Isshiki, R. Saito, T. Kimura, *J. Appl. Phys.* **70**(11), p. 6993 (1991).
- [10] S. M. Sze, *Physics of Semiconductor Devices* Wiley, New York, (1981).
- [11] A.G. Milnes, *Deep Impurities in Semiconductors* Wiley, New York (1973).
- [12] A. Rickman, G.T. Reed, B.L. Weiss, *IEEE Photonics Technology Letters* **4** (6), 633 (1992).

EXCITATION AND RELAXATION PROCESSES OF IMPACT EXCITATION EMISSION OF Er^{3+} IONS IN InP

T. KIMURA, H. ISHIDA, S. YUGO, R. SAITO, H. ISSHIKI* AND T. IKOMA**

University of Electro-Communications, Department of Electronics Engineering, 1-5-1 Chofugaoka, Chofu-shi, Tokyo 182, Japan, * Frontier System, Riken Institute, 2-1 Hiro-sawa, Wako-shi, Saitama 351-01, Japan, ** Institute of Industrial Science, University of Tokyo, 7-22-1 Roppongi, Minatoku, Tokyo 106, Japan

ABSTRACT

Time-resolved excitation and relaxation processes of the impact excitation emission (EL) at $1.54\mu\text{m}$ of Er^{3+} ions doped in InP were investigated in the temperature range from 77K to 330K. The decay process was almost exponential in all the measured temperature range and showed little thermal quenching. The decay time of 2ms at 77K decreased only to 1ms at 330K. This result contrasted with the large thermal quenching and nonexponential characteristics of the photoluminescence (PL) time decay at higher temperatures, suggesting different Er^{3+} centers excited between EL and PL. A two-emission-center model is proposed and the different behaviors of thermal quenching and time decay between EL and PL emissions are consistently explained.

INTRODUCTION

Studies on the emission of rare earth (RE) ions in III-V compounds have mostly been carried out by means of photoluminescence (PL) technique. However, the impact excitation emission (electroluminescence-EL) at $1.54\mu\text{m}$ of Er^{3+} ions doped in InP which we have observed for the first time [?],[2] shows different emission characteristics from those of PL emission; little thermal quenching of the EL emission intensity in contrast to strong thermal quenching of PL and different fine structures of PL and EL emission spectra from the same sample. It was considered that Er^{3+} ions located on different lattice sites were excited between EL and PL. Similar differences have also been presented recently for Er ions doped in MOCVD GaAs [3], and the above characteristics may, therefore, be common to rare earth ions doped in III-V compounds. It is expected that the analysis of the excitation and relaxation processes of EL emission in comparison with those of PL emission will give us some clue to the mechanisms for the excitation and relaxation processes and physical key factors limiting the emission efficiency of RE ions doped in III-V semiconductors.

This paper deals with the time-resolved characteristics of the $1.54\mu\text{m}$ EL emission processes. The temperature dependence of the time decay is presented and the different behaviors of the relaxation process between EL and PL are discussed. A two-emission-center model is proposed to explain differences in the relaxation processes between PL and EL.

SAMPLE FABRICATION AND MEASUREMENTS

Er ions were implanted into n-type ($n \sim 5 \times 10^{15}/\text{cm}^3$) InP at 150 keV to a dose of $7 \times 10^{14}/\text{cm}^2$ and thereafter annealed at 600°C for 20 hrs in a quartz ampoule with As over pressure. Au/Sn ohmic contacts were evaporated and alloyed on both surfaces. As the Er^{3+} -implanted region became high resistive, the voltage applied was almost across the implanted region. The EL emission at $1.54\mu\text{m}$ was detected with a liquid-nitrogen cooled germanium detector. Emissions other than the $1.54\mu\text{m}$ emission were cut off using an

interference filter and an Si wafer. Electrical pulses of 2-4 ms on-time and 6 ms off-time durations were applied to the samples and the time response of the RE emission was measured in the temperature range from 77K to 330K. The time response of the detecting system was $<70\mu\text{s}$.

RESULTS AND DISCUSSION

EL Decay Time

As is shown in our previous paper [2], the EL emission intensity shows little thermal quenching up to 330K. The EL emission is observed above a critical current (voltage). The measured decay process is exponential and its decay time is constant irrespective of the excitation current. Fig.1 shows decay curves at different temperatures between 77K and 330 K. The decay process is almost exponential in all the measured temperature range. This result contrasts essentially with PL decay curves of RE in III-V compounds. They are, in general, exponential at low temperatures, however, they become nonexponential at higher temperatures (GaAs:Er [4], Yb:InP [5], Nd:GaP [6]). The measured EL decay time is plotted as a function of temperature in Fig.2. Also plotted is the PL decay time of Er doped in GaAs [7] and GaAlAs [8] for comparison. The EL decay time at 77K ($\sim 2\text{ms}$) is nearly the same as that of PL ($\sim 1\text{ms}$), but decreases only slightly with increasing temperature (1ms at 330K). This result is similar to that of Er ions in glass [9] where Er ions are excited directly with light, but very different from the strong thermal quenching characteristics observed in the PL decay time where Er ions are excited indirectly via RE traps.

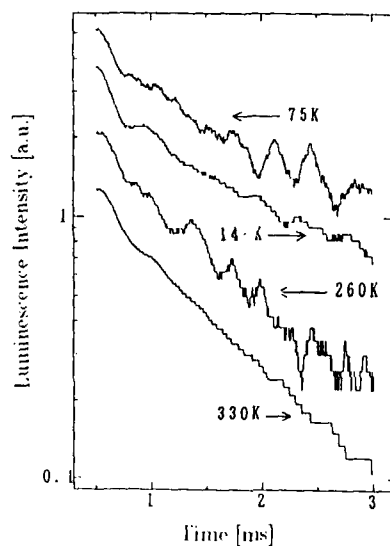


Fig.1 EL decay curves of Er^{3+} ions in InP at different temperatures between 77K and 330K. The decay is almost exponential irrespective of excitation current and temperature.

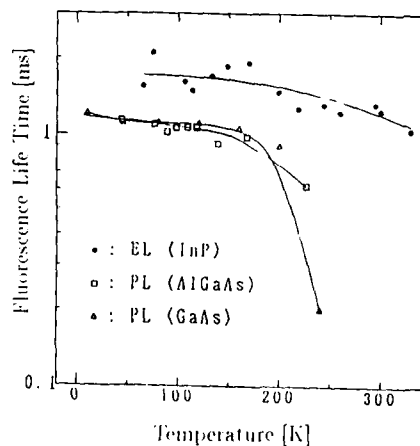
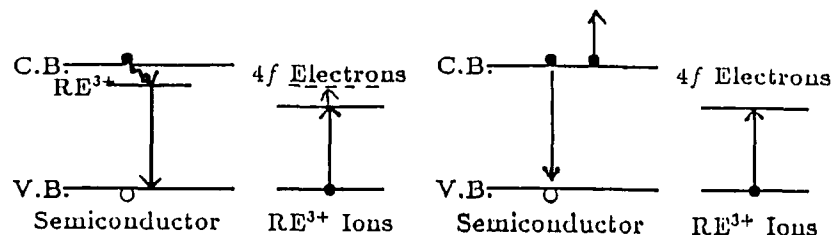


Fig.2 EL decay time as a function of temperature. Reported PL decay time of Er:GaAs and Er:GaAlAs is also plotted for comparison.

As have been shown in our recent paper [2], the $1.54\mu\text{m}$ EL emission is due to direct impact excitation of Er^{3+} 4f-electrons from the ground state ($^4I_{15/2}$) to the first excited state ($^4I_{13/2}$) through collision with energetic free electrons in the conduction band. On the other hand, in PL emissions the 4f-electrons are indirectly excited by the recombination energy of electrons and holes which are formed by illumination of above-bandgap energy light. Judging from the different quenching behaviors as well as different emission spectra between direct and indirect excitations, it is considered that different emission centers are excited between EL and PL.

Two-Emission-Center Model

We consider here P- and E-centers as shown in Fig.3. P-centers have RE traps (electron traps formed by RE ions) proposed by Takahei et al.[10] for Yb^{3+} in InP and the coupling between host semiconductors and 4f-electrons of RE ions is strong. The transfer of energy released through electron-hole recombination to 4f electrons of P-centers takes place easily via RE traps and therefore these centers illuminate well in PL. However, they also act as intermediates for the relaxation energy of 4f-electrons to back transfer nonradiatively to carriers in the host semiconductors. The higher the temperatures, the stronger, this nonradiative transition because of increased thermal phonon energy. This makes the fluorescence lifetime shorter and the PL emission efficiency lower at higher temperatures. E-centers are those which don't have such RE traps and couple very loosely with host semiconductors. They can be excited without no problem by collision with energetic electrons or direct illumination of photons of appropriate energy, but in an extremely small portion (but not zero) by PL because of a large energy discrepancy between bandgap and 4f-transition energy. In the impact excitation, both E- and P-centers can be equally excited. The nonradiative relaxation of the 4f-electrons of these centers may occur through Auger excitation of conduction electrons and its probability is much lower than the nonradiative relaxation on P-centers via RE traps. The above difference between P- and E-centers may originate in their different lattice sites. It has been shown that the direct optical excitation of 4f-electrons is very efficient than PL excitation [11]. We therefore consider that the density of P-centers is much lower than that of E-centers.



P-Center: It forms a RE-trap in the bandgap of the host semiconductor and is effectively excited by PL as well as by EL.

E-Center: It doesn't form a RE trap. It can be excited by EL but is hardly excited by PL.

Fig.3 Two-Emission-Center Model

Simulation of Steady State and Decay Process

Let us limit the transition of 4f-states only between the ground and the first excited states for simplicity. The rate equation is given by the following equation;

$$\frac{dN_2}{dt} = R N_1 - \frac{N_2}{\tau_{\text{fl}}} = R N_T - (R + \frac{1}{\tau_{\text{fl}}}) N_2, \quad (1)$$

where N_1 and N_2 are the densities of 4f electrons in the ground and excited states, respectively, $N_1 + N_2 = N_T$ the total density of optically active Er^{3+} ions, R the excitation rate and τ_{fl} the fluorescence lifetime which is related with the radiative and nonradiative lifetimes, respectively τ_{rad} and τ_{nrad} , via

$$\frac{1}{\tau_{\text{fl}}} = \frac{1}{\tau_{\text{rad}}} + \frac{1}{\tau_{\text{nrad}}}. \quad (2)$$

The solution of this equation for a steady state with excitation rate R is given by

$$N_{2,\text{steady}} = \frac{R}{R + \frac{1}{\tau_{\text{fl}}}} N_T. \quad (3)$$

In the decay process ($R = 0$ and $N_2 = N_{2,\text{steady}}$ at $t = 0$),

$$N_2(t) = \frac{R}{R + \frac{1}{\tau_{\text{fl}}}} N_T \exp(-\frac{t}{\tau_{\text{fl}}}). \quad (4)$$

Note that an Er ion is either in the ground or excited state and that its fluorescence decay time τ_{fl} can be considered independent of the degree of excitation or the number of Er-ions in the excited state.

In our two-emission-center model, E- and P-centers have different densities and different nonradiative lifetimes with each other. The total number of excited Er ions at steady state or dc is given by

$$N_{2,\text{dc}} = \frac{R\tau_{\text{fl,P}}}{1 + R\tau_{\text{fl,P}}} N_P + \frac{R\tau_{\text{fl,E}}}{1 + R\tau_{\text{fl,E}}} k_E N_E, \quad (5)$$

and the corresponding dc emission intensity is given by

$$L_{\text{dc}} = h\omega \eta_{\text{ex}} S w R \left\{ \frac{\eta_{\text{fl,P}}}{1 + R\tau_{\text{fl,P}}} N_P + \frac{\eta_{\text{fl,E}}}{1 + R\tau_{\text{fl,E}}} k_E N_E \right\}, \quad (6)$$

where $h\omega$ is the photon energy, η_{ex} the external efficiency, S the current flowing area, w the effective thickness of the Er^{3+} implanted region, $\eta_{\text{fl,P,E}} = \tau_{\text{fl,P,E}}/\tau_{\text{rad}}$ the fluorescence efficiency, $N_{\text{P,E}}$ is the density of emission centers and $\tau_{\text{fl,P,E}}$ the fluorescence lifetime. The subscripts P and E are for P- and E-centers, respectively. k_E is a portion of the E-centers which are excited. The fluorescence decay of the emission intensity is similarly given by

$$L_{\text{decay}}(t, T) = h\omega \eta_{\text{ex}} S w R \left[\frac{\eta_{\text{fl,P}}(T)}{1 + R\tau_{\text{fl,P}}(T)} N_P \exp(-\frac{t}{\tau_{\text{fl,P}}(T)}) + \frac{\eta_{\text{fl,E}}(T)}{1 + R\tau_{\text{fl,E}}(T)} k_E N_E \exp(-\frac{t}{\tau_{\text{fl,E}}(T)}) \right]. \quad (7)$$

The nonradiative lifetimes of E- and P-centers are assumed as follows;

$$1/\tau_{\text{nrad,E}} = A_E \exp(-E_{\text{a,E}}/kT), \quad 1/\tau_{\text{nrad,P}} = A_P \exp(-E_{\text{a,P}}/kT), \quad (8)$$

where $E_{A,E}$ and $E_{A,P}$ are the activation energies and A_E and A_P are the pre-exponential coefficients for E- and P-centers, respectively.

The calculated results of the dc emission intensity as a function of temperature $L_{dc}(T)$ for various k_E and the EL and PL decay curves $L_{decay}(t)$ at various temperatures with $k_E = 1$ and 10^{-6} , respectively, are shown in Fig.4-a,b. The EL decay is almost independent of temperature. The PL decay curve at 77K agrees with the EL decay curve at 77K, but the former shows a large thermal quenching at higher temperatures. The values used in the calculation are listed in Table I. The activation energies of E- and P-centers are determined from the temperature dependence of the emission intensity of EL and PL, respectively. The ratio of $N_E/N_P = 1000$ is based on the data by Taniguchi et al. [11] who observed that that direct optical excitation is ~ 1000 times more efficient than PL. We also assume judging from the excitation mechanisms that EL-excitation excites both E- and P-centers equally ($k_E = 1$), whereas PL-excitation excites only the P-centers effectively but E-centers in an extremely small portion ($k_E N_E$ where $k_E \ll 1$). The value of $k_E \sim 10^{-6}$ reproduces both the EL and PL results consistently.

Table I Parameters used in the simulation

	N (relative value)	E_a [eV]	A [1/sec]	k_E (typical)
E-Center	1000	0.04	4×10^3	10^{-6}
P-Center	1	0.12	2×10^8	—

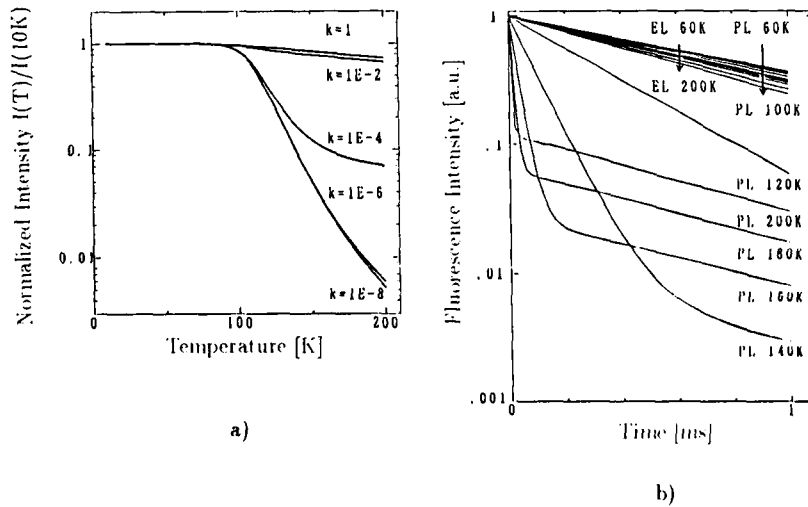


Fig.4 a) Steady state emission intensity as a function of temperature and b) emission decay curves for EL and PL that are simulated after two-emission-center model.

The simulated results of Fig.4 reproduce clearly the different features between the experimental EL and PL results qualitatively. We observe that the dc emission intensity is governed mostly by the major emission centers related with the excitation, namely by E-centers in EL and by P-centers in PL. As for time decay, the EL time decay is exponential and is characteristic of E-centers. The PL time decay is exponential at low temperatures, characteristics of P centers alone, but becomes nonexponential at higher temperatures. The fast decay in the initial stage is of P-centers, but the following slow decay is due to E-centers. The present simulation indicates that the characteristics of the E-centers appear in PL at high temperatures even if only a very small number of them are excited compared to the number of P-centers.

In order to explain a nonexponential decay of RE emissions with a one-emission-center model, we need a saturation of energy backflow from 4f-electrons to RE traps. Since one RE-trap is considered to be related to one RE-ion, such a saturation phenomenon is difficult to consider.

CONCLUSION

Time dependence of the EL emission of Er^{3+} ions doped in InP has been measured for the first time. The decay was almost exponential between 77K and 330K. The decay time of 2ms at 77K, nearly the same order as that of the PL decay time, decreased only to 1 ms at 330K. This small thermal quenching contrasted very much with the large thermal quenching of the PL decay time. A two-emission-center model with different excitation and relaxation processes could explain the different behaviors between EL and PL qualitatively.

Acknowledgements - The authors wish to thank Dr. K. Takahei, Dr. A. Taguchi and Dr. M. Taniguchi for helpful discussions.

REFERENCES

- 1) H. Isshiki, H. Kobayashi, S. Yugo, T. Kimura and T. Ikoma, *Appl. Phys. Lett.* **58**, 484 (1991)
- 2) H. Isshiki, R. Saito, T. Kimura and T. Ikoma, *J. Appl. Phys.* **70**, 6993 (1991)
- 3) M. Taniguchi, K. Takahei, J. Nakata and Y. K. Su, to be presented in MRS '93 Spring Meeting
- 4) K. Takahei, (private communication)
- 5) P.B. Klein, *Solid State Commun.* **65**, 1097 (1988)
- 6) M. Taniguchi, H. Nakagome, and K. Takahei, *Jpn. J. Appl. Phys.* **30**, 3788 (1991)
- 7) K. Takahei, P. Whitney, H. Nakagome, and K. Uwai, *Springer Proceedings in Physics*, Vol.38, *Electroluminescence* edited by S. Shionoya and H. Kobayashi (Springer-Verlag Berlin, Heidelberg 1989) p.382
- 8) T. Benyattou, D. Seghier, G. Guillot, R. Moncorge, P. Galtier and M.N. Charasse, *Appl. Phys. Lett.* **58**, 2132 (1991)
- 9) C. R. Giles, E. Desurvire, and J. R. Simpson, *Opt. Lett.*, **14**, 880 (1989)
- 10) K. Takahei, A. Taguchi, H. Nakagome, K. Uwai and P. S. Whitney, *J. Appl. Phys.* **66**, 4941 (1989)
- 11) M. Taniguchi, H. Nakagome, and K. Takahei, *Extended Abstracts (The 38th Spring Meeting, 1991)*, The Japan Society of Applied Physics and Related Societies (1991), p.1187

Impact excitation of Er-doped GaAs and the rare-earth sites in III-V compound semiconductors

S. J. Chang^{*,**}, K. Takahei^{**}, J. Nakata^{***} and Y. K. Su^{*}

^{*}Department of Electrical Engineering

National Cheng Kung University, Tainan, Taiwan, ROC

^{**}NTT Basic Research Laboratories, Musashino-Shi, Tokyo, Japan

^{***}NTT LSI Laboratories, Atsugi-shi, Kanagawa, Japan

Abstract

We report the first study of impact excitation of Er ions in GaAs. The MOCVD-grown, p⁺-n structured EL devices were fabricated by growing, at different temperatures, GaAs:Er layers on top of the n⁺ GaAs substrates. P⁺ layers were made by Zn diffusion from the top surfaces. When we forward biased these diodes, their EL spectra were similar to their respective PL spectra for each sample but different from each other's. However, when we reverse biased these diodes, EL spectra obtained from all samples are the same, which were different from their PL spectra. These results indicate that the Er center(s) excited by direct impact is different from the Er center(s) excited through electron-hole recombination and subsequent energy transfer. By using RBS channeling, we found that most of the Er ions, in our MOCVD-grown GaAs:Er samples, occupy a displaced tetrahedral interstitial site. From these PL, EL and RBS results, we conclude that only a small amount of Er ions emit luminescence when they are indirectly excited through energy transfer.

1. Introduction

In recent years, many studies have been devoted to the physical properties of rare-earth (RE)-doped III-V compound semiconductors [1-3]. Due to the screening effects by the outer 5s² and 5p⁶ electrons, the transitions between the incompletely filled RE 4f-shell electrons emit sharp and temperature stable luminescence that is insensitive to the surrounding host environment. Such properties make the RE-doped III-V compounds promising and potentially useful in optoelectronic applications. Among the various RE ions, Er attracted most attentions since it emits luminescence at 1.54 μ m which corresponds to the minimum absorption region of the silica-based optical fibers. Using Er-doped III-V compounds as the optical source can also perfectly match the Er-doped fiber amplifiers which have been widely used in optical communication. To electrically excite the RE ions in III-V host, we can either inject minority carriers [4] (i.e. light emitting diodes) or inject high energy electrons [5] (i.e. electroluminescence devices) into the III-V compound semiconductors. In the former case, RE ions are excited when the electron-hole pairs recombine and part of the recombination energy is transferred to the RE ions. In the latter case, RE ions are impact excited when the high energy electrons collide with the RE ions. For light emitting diodes, Er-doped GaAs, Al_xGa_{1-x}As, InP and Si have all been reported [4,6,7]. However, for electroluminescence (EL) devices, only Er-doped InP has been reported [5]. Also, the previously reported InP:Er EL devices were prepared by ion

implantation which might cause unrecoverable damage even after post-implantation annealing. In this work, we performed the first impact excitation study of Er-doped GaAs grown by metalorganic chemical vapor deposition (MOCVD). The fabrication of GaAs:Er EL devices and their optical properties as well as the Er lattice sites in the host GaAs are also reported.

II. Device fabrication and experiment

The Er-doped GaAs samples used in this study were grown on n^+ (100) oriented GaAs substrates by low pressure MOCVD at different temperatures [1]. P^+ layers were made by Zn-diffusion from the top surface at 600°C for four hours using $ZnAs_2$ as the zinc source [8]. P-side and n-side contacts were made by depositing Au/Zn and Au/Ge on the front surface and back side substrate, respectively. The structure of the devices used in this study is shown in Fig. 1. Since these devices are all p+-n structured, we can apply both forward bias and reverse bias. When we apply a forward bias, the RE ions are excited through electron-hole pair recombination and subsequent energy transfer [1]. When we apply a reverse bias, the RE ions are excited through direct impact excitation [5]. For comparison, the photoluminescence properties of these samples were also studied. In photoluminescence, a HeNe laser was used as the pumping source. The samples were placed in a cryostat in which the sample temperature was adjustable from 2K to room temperature during both PL and EL experiments. A 0.25m spectrometer was used to disperse the luminescence and a liquid nitrogen cooled Ge PIN detector was used for signal detection. Furthermore, Rutherford backscattering (RBS) channeling study was also performed to study the lattice sites of Er ions [9]. In RBS measurement, samples were mounted on a 3-axes goniometer and a well collimated ($<0.03^\circ$) 2.0MeV He^+ beam of 1mm diameter was irradiated from a Van de Graaff accelerator with a maximum acceleration energy of 2.5MeV. The backscattered He ions were detected with a Silicon Surface Barrier (SSB) detector set at a 170° angle to the incident probe He beam.

III. Results and Discussions

The secondary ion mass spectroscopy (SIMS) data of a typical sample used in this study is shown in Fig. 2. Fig. 3(a) and 3(b) show the PL spectra of two different samples. Sample A was grown at 500°C and sample B was grown at 600°C. Although both samples emit photoluminescence at 1.5 μ m, their PL spectra are different. This indicates that different Er center(s) emit PL depending on the growth conditions [1]. The EL spectra obtained under forward bias, by injecting minority carriers into GaAs hosts, of these two samples are shown in Fig. 4(a) and 4(b). Similar to PL spectra, the EL spectra, obtained by injecting minority carriers into GaAs hosts, are different for different samples. However, comparing Fig. 3(a), 3(b) with Fig. 4(a), 4(b), we found that the PL spectra and EL spectra obtained under forward bias are the same for the same sample. This is not surprising since, in both cases, the Er center(s) are excited through electron-hole recombination and subsequent energy transfer from the host GaAs to the Er center(s). On the other hand, the EL spectra obtained under reverse bias, by injecting high energy electrons into GaAs hosts, for these two samples are shown in Fig. 5(a) and 5(b). In contrast to PL spectra, the reverse biased

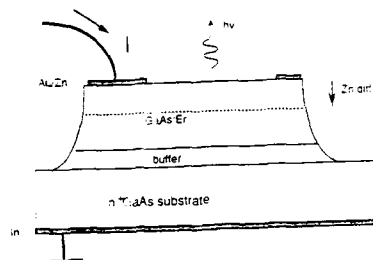


Fig 1. The device structure used in this study.

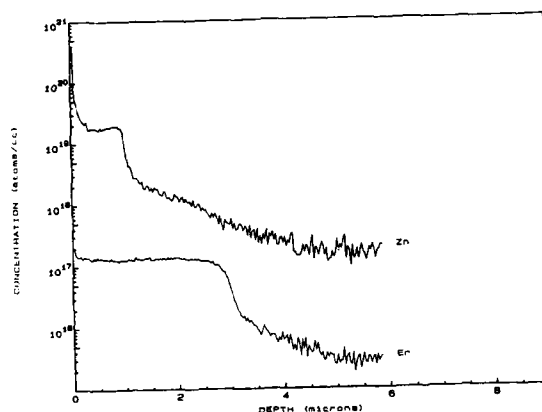


Fig. 2. SIMS profile of a typical sample used in this study, where both Zn and Er are uniformly distributed.

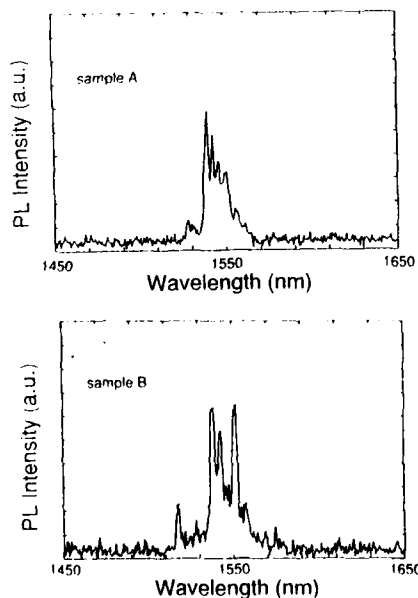


Fig. 3. The PL spectra of two different samples where (a) sample A was grown at 500°C and (b) sample B was grown at 600°C.

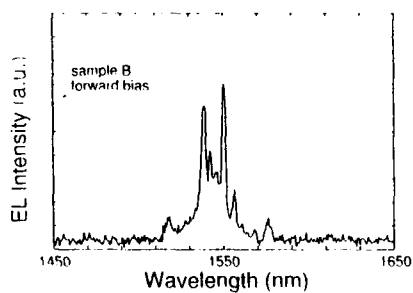
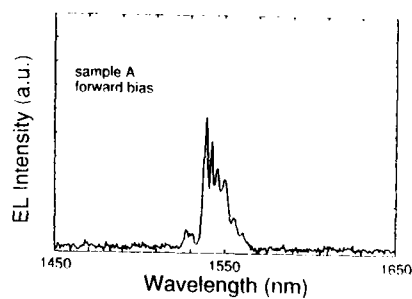


Fig. 4. The EL spectra, obtained under forward bias, of (a) sample A and (b) sample B.

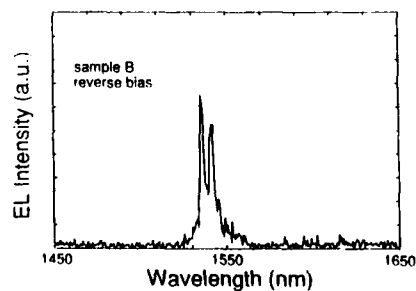
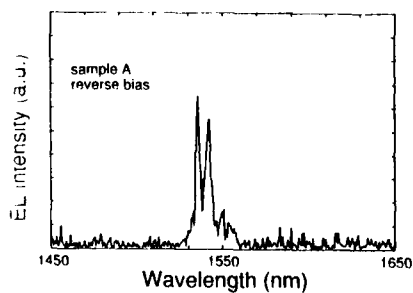


Fig. 5. The EL spectra, obtained under reverse bias, of (a) sample A and (b) sample B.

EL spectra are the same in Fig. 5(a) and Fig. 5(b) although the growth conditions are different for these two samples. Comparing Fig. 5(a), 5(b) with Fig. 3(a), 3(b), we found that the impacted excited EL spectra are different from the PL spectra. Other samples also show similar results. Such an observation suggests that the Er center(s) emitting luminescence under direct impact excitation is different from those Er center(s) emitting luminescence under host energy transfer even for the same sample. This result is in agreement with the earlier report of Nd-doped GaP where resonant photons were used to directly excite Nd ions optically [10].

To further clarify the Er lattice site in GaAs, RBS channelling experiment was performed. Fig. 6 shows the $\langle 100 \rangle$, $\langle 110 \rangle$ channeling spectra and 45° random spectrum of a MOCVD grown 150nm-thick GaAs:Er sample. The minimum channeling yield of 2.1% in $\langle 100 \rangle$ and 3.0% in $\langle 110 \rangle$ direction suggests good crystallinity in our samples. Fig. 7 shows the Er-related part of $\langle 110 \rangle$, $\langle 111 \rangle$ channeling spectra, and 45° random spectrum. In this figure, one channel is equal to the energy depth of 4KeV in the present experimental conditions. We can clearly see that the Er $\langle 110 \rangle$ channeling yield is larger than the 45° random yield. Such a strong flux peaking effect excludes the possibility of Er ions occupying the substitutional sites. It is likely that most Er ions occupy a somewhat displaced tetrahedral interstitial site by forming some kinds of native defects in our MOCVD grown GaAs:Er samples [9].

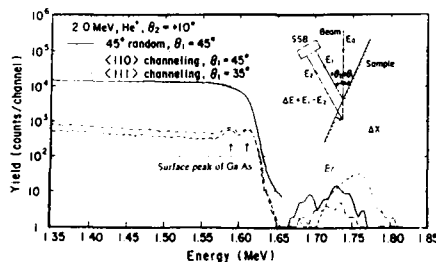


Fig. 6. The $\langle 100 \rangle$, $\langle 110 \rangle$ RBS channeling spectra and 45° random spectrum of a MOCVD grown 150nm thick GaAs:Er sample.

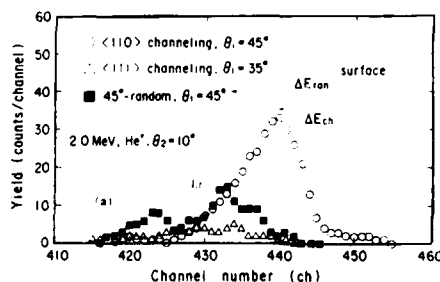


Fig. 7. The Er related part of the $\langle 110 \rangle$, $\langle 111 \rangle$ channeling spectra and 45° random spectrum. A strong flux peaking effect was observed.

From the PL, EL and RBS results, we believe that the majority of the Er ions which occupy the displaced tetrahedral interstitial site can not be excited by electron-hole recombination and subsequent energy transfer. However, they can be excited through direct impact excitation. The luminescence signals, observed by applying a reverse bias to the EL devices, were emitted from the dominant Er center. This dominant exists in the two kinds of MOCVD grown GaAs:Er samples measured in this study since the observed EL spectra were the same under reverse bias. On the other hand, only a small amount of Er ions form other centers that can be excited through host energy transfer. Those centers emit luminescence then we apply a forward bias to the GaAs:Er LEDs or irradiate laser light to excite the Er ions in GaAs hosts indirectly. These minority Er ions form different luminescence centers depend strongly on the sample growth conditions. In GaP:Nd, similar conclusion has been reported [9].

IV. Summary

In summary, we reported the first study of impact excited GaAs:Er EL devices. It was found that different Er center(s) emit luminescence when we use different excitation methods. A strong flux peaking effect was observed in RBS channeling experiment which indicates that most Er ions occupy a somewhat displaced tetrahedral interstitial site in our MOCVD grown GaAs:Er samples. Combining the PL, EL and RBS results, we conclude that only a small amount of Er centers emit luminescence when they are indirectly excited through host energy transfer.

Acknowledgements

The authors would like to thank A. Taguchi, H. Kanbe, Y. Horikoshi and T. Kimura for their helpful discussions. The work at NCKU is supported by National Science Council under contract number NSC 82-0404-E-006-306-T.

1. K. Takahei and A. Taguchi, Mater. Sci. Forum, **83-87**, 641 (1992)
2. H. Ennen and J. Schneider, J. Elecron. Mater., **A14**, 115 (1985)
3. M. Taniguchi and K. Takahei, J. Appl. Phys., **73**, 943 (1993)
4. A. Rolland, A. LeCorre, P. N. Favennec, M. Gaunneau, B. Lambert, D. Lecrosnier, H. L'Haridon, D. Moutonnet and C. Rochaix, Electron Lett., **24**, 956 (1988)
5. H. Isshiki, H. Kobayashi, S. Yugo, T. Kimura and T. Ikoma, Appl. Phys. Lett., **58**, 484 (1991)
6. P. Galtier, J. P. Pocholle, M. N. Charasse, B. deCremoux, J. P. Hirtz, B. Groussin, T. Benyattou and G. Guillot, Appl. Phys. Lett., **55**, 2105 (1989)
7. H. Ennen, G. Pomrenke, A. Axmann, K. Eisele, W. Haydl and J. Schneider, Appl. Phys. Lett., **46**, 381 (1985)
8. Y. Yamamoto and H. Kanbe, Jpn. J. Appl. Phys., **19**, 121 (1980)
9. J. Nakata, M. Taniguchi and K. Takahei, Appl. Phys. Lett., **61**, 2665 (1992)
10. M. Taniguchi, H. Nakagome and K. Takahei, Jpn. J. Appl. Phys., **30**, 3788 (1991)

PART V

Novel Structures and Devices

**NOVEL ELECTRONICS
ENABLED BY
RARE EARTH ARSENIDES BURIED IN III-V SEMICONDUCTORS**

S. JAMES ALLEN*, DAN BREHMER* AND C.J. PALMSTRØM**

*Physics Department, UCSB, Santa Barbara, CA 93106

** Bellcore, 331 Newman Springs Rd., Redbank, NJ, 07701

ABSTRACT

Heterostructures consisting of III-V semiconductors and epitaxial layers of the rare earth monoarsenides can be grown by molecular beam epitaxy. By alloying ErAs with ScAs, lattice match can be achieved with (Al,Ga)As. Using magneto-transport measurements, we show that these layers are semi-metallic with equal electron and hole concentrations, $3.0 \times 10^{20} \text{ cm}^{-3}$. Shubnikov-de Haas oscillations are used to confirm the predicted Fermi surface geometry and measure the electron effective mass and the coupling to the 4f spin on the Er^{3+} ion. Remarkably, the material shows no transition from semimetal to semiconductor as the film thickness is reduced to three monolayers. Below three monolayers the films are not uniform and are believed to consist of islands three monolayers high.

This system provides a unique opportunity to explore novel electronics based on controlled transport through semimetal/semiconductor heterostructures. Lateral transport through semimetal islands immersed in a δ -doped layer may provide a fast non-linear material for THz electronics. Vertical transport through thin epitaxial layers may enable resonant tunneling hot electron transistors with a semi-metal base. Preliminary experiments on transistor like test structures measure some transfer through a 10 monolayer thick semi-metal base. They also identify overgrowth of the III-V semiconductor on the semimetal layer as the key materials issue.

INTRODUCTION

Although metal/semiconductor junctions are ubiquitous in photonics and electronics, they usually play a passive role as ohmic contacts or Schottky barriers. Beginning with the early proposal of Mead¹ and experimental work of Sze and Gummel², the development of semiconductor electronics has been punctuated with attempts to incorporate metals in a more active role; primarily as metal base transistors. These attempts have met with marginal but insufficient success to warrant a serious attempt to replace homojunction or heterojunction bipolar transistors. At the same time a technology thrust has emerged, that focuses on quantum transport devices, like resonant tunneling transistors. Here, the "wished-for-break-through's" are devices with gain as well as multivalued operating points that will increase functionality.^{3,4,5} An obstacle to this kind of device is the necessity to selectively connect to an ultra thin layer, that supports quantum transport, and that is not so resistive that the device is prohibitively slow. Epitaxial, buried metal films compatible with III-V heterostructures may satisfy this need.

Recently, we have shown that the rare-earth arsenides can be epitaxially grown inside III-V heterostructures⁶ and may provide a material system to enable three terminal quantum devices as well as other novel metal/semiconductor devices.⁷ In the following we first review the structural and electrical properties of these materials. Then we specifically address two novel device structures based on ultra thin buried metal layers in III-V semiconductors. The first takes advantage of "island growth" at monolayer coverage to

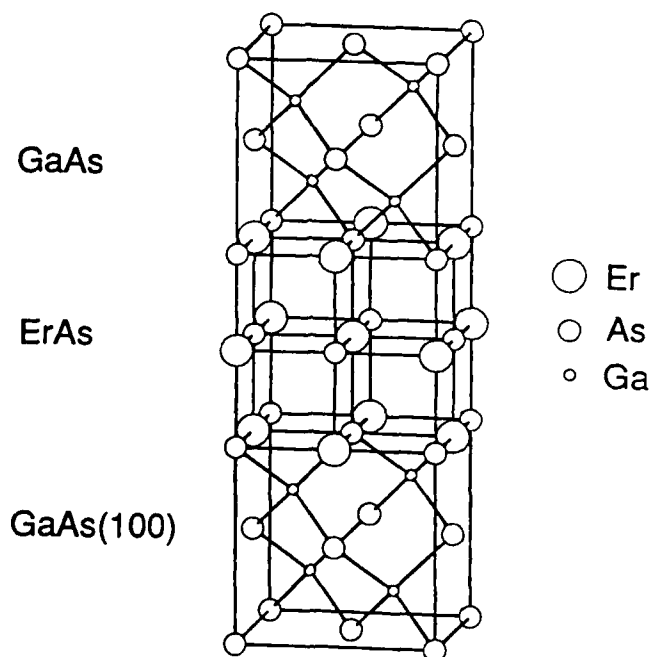


Fig. 1. Alignment of an Er,ScAs layer, three monolayers thick, with respect to the GaAs substrate.

produce a self assembling, random, "quasi optical array" of Schottky diodes for terahertz non-linear electronics. The second describes an attempt to make a hot electron transistor structure with a 10 monolayer, semi-metal base. The key material issues required for success are identified.

RARE-EARTH MONOARSENIDE EPITAXIAL FILMS

Although the rare earth arsenides crystallize into the rock salt structure, they can be epitaxially grown on zinc blende, GaAs and Al,GaAs surfaces. The orientation and disposition of the rare earth arsenide is such as to leave the As sublattice in the composite material unperturbed. Figure 1 shows the relative orientation of the substrate and film.

Magneto-transport as a function of magnetic field and temperature⁸ can be modeled by a semi-metal with electron and hole surfaces, shown in Figure 2, based on the band structure calculation of Hasegawa and Yanase.⁹ Electrons are expected in ellipsoids at the zone boundary at X, while the holes are expected to occupy the volume at Γ . Using this model as a guide, we extract the electron and hole concentrations and mobilities shown in Figure 3.

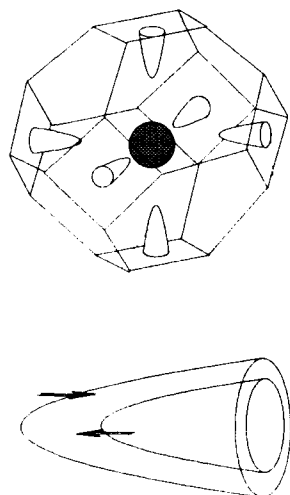


Fig. 2 The Fermi surface of the rare earth arsenides after Hasegawa and Yanase⁷. The holes are found at Γ and the electrons at X. The spin splitting of the electron ellipsoid is enhanced by exchange interactions with the Er 4f spin.

The striking beat oscillation is caused by a large spin splitting of the electron ellipsoid. (Figure 2.) The effective g-factor is measured to be $g_{\text{eff}} = 40$ and amplified by the exchange interaction between the conduction electrons and the 4f spins on the Er^{3+} ion. If we represent the interaction by $\Gamma \bar{S}_i \cdot \bar{s} \delta(\vec{r} - \vec{r}_i)$ where \bar{S}_i is the 4f spin on the i^{th} site located at \vec{r}_i , \bar{s} is the conduction electron spin at \vec{r} and Γ is the exchange interaction. The exchange enhanced spin splitting requires $\Gamma = 6.5 \text{ eV} \cdot \text{\AA}^3$. This is comparable to values found in rare earth metals.

Bogaerts et al. has measured Shubnikov-de Haas oscillations in magnetic fields up to 46 Tesla.¹⁰ At these large magnetic fields, oscillations from the hole surfaces emerge. While confirming the overall picture obtained at lower magnetic fields, they find that the electron and hole densities are not precisely equal, that they exhibit quantum confinement and that the exchange splitting of the Shubnikov-de Haas frequencies scale with Er concentration.

The two different electron mobilities are referenced to the long and short axes of the ellipsoids shown in Figure 2. The high electron mobility is obtained along the short axis and the low along the long axis.

In alloys of $\text{Sc}_x\text{Er}_{1-x}\text{As}$, lattice matched to GaAs, Shubnikov-de-Haas oscillations can be observed in the longitudinal magneto-resistance. (Figure. 4.) The period of these oscillations is a measure of the cross sectional area of the electron ellipsoid at the zone boundary. The temperature dependence yields an effective mass of $m^* = 0.17 m_0$, where m_0 is the free electron mass.

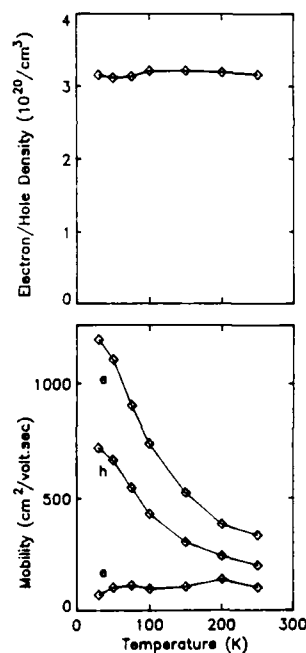


Fig. 3. Top: Electron and hole concentrations as a function of temperature. Bottom: Hole (h) and electron (e) mobilities as a function of temperature.

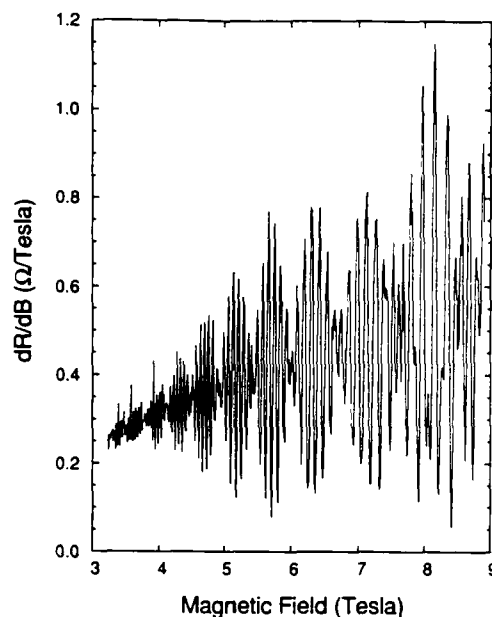


Fig. 4. Shubnikov-de Haas oscillations in the longitudinal magneto-resistance at 1.2° K. The beat oscillation is caused by the large exchange enhanced spin splitting.

Remarkably there is no semi-metal to semiconductor transition as the epitaxial films become very thin.¹⁰ To appreciate the scale of energy and thickness involved in the transition we refer to Figure 5. In a simple semi-metal where the electrons and holes would be described by simple parabolic bands, confinement to a thin quantum well would drive the electron states up and the hole states down. Eventually, the overlap of the electron and hole bands, that produced the semi-metallic behavior in the bulk, would be removed and a semiconductor would emerge. For ErAs, we estimate that this cross-over would occur at 5 to 6 monolayers, with the quantum confined energy gap rising to electron volts at three monolayers and below. Contrary to this expectation epitaxial films show metallic transport down to three monolayers. (See Figure 6.)

The failure to produce a transition to semi-conducting behavior is most likely related to the complexities of the real band structure, especially at the X-point, and the character of the interface between the rare earth arsenide and the GaAs. Indeed, Xia and co-workers have produced a tight binding model of rare earth arsenide quantum wells in GaAs and find that the material remains a semi-metal.¹¹ On the other hand, this result is very important from a technical point of view. Projected applications include transistor like structures where electrons are injected through ultra thin semi-metal films. If these films reverted to a semiconducting state, their potential impact in resonant tunneling hot electron transistors would be lost.

Below 3 monolayers the conductance becomes thermally activated indicating that the ErAs film has become somewhat disconnected. Indeed the prevailing view of the growth of ErAs on GaAs is that the first one or two monolayers are not continuous but form islands 3

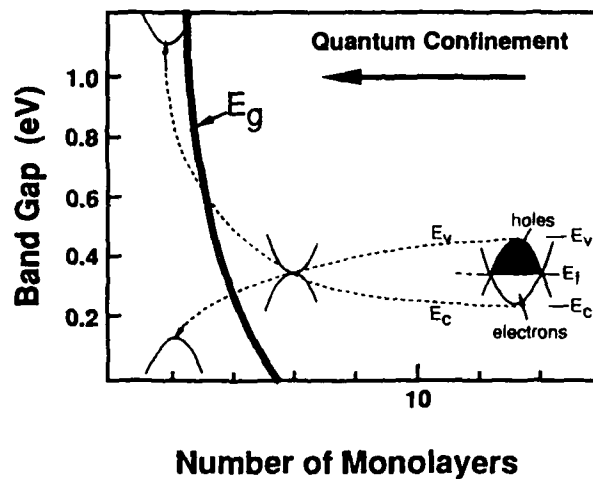


Fig. 5. Electron states and hole states are driven apart by quantum confinement. At 5 monolayers a gap appears and grows to electron-volts at film thicknesses of 3 monolayers.

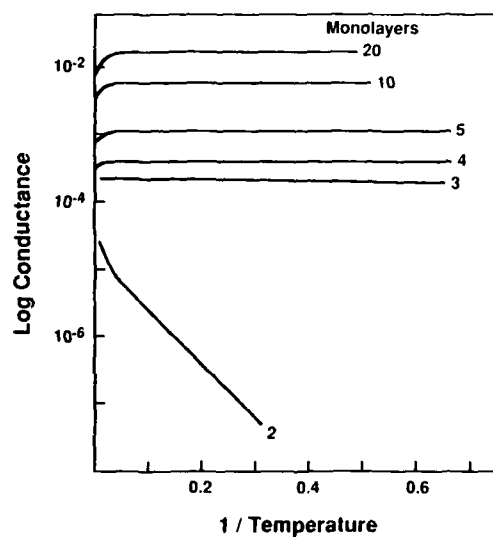


Fig. 6. Log of the conductance as a function of $1/T$ with thickness as a parameter. Metallic behavior is preserved down to 3 monolayers.

monolayers high. Only at 3 monolayers does the coverage become complete and then proceed to grow monolayer by monolayer. We will use this to our advantage in the next section where we speculate on some novel applications of a random 2- dimensional array of semi-metal islands buried inside a semiconductor.

Below we enumerate the established properties of epitaxial buried Er,ScAs films, some of which are reviewed above.

- Lattice matched semi-metal/semiconductor heterostructures.
- Band structure and Fermi surface.
- Conduction band/4f spin exchange.
- No semi-metal/semiconductor transition for monolayer coverage.
- Island hopping transport below 3 monolayers.
- Classic spin disorder scattering contribution to the resistivity.
- Depression of the Néel point at monolayer coverage.
- Bound magnetic polarons at monolayer coverage.

The underlined properties are critical to the novel electronics discussed in the next section.

NOVEL ELECTRONICS ENABLED BY BURIED SEMIMETALS

We can identify two areas in which semi-metal nano-structures buried inside compound semiconductors may have potential applications:

- i) Non-linear terahertz electronics in lateral composites comprised of semimetal and doped semiconductor, and
- ii) Resonant tunneling hot electron transistors with an ultra thin semi-metal base.

Non-linear terahertz electronics

A technology drive in submillimeter wave electronics distributes discrete semiconductor devices in a two-dimensional array^{12,13}. If the wavelength of the radiation is larger than the period of the array and its frequency below array resonances, the interaction of an incident plane wave with the structure can be modeled by the single device in a unit cell of the array. Expected improvements in performance over single elements are improved power handling, potential for power combining, improved dynamic range and broad band response below array resonances. Schottky diodes are the simplest devices that can be distributed over such an array.

Motivated by this technology thrust, we recognize that if the rare-earth monoarsenides are less than three monolayers and grown in a δ -doped layer they will constitute a random Schottky diode array, (Figure 7.). The strength of the non-linear response is controlled by the random Schottky diodes. Unlike the lithographically defined array, these arrays will appear more like an array of back-to-back Schottky diodes and strong non-linearities will

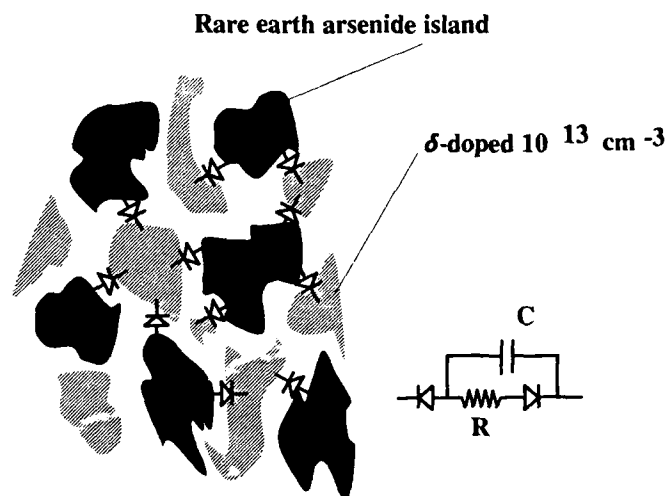


Fig. 7. 2-Dimensional random array of Schottky diodes formed by islands of semi-metal immersed in a δ -doped layer inside GaAs.

only appear if the doping level is sufficient to establish reverse biased tunnel currents, $> 10^{13}$ electrons/cm². Under these conditions the material will simulate an array of backward diodes which are known to be effective non-linear elements at microwave frequencies.¹⁴ The RC roll off is controlled by the sheet conductance of the δ -doped layer and capacitance between the islands and estimated to be > 10 THz. (A similar structure can be formed by precipitating As micro crystals from low-temperature grown GaAs in a δ -doped layer.¹⁵)

Non-linear response of a composite material at the percolation threshold is an important scientific issue, while the technology impact will rest on the frequency response and the strength of the non-linearities.

Metal Base Quantum Transport Devices

As mentioned in the introduction, previous attempts to fabricate metal base transistors have not met with the success necessary to contemplate replacing conventional transistors. However there is an emerging technology thrust that focuses on quantum transport devices like resonant tunneling, hot electron transistors. Selective contact to a highly conducting but ultra thin semi-metal layer, that supports quantum transport, could provide a material system to facilitate this technology.

To identify the materials and processing issues that will arise in producing this type of device, we have made an attempt to fabricate a rare earth arsenide, semi-metal base, heterojunction hot electron transistor. The layer sequence is shown in Figure 8. The emitter was designed to have a conduction band approximately .3 eV above the collector to minimize the effect of energy loss in the 10 monolayer base. (Theoretical estimates place the mean free path at 100 nm, much larger than the semi-metal thickness and we do not expect this to

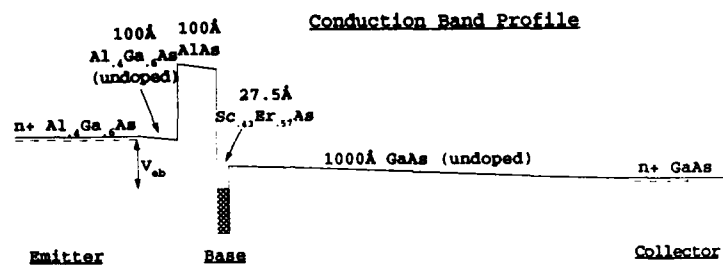


Fig. 8. Conduction band profile through the "transistor like" structure with a rare-earth arsenide base.

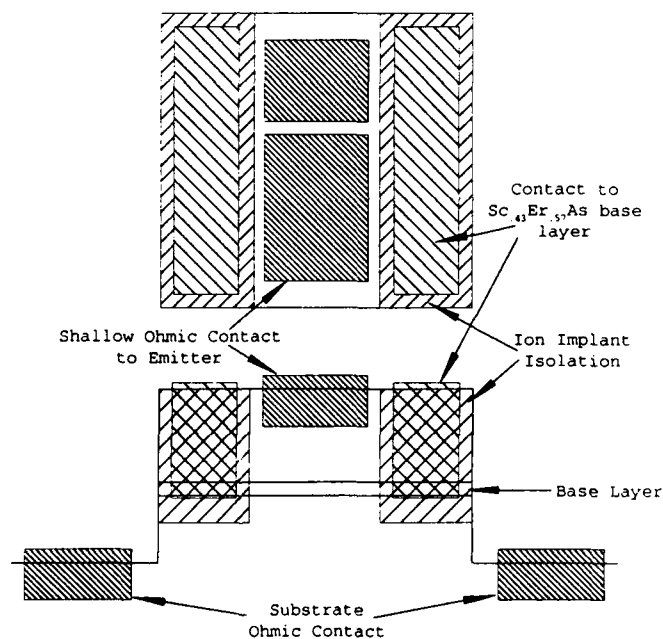


Fig. 9. Top and cross-sectional view showing emitter, base and collector contacts, and implant isolation of the ultrathin semi-metal base.

be a critical issue.¹⁶⁾ A tunnel barrier was placed at the emitter base junction to limit the current flow and allow some degree of control over the electron injection energy.

A clear material advantage of these buried semi-metal layers is the potential for selective and specific contact to nanometer thick highly conducting layers. Indeed this was realized in a straight forward and effective way. Rare-earth arsenides as thin as 5 monolayers were

exposed to proton implant at energies and fluences sufficient to render doped GaAs insulating. The sheet resistance changed less than 10%. This opened the door for a process whereby the (Al,Ga)As could be rendered insulating leaving an ultra thin plane of semimetal extending into this region from the base. (See Figure 9.) To electrically contact this thin semi-metal sheet, Ni was evaporated to the thickness required to form a compound alloy contact down to the metal layer. Alloying at 200°C for about one-half hour created a reliable and ohmic contact to 10 monolayers of rare earth arsenide without shorting to the collector.

The test structure had pairs of contacts to the emitter and to the base so that various configurations of current flow and base transfer could be measured. In this way experimental artifacts masquerading as base transfer could be excluded. The essential results are shown in Figure 10. For electrons injected into the base, a transfer coefficient of $\alpha = .02$ was measured. The horizontal shift in the I-V characteristic is caused by the IR drop in the metal base whereas the vertical rise is caused by base transfer.

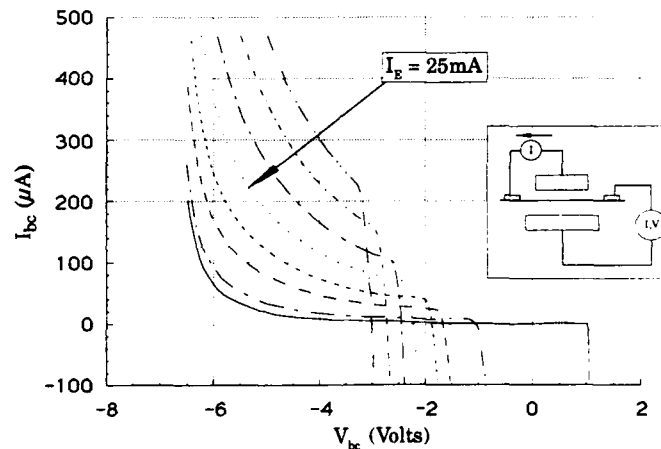


Fig. 10. Common base characteristics, at 4.2° K, displaying a base transfer characteristic of about $\alpha = .02$

It is clear that this base transfer is limited by the poor overgrowth of (Al,Ga)As on the rare earth arsenide. Structural information gained from transmission electron micrographs show a very defective overgrowth. This would cause most of the emitter/base current to flow through resistive channels and not be injected into the base at high energy. Only at high currents are there sufficient electrons injected into the base to be collected by the collector.

These experiments have served to highlight two key issues.

- Selective and specific contact to ultra thin, buried, rare earth arsenide layers can be achieved in rare earth arsenide/III-V heterostructures.
- Overgrowth of III-V semiconductors on the rare earth arsenides is the key materials issue to successfully realizing vertical quantum transport devices.

SUMMARY

Lateral magneto-transport measurements have shown that high quality ultra thin films of rare earth arsenides can be epitaxially grown inside (Al,Ga)As heterostructures. The essential electronic properties are those of a semi-metal with electron and hole concentrations of $3 \times 10^{20} \text{ cm}^{-3}$. Transport measurements display rich phenomena including spin disorder scattering, Shubnikov-de Haas oscillations, quantum confinement and enhanced exchange splitting. If rare-earth arsenide thin films were to undergo a transition to a semiconducting state, they would be of little value in quantum transport electronics. A critical feature is the persistence of metallic transport in quantum confined ultra thin films.

We have speculated on two potential applications of buried, semi-metallic, rare earth arsenide films. In the first we take advantage of the island growth of rare earth arsenides at coverage less than three monolayers. By imbedding these islands in a heavily δ -doped layer a random array of nano-structured Schottky diodes can be fabricated with intrinsic high frequency roll-off's at 10's of terahertz and with potentially large non-linearities. In this form these materials may be important for non-linear electronics at terahertz frequencies.

In the second we have addressed the issue of using ultra thin, semimetal layers in quantum transport electronics such as resonant tunneling hot electron transistors. The advantage that these films bring to this technology is the relative ease of selectively and specifically contacting highly conducting, nanometer thick control electrodes. By fabricating "transistor like" test structures we have confirmed this fact but have also revealed a critical materials issue, overgrowth of the GaAs on the rare earth arsenide.

ACKNOWLEDGEMENT

Work performed at UCSB is supported by the Office of Naval Research, (N00014-92-J-1452, N00014-93-10497) and the Air Force Office of Scientific Research (F49620-93-1-0329DEF).

1. C.A. Mead, Proc. IRE 48,359 (1960).
2. S.M. Sze and H.K. Gummel, Solid State Electron. 9, 751 (1966).
3. A.C. Seabaugh, J.H. Luscombe and J.N. Randall, to be published Future Electron Devices Journal.
4. F. Capasso, S. Sen, and F. Beltram, "Quantum-Effect Devices" in High Speed Semiconductor Devices, edited by S.M. Sze (John Wiley & Sons, New York, 1990), p. 465.
5. A.C. Seabaugh and M. Reed, "Resonant Tunneling Transistors", to be published in Heterostructure and Quantum Devices, edited by N.G. Einspruch and W.R. Frensley.
6. C.J. Palmström, S. Mounier, T.G. Finstad, P.F. Miceli, Appl. Phys. Lett. 56, 382 (1990).
7. T. Sands, C.J. Palmström, J.P. Harbison, V.G. Keramidas, N. Tabatabaie, T.L. Cheeks, R. Ramesh and Y. Silberberg, Mat. Sci. Rep. 2, 99 (1990).

8. S.J. Allen, Jr., F. DeRosa, C.J. Palmstrøm, and A. Zrenner, Phys. Rev. **B43**, 9599 (1991).
9. A. Hasegawa and A. Yanase, J. Phys. Soc. Jpn. **42**, 492 (1977).
10. R. Bogaerts, L. Van Bockstal, F. Herlach, F.M. Peeters, F. DeRosa, C.J. Palmstrøm and S.J. Allen, Jr., Physica **B177** 425 (1992).
11. S.J. Allen, Jr., N. Tabatabaie, C.J. Palmstrom, G.W. Hull, T. Sands, F. DeRosa, H.L. Gilchrist and K.C. Garrison, Phys. Rev. Lett. **62**, 2309 (1989).
12. J.-B. Xia, S.-F. Ren and Y.C. Chang, Phys. Rev. **B43**, 1692 (1991).
13. J.B. Hacker, R.M. Weikle, II, M. Kim, M.P. DeLisio and D.B. Rutledge, IEEE Trans. Microwave Theory Tech., **39**, 557 (1992).
14. R.M. Weikle, II, M. Kim, J.B. Hacker, M.P. DeLisio, Z.B. Popovic and D.B. Rutledge, Proc. IEEE, **80**, 1800 (1992).
14. S.M. Sze, Physics of Semiconductor Devices, John Wiley & Sons, New York, 1981, p.537.
15. M.R. Melloch, N. Otsuka, K. Mahalingam, C.L. Chang, P.D. Kirchener, J.M. Woodall and A.C. Warren, Appl. Phys. Lett. **61**, 177 (1992).
17. J.J. Quinn, Phys. Rev. **126**, 1453 (1962).

STUDY OF $\text{Sr}_{1-x}\text{Er}_x\text{F}_{2+x}$ LUMINESCENT THIN FILMS EPITAXIALLY GROWN ON InP (100).

A.S. BARRIERE*, B. MOMBELLI*, B.Y.KIM*, S. RAOUX* and A. GARCIA **

* LEMME, ** LCS, Univ. Bordeaux I, 351 Crs de la Liberation 33405 Talence, France.

ABSTRACT

Erbium-substituted $\text{Sr}_{1-x}\text{Er}_x\text{F}_{2+x}$ strontium fluoride layers were grown on InP(100) substrates by sublimation under ultra-high vacuum of high purity solid solution powders.

Their composition and the spatial distribution of the basic components were deduced from Rutherford backscattering (RBS), using a nuclear microprobe, and secondary ion mass spectrometry (SIMS). For x lower than 20% it is shown that the film composition is analogous with the initial sintered material and quite homogeneous. The ageing in air of the films was followed by infrared absorption studies. No significant water adsorption was revealed.

The texture of the layers was studied by RBS in channelling condition. For x as high as 15% it is shown that the films are well crystallized and well epitaxially grown on InP (100) substrates.

Infrared emission due to the $^4\text{I}_{13/2}$ - $^4\text{I}_{15/2}$ electronic transition on the $4f^{11}$ inner shells of Er^{3+} ions ($1.53\mu\text{m}$), which presents potential applications for optical communications, was studied at room temperature as a function of x . It is demonstrated that the highest luminescence efficiency of these layers corresponds to x upper than 20%.

INTRODUCTION

Growth and characterization of insulating epitaxial fluoride layers such as BaF_2 , SrF_2 and CaF_2 on semiconductor surfaces have received considerable attention, and the potential technological applications have been rapidly developed. Such structures can act to match lattice of dissimilar materials [1] ; as insulator, they offer new possibilities for metal-insulator-semiconductor field effect transistor (MISFET) and lead to the realization of completely monolithic three dimensional circuits.

In other respect, the spectroscopic properties of rare-earth (RE) ions in ionic bulk crystals have been extensively investigated. A large number of fluoride matrix-RE combinations was studied for their high luminescence efficiency due to intra- $4f$ -shell transitions of RE ions which give rise to luminescence in UV, visible, and near-infrared spectral regions. Moreover, laser action was demonstrated [2].

In order to realize luminescent components on semiconductors, we have studied the epitaxial growth of $\text{Sr}_{1-x}\text{Er}_x\text{F}_{2+x}$ /InP (100) substrates and the luminescence of Er^{3+} ions which presents an emission at $1.53\mu\text{m}$. This radiation corresponds to the optical range for minimum absorption in silica-based optical fibres and presents a great interest for optical communications.

The composition and the thickness of the layers were deduced from Rutherford back scattering (RBS) of 2 MeV $^4\text{He}^+$ particles. This analysis technique and apparatus was described in refs [3] and [4]. The spatial distribution of the basic components was studied by RBS, using a nuclear microprobe allowing to reduce the spot of the incident beam at $2.25\mu\text{m}^2$.

and by secondary ion mass spectrometry (SIMS) using a CAMECA IMS4F apparatus. The epitaxial quality of the layers was deduced from a RBS study in channelling condition. The ageing in air of the film was followed by IR absorption using a PERKIN-ELMER 983 system for wave number varying from 4000 to 400 cm^{-1} . The obtained physico-chemical results will be presented below.

Finally, we will present the photoluminescence (PL) results, characteristic of erbium in $\text{Sr}_{1-x}\text{Er}_x\text{F}_{2+x}/\text{InP}$. The luminescence efficiency of Er^{3+} ions, as a function of x , will be discussed for different transitions on the $4f^{11}$ inner-shell.

RESULTS AND DISCUSSION.

Growth and characterization

Thin films were grown on InP(100) substrates in a ultra-high-vacuum system(UHV). The substrates were classically cleaned (degreasing, etching, deoxidisation) [5] under a dry nitrogen atmosphere before surface rebuilding controlled by RHEED under vacuum at 350°C. The initial powders of SrF_2 and ErF_3 were mixed with appropriate proportion between 1 and 20 mol%, then evaporated under UHV at 1250°C from platinum crucibles. The growth rate was 0.1 nm.s^{-1} and the temperature of the substrate during the growth was 300°C.

The first characterizations of the obtained thin films were deduced from RBS measurements. The scattering angle θ_L in the laboratory coordinates was 160°. The surface barrier detector has a resolution of 13.5 keV checked with a ^{241}Am source. For example, Fig. 1 shows the RBS spectrum of a 480 nm thick $\text{Sr}_{0.96}\text{Er}_{0.04}\text{F}_{2.04}/\text{InP}(100)$ structure. The comparison of the areas of the RBS steps corresponding to the different components shows, whatever x varying from 1 to 20%, that the erbium, strontium and fluorine contents are analogous to those of the initial mixtures. Moreover, we have verified that their global atomic ratios are constant in the depth of the films. No significant traces of impurities, in particular oxygen, were revealed with this analysis technique in the bulk of the samples.

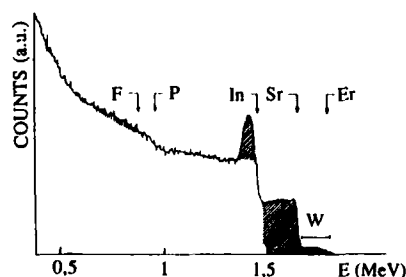


Fig. 1 RBS spectrum of a 480 nm thick $\text{Sr}_{0.96}\text{Er}_{0.04}\text{F}_{2.04}/\text{InP}(100)$ structure

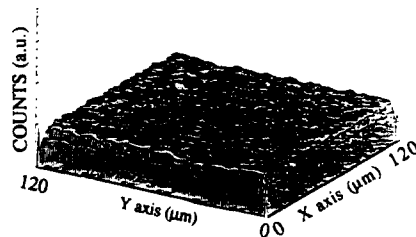


Fig. 2 Evolution of erbium concentration at the surface of the film

The spatial distribution of the main components at the surface of the films was studied by means of a nuclear microprobe which allows to reduce the lateral sizes of the beam at 2.25 μm^2 [6]. Fig. 2 was obtained on the basis of an energy window W corresponding, in Fig.1, to the response of erbium present in the first 200 nm of the film. This picture shows that the surface distribution of this element, on a $120 \times 120 \mu\text{m}^2$ sample area, does not vary significantly in the different points of the studied structure.

SIMS measurements were performed under pulverization of either oxygen or caesium ions, in order to determine the in-depth distribution of the different components of the layers. Whatever x , only the basic components (erbium, strontium and fluoride) and traces of carbon and oxygen were revealed. For a 470 nm thick layer of $\text{Sr}_{0.99}\text{Er}_{0.01}\text{F}_{2.01}/\text{InP}(100)$, Fig. 3 shows that the erbium concentration fluctuates lightly in the depth of the film. This is certainly due to the low quantity of erbium in this sample. Indeed, for higher substitution rates such a phenomenon was not observed. In other respect we can remark an anomaly near the interface between the film and the substrate on the strontium, erbium and oxygen profiles. This could be explained by a modification of the texture of the first layers of the film, enhancing the pulverization efficiency. Indeed, a RBS study in channelling condition, performed elsewhere [7], showed that in such films, which are not constraint on the substrate, crystalline defects appear near the interface. No diffusion of the chemical species in the bulk of the substrate was revealed with this analysis technique. The interfaces between the films and the substrates seem to be abrupt.

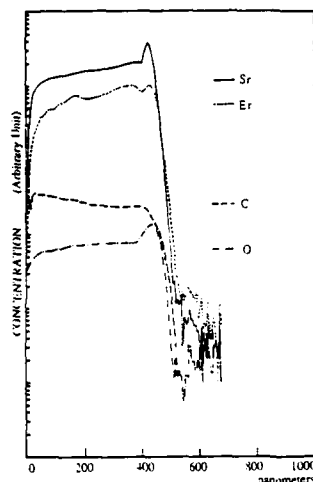


Fig. 3 SIMS profile of a 470 nm thick layer of $\text{Sr}_{0.99}\text{Er}_{0.01}\text{F}_{2.01}/\text{InP}(100)$

Channelling effect measurements were used to study the epitaxial quality of the films on $\text{InP}(100)$ substrates as a function of the substitution rate. Fig. 4 shows the evolution of the random (α) and aligned (β) spectra for x varying from 1% to 13%. We can observe that, for $x < 6\%$, the minimum yield χ_{\min} , which measure the ratio $\text{H}_\alpha/\text{H}_\beta$ (see Fig. 4 a), stays lower than 0.1, characteristic of a relatively good epitaxy of the film. For $6\% < x < 15\%$, the χ_{\min} variation is fast growing from 0.1 to 1. For $x > 15\%$ the channelling effect has completely disappeared, traducing a deterioration of the crystalline quality of the films. It is to note that the increase of χ_{\min} with erbium substitution rate is also due to the presence of interstitial fluorine atoms in the matrix, defocusing more and more the incident particles when the concentration of erbium becomes too high.

To ensure that the films are well ageing in air and notably that a water adsorption does not influence the crystallographic and luminescence properties of the layers, we have performed IR absorption measurements. After an ageing several weeks in moist air, 80% relative humidity, it has been impossible to detect any OH^- groups ($3600\text{--}3200\text{ cm}^{-1}$ band) and H_3O^+ groups ($1800\text{--}1600\text{ cm}^{-1}$ band). This shows the insensibility of the samples to the natural humidity.

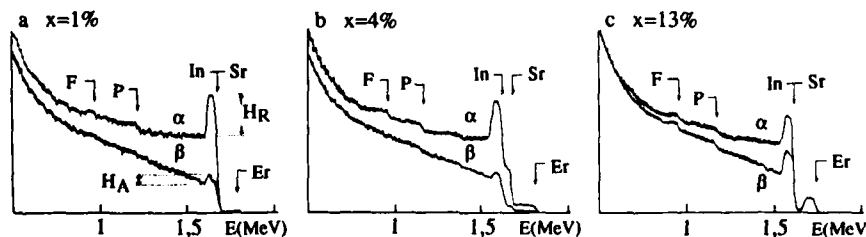


Fig. 4 RBS spectra random (α) and aligned (β) of $\text{Sr}_{1-x}\text{Er}_x\text{F}_{2+x}/\text{InP}(100)$ structures : (a) $x=1\%$, (b) $x=4\%$, (c) $x=13\%$

Luminescence properties

The photoluminescence study was recorded by means of the 488-nm line of an Ar⁺-ion laser as excitation source of the $^4F_{7/2}$ level of Er³⁺ ($4f^{11}$) ions. For the photon detection, a cooled GaAs photo-multiplier and a cooled Ge detector were used in the visible and in the near-infrared spectral regions respectively. The measurements were performed at room temperature (RT).

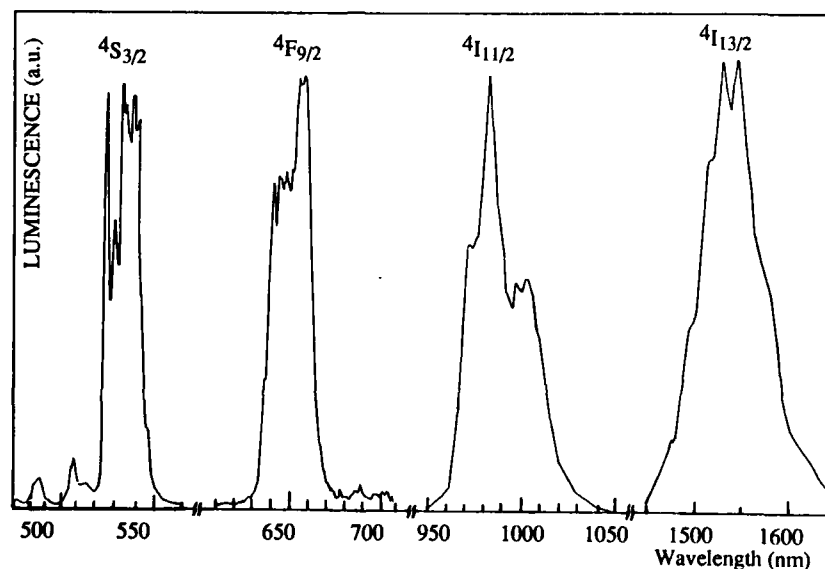


Fig. 5 PL spectra of a $Sr_{0.85}Er_{0.15}F_{2.15}/InP(100)$ structure at RT

Fig. 5 shows the four most intensive luminescence lines of Er³⁺ ions in $Sr_{1-x}Er_xF_{2+x}$ layers. They correspond to the transitions between the $^4S_{3/2}$, $^4F_{9/2}$, $^4I_{11/2}$ and $^4I_{13/2}$ excited levels and the $^4I_{15/2}$ ground state (533, 650, 980 and 1530 nm respectively).

With respect to the different potential applications, it was useful to determine the optimal values of the erbium concentration conducting to the maximum of luminescence intensity. Fig. 6 shows the evolution of luminescence intensity for the visible transitions and the 1.53 μ m radiation, versus x .

Due to the dipole-dipole interactions, the energy transfer between Er³⁺ ions becomes of high importance for high erbium concentrations and limits the incorporation of efficient active centres. The well-known concentration quenching [8] and cross relaxation phenomena [9,10-13] are responsible for the evolution of luminescence efficiency shown in Fig. 6. Because of the multiplicity of excited levels of Er³⁺ ions, and so the great number of cross relaxations [10], it is difficult to isolate one phenomenon from the others. But, we observe a different behaviour for the visible lines and for the IR one which is certainly due to the depopulation of the higher energy levels to the benefit of the $^4I_{13/2}$ - $^4I_{15/2}$ transitions. It is found that the maximum of luminescence for the 1.53 μ m radiation correspond to x_{max} upper than 20%. Such a result seems very attractive since, in these solid solution thin films, the maximum of photoluminescence intensity is obtained for an erbium concentration of three order of magnitude greater than in the case of erbium-doped classical semiconductors [14-16].

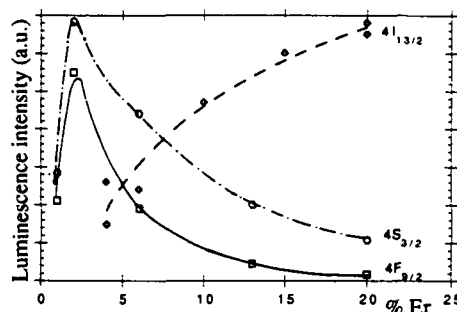


Fig. 6 Evolution of luminescence intensity versus erbium concentration for the $4F_{9/2}$, $4S_{3/2}$, $4I_{13/2}$ to $4I_{15/2}$ transitions.

of sintered materials $\text{Ca}_{1-x}\text{RE}_x\text{F}_{2+x}$ involving an RE^{3+} cation of small size. It consists in a progressive transformation with increasing x of (4:4:3:0) clusters into (8:12:1:0) cubooctahedral clusters (C_{3v} symmetry group) [19]. In fact, the proportion of pairs and clusters is evolving with erbium concentration. We have previously demonstrated the predominance of C_{4v} symmetry in $\text{Ca}_{1-x}\text{Er}_x\text{F}_{2+x}/\text{Si}$ samples [10], allowing the fact that the clusters concentration is relatively low considering the growth technique. The same behaviour was proved in $\text{Nd}:\text{CaF}_2$ epitaxial layers [20] and is attempted on $\text{Sr}_{1-x}\text{Er}_x\text{F}_{2+x}/\text{InP}$ samples. Photoluminescence measurements at low temperatures (2 K) are now in progress. They allow us to study the clustering processus and its effect on the cristal field splitting.

It is well known that a charge compensation mechanism is required when a rare-earth trivalent ion substitutes for a divalent ion in the fluoride matrix [9,17,18]. In our case, charge compensation mechanism is assumed by introduction of supplementary F^- ions in F' or F'' sites (F' and F'' sites are displaced positions from the ideal cubic empty position (1/2 1/2 1/2) (C_{4v} symmetry group) into respectively the $\langle 110 \rangle$ and $\langle 111 \rangle$ directions). For higher substitution rates, these pairs are associated in extended defects or clusters. A processus of clustering has been shown in the series

CONCLUSION

We have demonstrated that the prepared $\text{Sr}_{1-x}\text{Er}_x\text{F}_{2+x}$ thin films are homogeneous, dealing with their atomic concentration and spatial distribution. Moreover, a relatively good epitaxy is obtained for $x < 15\%$ and when the thickness of the film stays lower than 500 nm. Photoluminescence under excitation of an argon ion laser and cathodoluminescence have shown that erbium ions present strong luminescence lines in the visible and near-infrared spectral regions at room temperature. This last emission must be used for optical communications. The luminescence in the visible range can act to detect ions or electrons beams. It is already used for focusing the nuclear microprobe described in ref [6]. Finally, we have shown the predominance of cross relaxation phenomena at high erbium concentrations.

REFERENCES

- [1] T. Asano, H. Ishiwara, H.C. Lee, K. Tsutsui and S. Furukawa, Jpn. J. Appl. Phys. 25 (1986) L139.
- [2] A.A. Kaminskii, Laser crystals (Springer, New York, 1981).
- [3] G. Gevers, A.S. Barrière, J. Grannec, L. Lozano, B. Blanchard, Phys. Stat. solidi A81 (1984) 105.
- [4] H. Guégan, Ph. D. Thesis, University of Bordeaux I - 1990.
- [5] A.S. Barrière, B. Desbat, A. EL Fajri, H. Guégan and V. Tournay Appl. Surf. Sc., 64 (1993) 225.

- [6] Y. Llabador, D. Berthault, J.C. Gouillaud, P. Moretto
Nuclear. Inst. and Meth. B49 (1990) 435-440.
- [7] A.S. Barrière, A. EL Fajri, H. Guegan, B. Mombelli, S. Raoux
J. Appl. Phys. 71, 2 (1992) 709.
- [8] G. Blasse, A. Bril
Philips Tech. Rev. 31, 10 (1970) 304.
- [9] M.R. Brown, H. Thomas, J.S.S. Whiting, W.A. Shang
J. Chem. Phys. 50, 2 (1969), 881
- [10] Inta-4f-shell transitions of ER_{3+} ions in $Ca_{1-x}Er_xF_{2+x}$ thin films grown on Si(100).
A.S. Barrière, S. Raoux, A. Garcia, H. L'Haridon, B. Lambert and D. Motonnet
Proposed for publication, J. Appl. Phys (01/02/93)
- [11] M.P. Miller, J.C. Wright
J. Chem. Phys. 71 (1) (1979) 324.
- [12] M.R. Brown, H. Thomas, J.M. Williams, R.J. Woodward, W.A. Shand
J. Chem. Phys. 31 (8) (1969) 3321.
- [13] F. Auzel
J. of Lumin. 31-32 (1984) 759-761.
- [14] P.N. Favennec, H. L' Haridon, D. Moutonnet, A. Salvi, M. Gauneau
Jap. J. of Appl. Phys 29-4 (1990) L524.
- [15] P. Galtier, J.P. Pocholle, M.N. Charasse, R. de Cremoux, J.P. Hirtz, B. Groussin, T. Benyattou, G. Guillot
Appl. Phys. Lett. 55-20 (1989) 2105.
- [16] C. Rochaix, A. Rolland, P.N. Favennec, B. Lambert, A. Le Corre, H. L' Haridon, M. Salvi
J. Elect. Mat. 17-5 (1988) 351.
- [17] M.D. Kurz, J.C. Wright
J. of Lumin. 15 (1977) 169-186.
- [18] N.C. Amaral, B. Maffeo, D. Guenzburger
Phys. Stat. Sol. B117, 141 (1983).
- [19] J.M. Reau, M. Wahbi, J. Sénégas and P. Hagenmüller
Phys. Stat. Sol. (b) 169, 331 (1992).
- [20] L.E. Bausa, R. Legros, A. Munoz-Yague
J. Appl. Phys. 70 (8)- 1991, 4485.

OPTICAL AND STRUCTURAL PROPERTIES OF $\text{CaF}_2\text{:Nd}$ FILMS ON SI-BASED SUBSTRATES

C.-C. CHO, W.M. DUNCAN and H.-Y. LIU

Central Research Laboratories, Texas Instruments, P.O. Box 655936, MS 147, Dallas,
Texas 75265.

ABSTRACT

By thermally evaporating CaF_2 and NdF_3 , we have grown Nd-doped CaF_2 films on Si(111), Al/Si(111) and quarter-wavelength $\text{Ta}_2\text{O}_5/\text{SiO}_2$ multilayer Bragg reflectors. The optical and structural properties of the $\text{CaF}_2\text{:Nd}$ films are characterized by photoluminescence spectroscopy (PL) and x-ray diffraction. The effects of different Nd concentration, growth temperatures and post-annealing were studied. Regardless of the substrates, the as-grown films show emission lines at wavelengths similar to bulk $\text{CaF}_2\text{:Nd}$. Annealing the films at 700°C in forming gas results in a new emission pattern. Little difference between the PL spectra of polycrystalline and single crystal $\text{CaF}_2\text{:Nd}$ films is observed, indicating that the luminescence efficiency is insensitive to the crystalline quality of the films.

INTRODUCTION

Since CaF_2 can be grown epitaxially on Si, and vice versa, the epitaxial growth and the electrical properties of CaF_2 on Si-based substrates have been widely studied for their possible applications in high speed electronics devices.^{1,2} In addition to their usage in electronics devices, several recent papers have reported the luminescence properties of rare earth doped fluorides³⁻⁶ and discussed the feasibility of employing these materials as the optical sources for Si-based optoelectronics. Optical devices made of these materials may also provide light sources at wavelengths where semiconductor lasers do not exist or perform poorly.

These studies have shown that rare earth ions can be incorporated into epitaxial fluoride films by using molecular beam epitaxy (MBE).³⁻⁶ For Nd-doped CaF_2 films,⁴⁻⁶ strong emission intensities with luminescence at wavelengths similar to bulk $\text{CaF}_2\text{:Nd}$ were observed. In contrast to the low quenching concentration, charge compensation and Nd aggregation problems observed in bulk $\text{CaF}_2\text{:Nd}$, high Nd concentrations are obtainable in the MBE grown films with less Nd aggregation and no charge compensation.

In this paper, we report the effects of post-annealing, different growth temperatures and crystalline quality on the photoluminescence (PL) properties of these films. The PL spectra from three different substrates, i.e., Si(111), Al(111) and $\text{Ta}_2\text{O}_5/\text{SiO}_2$, were studied, and found to exhibit similar emission patterns but with

different intensities. Growing the films at various temperatures from 100°C to 700°C did not change the emission pattern either. In contrast, when the films were annealed at 700°C in forming gas after they were deposited, the PL spectra of the post-annealed films are very different from the PL spectra of the as-grown films. By comparing the films grown at different temperatures, we found the crystalline quality of the films do not noticeably affect their PL properties.

EXPERIMENT

The Nd-doped CaF_2 films were grown by thermally evaporating CaF_2 and NdF_3 from two effusion cells.⁶ Since the fluorides do not dissociate during the growth process, the deposition rates and film compositions can be controlled simply by the cell temperatures, with two ion gauges monitoring the flux pressures of CaF_2 and NdF_3 . Composition and thickness of the films were determined by x-ray fluorescence spectroscopy and a surface profilometer, respectively. $\text{Si}(111)$, $\text{Al}(111)/\text{Si}(111)$ and 10.5 pairs of quarter-wavelength $\text{SiO}_2/\text{Ta}_2\text{O}_5$ multilayer Bragg reflectors on $\text{Si}(100)$ were used as the substrates. $\text{Si}(111)$ were prepared by a typical high temperature cleaning process in the MBE chamber.² $\text{Al}(111)$ was grown on the cleaned $\text{Si}(111)$ at 300°C.⁷ Single crystal $\text{CaF}_2:\text{Nd}$ on the $\text{Al}(111)$ was obtained by ramping the substrate temperature from 100°C to 300°C in five minutes and then maintaining at 300°C until the end of the growth, as reported for the epitaxial growth of CaF_2 on $\text{Al}/\text{Si}(111)$.⁸ The $\text{Ta}_2\text{O}_5/\text{SiO}_2$ Bragg reflectors were grown by electron beam evaporation with the substrate temperature at 280°C. The reflector was designed to have the maximum reflectivity around 1046 nm. X-ray diffraction was carried out by using a $\text{Cu K-}\alpha_1$ source and a germanium monochromator. PL spectra were taken with a Ge detector and the 514.5 nm line of an Ar ion laser as the excitation source.

RESULTS AND DISCUSSION

Figure 1 shows the room temperature PL spectrum of a 1 μm thick $\text{CaF}_2:\text{Nd}$ (0.96 wt.%) film grown on $\text{Si}(111)$ at 100°C. The $^4\text{F}_{3/2} \rightarrow ^4\text{I}_{9/2}$, $^4\text{F}_{3/2} \rightarrow ^4\text{I}_{11/2}$ and $^4\text{F}_{3/2} \rightarrow ^4\text{I}_{13/2}$ transitions are observed at around 900 nm, 1060 nm and 1350 nm, respectively. The emission wavelengths from the films are closely correlated with the emission wavelengths observed from bulk $\text{CaF}_2:\text{Nd}$.⁹⁻¹¹ This type of close correlation has also been observed between $\text{Er}_x\text{La}_{(1-x)}\text{F}_3$ ³ and $\text{Er}_x\text{Ca}_{(1-x)}\text{F}_{(2+x)}$ ¹² films grown by MBE and their corresponding bulk materials. PL spectra of $\text{CaF}_2:\text{Nd}$ films taken at 4.2 K and 77 K show more well-separated peaks with narrower linewidths and similar emission wavelengths.⁶ For example, linewidths of the 1046.1 nm peak are 1.5 nm at room temperature, 0.44 nm at 77 K and 0.12 nm at 4.2 K. As observed from bulk $\text{CaF}_2:\text{Nd}$,¹¹ this peak shift toward 1045.7 nm when the films were cooled down to 4.2 K.

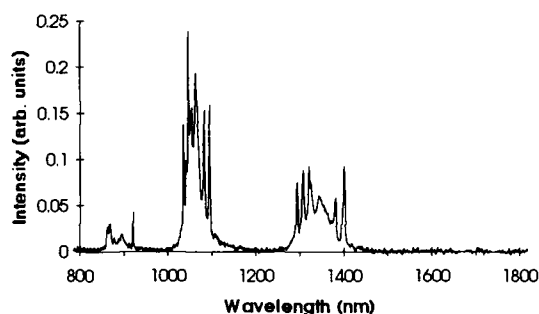


Figure 1
Room temperature
PL spectrum of a 1
 μm thick $\text{CaF}_2\text{:Nd}$
(0.96 wt.%) film
grown on Si(111) at
 100°C .

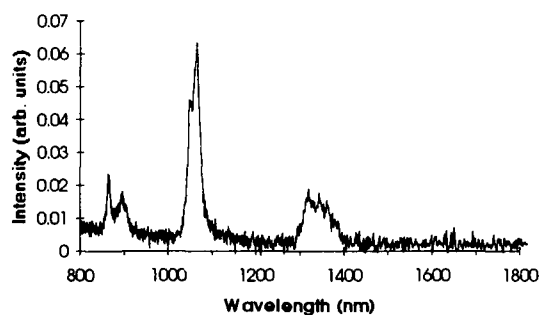


Figure 2
Room temperature
PL spectrum of a 1
 μm thick $\text{CaF}_2\text{:Nd}$
(33 wt.%) film
grown on Si(111) at
 100°C .

When the Nd concentration increases above 3.8 wt.%, the sharp emission line at 920.9 nm in the $^4\text{F}_{3/2} \rightarrow ^4\text{I}_{9/2}$ region; the lines at 1035.2 nm, 1046.1 nm, 1081.9 nm and 1093.8 nm in the $^4\text{F}_{3/2} \rightarrow ^4\text{I}_{11/2}$ region; and the lines at 1293.5 nm, 1307.2 nm, 1320.2 nm, 1380.3 nm and 1400.4 nm in the $^4\text{F}_{3/2} \rightarrow ^4\text{I}_{13/2}$ region disappear. Weak emission bands from aggregated Nd-F at wavelengths similar to those of NdF_3 were observed. A PL spectrum of a 1 μm thick $\text{CaF}_2\text{:Nd}$ (33 wt.%) film grown on Si(111) at 300°C is shown in figure 2. Similar pattern was observed from films of Nd concentrations from 7.6 wt.% to 33 wt.%.

The films grown at various temperatures show very similar emission pattern but different intensities when the Nd concentration is the same. Figure 3 shows the intensities of the peak at 1046.1 nm from $\text{CaF}_2\text{:Nd}$ (0.96 wt.%) and the intensities of the peak at 1064.5 nm from $\text{CaF}_2\text{:Nd}$ (33 wt.%) grown at various temperatures. When the Nd concentration is 0.96 wt.%, the maximum intensity is observed from the films grown at 500°C . When the Nd concentration is 33 wt.%, the intensities at 1064.5 nm increase as the growth temperatures increase.

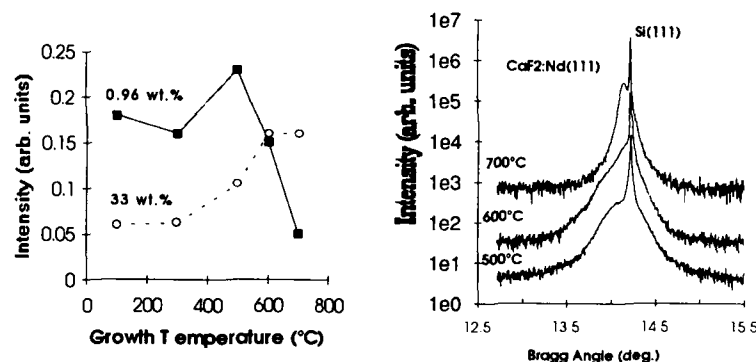


Figure 3 PL intensities at 1046.1 nm from 1 μm thick $\text{CaF}_2\text{:Nd}$ (0.96 wt.%) films; and at 1064.5 nm from 0.2 μm thick $\text{CaF}_2\text{:Nd}$ (33 wt.%) films grown at various temperatures.

Figure 4 X-ray rocking curves of $\text{CaF}_2\text{:Nd}$ (0.96 wt.%) films grown on Si(111) at 500°C, 600°C and 700°C.

When $\text{CaF}_2\text{:Nd}$ films of the same thickness and Nd concentration were grown on Si(111), Al(111) and quarter wavelength $\text{Ta}_2\text{O}_5/\text{SiO}_2$ reflectors at the same growth temperature, the PL spectra of the films show similar pattern but different intensities. The relative intensities of the 1046.1 nm peak for 1 μm thick $\text{CaF}_2\text{:Nd}$ (0.96 wt.%) films grown on Si, Al and the $\text{Ta}_2\text{O}_5/\text{SiO}_2$ reflectors are 1.0, 3.3 and 9.8, while the reflectivity of the substrates at this wavelength are 28%, 90% and 99%, respectively.

X-ray diffraction analysis of 1 μm thick $\text{CaF}_2\text{:Nd}$ (0.96 wt.%) films on Si(111) shows that the films grown at and above 300°C are epitaxial. The crystalline quality of the epitaxial films improves as the growth temperatures increase from 300°C to 700°C. Figure 4 shows the x-ray rocking curves of the films grown at 500°C, 600°C and 700°C. While the Bragg angle of the $\text{CaF}_2\text{:Nd}(111)$ peaks remains at 14.14 degree, the peak intensity increases from 275 to 595 and 1350 counts per second as the growth temperature increases from 500°C to 600°C and 700°C. The widths of the peaks decrease as the temperatures increase. These rocking curves show that the $\text{CaF}_2\text{:Nd}$ film grown at 700°C has the best crystalline quality. In comparison with $\text{CaF}_2(111)$ films grown on Si(111) at 700°C, the Bragg angle of the $\text{CaF}_2\text{:Nd}(111)$ peak is very close to that of a $\text{CaF}_2(111)$ grown on Si(111) at 700°C. However, the intensity of the $\text{CaF}_2\text{:Nd}(111)$ peak is approximately half the intensity of the $\text{CaF}_2(111)$ peak, indicating that adding 0.96 wt.% of NdF_3 slightly degrades the crystalline quality of the film, even though the halfwidth of the $\text{CaF}_2\text{:Nd}(111)$ peak (305 arc sec) is not much worse than the halfwidth of the $\text{CaF}_2(111)$ peak (285 arc sec).

The results of figure 3 and figure 4 show that the PL intensity is independent of the crystalline quality. Although the film grown at 700°C shows the best crystalline quality, the PL intensity of this film is lower than the PL intensities of the film grown at 500°C and the polycrystalline film grown at 100°C. The same insensitivity to crystalline quality was confirmed by comparing the PL spectra of epitaxial and polycrystalline $\text{CaF}_2\text{:Nd}$ films grown on Al(111)/Si(111) substrates.

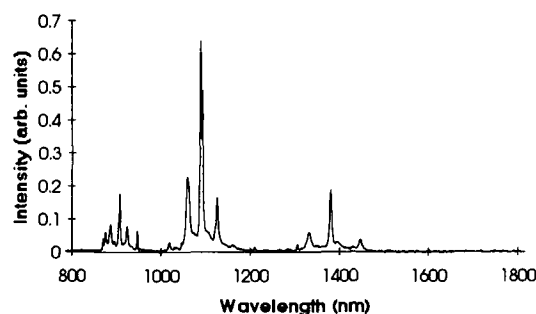


Figure 5
Room temperature
PL spectrum of a 1
 μm thick $\text{CaF}_2\text{:Nd}$
(0.96 wt.%) film
grown on Si(111) at
100°C and post-
annealed in forming
gas at 700°C for 30
min.

Although annealing the $\text{CaF}_2\text{:Nd}$ films in forming gas (90% N_2 + 10% H_2) at 450°C did not induce any change in their PL spectra, annealing at 700°C resulted in a very different emission pattern (figure 5). Although the emission lines are still around 900 nm, 1060 nm and 1350 nm regions, as the as-grown films, the wavelengths of the peaks for the annealed films do not match with those for the as-grown films. Sharp new peaks at 870.5 nm, 875.8 nm, 886.9 nm, 896.1 nm, 907.7 nm, 924.6 nm and 947.1 nm in the $^4\text{F}_{3/2} \rightarrow ^4\text{I}_{9/2}$ region; 1030.7 nm, 1059.4 nm, 1088.7 nm, 1092.4 nm and 1126.1 nm in the $^4\text{F}_{3/2} \rightarrow ^4\text{I}_{11/2}$ region; and 1306.6, 1332.1 nm, 1381.0 nm and 1447.3 nm in the $^4\text{F}_{3/2} \rightarrow ^4\text{I}_{13/2}$ region were detected. The origin of these emission lines is being investigated and will be reported elsewhere.

CONCLUSION

We have grown epitaxial and polycrystalline $\text{CaF}_2\text{:Nd}$ films on Si(111) , Al(111)/Si(111) and $\text{Ta}_2\text{O}_5/\text{SiO}_2$ Bragg reflectors by co-evaporation of CaF_2 and NdF_3 . The PL spectra from these films show emission lines at wavelengths similar to those of bulk $\text{CaF}_2\text{:Nd}$, but the films show higher quenching concentration and less Nd aggregation problem. While the PL spectra from the films on the different substrates display similar emission pattern, the PL intensity increases significantly as the substrate reflectivity increases. Post-annealing $\text{CaF}_2\text{:Nd/Si(111)}$ at 700°C changes the emission pattern significantly. We also found that the PL efficiency is insensitive to the crystalline quality of

the films. The strong emission intensity of the films and the possibility of fabricating electroluminescence devices from these high doping-concentration films make them attractive for optical and optoelectronics applications. Since the strong emission can be obtained from polycrystalline films, they can be used for Si-based or polymer-based circuits without the restraint of epitaxial growth processes.

ACKNOWLEDGMENTS

The authors are indebted to M. Howell, Q. Montague and D. Smith for their technical assistance. Thanks also to T.-H. Lin, S.K. Fan, J.-Y. Yang and B. E. Gnade for many helpful discussions.

REFERENCES

1. L. J. Schowalter and R.W. Fathauer, *CRC Critical Reviews in Solid State and Materials Sciences*, **15**, 367 (1989).
2. C.-C. Cho, H.-Y. Liu, B.E. Gnade, T.S. Kim and Y. Nishioka, *J. Vac. Sci. Technol. A* **10**, 769 (1992).
3. H.D. Müller, J. Schneider, H. Luth and R. Strumpler, *Appl. Phys. Lett.* **57**, 2422 (1990).
4. L. E. Bausá, R. Legros and A. Muñoz-Yagüe, *Appl. Phys. Lett.* **59**, 152 (1991).
5. L. E. Bausá, C. Fontaine, E. Daran and A. Muñoz-Yagüe, *J. Appl. Phys.* **72**, 499 (1992).
6. C.-C. Cho, W. M. Duncan, T.-H. Lin and S.-K. Fan, *Appl. Phys. Lett.* **61**, 1757 (1992).
7. C.-C. Cho and H.-Y. Liu, *Mat. Res. Sym. Proc.* **221**, 87 (1991).
8. C.-C. Cho, H.-Y. Liu and H.-L. Tsai, *Appl. Phys. Lett.* **61**, 270 (1992).
9. Yu. K. Voron'ko, A. A. Kaminskii and V. V. Osiko, *Sov. Phys. JETP* **22**, 295 (1966).
10. C. A. Freeth and G. D. Jones, *J. Phys. C*, **15**, 6833 (1982).
11. A. A. Kaminskii, L.S. Kornienko and A.M. Prokhorov, *Sov. Phys. JETP* **21**, 318 (1965).
12. C.-C. Cho and W.M. Duncan, submitted to *Appl. Phys. Lett.*

MBE GROWTH OF RARE-EARTH DOPED FLUORIDE INSULATORS ON SEMICONDUCTORS FOR LASER APPLICATIONS

M. LUI, R.A. MCFARLANE, AND D. YAP*

*Hughes Research Laboratories, 3011 Malibu Canyon Road, Malibu, CA 90265.

ABSTRACT

With the recent success of using rare-earth doped fluoride crystals as high power visible upconversion lasers, we have explored the use of MBE grown fluoride layers for a possible waveguide laser. By confining the pumped light in a waveguide with dimensions on the order of a few micron, the pump power density will increase promoting higher efficiencies at room temperatures. Initially, we have grown planar waveguides of erbium doped ZnF_2 on MgF_2 substrates using molecular beam epitaxy and have formed channel waveguides by ion milling. By exciting individual channels with an 800 nm pump, we have generated strong upconversion fluorescence at 410 nm, 550 nm and 670 nm and at numerous weaker peaks. The fabrication techniques can be adapted to semiconductor substrates for making compact diode-pumped visible and infrared lasers. A number of fluoride materials that are useful as laser host crystals are lattice matched to GaAs (100) and GaAs (111) offering the possibility of integrating the channel waveguide laser with the semiconductor diode laser pump source. For example SrF_2 may be grown on GaAs (100) as a cladding layer followed by PbF_2 doped with a rare-earth ion. Also LaF_3 may be grown on GaAs (111) followed by CeF_3 doped with a rare-earth ion. Both PbF_2 and CeF_3 have low phonon energies and a higher index of refraction than their respective lattice matched cladding layers and should be capable of provide an attractive upconversion laser waveguide system. Our initial upconversion luminescence results on erbium doped PbF_2 on GaAs (100) using a intervening SrF_2 cladding layer are also reported.

INTRODUCTION

Laser operation at wavelengths shorter than the pumping wavelength is accomplished in a new class of laser called an "Upconversion Laser." The laser operates by combining the energy of two or more infrared pump photons to produce an excited state of an impurity ion in an appropriate laser host material that is greater than the energy of one pump photon alone. This can occur by several excitation pathways. The most obvious route is a stepwise absorption of several pump photons in a system that has adequately long lifetimes at intermediate energy level positions and favorable level spacings and decay characteristics. This sequential absorption enables a stepwise excitation process to higher ionic energy levels, and is typically realized in fiber systems where doping levels are low (0.1% or less). In bulk crystals having rare earth doping levels of 1 to 10%, energy contained in two or more ions, each having absorbed one pump photon, can be accumulated by a single ion through energy exchange processes that are able to efficiently excite the ion to an energy level well above the single pump photon excitation level.

Initial upconversion lasers operated at cryogenic temperatures, typically 10-100K.¹⁻⁷ The necessity of low temperatures arises from the fact that the population decays from the desired upper laser level via nonradiative mechanism associated with crystal lattice vibrations. This loss is reduced at lower operating temperatures because of the reduction of the phonon density in the host crystal. Room temperature operation of these lasers using bulk materials has been reported for one specific crystal host⁸ but for the most part, visible room temperature upconversion lasers have been operated using rare earth doped ZBLAN fluorozirconate single mode fibers.⁹⁻¹² The combination of lower phonon energy glass and small laser mode cross section, which leads to very high pump power density, enables modest pumping powers to overcome the deleterious effects of the nonradiative decay processes that tend to reduce the population inversion available for establishing the needed laser gain.

It is this same combination of high pump power density and low phonon energy that may be exploited in MBE grown planar and channel waveguides investigated in this work. We believe that the use of planar and channel waveguides can reduce the pump power threshold to the 100 milliwatt level for visible upconversion lasers and to the milliwatt level for IR lasers (downconversion) using waveguide channels. We have produced channels using ion milling techniques and have demonstrated confined propagation of the pump source and a clear guiding of the visible fluorescence resulting from the upconversion in erbium.¹³ While some reports by European workers have appeared on infrared lasers using channels in LPE grown Nd:YAG,^{14,15} and in erbium-titanium diffused LiNbO₃ waveguides,^{16,17} the dimension control of guide thickness using MBE is superior and certainly can achieve much better control of dopant distribution than is possible using the Er:Ti co-diffusion methods. The ion milling techniques permit single guides or linear arrays to be fabricated on a given GaAs wafer and even permit arrays of differing dopants to produce multiple color laser output.

MOLECULAR BEAM EPITAXY OF FLUORIDE SYSTEMS

The replacement of silica and fluorozirconate glass fiber waveguide materials by MBE grown laser host crystals demands the preparation of doped halide hosts in planar structures that can, if desired be fabricated into channel guides, either singly or in multiple parallel arrays. To date only limited work on achieving this has been reported. Published reports by a group in France¹⁸ and by TI researchers¹⁹ discuss low temperature photoluminescence measurements (10K) made on Nd doped homoepitaxial grown layers of CaF₂ on CaF₂ and Si substrates. Our own work is, to our knowledge the first report of room temperature observation of upconversion luminescence in any MBE prepared fluoride system, particularly for materials grown on a semiconductor substrate. The potential for integrating visible and near IR lasers on GaAs substrates can be seen from the following table that considers the lattice parameters of the materials in question.

Table I
Substrate and MBE Cladding/Active Layers for Channel Waveguide Lasers.

Materials approximately lattice matched to GaAs(111) and Silicon(111)

	<u>Mismatch GaAs</u>	<u>Mismatch Si</u>
LaF ₃	3.6%	8.0%
CeF ₃	2.8%	7.0%
NdF ₃	1.5%	5.7%

Materials approximately lattice matched to GaAs(100, a=5.65Å),
Si(100, a=5.43Å), or InP(100, a=5.87Å)

CaF ₂	a=5.46Å
BaF ₂	a=6.20Å
SrF ₂	a=5.80Å
PbF ₂	a=5.93Å

The alloyed system Ca_xSr_{1-x}F₂ may be precisely lattice matched to GaAs(100) by selecting the proper stoichiometry of the mixed fluorides.

EXPERIMENTAL RESULTS AND DISCUSSION

The first waveguide we have prepared by MBE employed Erbium doped ZnF₂ deposited on MgF₂. The ZnF₂/MgF₂ material system was chosen because of our experience in growing it in earlier work by Lui et al²⁰ for magnetic studies of antiferromagnetic films. The refractive index of MgF₂ is less than that of ZnF₂ making it possible to confine light in the planar ZnF₂ waveguide. Lederman²¹ has shown that by using a high index coupling prism, it is possible to launch laser light into these ZnF₂ films.

The (001) MgF_2 substrates were obtained from Optovac, Inc.²² and were carefully aligned with the *c*-axis perpendicular to the substrate surface using an X-ray Laue Camera. The substrates were mechanically polished using diamond paste on a custom polishing system. A combined mechanical/chemical etching technique was used as the last polishing step in order to remove damage left by the mechanical polishing steps. A 20% HCl solution was used in conjunction with a custom etch polishing system. A final free etch in 20% HCl was used before loading the substrate into the high vacuum MBE growth chamber. The necessity for such an elaborate polishing scheme for preparing high quality layers was established during capacitance studies on FeF_2 epitaxial films.²³

The $\text{ZnF}_2\text{:Er}$ epitaxial films were grown in an MBE chamber originally setup to grow transition metal difluorides for magnetic studies.²⁴ This system was relatively primitive, lacking many of the in-situ characterization features and sophisticated control setup found on a typical III-V semiconductor system. Growth must take place in an UHV ($<10^{-8}$ Torr) chamber in order to place the process in the molecular regime and more importantly to allow oxide removal of the substrate prior to growth. The oxide layer is removed by heating the substrate in an oxygen free environment thereby vaporizing any residual oxide on the surface. A cryoshroud is installed in the chamber in order to reduce outgassing during any of the heating processes. High quality source material is essential for epitaxial film growth. The source materials were purified by sintering in an HF environment, to reduce any impurities present in the starting fluoride materials. The source materials were vaporized during growth from a heated carbon crucible which had been previously pyrolyzed and fired under vacuum to a temperature higher than the growth conditions.

Optimum growth conditions were established during previous magnetic studies.²⁵ The MgF_2 substrate oxide layer was removed by heating to 550°C for 20 minutes. A $1.0\ \mu\text{m}$ MgF_2 buffer layer was grown with the substrate at 350°C in order to improve surface quality for the final epitaxial layer. A $1.0\ \mu\text{m}$ $\text{ZnF}_2\text{:Er}$ layer was grown using a ZnF_2 and ErF_3 source simultaneously with the substrate held at 300°C . Based on deposition measurements using a quartz crystal oscillator, the erbium doping is estimated to be approximately 20%.

To configure the material for laser experiments, it was cut into $2 \times 3\ \text{mm}$ rectangular samples with the $2\ \text{mm}$ face polished to an optical finish. This facilitates end pumping of the planar waveguide using a microscope objective to introduce the pump beam. To further confine the pump light along the planar dimension, and increase the pump power density, the $\text{ZnF}_2\text{:Er}$ film was channelized using ion milling into a series of $0.5\text{--}20\ \mu\text{m}$ wide waveguide structures separated by $50\ \mu\text{m}$. As an etch mask, a $2\ \mu\text{m}$ thick layer of photolithographically patterned resist was applied to the planar structure in a rib pattern. Waveguide channels having widths between $0.5\ \mu\text{m}$ and $20\ \mu\text{m}$ were formed by etching with an Ar ion beam incident perpendicular to the sample surface and having an energy of $500\ \text{eV}$ with a beam current of $100\ \text{mA}$. Waveguides were etched through the ZnF_2 layer to a total height of $1.3\ \mu\text{m}$.

The pump was coupled to individual channel waveguides using the microscope objective and a sharp line of visible upconversion fluorescence was seen along the driven channel, confirming pump confinement to the selected channel. The upconversion emission spectrum for the channelized waveguide structure pumped at $800\ \text{nm}$, is shown in Fig. 1.

The potential for visible and UV laser operation can be seen from these measurements. The earlier reports on IR laser operation of these types of structures suggests that even lower pump thresholds could be found for IR laser operation of the MBE channels. Waveguiding of the $800\ \text{nm}$ pump results in upconversion fluorescence at $410\ \text{nm}$, $550\ \text{nm}$, and $670\ \text{nm}$. The relevant energy levels of the Er^{3+} ion are shown in Fig. 2. Pairs of $^4\text{I}_{9/2}$ ions that are directly excited by the pump, share their energy to produce a population in the $^2\text{H}_{9/2}$ level. These are the source of the observed $410\ \text{nm}$ emission. Nonradiative decay to $^4\text{F}_{5/2}$, $^2\text{H}_{11/2}$, $^4\text{S}_{3/2}$ and $^4\text{F}_{9/2}$ ions leads to spontaneous emission at $455\ \text{nm}$, $530\ \text{nm}$, $550\ \text{nm}$ and $670\ \text{nm}$. Laser emission is expected to be possible at room temperature at wavelengths of $550\ \text{nm}$ and $670\ \text{nm}$ with the $^4\text{S}_{3/2}$ level and the $^4\text{F}_{9/2}$ level as the upper laser levels respectively, as reported in the bulk crystal systems.³ Other transitions, particularly at $410\ \text{nm}$ and $560\ \text{nm}$, demonstrate significant spontaneous emission that originates in the $^4\text{H}_{9/2}$ level, and are also possible laser candidates. The latter is particularly interesting since the laser would terminate on the $^4\text{I}_{13/2}$ level, not otherwise populated at room temperature. Emission near $380\ \text{nm}$ from the $^4\text{G}_{11/2}$ level in the vicinity of $26500\ \text{cm}^{-1}$ shows the presence of higher order energy pooling mechanisms operative for $800\ \text{nm}$ excitation.

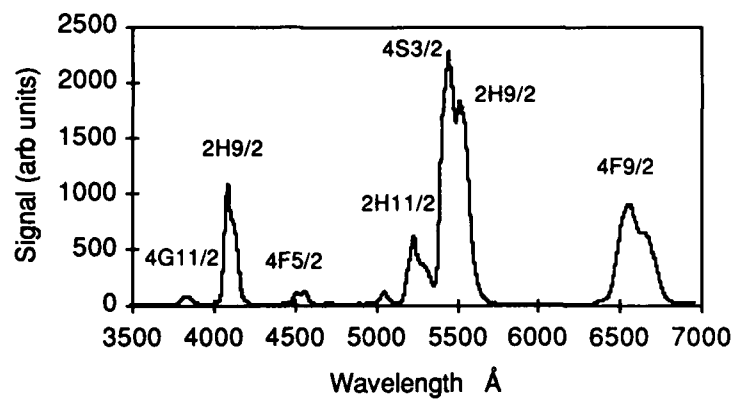


Figure 1. Upconversion spectrum of 20% Er:ZnF₂ MBE channel waveguides. Upper states of emission systems are identified.

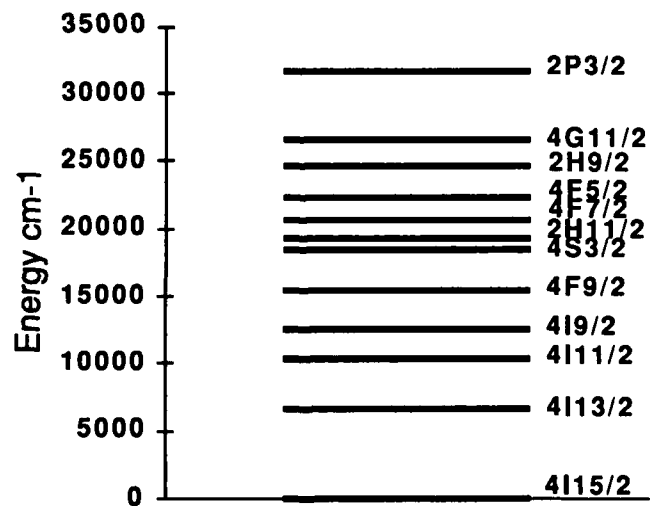


Figure 2. Energy levels of the erbium ion.

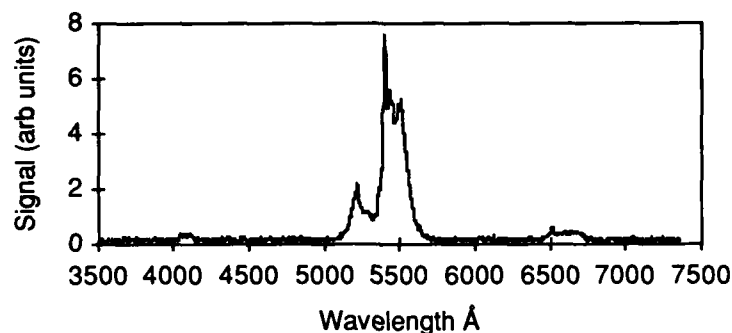


Figure 3. Upconversion spectrum of $\text{PbF}_2\text{:Er 1\%}$ on CaSrF_2 cladding on GaAs (100). Excitation at 972 nm.

The first rare-earth doped fluoride grown on GaAs (100) were PbF_2 doped with 1-5% erbium with an intervening SrF_2 cladding layer. Both of these fluoride materials are approximately lattice matched to GaAs as can be seen in Table 1. The SrF_2 cladding layer provides a lower index material to allowing guiding in the PbF_2 layer. A $\text{Ca}_{0.44}\text{Sr}_{0.56}\text{F}_2$ cladding layer was also used to allow a precise lattice match to the GaAs substrate. The epitaxial fluoride films were grown in a custom solid source MBE system. The system is capable of handling up to four effusion cells and has insitu RHEED analysis. The film thicknesses are determined using a laser reflection technique.

Photolithographic techniques were used to make a series of channel waveguides in these layers and we find that it is possible to cleave the GaAs wafer and achieve a very good surface at the waveguide end as the interface propagates through the grown layers. This result is a particularly significant one, as all other planar and channel structures that have been reported, grown for example using LPE (as for Nd:YAG) have required a particularly difficult polishing operation in order to attain a smooth finished guide end through which the pump power can be introduced and mirrors fastened for laser operation. This system grown on GaAs shows upconversion luminescence when pumped at 800 nm. or at 970 nm. The spectrum, shown in Fig. 3, is similar to that found for the ZnF_2 . The sharp luminescence features in the PbF_2 are particularly encouraging suggesting that inhomogeneous broadening is not too significant. A similar spectrum is observed for 800 nm excitation.

CONCLUSION

This work opens up the possibility of a compact room temperature visible laser source excited by semiconductor diode laser pumps. Other materials are available that provide a site for the rare earth dopant that is substitutional and does not require the charge compensation of the ZnF_2 and PbF_2 systems. A particularly attractive combination of a cladding and active layer pair is LaF_3 and CeF_3 . Both are closely lattice matched to GaAs(111) and grow in a hexagonal structure on this substrate. In addition, over the spectral range of 0.4 to 1.6 microns, there is a refractive index differential of 0.02 which provides for optical confinement in a rare earth doped CeF_3 waveguide. To exploit the efficient transfer of energy that occurs between Ytterbium and other rare earths, and to utilize the broad absorption band of the Yb^{3+} ion in the 970 nm region that is accessible with semiconductor diode pump lasers, the fluoride host may be co-dope with Yb and a rare-earth ion. Since it is also possible to dope the fluoride epitaxial layers with transition metals such as Cr, Ti, Mn, Fe, V, Co or Ni, there is the

possibility of constructing tunable MBE waveguide lasers or employing transition metal donor ions that have broad pumping bands to efficiently transfer energy to rare earth ions such as Nd and Er as has been reported for optically pumped bulk crystals.

REFERENCES

1. A.J. Silversmith, W. Lenth, and R.M. Macfarlane, *Appl. Phys. Lett.* **51**, 1977 (1987).
2. R.M. Macfarlane, F. Fong, A.J. Silversmith, and W. Lenth, *Appl. Phys. Lett.* **52**, 1300 (1988).
3. R.A. McFarlane, *Appl. Phys. Lett.* **54**, 2301 (1989).
4. D. C. Nguyen, G.E. Faulkner and M. Dulick, *Applied Optics* **28**, 3553 (1989).
5. R.A. McFarlane, *Optics Lett.* **16**, 1397 (1991).
6. T. Hebert, R. Wannemacher, R.M. Macfarlane, and W. Lenth, *Appl. Phys. Lett.* **60**, 2592 (1992).
7. P. Xie and S.C. Rand, *Optics Lett.* **17**, 1198 (1992).
8. R. J. Thrash, *Compact Blue-Green Laser Technical Digest* **6**, 17 (1992).
9. T.J. Whitley, C.A. Millar, R. Wyatt, M.C. Brierley, and D. Szebesta, *Electron. Lett.* **27**, 1785 (1991).
10. S.G. Grubb, K.W. Bennett, R.S. Cannon and W.F. Humer, *Electron. Lett.* **28**, 1243).
11. J.Y. Allain, M. Monerie and H. Poignant, *Electron. Lett.* **26**, 261 (1990).
12. R. G. Smart, D.C. Hanna, A.C. Tropper, S.T. Davey, S.F. Carter and D. Szebesta, *Electron. Lett.* **27**, 1307 (1991).
13. M. Lui, R.A. McFarlane and D. Yap, *Electron. Lett.* **29**, 172 (1993).
14. I. Chartier, B. Ferrand, D. Pelenc, S.J. Field, D.C. Hanna, A.C. Large, D.P. Shepherd, A.C. Tropper, *Optics Lett.* **17**, 810 (1992).
15. S.J. Field, D.C. Hanna, A.C. Large, D.P. Shepherd, A.C. Tropper, P.J. Chandler, P.D. Townsend and L. Zhang, *Electron. Lett.* **27**, 2375 (1991).
16. S.J. Field, D.C. Hanna, A.C. Large, D.P. Shepherd, A.C. Tropper, P.J. Chandler, P.D. Townsend and L. Zhang, *Optics Lett.* **17**, 52 (1992).
17. R. Brinkmann, W. Sohle and H. Suche, *Electron. Lett.* **27**, 415 (1991).
18. L.E. Bausa, R. Legros, and A. Munoz-Yague, *Appl. Phys. Lett.* **59**, 152 (1991).
19. C.C. Cho, W.M. Duncan, T.H. Lin, and S.K. Fan, *Appl. Phys. Lett.* **61**, 1757 (1992).
20. M. Lui, C.A. Ramos, A.R. King, and V. Jaccarino, *J. Appl. Phys.* **67**, 5518 (1990).
21. D. Lederman and A. Nikroo (to be published).
22. Optovac, Inc., North Brookfield, MA 01535.
23. M. Lui, A.R. King, V. Jaccarino, and G.L. Snider, *Phys. Rev.* **B40**, 4898 (1989).
24. M. Lui, thesis (unpublished), University of California, Santa Barbara, 1989.
25. M. Lui, A.R. King, V. Jaccarino, R.F.C. Farrow, and S.S.P. Parkins, *Mat. Res. Soc. Symp. Proc.* **187**, 267 (1990).

ERBIUM DOPED GALLIUM ARSENIDE A SELF-ORGANISING LOW DIMENSIONAL SYSTEM

A.R. PEAKER*, H.EFEOGLU*, J.M. LANGER**, A.C. WRIGHT***, I. POOLE* AND
K.E. SINGER*

* Centre for Electronic Materials and Electrical Engineering & Electronics Department,
UMIST, Manchester, M60 1QD, England

** Institute of Physics, Polish Academy of Science, Al Lotnikow 32/46, Warsaw 02668,
Poland

***Advanced Materials Laboratory, North East Wales Institute, Connah's Quay, Wales

ABSTRACT

The growth of erbium doped gallium arsenide by MBE at normal substrate temperatures ($\sim 580^\circ\text{C}$) is constrained by a solubility limit of $8 \times 10^{17} \text{ cm}^{-3}$. This is much less than is desirable for optical emitters using the forbidden $4f$ transitions of Er^{3+} to produce radiation at $1.54\mu\text{m}$. We have developed an MBE technique where it is possible to produce spherical mesoscopic precipitates containing erbium as a matrix element within the gallium arsenide. Structural and analytical studies indicate that the precipitate is cubic (rock salt) erbium arsenide. The physical size of the precipitates is self limiting as a result of surface migration occurring during MBE growth. By adjusting the growth conditions it is possible to produce an array of uniform erbium arsenide quantum dots of a size chosen from the range $10\text{-}20\text{\AA}$. The dot density can be varied by changing the erbium flux.

INTRODUCTION

Semiconductors doped with rare earths can provide temperature insensitive luminescence with narrow, almost atomic-like, linewidths. This is because the luminescence derives from the internal f shell transitions which are well screened from the matrix lattice. As a result the emission is almost host independent. Erbium is of particular interest because it has a characteristic emission at $1.54\mu\text{m}$ which is near to the minimum absorption window of silica-based optical fibres. A wide variety of experimental techniques, including liquid phase epitaxy (LPE)¹, ion implantation², metal organic chemical vapour deposition (MOCVD)³ and molecular beam epitaxy (MBE)^{4,5}, have been employed to incorporate erbium into the binary semiconductor gallium arsenide. For the latter technique, optimum growth conditions and erbium concentrations for maximum luminescence efficiency have been deduced⁴, but few structural studies have been undertaken.

Using MBE we have grown and undertaken detailed structural characterisation of gallium arsenide doped with erbium in the range $4 \times 10^{16} \text{ cm}^{-3}$ to $2 \times 10^{20} \text{ cm}^{-3}$. Secondary ion mass spectroscopy (SIMS) has been used to study the concentration of erbium incorporated into gallium arsenide as a function of both substrate and erbium cell temperature. Transmission electron microscopy (TEM) has been used to determine the concentration, size and chemical composition of erbium-related micro-precipitates present in the gallium arsenide doped with erbium at concentrations beyond the solubility limit.

EXPERIMENTAL

The samples were grown in a RIBER 2300 MBE system employing conventional thermal effusion cells. Elemental erbium of 4N purity obtained from Rare Earth Products Ltd, Widnes, England was used. The samples were grown on (100) orientated gallium arsenide substrates. Three types of substrate were used to enable a range of electrical measurements to be undertaken, these were: semi-insulating, Te-doped n^+ or Zn-doped p^+ . Prior to growth the substrates were degreased, etched then mounted with indium to the substrate holders. An initial 30 minute outgassing at 350°C was performed before the samples were transferred to the growth chamber where the oxide was removed by heating to 600°C. The samples were further outgassed for 5 minutes at 620°C (as determined by an optical pyrometer) before the substrate temperature was reduced to that required for growth.

In order to study the incorporation of erbium into gallium arsenide a number of multilayer structures were grown in which one growth parameter was varied while the others were kept constant. Non erbium-doped layers were grown between the erbium containing regions to allow clear delineation of the different erbium-doped layers and to indicate whether any substantial diffusion of the dopant was occurring. A typical sample structure is shown as Figure 1, in general each region was made approximately 1 μm wide. Thick, uniformly erbium-doped layers were also grown to permit the detailed optical and electrical assessment of the material. This is reported elsewhere⁶.

Compositional analysis of the layers by dynamic secondary ion mass spectroscopy (SIMS) was performed by Cascade Scientific Ltd, Uxbridge, England using a 3-10 keV O_2^+ primary beam with a raster size of 175 μm^2 , the secondary ion count from the central 60 μm diameter area being analyzed. In order to calibrate accurately the erbium concentrations, gallium arsenide ion implanted with erbium were produced as reference samples by two independent implantation systems; one at Surrey University using $10^{15} \text{ atom cm}^{-2}$ of $^{167}\text{Er}^{++}$ at 250keV and one at Maier Institute where $10^{14} \text{ atoms cm}^{-2}$ of $^{168}\text{Er}^+$ at 350keV were employed. These were profiled under the same SIMS conditions as the grown layers and provided an erbium calibration of the MBE grown samples accurate to $\pm 20\%$. Calibration of the depth axis of the profile was achieved by measurement of the total crater depths on a Tensor Alpha-step 200RD profileometer.

Microstructural characterisation of the samples was performed using a Philips EM430 transmission electron microscope. Cross-sectional specimens of selected samples were prepared using conventional mechanical polishing down to 25 μm thickness. This was followed by ion milling at 13.5° with 5 keV argon ions and then with iodine ions to improve sample quality by the reduction of ion damage. Several different beam conditions were employed for viewing the TEM specimens. It was found that bright field imaging was only able to reveal the presence of the more heavily erbium-doped layers when using the (220) and (004) reflections. Better contrast was obtained using these reflections in the dark field mode. The best

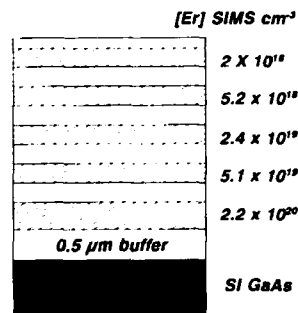


Figure 1. Structure of sample #2054 which is typical of the MBE multilayers grown for this investigation

contrast, however, was achieved by using the (002) reflection in the centred dark field mode.

RESULTS AND DISCUSSION

Erbium Doping Processes

Figure 2 shows a SIMS depth profile of the erbium concentration of the multilayered gallium arsenide sample #2054, the same sample whose structure is shown schematically in figure 1. The sample was grown at a constant substrate temperature of 580°C as determined by an optical pyrometer. This growth temperature has previously been reported to be the optimum T_{sub} for strong erbium related photoluminescence⁴. During growth the erbium cell temperature was reduced in an incremental manner from 950°C for the erbium-doped layer nearest the substrate down to 780°C for the erbium-doped layer nearest to the surface.

The undulation in the highest concentration region in the sample shown in Figure 2 at ~5µm from the surface was due to an interruption of the erbium flux while the V/III ratio was increased from 2.5:1 to approximately 5:1 by an intentional increase in the arsenic flux. Using RHEED, the growth conditions were adjusted initially to be arsenic stable without erbium. When the erbium flux, at a level necessary to produce an erbium concentration of $2 \times 10^{20} \text{ cm}^{-3}$, was initiated, the RHEED pattern degraded consistent with an arsenic deficiency. Although we have not, as yet, carried out a detailed investigation, there is no evidence from our measurements for a substantial dependence of erbium incorporation on arsenic to gallium ratio. We have grown layers over the range of arsenic to gallium ratios from just arsenic stable to four times arsenic stable (measured by RHEED).

There is no evidence for large scale, long range diffusion of erbium into the undoped gallium arsenide spacer layers at this growth temperature, the apparent presence of an erbium signal on the substrate side of the step profiles in some of the layers is due to SIMS broadening in cases where a high primary ion beam energy was used.

There are, however, some interesting features in the detailed SIMS profile which cannot be explained by instrumental factors. In other SIMS profiles, there is evidence of non-uniformity of the erbium concentration in the layer. This takes two forms, the first being a gradual decrease in the magnitude of the erbium concentration during the growth of the 0.5µm region, the last grown (near surface) part of the region showing a decrease of up to 30% in erbium concentration. An example of the effect can be seen in the region

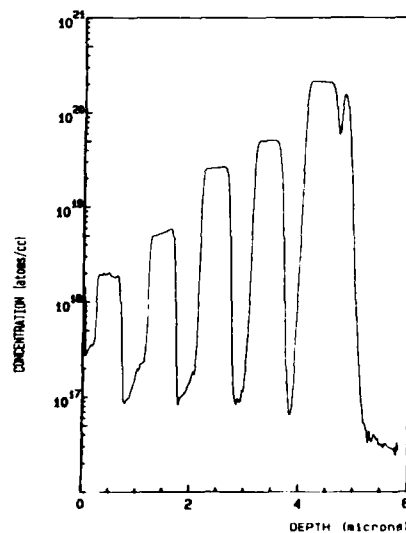


Figure 2. SIMS depth profile of the sample shown in figure 1 using O_2^+ as the primary bombarding species at 10keV

between 1.3 and 1.8 μm in Figure 1. The other aspect of the non-uniformity (not evidenced in the example shown) is a pronounced rounding of the SIMS erbium profile of the last grown edge of the erbium doped layers.

We do not believe these effects are in any way artifacts of the SIMS measurement because they do not change with measurement conditions but are different in different layers indicating some transient (on a time scale of minutes) in the erbium incorporation. We do not attribute it to diffusion because of the asymmetry of the first and last grown edges of the erbium bearing regions. Changing the SIMS primary ion energy does produce some variation in the well known 'SIMS broadening' but does not change the shape of the peaks. Measurements on some samples were performed with a reduced primary ion beam energy of 3 keV which has resulted in a reduction of the SIMS broadening evident in the profile edge nearest the substrate but only at a level one and a half orders of magnitude in concentration below the peak. Repeating the measurement with an 8 keV beam increased the broadening effect but did not alter the shape of the individual erbium-doped layer profiles under discussion.

To study erbium incorporation in MBE gallium arsenide as a function of substrate temperature, the erbium cell was maintained at 880°C during the growth of an erbium-doped multi-layer structure while T_{sub} was varied incrementally between 540°C for the layer nearest to the substrate up to 630°C for the uppermost erbium-doped layer. There is no measurable change in the level of erbium incorporation (measured at the peak of the profile) with increasing T_{sub} in the range 540 - 630°C.

It is also evident from this study that at substrate temperatures $\geq 605^\circ\text{C}$ that the non-uniformity in erbium concentration referred to in the previous paragraph is much reduced compared to layers grown at 580°C also, in general, the non-uniformity increases as the temperature is reduced below 580°C although the results we obtain are not wholly consistent possibly due to different behaviour under different V/III ratios. Results which are possibly related to these effects has been reported by Galtier et al.⁵

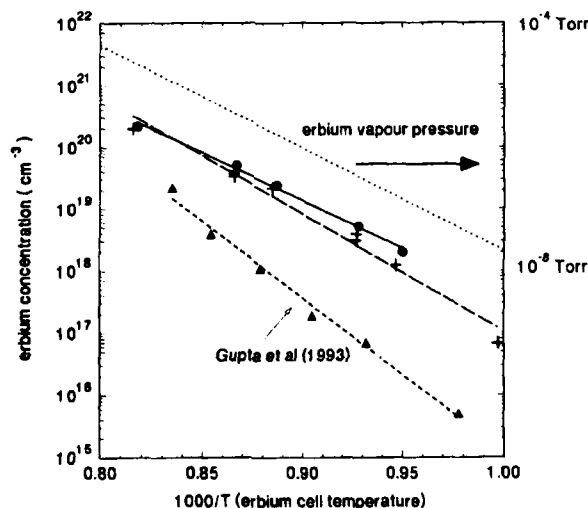


Figure 3 Summary of SIMS calibrations undertaken by us in 1990(+) and 1993 (●) compared with data from ref 8 (+) and the erbium vapour pressure

in erbium-doped gallium arsenide quantum wells grown by MBE.

Another multilayer sample was co-doped with silicon at 10^{17} cm^{-3} . The SIMS profile, shows that the intentionally introduced silicon concentration was constant through the top seven epilayers (erbium concentrations from zero to $4 \times 10^{19} \text{ cm}^{-3}$) clearly demonstrating that the presence of erbium as a co-dopant does not affect the total silicon incorporation. Conversely, from the excellent agreement in the erbium concentration versus the erbium cell temperature data between this layer and the non-silicon doped multilayer structures grown before and after this sample shows that the incorporation of erbium at the growing surface is not affected by the presence of silicon in these concentrations.

In order to calibrate the erbium concentrations in the layers against the erbium cell temperatures from this data the total number of erbium atoms in each region was used in preference to an estimated layer concentration at some arbitrary point. When this is done the erbium cell calibration data shown in Figure 3 is obtained. Two of our data sets are shown, one which derives from work done in 1990 and the other from our most recent measurements taken in 1993. Least mean square fits are shown for the separate data sets. The variation in slope is due primarily to the low concentration point which was taken near the limit of measurement of the SIMS system. The published vapour pressure data⁷ is shown for comparison and the slope is almost identical to that derived from the high concentration MBE data points.

Also shown in figure 3 are data from Gupta et al.⁸ The magnitude of the erbium concentration in the gallium arsenide for a given erbium source temperature is between one and two orders less than our results. In addition the slope of the relationship is distinctly different to both the vapour pressure line and our results. One factor which does appear to be different is the V/III ratio. Gupta et al. state they used a V/III flux ratio of ~ 30 , our ratios based on RHEED are ~ 4 for the 1993 work and less for the 1990 calibration. The discrepancy with Gupta's results is obviously an issue which requires further investigation.

From these average concentration data, for erbium concentrations up to $2 \times 10^{20} \text{ cm}^{-3}$, there is no evidence for an upper limit to incorporation in MBE grown gallium arsenide.

Structural Properties

Figure 4 is a cross sectional TEM micrograph of a region of a multilayered gallium arsenide sample obtained using the (002) reflection in the centred dark field mode. This picture and high resolution lattice imaging at higher magnifications shows very clearly that these layers are not homogeneous but consist of small precipitates. These precipitates were observed in a layer where the average erbium concentration was $1.2 \times 10^{18} \text{ cm}^{-3}$ and in all the erbium-doped layers more heavily doped than this. No precipitates were observed in the layers which contained less erbium. The concentration of the precipitates increased with the erbium doping level. Extrapolation of the precipitate volume to zero (measured by high resolution and convergent beam TEM) gives an erbium solubility in gallium arsenide at 580°C of $8 \times 10^{17} \text{ cm}^{-3}$.

A sequence of layers was grown with a constant erbium concentration but at differing substrate temperatures. Erbium-doped layers grown at temperatures $\leq 605^\circ\text{C}$ exhibit uniform precipitation within each layer. However, an erbium containing layer grown at 630°C is shown in figure 5. The size of the precipitates is greater than in the lower temperature layers and the particles are typically elongated as distinct from the near spherical form in the other layers as shown in the dark field (002) beam image of Figure 4. Dislocations can also be observed and probably originate as a result of

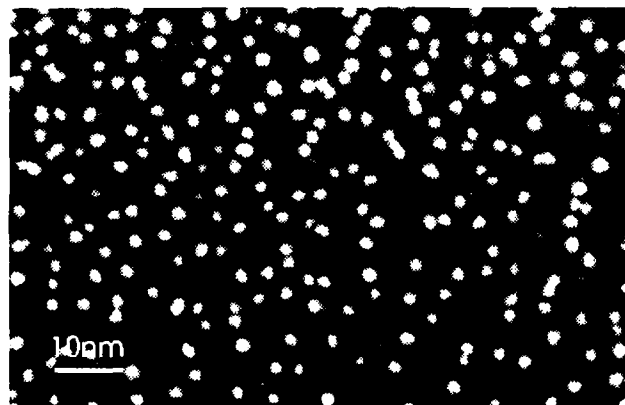


Figure 4 A TEM micrograph of a sample grown with a substrate temperature of 580°C. The erbium concentration is $2 \times 10^{20} \text{ cm}^{-3}$

misfit between the particles and the gallium arsenide matrix. This will only occur when the precipitate exceeds a critical size.

When using the (002) beam, the precipitates were observed as bright spots indicating that their (002) structure factor is greater than that of the surrounding gallium arsenide lattice. By imaging with the (111) beam, the precipitates can be seen as dark spots on a bright background so displaying reversed contrast. These observations are consistent with the precipitates having rocksalt structure. Erbium arsenide has the rocksalt structure, $a_0 = 5.732 \text{ \AA}$, and thus is easily accommodated as a precipitate in the gallium arsenide matrix, $a_0 = 5.653 \text{ \AA}$, when the particle sizes are as small as is seen here. The structure factors for the (002) and (111) reflections in erbium arsenide are large and small respectively, being the reverse of the gallium arsenide matrix, and are thus expected to give the observed contrast when used to

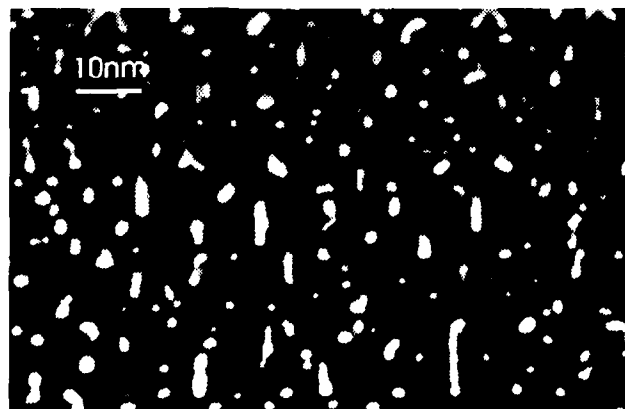


Figure 5 Micrograph of a sample grown with a substrate temperature of 630°C and an erbium concentration of $3 \times 10^{19} \text{ cm}^{-3}$

form an image. These observations are consistent with the chemical composition of the precipitates being erbium arsenide.

Other possible structures are metallic erbium or some other erbium arsenide. Metallic erbium is hexagonal and would be expected to form platelets, probably on {111} planes as observed in the case of ErSi_2 in heavily erbium doped silicon grown by MBE⁹. The fact that the particles observed here are clearly spheroidal seems to rule this out. Other possible arsenides are Er_3As_4 which has the Th_3P_4 structure and a lattice constant of 8.5Å. This would generate considerable strain in the surrounding gallium arsenide matrix, even with the very small particle sizes observed here. Thus the more open structure of Er_3As_4 would tend to be unstable with respect to the more closely packed rocksalt erbium arsenide structure which has a smaller misfit to the gallium arsenide matrix. Therefore, these considerations rule out the possibility of the non-rocksalt structured erbium arsenides.

While microdiffraction, e.g. in STEM mode, could in principle be used to obtain diffraction patterns from the particles, in practice this is complicated by the fact that they are embedded in a gallium arsenide matrix which will tend to mask the expected intensity changes in the diffraction pattern. For similar reasons microanalysis by EDX spectroscopy will also be difficult. Double crystal X-ray measurements on the layer reveal a gradual broadening of the gallium arsenide diffraction peak with increasing erbium concentration for concentrations above $3 \times 10^{17} \text{ cm}^{-3}$. The measurements were done on erbium bearing layers 2.5µm thick which would contain, in total, an inadequate volume of ErAs to produce a measurable diffraction peak attributable to the 5.732Å rocksalt lattice.

By taking a large number of high magnification images of the precipitates in the various regions of the samples the average diameter per layer of these roughly spherical particles was determined. The particle sizes in sample #1788 are detailed in Figure 6. The erbium-doped layers were grown with a constant erbium flux but at different substrate temperatures. The average particle size was seen to increase with increasing substrate temperature. The largest precipitate diameter varies significantly from this relationship possibly due to the onset of dislocation in the grown layer.

It is very tempting to ascribe this overall behaviour to the traditional concept of bulk precipitation coarsening namely that a nucleus of a critical size occurs and then this grows by the short range diffusion of (in this case) erbium from the matrix or from the dissolution of smaller precipitates in the immediate vicinity. The conditions under which the experiments were done rule out such a mechanism. The sample #1788 was grown as a multilayer structure with the lowest temperature layer grown first. Consequently, the smallest precipitates were subjected to annealing at just as high a temperature as the larger precipitates and on average for a longer period of time. Therefore, it seems that the well established mechanism of precipitate coarsening or "Ostwald ripening" is not the dominant mechanism in this case.

If the relationship shown in figure 6 is examined as an Arrhenius plot, the lower temperature data (540-605°C) are characterised by a slope (activation energy) of 0.63eV. The concept of an activation energy needs careful consideration here because we are plotting the log of a diameter against the reciprocal temperature. For a bulk process the measure of diameter reduces the problem to a one dimensional system and so is therefore directly comparable with a diffusion activation energy if identical times are involved for each layer. However, it is much more likely in our case that the nucleation and maturation of the precipitates occurs at the growing surface. Here, the concept of an activation energy derived from the data of figure 6 is somewhat dubious. Our measure of size is the diameter but, unlike the bulk case, the mass flow at the surface is planar i.e. in two dimensions but growth is in three. Therefore a more

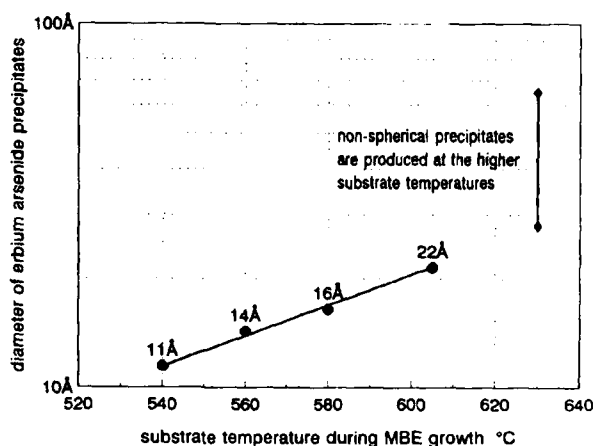


Figure 6 The dependence of precipitate size on substrate temperature during growth.

detailed knowledge of the processes involved is necessary before a realistic interpretation of the activation energy can be made. However, the apparent energy of 0.63 eV derived from our data is a sensible value for an activation energy of migration of a large atom on a gallium arsenide surface.

We have also grown multi-layer structures with a constant substrate temperature but changed the erbium flux to alter the erbium concentration by two orders of magnitude. The most heavily doped layer was grown first and therefore was held at the growth temperature for the longest period of time, 300 min. The combined effects of a greater supply of erbium and a substantial increase in the anneal time produced an increase in the precipitate size of < 20% a figure comparable with the scatter in the data. However, the precipitate density increased with erbium flux as would be expected.

From the preceding results it appears that any erbium in excess of the solubility limit is incorporated in the gallium arsenide lattice, presumably as erbium arsenide microprecipitates, which arise initially from statistical fluctuations in the surface erbium concentration. Upon reaching a critical nucleus size beyond which they cannot be dissolved by the host lattice, the precipitates continue to grow as a result of the surface migration of erbium. The size of these particles is a function of the substrate temperature which would be expected to dominate the mobility of the erbium species on the growing surface. This mechanism would predict a linear dependence on growth rate and a possible dependence on V/III ratio. We have not as yet been able to test this hypothesis.

The proposed incorporation mechanism explains the lack of saturation evident in the erbium cell calibration data shown in Figure 4. Erbium dopant atoms in excess of the solubility limit are preferentially incorporated in the lattice in the observed precipitates of ErAs and the similar lattice constants facilitate the incorporation as near spherical particles.

CONCLUSIONS

The incorporation of erbium in gallium arsenide grown by MBE and the subsequent structural characteristics of the material have been investigated by a combination of SIMS and TEM measurements. SIMS analysis revealed no incorporation dependence on substrate temperature in the range 540 - 630°C and no upper limit to erbium incorporation in gallium arsenide up to $2 \times 10^{20} \text{ cm}^{-3}$. A transient increase in erbium concentration towards the substrate was detected in epilayers grown at substrate temperatures $\leq 580^\circ\text{C}$ in some cases.

TEM measurements revealed a solubility limit of erbium in gallium arsenide of $8 \times 10^{17} \text{ cm}^{-3}$ at 580°C. Erbium concentrations in excess of this figure formed near spherical micro-precipitates whose structure, as observed by TEM, was consistent with their chemical composition being erbium arsenide. The size of these precipitates increased with substrate temperature with an activation energy of 0.63eV which we associate with erbium transport on the surface during growth. At $T_{\text{sub}} = 630^\circ\text{C}$ the morphology of the precipitates changed and larger elongated particles were observed in the erbium-bearing epilayers.

The presence of erbium arsenide micro-precipitates of controllable size in the mesoscopic range provides a novel method for the growth of quantum dots using the mechanism as a self-organising system.

ACKNOWLEDGEMENTS

We would like to acknowledge the valuable contributions to the SIMS measurements by S.D. Littlewood of Cascade Scientific Ltd, W. Gillin of Surrey University, and B. Clegg of Philips Research Laboratories, Redhill. We are also pleased to acknowledge useful discussions with M.R. Brozel and G. Lorimer of UMIST. This work has been supported by the UK Science and Engineering Research Council and by European ESPRIT research programme.

REFERENCES

- 1 F. Bantien, E. Bauser and J. Weber, *J. Appl. Phys.* **61** 2803 (1987)
- 2 P.B. Klein, F.G. Moore and H.B. Dietrich, *Appl. Phys. Lett.* **58** 502 (1991)
- 3 K. Uwai, H. Nakagome and K. Takahei, *J. Crystal Growth* **93** 583 (1988)
- 4 R.S. Smith, H.D. Muller, H. Ennen, P. Wennekers and M. Maier, *Appl. Phys. Lett.* **50** 49 (1987)
- 5 P. Galtier, M.N. Charasse, J. Chazelas, A.M. Huber, C. Grattepain, J. Siejka and J.P. Hirtz, *Inst. Phys. Conf. Ser.* **96** 61 (1988)
- 6 I. Poole, H. Efeoglu, K.E. Singer and A.R. Peaker to be published *J. Crystal Growth* 1993 (Proceedings of MBE-VII 1992)
- 7 *Selected Values of the Thermodynamic Properties of the Elements*, Ed. R. Hultgren (American Society for Metals, New York 1973) p.168.
- 8 S. Gupta, S. Sethi and P.K. Battacharya, *Appl. Phys. Lett.* **62** 1128 (1993)
- 9 H. Efeoglu, J.H. Evans, T.E. Jackman, B. Hamilton, D.C. Houghton, J.M. Langer, A.R. Peaker, D. Perovic, I. Poole, N. Ravel, P. Hemment and C.W. Chan, *Semicond. Sci Technol.* **8** 236 (1993)

Er-DOPED GaAs FOR HIGH SPEED PHOTOCONDUCTOR APPLICATIONS

S. Gupta, S. Sethi, P. K. Bhattacharya and S. Williamson
Solid State Electronics Laboratory, Department of Electrical Engineering and Computer
Science, University of Michigan, Ann Arbor, MI 48109-2122

ABSTRACT

The observation of 1.54 μm luminescence in erbium-doped-GaAs (GaAs:Er) and $\text{Al}_x\text{Ga}_{1-x}\text{As}$, has stimulated research efforts because of their potential application to light sources in optical communications. In this paper, we study a different aspect of the photoresponse behavior of this material. The dependence of the carrier lifetime on the doping concentration of Erbium is investigated in GaAs:Er grown by MBE. A reduction in the carrier lifetime down to ~ 1 ps is observed for the highest doping ($\sim 5 \times 10^{19} \text{ cm}^{-3}$) investigated. Together with the high-resistivity observed for the higher doping values, this material serves as a novel photoconductor material for high-speed optoelectronics.

GaAs:Er Growth by molecular-beam-epitaxy

In recent years, the successful incorporation of rare-earth elements in III-V compound semiconductors and the tailoring of their luminescence properties have lead to an interest in these material systems¹⁻⁴. The rare-earths can be incorporated in III-V semiconductors by a number of methods : ion-implantation, during liquid-phase-epitaxial (LPE) growth, and during molecular-beam-epitaxial (MBE) growth. Due to the large ionic radius of Er^{3+} (0.88 Å) compared to Ga^{3+} (0.62 Å), the solid-solubility limit of Er in GaAs is $\sim 10^{17} \text{ cm}^{-3}$. Hence the upper limit of Er-incorporation in an equilibrium growth process like LPE is near the above value. Ion-implantation at high doses leads to extensive damage to the crystal structure, and the post-implantation anneal require to electrically activate the implanted Er, would lead to segregation of the Er due to its low solid-solubility. On the other hand being primarily a reaction-kinetics controlled growth process, MBE allows a wide-range of rare-earth doping in III-V semiconductors.

For our study, 1- μm thick GaAs:Er epilayers were grown on (001) oriented SI-GaAs substrates. The substrate temperature was 600°C and the As/Ga flux ratio ~ 30 . The Er-source temperature was varied from 750°C to 950°C to cover the range of doping from 7×10^{16} to $5 \times 10^{19} \text{ cm}^{-3}$. This Er incorporation has been verified by secondary-ion-mass-spectroscopy (SIMS). A uniform doping profile throughout the epilayer is obtained. The source cell temperature versus the measured Er-concentration is plotted as shown in Fig.1. It is to be remembered that SIMS gives a measure of the total amount of chemical species present in the epilayer, and not the electrically or optically activated fraction responsible for the respective properties.

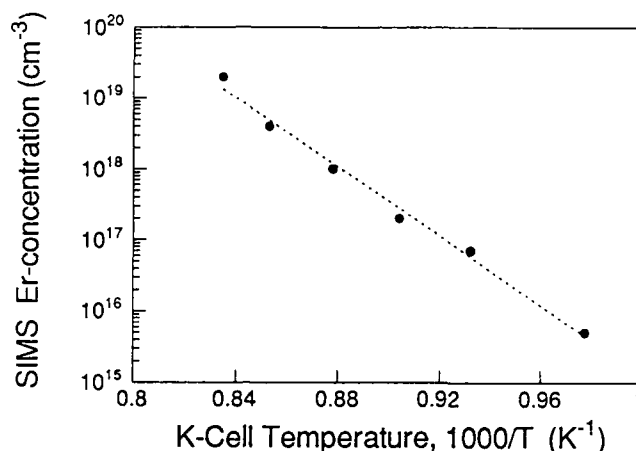


Fig.1 Erbium concentration in GaAs epilayers, measured by SIMS, as a function of the MBE source cell temperature.

Experiment

To study the dependence of the carrier lifetime on the doping concentration, the technique of time-resolved photoluminescence can be used. However it is observed that in the doping range studied, the GaAs band-edge luminescence disappears. Alternatively, one can measure the transient photoconductive current induced by a short pulse laser to determine the carrier lifetime⁵. Metal electrodes in a coplanar-strip configuration having a 30- μm width and 15- μm separation is deposited on these epilayers using 500Å/3000Å Ti/Au metallization, defined by photolithographic techniques. A 15- μm gap in one electrode serves as the photoconductor gap in the biased electrode, with the other electrode serving as the ground. This photoconductor gap is optically excited by ~100fs wide optical pulses from a colliding-pulse-mode-locked (CPM) dye laser operating at $\lambda = 620 \text{ nm}$, and a repetition rate of 100 MHz. The average power in the excitation beam is ~5 mW. The photogenerated carriers in the gap are swept by the applied bias across the gap, and part of them recombine in the gap, and the rest are collected by the other electrode, resulting in a current pulse and hence a voltage pulse travelling down the broadband transmission line structure. From the decay of the photoconductive transient, the carrier lifetime can be measured. To detect this electrical pulse the technique of external-electro-optic sampling is used⁶.

Results and Discussion

The measured photoconductive transient⁷ for an applied modulated-dc bias of 15 V across the 15- μm gap is shown in Fig.2, for the samples with a doping of $2 \times 10^{17} \text{ cm}^{-3}$ and $5 \times 10^{19} \text{ cm}^{-3}$.

Note the difference in the time scales. It is clearly observed that for the doping range investigated, the free carrier lifetime is in the picosecond domain, with a decrease in the lifetime observed with increased doping. From the $1/e$ decay time of the transient, the carrier lifetime can be plotted as a function of the doping concentration. This is shown in Fig.3 on a log-log plot. Note the linear curve obtained for the doping range investigated.

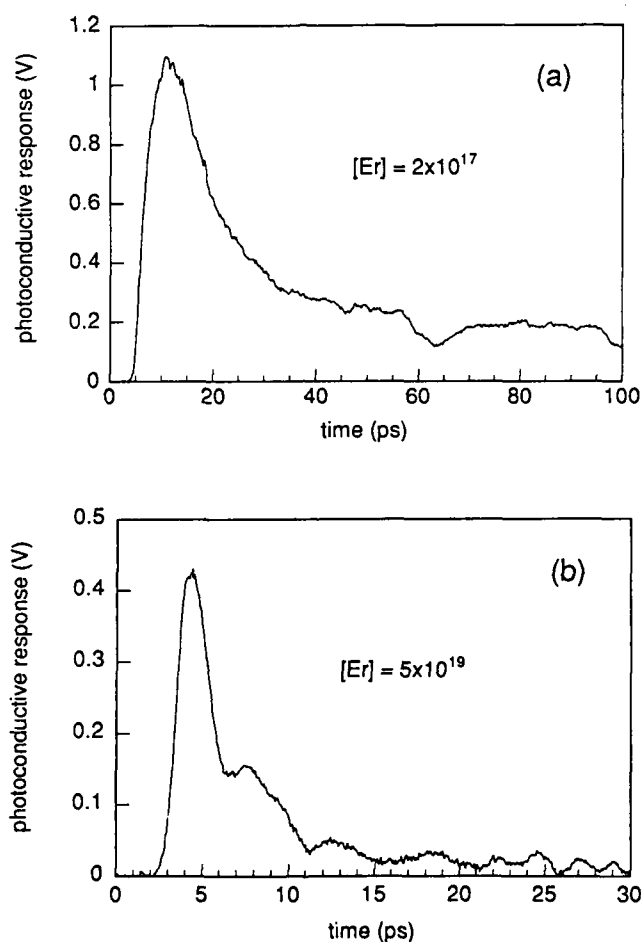


Fig.2 Photoconductive switching transient as measured by electro-optic sampling for GaAs:Er epilayer with (a) $[Er] = 2 \times 10^{17} \text{ cm}^{-3}$, and (b) $[Er] = 5 \times 10^{19} \text{ cm}^{-3}$.

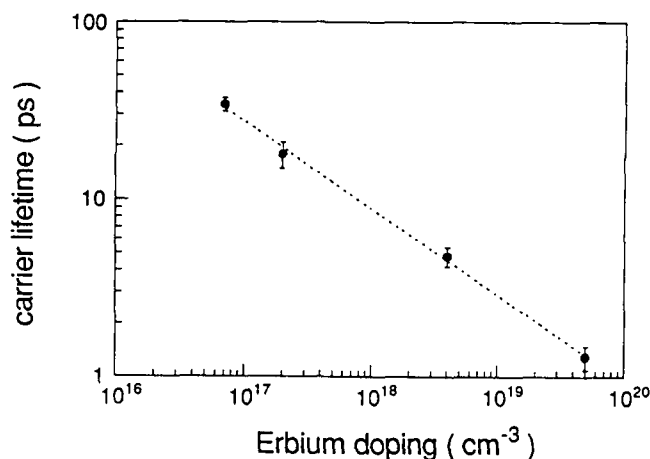


Fig.3 Dependence of the carrier lifetime on the erbium-doping concentration, in the MBE grown GaAs:Er epilayers.

To explain the observed ultrafast recombination of photogenerated carriers, if one assumes the Shockley-Read-Hall theory of recombination at a single deep-level, the minority carrier lifetime τ_r is given by, $\tau_r = 1 / N_t v_{th} \sigma$, where N_t is the trap density, v_{th} is the thermal velocity $\sim 10^7$ cm/s at 300 K, and σ is the capture cross-section. Hence a plot of τ_r versus N_t would be linear on a log-log plot, as shown in Fig.3, assuming that all the Er-incorporated contributes to the trapping/recombination, *i.e.* $N_t = [\text{Er}]$. It is not known what particular Er-species is responsible for the observed recombination, *e.g.* Er^{3+} , etc. The linearity of the curve would support a simple picture as given by Eqn.(1). However the measured slope of $-1/2$ is not expected from Eqn.(1), which predicts a slope of -1 . This discrepancy in the slope could be due to the deviation from such a simple approximation, or possibly due to the fact that the concentration of traps responsible for this behavior, N_t , is not a linear function of the Er-concentration.

Further work is in progress to determine the nature of levels responsible for the ultrafast carrier trapping/recombination properties in this material and its high-resistivity behavior. DLTS measurements do not indicate the presence of a sufficient density of Er-impurity related discrete deep-level states to account for the short recombination times. Double-crystal X-ray diffraction measurements (Fig.4) show a large residual compressive strain ($\sim 0.05\%$), especially for the higher Er-dopings. Strain-induced defects may be responsible for the observed short lifetime, although this needs to be confirmed. Photocurrent spectroscopy has also been performed on interdigitated electrode structures in order to determine if band tail states could be responsible for the high resistivity and short carrier lifetimes (as has been shown to be the case in LT-GaAs⁸). The absorption edge was found to be unaffected, however, eliminating this possibility.

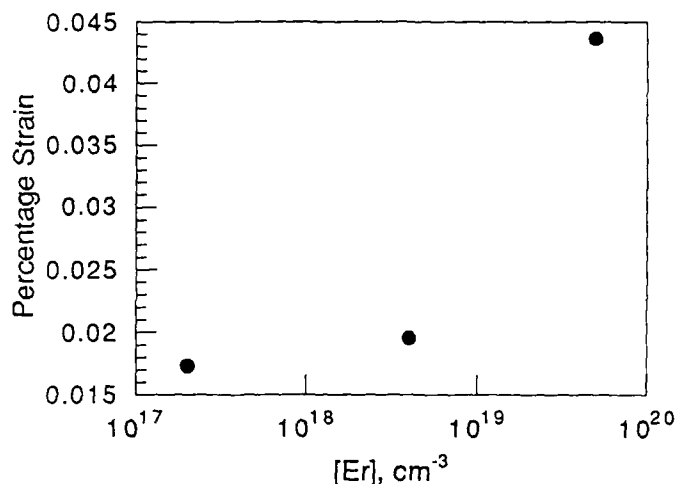


Fig.4 Strain as calculated from double-crystal X-ray rocking curves, as a function of [Er].

Although this deviation from the behavior as predicted by Eqn.(1) is not understood at present, this material has important implications for use in ultrafast optoelectronics. From Fig.2(b), for the $5 \times 10^{19} \text{ cm}^{-3}$ doped sample, nearly 0.5V is switched from a 15V bias across a 15- μm gap, using only a 50 pJ/pulse of optical energy. This is similar to the best material to date for photoconductive switching purposes, low-temperature MBE grown GaAs⁹. It needs to be seen if further optimization of the MBE growth, and possible annealing conditions might improve the responsivity without sacrificing the high-resistivity and short carrier lifetime properties. In addition, this material has practical advantages when used for high-speed photoconductive switching purposes. From Fig.3 it is observed that the carrier lifetime is a smooth function of the doping, and hence it is possible to 'tune' the carrier lifetime for the desired application. This can lead to optimizing the response speed of optoelectronic devices e.g. the bandwidth of integrated detector-amplifier configuration.

Similar behavior for the carrier lifetime was also expected in other erbium doped III-V compounds e.g. $\text{In}_{0.53}\text{Ga}_{0.47}\text{As}$, thereby enabling the realization of fast photoconductive detectors with low dark currents for the longer wavelength region without using complicated barrier designs and processing techniques. However, as shown in Fig. 5, electro-optic sampling measurements on MBE-grown Er-doped $\text{In}_{0.53}\text{Ga}_{0.47}\text{As}$ indicate carrier lifetimes in excess of ~100 ps for the doping range of 10^{17} - 10^{19} cm^{-3} . The resistivity of these films was also quite low, from 10-500 $\Omega\text{-cm}$ for the same doping range.

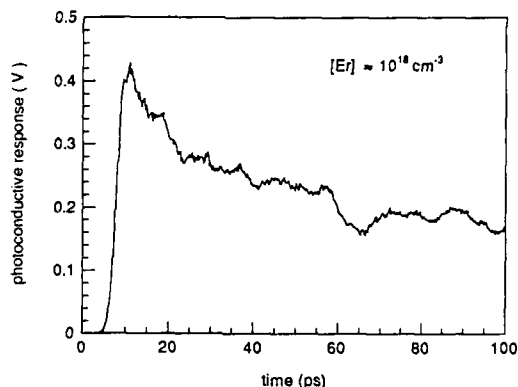


Fig.5 Photoconductive switching transient as measured by electro-optic sampling for $\text{In}_{0.53}\text{Ga}_{0.47}\text{As} : \text{Er}$ epilayer, with $[\text{Er}] = 10^{18} \text{ cm}^{-3}$. Similar data is obtained in the doping range of $10^{16} - 10^{19} \text{ cm}^{-3}$.

Conclusions

In conclusion, we have studied the dependence of the free-carrier lifetime on the erbium doping concentration in $\text{GaAs}:\text{Er}$. The lifetime decreases smoothly as the doping is increased. MBE growth allows very high doping of up to $5 \times 10^{19} \text{ cm}^{-3}$, without deteriorating the crystallinity, and at these doping levels, carrier lifetimes of $\sim 1 \text{ ps}$ are obtained. Therefore, this material when used as a photoconductive switch leads to efficient generation of picosecond transients.

This work was supported by the National Science Foundation under grant ECS-9014069 and by the Air Force Office of Scientific Research (AFOSR), University Research Initiative under Contract No. AFOSR-90-0214.

References

- [1] C. Lhomer, B. Lambert, Y. Toudic, A. LeCorre, M. Gauneau, F. Clerot, and B. Sermage, *Semicond. Sci. Technol.* **6**, 916 (1991).
- [2] P. Galtier, T. Benyattou, J. P. Pocholle, M. N. Charasse, G. Guillot, and J. P. Hirtz, *GaAs and Related Compounds, 1989*, IOP Publishing Ltd., Bristol, England, pp.327.
- [3] T. Benyattou, D. Seghier, G. Guillot, R. Moncorge, P. Galtier, and M. N. Charasse, *Appl. Phys. Lett.* **60**, 350 (1992).
- [4] G. S. Pomrenke, H. Ennen, and W. Haydl, *J. Appl. Phys.* **59**, 601 (1992).
- [5] D. H. Auston, *Picosecond Optoelectronic Devices*, ed. C. H. Lee, Academic Press, Orlando, 1984, Chap.4.
- [6] J. A. Valdmanis, *Electronics Letters* **23**, 1308 (1987).
- [7] S. Sethi, S. Gupta, and P. K. Bhattacharya, *Appl. Phys. Lett.* **62**, 1128 (1993).
- [8] F. W. Smith, Ph.D. thesis, MIT, 1990.
- [9] S. Gupta, J. F. Whitaker, G. Mourou, *IEEE J. Quant. Electron.* **28**, 2464 (1992).

EuTe/PbTe SUPERLATTICES: MBE GROWTH AND OPTICAL CHARACTERIZATION

G. SPRINGHOLZ, SHU YUAN, G. BAUER, M. KRIECHBAUM* AND H. KRENN

Institut für Halbleiterphysik, Johannes Kepler Universität Linz, A - 4040 Linz, Austria

** Institut für Theoretische Physik, Karl Franzens Universität Graz, A - 8010 Graz, Austria*

ABSTRACT

The heteroepitaxial growth of EuTe on PbTe (111) by molecular beam epitaxy (MBE) was investigated using in situ reflection high energy electron diffraction (RHEED). As a function of substrate temperature and Te₂ flux rate, the resulting EuTe (111) surfaces exhibit several different surface reconstructions corresponding to Te-stabilized or Eu-stabilized surfaces. The Eu-stabilized surface shows a $(2\sqrt{3} \times 2\sqrt{3})R30^\circ$ surface reconstruction. Because of the strain induced tendency for 3D islanding, only in a narrow window of MBE growth parameters perfect 2D layer-by-layer heteroepitaxial growth exists. Using such optimized MBE growth conditions, we have fabricated a series of PbTe/EuTe superlattices. In such superlattices the wide band gap EuTe layers act as barriers and the narrow band gap PbTe as quantum wells. The superlattices were investigated by high resolution x-ray diffraction, showing their high structural perfection. Modulated low temperature Fourier transform infrared reflection measurements were performed in order to determine the confined energy levels in the PbTe quantum wells. The measurements indicate that mini-subbands are formed in the PbTe quantum wells with a mini-band width of 22 meV in agreement with envelope function calculations.

1. INTRODUCTION

Advances in molecular beam epitaxial (MBE) growth techniques have recently led to the fabrication of lead salt heterostructure quantum well diode lasers [1]. In such structures, usually PbTe is used for the quantum wells and the ternary $\text{Pb}_{1-x}\text{Eu}_x\text{Te}$ with $x < 0.05$ for the barriers. Because of the rapid increase of the energy gap with Eu content [1], $\text{Pb}_{1-x}\text{Eu}_x\text{Te}$ is an attractive material in this context. Recently, also PbTe/EuTe superlattices, have been used in such structures [2], as well as in PbTe-EuTe transistor structures [3]. Because of the large difference of the energy band gaps (PbTe: $E_g = 190$ meV and EuTe: $E_g = 2.0$ eV), very large confinement energies of more than 1 eV can be achieved in EuTe/PbTe quantum well structures. In addition, the EuTe - PbTe system has attracted attention because of the interesting combination of an antiferromagnetic (EuTe) and a diamagnetic (PbTe) material [5,6], which offers the possibility to study the influence of low dimensionality on the magnetic behaviour in short period EuTe/PbTe superlattices. In terms of heteroepitaxy, both materials crystallize in the fcc rocksalt crystal structure and their lattice mismatch is only 2.1%.

2. EXPERIMENTAL

Our experiments were carried out in a Riber MBE growth chamber and custom-built preparation and load-lock chambers. For optimum PbTe MBE growth, it is of crucial importance to achieve an as close as possible stoichiometric flux [7]. Therefore, we use a Te₂ effusion cell in addition to a PbTe compound effusion cell in order to fine adjust the beam flux composition. Under these conditions we have recently demonstrated the MBE growth of very high mobility PbTe epilayers with Hall mobilities of up to 1.98×10^6 cm²/Vs [7]. For EuTe growth, elemental Eu and another Te₂ effusion cell are used, since the EuTe compound itself has a very low vapor pressure at temperatures below 1000°C. The beam flux rates from the different effusion cells were measured with a quartz crystal thickness monitor, which was also used to calibrate the ion gauge beam flux monitor. In situ RHEED surface studies were carried out with an electron gun operated at 35 keV. For all samples, first thick PbTe buffers were deposited on freshly cleaved (111) BaF₂ (lattice mismatch of 4.2%) substrates. This ensures complete strain relaxation of the buffer and a very high perfection of the surface of the epitaxial layer [7].

3. THE SURFACE RECONSTRUCTIONS OF EuTe (111)

The heteroepitaxial growth of EuTe on relaxed PbTe buffers was studied for a wide range of growth conditions by in-situ RHEED. For the static as well as the growing EuTe (111) surface

we generally can distinguish two different surface states: (1) a Te-stabilized surface and (2) an Eu-stabilized surface, each exhibiting a different type of surface reconstruction [8]. The Te-stabilized surface occurs only with an impinging Te_2 flux for a quite narrow regime of substrate temperatures just above the Te_2 condensation temperature (which is dependent on the impinging Te_2 flux rate). This is similar to the behaviour of the PbTe or the $\text{Pb}_{1-x}\text{Eu}_x\text{Te}$ (111) surfaces [9]. The Te-stabilized EuTe (111) surface has a complicated surface reconstruction with quite weak fractional order streaks in the RHEED patterns. In the $[-110]$ azimuth we observe $1/3$ and $1/4$ order streaks, in the $[-321]$ azimuth $1/3$ and $1/2$ order streaks. In the $[-211]$ azimuth only weak $1/2$ order streaks appear. These observations can be very well explained by a multi-domain $(3 \times 4)/(4 \times 3)$ surface reconstruction for the Te-stabilized EuTe (111) surface.

With substrate temperatures about 30°C above the Te_2 condensation points, the redesorption rate of the chemisorbed Te-adatoms on the EuTe surface is already so high, that the equilibrium Te surface coverage at the impinging Te_2 flux rate decreases and the surface changes to the Eu-stabilized state. The corresponding RHEED patterns for the different azimuths are shown in Fig.1 with the integral order diffraction streaks being indicated by their corresponding 2D indices. In the $[-110]$ azimuth (Fig.1(a)), bright $1/2$ order streaks are observed, whereas in the $[-211]$ azimuth (Fig.1(b)) $1/6$ order streaks appear. This indicates that the unit cell of the reconstructed surface is rotated by 30° with respect to the unreconstructed surface unit cell, with the basis vectors of the reconstructed unit cell oriented parallel to the $[-211]$ directions. Since the $1/2$ ($\approx 3/6$) order streaks observed in the $[-211]$ azimuth are much stronger than the other $1/6$ order streaks, the surface unit cell of the reconstruction seems to be nonprimitive. The RHEED pattern observed in the $[-321]$ azimuth is shown in Fig.1(c). In this azimuth again only strong $1/2$ order streaks are observed (bright streaks directly at the shadow edge). However, also diffraction streaks from the higher order Laue zones, namely the $1/6^{\text{th}}$, $2/6^{\text{th}}$ and the $3/6^{\text{th}}$ order Laue zones, are observed for the higher order

Laue zones the same patterns as for the 0^{th} order Laue zone are observed only successively shifted by small angles parallel to the shadow edge. From these RHEED patterns the occurrence of a clear $(2\sqrt{3} \times 2\sqrt{3})R30^\circ$ surface reconstruction for the Eu-stabilized EuTe surface is deduced. This surface reconstruction is stable up to substrate temperatures of about 140°C above Te_2 condensation temperatures. At higher temperatures the fractional order streaks in the RHEED patterns eventually disappear, indicating a transition to an unreconstructed Eu-stabilized EuTe surface.

4. HETEROEPITAXY OF EuTe ON PbTe (111)

The nucleation and growth behaviour of strained EuTe on PbTe (111) was studied for a wide range of growth temperatures between 220°C and 380°C , and different Te_2 -to-Eu beam flux ratios from 1.2 to 16. We found that perfect 2D nucleation and layer-by-layer growth occurs only in a small range of substrate temperatures up to about 60 to 80°C above the Te_2 condensation points, depending on the Te_2 -to-Eu flux ratio used [8]. At higher substrate temperatures 3D nucleation occurs, which is followed by a only very slow reformation of a smooth surface after continued growth. With substrate temperatures below the Te_2 condensation points, polycrystalline growth with tellurium precipitates is observed. Like for the static surface, the steady state growing surface in the 2D growth and nucleation regime can be either Te- or Eu-stabilized.

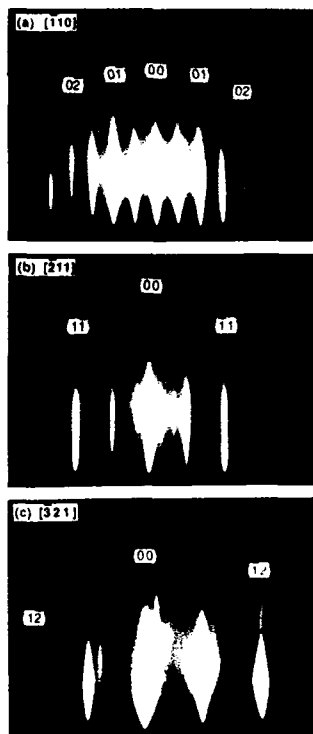


Figure 1: RHEED patterns (35 keV) observed for the Eu-stabilized EuTe (111) surface for different azimuth directions of the electrons: (a) $[-110]$ azimuth, (b) $[-211]$ azimuth and (c) $[-321]$ azimuth. The corresponding EuTe (111) surface reconstruction is a $(2\sqrt{3} \times 2\sqrt{3})R30^\circ$ reconstruction.

For substrate temperatures up to 20°C above the Te₂ condensation temperature the growth proceeds in the Te-stabilized mode and for higher substrate temperatures in the Eu-stabilized growth mode characterized by the $(2\sqrt{3} \times 2\sqrt{3})R30^\circ$ reconstruction, details are given in Ref.8.

The critical layer thickness for MBE growth of fully strained EuTe on relaxed PbTe buffer layers was determined using in situ RHEED. We found a maximum critical layer thickness of 52 EuTe monolayers (198 Å) when the growth conditions were set such that EuTe surface is just at the transition between the Eu-stabilized and the Te-stabilized state. For these growth conditions we also observe a maximum number of RHEED intensity oscillations. In addition, an abrupt surface roughening occurs at the critical EuTe layer thickness, as is indicated by the appearance of 3D transmission spots in the RHEED patterns. This fact indicates, that the initial strain relaxation is not caused by misfit dislocations but rather by coherent 3D islanding of the surface [9]. With increasing substrate temperature we found a strong increase of the damping of the RHEED intensity oscillations, which indicates a strong increase of the diffusion lengths of the surface adatoms. This explains the experimentally observed strong decrease of the critical layer thickness with increasing substrate temperature, since within the model of coherent 3D islanding the increasing mobility of the surface adatoms results in a strongly enhanced tendency for 3D islanding. For substrate temperatures only about 60 to 80° above the Te₂ condensation points, the RHEED patterns changes during the nucleation of EuTe on PbTe (111) already within 2 - 5 ml of EuTe growth from the streaked PbTe RHEED pattern to a spotty transmission pattern for the EuTe surface, i.e. 3D nucleation and growth occurs. This limit for 2D layer-by-layer growth can be explained by the drastically increased surface diffusion, leading to 3D surface islanding and 3D growth within few monolayers. As a result, for optimum heteroepitaxial growth of EuTe/PbTe heterostructures, the growth conditions have to be precisely controlled, such that the EuTe growth proceeds in the Eu-stabilized growth mode, with the substrate temperatures not more than 30°C above the transition to the Te-stabilized mode.

5. EuTe/PbTe SUPERLATTICES: MBE GROWTH AND STRUCTURAL CHARACTERIZATION

A series of EuTe/PbTe superlattices were grown on thick ($> 4 \mu\text{m}$), fully relaxed PbTe buffer layers, predeposited on BaF₂ (111) substrates at $T_s = 350^\circ\text{C}$. In order to achieve optimum 2D nucleation and layer-by-layer growth of EuTe on PbTe, the substrate temperature was reduced to 255-270°C for the growth of the EuTe/PbTe superlattices. This substrate temperature is about 30-45°C above the Te₂ condensation points for the Te₂ flux rates used, serving as a reference point. The PbTe layers were grown at a growth rate of 0.62 ml/sec - 0.80 ml/sec (1 monolayer (ml) = 3.731 Å for PbTe (111)). The EuTe layers were grown with 0.4 ml/sec (= 1.52 Å/sec), which is given by the Eu flux rate from the effusion cell, and using a Te₂ to Eu flux ratio of 3. This results in an Eu-stabilized growth, as is evident from the appearance of the corresponding $(2\sqrt{3} \times 2\sqrt{3})R30^\circ$ surface reconstruction. During the growth of the PbTe layers, the surface state changes to the typical unreconstructed Pb-stabilized PbTe surface. Since in our superlattices the EuTe layer thicknesses do not exceed the EuTe critical layer thickness, the EuTe layers are fully strained with respect to the PbTe layers. During the whole growth procedure, the RHEED patterns remained totally streaked and no indications of 3D transmission patterns were observed. This indicates the persistence of a very smooth surface during every stage of the superlattice growth. Consequently, very smooth PbTe/EuTe heterointerfaces can be expected.

In the following we present the experimental results for three different EuTe/PbTe superlattices. In all the three superlattices, the PbTe quantum wells with well widths between 56 Å and 290.5 Å were separated only by 9.5 Å to 19 Å wide EuTe barrier layers, which results in a significant coupling between the quantum wells. The number of superlattice periods ranges from $N = 20-80$, so that the total thickness of the superlattice stack was between 0.5 - 1 μm . The

Table I: EuTe/PbTe superlattice sample parameters

sample	d_{buffer}	$d_{\text{SL-period}}$	$d_{\text{PbTe QW}}$	$d_{\text{EuTe barr.}}$	period	$a_{\text{n,SL}}$	FWHM_{SL0}	$d_{\text{tot,SL}}$	$\Delta a_{\text{SL}}/a_{\text{PbTe}}$
	[μm]	[Å]	[Å]	[Å]	numb.	[Å]	[arcsec]	[μm]	[%]
#183	4.5	300	290.5	9.5	20	6.475	68	0.60	0.07
#210	5.9	131	112	19	80	6.490	180	1.05	0.32
#255	4.1	75	56	19	70	6.507	277	0.525	0.56

detailed sample parameters are listed in Table I. Fig.2 shows the $\Omega/2\theta$ x-ray diffraction patterns in the vicinity of the Bragg (222) reflection, determined using a high resolution Philips MRD diffractometer employing $\text{CuK}\alpha_1$ radiation. The detector opening angle was 0.45° .

Apart from the diffraction peaks of the BaF_2 substrate and the relaxed PbTe buffer layer, several superlattice satellite peaks are observed, from which the superlattice period was determined. Due to the decrease of the superlattice period from 300\AA for sample #183 (Fig.2(a)) to 75\AA for sample #255 (Fig.2(c)), the spacing of the superlattice satellite peaks increases strongly for Fig.2(a) to (c). For the sample #183 to #255 the thickness of the PbTe layers in the superlattice decreases strongly, whereas the EuTe layer thickness was kept roughly the same. Therefore, the overall EuTe content in the superlattice stack increases strongly from sample #183 to #255, resulting in a shift of the 0th order superlattice SLO peak to lower angles, since the lattice constant of EuTe (6.598\AA) is larger than for PbTe (6.462\AA). The average normal lattice constant of the superlattice stack $a_{n,SL}$ obtained from the x-ray data is given in Table I. In addition, a significant increase of the full width at half maximum (FWHM) of the SLO peak with increasing EuTe content in the SL is observed (see Table I). This is similar to the behaviour of ternary $\text{Pb}_{1-x}\text{Eu}_x\text{Te}$ alloy epitaxial layers, for which we also have observed a very strong increase of the FWHM of the Bragg (222) reflection with increasing Eu-content.

For sample #183 the EuTe content in the superlattice is very small. Therefore, it can be assumed, that the whole superlattice stack is fully strained with respect to the PbTe buffer layer, with the in-plane lattice constant in the SL stack being equal to the bulk PbTe lattice constant of the buffer layer. This has been shown in detail for a similar sample

in Ref. [12]. Consequently, the individual PbTe and EuTe layer thicknesses in the SL could be determined from the position of the SLO diffraction peak. The quoted assumption, however, does not hold for the other two superlattice samples, since the lattice mismatch between the superlattice stack and the PbTe buffer layer of 0.32% and 0.55% for samples #210 and #255, respectively, can no longer be neglected for the superlattice stack thicknesses $d_{tot,SL}$ of 1.05 and $0.525\text{ }\mu\text{m}$, respectively. The lattice mismatch of the SL was calculated using the nominal EuTe and PbTe layer thicknesses (see Table I) for the calculation of the in-plane lattice constant and assuming a corresponding free standing superlattice. Comparing the calculated averaged normal superlattice lattice constant with those experimentally obtained (see Table I), it is concluded, that for these two samples the superlattice stack is neither freestanding nor fully strained with respect to the PbTe buffer layer and that a partial relaxation of the SL stack has occurred.

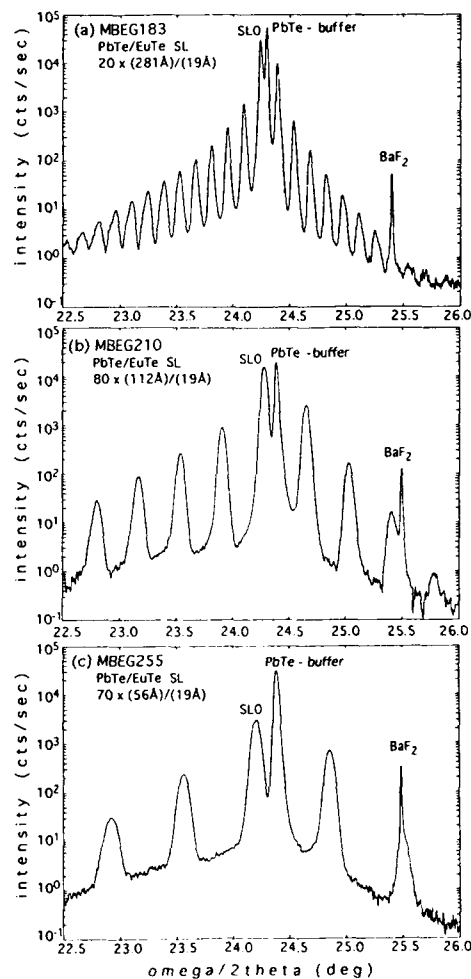


Figure 2: $\Omega/2\theta$ x-ray diffraction patterns in the vicinity of the Bragg (222) reflection for the three EuTe/PbTe superlattice samples (a) #183, (b) #210 and (c) #255 with the exact sample parameters given in Table I. The superlattices were grown on thick fully relaxed PbTe buffer layers on a $\text{BaF}_2(111)$ substrates.

6. OPTICAL PROPERTIES: MODULATED REFLECTIVITY

Since the three superlattice samples were grown on thick PbTe buffers, no infrared transmission experiments could be performed in order to deduce the interband transitions between confined states in the PbTe wells, which occur at higher energies than the bulk PbTe energy gap. In addition, the highly conducting PbTe buffer rules out the use of frequency dependent photoconductivity measurements. Therefore, only reflectivity measurements could be performed using Fourier transform spectroscopy. However, since the change of the refractive index due to interband absorption are comparatively small and therefore induce only small changes in the reflectivity spectrum, reflectivity modulation techniques were applied. In this work we applied temperature modulation, i.e. reflectivity spectra were taken at $T = 5$ K and $T = 29$ K, changing the energy gap of PbTe from 190 meV to 195 meV. Consequently, the interband transition energies between the confined levels change as well and therefore, the difference reflectivity $\Delta R_{(5K,29K)} / R_{(5K)}$ exhibits distinct signatures at the electronic interband transition energies.

The measured reflectivity spectra show interference fringes at photon energies below the energy gap of the PbTe buffer resulting from the step like changes of the optical constants at the air-substrate-buffer-multilayer stack interfaces. The spectra can be reproduced quite well with calculated spectra based on the model described by Yuan et al. [13], i.e. on using model dielectric functions for the buffer, the barriers and the quantum wells. The absorption due to the interband transitions in the QW's results in changes of the refractive index $n(\omega)$ as well [13], and is taken into account using the Kramers Kronig transformation of $\alpha(\omega)$. The reflectivities of the whole samples was then calculated using the transfer matrix method and matching the electromagnetic fields at all interfaces. Because of the much larger energy gap, the absorption in the EuTe barriers in the frequency range of interest was neglected [5].

In Fig.3 the modulated reflectivity spectrum $\Delta R/R$ is shown for sample #210 on a very enlarged scale. The fringes below about 1600 cm^{-1} are due to interference fringes in the optical spectra of the PbTe buffer and EuTe/PbTe superlattice. Above the energy gap of the buffer (1530 cm^{-1}) the variation of $\Delta R/R$ is comparatively small, however, showing a prominent structure around 2500 cm^{-1} . Fig.3 (a) and (b) compares the fits of the experimental spectrum (dots) using two different model calculations. In Fig.3(b) the calculation for $\Delta R/R$ is based only on the optical properties of the wells, the barriers and the buffer, neglecting electronic inter band transitions between confined levels within the quantum wells. It is evident that the structure between 2000 cm^{-1} and 2700 cm^{-1} cannot be reproduced. For the second fit shown in Fig.3(a), inter band transitions are included, now reproducing the main features of the modulated reflectivity spectrum. From reflectivity measurements on $\text{PbTe}/\text{Pb}_{1-x}\text{Eu}_x\text{Te}$ MQW's it has been

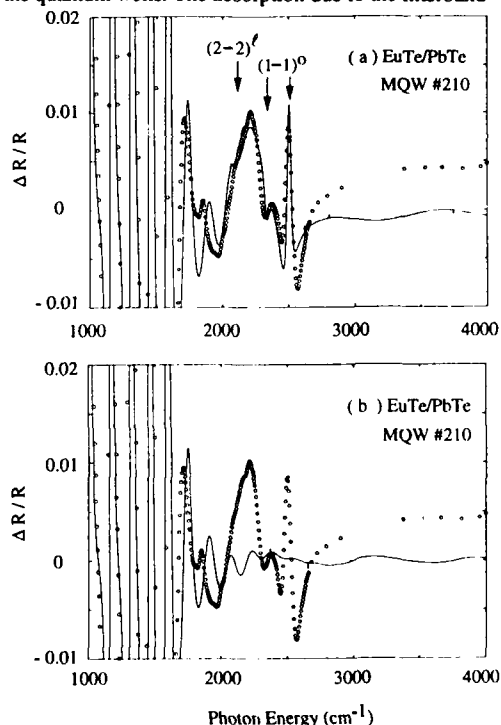


Figure 3: Modulated reflectivity spectrum $\Delta R/R$ for EuTe/PbTe superlattice sample #210 shown on a very enlarged scale. (a) Experimental data (dots) and calculated spectrum (full line) including inter band transitions between confined energy levels (indicated by arrows). (b) Experimental data (dots) and calculated spectrum (full line) neglecting inter band transitions between confined energy levels.

shown [14], that interband transitions between electronic subbands belonging to the three oblique (o) valleys (with respect to the [111] growth direction) in the band structure of the PbTe wells cause the strongest changes in $R(\omega)$. On the contrary, the transitions involving the subbands of longitudinal (l) valley are usually barely seen in the reflectivity spectrum [14]. Indeed, an envelope function calculation for this sample confirms that in the range marked by the arrows in Fig. 3 the interband transitions $(1-1)^o$ and $(2-2)^l$ occur.

Because of the small thicknesses (19 \AA) of the EuTe barriers, our envelope function calculations show, that the oblique $n=1$ subbands both in the conduction band and valence bands are actually minibands with widths of 3 meV and 2 meV, respectively, for an offset assumed to be $\Delta E_c/\Delta E_g = 0.5$. Assuming an offset of 0.9, the corresponding values are 3.5 meV and 9 meV, respectively, for an EuTe energy gap of 5 eV at the L points of the Brillouin zone. Thus in modelling the modulated reflectivity, we take instead of one $(1-1)^o$ transitions actually *two* $(1-1)^o$ transitions, corresponding to the extrema of the miniband dispersions along K_z ($z \parallel$ to the [111] - growth direction) at the edges of the mini Brillouin zone ($K_z=0$ and $K_z=\pi/D$, D is the superlattice period). The experimentally obtained transition energies for the $(1-1)^o$ transition at the mini Brillouin zone edges of 288 meV at $K_z=0$ and of 310 meV at $K_z=\pi/D$ fit well to the corresponding transition energies obtained from our calculations (293 meV at $K_z=0$ and 305.5 meV at $K_z=\pi/D$). For the $(2-2)^l$ transition the calculated value is 266 meV. Similar modulated reflectivity measurements were also carried out for the other two EuTe/PbTe superlattice samples #183 and #255.

7. CONCLUSION

In conclusion we have shown, that 2D layer-by-layer heteroepitaxial growth of EuTe on PbTe (111) is achieved only in a quite narrow regime of growth conditions. The optimum growth conditions are close to the transition regime between the Te-stabilized and the Eu-stabilized growth modes, which can be distinguished by in-situ RHEED because of their different surface reconstructions. Using optimized growth conditions, we have grown strained PbTe/EuTe superlattices with excellent structural properties, as shown by x-ray diffraction. Information on confined energy levels in the PbTe/EuTe superlattices was obtained by modulated reflectance spectroscopy and compared with EFA calculations.

ACKNOWLEDGEMENTS

We acknowledge support by the Fonds zur Förderung der wissenschaftlichen Forschung.

REFERENCES

1. D. L. Partin, IEEE J. Quantum Electronics **QE 24**, 1716 (1988).
2. A. Ishida, S. Matsuura, H. Fujiyasu, H. Ebe and K. Shinohara, Superlatt. Microstr. **2**, 574 (1986).
3. D. L. Partin, J. Heremans, C. M. Thrush, L. Green and C. H. Olk, Phys. Rev. B **38**, 3549 (1988).
4. J. Heremans and D. L. Partin, Phys. Rev. B **37**, 6311 (1988).
5. A. Mauger and C. Godart, Physics Reports **141**, 51 (1986).
6. See, e.g. *Physics of IV-VI Compounds and Alloys*, edited by S. Rabi (Gordon and Breach, 1974).
7. G. Springholz, G. Bauer and G. Ihninger, J. Cryst. Growth, (1992) in press.
8. G. Springholz and G. Bauer, Appl. Phys. Lett. (1993) in print.
9. G. Springholz and G. Bauer, Appl. Phys. Lett. **60**, 1600 (1992).
10. C. W. Snyder, B. G. Orr, D. Kessler and L. M. Sander, Phys. Rev. Lett. **66**, 3032 (1991).
11. G. Springholz and G. Bauer, Proc. Mat. Res. Soc. (1993), in print.
12. E. Koppenteiner, G. Springholz, P. Hamberger and G. Bauer, submitted to J. Appl. Phys.
13. Shu Yuan, G. Springholz, H. Krenn, G. Bauer, M. Kriechbaum, Appl. Phys. Lett. **62**, 885 (1993).
14. Shu Yuan, G. Springholz, N. Frank, H. Krenn, G. Bauer, M. Kriechbaum, Mat. Res. Soc. Proc. Proceedings, San Francisco, (1993), submitted.

EFFECTS OF MICROSTRUCTURE ON PHOTOLUMINESCENCE OF $\text{SrS:Eu}^{2+}, \text{Sm}^{3+}$ THIN FILMS

SUSAN Z. HUA*, L. SALAMANCA-RIBA*, M. WUTTIG* and P. K. SOLTANI**

*Department of Materials and Nuclear Engineering, University of Maryland, College Park,
MD 20742-2115

**Quantex Corporation, Rockville, MD 20850

Abstract

The microstructure and its effects on the photoluminescence properties of $\text{SrS:Eu}^{2+}, \text{Sm}^{3+}$ thin films grown with different conditions were studied by transmission electron microscopy, x-ray diffraction and photoluminescence techniques. The $\text{SrS:Eu}^{2+}, \text{Sm}^{3+}$ thin films were prepared by e-beam evaporation at different substrate temperatures and growth rates. Both of these growth conditions affect the crystallinity of the thin films. The Sm^{3+} emission is stronger in the films grown at higher growth rates and at an optimum substrate temperature. We believe that the stronger Sm^{3+} emission is due to the higher population of Sm^{3+} trivalent charge states in the films. Further increase of the substrate temperature increases the grain size in the films, but has no significant effect on the PL emission properties. In contrast, the Eu^{2+} emission is less sensitive to growth conditions.

Introduction

Recent developments in thin-film electroluminescence technology have renewed interest in rare-earth doped alkaline-earth sulfides in the form of thin films, because the quality of the thin films directly determines the luminescence characteristics and the performance of the devices [1, 2]. For optical memory devices, such as optically stimulated radiation dosimeters, infrared sensors and near-infrared image intensifiers, which require doubly doped phosphors, the charge states of each dopant and the probability of electronic transitions between dopants are very important. The growth conditions affect the crystallinity of the thin films and, therefore, it is expected that they also affect the emission efficiency and electron transfer processes. In order to increase the emission efficiency and improve the performance of the films, the effects of several parameters of deposition, such as substrate temperature and sulfur coevaporation, have been studied [3, 4]. However, no systematic study has been carried out on the dependence of the photoluminescence (PL) characteristics upon microstructure, and various growth parameters. In this paper, we report on the effects of growth rate and substrate temperature on the crystallinity and orientation of SrS films by transmission electron microscopy (TEM), and x-ray diffraction. The effects of microstructure on the charge states of the dopants are also studied by photoluminescence technique.

Experimental

The $\text{SrS:Eu}^{2+}, \text{Sm}^{3+}$ thin films were deposited by the e-beam evaporation method on BaF_2 substrates [5]. In order to study the effects of growth conditions on the optical properties, the substrate temperature was varied from 500°C to 600°C , and the deposition rate was changed in the range of $15\text{\AA}/\text{s}$ to $30\text{\AA}/\text{s}$. The film thickness was either $2.3\text{ }\mu\text{m}$ or $3.7\text{ }\mu\text{m}$ and the Eu^{2+} and Sm^{3+} concentrations were $0.002\text{mol}\%$ and $0.004\text{mol}\%$, respectively.

The PL spectra were obtained by a scanning spectra system which is composed of an Acton SpectraPro 275 Digital Scanning Monochromator and a Hamamatsu RS636 GaAs photomultiplier. A direct observation of the microstructure of the films was carried out by cross-sectional TEM. Both dark field and bright field TEM micrographs were obtained using a JEOL JEM-2000FXII TEM. X-ray diffraction spectra were obtained from all the thin film samples and compared with powder target materials to study the crystallinity and preferred orientation of the films.

Results and discussions

The microstructure of thin films depends primarily on the condensation conditions of the evaporated beam, which in turn depend on parameters such as substrate temperature, deposition rate, and the physical and chemical properties of the substrate. The effects of the parameters were studied as follows.

(a) Effects of Deposition Rate

PL spectra are shown in Fig. 1 for $\text{SrS:Eu}^{2+}, \text{Sm}^{3+}$ thin films grown at different deposition rates, 15 \AA/s (Fig. 1(a)) and 30 \AA/s (Fig. 1(b)). The film thickness of these samples was approximately the same. The emission spectra were obtained under the same conditions with an excitation energy of 5 eV (UV) at room temperature. The broad emission peak centered at 2.0 eV is identified as Eu^{2+} emission [6], and the three sharp peaks centered at 1.88 eV , 2.04 eV and 2.18 eV are identified as Sm^{3+} emissions [7]. Fig. 1 shows that the Eu^{2+} emission is almost the same for both samples. However, the emission of Sm^{3+} is very sensitive to the growth rate. Very low intensities of Sm^{3+} emission were observed from the samples grown at 15 \AA/s , while very strong emission of Sm^{3+} was obtained from the samples grown at 30 \AA/s .

The microstructure produced by different deposition rates was investigated by TEM observation. Fig. 2 shows cross-section TEM micrographs of the sample grown at 15 \AA/s (Fig. 2(a)) and 30 \AA/s (Fig. 2(b)). Both figures show a columnar structure of the film. The grains in the film grown at 30 \AA/s have larger diameter than those grown at 15 \AA/s , and most of the columns are well aligned and extend from the interface to the free surface of the film.

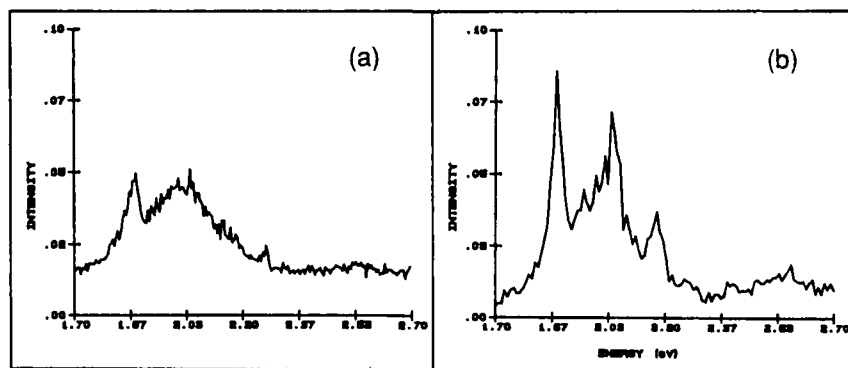


Fig. 1 PL spectra of $\text{SrS:Eu}^{2+}, \text{Sm}^{3+}$ thin films grown at different growth rates: (a) 15 \AA/s and (b) 30 \AA/s on BaF_2 substrates at 550°C .



(a)



(b)

Fig. 2 Cross-section TEM micrographs of $\text{SrS:Eu}^{2+}, \text{Sm}^{3+}$ thin films grown at 550°C and with different growth rates: (a) 15 \AA/s and (b) 30 \AA/s on a BaF_2 substrate. The interface is indicated by the arrows.

Other samples with different doping concentrations of Sm^{3+} and Eu^{2+} were studied using TEM and showed the same results. These results suggest that with good crystallinity and large grain size, the Sm^{3+} has high emission efficiency, whereas, with small grain size and poor crystallinity, Sm^{3+} shows low emission efficiency. Namely, there are more effective Sm^{3+} emission centers in samples with better crystalline quality. The reason for this can be explained by the existence of mixed valence states of Sm in the SrS host material. The trivalent state of Sm is energetically favored over the bound state in a crystal. Disturbances in the coordination, as it occurs on the surface or at grain boundaries, will tilt the balance of Sm to the divalent state [8]. X-ray photoemission spectroscopy (XPS) studies have revealed that there is a large divalent component on the surface of Sm metal even though it has trivalent configuration in the bulk [9]. In alkaline-earth sulfides, such as CaS, the Sm ions have been identified in both the trivalent and the divalent states [10]. From our results, we believe that films with small grain sizes have more Sm ions in the Sm^{2+} state at grain boundaries than films with larger grain sizes even for the same total Sm concentration. The Sm^{3+} emission intensity, therefore, decreases in the films with small grain sizes.

In contrast, Eu^{2+} emission is not as sensitive to the grain size and we observed the same PL intensity of Eu^{2+} in samples grown at different deposition rates. In the case of Eu^{2+} the 4f level is exactly half filled with 7 electrons resulting in a favorable energy state for the ion in the crystal.

(b) Effects of Substrate Temperature

A TEM study was also carried out on films grown at different substrate temperatures and

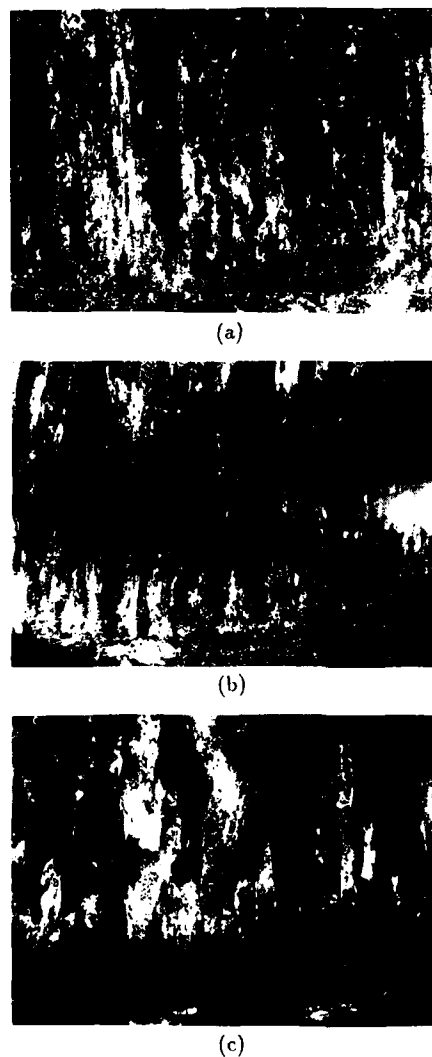


Fig. 3 Cross-section TEM micrographs of SrS: $\text{Eu}^{2+}, \text{Sm}^{3+}/\text{BaF}_2$ thin films grown at : (a) 500°C , (b) 550°C and (c) 600°C . The interface is indicated by the arrows.

for a low growth rate of $15\text{\AA}/\text{s}$. Figure 3 shows cross-sectional TEM micrographs from samples grown at 500°C , 550°C , and 600°C , respectively. As expected, an increase in grain size was observed with increasing substrate temperature. A detailed observation of these micrographs shows that although the diameter of the grains increases with substrate temperature, the grains are no longer well aligned columns, at the highest temperature. We

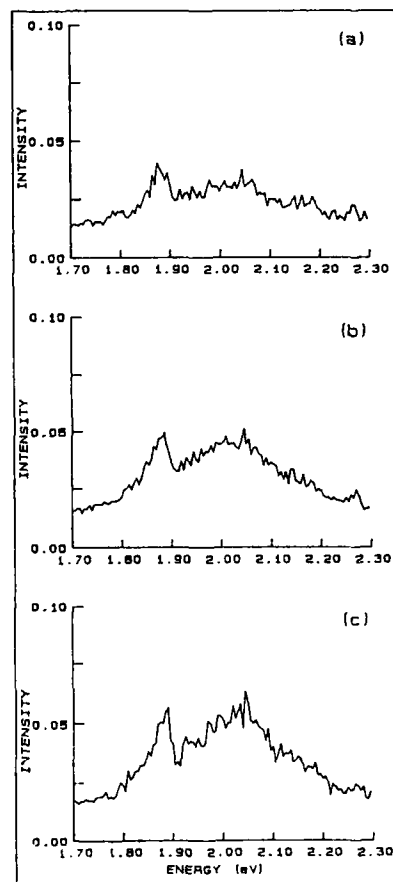


Fig. 4 Intensity of total PL emission dependence on substrate temperature (a) 500°C ; (b) 550°C ; (c) 600°C .

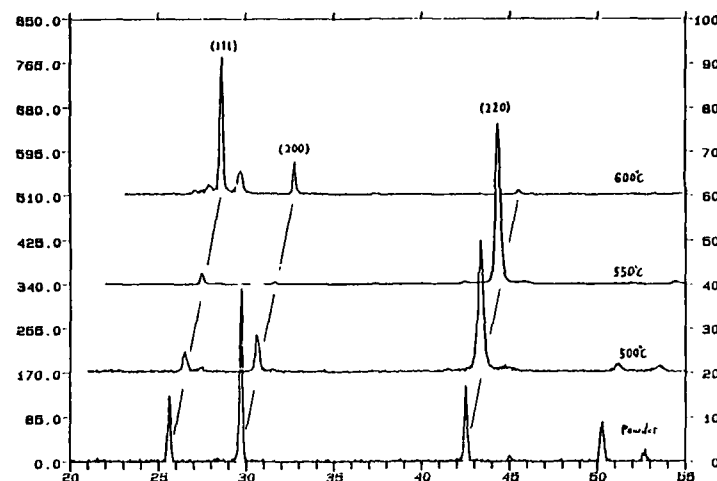


Fig. 5 X-ray diffraction spectra from SrS thin films grown at different substrate temperatures and for SrS powder.

also found a strong tendency of uniaxial grain growth at high substrate temperature. The PL spectra of these samples are shown in Fig. 4. The Eu^{2+} emission intensity increased somewhat with substrate temperature due to the improvement of the crystallinity. However, no obvious increase of Sm^{3+} emission was observed when the substrate temperature was raised to 550°C . It is known that grain growth in this temperature range is mainly due to surface diffusion [11]. At low growth rates and high temperatures, surface diffusion is large, and the Sm ions have more opportunity to move to the surface and to grain boundaries by surface diffusion to form Sm^{2+} or possibly SmS. Therefore, at low growth rates, the Sm^{3+} population is lower even when the grain size is large. We can conclude that the emission intensity of Sm^{3+} depends on both crystallinity and growth conditions. Only at high growth rates and optimum substrate temperature, we can get maximum Sm^{3+} emission. It is also possible that the PL of Sm^{3+} in films grown at high temperatures is more affected by scattering by defects within the grains.

The preferred film orientation was studied using x-ray diffraction for films grown at different substrate temperatures. Fig. 5 shows x-ray diffraction spectra of $\text{SrS:Eu}^{2+}, \text{Sm}^{3+}$ films deposited at different temperatures. A typical spectrum of $\text{SrS:Eu}^{2+}, \text{Sm}^{3+}$ powder is also shown in Fig. 5 for comparison. The diffraction spectrum from the powder sample shows maximum intensity for the (200) reflection followed by (220) and (111), which correspond to a rock salt crystal structure. The spectrum from the films deposited at 500°C and 550°C show a maximum intensity for the (220) reflection, whereas, the diffraction spectrum from the film deposited at 600°C shows the maximum at (111). These results suggest that the thin films are highly oriented along the (110) direction between 500°C and 550°C , and the preferred orientation changes to (111) when the substrate temperature is increased to 600°C . The stronger PL intensity of Eu^{2+} at higher temperature (see Fig. 4) is caused by larger grain size and may also be related to the (111) orientation of $\text{SrS:Eu}^{2+}, \text{Sm}^{3+}$ thin films [12].

Acknowledgments

This work was supported by NSF DMR 9020304.

Conclusions

The effects of growth conditions on microstructure and luminescence properties of SrS:Eu^{2+} , Sm^{3+} thin films were studied using TEM, x-ray and PL measurements. The PL emission intensity of Sm^{3+} is very sensitive to deposition rate. High emission intensity was observed on samples grown at higher growth rate of $30\text{\AA}/\text{s}$. Good crystallinity was also obtained for this growth condition. We suggest that under this growth condition the concentration of Sm^{3+} is higher. However, at lower growth rates the intensity of the Sm^{3+} emission is low, even when the grains are large. We believe that this is because some Sm ions are in divalent states at the grain boundaries. The substrate temperature does not have a strong effect on the Sm charge states, but affects the orientation of the thin films. Between 500°C and 550°C the films tend to have (110) orientation. Above 600°C , the films are strongly oriented to the [111] direction. In contrast, the brightness of the Eu^{2+} emission increased with increasing substrate temperature.

References

- [1] K. Onisawa, K. Taguchi, M. Fuyama, K. Tamura, Y. Abe, and Y. A. Ono, *J. Electrochem. Soc.* **136**, 2736 (1989).
- [2] K. Onisawa, M. Fuyama, K. Taguchi, K. Tamura, and Y. A. Ono, *J. Electrochem. Soc.: Solid State Science and Tech.* **135**, 2631 (1988).
- [3] S. Tanaka, *J. Crystal Growth*, **101**, 958 (1990).
- [4] H. Kobayashi, S. Tanaka, V. Shanker, M. Shiiki and H. Deguchi, *J. Crystal Growth*, **72**, 559 (1985).
- [5] Z. Hua, L. Salamanca-Riba, M. Wuttig, and P. K. Soltani, *J. Opt. Soc. America, B*, (in the press).
- [6] W. Lehmann and F. M. Ryan, *J. Electrochem. Soc.: Solid State Science*, **118**, 477 (1971).
- [7] N. Yamashita and S. Asano, *J. Phys. Soc. Jpn.* **56**, 352 (1987).
- [8] J. W. Allen, L. I. Johansson, I. Lindau and S. B. Hagstrom, *Phys. Rev. B*, **21**, 1335 (1980).
- [9] G. K. Wertheim and G. Crecelius, *Phys. Rev. Lett.* **40**, 813 (1978).
- [10] W. Lehmann, *J. Lumin.* **5**, 87 (1972).
- [11] J. A. Thornton, *Ann. Rev. Mater. Sci.* **7**, 239 (1977).
- [12] K. Tanaka, A. Mikami, T. Ogura, K. Taniguchi, M. Yoshida, and S. Nakajima, *Appl. Phys. Lett.* **48**, 1730 (1986).

MICROELECTRONIC DEVICES : PROSPECTS FOR RARE-EARTHS

LEO ZAKHARENKOV, VALERI GOLUBEV, VITALI KOZLOVSKII

St. Petersburg Technical University, Experimental Physics Dept., Radio & Physical Dept., Polytechnicheskaya St., 29, St. Petersburg, 195251, Russia.

The report submitted contributes to the series of research works in the spheres of rare-earth (RE) application to electronic industry, and namely, to the production of such devices as surface-barrier structures, solar cells' elements.

Schotky barriers.

Schotky barriers (SB) based on III-V compounds are of interest both as discrete devices, and as integral microelectronics elements. It has been found out that the main impediment to manufacturing of SB-containing structures, such as InP-based ones, is due to the fact that their parameters are much more susceptible to the environment of their formation, than those of other semiconductors. This results in the failure to reproduce their characteristics. Furthermore, it impedes the attempts to develop their industrial fabrication know-how.

Most frustrating of all the properties of the existing III-V semiconductor-based barrier structures are the following :

- impurities diffusion out of the semiconductor bulk to the barrier area, with the structure keeping operating (this drawback is inherent in the structures of all devices);
- conductive non-stable native oxides (NO) available on the surface of the semiconductor (the more so with regard to indium-based compounds), which considerably reduce the SB parameters and deteriorate the degradation qualities of the devices.

To improve the electric and physical parameters of SB, containing InP and InGaAs, RE have been applied, standard Au-n-InP(InGaAs) SB being chosen as the elements to compare them with. Au-Ni-Yb-n-InP(InGaAs) surface barrier structures were fabricated by vacuum evaporation of metals onto the wafer, heated to 70°-100°C, within one technological package. All the structures were subsequently heat-treated in vacuum.

I-V, C-V characteristics have been read on the structures obtained, the most attention being paid to leakage currents and break-down voltage. The results of the experiments are demonstrated in table I, fig. 1.

Presented are SB parameters with RE (Yb) optimum thickness of 15-20 nm. Increase of RE layer thickness brings about the decrease of reverse currents, growth of the imperfection factor and deterioration of C-V characteristics.

The temperature range changing from 77 to 350K, the reverse curve of I-V and break-down voltage of RE containing structures demonstrate the same character of temperature dependence as that of Au-n-InP, while the temperature coefficient of break-down voltage keeps within the limits calculated for Au-InP $\sim (2-3) \cdot 10^{-2}$ eV/K. Grounding on the results of the measurements taken after one hour period of 200°, 300°, 400°C heat treatments, it is demonstrated that multilayered M-RE-InP structures exhibit higher thermal stability in comparison with M-InP. The transformations in the reverse curve of I-V are observed only after a half an hour period of over 480-500°C heat treatment.

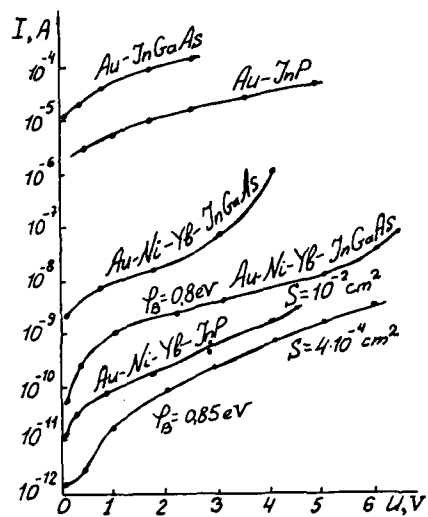


Fig. 2.

C-V characteristics of structures :

- 1 - Au-SiO₂-InP
- 2 - Au-Yb₂O₃-InP

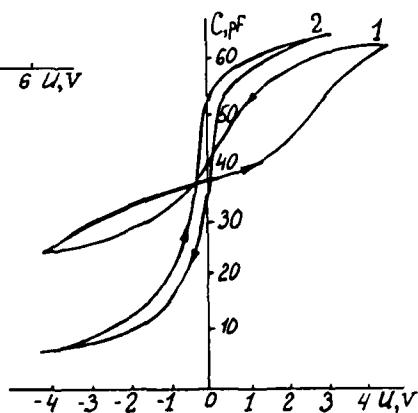


Fig. 3.

C-V characteristics of structures :

- 1 - Al-SiO₂-GaAs
- 2 - Al-ErF₃-GaAs

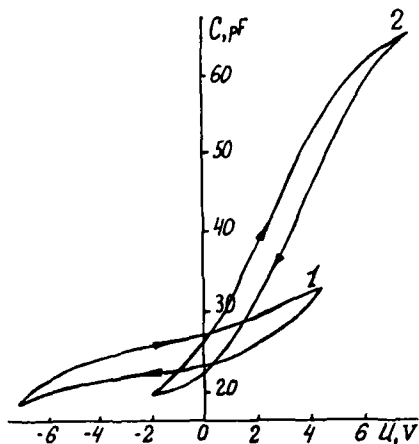


Table I
Vacuum evaporated InP based Schotky
barriers parameters (300K).

Structure	Electron concentra- tion, cm^{-3}	Imperfec- tion factor	Barrier's height, eV		Break-down voltage, V	Leakage current, A
			I-V	C-V		
Au-n-InP (100)	$8 \cdot 10^{15}$	1.08	0.65	0.656	12-14	10^{-5}
	$2 \cdot 10^{16}$	1.12	0.64	0.62	6-8	$10^{-5}-10^{-6}$
	$8 \cdot 10^{16}$	1.22	0.59	0.62	5-6	10^{-5}
	$2 \cdot 10^{17}$	1.27	0.57	0.61	3-4	10^{-4}
	$2 \cdot 10^{18}$	1.34	0.52	0.58	2-3	10^{-4}
Au-Ni-Yb-n-InP (100)	$8 \cdot 10^{15}$	1.12-	0.83-	0.85-	16-18	$10^{-10}-10^{-12}$
$d_{Yb}=15-20\text{nm}$	$2 \cdot 10^{16}$	1.4	0.91	1.03		

There are similar corrections of all SB parameters on Au-Ni-Yb-n-InGaAs with $n \sim (0.4-1) \cdot 10^{16} \text{cm}^{-3}$.

What is the role of RE, as we see it ?

First, RE play the part of the inner getter of uncontrolled impurities in the surface area of the wafer, generating the pure contact adjacent zone for SB's formation. With RE atoms distributed inside the semiconductor deep from the surface, the diffusion barrier is formed for the impurities, diffusing from the bulk SB zone, thus resulting in the degradation properties improvement.

Secondly, the subsequent heat treatment of the barrier brings about chemical interaction between RE and unstable native oxides In_2O_3 and Ga_2O_3 and their substitution for an oxide of Yb_2O_3 type with good dielectrical properties. Actually, heat treatment occurs simultaneously with the partial diffusion of RE into the bulk of the semiconductor, which results in the effect, demonstrated in p.1.

Thirdly, RE layer impedes Me(Au) and III-V atoms mutual diffusion, which reduces the smearing of contact-adjacent zone.

MIS - structures.

In view of the change-over from silicon to III-V compounds for MIS-structures, it becomes pressing to develop the low-temperature technique for manufacturing of dielectric layers.

Native conducting oxides, available on the surface of a semiconductor, as well as the variation of the barrier stoichiometry during heat treatments in the process of the dielectric layer formation, give rise to instability of electric characteristics, high surface states density (N_{ss}), coming over $10^{12} \text{eV}^{-1} \cdot \text{cm}^{-2}$, and the larger hysteresis value.

In this case, RE or rather their oxides, turn out to be the most promising to be applied in MIS-technology.

It should be noted that RE oxides have the following advantages : high thermostability, relative simplicity of their manufacturing at low temperatures, binding defects into electrically inactive compounds due to gettering properties inherent in RE. Besides, RE oxides have the dielectric constant (3-4) times larger than SiO_2 , with considerable electric strength of their layers ($E_{br-down} = 1 - 3 \cdot 10^6 \text{V} \cdot \text{cm}^{-1}$).

Dielectric layers of RE oxides have been manufactured by two methods :

a) oxidizing RE layers produced by thermal evaporation in vacuum in the open at $T = 250^\circ\text{C}$,

b) evaporizing of RE at temperature in the zone of oxygen fed onto unheated wafer (so called, "oxygen shower").

Apart from RE oxides, there have also been involved the evaporized RE fluorides - LaF_3 , YF_3 , DyF_3 , ErF_3 . To control electric and physical parameters of the surface of InP and GaAs wafers, MIS-structures containing such traditional dielectrics as SiO_2 , ZnSe, GeO and amber, have been chosen as the compounds, subjected to the test.

Dielectric-semiconductor interface has been investigated by C-V and G-V techniques at wide frequency (200Hz - 1 MHz) and temperature (77-300K) range.

The specifications for manufacturing, as well as the parameters of MIS-structures, are demonstrated in Table II, fig. 2,3.

Table II.
Specifications for manufacturing of InP & GaAs - based
MIS-structures and their parameters.

Structure, the method of dielectric manufacturing	$N_{ss}^{\text{min}}, \text{eV}^{-1}\text{cm}^{-2}$	N_{tr}, cm^{-2}	$Q_F, \text{cm}^{-2}\text{Coul}$	$\rho_{\text{diel}}, \text{Ohm}\cdot\text{cm}$
Vacuum evaporation Al- SiO_2 -n-InP Al-GeO-n-InP Al-ZnSe-n-InP Al-amber-n-InP	$(0.5-1)\cdot 10^{11}$ $3.7\cdot 10^{10}$ $> 10^{10}$ $3.5\cdot 10^{10}$	10^{12} $1.3\cdot 10^{12}$ $5\cdot 10^{11}$ $1.3\cdot 10^{12}$	(+)	10^{15}
Al- Yb_2O_3 -n-InP a) thermal Yb oxidation b) Yb evaporation in "oxygen shower"	$6.6\cdot 10^{11}$ $1.5\cdot 10^{10}$	$2.3\cdot 10^{11}$ $2.5\cdot 10^{11}$	$(+)6.1\cdot 10^{11}$	10^{13} 10^{15}
Vacuum evaporation Al- ErF_3 -InP	$2\cdot 10^{10}$	-	$(+)1.8\cdot 10^{11}$	
Vacuum evaporation Al- SiO_2 -n-GaAs Al-amber-n-GaAs	$6\cdot 10^{12}$ $4\cdot 10^{12}$	$4\cdot 10^{12}$ $> 10^{12}$	(+)	10^{15}
Al- Yb_2O_3 -n-GaAs a) Yb evaporation in "oxygen shower" b) additional annealing in the open at $T = 400^\circ\text{C}$	$2\cdot 10^{12}$ 10^{12}	$> 10^{12}$ $> 10^{12}$	(+)	10^{15}
Vacuum evaporation Al- ErF_3 -n-GaAs	$6\cdot 10^{11}$	$< 10^{12}$	(+)	-

Note: $d_{\text{diel}} = 1000-2000\text{\AA}$, N_{ss} - surface states density related to eV , N_{tr} - traps density, Q_F - fixed charge in dielectric.

The comparative analysis demonstrates, that RE application in the "oxygen shower" technique makes it possible to get N_{ss} one-second - one-third of its previous value and to reduce the density of traps (3-4) times for MIS-InP with the traditional dielectrics.

In reference to GaAs, reduction of these parameters is less tangible. Presumably, that is a consequence of non-optimal heat treatment regimes of the structures, heat treatment following the isolating layer evaporation.

InP- and GaAs- based RE fluorides application proceeds from the modification activity of fluoride ions with regard to the native oxides of the semiconductor.

For all the set of fluorides, InP structures had the lowest N_{ss} . The minimum value of N_{ss} for GaAs ran $\sim 6 \cdot 10^{11} \text{ eV}^{-1} \cdot \text{cm}^{-2}$, which is several times less than for RE oxides containing structures.

Hysteresis on C-V parameters was smaller with regard to RE containing structures.

RE application as dielectrics contributed to the structure formation with positive charge, capable of shifting to the Yb_2O_3 (ErF_3) - InP interface due to the electric field, and acting as surface states.

The opportunity to monitor the amount of mobile positive ions, to shift them towards the interface with a semiconductor or to confine them to the bulk of the isolator, "freezing" them at low temperatures, gives the necessary prerequisites for different devices to be generated, e.g. for charge transferred devices.

InP (GaAs) RED structures in the state of disbalanced exhaustion are distinguished by their high illumination responsivity and can be used as photodetectors.

In general, RE containing dielectric layers are peculiar for their better adhesion with semiconductors and higher ruggedization, comparing with conventional isolators.

Radiation resistant (RR) material for solar cells.

One of the main considerations, accounting for the persistent interest to RE, is their ability to stimulate resistance to irradiation within semiconducting materials and devices (e.g. within silicon). Such influence hasn't been observed so far for GaAs devices.

The cause of the influence deficiency has been so far considered to be the behaviour of RE atoms, as inefficient sinks of radiation defects (RD) in n-GaAs lattice. We have come to the idea that the cause is something quite different. Rather, it is due to low mobility of the primary RD, generated in n-GaAs by irradiation. It is well known that RD, generated in n-GaAs by irradiation are point Frenkel pair defects (FP), which are stable at room temperature, and dissociate into mobile components, as vacancy and interstitial type defects, at $T = 80-100^\circ\text{C}$.

This assumption has contributed to launching a set of experiments in the investigation of the effect, produced by RE atoms upon the character of RD formation in n-GaAs at the elevated irradiation temperatures, and the subsequent instructions how to improve RR semiconductor devices, e.g. solar cells at the space stations, operating in the zones of elevated temperatures.

We have researched the conductivity compensation of n-GaAs epitaxial layers due to electron irradiation at temperatures ranging from 20° to 250°C . The layers have been produced by liquid phase epitaxy with Yb doping in the concentrations of $3 \cdot 10^{-3} - 5 \cdot 10^{-2} \text{ wt.}$

Figure 4 illustrates the results of the experiments performed, presented as the ratio (η) of the charge carrier removal velocity in Yb - containing specimens numbering $5 \cdot 10^{-2} \text{ wt.}$ (curve 1) and $3 \cdot 10^{-3} \text{ wt.}$ (curve 2) to the charge carrier removal velocity in undoped samples depending on the irradiation temperature (Q).

The layout makes it clear that there is an abrupt change in the behaviour of the curves with Q increase over 100°C . $(\partial \eta / \partial Q)_{\text{Yb}}$ value decreases faster than $\partial \eta / \partial Q$ and at $Q = 150^\circ\text{C}$ η is ~ 0.4 for $C_{\text{Yb}} = 5 \cdot 10^{-2} \text{ wt.}$, and η is 0.6 for $C_{\text{Yb}} = 3 \cdot 10^{-3} \text{ wt.}$. Further increase of Q to 200°C results in the increase of η up to 0.5 and 0.7 respectively, reaching $\sim (0.8-0.9)$ at $Q = 250^\circ\text{C}$.

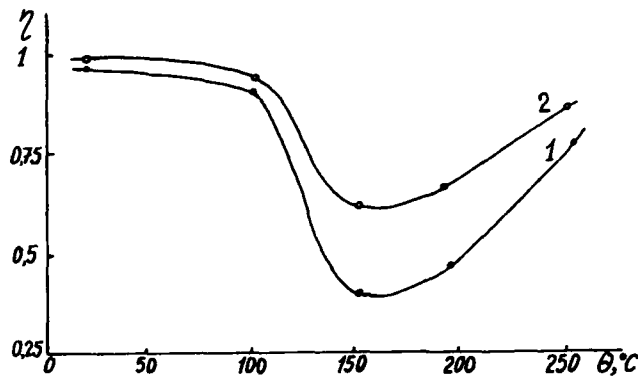


Fig 4.

Ytterbium influence
on the parameters
stability of solar
cells

- 1 - [Yb] = $5 \cdot 10^{-2}$
wt. %
2 - [Yb] = $3 \cdot 10^{-3}$
wt. %

Assuming that each RD, accounting for n-GaAs conductivity compensation, generates single-charged deep trapping level, the charge carrier removal velocity $\partial n / \partial t$ becomes equal to the RD introduction rate.

Quasi-balanced RD concentration determining the removal carriers concentration can be found from the continuity equation $\partial N / \partial t = G - N / \tau$, where G , τ are the generation tempo and RD lifetime, with $N = G \cdot \tau$ under stationary conditions. Since under fixed irradiation conditions G does not actually transform with the change of C_{Yb} and Q at temperatures ranging from 20° to 250°C, hence $\partial n / \partial t$ transformations are due to solely τ change.

FP's lifetime is attributed to two main processes - dissociation and annihilation of FP components with E_d and E_p energy barriers for these processes reaching the value, when the generated FP are stable at room temperature. It is known from the previous publications, that the utter lowest limit of the temperature activation of FP components in n-GaAs reaches the value of 80° - 100°C. That is why irradiation at $Q > 100^\circ\text{C}$ results in FP dissociation. Their mobility grows with Q rise. They have better chance to overtake the impurity atoms, forming complex defect compounds.

Dramatic η decrease, observed in Yb doped specimens at $Q > 100^\circ\text{C}$ testifies on behalf of this model. η - C_{Yb} relation at fixed irradiation temperatures (ranging from 100° to 250°C) demonstrates high efficiency of Yb atoms as either annihilation centres, or capture centres.

At higher irradiation temperatures (250°-350°C) $\partial n / \partial t$ distinctions for doped and undoped specimens are actually negligible and η value tends to unit.

To supply an adequate explanation for it, it is not enough to allow for only the dissociation process, which dominated at low Q .

It has to be presumed that the dramatic growth of annihilation processes at $Q > 250^\circ\text{C}$ seems to be due to decrease of E_p energy barrier following the change in the charge states of the interacting defects.

Thus, the results obtained demonstrate that ytterbium atoms in n-GaAs considerably reduce the rate of RD addition, therefore, making it possible to improve the parameters of irradiation responding devices.

It is well known that photo current of solar cells is determined by the diffusion length (or lifetime) of excess minority carriers and decreases abruptly with RD concentration growth.

The results and conclusions, we have come to in the present investigation, may be of interest for stability enhancement of n-GaAs based devices, operating at $Q > 100^\circ\text{C}$, namely solar cells.

The authors are thankful to Eng. A.Sokolov for manufacturing all MIS-structures.

PART VI

Theory and Models

ELECTRON STRUCTURE AND MECHANISM OF EXCITATION OF THE RARE-EARTH IONS IN THE III-V SEMICONDUCTORS

VADIM F. MASTEROV

State Technical University, Experimental Physics Department, 195251
St. Petersburg, Russia

ABSTRACT

The review of results of EPR, ODMR, RBS and PL investigations of the III-V semiconductors doped with rare-earth elements is represented. The possible sites of RE related centers in hosts are discussed. The possible mechanism of excitation of intrashell f-f transitions is considered. The simple theoretical model of the substitutional RE center in a binary semiconductors is discussed.

INTRODUCTION

There are two main reasons of an interest of researchers to semiconductors doped with rare-earth (RE) atoms. The first, its electron structure is differenced from other impurities. The second, a possibility of preparing semiconductors having new magnetic and optical properties.

In the last few years RE doped semiconductors have attracted much attention for their potential application to light emitting devices with temperature stable wavelengths. These materials combine the advantages of atom-like, intra-4f-shell transitions of RE-dopands with ability of semiconductors to activate the emission by minority-carrier injection.

Systematic investigations of semiconductors doped with rare-earth elements had started over a decade ago. Over the next some years several technology methods were used for preparing these materials. At the same time an assortment of the experimental methods used for investigation of the states RE dopands in semiconductors increased. In parallel with traditional radio- and optical spectroscopy the Rutherford backscattering channeling and photo electron spectroscopy have started use at the last few years. The number of investigating materials have increased also. The states of RE impurities are researching in solid solutions on base III-V compounds, in III-VI compounds among silicon and III-V's.

In this work we consider an electron structure of some types of RE centers in semiconductors and a possible mechanism of activation of the f-f luminescence in binary III-V compounds according to an analyses experimental results and simple theoretical model of the RE center in these materials. In conclusion some ways of development of studies RE doped semiconductors are discussed.

CHARACTERISTIC OF THE TECHNOLOGY OF SEMICONDUCTORS DOPED WITH RARE-EARTH ELEMENTS

Rare-earth-doped single crystal and epitaxial films have been grown using all the technological methods: growth of dendritic GaP and InP crystals from nonstoichiometric melts [1,2]; the Czochralski method in the case purity III-V's [3]; synthesis and diffusion through the melt of GaAs and InP [4]; horizontal zone melting of GaAs and GaSb [5]; molecular beam epitaxy III-V's and Si [6]; ion-implantation doping of III-V's and Si [7,8]; MOCVD [9,10] et al.

The main difficulty in using rare-earth elements is their extremely high chemical activity. Consequently, serious problems are encountered in the preparation of ultra pure RE elements and their storage. A special problem in the technology of RE-doped semiconductors is the selection of the container material. The usual quartz equipment is chemically reduced by rare-earth, which results in contamination of growth crystal with silicon.

whereas the RE elements becomes bound forming complexes with oxygen. That's why the methods using noncontact material of container and semiconductor (MBE, MOCVD) are preferred.

THE EXPERIMENTAL RESULTS REVIEW

Electron paramagnetic resonance (EPR) is most effective method of an investigation of ground state of paramagnetic centers, their symmetry and charge state. The useful information on excited states of RE ions in semiconductors may be obtained by ODMR and Zeeman spectroscopy.

The EPR studies of InP:Yb [11-15]; InP:Gd [16]; InP:Er [17]; GaAs:Er [18,19] have shown that these centers have charge state 3+ and this state is independent of conductivity of material (n- or p-type). The parameters of EPR spectra are represented in Table.

Center	g-factor	$A, 10^{-4} \text{ cm}^{-1}$	B.Oe	$\Delta H_{pp}, \text{Oe}$	λ	Ref.
Ground state						
InP:Yb ³⁺ (cub)	3.291	886(¹⁷¹ Yb) 247(¹⁷³ Yb)	3-4	3	≤0.05	[13]
InP:Yb ³⁺ (ax)	3.09(1) 3.39(1)	910(¹⁷¹ Yb) 249(¹⁷³ Yb)	0.1(1) 12(1)	12	0.05	[14]
InP:Er ³⁺ (ax)	5.899(1) 5.954(1)	210(¹⁶⁷ Yb)	-	12	0.05	[17]
GaAs:Er ³⁺	5.921	208(¹⁶⁷ Yb)	-	11		[19]
Excited state						
InP:Yb ³⁺	$g_J(5/2)=0.578$ $g_J(5/2)=0.62$				0.244 0.21	[20] [21]

A - hyperfine constant; B - superhyperfine constant;
 λ - hybridization degree.

It should be noted that the line-width of EPR for RE³⁺ centers in III-V's is order of magnitude less than the line-width for transition metal centers in the same materials (for example, 120 Oe for InP:Fe).

Therefore, we can note for ground states of RE centers the next conclusions:

1. The charge state of the RE centers in III-V's is 3+.
2. The hybridization degree of the ground state of rare-earth ion with the host states is very weak ($\lambda \approx 0.05$).
3. The RE centers registrant by EPR have cubic or weakly distorted cubic symmetry.

The special interest represents a determination of the parameters of the excited states of the RE centers in semiconductors. These data were obtained by the optical detection EPR method (ODMR) [20] and the study of Zeeman effect involving intra-center transitions [21]. The results of these investigations are shown in the Table. They indicate that delocalization of f-electrons in excited state of the Yb³⁺ in InP is considerably greater than in the ground state ($\lambda \approx 0.24$).

The important problem is a determination location of an RE atom in host. The most reliable method for it is Rutherford backscattering (RBS) and channeling. Analyses of RBS data has revealed that ytterbium in InP is in substitutional site, probably substituting for In [22]. Recently the results of RBS studies for GaAs:Er were reported [23,24]. Authors of these works have shown that Er atoms occupy a different sites: 4As or 4Ga tetrahedral interstitial; tetrahedral interstitial with defect or impurity; substitutional in segregated ERAs. But there is no Ga atom in substitutional site at all. The same results have been obtained for GaAs:Yb [25]. There are not RBS data for InP:Er. At the same time the parameters of EPR spectra for cubic centers Er in InP and GaAs are quit closed (see Table) and it is felt that they occupy the same sites in the both materials. However, the fact of the different Er- and Yb- sites in InP is incomprehensible.

Summing the results of KPR and RBS studies, we would note:

1. The Yb atoms substitute the In atoms in InP.
2. The Kr atoms in GaAs place several sites and tetrahedral interstitial also.
3. The one of centers Er in InP has cubic symmetry and its EPR parameters quite closed to cubic Er center in GaAs.
4. The other RE impurities or Yb and Er in other materials have noncubic symmetry interacting, probably, with defects or impurities.
5. The degree of hybridization of ground states RE ions with host states is weakly ($\lambda \leq 0.05$). On the other hand, the excited state of Yb ion in InP is considerable delocalized ($\lambda \approx 0.24$).

The main interaction splitting the terms of the RE ions is spin-orbital interaction. The both ground and excited states are splitting in crystal field additionally. The energetic diagram for the some RE ions is represented in Fig.1 (splitting in crystal field is not shown). At the present time the intrashell photo-luminescence (PL) of trivalent ions Yb,

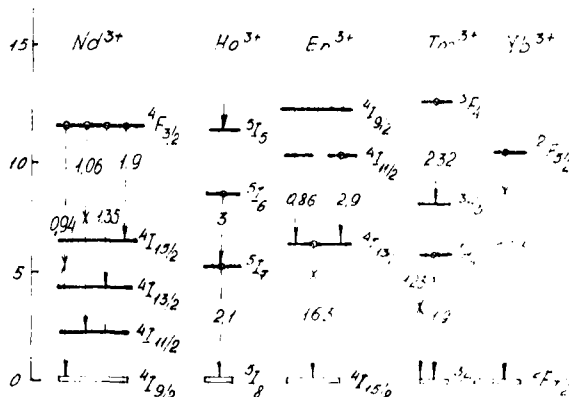


Fig.1 Laser's channels of RE^{3+} ions in crystal of type $Y_3Al_5O_{12}$ [27].

The transition energies show in μm ; x-transitions observed in semiconductors.

Kr, Tm, Nd in III-V's have been studied.

The relative energies of the levels shown in Fig.1 are little affected by the host because they determined mainly by spin-orbital interaction and may be changed only if wave functions of "f-electrons" of RE center in crystal are not pure f-functions and they are mixed with host wave functions.

As noted above, Yb atom substitutes In atom in InP and its solubility is of the order $10^{19} - 10^{20} \text{ cm}^{-3}$ by RBS [22] and KPR [13]. The excitation of 4f-electrons can be produced by either direct photo-excitation, if the photon energy is equal to distance between F(7/2) and F(5/2) levels, or excitation of host and energy transfer from it to RE f-electrons. The main peculiarities of the Yb PL spectrum are:

1. When monitoring the intensity of the major luminescence line, efficient excitation is accomplished only via the band gap and near band gap region. Maximum signal is observed for excitation with energy of the free exciton (FE) or near to it [26].

2. The n-type samples InP:Yb almost constant intensity for temperatures between 4 and 40K was observed [26]. After slow decrease in the intensity between 40 and 80K a step drop-off takes place. A satisfactory theoretical fit to the data can only be obtained assuming a thermally activated dissociation of the luminescent complex according to formula [26]

$$I_{PL} \propto [1 + c_1 \exp(-E_1/kT) + c_2 \exp(-E_2/kT)]^{-1}, \quad (1)$$

where $E_1 = (7-19)\text{meV}$ (in different Refs); $E_2 = (119 \pm 10)\text{meV}$ [26].

However, there is not decrease in intensity of luminescence for temperatures between 4 and 80K for high doped samples InP:Yb, as it is shown in fig.2 [27].

3. There is a minimum of conductivity near FE energy in photoconductivity spectrum [26]. It follows from these data that free excitons trapped immediately after their generation very efficiently.

The other situation takes place in III-V's doped with erbium. Sometimes the Er-related luminescence was not observed at all, although in the same samples the KPR spectrum of the cubic (or almost cubic) centers of trivalent erbium was indicated very well [13,18]. When Er-related emission due to transitions between $^4I_{13/2}$ and $^4I_{15/2}$ levels has observed, erbium centers are noncubic. The main peculiarities of the Er-related luminescence:

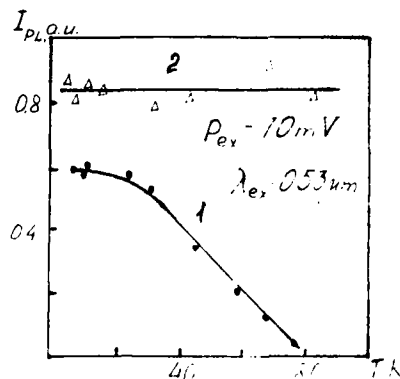


Fig.2 The temperature dependence of the integral intrashell luminescence main line for samples InP:Yb

1- $n[\text{Yb}] = 10^{18} \text{ cm}^{-3}$ (cubic KPR-centers);
2- $n[\text{Yb}] = 5 \cdot 10^{19} \text{ cm}^{-3}$ (axial KPR-centers) [27].

1. The Er-related emission in III-V's at $\lambda = 1.54\mu\text{m}$ is observed at the room temperature.

2. The PL intensity and the PL decay time constant are not changed for temperatures between 4 and 200K. In MOCVD layers InP:Er it was obtained the Er-related PL intensity increases nearly to erbium concentration with minor saturation of higher doping levels. At about 10^{18}cm^{-3} , however, the PL intensity saturates and shows an abrupt decrease at concentrations between $5 \cdot 10^{18}\text{cm}^{-3}$ and $1 \cdot 10^{19}\text{cm}^{-3}$ [28].

The Nd-related PL spectrum for GaP consists of two groups of lines at regions of wavelengths $0.9\mu\text{m}$ and $1.1\mu\text{m}$ [29]. These groups of lines are due to the transitions between $^4F_{3/2}$ and $^4I_{9/2}$, $^4I_{11/2}$ states of noncubic Nd^{3+} centers. The same spectrum was observed in MOCVD layers GaAs:Nd [30]. Quite recently [31] it was noted that the energy separation between the spin-orbit-splitting levels are smaller for "dominant" Nd center in GaP when compared with the corresponding energy separation of Nd in ionic crystals. It is possible if only the f-state of Nd center is mixed with host states. Really, spin-orbit-interaction operator is

$$V_{sl} = \sum \alpha_1 l_1 s_1, \quad (2)$$

where

$$\alpha_1 \propto dU/dr_1 \times \hbar^2 / 2m^2 c^2 r_1. \quad (3)$$

Therefore, in order to the spin-orbit-splitting decrease the radius of the f-electrons r_1 must be increased. It is possible if these states are not a pure f-states but its wave functions are linear combination of atomic orbits including the orbits of neighbors.

The characteristic 4f transitions of trivalent thulium InGaAs, AlGaAs, InP, GaP and Si substrates implanted with Tm [32] and MOCVD layers InP, GaAs, GaP and GaInP doped with Tm [33] were reported quite recently. The emissions, which are due to spin-orbit levels $^3H_5 - ^3H_6$ of $\text{Tm}^{3+}(4f^{12})$ are centered around $1.23\mu\text{m}$ and vary in structure from host due to the difference in crystal field. Additionally authors of [33] the Tm-related emissions at $1.9\mu\text{m}$ both in GaAs and GaInP observed. These emissions are due to $^3H_4 - ^3H_6$ electronic transitions [33].

The experimental fact that f-f emissions are observed by excitation energy corresponding to band-band transitions indicates the possibility of observation of electroluminescence (EL) related to RE ions in semiconductors. Really, in the first experiment the EL was obtained in InP:Yb [34]; later the same results were obtained in p-n structures on base Si:Er [35], GaAs:Er [36], InP:Yb [37]. Authors [38] had prepared the emission structure on base of InP:Er - n-InP (structure n n⁺). It should be noted that in this case the emission intensity of the Er related EL at $1.54\mu\text{m}$ was observed up to the temperature higher than 300K (see Fig.3). The important result of these studies is that EL efficiency decrease more slowly with increasing temperature than the PL intensity does.

THE THEORETICAL MODEL OF RE-CENTER IN BINARY SEMICONDUCTOR

The purpose of this part is to present a simple model of the ground state for a rare-earth substitutional center in a binary semiconductor by taking into account:

1. The effects of intra-atomic correlation leading to the energy

difference between the occupied and empty f-levels.

2. The stabilizing electrostatic field produced by the trivalent RE ion environment in the host.

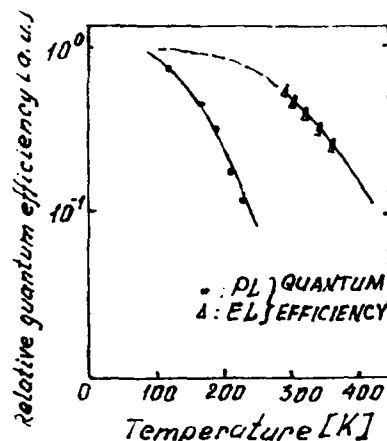


Fig.3 The temperature dependencies of PL (1) and KL (2) efficiency for structure InP:Er - n-InP from work [38].

We use now the principle "local ion bonding" and we don't take into account the d-states of rare-earth atom, which was been used in work [39]. The principle "local ion bonding" is result of an analyses of the experimental data: the hybridization degree of the ground state RE ion with host states is very weak. Therefore, we would be take into account only interaction of s-electrons of the impurity atom with sp^3 -hybrid states of a neutral metal vacancy in binary semiconductor; also we take into account that one of f-electrons is promoted in sp^3 -state. This process is shown in Fig.4. The energy diagram corresponding to formation of the RE center in III-V compounds is represented in the same figure.

In order to describe the ground state of the RE ion in III-V's we are using the method, which was suggested ourselves in work [40] to find the position of levels produced by local perturbation in allowed band scheme of binary semiconductor [41]. Later this method was applied to calculate the state of transition metal and rare-earth elements in III-V's [42,43]. Here we discuss this method very shortly.

Two-band model of an ideal binary semiconductor can be introduced by set of the Green functions $G_0^\alpha(E)$ defined by the relation

$$G_0^\alpha(E) = \{E - \Delta - b_1^2 [E + \Delta - b_2^2 G_0^\alpha(E)]^{-1}\}^{-1}, \quad (4)$$

but with the different positions of midgap point $E=0$ with respect to the vacuum level for each α [index an irreducible representation (a_1 or t_2)]. Parameters Δ , b_1 and b_2 are related to the position of the band edges. We pass to the Green functions (4) for a rare-earth impurity center by inserting the effective energies E_r^α for 6s or 4f electrons instead of the parameter Δ in formula (4):

$$G_r^\alpha(E) = \{E - E_r^\alpha - b_1^2 [E + \Delta - b_2^2 G_0^\alpha(E)]^{-1}\}^{-1}. \quad (5)$$

Here we take into account 1) the perturbation of the bonding ($b_{1\alpha}^2 \neq b_{1\alpha}^2$); 2) the possible charge transfer from the impurity atom to the surrounding B-atoms ($\Delta \neq \Delta$). We use for 4f only t_2 representation, because a_2 and t_1 representations are not hybridized with host states at all.

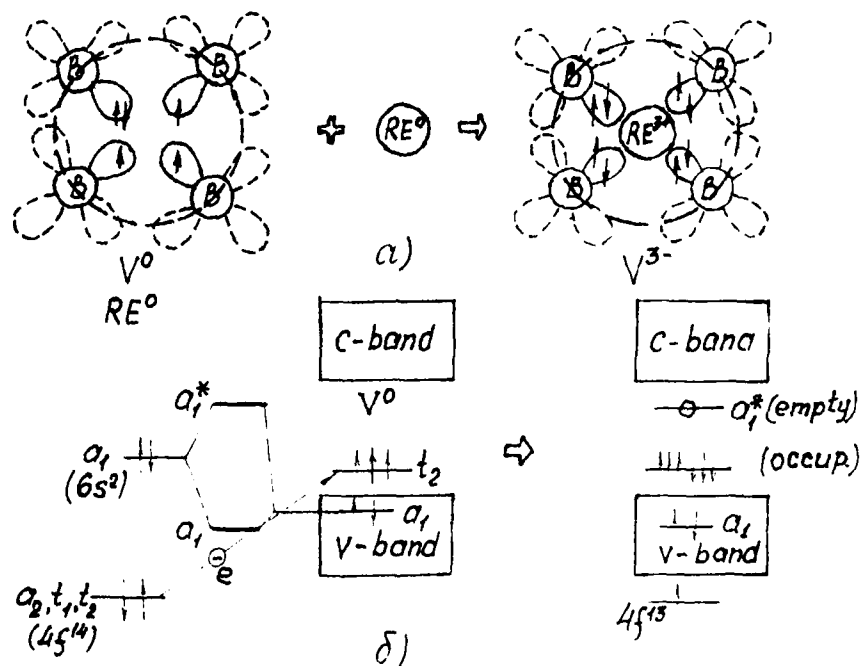


Fig.4 The process of formation RE center in III-V's (a) and the energy diagram corresponding to formation RE center (b).

The poles of G_r^α at $\alpha = a_1$ provide s-like levels a_1 and a_1^* (see Fig.4) which do not enter the subsequent calculations. Our main interest is to estimate the position of the poles $G_r^\alpha(E)$ for $\alpha = t_2$. In this case we can put $(b_{1\alpha})^2 = 0$, because the hybridization of f-states with host states is very weak. Then, we get a pure f-level of t_2 symmetry with energy $E_f^\alpha = E_f$ and t_2 level of sp^3 -hybrid orbital of cation vacancy with energy:

$$E_V = 1/2\delta(b_1^2 + \delta^2 - [(b_1^2 - \delta^2 + 2\Delta\delta)^2 + 4\delta^2 b_2^2]^{1/2}), \quad (6)$$

where $\delta = \Delta - \Delta^* = (U_B - \rho)q$ characterizes the perturbation produced by the transfer of a charge q from a rare-earth atom to B-atoms. The U_B is an intra-atomic integral and a parameter ρ accounts for electrostatic interaction between f-electrons and the electrons of the charged vacancy.

The effective energy E_f in crystal can be written as depending on the

occupation number n_i :

$$E_{f1} = E_f^{\text{core}} + U_{fs} N_s + U_{ff} (N_f - n_i) + \rho_i q, \quad (7)$$

where $N_f = \sum n_i$ and $q = N_f^0 + N_s^0 - N_f - N_s$; $N_{f,s}^0$ is a number of 6s and 4f electrons in a free RE atom; $N_{f,s}$ is the same quantity in the RE ion. We put $N_s = 0$, because a s_1 level is empty.

Using the expressions given above we can obtain the values of energies both for occupied (E_f) and empty (E_f^*) f-levels for Yb impurity in InP. For numerical estimation we use $U_{ff} = 18.5\text{eV}$ and $E_f^0 - 2U_{fs} = -I_f = -19.3\text{eV}$ obtained by us from the data on a free ytterbium atom [43]. The obtained positions of E_f and E_v levels for both $\text{Yb}^{3+} - \text{V}^{3-}$ and $\text{Yb}^{2+} - \text{V}^{2-}$ systems are shown in Fig.5.

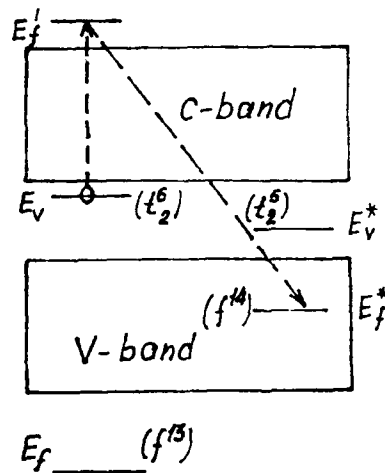


Fig.5 The position of characteristic level for $\text{Yb}^{3+} - \text{V}_A^{3-}$ (left) and $\text{Yb}^{2+} - \text{V}_A^{2-}$ (right)

The last step is to estimate the change of a total electron energy E at transition $\text{Yb}^{3+} \Rightarrow \text{Yb}^{2+}$. Here we use Slater-Janeek theorem, which was substantiated for our model in the previous paper [44]:

$$\partial E / \partial n_i = E_{f1}. \quad (8)$$

Then

$$\Delta E = \int_0^1 E_{f1} dn_i + \int_0^2 E_v(q) dq = \Delta E_f + \Delta E_v, \quad (9)$$

where we used that $dq = -dn_i$.

The first term can be calculated analytically by integration of (7) that leads to an expression:

$$\Delta E_f = -I_f + 2.5\rho. \quad (10)$$

The second term is less than the first and we can neglect it. In result we can come to the conclusion that $\Delta E > 0$ if $\rho > 8\text{eV}$.

We see that in this model 1) a strong electrostatic interaction between f-electrons and electrons localized on sp-hybrids of a charged vacancy is necessary to stabilize the trivalent state of ytterbium impurity with respect to divalent one; 2) the hybridization of 6s electron state with a_1 state of a vacancy can lead to formation of an electron trap level.

ON MECHANISM OF EXCITATION OF f-f EMISSION IN SEMICONDUCTOR

We discuss now the possible mechanism of excitation of f-f transitions on the example of ytterbium impurity in InP. This material is the most studied by EPR, RBS, PL and KL. There are some models of mechanism of excitation of emission for InP:Yb [26,45,46], which are combined by a general assumption: the excitation energy is transferred to RE center from host by Auger process. Here we discuss this process in more detail using the results represented in the previous sections. As it was noted above the emission f-f transitions in trivalent ytterbium ions allowed because its excitation state is hybridized with host state and the crystal has not a center of inversion. That's why the main task now is to describe the process of excitation with the electron structure of Yb ion in general energy scheme of crystal, shown in Fig.6.

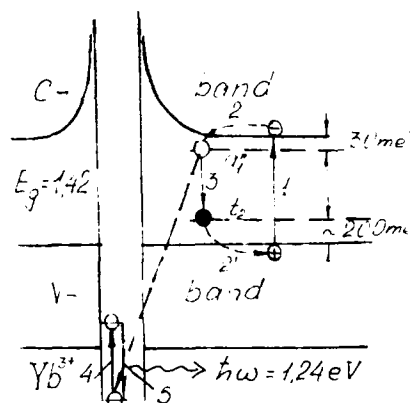


Fig.6 The scheme of excitation of Yb^{3+} in InP; 1-process of excitation of host producing a free exciton or electron-hole pair; 2-trapping of electron on the a_1 level [$E(a_1)=10\text{meV}$]; 2'-trapping of hole [$E(t_2) = 200\text{meV}$]; electron-hole annihilation; 3-the energy transfer to f-electron; 4-excitation of ytterbium ion; 5-photon emission.

In order to estimate the rate of Auger recombination the potential of impurity center can be approximated as zero radii potential[47]:

$$U(r) \propto \delta(r). \quad (11)$$

Then

$$\Psi(r) \approx (2\pi r_0)^{-1/2} r^{-1} \exp(-r/r_0), \quad (12)$$

where $r_0 = \hbar/(2m\varepsilon)^{1/2}$ - size of localized state; ε - energy of impurity center.

In case a) $r_0 \sim a$ (a - lattice constant);

b) $r_0 \sim a_B$ (a_B - Bohr radii)

the rate of Auger recombination may be represented in form:

$$G \propto (E_B/\hbar) \lambda_{ee}^6 n p N I_{cc} I_{ch}, \quad (13)$$

where E_B - Bohr energy of electron-electron interaction; n - electron concentration; p - hole concentration; N - impurity concentration; I_{cc} - overlap integral of an electrons of impurity center; I_{ch} - overlap integral of an electron of conduction band and hole from valence band; λ_{ee} - characteristic length of electron-electron interaction, it is evident that $\lambda_{ee} \propto r_0$ in this case. Then

$$G \propto (E_B/\hbar) r_0^6 n p N I_{cc} I_{ch} \quad (14)$$

where $I_{cc} \approx 1$. In the bulk semiconductor we have: $I_{ch} \propto (kT/E_g)$ and

$$G^0 \propto (E_B/\hbar) r_0^6 n p N (kT/E_g). \quad (15)$$

The other situation takes place in a quantum well. In this case $I_{ch} \propto (\varepsilon_0/E_g)$, where $\varepsilon_0 \propto (\pi\hbar)^2/md^2$; d - width of the well. If the well is rather narrow ($\varepsilon_0 \gg kT$), that the rate of Auger recombination in the well is higher than in a bulk:

$$G^{qw} \propto (E_B/\hbar) r_0^6 n p N (\varepsilon_0/E_g) \cdot G^0 \quad (16)$$

At $E_B \propto 10 \text{ meV}$; $r_0 \propto 5 \cdot 10^{-7} \text{ cm}$; $n=p=10^{18} \text{ cm}^{-3}$; $N=10^{19} \text{ cm}^{-3}$; $T=300\text{K}$; $E_g \propto 1 \text{ eV}$ we have $G^0 \propto 4 \cdot 10^{28} \text{ cm}^{-3} \text{ s}^{-1}$. If the well width is 100\AA we have $G^{qw} \propto 4 \cdot 10^{29} \text{ cm}^{-3} \text{ s}^{-1}$.

In conclusion of this section note some ways of increasing of efficiency of RE related emission in semiconductors:

1. The one of the ways of increasing of efficiency of the RE related emission in semiconductors is producing quantum size structures on their base. The difference of temperature dependencies of PL and EL of the structure on base InP:Er (Fig.3) can be explained by this way, we think. Actually, the effect of heteroboundary on nonradiative recombination of nonequilibrium carries in semiconductor structures was reported in the work [48]. It was shown that the presence of the heteroboundary results in the appearance of a new no-threshold mechanism of Auger recombination: an electron-hole pair is annihilated in the volume of the narrow-band-gap semiconductor and a fast Auger particle is ejected from the subbarrier-motion region located next to the heteroboundary. It was established that the new recombination mechanism has weak power-law temperature dependence and, owing to the efficient long-range action, it is dominant process of nonradiative recombination in micron-size heterostructures.

2. The semiconductor quantum-size structures having varying quantum well depth are of interest to produce a high efficiency RE related emission. In this case the value of a gap (E_g) of the narrow-band-gap semiconductor can be comparable with an energy of excitation of f-f transition.

3. Double doping with both erbium and ytterbium is of interest to excite the Er ion by an emission from Yb, because $\hbar\omega_{em}(\text{Yb}^{3+}) = \hbar\omega_{ex}(\text{Er}^{3+})$.

REFERENCES

1. V.F. Masterov, V.V. Romanov and B.K. Samorukov. *Sov. Phys.-Semicond.* 12, 955 (1978)
2. V.A. Kasatkin, F.P. Kesamanly, V.F. Masterov et al. *Izv. Acad. Nauk SSSR, Neorg. Mater.* 16, 1901 (1980)
3. L.F. Zakharenkov, V.F. Masterov and O.D. Khokhryakova. *Sov. Phys.-Semicond.* 21, 211 (1987)
4. A. Stapor, J. Raczynska, H. Przybylinska et al. *Mater. Sci. Forum.* 10-12, 633 (1986)
5. G. Jsirolek, J. Raczynska and J. Gorecka. *J. Cryst. Growth* 78, 105 (1986)
6. H. Ennen, J. Wagner, H.D. Muller et al. *J. Appl. Phys.* 61, 4877 (1987)
7. H. Ennen, J. Schneider, G. Pomrenke et al. *Appl. Phys. Lett.* 43, 943 (1983)
8. G. Pomrenke, H. Ennen and W. Haydl. *J. Appl. Phys.* 59, 601 (1986)
9. K. Uwai and K. Takahai. *Appl. Phys. Lett.* 51, 977 (1987)
10. K. Uwai, H. Nakagome and K. Takahai. *Appl. Phys. Lett.* 51, 1010 (1987)
11. V.A. Kasatkin, V.F. Masterov, V.V. Romanov et al. *Sov. Phys.-Semicond.* 16, 106 (1982)
12. V.F. Masterov, V.V. Romanov and K.F. Shtel'makh. *Sov. Phys.-Solid State* 25, 824 (1983)
13. V.F. Masterov, V.P. Savel'ev, K.F. Shtel'makh and L.F. Zakharenkov. *Sov. Phys. - Semicond.* 23, 1381 (1989)
14. V.F. Masterov, K.F. Shtel'makh, L.F. Zakharenkov et al. *Sov. Phys.-Semicond.* 25, 225 (1991)
15. B. Lambert, Y. Toudie, G. Grandpierre, A. Rupertand A. LeCorre. *Electron. Lett.* 24, 1446 (1988)
16. V.F. Masterov, V.V. Romanov, B.K. Samorukov et al. *Sov. Phys. - Semicond.* 17, 596 (1983)
17. V.F. Masterov, K.F. Shtel'makh and L.F. Zakharenkov. *Sov. Phys.-Semicond.* 21, 223 (1987)
18. M. Baessler, J. Schneider, F. Kohl et al. *J. Phys. C: Sol. St. Phys.* 20, L963 (1987)
19. P.B. Klein, F.G. Moore and H.B. Dietrich. *Appl. Phys. Lett.* 58, 502 (1991)
20. R. Kullenbach, H.J. Reyher, J. Unruh et al. *Proc. 14th Int. Conf. Def. Semicond. Paris. 1986*, p.214
21. G. Azzodi, J. Weber, Ch. Uihlein et al. *Phys. Rev. B.* 31, 7767 (1985)
22. A. Kozanecki and R. Groetzschel. *J. Appl. Phys.* 68, 517 (1990)
23. A. Kozanecki, M. Chan, C. Jeynes, B. Sealy and K. Homewood. *Solid St. Comm.* 78, 763 (1991)
24. J. Nakota, M. Taniguchi and K. Takahai. *Appl. Phys. Lett.* 61, 2665 (1992)
25. A. Kozanecki and R. Groetzschel. *J. Appl. Phys.* 64, 3315 (1988)
26. K. Thonke, K. Pressel, G. Bohnert et al. *Semicond. Sci. Techn.* 5, 1124 (1990)
27. A.A. Kaminaki, A.K. Aminov, V.L. Ermolaev et al. *Physics and spectroscopy of laser crystal. Moscow, 1986*, p.23
28. K. Uwai, H. Nakagome and K. Takahai. *J. Cryst. Growth.* 93, 583 (1988)
29. J. Wagner, H. Ennen and H.D. Muller. *J. Appl. Phys.* 59, 1202 (1986)
30. M. Taniguchi, H. Nakagome and K. Takahai. *Appl. Phys. Lett.* 58, 2930 (1991)
31. M. Taniguchi and K. Takahai. *J. Appl. Phys.* 73, 943 (1993)
32. G.S. Pomrenke, E. Silkowski, J.R. Colon, D.J. Topp, Y.K. Yeo and R.L. Henggehold. *J. Appl. Phys.* 71, 1919 (1992)
33. K. Pressel, J. Weber, C. Hiller et al. *Appl. Phys. Lett.* 61, 560 (1992)
34. A.G. Dmitriev, L.F. Zakharenkov, V.A. Kasatkin et al. *Sov. Phys.- Semicond.* 17, 1201 (1983)
35. H. Ennen, G. Pomrenke, A. Ammann et al. *Appl. Phys. Lett.* 46, 361 (1985)
36. K. Takahai, P. Whitney, H. Nakagome and K. Uwai. *J. Appl. Phys.* 65, 1257 (1989)
37. W.H. Haydl, H.D. Muller, H. Ennen, W. Korber and K.W. Benz. *Appl. Phys. Lett.* 46, 870 (1985)
38. H. Isahiki, H. Kobayashi, S. Yugo, K. Kimura and T. Ikoma. *Jap. J. Appl. Phys.* 30, L225 (1991)

- 39. C. Delerue and M. Lannoo. Phys. Rev. Lett. 67, 3006 (1991)
- 40. N. P. Ilyin, V. F. Masterov and A. E. Vasilyev. Sov. Phys.-Semicond. 26, 1866 (1992)
- 41. N. P. Ilyin, V. F. Masterov and A. E. Vasilyev. Sov. Phys.- Semicond. 25, 185 (1991)
- 42. N. P. Ilyin and V. F. Masterov. Semicond. Sci. Tech. (in the press)
- 43. A. A. Radzig and V. M. Smirnov. Parameters of Atoms and Atomic Ions. M. 1986, p. 344 (in Russian)
- 44. A. E. Vasilyev, N. P. Ilyin and V. F. Masterov. Sov. Phys.- Semicond. 22, 1253 (1988)
- 45. V. A. Kasatkin, V. F. Masterov, V. P. Savelyev and V. A. Kharchenko. Abstracts of papers presented at Seventh All-Union Symposium on Spectr. of Crystals. 1982, p. 167 (in Russian)
- 46. K. Takahashi and A. Taguchi. Mat. Sci Forum. 83-87, 641 (1992)
- 47. G. G. Zegrya (unpubl.)
- 48. G. G. Zegrya and V. A. Kharchenko. Sov. Phys. JETP. 74, 173 (1992)

THE THEORY OF RARE-EARTH IMPURITIES IN SEMICONDUCTORS

MICHEL LANNOO AND C. DELERUE

Institut d'Electronique et de Microelectronique du Nord (U.M.R. CNRS 9929), Département ISEN, 41, boulevard Vauban, 59046 Lille Cedex, France.

ABSTRACT

The chemical trends of rare-earth impurities in semiconductors are analyzed on the basis of a selfconsistent tight-binding Green's function technique. The 4f states are treated as a frozen core and we get essentially no 5d derived states in the gap. We calculate the 4f ionization levels in the solid and conclude that the stable state is mostly 3+. We then describe the results of a LDA calculation for Er in silicon which we find to be stable in the interstitial position. Finally we consider in some detail the case of Yb in InP where we discuss the possible origin of the shallow gap levels and the mechanisms for luminescence excitation and quenching.

I - INTRODUCTION

The understanding of rare earth (R.E.) impurities in semiconductors is still a challenge both from the theoretical and experimental point of views. Experimentally the most clear-cut case is Yb in InP (see recent reviews in [1, 2]) which is believed to be substitutional on the cation site, contrary to Er for instance which is found to be at several distinct sites, in particular at interstitial positions. On the theory side the first calculation for Yb in InP was made by Hemstreet [3] while, more recently, we have performed a more systematic tight binding study of the chemical trends [4]. In the present paper we first summarize this analysis and show that it is confirmed by independent studies. We then present the results of an LDA calculation for Er in silicon which shows that the stable position is interstitial, leading to gap states in agreement with tight binding. Finally we concentrate on Yb in InP discussing in detail the available experimental data.

II - CHEMICAL TRENDS

If we take the convention that a free neutral R.E. atom has $n+3$ electrons in the 4f, 5d, 6s shells the ground state configuration is $4f^{n+1}6s^2$ for most of these elements. The 4f shell is very contracted on the atom and this contraction increases with atomic number. This is such that, already for Nd ($4f^4 6s^2$), the 4f wave function has its maximum within the $5s^2 5p^6$ closed shell of the Xe structure [5], which thus leads to shielding of the crystal field influence on the f electrons. Contrary to the 4f orbitals, the 6s orbitals are fairly extended (the 6s maximum for Gd lies at 1.8 Å from the nucleus compared to 0.3 Å for the 4f orbitals which can be treated as core orbitals). Finally the 5d states are intermediate, being however more extended than the 3d states of transition metals.

Our description of the chemical trends is based on a tight binding formulation. In this framework the different atomic states (*i.e.* 4f, 5d and 6s) have to be treated in a different way in view of their widely varying extension in space. First of all the 4f states must have fairly small overlap with the s,p states of the neighboring atoms. We thus ignore, in a first step, this overlap and treat them as a frozen core which can be occupied by different numbers of electrons. At the opposite the 6s state is so extended that it will couple strongly and will be spread equally over the valence band bonding states and the conduction band antibonding states. In this tight binding view the electron population of the 6s shell for the atom in the solid

is thus $6s^1$ as is the case for the R.E. metals [6] and the mixed valence compounds [7]. Finally the 5d states, in view of their intermediate behavior, must experience substantial covalent coupling which has to be analyzed in some detail.

From this the physical description becomes very simple. For the opposite reasons discussed above the 4f and 6s states are discarded from the tight binding coupling matrix (4f because they remain atomic like, 6s because they cannot induce states close to the gap and lead to a $6s^1$ configuration). We are thus left with the 5d states which thus represents exactly the same problem as TM (transition metal) impurities, treated with success in ref. [8] on a selfconsistent tight binding basis. The essential difference however is that, for RE impurities, one has to perform several calculations corresponding to different electron populations of the 4f core and ultimately determine which one is the most stable. In the following we consider three possible configurations of the 4f core: $4f^{n-1}$, $4f^n$ and $4f^{n+1}$. As, in our notations, the valence population of the neutral atom is $n+3$, these respectively correspond to the $4+$, $3+$ and $2+$ oxidation states since, in the conventional definition of the oxidation states all valence electrons other than the 4f electrons are assumed to be transferred to the more electronegative neighbors.

Let us then discuss, for a fixed configuration of the 4f core, the nature of the states induced by the coupling of the 5d orbitals with their neighbors. We consider the substitutional case on the cation site. As for TM impurities this can be best understood from a defect molecule model [9] as shown on Fig. 1. The d states behave as e (doubly degenerate) and t_2 (triply degenerate) in T_d symmetry. Their interaction with the t_2 combination of the neighboring sp^3 hybrids gives, in increasing order of energies: a bonding state t_2 , an atomic like state e and an antibonding state t_2^* . This picture essentially reproduces what is obtained from our self-consistent tight binding Green's function calculations. For T.M. impurities the t_2 bonding state falls within the valence band while, eventually, e and t_2^* are found in the forbidden gap [4]. The situation is dramatically different for R.E. substituted on cation sites where we find no gap levels, the bonding state t_2 being still in the valence band while e and t_2^* are now in the conduction band.

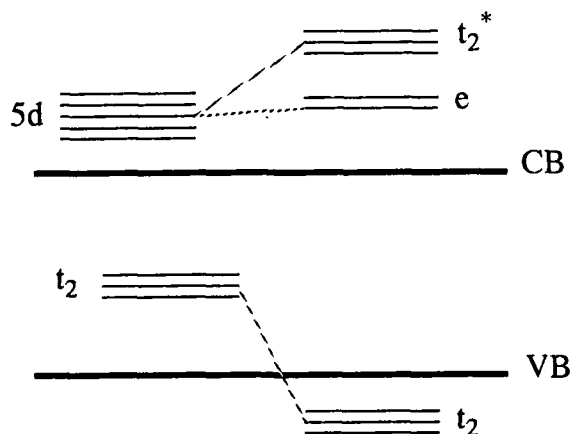


Fig. 1 - Level structure in the defect molecule model.

To understand this we have to make a short comment about the determination of the tight binding parameters. As usual we consider that the atomic energy of the d states in the solid varies linearly with the excess d electron population Δn_d

$$E_d = E_{d0} + U_{dd}\Delta n_d \quad (1)$$

where E_{d0} is taken from the neutral free atom values calculated by Herman and Skillman [10] corresponding to the chosen configuration of the 4f core. Thus U_{dd} is the Coulomb term which accounts for deviations from the neutrality of the atom and is given here the value of 8 eV as in ref. [8] but the results are rather insensitive to the value of this parameter as long as it is large enough. To obtain the tight binding matrix elements coupling the impurity d states to the s,p states of the neighbors we scale them from their known values for TM impurities by means of the Wolfsberg-Helmholtz formula [11]. In this way we find that the ratio of the R.E. to the T.M. values is quite large, of order 2.5. Finally we determine the relative position of E_{d0} with respect to the band structure by calculating the average sp atomic energy of the host semiconductor with the same Herman Skillman procedure which ensures a coherent description.

With all this the reasons why we get no d gap states are twofold: E_d is higher for R.E. than T.M. impurities and the covalent coupling is much larger. This means that the t_2 bonding state remains in the valence band while e and t_2^* of Fig. 1 are pushed to higher energies, i.e. outside the gap. This means that the charge state of the R.E. is completely determined by the core configuration and the nature of the host semiconductor. For a $4f^m$ core configuration (i.e. the $3+$ oxidation state) of a R.E. ion substituted to a cation in III-V materials the 3 extra valence electrons belong to a closed shell as was the case for the cation itself. This corresponds to a neutral charge state of the impurity while, by comparison, the same situation in IV and II-VI semiconductors respectively leads to - and + charge states respectively.

We now have to determine what is the stable configuration of the 4f core. For this we need to calculate the total energy $E(m)$ of the system as a function of the configuration $4f^m$ (with $m = n-1, n, n+1$) of the f core. The next step is to determine the ionization energies $E_{m, m-1}$ defined as

$$E_{m, m-1} = E(m) - E(m-1) \quad (2)$$

whose position with respect to the Fermi level E_F determines the actual stable configuration m : if $E(m, m-1) < E_F$ then one gets the configuration $4f^m$ while one gets $4f^{m-1}$ in the opposite situation. To calculate this quantity (analogous to a one-electron level) we write an equation similar to (1) i.e.

$$E_{m, m-1} = E_{m, m-1}^0 + U_{fd}\delta n_d \quad (3)$$

where $E_{m, m-1}^0$ is deduced from the neutral free atom situation and thus corresponds to an electron transfer from the d to the f shell while $U_{fd}\delta n_d$ is the shift in f level due to the excess δn_d of d electrons on the R.E. impurity. We deduce $E_{m, m-1}^0$ and U_{fd} from free-atom calculations [6,10] while δn_d is deduced from a selfconsistent calculation in the intermediate state $m-1/2$ (for more details see [8, 12]). We perform this calculation for the three configurations $m = n-1, n, n+1$ which correspond to the oxidation states $4+, 3+, 2+$. The results for $E_{n, n-1}$ and $E_{n+1, n}$ which can also be labelled in a more transparent way $E(3+, 4+)$ and $E(2+, 3+)$ are plotted in Figure 2 for Si, InP and CdTe. In fact we found that the chemical trends along the R.E. series are exactly identical within 0.2 eV irrespective of the host

semiconductor, except for a rigid shift of its band structure. This allows to plot the results on a unique diagram for these three and even for all IV, III-V and II-VI semiconductors. This is similar to what was obtained for the d gap states of T.M. impurities and was shown to be due to strong screening occurring at such impurities [4]. The central result of Fig. 2 is that, in most situations, the $E(2+, 3+)$ level falls in the conduction band while $E(3+, 4+)$ lies in all cases within the valence band, the large value of the difference $E(2+, 3+) - E(3+, 4+)$ reflecting the strong Coulomb electron-electron repulsion in the f shell. As the Fermi energy E_F falls within the gap the conclusion is that most R.E. impurities should be in the $3+$ state with possible exceptions near the center and the end of the series and this most probably in the wide gap semiconductors. This conclusion is in fairly good overall agreement with available experimental data as discussed in the following.

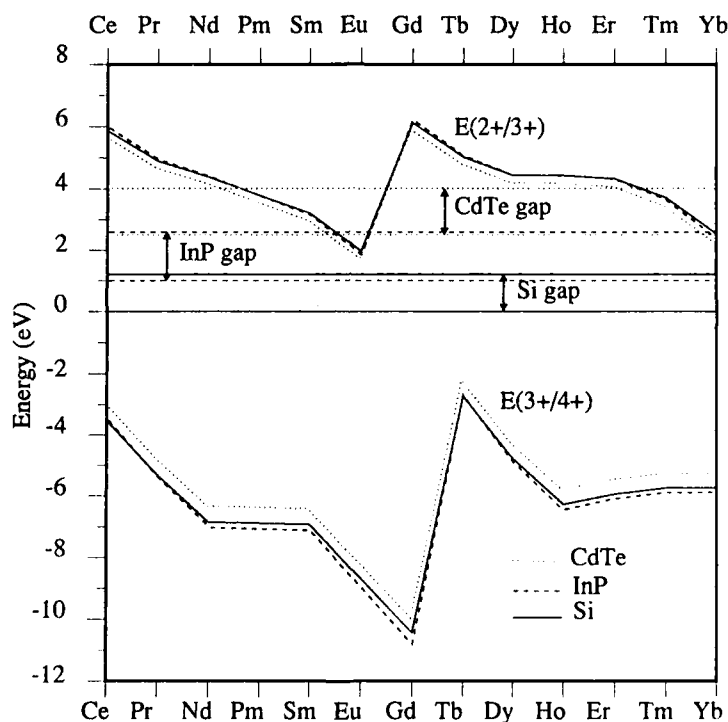


Fig. 2 - Trends in the $E(2+, 3+)$ and $E(3+, 4+)$ levels for different semiconductors

Although our TB calculation can be expected to provide an accurate description of the chemical trends there can be an uncertainty (estimated to be of order 0.5 eV) with regard to the exact location of the curve $E(2+, 3+)$ with respect to the band gap of the host semiconductors. This point was further discussed recently by Langer [13] who based his analysis on the fact that, as demonstrated for T.M. impurities and shown by our calculations, the R.E. ionization energies in the series of isovalent compounds (e.g. III-V or II-VI

semiconductors) should follow a unique curve once the host band structures are shifted by their natural band offsets. This is shown on Fig. 3 (taken from ref. [13]) where are drawn: *i*) our predicted values for CdTe, *ii*) the band gaps of other II-VI semiconductors shifted from CdTe by their natural band offsets and *iii*) our predicted $E(2+, 3+)$ shifted by + 0.6 eV to reproduce the few known experimental values. This shifted curve might then represent a fairly accurate determination of the ionization level $E(2+, 3+)$.

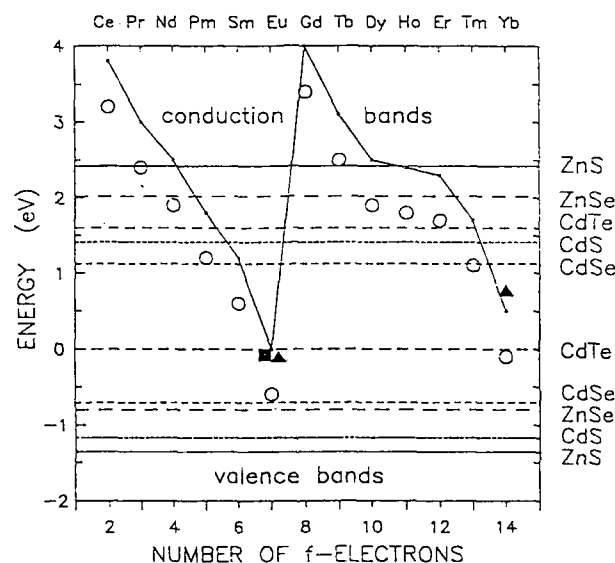


Fig. 3 - Trends in $E(2+, 3+)$ for the II-VI semiconductors.- open circles: our calculated values - full lines: the same curve shifted by + 0.6 eV - filled squares and triangles: experimental values

These general trends are confirmed by experimental observations: in Si, Er is observed in the +3 state, but it seems that most of the impurities are on interstitial sites [17].

In III-V materials one observes Er^{3+} in InP [14, 15], GaAs [15, 16, 17], and GaP [16]; Nd^{3+} in GaAs [16] and GaP [16, 18]; Tm^{3+} in GaAs [16]; and Pr^{3+} in GaP [19]. An interesting case is Yb which seems to be trivalent in GaAs and GaP [20] as well as in n-type or p-type InP [20-24]. Our results agree with this conclusion.

In II-VI semiconductors there is much information for CdTe [25, 26]; Nd, Gd, Er, and Yb are found in the +3 state; Eu always in the +2 state, even in other compounds; and Tm also in the +2 state, but the atomic site is uncertain. These trends are consistent with our results except for Yb which we predict to be Yb^{2+} . One should also note that, for ZnS, there is some evidence [27, 28] that the $E(2+, 3+)$ level lies in the forbidden gap for Eu and Yb, in correspondence with the general trend exhibited by Fig. 2 and 3.

Finally, it is interesting to compare this work to other theoretical studies. The only existing calculation in semiconductors concerns Yb in InP [3] and is based on the X_α scattered wave cluster method. The main conclusion of this study was that some of the 4f states are substantially delocalized, in apparent contradiction with experimental evidence coming from extremely sharp internal transitions. This is probably overestimated, due to the fact that, in this work, the radius of the muffin-tin spheres was arbitrarily modified to adjust the small cluster gap to the experimental one, resulting in an overestimate of the interatomic coupling and thus of the delocalization of the 4f states. However, as discussed in the last section, there must be some amount of delocalization of the 4f shell to interpret the experimental data.

III - ERBIUM IN SILICON

This part summarizes the work described in more detail in ref. [29]. Erbium luminesces in many materials, with a line width and frequency approximately independent of the host [30]. In silicon, it is believed that the erbium defect captures an exciton created either by light or by carrier injection and the recombination energy is transferred to the 4f shell electrons, which are promoted from their $^4I_{15/2}$ Er^{3+} ($4f^{11}$) ground state [31] in the crystal. A photon ($\sim 1.54 \mu$) is emitted when the 4f electrons relax from the $^4I_{13/2}$ Er^{3+} ($4f^{11}$) excited state. This transition is forbidden by electric dipole selection rules for an isolated atom. However, it becomes allowed because the crystal field mixes states of opposite parity. The otherwise weak influence of the host is understandable because the 4f electrons are strongly localized inside the atom and play a minor role in bonding. Little is known about the chemical nature of erbium impurities in silicon: the site where erbium sits, substitutionally or interstitially, the "charge state" or the fact that it exists as an isolated defect or whether it precipitates into a silicide or with other impurity atoms. One can obtain some information by calculating the total energy of erbium at several sites in the silicon lattice to predict among these the lowest energy configuration. The approach is based on the local density approximation (L.D.A.) and the use of optimized ab initio norm-conserving pseudopotentials [32]. The calculation is performed on a 32 atoms supercell and a special k point scheme (eventually 64 atoms and 2 k points to check convergence) with the quantum molecular dynamics technique [33]. More technical details can be found in [29].

Three high symmetry geometries for the Er atom were considered : the tetrahedral (T_i) and the hexagonal (H_i) interstitial sites and the (tetrahedral) substitutional (T_s) site. Additionally, there is the possibility that the total energy could be lowered if one electron in the 4f shell could be promoted to a valence level in order to participate in bonding. Since the calculations are done within pseudopotential theory where the f states are treated as core states, one must perform separate calculations for each "oxidation state". Two oxidation states were investigated: Er^{2+} and Er^{3+} . The cohesive energy of the erbium atom in the silicon lattice was computed for these six distinct cases. Both atomic and electronic degrees of freedom are completely relaxed for all six configurations. The cohesive energy of the erbium atoms is calculated using the free atom $4f^{12}6s^2$ (*i.e.* $2+$) as the reference and is thus obtained as :

$$E_{\text{coh}}^{2+} = \left[E(\text{Er}^{2+})_{\text{psat}} + nE(\text{Si})_{\text{pscr}} \right] - E(\text{Er}^{2+} + n\text{Si})_{\text{pscr}} \quad (4)$$

$$E_{\text{coh}}^{3+} = \left[E(\text{Er}^{3+})_{\text{psat}} + nE(\text{Si})_{\text{pscr}} \right] - E(\text{Er}^{3+} + n\text{Si})_{\text{pscr}} + \left[E(\text{Er}^{3+})_{\text{atom}} - E(\text{Er}^{2+})_{\text{atom}} \right]$$

where psat and pscr refer to pseudoatom and pseudocrystal, respectively and n is the number of silicon atoms per supercell. These energies were calculated for a neutral cell and thus cannot be identified directly to the $E(m)$ of section II (we will come back to this point later). The last term in the equation defining E_{coh}^{3+} is the energy needed to promote an electron from the 4f shell to the 5d shell in the free atom, i.e. the difference between the lowest energy $4f^{12}6s^2$ multiplet and the lowest energy $4f^{11}6s^25d^1$ multiplet which is known experimentally to be 0.89 eV [34]. Table 1 shows that the lowest energy site is the tetrahedral interstitial, being one eV or more lower than the other two sites. The Er^{3+} oxidation state is lower than the Er^{2+} state for each of the sites investigated. This result is in agreement with the interstitial position predicted by He channeling experiments [35] and the tetrahedral symmetry inferred by the splitting of the luminescence lines [36].

For this minimum energy configuration, the erbium slightly distorts the silicon lattice. No Si-Si bonds are broken but the cage of ten silicon atoms surrounding the erbium atom relaxes outward. The four tetrahedrally-coordinated Si atoms move 0.16 Å from their ideal crystalline positions and the Er-Si distance is 2.48 Å.

This confirms the simple view that Er is a bigger atom than Si and that the size effect is such that the nearest neighbors should relax outward.

Some other results of ref. [29] are interesting to comment since they essentially confirm the point of view of section II. First this calculation confirms that the 6s state plays no role in the gap region and mixes quite strongly with the states of the host crystal. Second the 5d atomic state is found to lie high (several eV) in the conduction band. For the tetrahedral interstitial site its interaction with bulk antibonding states of the conduction band lowers a t_2 combination of such states in the band gap at $E_c - 0.2$ eV. We find the same behavior in the T.B. calculation of section II when applied to the T_i case, again confirming the similarity of results. Finally a most interesting point is to deduce from Table 1 an idea of the position of the ionization level $E(2+, 3+)$. For this it is important to notice that, in a neutral cell, the $2+ \Rightarrow 3+$ transformation is obtained by changing the core from $4f^{12}$ to $4f^{11}$ and putting the extra electron on the lowest empty level which we call E_u . From this we can write

$$E(2+, 3+) = E_{\text{coh}}^{3+} - E_{\text{coh}}^{2+} + E_u \quad (5)$$

Within a few tenths of eV E_u is located near the bottom of the conduction band E_c . The results of table I then show that $E(2+, 3+) - E_c$ is of order 0.9 eV, 0.7 eV and 1.7 eV for the T_i , H_i and T_s sites respectively. This last result agrees with the T.B. conclusion of section I that $E(2+, 3+)$ is relatively high above E_c but differs somewhat in the actual number (1.7 eV against 3 eV for the T.B. value of section II). Part of this difference might be due to atomic relaxation but more work is needed for better understanding.

Table I - Cohesive energy of an erbium atom at various positions in Si

configuration	Er^{2+}	Er^{3+}
T_i	2.54 eV	3.47 eV
H_i	0.65 eV	1.31 eV
T_s	0.82 eV	2.55 eV

IV - THE CASE OF Yb IN InP

We concentrate on this system which is the most extensively studied (for a detailed account of the experimental observations see the review papers [1, 2]). One reason is certainly the fact that the difference in size between the Yb and In ions is relatively small so that Yb is probably incorporated mostly as substitutional on the cation site as shown by Rutherford Backscattering experiments [37] and also evidence of the site symmetry from Zeeman splitting of luminescence lines [22]. Deep level transient spectroscopy and Hall measurements [38] agree, at least in n type materials, on the existence of an acceptor-like electron trap (AE) located 30 meV below the conduction band. At first sight this trap could be thought to be related to the ionization level $E(2+, 3+)$ discussed in section II which might well lie slightly below the conduction band for the Yb case. However electron paramagnetic resonance measurements [21] unambiguously show that Yb remains in its Yb^{3+} core state for all positions of the Fermi level within the band gap. This AE level must then either be due to the 5d related states or to other possible reasons invoked in the literature and which we discuss later. Furthermore there is also evidence in p samples for a hole trap lying 50 meV above the valence band [39]. If both trap states correspond to the same isolated substitutional Yb then one would have the interesting picture of an isoelectronic center (Yb^{3+} is isoelectronic to In^{3+}) capable of trapping symmetrically both types of carriers.

Before discussing this peculiar behavior let us now summarize the present understanding of the transfer mechanisms for intra-4f shell luminescence excitation and quenching in n type InP. As discussed in detail in several papers [2, 40-44] the situation is the one pictured in figure 4. Let us then describe the excitation mechanism first. This proceeds in several steps:

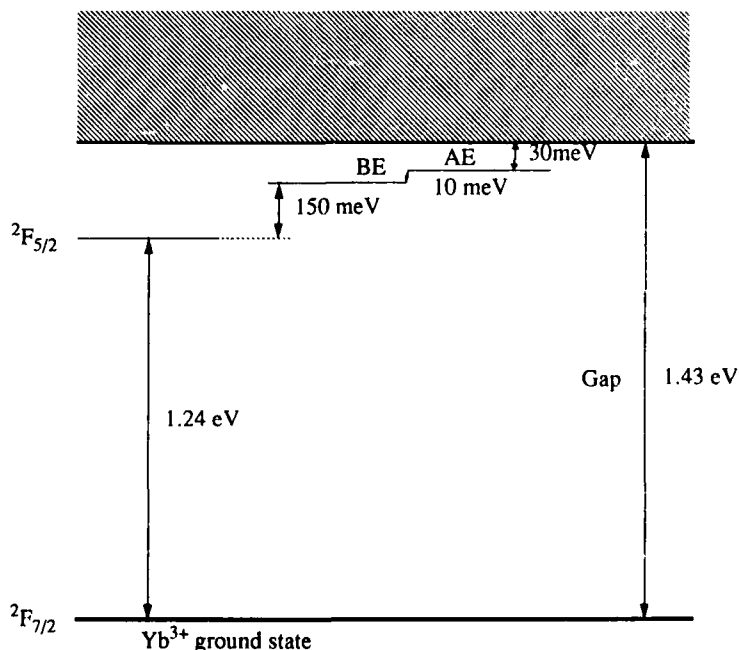


Fig. 4 - The different energy levels characteristic of Yb in InP.

- 1) photoexcitation of free electron-hole pairs for instance
- 2) capture of the electron in the A.E. trap
- 3) the center being now negatively charged traps a hole in a shallow state forming an exciton bound to the Yb^{3+} core (B.E.).
- 4) the bound exciton relaxes, transferring most of its energy to excite the 4f core from its $^2F_{7/2}$ ground state to its $^2F_{5/2}$ excited state
- 5) Luminescence occurs in the 4f shell.

This mechanism seems to be well established and photoluminescence excitation studies [43] directly show the role of the A.E. level in this process. This is even further confirmed by studies of the quenching of luminescence versus temperature showing that there is an intrinsic mechanism operating at high temperature which is thus the reverse of the one just described. However each one of the steps 2 to 5 asks for a quantitative theoretical study.

Before attempting to discuss these questions let us remind the results of section II for Yb in InP. Assuming a 4f core completely decoupled from the host states we obtained an $E(2+, 3+)$ ionization level just above the bottom of the conduction band. This is in complete agreement with the fact that only Yb^{3+} is found experimentally [21]. However analysis of the Zeeman splitting of the luminescence [22] indicates that the Yb^{3+} ground state $^2F_{7/2}$ has an orbital reduction factor of 0.95 which becomes 0.75 in the excited state in some contradiction with the hypothesis of a 4f frozen core. Furthermore our calculation predicts no 5d or 6s derived gap states while experimentally there is evidence for the A.E. electron trap and probably for a hole trap too. We have thus to examine if and how these points can be explained by theory.

Let us consider first the possible origin of the apparent delocalization of the wave function observed in e.p.r. or Zeeman experiments. In the frozen core approximation the $^2F_{7/2}$ and $^2F_{5/2}$ states lead to a pure f contribution. Any small perturbation V not included in this scheme can be analyzed by perturbation theory and would lead to a change in effective orbital momentum proportional to V/Δ where V is the coupling parameter and Δ some average distance in energy to the higher contributing states. Since, as shown on Fig. 4, the distance in energy to the continuum is much smaller (~ 0.2 eV) for $^2F_{5/2}$ than for $^2F_{7/2}$ (1.4 eV) the effect should be much larger in the excited state. The experimental ratio is 0.25/0.05 i.e. 5 in good correspondence with the ratio of the two energies (~ 7).

Let us now turn to the other point, i.e. the existence of A.E. and hole trap states. The first explanation which comes to mind is that they could originate from 5d derived states in spite of the fact that our calculation predicts that such states lie relatively deep in the conduction and valence band. If we admit that such a large error occurs in the calculation, then the A.E. level would be the "e" level and the hole trap would correspond to the bonding level t_2 of figure 1. However, in such a scheme it is difficult to accept that both would accidentally give rise to shallow states at the same time. If only the A.E. trap would exist then such an explanation would become more plausible.

Among the possible reasons which can be invoked to explain the existence of two shallow levels for this isoelectronic center none seems to be really convincing. *i)* the electronegativity rule: this is implicitly included in our T.B. treatment and the previous discussion applies *ii)* the size difference leading to a long range strain field. Here the Yb atom is larger than In and the strain field would correspond to compression of the bonds. The corresponding deformation potentials for the band edges of InP are known and correspond to repulsive potentials which cannot bind carriers.

Other explanations could be invoked. One is that a strong local lattice distortion could occur, stabilizing a 5d derived state. This should be ruled out for the A.E. level since the activation energy of the Hall measurements and DLTS are the same and small (30 meV) indicating a non activated capture cross section. Another appealing possibility might be that the Yb center leads to a local positive change $\delta\alpha$ in polarisability with respect to the host material.

Then any type of carrier of charge $q = \pm e$ at a distance r will induce a field q/r^2 at the Yb site, giving rise to a polarization energy $-1/2 \delta\alpha q^2/r^4$. This potential is attractive for both carriers and of relatively short range. A rough preliminary estimation however seems to show that, with a reasonable estimate of $\delta\alpha$ and properly dividing by the bulk dielectric constant, the resulting potential is too small to give the observed binding energies. However a more careful examination of this possibility is needed before reaching any firm conclusion.

Finally we can try to comment upon the excitation mechanism itself. If one agrees that the first step is the capture of the electron in the AE level two possibilities occur:

i) a hole is trapped by the corresponding negatively charged center giving a bound exciton (BE). There is then transfer from this BE to be the excited state $^2F_{5/2}$. Such transfer can only be provided by multiphonon processes, the energy difference being 150 meV between the two states

ii) there is a direct transition between the system AE+ free hole to the $^2F_{5/2}$ excited state. This is an Auger process which must also be phonon assisted to provide the difference in energy, again of order 150 meV.

Both mechanisms require the understanding of the AE origin and of its possible electron-phonon coupling. If the capture in this AE state results from multiphonon processes the fact that Hall and DLTS measurements give the same energy 30 meV indicates that the activation barrier for capture is zero. This means that the Franck-Condon shift is also 30 meV. This value is small and should be incorporated in the theory for the excitation mechanism.

V - CONCLUSION

We have calculated the chemical trends for the RE impurities and derived an overall description compatible with experiment. LDA calculations for Er in silicon give a stable interstitial position in agreement with observations. Finally we have discussed the fairly detailed picture of Yb in InP on the basis of our results.

Bibliography

1. V.F. Masterov and L.F. Zakharenkov, *Sov. Phys. Semicond.*, **24**, 383 (1990).
2. K. Takahei, *Proceedings of the 21th International Conference on the Physics of Semiconductors*, Beijing (1992).
3. L.A. Hemstreet, in *Material Science Forum*, edited by H.J. von Bardeleben (Trans. Tech. Publications, Switzerland 1986), Vols. 10-12, p. 85.
4. C. Delerue and M. Lannoo, *Phys. Rev. Lett.*, **67**, 3006 (1991).
5. B.G. Wybourne, *Spectroscopic Properties of Rare Earths*, Interscience Publishers, John Wiley and Sons, Inc., New-York (1965).
6. J.F. Herbst, D.N. Lowy and R.E. Watson, *Phys. Rev. B* **6**, 1913 (1972); J.F. Herbst, R.E. Watson and J.W. Wilkins, *Phys. Rev. B* **13**, 1439 (1976) and **17**, 3089 (1978).
7. *Valence fluctuations in Solids*, edited by L.M. Falicov et al., North Holland, Amsterdam, (1981).
8. C. Delerue, M. Lannoo and G. Allan, *Phys. Rev. B* **39**, 1669 (1989).
9. G. Picoli, A. Chomette and M. Lannoo, *Phys. Rev. B* **30**, 7138 (1984).
10. F. Herman and S. Skillman, *Atomic Structure Calculations*, Prentice Hall, New York, (1963).
11. M. Wolfsberg and L. Helmholz, *J. Chem. Phys.* **20**, 837 (1952).
12. C. Delerue and M. Lannoo, to be published
13. J. Langer, to be published.

14. B. Lambert, A. Le Corre, Y. Toudic, C. Lhomer, G. Grandpierre and M. Gauneau, *J. Phys. Condensed Matter*, **2**, 479 (1990).
15. G. Pomrenke, H. Ennen, and W. Haydl, *J. Appl. Phys.*, **59**, 601 (1986).
16. M. Ennen and J. Schneider, in Proceedings of the Thirteenth International Conference on Defects in Semiconductors, Coronado, CA, 1984, edited by L.C. Kimerling and J.M. Parsey (Metallurgical Society of AIME, New York, 1985), Vol. **14a**, p. 115.
17. H. Ennen, J. Wagner, H.D. Mueller and R.S. Smith, *J. Appl. Phys.*, **61**, 4877 (1987).
18. J. Wagner, H. Ennen, and H.D. Müller, *J. Appl. Phys.*, **59**, 1202 (1986).
19. V.A. Kasatkin, F.P. Kesumanly, and B.E. Samorukov, *Fiz. Tekh. Poluprovodn.* **15**, 616 (1981) [*Sov. Phys. Semicond.* **15**, 352 (1981)].
20. H. Ennen, G. Pomrenke, and A. Axmann, *J. Appl. Phys.*, **57**, 2182 (1985).
21. B. Lambert, Y. Toudic, G. Grandpierre, A. Rupert, and A. Le Corre, *Electron. Lett.*, **24**, 1446 (1988).
22. G. Aszodi, J. Weber, Ch. Vihlein, L. Pu-Lin, H. Hennen, U. Kaufman, J. Schneider, and J. Windscheif, *Phys. Rev. B* **31**, 7767 (1985).
23. W. Kröber and A. Hangleiter, *Appl. Phys. Lett.*, **52**, 114 (1988).
24. P.B. Klein, *Solid State Commun.*, **65**, 1097 (1988).
25. R. Boyn, *Phys. Status Solidi*, **148**, 11 (1988).
26. R.S. Title, in Physics and Chemistry of II-VI Compounds, edited by M. Aven and J.S. Prener, (North-Holland, Amsterdam, 1967).
27. M. Godlewski and D. Hommel, *Phys. Status Solidi (a)*, **95**, 261 (1986).
28. H. Przybylinska, M. Godlewski, and A. Stapor, in Proceedings of the Twenty-Sixth School on the Physics of Semiconductor Compounds, Jaszowiec (Polish Scientific, Krakow, 1987).
29. M. Needels, M. Schlüter and M. Lannoo, *Phys. Rev.*, to be published.
30. J. Michel, J.L. Benton, R.F. Ferrante, D.C. Jacobson, D.J. Eaglesham, E.A. Fitzgerald, Y.H. Xie, J.M. Poate, and L.C. Kimerling, *J. Appl. Phys.*, **70**, 2672 (1991).
31. J.L. Benton, J. Michel, L.C. Kimerling, D.C. Jacobson, Y.H. Xie, D.J. Eaglesham, E.A. Fitzgerald and J.M. Poate, *J. Appl. Phys.*, **70**, 2667 (1991).
32. L. Kleinman and D.M. Bylander, *Phys. Rev. Lett.*, **48**, 1425 (1982); D.C. Allan and M.P. Teter, *Phys. Rev. Lett.*, **59**, 1136 (1987); A.M. Rappe, K.M. Rabe, E. Kaxiras, and J.D. Joannopoulos, *Phys. Rev. B* **41**, 1227 (1990).
33. R. Car and M. Parrinello, *Phys. Rev. Lett.*, **55**, 2471 (1985).
34. C.E. Moore, Ed., *Atomic Energy Levels*, U.S. Government Printing Office, Washington, DC, (1971).
35. D.J. Eaglesham, private communication.
36. Y.S. Tang, J. Zhang, K.C. Heasman, and B.J. Sealy, *Sol. St. Com.* **72**, 72 (1989).
37. A. Kozanecki and R. Grotzschel, *J. Appl. Phys.*, **68**, 517 (1990).
38. P.S. Whitney, K. Uvagi, H. Nakagome and K. Takahei, *Appl. Phys. Lett.*, **53**, 2074 (1988).
39. D. Seghier, T. Benyattou, G. Bremond, F. Ducroquet, J. Gregoire, G. Guillot, C. Lhomer, B. Lambert, Y. Toudic and A. Le Corre, *Appl. Phys. Lett.*, **60**, 983 (1992).
40. K. Takahei, A. Taguchi, H. Nakagome and P.S. Whitney, *J. Appl. Phys.*, **66**, 4941 (1989).
41. B.J. Heijmink Liesert, M. Godlewski, A. Stapor, T. Gregorkiewicz, C.A.J. Ammerlaan, J. Weber, M. Moser and F. Scholz, *Appl. Phys. Lett.*, **58**, 2237 (1991).
42. B.J. Heijmink Liesert, M. Godlewski, T. Gregorkiewicz and C.A.J. Ammerlaan, *Appl. Phys. Lett.*, **59**, 3279 (1991).
43. A. Kozanecki, K. Karpinska and Z. Kalinski, *Appl. Phys. Lett.*, **62**, 84 (1993).
44. A. Taguchi, M. Taniguchi and K. Takahei, *Appl. Phys. Lett.*, **60**, 965 (1992).

KINETICS OF THE LUMINESCENCE OF ISOELECTRONIC RARE-EARTH IONS IN III-V SEMICONDUCTORS

H. J. Lozykowski, Department of Electrical and Computer Engineering, and Condensed
Matter & Surface Sciences Program Ohio University Athens, Ohio 45701

ABSTRACT

In this work we have developed a model for the kinetics of the energy transfer from the host lattice to the localized core excited states of rare earth isoelectronic structured traps (REI-trap). We have derived a set of differential equations for semi-insulating semiconductor governing the kinetics of rare earth luminescence. The numerically simulated rise and decay times of luminescence show a good quantitative agreement with the experimental data obtained for InP:Yb, over a wide range of generation rates.

INTRODUCTION

The investigation of the luminescence properties of rare earth doped III-V is of great interest both from scientific and application points of view. The scientific interest is related to the uniqueness of optical and electrical properties of rare earth impurities in semiconductor hosts. Among the rare earth doped III-V semiconductors InP:Yb has been the most extensively studied [1-6]. In this paper we discuss only the structured isoelectronic traps (REI-trap) in III-V semiconductors introduced by RE^{+3} ions replacing the element from column III. Furthermore, we develop a model of the luminescence kinetic that describes the energy transfer from the host to the REI-trap core states, and the recombination and quenching processes. Study of the rise and decay times at different excitation intensities, temperatures, can provide important information about the energy transfer and recombination (radiative, and non-radiative) processes.

THEORETICAL FORMULATION

An isoelectronic center can form bound states because of a short range central-cell potential. According to Thomas [7], the primary factors affecting the binding potential are the electronegativity and the size differences between the impurity and the host ion which it replaces. It is found experimentally that only very large atoms or very small atoms produce isoelectronic traps because they create large lattice distortion induced by the substitution. The above conclusion is supported by the fact that the atomic covalent radii (ionic RE^{+3}) for all rare earths are bigger than atomic radii of Ga and In that they are replacing. Pauling's electronegativity of rare earth elements is in the range of 1.1-1.25, and is smaller than Ga (1.81) and In (1.78) for which it substitutes. If the rare earth ions replace the element from column III in III-V compounds (that are isovalent concerning outer electrons of RE^{+3} ions), they create isoelectronic traps. The rare earth isovalent traps that we can call isoelectronic "structured" impurities [8] possess unfilled 4f core shells. The luminescence structure arises from intra-configurational f-f transitions in the core of the isoelectronic "structured" impurities.

The striking feature of excitons bound to the isoelectronic traps is a long luminescence decay time, ranging from a few hundred to few thousand nanoseconds [9,10-12]. The lifetimes of neutral donor or acceptor bound excitons in direct gap semiconductors are in the range of nanoseconds. The "simple" isoelectronic center in III-V materials can exist in three possible states instead of two as in the case of the Shockley-Read-Hall (SRH) recombination model [11]. In the case of rare earth isoelectronic traps, the kinetics model is even more complicated because of an energy transfer processes between the localized state in the forbidden gap of the host, and the localized core state of structured isoelectronic impurities. There are three possible mechanisms of energy transfer. The first is the energy transfer from excitons bound to "structured" isoelectronic centers to the core electrons. It takes place as a result of the electrostatic perturbation between the core electrons and the

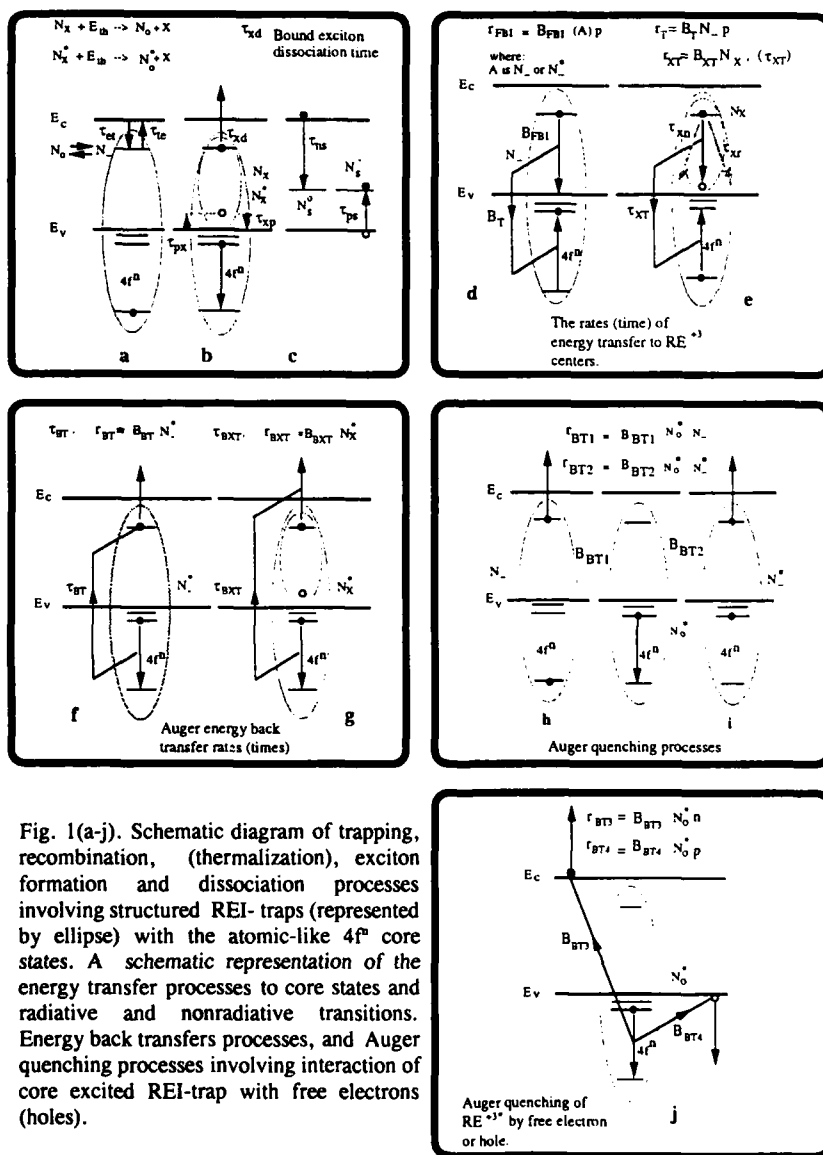


Fig. 1(a-j). Schematic diagram of trapping, recombination, (thermalization), exciton formation and dissociation processes involving structured REI-traps (represented by ellipse) with the atomic-like $4f^n$ core states. A schematic representation of the energy transfer processes to core states and radiative and nonradiative transitions. Energy back transfers processes, and Auger quenching processes involving interaction of core excited REI-trap with free electrons (holes).

exciton, (effective-mass-like particles) [8]. The second mechanism is the transfer of energy to the core electrons involving the "structured" isoelectronic trap occupied by electron (hole) and free hole (electron) in the valence (conduction) band. The third mechanism is the transfer through an inelastic scattering process in which the energy of a free exciton near a "structured" trap is given to the localized core excited states [8]. If the initial and final states are not resonant, the energy mismatch must be distributed in some way, e.g. by phonon emission or absorption [8,13]. If the atomic core excitations are strongly coupled to the host phonons, the energy transfer probability is likely to be higher [8]. Strong phonon coupling may also be desirable in ensuring that relaxation down the ladder of core excited states occurs quickly, thus preventing back transfer. However, for efficient radiative recombination, the phonon coupling should not be strong, in order to prevent core de-excitation by nonradiative multiphonon emission. In this regard the rare earth "structured" impurity seems to be ideal.

KINETIC MODEL AND COMPUTATION RESULTS

The luminescence kinetic model involving RE^{+3} "structured" isoelectronic centers, is complicated because the center can exist in six possible states. Furthermore the energy transfer processes between the localized state in the forbidden gap and core states complicate the model. We assume that the isoelectronic trap is an electron trap such as Yb^{+3} in semi-insulating (SI) InP. This trap may exist in six distinct states: (1) neutral unoccupied trap (concentration N_0), (2) negatively charged (concentration N_-), (3) exciton occupied (concentration N_x), (4) neutral excited (concentration N_0^*), (5) excited negatively charged (concentration N_-^*), and (6) excited exciton occupied (concentration N_x^*). When isoelectronic traps are present in n or p-type materials the model will be different. The asymmetry between n and p type semiconductors results from the fact that the isoelectronic center binds only an electron (hole). Thus in a n-type material, a fraction of the isoelectronic traps will be occupied by electrons even before the sample is excited, while in p-type material, all the isoelectronic centers will be empty. Figure 1 shows the physical models, symbols, and definitions used in the analysis of excitation, recombination and quenching of "structured" isoelectronic centers. By fitting the calculation to the experimental data, we can estimate important parameters related to energy transfer from the lattice to RE^{+3} centers, the Auger processes, and the temperature quenching mechanisms. The N_0 center can be transformed to the neutral rare earth core excited center N_0^* , through an Auger process where the recombination energy of the bound electron with free hole is transferred nonradiatively to the core states. The N_0 may also recombine radiatively or nonradiatively with a hole in the valence band. The last three processes transform N_0 center into N_0^* neutral trap. The N_0^* may capture an electron and be transformed into N_-^* center. The N_-^* may lose the electron through processes described above, or by auto de-ionization Auger process. This Auger nonradiative luminescence quenching mechanism of the excited REI-trap with characteristic time τ_{BT} is shown in Fig. 1f. The exciton bound to a REI-trap with excited core states (N_x^*), can back transfer energy from core excitations to the exciton, and dissociate it, with the liberation of an electron or hole. Once formed, the N_- and N_-^* states can also be converted into N_0 and N_0^* states, respectively, by thermal ionization or to N_x and N_x^* , respectively, by capturing a hole from the valence band with time τ_{px} . The second most important energy transfer process is shown in Fig. 1e. In this process energy is transferred from the bound exciton (on isoelectronic trap N_x) to the core states with the rate r_{iT} . The exciton bound to isoelectronic traps N_x and N_x^* can thermally dissociate by several processes. It can dissociate into a free exciton (X) and neutral N_0 , or neutral excited (N_0^*) REI-trap respectively. The REI-traps N_0^* , N_-^* and N_x^* may also be de-excited to N_0 , N_- and N_x respectively by radiative transitions (time τ_j) between the $4f^n$ core states. The nonradiative decay channel of free carriers through an additional type of trap N_t , the "shunt path" is shown in Fig. 1c. Figure 1.h,i,j show examples of nonradiative recombination involving the interaction of a core excited REI-trap (N_0^*) with an electron trapped on a separate center (N_-), an electron trapped on a core excited

$$\begin{aligned} \frac{dN_-}{dt} = & \frac{n}{\tau_{\alpha}} \left(\frac{N_0}{N} \right) + \frac{N_-^*}{\tau_3} + \frac{1}{\tau_{\beta}} \left(\frac{N_x}{N} \right) \frac{N_v}{\beta_h} \exp \left(-\frac{E_h}{kT} \right) - \frac{1}{\tau_{\alpha}} \left(\frac{N_-}{N} \right) \beta_r N_c \exp \left(-\frac{E_i}{kT} \right) \\ & - \frac{p}{\tau_{\mu}} \left(\frac{N_-}{N} \right) - B_{FB}(N_-)p - B_T(N_-)p - B_{BT}(N_0^*)N_- \end{aligned} \quad (1)$$

$$\frac{dN_x}{dt} = \frac{N_x^-}{\tau_3} + \frac{p}{\tau_{\mu}} \left(\frac{N_-}{N} \right) - N_x \left(\frac{1}{\tau_2} + \frac{1}{\tau_{xT}} + \frac{1}{\tau_{x\mu}} \right) - \frac{1}{\tau_{\beta}} \left(\frac{N_x}{N} \right) \frac{N_v}{\beta_h} \exp \left(-\frac{E_h}{kT} \right) \quad (2)$$

$$\begin{aligned} \frac{dN_0^*}{dt} = & \frac{N_x}{\tau_{xT}} + B_T(N_-)p + \frac{1}{\tau_{\alpha}} \left(\frac{N_-^*}{N} \right) \beta_r N_c \exp \left(-\frac{E_i}{kT} \right) - \frac{n}{\tau_{\alpha}} \left(\frac{N_0^*}{N} \right) - \frac{N_0^*}{\tau_3} \\ & - B_{BT}(N_0^*)N_- - B_{BT}(N_0^*)n - B_{BT}(N_0^*)p \end{aligned} \quad (3)$$

$$\begin{aligned} \frac{dN_-^*}{dt} = & \frac{n}{\tau_{\alpha}} \left(\frac{N_0^*}{N} \right) + \frac{1}{\tau_{\beta}} \left(\frac{N_x^*}{N} \right) \frac{N_v}{\beta_h} \exp \left(-\frac{E_h}{kT} \right) - \left(\frac{1}{\tau_3} + \frac{1}{\tau_{BT}} \right) N_-^* \\ & - \frac{p}{\tau_{\mu}} \left(\frac{N_-^*}{N} \right) - \frac{1}{\tau_{\alpha}} \left(\frac{N_-^*}{N} \right) \beta_r N_c \exp \left(-\frac{E_i}{kT} \right) - B_{BT}(N_0^*)N_-^* - B_{FB}(N_-^*)p \end{aligned} \quad (4)$$

$$\frac{dN_x^*}{dt} = \frac{p}{\tau_{\mu}} \left(\frac{N_-^*}{N} \right) - N_x^* \left(\frac{1}{\tau_2} + \frac{1}{\tau_3} + \frac{1}{\tau_{BXT}} + \frac{1}{\tau_{x\mu}} \right) - \frac{1}{\tau_{\beta}} \left(\frac{N_x^*}{N} \right) \frac{N_v}{\beta_h} \exp \left(-\frac{E_h}{kT} \right) \quad (5)$$

$$\frac{dn}{dt} = G + N_x^* \left(\frac{1}{\tau_{x\mu}} + \frac{1}{\tau_{BXT}} \right) + \left(\frac{N_- + N_-^*}{N} \right) \frac{1}{\tau_{\alpha}} \beta_r N_c \exp \left(-\frac{E_i}{kT} \right) \quad (6)$$

$$+ \frac{N_x}{\tau_{x\mu}} + \frac{N_-^*}{\tau_{BT}} - \frac{n}{\tau_{\alpha}} \left(\frac{N_0 + N_0^*}{N} \right) - \frac{n}{\tau_{\alpha}} \left(\frac{N_s^0}{N_s} \right) + B_{BT}(N_0^*)N_-^* + B_{BT}(N_0^*)N_-$$

$$\begin{aligned} \frac{dp}{dt} = & G + \frac{1}{\tau_{\beta}} \frac{N_v}{\beta_h} \exp \left(-\frac{E_h}{kT} \right) \left(\frac{N_x + N_x^*}{N} \right) - \frac{p}{\tau_{\mu}} \left(\frac{N_- + N_-^*}{N} \right) - \frac{p}{\tau_{\mu}} \left(\frac{N_s - N_s^0}{N_s} \right) \\ & - B_T(N_-)p - B_{FB}(N_- + N_-^*)p \end{aligned} \quad (7)$$

$$\frac{dN_s^0}{dt} = \frac{p}{\tau_{\mu}} \left(1 - \frac{N_s^0}{N_s} \right) - \frac{n}{\tau_{\alpha}} \left(\frac{N_s^0}{N_s} \right) \quad (8)$$

$$\left. \begin{aligned} N_0 &= N - N_- - N_x - N_0^* - N_-^* - N_x^* \\ N_s &= N_s^0 + N_s^- \end{aligned} \right\} \quad (9)$$

$$p = n + N_- + N_-^* + \left(1 - \frac{N_s^0}{N_s} \right) N_s \quad (10)$$

Table I Parameters Describing Rise and Decay Kinetics of InP : Yb.

Symbol	Unit	Parameter Value
τ_2	sec	2×10^{-7}
τ_3	sec	11.6×10^{-6}
τ_{BT}	sec	1×10^{-7}
τ_{BTX}	sec	1×10^{-7}
τ_{a0}	sec	5×10^{-6}
τ_{p0}	sec	3×10^{-8}
τ_{XT}	sec	1.25×10^{-9}
τ_{ex}	sec	5×10^{-11}
τ_{pk}	sec	5×10^{-11}
B_T	cm^3/sec	4×10^{10}
B_{FBI}	cm^3/sec	1×10^{-11}
B_{BT1}	cm^3/sec	1.2×10^{-13}
B_{BT2}	cm^3/sec	1.2×10^{-13}
B_{BT3}	cm^3/sec	4×10^{-13}
B_{BT4}	cm^3/sec	4×10^{-13}
N_s	cm^{-3}	8×10^{16}
N	cm^{-3}	5×10^{17}
G	# photons / $(\text{cm}^3 \cdot \text{sec})$	$2 \times 10^{20} - 1.5 \times 10^{25}$

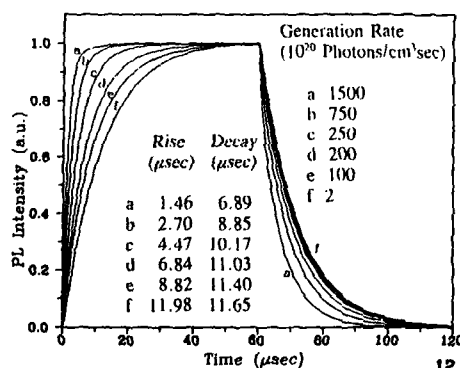
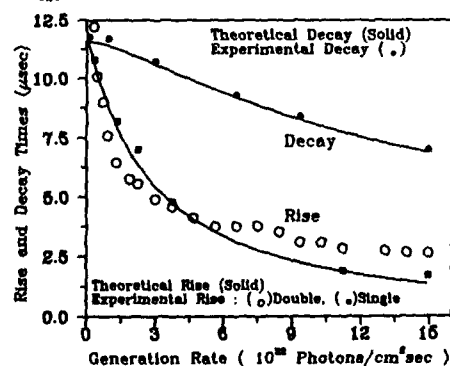


Fig. 3 The numerically computed rise and decay times (solid lines) as a function of generation rates. The experimental values of rise times (circles-single exp. f.), (squares-double exp. f.) The dots stand for the decay times constant of the dominant component of the experimental data fitted to double exponential function.

Fig. 2. Numerical solutions of Eqs.(1)-(10). The rare earth luminescence intensity versus time for the set of parameters shown in Table I. The set of computed profiles (normalized to unity at maximum), showing the buildup of luminescence, the steady state value, and the decay after switching off (at 60 μs) the excitation pulse.



REI-trap (N_t^*), or the free electrons (holes) with Auger coefficients $B_{BT3}, (B_{BT4})$ [14,15]. By consulting Figs.1, we can now complete the formal description of the model by deriving the differential equations for the REI-trap kinetics. To solve this system, we assumed, excitations take place at a low enough temperatures (8.6 K) that thermal activation of the trapped carriers is negligible. That is, terms explicitly dependent on temperature were ignored, and only trapping, transferring and recombination transitions were considered. The numerical solution of equations was obtained using the parameters shown in Table I by repeating the numerical calculations for different values of the generation rate. The luminescence intensities are proportional to N_t^* , N_t^* , and N_t^* . Figure 2 shows the computed luminescence rise and decay as a function of the generation rate. In figure 3, the solid lines are the computed rise and decay times (the experimental data are imposed on the computed curves). The circles shown in Fig.3 represent the experimental rise time obtained from fitting to a single exponential function. The squares stand for the rise time of the dominant component of the experimental data fitted to double exponential function. The dots represent the experimental decay time of the dominant component of the double exponential fitting. The numerically simulated luminescence rise and decay measurements show a good quantitative agreement with experiment over a wide range of generation rates.

For n-type material the equations are even more complicated, similar equations hold for p-type material. Such systems of coupled, first order stiff nonlinear differential equations require specialized numerical integration routines designed specifically for stiff systems.

The detailed analysis of the parameters and their influences on the rise time, the efficiency of the steady state luminescence, and decay time will be published elsewhere. Finally, the proposed model can be refined by taking into account the surface recombination and carrier diffusion processes, which may play important roles in the reduction of the overall photoluminescence emission.

This work was supported by AFOSR grant No 90-0322.

REFERENCES

1. H. Ennen, G. Pomrenke and A. Axmann, *J. Appl. Phys.*, 57, 2182, (1985).
2. P. B. Klein, *Solid State Commun.*, 65, 1097, (1988).
3. P. S. Whitney, K. Uwai, H. Nakagome, and K. Takahei, *Appl. Phys. Lett.*, 53, 2074 (1988).
4. K. Thonke, K. Pressel, G. Bohnert, A. Stapor, J. Weber, M. Moser, A. Malassioti, A. Hangleiter and F. Scholtz, *Semicond. Sci. Technol.*, 5, 1124 (1990).
5. C. Lhomer, B. Lambert, Y. Toudic, A. LeCorre, M. Gauneau, F. Clerotand, B. Sermage, *Semicond. Sci. Technol.*, 6, 916, (1991).
6. H. J. Lozykowski, A. K. Alshawa, G. Pomrenke, and I. Brown, *Bulletin American Phys. Soc.*, Vol. 36, C54, 2167, (1991), *ibid.*, E 4.4.
7. D. G. Thomas, *J. of the Phys. Soc. of Japan*, 21, 265 (1966).
8. D. J. Robbins and P. J. Dean, *Adv. in Physics*, 27 (4), 499 (1978) and references therein.
9. J. D. Cuthbert and D. G. Thomas, *Phys. Rev.*, 154 (3), 763, (1967).
10. J. Jayson, R. Bhargava, and R. Dixon, *J. Appl. Phys.*, 41, 4972, (1970).
11. J. M. Dishman and M. DiDomenico, Jr., *Phys. Rev. B*, 1, 3381, (1970).
12. J. S. Jayson and R. Z. Bachrach, *Phys. Rev. B*, 4(2), 477, (1971).
13. T. Holstein, S. Lyo, and R. Orbach, Excitation in Disorder Systems, in *Laser Spect. of Solids*, edited by W. Yen and P. Selzer, Springer-Verlag, Berlin, 1981, p., 39.
14. J. M. Langer, *Springer Proceedings in Physics* Vol. 38, Electroluminescence, Editors: S. Shionoya and H. Kobayashi Springer-Verlag, 1989 and references cited therein.
15. J. M. Langer and Le Van Hong, *J. Phys. C: Solid State Phys.*, 17, L923, (1984).

ELECTRONIC STRUCTURE OF SI DOPED BY RARE-EARTH Yb^{3+}

SHANG YUAN REN AND JOHN D. DOW

Department of Physics and Astronomy, Arizona State University, Tempe,
Arizona 85287-1504, U.S.A.

ABSTRACT

The electronic structure of Yb^{3+} -doped Si is elucidated in terms of level repulsion between the Si vacancy's deep levels (and spectral density) and the Yb^{3+} levels, both for bulk Si and for small clusters. The $^2\text{F}_{5/2}$ level of Yb^{3+} splits into a Γ_8 level and a Γ_6 level, with the Γ_6 repelled most, by the nearby Γ_6 (A_1) level of the Si vacancy. The level-repulsion is either upwards or downwards in energy, depending on whether the A_1 -like vacancy level lies below or above this Yb^{3+} level. The $^2\text{F}_{7/2}$ Yb^{3+} level is split into Γ_6 , Γ_7 , and Γ_8 sub-levels, all moving downwards in energy, with Γ_6 moving most, again due to strong level repulsion from the nearby A_1 -like vacancy level, while the more-distant, higher-energy T_2 -like (Γ_7 and Γ_8) vacancy level produces a weaker repulsion. In small clusters, the Si-vacancy's wavefunctions and deep level energies are sensitive to cluster-size, and changes in them alter the level repulsion experienced by the Yb^{3+} levels, even though the 4f electrons are localized.

I. INTRODUCTION

Rare-earth doped semiconductors, particularly rare-earth-doped Si, have attracted considerable attention recently for potential applications in optical-interconnect computing: electronic computation in the Si proceeds rapidly and inexpensively, while communication over optical fibers using luminescence from a rare-earth impurity, such as Er^{3+} , leads to fast storage of information. The substitutional rare-earth dopants are different from conventional s- and p-bonded impurities [1] in two important ways: (i) their relevant electrons are f-electrons, rather than s- or p-electrons; and (ii) these f-electrons generally occupy spatially localized states, and have very large total orbital angular momentum L . Therefore, we start first by treating a rare-earth whose total orbital angular momentum is only modestly large: Yb^{3+} , with $L=3$, an F-state. Subsequent work will discuss other rare-earth impurities of higher angular momentum, e.g., Er^{3+} with $L=6$. Our goal is to obtain a simple physical understanding of which factors determine the electronic structure and level spectrum of the Yb^{3+} impurity in Si, and to establish an intellectual framework for treating other rare-earth impurities with arbitrary orbital angular momentum. We shall be particularly interested in the additional level-splittings of the rare-earth's spin-orbit split energy levels, caused by interaction of the f-electron system with the sp^3 hybrids of the Si host.

II. SYMMETRY AND MATRIX ELEMENTS

Yb^{3+} has a configuration $4f^{13}$, which forms a spin doublet, and the term ^2F . This term has two spin-orbit split levels $^2\text{F}_{5/2}$ and $^2\text{F}_{7/2}$, with the latter being at lower energy by 1.27 eV. At a substitutional site in a diamond crystal field, the levels split further on a scale small compared with 0.1 eV (as we shall see):

$$^2\text{F}_{5/2} \rightarrow \Gamma_6 + \Gamma_8 \text{ and } ^2\text{F}_{7/2} \rightarrow \Gamma_6 + \Gamma_7 + \Gamma_8,$$

where we have used the tetrahedral (T_d) double-group notation of Tinkham [2].

The main contribution to the crystal-field splitting is due to the interaction of the substitutional Yb^{3+} with the sp^3 hybrids of its four nearest-neighbor Si atoms. Here we neglect the contributions of more-distant neighbors. Indeed, of the orbitals centered on each nearest-neighbor, the linear combination h_1 of four orbitals that are inward-

directed toward the Yb^{3+} at each site are the most important ones, and form an A_1 and a T_2 state; in the double group, A_1 becomes Γ_6 and T_2 becomes Γ_7 and Γ_8 . These inward-directed orbitals are the dangling bonds of the Si-vacancy deep level.

There are four sp^3 orbitals centered on each of the four neighbors, making a total of sixteen orbitals, or thirty-two spin-orbitals. Thus, if we project from these thirty-two spin-orbitals the various partners of specific rows of the irreducible representations Γ_6 , Γ_7 , and Γ_8 , then we know from group theory that each of those partners couples only with corresponding partners for the rare-earth ion: namely the ones that transform according to the same row of the same representation.

The four nearest-neighbor Si atoms with four hybrids each, have orbitals that transform according to

$$2A_1 + E + T_1 + 3T_2 \rightarrow 3\Gamma_6 + 3\Gamma_7 + 5\Gamma_8.$$

where A_1 is one-dimensional, E is two-dimensional, and T_1 and T_2 are three-dimensional representations of the tetrahedral (T_d) group, and Γ_6 , Γ_7 , and Γ_8 are irreducible representations of the T_d double group with dimensions 2, 2, and 4. Using projection-operator techniques, we have organized the hybrids of the neighboring host Si atoms according to the irreducible representation Γ_6 , Γ_7 , and Γ_8 [3].

To calculate the energy levels of Yb^{3+} at a substitutional site in Si, we assume an unperturbed Hamiltonian $H_0 = H_{\text{ion}} + H_{\text{Si}}$, where H_{Si} is the Hamiltonian of Si with a single vacancy at its center. The Yb^{3+} ion is inserted into the vacancy, but not (yet) coupled to the Si. Thus the unperturbed spectrum is the combined spectrum of the Yb^{3+} free ion plus the spectrum of Si with a vacancy. For the Si Hamiltonian, we use the empirical tight-binding model of Vogl *et al.* [4]. The zero of energy of this Si Hamiltonian is the top of the valence band. While the energies of the $2F_{5/2}$ and $2F_{7/2}$ levels of Yb^{3+} are known to be 1.27 eV apart, the energy of either level with respect to the top of the Si valence band is unknown. That is, the energy line-up of Yb^{3+} and Si is not accurately known, and is difficult to compute precisely — much as the energy line-ups of two different semiconductors are difficult to determine theoretically. Thus we take the energy offset $E(2F_{5/2})$, namely the energy of the $2F_{5/2}$ level with respect to the Si valence band maximum, as a parameter that we vary over a range from -1.55 eV to -0.65 eV, to see how the energy levels of Yb^{3+} in Si are affected by the choice of $E(2F_{5/2})$. We note that this range of energies was determined to be reasonable by examining the spectrum of free Yb^{3+} and by executing calculations which treated Coulomb effects in a mean-field approximation.

The perturbation coupling the Si and the Yb^{3+} is a matrix V :

	$2F_{5/2}$		$2F_{7/2}$		
	Γ_6	Γ_8	Γ_6	Γ_7	Γ_8
$\Gamma_6(A_1)h_1$:	$\alpha V_{h1f\sigma}$	0	$-\alpha\beta V_{h1f\sigma}$	0	0
$\Gamma_6(A_1)h_2$:	$\alpha V_{h2f\sigma}$	0	$-\alpha\beta V_{h2f\sigma}$	0	0
$\Gamma_6(T_1)p$:	$\alpha\beta V_{pf\pi}$	0	$\alpha V_{pf\pi}$	0	0
$\Gamma_7(T_2)h_1$:	0	0	0	$\lambda V_{h1f\sigma}$	0
$\Gamma_7(T_2)h_2$:	0	0	0	$\lambda V_{h2f\sigma}$	0
$\Gamma_7(T_2)p_\pi$:	0	0	0	$2V_{pf\pi}/3$	0
$\Gamma_8(T_2)h_1$:	0	$\nu V_{h1f\sigma}$	0	0	$\mu V_{h1f\sigma}$
$\Gamma_8(T_2)h_2$:	0	$\nu V_{h2f\sigma}$	0	0	$\mu V_{h2f\sigma}$
$\Gamma_8(T_2)p_\pi$:	0	$\rho V_{pf\pi}$	0	0	$\tau V_{pf\pi}$
$\Gamma_8(T_1)p$:	0	$-\nu V_{pf\pi}$	0	0	$\omega V_{pf\pi}$
$\Gamma_8(E)p$:	0	0	0	0	0

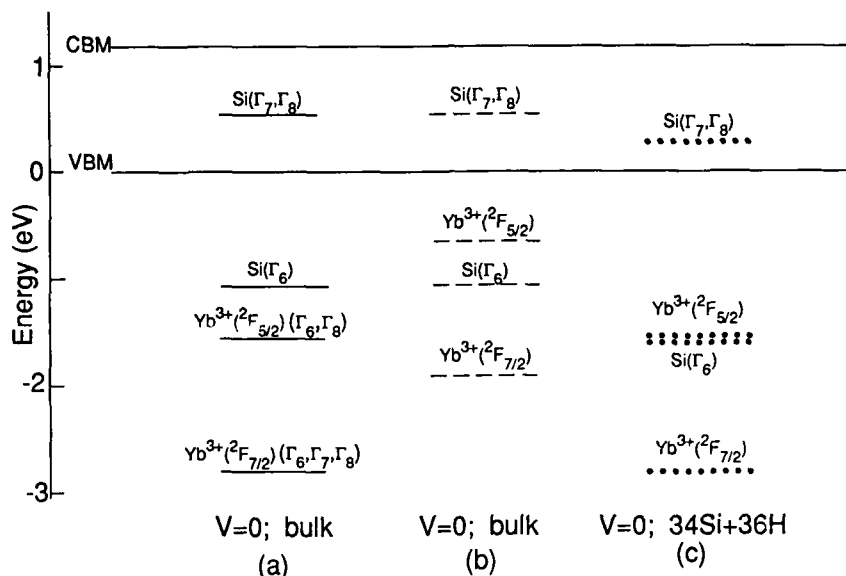


Fig. 1. Principal energy levels, in the limit $V \rightarrow 0$, of the Si vacancy and the Yb³⁺ ion. (a) Solid lines: the case of $E(^2F_{5/2}) = -1.55$ eV for the "bulk," namely 524Si+276H; (b) Dashed lines: $E(^2F_{5/2}) = -0.65$ eV for "bulk" Si; and (c) Dotted lines: $E(^2F_{5/2}) = -1.55$ eV for a 34Si+36H cluster.

This matrix couples the relevant ionic states to the relevant linear combinations of spin-orbitals formed from the nearest-neighbor Si hybrids. As mentioned above, we need only consider the relevant spin-orbitals, namely those that transform according to a specific row of a specific representation. Here the inward-directed hybrids of the nearest-neighbors are h_1 , the outward-directed hybrids are h_2 , and the remaining combinations of eight p-orbitals are p and p_π . We also have $\alpha = \sqrt{(20/21)}$, $\beta = 2/\sqrt{3}$, $\lambda = (4\sqrt{3})/9$, $\mu = \sqrt{(40/189)}$, $\nu = \sqrt{(8/21)}$, $\rho = \sqrt{(2/7)}$, $\tau = \sqrt{(10/63)}$, $v = \sqrt{(50/63)}$, and $\omega = \sqrt{(10/7)}$. For the matrix elements, we have $V_{h1f\sigma} = (V_{sf\sigma}/2) + \sqrt{3}V_{pf\sigma}/2$ and $V_{h2f\sigma} = (\sqrt{3}V_{sf\sigma} - V_{pf\sigma})/2$. These matrix elements describe the interaction between the central rare-earth impurity Yb³⁺ and the s- and p-orbitals associated with the four nearest-neighbor Si atoms and belonging to the same row of the same irreducible representation of the T_d double group [5].

The critical matrix elements were chosen [3] using the theory of Harrison *et al.* [6] as a guide. Their values are $V_{h1f\sigma} = 0.12$ eV, $V_{h2f\sigma} = 0.024$ eV, and $V_{pf\pi} = -0.024$ eV for the interactions of Yb³⁺ with Si.

III. RESULTS AND DISCUSSION

At this point it is simply a matter of deciding how to solve the coupled Hamiltonian problem, $H = H_0 + V$. Because we are interested in Yb³⁺ both at the center of clusters of Si atoms and in bulk Si, we choose the Yb³⁺ site at the center of a cluster, and terminate the surface of the cluster with H atoms [7]. The parts of the cluster Hamil-

tonian that transform according to Γ_6 , Γ_7 , and Γ_8 are each diagonalized, as discussed in Ref. [7]. We have used four different cluster sizes: (i) 34 Si atoms, one vacancy at the center, and 36 H atoms at the surface, denoted 34Si+36H; (ii) 86Si+76H; (iii) 238Si+196H; and (iv) 524Si+276H. Here we report results for (i) and (iv).

We note that the cluster of 524Si+276H, with an additional Si atom at its center, has essentially the spectrum of bulk Si, with band edges virtually at the experimental energies of empirical tight-binding theory [7]. Thus the cluster calculations, by construction, reproduce the spectrum of bulk Si in the empirical tight-binding limit when the cluster is very large. That is, they do a good job of reproducing the valence band structure, and an adequate job of simulating the lowest conduction band [4].

With this theoretical approach, we vary the energy line-up $E(2F_{5/2})$ and the cluster size, and then compute the energy levels and central-site partial density of states spectrum versus energy E . The resulting spectral-peak energies are displayed below.

III.a. Case of both Yb levels below the Si vacancy's deep levels

The range of possible energies of the $2F_{5/2}$ level of Yb^{3+} in solid Si allows for this level to fall either (a) below the energies of both the A_1 (Γ_6) and T_2 (Γ_7 and Γ_8) energy levels of the vacancy in Si; or (b) above the A_1 (Γ_6) vacancy level, but below the T_2 ($\Gamma_7+\Gamma_8$) level. In this section, we discuss case (a). (See Fig. 1.) Fig. 2 shows the results of our calculations for this case, for a "bulk" 524Si+276H cluster and for a 34Si+36H cluster.

In the limit $V \rightarrow 0$ the principal features of the spectrum are, in order of descending energy, (i) the T_2 -like or Γ_7 - and Γ_8 -symmetric level of the Si vacancy near mid-gap (0.5 eV); (ii) the A_1 -like or Γ_6 -symmetric level of the vacancy about 1.1 eV below the valence band maximum; (iii) the $2F_{5/2}$ level ($\Gamma_6+\Gamma_8$) at the assumed energy of 1.55 eV below the valence band maximum of Si; (iv) its spin-orbit-split $2F_{7/2}$ partner 1.27 eV lower in energy ($\Gamma_6+\Gamma_7+\Gamma_8$). See Fig. 1.

Turning on the coupling V in steps (Fig. 2), we find that the effect of the inward-directed orbitals centered on the nearest-neighbors is to split the $2F_{5/2}$ state into (i) a Γ_8 level at almost the same energy as the $2F_{5/2}$ level, but shifted downwards slightly in energy; and (ii) a Γ_6 level shifted more, downwards in this case. The Γ_6 shift is much larger than the Γ_8 shift because the $2F_{5/2}$ level is interacting with the spectrum of the Si-vacancy whose dominant features are the A_1 (Γ_6) and T_2 ($\Gamma_7+\Gamma_8$) vacancy deep levels. The A_1 -like Γ_6 vacancy level is much closer than the T_2 -like Γ_7 and Γ_8 level to the $2F_{5/2}$ Yb^{3+} level, and so repels the nearby $2F_{5/2}$ level more. (Recall that levels repel in perturbation theory.) In this case, both Yb^{3+} levels move downwards as a result of coupling to Si, because the Si-vacancy levels both lie above them: The $2F_{7/2}$ level is likewise shifted downwards and split, with the Γ_6 sub-level split most.

The coupling to the inward-directed hybrids ($h_{1\sigma}$) shifts and splits the levels (Fig. 2), and the addition of the outward-direct hybrids ($h_{1\sigma}+h_{2\sigma}$) and the other p-orbitals p and p_π ("all") leads only to modest quantitative corrections to the physics of the inward-directed hybrids. Thus the most important parts of the coupling matrix V are the terms proportional to $V_{h_{1\sigma}}$, and the Γ_6 component of the $2F_{5/2}$ level will normally shift more than the Γ_8 component because the coefficient α is larger than ν , and because the $2F_{5/2}$ level is closer to the Γ_6 Si-vacancy level. Similarly for $2F_{7/2}$, Γ_6 is expected to shift the most, and Γ_8 the least because $\alpha\beta > \lambda > \mu$ and because the Γ_6 -symmetric vacancy level is closer to the $2F_{7/2}$ level of Yb^{3+} .

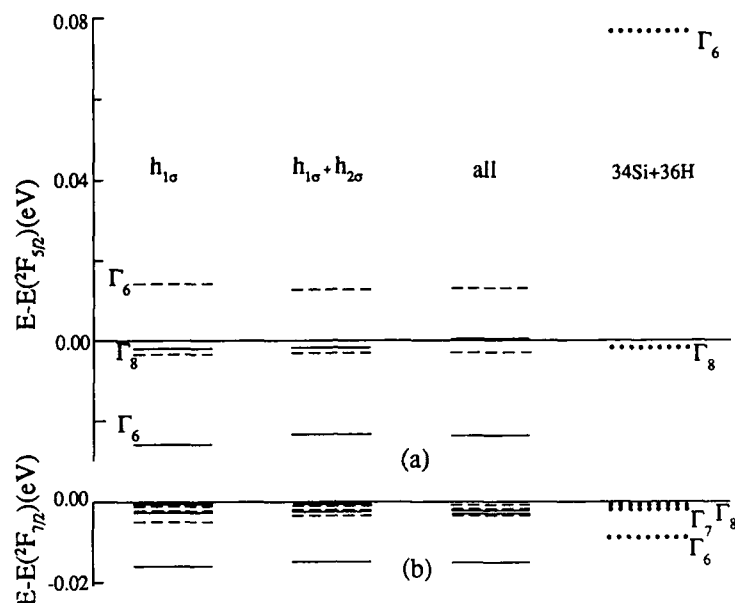


Fig. 2. Energies E (in eV) relative to the assumed Yb^{3+} free-ion energies (a) $E(2F_{5/2})$ and (b) $E(2F_{7/2})$ computed for $E(2F_{5/2}) = -1.55$ eV (solid lines) and $E(2F_{5/2}) = -3.65$ eV (dashed), and for the cases ($h_{1\sigma}$) inward-directed nearest-neighbor hybrids, ($h_{1\sigma} + h_{2\sigma}$) outward-directed hybrids as well, and (all) all nearest-neighbor hybrids. Each of the above cases is for "bulk" Si (524Si+276H). The right-most (dotted) lines are for $E(2F_{5/2}) = -1.55$ eV and a 34Si+36H cluster. The different signs of the level-shifts are a consequence of the corresponding level structures of Fig. 1. In (b), for all four cases, the Γ_7 levels lie between the lower-energy Γ_6 levels and the higher-energy Γ_8 levels.

III.b. Case of the higher Yb level above the lower Si vacancy deep level

When the $2F_{5/2}$ level lies between the A_1 -like (Γ_6) and T_2 -like (Γ_7 and Γ_8) levels of the Si-vacancy, the physics is changed somewhat. In this case, the Γ_6 (A_1 -like) level of the Si vacancy repels the $2F_{5/2}$ level of Yb^{3+} upwards in energy. (See Fig. 2.) Otherwise the physics is the same as in the case when both Yb^{3+} levels are below both vacancy levels. Note that non-vacancy deep level features of the spectral density cause the $2F_{7/2}$ level's Γ_6 component to split less than in the case of the $2F_{5/2}$ level at -1.55 eV.

III.c. Cluster-size effects

In small Si particles with Yb^{3+} at the center, the same physics holds as in bulk Si. However, although the 4f electrons of Yb^{3+} are localized, the wavefunction of the Si vacancy has anti-bonding character, is peaked on neighbors to the vacancy, and extends over a significant distance [1]. Therefore the Si vacancy's deep levels are sensitive to cluster size, even if the 4f electrons are not. This is depicted in Fig. 1, where, for "bulk" Si the Yb^{3+} levels are both above the Si-vacancy levels, but as the cluster-size decreases, the A_1 -like Γ_6 vacancy deep level descends below the free-ion $2F_{7/2}$ level of

Yb^{3+} . When this happens, the shift of the Γ_6 component of the $2F_{5/2}$ level changes sign. (See Fig. 2.)

IV. CONCLUSIONS

The $2F_{5/2}$ and $2F_{7/2}$ levels of Yb^{3+} are influenced via level repulsion by the Si spectral density of states with the same symmetry. The most prominent features of these densities of states are the A_1 -like (Γ_6) deep level of the vacancy in the valence band, and the T_2 -like (Γ_7 and Γ_8) vacancy deep level near mid-gap.

The inward-directed hybrids of the nearest-neighbor Si account for all of the major qualitative features of the coupling, although the other hybrids centered on those neighbors are needed for a quantitative evaluation of the shifts and splittings.

When both of the Yb^{3+} levels lie below both of the Si-vacancy levels, the effect of coupling between the Yb^{3+} and the Si is to repel the Yb^{3+} levels downwards in energy. The Γ_6 levels of Yb^{3+} are most severely affected, because of their proximity to the Γ_6 A_1 -like Si-vacancy deep level about 1.1 eV below the valence band maximum. The Γ_7 and Γ_8 states are perturbed less by the coupling, because they sense only the T_2 -like levels of the host, and the T_2 -like vacancy level is distant, near mid-gap.

When the A_1 -like vacancy level of Si lies below the $2F_{5/2}$ level of Yb^{3+} , being of Γ_6 symmetry, it repels the Γ_6 component of $2F_{5/2}$ upwards in energy.

For Yb^{3+} at the center of a cluster of Si, as the cluster size decreases, the vacancy levels, being antibonding in character, sense the reduced size, even when the 4f electrons of Yb^{3+} do not. This reduced size can cause the Si vacancy's deep levels to shift, in particular the A_1 -like level can descend below the $2F_{5/2}$ level of Yb^{3+} , leading to a sign reversal of the shift of the Γ_6 component of $2F_{5/2}$.

Future theoretical work on substitutional rare-earth impurities will deal with (i) extending the present analysis to rare-earths with high angular momenta, and (ii) determining line-ups of rare-earth energy levels relative to their semiconductor hosts [3].

Acknowledgements -- We are grateful to the U.S. Air Force Office of Scientific Research for their generous support of this work (Contract No. AFOSR-91-0418).

REFERENCES

- [1] H. P. Hjalmarson, P. Vogl, D. J. Wolford, and J. D. Dow, Phys. Rev. Letters **44**, 810 (1980); see also W. Y. Hsu, J. D. Dow, D. J. Wolford, and B. G. Streetman, Phys. Rev. B **16**, 1597 (1977).
- [2] We use the notation of M. Tinkham, *Group Theory and Quantum Mechanics*, (McGraw-Hill, New York, 1964).
- [3] S. Y. Ren and J. D. Dow, to be published.
- [4] P. Vogl, H. P. Hjalmarson, and J. D. Dow, J. Phys. Chem. Solids **44**, 365 (1983).
- [5] K. Takegahara, Y. Aoki, and A. Yanase, J. Phys. C **13**, 583 (1980).
- [6] W. A. Harrison and G. K. Straub, Phys. Rev. B **36**, 2695 (1987); G. K. Straub and W. A. Harrison, Phys. Rev. B **31**, 7668 (1985).
- [7] S. Y. Ren and J. D. Dow, Phys. Rev. B **45**, 6492 (1992).

SIMPLE MODEL FOR RARE-EARTH IMPURITIES IN THE COMPOUND SEMICONDUCTORS

NICOLAS P. ILYIN and VADIM F. MASTEROV

State Technical University, Experimental Physics Department,
195251 St. Petersburg, Russia

ABSTRACT

A model of the ground state for a rare-earth element in a binary semiconductor is suggested and illustrated for ytterbium in InP. It is shown that the charge state of Yb^{3+} with $4f^{13}$ shell is more stable than the state of Yb^{2+} with f^{14} shell.

MODEL

The purpose of this paper is to present a simple model of the ground state for a rare-earth element in a binary semiconductor by taking into account:

- i) the effects of intra-atomic correlation leading to the energy difference between the occupied and empty f -levels;
- ii) the stabilizing electrostatic field produced by the RE^{3+} ion environment in the matrix. The general formulation of the model is completed by semi-quantitative estimates for an ytterbium atom in indium phosphide.

Two-band model of an ideal binary semiconductor can be introduced by a set of Green function $G_0^\alpha(E)$ defined by the same relation:

$$G_0^\alpha(E) = [E - \Delta - b_1^2 [E + \Delta - b_2^2 G_0^\alpha(E)]^{-1}]^{-1}, \quad (1)$$

but with the different positions of the midgap point $E = 0$ with respect to the vacuum for each α [1]. Here index α characterizes an irreducible representation (a_1 or t_2); parameters Δ , b_1 and b_2 are related to the position of the band edges. Two-band subsystem corresponding to each α is represented in Fig. 1; the realistic band structure is obtained by the superposition of such subsystems.

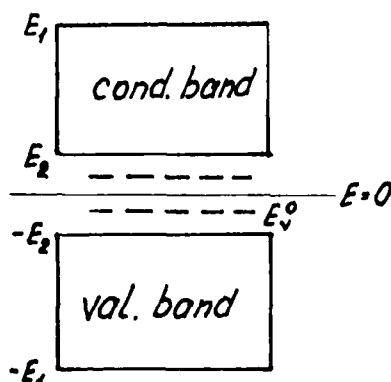


Fig. 1. Two-band subsystem for a particular α ; $E_v^0 = -\Delta$;

$$E_{1,2} = \sqrt{\Delta^2 + (b_1 \pm b_2)^2};$$

the "gap width"

$$E_g = \sqrt{\Delta^2 + (b_1 - b_2)^2}.$$

It should be noted that the energy $E_V^{\alpha} = -\Delta$ can be interpreted as a quasi-vacancy level (a_1 or t_2) corresponding to the removal of a neutral A atom from A^3B^5 matrix [2]. This energy is a pole of function:

$$G_V^{\alpha}(E) = [E + \Delta - b_2^2 G_0^{\alpha}(E)]^{-1}, \quad (2)$$

which can be called a "vacancy Green function".

We pass to the Green functions $G_r^{\alpha}(E)$ for a rare-earth impurity center by inserting the effective energies E_r^{α} for 6s ($\alpha = a_1$) or 4f ($\alpha = t_2$) electron instead of the first Δ in formula (1):

$$G_r^{\alpha}(E) = [E - E_r^{\alpha} - b_{1\alpha}^2 [E + \Delta' - b_2^2 G_0^{\alpha}(E)]^{-1}]^{-1}. \quad (3)$$

Here we also take into account the perturbation of the bonding with the nearest neighbors ($b_{1\alpha}^2 \neq b_2^2$); by inserting Δ' instead of the second Δ in (1) we account for the possible charge transfer from the impurity atom to the surrounding B atoms.

The poles of $G_r^{\alpha}(E)$ provide two s-like levels a_1 and a_1' which do not enter the subsequent calculations in this paper; it should be noted only that a_1 -level is fully occupied and a_1' -level is empty. It may play a role of the electron trap level observed experimentally [3].

Our main interest is to estimate the position of the poles of $G_r(E)$ at $\alpha = t_2$. It is known that the hybridization of f-states with the host states is very weak [4], so we can put $b_{1\alpha}^2 = 0$ for $\alpha = t_2$. In this case we get a pure f-level of t_2 symmetry with the energy $E_r^t = E_f$ and cation vacancy level of the same symmetry with the energy E_V related to the pole of the function

$$G_V^t(E) = [E + \Delta - b_2^2 G_0^t(E)]^{-1} \quad (4)$$

in the gap. We find for E_V an expression:

$$E_V = \frac{1}{28} [b_1^2 + \delta^2 - ((b_1^2 - \delta^2 + 2\Delta\delta)^2 + 4\delta^2 b_2^2)^{1/2}], \quad (5)$$

where $\delta = \Delta - \Delta' = (U_B - \rho)q$ characterizes the perturbation produced by the transference of a charge q from a rare-earth atom to the surrounding atoms. U_B is an intra-atomic integral for B-atom and a parameter ρ accounts for an electrostatic interaction between f-electron and the electron of sp^3 bonds pointing to the impurity. Fig.2 presents the dependence $E_V(\delta)$.

We pass now to the structure of the rare-earth levels. The distinction between the energies of occupied and empty f-level has a crucial meaning in our model. We can write for the energy of an occupied f-level in a free atom:

$$E_f^O = E_f^{\text{core}} + U_{fs} N_s^O + U_{ff} (N_f^O - 1), \quad (6)$$

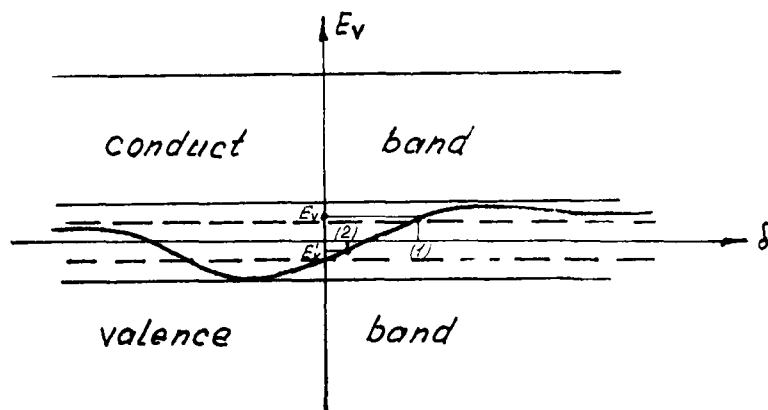


Fig.2. The position of a charged-vacancy level in the gap.
Special points are given for (1) $q = 1$ (2) $q = 2$.

where E_f^{core} is the atomic core potential; U_{fs} is the integral of interaction with external 6s-electrons (usually their number $N_s^0=2$); N_f^0 is a number of f-electrons in a free atom interacting through U_{ff} .

The effective energy E_f in crystal can be written as depending on the occupation number n_f :

$$E_{ff} = E_f^{\text{core}} + U_{fs} N_s + U_{ff} (N_f - n_f) + \rho q, \quad (7)$$

where $N_f = \sum n_f$ and $q = N_f^0 + N_s^0 - N_f - N_s$; N_s is a number of 6s-electrons retained by the rare-earth ion in accordance with our supposition about their character of a_1^* level we put $N_s = 0$.

ESTIMATES AND CONCLUSIONS

Now we consider a particular case of Yb^{+q} ($N_f^0=14$, $N_s^0=2$) in order to compare to charge states of this ion with $q=3$ (f^{13}) and $q=2$ (f^{14}) in InP. Using the expression given above we can obtain the values of energies both for occupied (E_f) and empty (E_f^*) f-levels. For numerical estimation we use $U_{ff}=18.5$ eV and $E_f^0 - 2U_{fs} = -I_f = -19.3$ eV obtained by us from the data on a free Yb atom [5].

For Yb^{+3} (f^{13}) we have got from (6-7) the following energy levels:

$$E_f = -I_f + 3\rho - U_{ff}, \quad (8a)$$

$$E_f^* = -I_f + 3\rho. \quad (8b)$$

The parameter ρ will be estimated later as being about 8-9 eV. So the

energy of occupied f-levels E_f lies far below the valence band and the energy of a single empty f-level E_f^+ lies high up in the conduction band (Fig.3). In this case the charged vacancy (V_A^{-3}) level E_v (of t_2 -symmetry) is fully occupied and lies in the upper part of the gap.

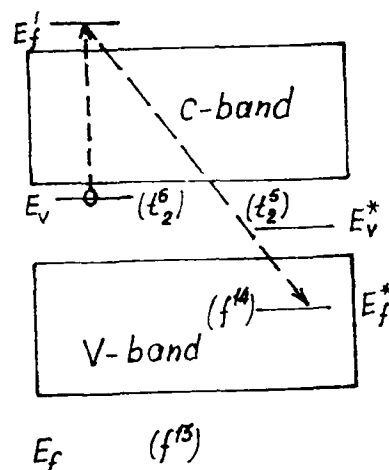


Fig.3. The position of characteristic levels for $Yb^{+3}-V_A^{-3}$ (left) and $Yb^{+2}-V_A^{-2}$ (right) systems.

The levels for $Yb^{+2} (f^{14})$ and V_A^{-2} system can be obtained by translating one electron from the level E_v to the empty level E_f^+ ; in result we got fully occupied f-shell with one-electron energy E_f which can be expressed as follows:

$$E_f^+ = -I_f + 2\rho \quad (9)$$

The vacancy level E_v^+ (for V_A^{-2}) is occupied by five electrons and lies a bit lower than fully occupied E_v -level (Fig.2 and 3).

The last step is to estimate the charge of a total electronic energy E by such a transition. Here we use Slater-Janek theorem which was substantiated for our model in the previous papers [6]:

$$\frac{dE}{dn_1} = E_{f1} \quad (10)$$

The expression for ΔE can be divided into two parts corresponding to the rear-earth ion and charged vacancy:

$$\Delta E = \int_0^1 E_{f1} dn_1 + \int_3^2 E_v(q) dq = \Delta E_f + \Delta E_v, \quad (11)$$

where we have used that $dq = -dn_1$.

The first term can be calculated analytically by integration of (7) that leads to an expression:

$$\Delta E_f = -I_f + 2.5\rho \quad (12)$$

The second term can be estimated graphically (Fig.2). In result we can come to the conclusion that $\Delta E > 0$ if $\rho > 8.5$ eV.

We see that in our model a strong electrostatic interaction between f-electrons of Yb atom and electrons localized on sp^3 -bonds pointing to the impurity center is necessary to stabilize the f^{13} -shell with respect to the f^{14} -shell.

REFERENCES

- [1] N.P.Ilyin, V.F.Masterov and A.E.Vasilyev, Sov.Phys.Semicond. 25 185, (1991)
- [2] N.P.Ilyin, V.F.Masterov and A.E.Vasilyev, Sov.Phys.Semicond. 25 1886, (1991)
- [3] P.S.Whitney, K.Uwai, H.Nakagome and K.Takachi. Appl.Phys.Lett., 21, 2074 (1988)
- [4] V.F.Masterov and Z.F.Zakharenkov, Sov.Phys.Semicond. 24, 610 (1990)
- [5] A.A.Rodtsig and V.M.Smirnov Parameters of Atoms and Atomic Ions (Moscow, 1986, 344 pages)
- [6] A.E.Vasilyev, N.P.Ilyin and V.F.Masterov, Sov.Phys.Semicond. 22, 1253 (1988)

Author Index

- Abe, K., 107
 Adams, Edward, 49
 Adler, D.L., 119
 Allen, S. James, 307
 Almonte, M., 119
 Alshawa, A.K., 263, 281
 Alves, E., 175
 Ammerlaan, C.A.J., 239
 An, C.Y., 213
 Anedda, Alberto, 207
 Asatsuma, T., 67

 Barberis, G.E., 213
 Barriere, A.S., 113, 319
 Bauer, G., 353
 Becker, Philippe C., 55
 Beldi, N., 133
 Bellani, V., 125
 Benton, J.L., 119
 Benyattou, T., 163
 Bhattacharya, P.K., 347
 Borschensky, V.V., 73
 Boyn, R., 269
 Brehmer, Dan, 307
 Brémond, G., 163
 Brinkevich, D.I., 73, 79
 Brown, Ian G., 39, 263, 281

 Caldwell, P.J., 257
 Campidelli, Y., 97
 Carnera, A., 125
 Chang, S.J., 299
 Cho, C.-C., 325
 Chroboczek, J.A., 97
 Citrin, P.H., 19
 Coffa, S., 125
 Colon, Jose E., 169, 251
 Coon, Victoria, 15
 Custer, J.S., 101

 d'Avitaya, Arnaud F., 97
 da Silva, M.F., 175
 Dauplaise, H.M., 151
 Davis, A., 151
 de Maat-Gersdorf, I., 239
 Delerue, C., 385
 Dodd, P., 67
 Donegan, J.F., 67
 Dörnen, Achim, 3, 195
 Dow, John D., 403
 Duncan, W.M., 325

 Eaglesham, D.J., 119
 Edwards, N.V., 257
 Efeoglu, H., 337
 Elsaesser, David W., 169, 251
 Evans, K.R., 175

 Fang, Xiao Ming, 15, 55

 Favenne, P.N., 97, 113, 133, 181
 Feuerstein, Robert, 287
 Franzó, G., 125

 Garcia, A., 319
 Gauneau, M., 133, 181
 Gennaro, A.M., 213
 Godlewski, M., 239, 275
 Golubev, Valeri, 365
 Greenwald, Anton C., 21
 Gregorkiewicz, T., 239
 Guillot, G., 163
 Gupta, S., 347

 Haase, Dieter, 195
 Hansenöhl, Stanislav, 27
 Hegarty, J., 67
 Hengehold, Robert L., 169, 251
 Hiller, Christoph, 195
 Hjelt, Kari T., 27
 Horrigan, J.A., 151
 Hua, Susan Z., 359

 Ikoma, T., 293
 Ilyin, Nicolas P., 409
 Ishida, H., 293
 Isshiki, H., 293

 Jacobson, D.C., 87, 119
 Jones, C.R., 175

 Kalboussi, A., 163
 Katsumata, H., 201
 Kazuchits, N.M., 79
 Kechouane, M., 133
 Kharchenko, T.D., 229
 Kim, B.Y., 319
 Kim, Hong Koo, 55
 Kimerling, L.C., 87
 Kimura, T., 293
 Kitagawa, H., 87
 Kolbas, R.M., 257
 Kozanecki, Adrian, 219
 Kozlovskii, Vitali, 365
 Krenn, H., 353
 Kriechbaum, M., 353
 Kumagai, M., 107, 201

 L'Haridon, H., 97, 113, 133, 181
 Lambert, B., 163
 Langer, Dietrich W., 15
 Langer, J.M., 337
 Lannoo, Michel, 385
 Lay, Uwe W., 21
 Le Corre, A., 163
 Lhomer, C., 163
 Li, Cheng Chung, 55
 Li, T., 281
 Li, Yabo, 15

- Liesert, B.J. Heijmink, 239
 Lipsanen, Harri K., 27
 Liu, H.-Y., 325
 Löbe, K., 269
 Lorenzo, J.P., 151
 Lozykowski, H.J., 263, 281, 397
 Lui, M., 331
 Lunney, J.G., 67

 Majima, A., 107, 201
 Marcus, M.A., 119
 Marrakchi, G., 163
 Martins, G.B., 213
 Masterov, Vadim F., 373, 409
 McFarlane, R.A., 331
 Melo, A.A., 175
 Michel, J., 87
 Mohammed-Brahim, T., 133
 Mombelli, B., 319
 Moneger, S., 163
 Monemar, B., 275
 Moutonnet, D., 97, 113, 181
 Moxey, D.E., 257

 Nakashima, Kenshiro, 61
 Nakata, Jyoji, 139, 299
 Noyori, Y., 201
 Nykolak, Gerald, 55

 Ootake, K., 107

 Palmstrøm, C.J., 307
 Pankove, Jacques I., 287
 Peaker, A.R., 337
 Petrov, V.V., 73, 79, 229
 Poate, J.M., 87, 119
 Polman, A., 101, 175
 Pomrenke, Gernot S., 169, 251, 263
 Poole, I., 337
 Pressel, Klaus, 3, 195
 Priolo, F., 125
 Prosolovch, V.S., 73
 Pyshkin, Sergei L., 207

 Ramseyer, G.O., 151
 Raoux, S., 113, 319
 Rees, Jr., William S., 21
 Ren, F.Y.G., 87
 Ren, Shang Yuan, 403
 Rettori, C., 213

 Rogers, Jim L., 49
 Ryabova, Ludmila I., 225

 Saito, R., 293
 Salamanca-Riba, L., 359
 Salvi, M., 133, 181
 Scholz, Ferdinand, 3, 195, 239
 Seghier, D., 163
 Sethi, S., 347
 Singer, K.E., 337
 Snoeks, E., 101
 Soares, J.C., 175
 Solomon, James, 55
 Soltani, P.K., 359
 Sopanen, Markku A., 27
 Spinella, C., 125
 Springholz, G., 353
 Su, Y.K., 299
 Sun, J., 257
 Sun-Paduan, Q., 87
 Świątek, K., 275

 Taguchi, Akihito, 139
 Takahai, Kenichiro, 139, 299
 Tamm, Marina E., 225
 Toudic, Y., 163
 Tsimperidis, I., 239
 Tuomi, Turkka O., 27

 Uekusa, S., 107, 201

 van den Hoven, G.N., 101, 175
 Varhue, Walter J., 49

 Wasiela, A., 97
 Weber, Jurgen, 3, 195
 Williamson, S., 347
 Wright, A.C., 337
 Wuttig, M., 359

 Yap, D., 331
 Yavid, V.Yu., 229
 Yeo, Yung Kee, 169, 251
 Yuan, Shu, 353
 Yugo, S., 293

 Zakharenkov, Leo, 33, 365
 Zhang, Tong, 257
 Zheng, B., 87
 Zimmermann, H., 269

Subject Index

- absorption coefficient, 107
- alloy disorder, 219
- aluminum gallium arsenide, 169, 257
- amorphous silicon, 133
- bound excitons, 163, 275
- cadmium
 - sulfide, 281
- calcium fluoride, 325
- cathodoluminescence, 269
- channeling, 175, 219, 299
- charge state, 385, 409
- chemical trends, 385
- crystal
 - field, 213, 409
 - growth, 33, 73, 79
- cyclopentadienyl erbium, 21
- de-excitation mechanisms, 239
- defects, 119
- devices, 55, 87, 119, 307, 331, 337, 347, 365
- donor(s), 119, 269
 - acceptor pairs, 269
- dysprosium, 213
- electrical properties, 151, 163, 207
- electron spin resonance, 213, 373
- electronic structure, 373, 385, 403
- electro-optic sampling, 347
- energy transfer mechanisms, 139, 275, 293, 397
- epitaxy, 101, 113, 319
- erbium(-)
 - amide, 21
 - arsenide, 307, 337
 - doped-
 - aluminum gallium arsenide, 169, 257
 - amorphous silicon, 133
 - fluorides, 113, 319
 - gallium arsenide, 15, 163, 251, 299, 347
 - indium phosphide, 3, 293
 - lead telluride, 213
 - silica films, 55
 - silicon, 49, 55, 61, 67, 87, 97, 101, 107, 119, 125, 287, 385
 - oxygen complexes, 61, 97, 139, 169
 - sources, 21
- europium, 275
- telluride, 353
- EXAFS, 119
- excitation mechanisms, 125, 239, 251, 269, 275, 287, 373
- fluorescence decay, 293, 397
- fluorides, 113, 319, 325, 331
- gadolinium, 73, 207
- doped silicon, 73
- gallium
 - arsenide
 - erbium doped, 15, 139, 163, 169, 175, 181, 251, 299, 337, 347
 - thulium doped, 3, 195
 - ytterbium doped, 163
 - phosphide, 207, 219
- germanium, 73, 229
- gettering, 79
- impact excitation, 287, 293, 299
- impurity gettering, 27, 73
- indium
 - gallium arsenide, 151
 - phosphide, 27
 - phosphide
 - erbium doped, 3, 293
 - ytterbium doped, 3, 139, 201, 219, 239, 263, 275, 385
- infrared reflectivity, 353
- intra atomic correlations, 409
- ion
 - beam induced epitaxy, 101
 - implantation, 39, 125, 133, 169, 181, 201, 251
- isoelectronic traps, 163, 293, 397
- kinetics, 293, 397
- lanthanum, 207
- laser
 - applications, 287, 331
 - doping, 67
- lattice location, 175, 195, 299, 385
- lead telluride, 225, 353
- level repulsion, 403
- light emitting diodes, 87
- LPE, 27, 151
- luminescence, 397
- magnetoresistance, 225
- MBE, 97, 175, 257, 325, 331, 337
- microstructures, 337, 359
- MOCVD, 15, 21
- MOVPE, 3
- neodymium, 229, 281, 325
 - doped germanium, 229
- optically detected magnetic resonance, 373
- optoelectronic devices, 119
- oxygen, 61, 87, 97, 125, 139, 169
- photoconductive switching, 347
- photoconductivity, 207

- photoluminescence
 - amorphous silicon, 133
 - excitation spectroscopy, 107, 195, 201
 - fluorides, 113, 319, 325
 - gallium
 - arsenide
 - erbium doped, 15, 139, 163, 169, 175, 251
 - thulium doped, 3, 195
 - ytterbium doped, 163
 - phosphide, 207, 219
 - indium phosphide
 - erbium doped, 3
 - ytterbium doped, 3, 139, 201, 219, 263, 275, 397
 - semiconductor alloys, 3, 27, 169, 219, 257
 - silica, 55
 - silicon
 - erbium doped, 55, 61, 67, 87, 97, 101, 107, 119, 125
 - ytterbium doped, 79
- plasma
 - deposition, 39
 - enhanced CVD, 49
- praseodymium dioxide, 27
- precipitates, 337
- processing, 87
- pulsed laser irradiation, 61
- purification, 33
- quantum dots, 337
- radiation effects, 79, 229
- rare earth
 - doping, 3, 39
 - ground state, 409
 - monoarsenides, 307
- resonant tunneling hot electron transistor, 307
- RF magnetron sputtering, 55
- Rutherford backscattering, 61, 175, 219, 299, 373
- samarium, 207
- scandium arsenide, 307
- Schottky barriers, 365
- semimetal-semiconductor heterostructures, 307
- silicon, 287, 385, 403
 - amorphous, 101, 133
 - erbium doped, 61, 67, 87, 97, 101, 107, 119
 - ytterbium doped, 79, 403
- solar cells, 365
- strontium sulfide, 359
- superlattices, 353
- surface
 - modification, 39
 - reconstruction, 353
- terahertz nonlinear electronics, 307
- thin film(s), 113, 359
 - optical amplifiers, 55
- thulium, 3, 195, 225, 269
 - doped
 - gallium arsenide, 195
 - zinc sulfide, 269
- x-ray diffraction, 325, 353
- ytterbium
 - doped-
 - cadmium sulfide, 281
 - calcium sulfide, 275
 - gallium
 - arsenide, 163
 - indium phosphide, 219
 - phosphide, 219
 - indium
 - arsenide phosphide, 219
 - phosphide, 3, 139, 201, 219, 239, 263, 275, 385
 - lead telluride, 213
 - silicon, 79, 403
 - strontium sulfide, 275
 - zinc sulfide, 275
- Zeeman spectroscopy, 195
- zinc sulfide, 275